DOE/ER-0313/22
Distribution
Categories
UC-423, -424

FUSION MATERIALS
SEMIANNUAL PROGRESS REPORT
FOR THE PERIOD ENDING
JUNE 30, 1997

Prepared for
DOE Office of Fusion Energy Sciences
(AT 60 20 00 0)

DATE PUBLISHED: AUGUST 1997

Prepared for
OAK RIDGE NATIONAL LABORATORY
Oak Ridge, Tennessee 37831
Managed by
Lockheed Martin Energy Research Corp.
for the
U.S. DEPARTMENT OF ENERGY
under Contract DE-AC05-96OR22464

FOREWORD

This is the tweny-second in a series of semiannual technical progress reports on fusion materials. This report combines the full spectrum of research and development activities on both metallic and non-metallic materials with primary emphasis on the effects of the neutronic and chemical environment on the properties and performance of materials for in-vessel components. This effort forms one element of the materials program being conducted in support of the Fusion Energy Sciences Program of the U.S. Department of Energy. The other major element of the program is concerned with the interactions between reactor materials and the plasma and is reported separately.

The Fusion Materials Program is a national effort involving several national laboratories, universities, and industries. A large fraction of this work, particularly in relation to fission reactor experiments, is carried out collaboratively with our partners in Japan, Russia, and the European Union. The purpose of this series of reports is to provide a working technical record for the use of the program participants, and to provide a means of communicating the efforts of materials scientists to the rest of the fusion community, both nationally and worldwide.

This report has been compiled and edited under the guidance of A. F. Rowcliffe by Gabrielle Burn, Oak Ridge National Laboratory. Their efforts, and the efforts of the many persons who made technical contributions, are gratefully acknowledged.

F. W. Wiffen
International and Technology Division

Reports previously listed in this series are as follows:

DOE/ER-0313/1	Period ending September 30, 1986
DOE/ER-0313/2	Period ending March 31, 1987
DOE/ER-0313/3	Period ending September 30, 1987
DOE/ER-0313/4	Period ending March 31, 1988
DOE/ER-0313/5	Period ending September 30, 1988
DOE/ER-0313/6	Period ending March 31, 1989
DOE/ER-0313/7	Period ending September 30, 1989
DOE/ER-0313/8	Period ending March 31, 1990
DOE/ER-0313/9	Period ending September 30, 1990
DOE/ER-0313/10	Period ending March 31, 1991
DOE/ER-0313/11	Period ending September 30, 1991
DOE/ER-0313/12	Period ending March 31, 1992
DOE/ER-0313/13	Period ending September 30, 1992
DOE/ER-0313/14	Period ending March 31, 1993
DOE/ER-0313/15	Period ending September 30, 1993
DOE/ER-0313/16	Period ending March 31, 1994
DOE/ER-0313/17	Period ending September 30, 1994
DOE/ER-0313/18	Period ending March 31, 1995
DOE/ER-0313/19	Period ending December 31, 1995
DOE/ER-0313/20	Period ending June 30, 1996
DOE/ER-0313/21	Period ending December 31, 1996
DOE/ER-0313/100	Technical Evaluation of the Technology of Vanadium Alloys for Use as Blanket Structural Materials in Fusion Power Systems

CONTENTS

1.0 VANADIUM ALLOYS

CHEMISTRY RELATED TO THE PROCUREMENT OF VANADIUM ALLOYS*, D.L. Smith, H.M. Chung, H.C. Tsai (Argonne National Laboratory)

OBJECTIVE

The objective of this work is to evaluate the chemistry of vanadium alloys as it relates to production capability and low-activation characteristics.

SUMMARY

Evaluation of trace element concentrations in vanadium alloys is important to characterize the low-activation characteristics and possible effects of trace elements on the properties. Detailed chemical analyses of several vanadium and vanadium alloy heats procured for the Argonne vanadium alloy development program were analyzed by Johnson-Matthey (UK) as part of a joint activity to evaluate trace element effects on the performance characteristics. These heats were produced by normal production practices for high grade vanadium. The analyses include approximately 60 elements analyzed in most cases by glow-discharge mass spectrometry. Values for molybdenum and niobium, which are critical for low-activation alloys, ranged from 0.4 to 60 wppm for the nine heats.

INTRODUCTION

Vanadium alloys offer a potential for both high performance and low activation characteristics for fusion power applications. Chromium and titanium, which are the primary alloying elements for the candidate alloys for fusion applications, also exhibit favorable long-term activation characteristics. Therefore, trace elements, such as niobium and molybdenum, are the primary contributors to the long-term activation characteristics of vanadium alloys. Certain trace elements may also affect the mechanical properties of vanadium alloys, particularly after irradiation. A joint effort was conducted by Argonne National Laboratory and Johnson-Matthey of the United Kingdom to evaluate the low activation potential of vanadium alloys. Samples of three heats of vanadium and six heats of vanadium alloys were prepared from materials used in the test program at Argonne for analysis by Johnson-Matthey. These materials were produced by standard procedures used at the time for production of vanadium and vanadium-alloys. An important aspect of this effort was to identify which elements in these materials are the major contributors to the long-term activation and to evaluate whether these elements could be further reduced if necessary. Related information has been reported by Murphy and Butterworth [1] and Attaya [2].

MATERIALS AND PROCEDURES

Materials used in this investigation were obtained from the ANL stock of material used in the vanadium alloy development program. Three heats of unalloyed vanadium and six heats of candidate vanadium alloys were included in this study. These materials, which were produced by standard procedures used at the time of production, are summarized in Table I. One of the vanadium heats (BL-20) was produced in the 1960's for the breeder reactor program. Low activation material was not an issue at the time. Alloys of V-Cr-Ti produced at ANL for the breeder program were made from this material. The other two heats of vanadium were produced from Teledyne Wah Chang (TWC). The heat designated BL-51 was obtained from

*Work supported by Office of Fusion Energy, U.S. Department of Energy, under Contract W-31-109-Eng-38.

one of the ~300 Kg ingots of vanadium being produced by TWC in the late 1980's when they were producing several hundred ton of vanadium. Four of the vanadium alloys were produced by TWC for the ANL fusion program, one alloy (BL-43) was produced by ANL from TWC vanadium (BL-51) before TWC started producing these alloys, and the other alloy (BL-24) was produced by ANL in the 1960's for the breeder program.

The analyses were performed predominately by glow discharge mass spectrometry (GDMS). Exceptions to this method are noted.

RESULTS AND DISCUSSION

The analytical results obtained for the three heats of vanadium and six heats of V-Cr-Ti alloys are presented in Table 2 in units of parts-per-million by weight. Results for the light elements $Z \leq 12$ were not reported. A few other elements could not be analyzed because of interference with the spectra. A large fraction of the elements were below the limit of detection. In these cases the results are reported as "less than" the detection limit, which is typically a few parts-per-billion.

The dominant trace impurities are Al (5.7-380 wppm), Si (3.3-560 wppm), and Fe (15-200 wppm). Values for Nb and Mo, which are critical for long-term activation varied from 0.056 to 40 wppm for Nb and 0.53 to 60 wppm for Mo. Although the values are low, possible contamination by Ta from instrument parts was noted for all specimens. For the case of BL-46 (V-5 Ti), analyses for Sr, Zr, Nb, Mo and Te were obtained by SSMS techniques. The values obtained by the SSMS technique on the V-5 Ti alloy tend to be considerably higher than the concentrations obtained from the other specimens by the GDMS technique. Significant amounts of copper detected in some alloys may result from the use of copper heat sinks used in the alloy melting processes. A very high tungsten concentration was obtained for one vanadium specimen. The source of W in this case has not been determined. It appears that higher concentrations of some elements (eg, Sn) in the alloys may have originated from Cr or Ti since the concentrations in unalloyed vanadium are quite low.

These results indicate that high purity vanadium alloys can be obtained by current production processes. Further investigations can be conducted to evaluate which trace elements, if any, need to be further reduced to provide desirable low-activation properties. The values given in Table 2 represent typical trace element concentrations obtained in the alloys tested. It has been noted that at TWC, for example, the vanadium is processed in the same facilities that are used for processing niobium and that in some cases significant contamination of niobium will occur in first batches of vanadium. This has been observed by R. Johnson [3] in the production of a 1200 Kg heat of V-4Cr-4Ti alloy. It has also been concluded by R. Peterson [4] that niobium and molybdenum can be controlled to a great extent by selection of the source of raw vanadium.

Based on the information presented here and other analyses of vanadium alloys, we have concluded that vanadium alloys can be produced with trace element concentrations presented in Table 3 without a significant cost penalty. Further analyses and evaluation can be conducted to determine the desirability and cost of selectively reducing any of the trace elements to lower levels. Calculations of residual radioactivity, nuclear afterheat, and dose in a vanadium alloy first wall with the trace element concentrations in Table 3 have been presented by Attaya [2]. These types of analysis also indicate that the activation levels decrease substantially from the first wall to the back of the blanket.

REFERENCES

[1] D. Murphy and G.J. Butterworth, J. Nucl. Mat., 191-194 (1992), p. 1444.

[2] H. Attaya and D. Smith, The Effects of Impurities on the Activation of SiC, Vanadium, and Ferritic Alloys, Fusion Materials Semiannual Progress Report, DOE/ER-0313/18, July 1995, pp. 107-117.

[3] W. R. Johnson, J.P. Smith and R.D. Stambaugh, Fusion Materials Semiannual Progress Report for period ending December 31, 1995, DOE/ER-0313/19, April 1995, pp. 5-11.

[4] J.R. Peterson and D.B. Smathers, J. Nucl. Mat. 141-143 (1986) pp. 1113-1116.

Table 1. Vanadium and vanadium alloys included in this evaluation of trace element concentrations

Specimen Designation	Specimen ID	Source of Material
V	BL-20	ANL inventory from Breeder Reactor Program in 1960's
V	BL-51	From ~300 Kg ingot purchased by ANL Fusion Program from TWC in late 1980's
V	BL-52	Purchased by ANL Fusion Program from TWC
V-5Ti	BL-46	Produced by TWC for ANL Fusion Power Program
V-4Cr-4Ti	BL-47	Produced by TWC for ANL Fusion Program
V-9Cr-5Ti	BL-43	Produced by ANL from Vanadium procured from TWC (BL-51)
V-11Cr-5Ti	BL-40	Produced by TWC for ANL Fusion Program
V-10Cr-10Ti	BL-44	Produced by TWC for ANL Fusion Program
V-14Cr-5Ti	BL-24	Produced by ANL breeder reactor program in 1960's

Table 2. Trace element analysis of vanadium and vanadium alloy heats.

ANL ID NO.	BL 20	BL 51	BL 52	BL 46*	BL 47	BL 43	BL 40	BL 44	BL 24
Nom. Composition (wt. %)	V	V	V	V-5Ti	V-4Cr-4Ti	V-9Cr-5Ti	V-11Cr-5Ti	V-10Cr-10Ti	V-14Cr-5Ti
Al	5.7	270	380	350	400	100	100	100	100
Si	3.3	560	300	300	90	80	80	80	80
P	<0.005	26	9	15	4	4	4	1	1
S	0.34	69	17	27	3	10	10	3	3
Cl	0.086	0.041	0.13	0.16	2	0.6	0.2	0.6	0.6
K	<0.01	<0.04	<0.032	<0.022	0.6	2	0.2	2	2
Ca	<0.96	<1.5	<1.3	<0.92	0.6	0.6	0.2	2	2
Sc	0.01	0.0078	0.0046	0.027	0.2	0.2	0.2	0.6	0.2
Ti	1.3	3.2	5.7	Matrix	Matrix	Matrix	Matrix	Matrix	Matrix
V	Matrix	Matrix	Matrix	Matrix	Matrix	Matrix	Matrix	Matrix	Matrix
Cr	----------	----------	----------	----------	Matrix	Matrix	Matrix	Matrix	Matrix
Mn	----------	----------	----------	----------	----------	----------	----------	----------	----------
Fe	15	23	28	86	100	30	80	200	200
Ni	2.1	0.66	0.83	6.4	3	3	3	3	3
Co	0.01	0.28	0.036	0.1	0.3	0.8	0.2	0.8	0.2
Cu	7.7	<0.018	0.33	40	0.4	10	1	40	100
Zn	0.16	<0.033	<0.032	0.58	0.6	0.5	0.5	2	0.5
Ga	----------	----------	----------	----------	----------	----------	----------	----------	----------
Ge	----------	----------	----------	----------	----------	----------	----------	----------	----------
As	----------	----------	----------	----------	----------	----------	----------	----------	----------
Se	----------	----------	----------	----------	----------	----------	----------	----------	----------
Br	<0.012	<0.017	<0.012	<0.012	<0.007	<0.006	<0.006	<0.006	<0.006
Rb	<0.001	<0.0022	<0.002	0.077	<0.005	<0.005	<0.005	<0.005	<0.005
Sr	0.018	0.012	0.038	0.05	<0.005	<0.004	<0.004	<0.004	<0.004
Y	3.8	2.2	4.2	0.2	<0.004	0.4	<0.04	<0.003	<0.003
Zr	0.65	2.1	12	20	3	2	7	7	0.7
Nb	0.056	5.4	18	40	4	0.4	1	4	4
Mo	0.53	3	34	60	6	2	20	20	50
Ru	<0.0098	<0.012	<0.0076	0.44	<0.03	<0.02	<0.02	<0.02	<0.02
Rh	0.032	<0.0016	<0.0014	0.18	<0.004	<0.04	<0.04	<0.04	<0.04
Pd	<0.0055	<0.0057	<0.0054	0.29	<0.02	<0.02	<0.02	<0.02	<0.02
Ag	<0.0078	<0.008	0.035	0.2	<0.009	0.08	<0.008	<0.008	<0.008
Cd	<0.032	<0.15	<0.14	<0.13	<0.02	<0.02	<0.02	<0.02	<0.02
In	<0.035	<0.036	<0.033	<0.031	<0.005	<0.005	<0.005	<0.005	<0.005
Sn	<0.041	<0.088	<0.081	0.93	<0.02	5	5	1	2
Sb	----------	----------	----------	----------	----------	----------	----------	----------	----------
Te	1.1	2.8	3.1	<0.006	<0.02	<0.02		<0.01	<0.01
I	----------	----------	----------	----------	----------	----------	----------	----------	----------
Cs	<0.001	<0.0026	0.12	0.33	<0.006	<0.005	<0.005	<0.005	<0.005
Ba	<0.001	<0.014	<0.014	0.29	<0.008	<0.05	<0.008	<0.007	<0.007
La	<0.001	<0.014	<0.0014	0.013	<0.006	0.6	<0.006	<0.005	<0.005
Ce	<0.001	<0.0014	<0.0013	0.03	<0.007	0.6	<0.006	<0.006	<0.006
Pr	<0.001	<0.0016	<0.0014	0.01	<0.006	<0.006	<0.006	<0.006	<0.005
Nd	<0.001	<0.0062	<0.0057	0.49	<0.02	0.7	<0.02	<0.02	<0.02
Sm	<0.0026	<0.0058	<0.0053	<0.0051	<0.02	8	<0.02	7	2
Eu	<0.0015	<0.0016	<0.003	0.025	<0.01	<0.01	<0.01	<0.01	<0.01
Gd	<0.0029	<0.0055	<0.0057	<0.0053	<0.03	<0.03	<0.03	<0.02	<0.02
Tb	<0.001	<0.0016	<0.0014	<0.0013	<0.007	<0.005	<0.006	<0.006	<0.006
Dy	<0.0025	<0.0055	<0.005	<0.0047	<0.03	<0.02	<0.02	<0.02	<0.02
Ho	0.0031	<0.0016	<0.0014	<0.0013	<0.007	<0.007	<0.007	<0.006	<0.006
Er	<0.0022	<0.0046	<0.0042	<0.0039	<0.02	<0.02	<0.02	<0.02	<0.02
Tm	<0.001	<0.0016	<0.0014	<0.0013	<0.008	<0.007	<0.007	<0.006	<0.006
Yb	<0.0023	<0.0049	<0.0045	<0.0042	<0.02	<0.02	<0.02	<0.02	<0.02
Lu	<0.001	<0016	<0.0014	<0.0014	<0.008	<0.007	<0.007	<0.007	<0.007
Hf	<0.0063	0.074	0.099	0.5	<0.02	<0.02	2	0.2	<0.02

*Sr, Zr, Nb, Mo and Te analyzed by SSMS for BL-46.

Table 2. Trace element analysis of vanadium and vanadium alloy heats. (Cont'd)

ANL ID NO.	BL 20	BL 51	BL 52	BL 46*	BL 47	BL 43	BL 40	BL 44	BL 24
Nom. Composition (wt. %)	V	V	V	V-5Ti	V-4Cr-4Ti	V-9Cr-5Ti	V-11Cr-5Ti	V-10Cr-10Ti	V-14Cr-5Ti
Ta	0.65	0.54	0.61	1.1	0.3	0.2	0.2	0.2	0.2
W	2800	0.21	1.8	8.2	<0.03	20	3	0.8	20
Re	<0.0016	<0.0025	<0.0023	<0.0021	<0.01	<0.01	<0.001	<0.01	<0.01
Os	<0.0018	<0.0038	<0.0035	<0.0032	<0.02	<0.02	<0.02	<0.02	<0.02
Ir	<0.0012	<0.0025	<0.0023	<0.0021	<0.01	<0.01	<0.01	<0.01	<0.01
Pt	1.1	<0.0046	<0.0042	<0.0039	<0.02	<0.02	<0.02	<0.02	<0.02
Au	23	0.072	0.032	0.067	<0.009	<0.008	<0.008	<0.008	<0.008
Hg	<0.011	<0.012	<0.011	<0.019	<0.03	<0.03	<0.03	<0.03	<0.03
Tl	----------	----------	----------	----------	----------	----------	----------	----------	----------
Pb	<0.0071	<0.015	<0.014	<0.013	<0.02	<0.02	<0.02	<0.02	<0.02
Bi	<0.0066	<0.014	<0.013	<0.012	<0.009	<0.008	<0.008	<0.008	<0.008
Th	<0.0018	<0.0023	<0.0014	<0.0013	<0.01	<0.009	>0.009	<0.009	<0.009
U	0.039	0.013	0.015	0.012	<0.01	<0.01	<0.01	<0.009	<0.009

*Sr, Zr, Nb, Mo and Te analyzed by SSMS for BL-46

Table 3. Trace element concentrations in vanadium alloys considered attainable by standard production practices.

	V4CR4Ti																
Element	C	N	O	Al	Si	P	S	Cl	K	Fe	Ni	Cu	As	Nb	Mo	Ta	W
wppm	50	100	200	100	500	30	10	.2	.1	40	4	1	0.1	1	4	2	2
appm	200	400	600	200	900	49	16	.29	.13	36	3.5	0.8	0.07	0.55	2.1	0.56	0.55

PRODUCTION AND FABRICATION OF VANADIUM ALLOYS FOR THE RADIATIVE DIVERTOR PROGRAM OF DIII–D — W.R. Johnson and J.P. Smith (General Atomics)

SUMMARY

V-4Cr-4Ti alloy has been selected for use in the manufacture of a portion of the DIII–D Radiative Divertor upgrade. The production of a 1200-kg ingot of V-4Cr-4Ti alloy, and processing into final sheet and rod product forms suitable for components of the DIII–D Radiative Divertor Program (RDP), has been completed by Wah Chang (formerly Teledyne Wah Chang) of Albany, Oregon (WCA). CVN impact tests on sheet material indicate that the material has properties comparable to other previously-processed V-4Cr-4Ti and V-5Cr-5Ti alloys. Joining of V-4Cr-4Ti alloy has been identified as the most critical fabrication issue for its use in the RDP, and research into several joining methods for fabrication of the RDP components, including resistance seam, friction, and electron beam welding, and explosive bonding is being pursued. Preliminary trials have been successful in the joining of V-alloy to itself by resistance, friction, and electron beam welding processes, and to Inconel 625 by friction welding. In addition, an effort to investigate the explosive bonding of V-4Cr-4Ti alloy to Inconel 625, in both tube-to-bar and sheet-to-sheet configurations, has been initiated, and results have been encouraging.

PROGRESS AND STATUS

1. Introduction

General Atomics (GA) has developed a plan for the utilization of vanadium alloys in the DIII–D tokamak. The plan is being implemented with the assistance of the Argonne, Oak Ridge, and Pacific Northwest National Laboratories (ANL, ORNL and PNNL), and will culminate in the operation of a water-cooled vanadium alloy structure in the DIII–D Radiative Divertor (RD) upgrade.[1,2] The use of a vanadium alloy will provide a meaningful step towards developing advanced materials for fusion power applications by 1) demonstrating the in-service behavior of a vanadium alloy (V-4Cr-4Ti) in a typical tokamak environment, and 2) developing knowledge and experience on the design, processing, and fabrication of full-scale vanadium alloy components.

The program currently consists of three phases: first, small vanadium alloy specimens and coupons have been and are continuing to be exposed inside the DIII–D vacuum vessel to evaluate the effects of the DIII–D vacuum environment; second, a small vanadium alloy component will be designed, manufactured, and operated in conjunction with the existing DIII–D divertor; and third, the upper private flux baffle of the new double-null, slotted divertor will be designed, fabricated from vanadium alloy product forms, installed in DIII–D, and operated. In addition, as part of a collaboration between GA and the Japan Atomic Energy Research Institute, small vanadium alloy specimens and coupons are being exposed inside the vacuum vessel of the JFT-2M tokamak in Japan to evaluate the effects of the vacuum environment for comparison with data obtained from DIII–D. A major portion of the program is research and development to support fabrication and resolve key issues related to environmental effects. The plan is being carried out by GA as part of the DIII-D Program, and with the support of ANL, ORNL, and PNNL, participants in the Materials Program of the Department of Energy's Office of Fusion Energy (DOE/OFE).

2. PHASE 1: Specimen and Coupon Exposures and Analysis

Minature Charpy V-notch (CVN) impact and tensile specimens of V-4Cr-4Ti alloy (ANL 500 kg heat)[3] were exposed/monitored in DIII–D in a position on the vessel wall behind the divertor baffle for ~9 months, experiencing a maximum temperature of ~350°C.[4] CVN tests conducted at ANL at temperatures over the range of –196 to +150°C indicated ductile behavior for all test temperatures, and tensile tests conducted at

ambient and elevated temperatures indicated values similar to that for unexposed material.[5] A new set of V-4Cr-4Ti alloy samples, installed during the January 1996 vent, is currently undergoing exposure to provide more data for confirmation and statistical verification.

In parallel to these exposures, additional V-4Cr-4Ti alloy samples underwent short-term exposures utilizing the DIII–D Divertor Material Exposure System (DiMES). A V-4Cr-4Ti alloy disc, and subsequently, miniature CVN specimens, were exposed/monitored during bakeout of the DIII–D vacuum vessel (maximum temperature of ~350°C).[4] CVN tests conducted at ANL at temperatures over the range of –196 to +150°C indicated ductile behavior for all temperatures.[5] A surface analysis (for hydrogen) of the V-4Cr-4Ti alloy disc specimen was completed at Sandia National Laboratory in Albuquerque, NM, and evaluation of that data was performed at ANL and reported previously.[5] Other DiMES exposures of V-4Cr-4Ti alloy are being considered to evaluate the effects of other DIII–D environmental conditions (e.g., discharge cleaning, boronization, etc.)

In addition, miniature and standard CVN specimens, miniature tensile specimens, standard bend specimens, and small coupons (for O and H analysis) of V-4Cr-4Ti alloy (GA 1200-kg heat) are being exposed/monitored in the Japanese tokamak JFT-2M in a position under the JFT-2M divertor baffle, where they will experience a maximum temperature of ~300°C. These specimens and coupons will be evaluated jointly by JAERI and GA after their removal.

3. PHASE 2: Small Component Exposure

A second step in the DIII–D Vanadium Plan is to install a small V-4Cr-4Ti alloy component in DIII–D. This component will be manufactured utilizing many of the methods proposed for the Phase 3 water-cooled private flux baffle. The component will be installed, exposed for some period of tokamak operations, and then removed. Samples from the component will be excised, and metallurgical analyses and property measurements will be made on the excised materials. Fabrication of this component is planned for the end of 1997, but a specific design for the component has not yet been defined.

4. PHASE 3: Radiative Divertor Program

The design, manufacture, and installation of a V-4Cr-4Ti alloy private flux baffle structure for the upper divertor of the RDP will be performed as the third phase of the vanadium alloy program. Details of the structural design of the toroidally-continuous, water-cooled and radiatively-cooled structural panels which make up the V-4Cr-4Ti alloy private flux baffle were presented in a previous report.[4]

The water-cooled panels for the V-4Cr-4Ti alloy baffle will be fabricated of sandwich construction from two 4.8 mm sheets, each containing a wide 1.5 mm deep slot milled into its face to provide an internal coolant channel. Resistance seam welding is the primary candidate process being considered for structurally joining the panel edges, with electron beam welding proposed for making a leak-tight perimeter seal. Other methods of joining are proposed for different areas of the design such as the graphite armor tile attachment studs and cooling water inlet and outlet manifolds. To facilitate installation, V-4Cr-4Ti alloy/Inconel 625 joints are planned to provide a bi-metallic tube nipple. This component will be used to transition V-alloy water-cooled panels to Inconel 625 tubes which provide a cooling water supply.

A. Fabrication of Product Forms for the Radiative Divertor

Processing of the V-4Cr-4Ti alloy by WCA was initiated in September 1995, and the finished sheet and rod product forms were completed and received by GA from WCA in October 1996. Complete details of the processing, including melting of the 1200-kg ingot, extrusion into billets, warm rolling of the billets into sheet bar material, warm processing (rolling and swageing) of sheet bar material into 4.8 mm thick sheet

and 11 mm diameter rod product forms, and chemical analysis of various processed forms, were presented in previous reports.[4,6,7] CVN tests were conducted at ANL on miniature specimens excised from sheet material to characterize the fracture behavior of the heat. Tests conducted at temperatures over the range of –196 to +25°C indicated ductile behavior for all temperatures. The GA heat exhibited a ductile/brittle transition (DBTT) temperature below -196C and an upper shelf energy of ~10 J. The DBTT of the GA heat was similar to that obtained for previously-processed V-4Cr-4Ti and V-5Cr-5Ti alloy heats whereas the upper shelf energy was slightly lower than observed for the other alloys (~12–16 J).[8] Support will be continued by ANL and ORNL in the development of basic engineering design properties for these product forms.

B. Manufacturing Technology Development

As manufacturing development is a major focus of this project a significant amount of research and development is being performed in this area. The RD structure will require many metal/metal joints, and joining development is therefore a key area of study. GA is using private IR&D funds to complement welding efforts at ANL and ORNL, investigating several different joining processes which are attractive for fabrication of RD components including resistance seam, friction, electron beam welding, and most recently, explosive bonding. Until just recently, i.e., prior to the receipt of the sheet and product forms from the GA heat, the scope of the GA joining development efforts had been limited by the availability of material, some of which has been purchased from WCA (V-5Cr-5Ti; Heat ID #932394) and some of which has been supplied by ANL (V-5Cr-5Ti alloy; Heat ID #832394 and V-4Cr-4Ti alloy; Heat ID #832665[3]). In addition, where required thicknesses of material were unavailable for weld trials, ORNL performed warm and/or cold rolling of available materials to required thicknesses.

Resistance Welding Studies

Resistance seam welding studies in air have been completed to develop the method for structurally joining sheets of vanadium alloy together to make the water-cooled panels for the RDP.

As reported previously,[4,6,7] spot weld trials were initially performed on 4.8 mm thick V-5Cr-5Ti alloy and V-4Cr-4Ti alloy sheet materials utilizing variations in power input (welding current and dwell time) and electrode pressure, producing diffusion bonds at low power levels and weld nuggets with minimal porosity at higher power levels. Both diffusion-bonded and fully-welded materials had similar strengths (~380 Mpa) in simple spot weld lap shear tests, well above that specified by American Welding Society standards for material of this strength level.

Resistance seam (overlapping spots) welds were then performed on similar 4.8 mm V-4Cr-4Ti alloy sheet using copper alloy wheel electrodes and a variety of power settings, and electrode (wheel) pressures, wheel diameters, and wheel radii. Although full melting (i.e., nugget formation) could not be achieved at the faying surfaces of the coupon samples without some melting of the copper electrodes and surface cracking, leak-tight seam diffusion bonds (~5 to 10 mm in width) were obtained which exhibited room-temperature lap shear test strengths comparable to that achieved for similar spot-welded (and spot-bonded) material.

In addition to the resistance welding studies, preliminary tests were completed at PNNL to study the potential for stress corrosion cracking of vanadium alloy resistance welds in DIII–D cooling water. PNNL performed several crack growth tests on specimens of V-4Cr-4Ti alloy (ANL 500 kg heat[3]) in DIII–D cooling water at a stress intensity of 30 Mpa-$\sqrt{m}$, a factor of ten times the calculated value based on stress analysis. No measurable crack growth, confirmed by SEM analysis of fracture surfaces obtained after the specimens were rapidly broken in tension, was observed during either test (32 and 60 days).[9]

Friction Welding Studies

Two types of friction welding trials are in progress. Inertia (shop) and portable friction welding have been selected as candidate processes for joining vanadium alloy to itself, and inertia welding has been selected as one method for creating a bi-metallic joint between vanadium alloy and Inconel 625. Initial rod-to-rod inertia weld trials of vanadium alloy (V-5Cr-5Ti alloy) bonded to itself, and to Inconel 625, were successful in air, without any protective environment. Metallography showed complete bonding with no indications of porosity or cracking, and mechanical tests at room temperature resulted in failures in material well away from the joint and HAZs, at stress levels greater than the strength of the V-alloy.

As reported previously,[4,6,7] inertia weld trials were performed to fabricate bi-metallic V-5Cr-5Ti alloy/Inconel 625 joints in a butt joint configuration which could be machined into a bi-metallic tube nipple, a component which could be joined to a V-alloy water-cooled panel (via a controlled shop weld, e.g., electron beam welding) and subsequently to an Inconel 625 cooling water tube (via a field tungsten-inert gas weld). After initial unsuccessful attempts, followed by a joint configuration change, joints were produced which were vacuum leak tight to DIII–D standards and exhibited strengths >~720 MPa in room-temperature tensile pull tests, with failures occurring in a ductile (tearing) mode in the V-alloy away from the joint.

As previously reported,[6,7] portable friction welding trials of vanadium alloy rod to plate were also performed to develop methods of *in-situ* replacement of studs on water-cooled panels. After several partially-successful trials, in which substantial bonding was achieved, but with attendant large hardness increases at the weld interface and thick heat-affected zones (HAZs), additional trials were performed using shorter welding times to reduce heat input, and ram pressures and rotational speeds were selected to be similar to that used for the successful inertia weld trials. These trials yielded several samples which were bonded over ~100% of the contacting areas, possessed no observable porosity, and exhibited a joint strength comparable to that of the V-4Cr-4Ti alloy. An additional set of ~40 trials, utilizing threaded studs similar to that to be used for fabricating the RD structure, is currently in progress.

Electron Beam Welding Studies

Preliminary electron beam welding trials on 6.35 mm V-5Cr-5Ti alloy sheet have been completed, and were reported previously.[6]

Explosive Bonding Studies

Explosive bonding is being investigated as an alternate method for producing a dissimilar metal joint between V-4Cr-4Ti alloy and Inconel 625 for application as a tube nipple/connector to transition a V-4Cr-4Ti alloy water-cooled RD panel to an Inconel 625 water supply tube. A lap joint for this tube-to-tube configuration may be more preferable for this application compared to the butt joint configuration developed by inertia welding because of its enhanced mechanical strength and potential for a longer (up to ~10 times) leak path between the cooling water inside the tube and the external vacuum environment of DIII–D.

As reported previously, [7] a preliminary explosive bonding trial of a V-4Cr-4Ti alloy tube (~150 mm long × 22.1 mm o.d. × 2 mm wall) to an Inconel 625 round bar was performed. This trial was partially successful, producing a vacuum leak tight joint with no porosity over about 1/2 of the length of the sample. Another bonding trial is being planned in which additional explosive material will be placed on the outer surface of the V-4Cr-4Ti alloy tube in order to bond the entire length of the sample. For this trial, 22 mm O.D. × 2 mm wall V-4Cr-4Ti alloy tubing is currently being fabricated (by cold drawing) from a section of 47 mm thick V-4Cr-4Ti alloy sheet bar longitudinally rolled from extruded billet material.

Another method being pursued for developing a V-4Cr-4Ti alloy/Inconel 625 tube nipple/connector involves the forming of explosively-bonded V-4Cr-4Ti alloy/Inconel 625 sheet material into a tubular shape by a deep drawing process. As part of this investigation, a preliminary explosive bonding trial of a V-4Cr-4Ti alloy sheet (380 mm × 125 mm × 2 mm thickness) to an Inconel 625 sheet (1.25 mm thickness) was performed. Ultrasonic testing of the explosively-bonded composite sheet showed no indications of debonding between the two materials, and metallography of samples excised from a number of locations in the sheet revealed no evidence of porosity at the bond line between the V-4Cr-4Ti alloy and the Inconel 625. Plans are currently underway to perform shear tests on strips excised and machined from the explosively-bonded sheet. In addition, another explosive bonding trial has recently been performed using larger pieces of sheet material (~360 mm × ~230 mm) in order to provide a sufficient amount of material for deep drawing studies. Evaluation of this bonding trial is currently in progress.

CONCLUSIONS

A program for utilizing vanadium alloys in DIII–D has been developed to assist the deployment of low activation alloys for fusion applications, and production of material for this program has been completed. A 1200-kg V-4Cr-4Ti alloy ingot of acceptable chemical composition has been melted, extruded into rectangular billets, and processed into sheet and rod product forms. CVN impact properties of the finished alloy are comparable to those of previously-processed V-4Cr-4Ti and V-5Cr-5Ti alloys. Preliminary successes have been achieved in developing similar and dissimilar metal welds in vanadium alloy by resistance, inertia, portable friction, and electron beam welding, and explosive bonding methods.

ACKNOWLEDGEMENTS

This is a report of work supported by the U.S. Department of Energy under Contract No. DE-AC03-89ER51114, and General Atomics under internal R&D funding.

REFERENCES

[1]J. P. Smith, W. R. Johnson, R. D. Stambaugh, P. W. Trester, D. Smith, and E. Bloom, "Vanadium Alloys For The Radiative Divertor Program of DIII–D," to be published in *Proc. of the 16th IEEE/NPSS Symposium on Fusion* Engineering, Champlain, Illinois, September 30 through October 5, 1995.

[2]J. P. Smith, W. R. Johnson, R. D. Stambaugh, P. W. Trester, D. Smith, and E. Bloom, "Utilization of Vanadium Alloys In The DIII–D Radiative Divertor Program," to be published in *Proc. of the 7th International Conf. on Fusion Reactor Materials* (ICFRM-7), Obninsk, Russia, September 25–29, 1995.

[3]H. M. Chung, H.--C. Tsai, D. L. Smith, R. Peterson, C. Curtis, C. Wojcik, and R. Kinney, "Fabrication of 500-kg Heat of V-4Cr-4Ti," in *Fusion Reactor Materials Semiannual Progress Report*, DOE/ER-0313/17, Oak Ridge National Laboratory, Oak Ridge, Tennessee (1994), p. 178–187.

[4]W. R. Johnson, J. P. Smith, and R. D. Stambaugh, "Production and Fabrication of Vanadium Alloys for the Radiative Divertor Program of DIII–D", in *Fusion Reactor Materials Semiannual Progress Report*, DOE/ER-0313/19, Oak Ridge National Laboratory, Oak Ridge, Tennessee (1995), p. 5–11.

[5]H. Tsai, D. L. Smith, W. R. Johnson, and J. P. Smith, "Performance of V-4Cr-4Ti Material Exposed to the DIII–D Tokamak Environment", in *Fusion Reactor Materials Semiannual Progress Report*, DOE/ER-0313/21, Oak Ridge National Laboratory, Oak Ridge Tennessee (1997). p. 10-14.

[6]W. R. Johnson, J. P. Smith, and R. D. Stambaugh, "Production and Fabrication of Vanadium Alloys for the Radiative Divertor Program of DIII–D", in *Fusion Reactor Materials Semiannual Progress Report*, DOE/ER-0313/20, Oak Ridge National Laboratory, Oak Ridge, Tennessee (1996), p. 3–10.

[7]W. R. Johnson, J. P. Smith, and P. W. Trester, "Production and Fabrication of Vanadium Alloys for the Radiative Divertor Program of DIII–D", in *Fusion Reactor Materials Semiannual Progress Report*, DOE/ER-0313/21, Oak Ridge National Laboratory, Oak Ridge, Tennessee (1996), p. 3–9.

[8] D.L. Smith, H.M. Chung, H. Matsui, and A.F. Rowcliffe, "Progress in Vanadium Alloy Development for Fusion Applications," to be published in *Proc. of the Fourth International Symposium on Fusion Nuclear Technology* (ISFNT-4), Tokyo, Japan, April 6–11, 1997.

[9] R. J. Kurtz and W. R., "An Evaluation of the Susceptibility of V-4Cr-4Ti to Stress Corrosion Cracking in DIII–D Cooling Water", to be published in *Fusion Reactor Materials Semiannual Progress Report*, DOE/ER-0313/21, Oak Ridge National Laboratory, Oak Ridge Tennessee (1997), p. 31-35.

REVISED ANL-REPORTED TENSILE DATA FOR V-Ti AND V-Cr-Ti ALLOYS*

M. C. Billone (Argonne National Laboratory)

SUMMARY

The tensile data for all irradiated vanadium alloy samples and several unirradiated vanadium alloys tested at Argonne National Laboratory (ANL) have been critically reviewed and revised, as necessary. The review and revision are based on re-analyzing the original load-displacement strip-chart recordings using a methodology consistent with current ASTM standards. No significant difference has been found between the newly-revised and previously-reported values of yield strength (YS) and ultimate tensile strength (UTS). However, by correctly subtracting the non-gauge-length displacement and linear gauge-length displacement from the total cross-head displacement, the uniform elongation (UE) of the gauge length decreases by 4-9% strain and the total elongation (TE) of the gauge length decreases by 1-7% strain. These differences are more significant for lower-ductility irradiated alloys than for higher-ductility alloys.

PROGRESS AND STATUS

Introduction

The results of tensile tests performed at Argonne National Laboratory (ANL) on unirradiated and irradiated V-Ti and V-Cr-Ti alloys have been reported in tabular and/or graphical form in the Fusion Reactor Materials Semiannual Progress Reports from the periods ending March 31, 1987 (DOE/ER-0313/2) to June 30, 1996 (DOE/ER-0313/20). Results can also be found in the open literature, but the Progress Reports contain the most detailed set of results for the tensile properties of interest: yield strength (YS), ultimate tensile strength (UTS), uniform elongation (UE), total elongation (TE) and reduction in area (RA). Recently, the methodology used to determine the UE and TE values has come into question. In the process of resolving the issue of whether tensile-machine displacement was properly subtracted from cross-head displacement in determining elongations, all tensile properties have been re-examined in the current work. Both published and unpublished load-displacement curves have been re-analyzed and re-evaluated to derive the revised set of tensile properties.

The one-third-size tensile specimens (SS3) used in all ANL tensile tests (except for the oxidation studies) have a gauge length of 7.62 mm and a cross-sectional area of about 1 mm^2 (0.9-1.4 mm^2). The Instron testing machine has a 500 kgf (4900 N) load cell. A uniform cross-head speed of 0.5 mm/minute was used for all tests, giving an effective gauge-length strain rate of 0.11%/second. Based on data in laboratory notebooks and on the original load-displacement curves, the load cell was varied during the tests from a full vertical scale (250 mm in height) of anywhere from 10 kgf to 250 kgf. Useful data for most tests were recorded with a full scale of 50 kgf for unirradiated material and 100 kgf for irradiated material. In terms of converted stress, this amounts to about 4 MPa per vertical grid mark. The strip chart recording speed was generally 50 mm/minute, although 100 mm/minute was used in several cases. At 50 mm/minute, each horizontal grid mark corresponds to a cross-head displacement of 0.02 mm and a gauge length strain of 0.262%. In general, the extensometer readings for cross-head displacement at the end of the test were consistent with the values determined from cross-head displacement rate and strip-chart recorder speed rate. For the oxidation studies, the gauge section of the samples is 19 mm in length, about 4.5 mm in width and about 1 mm in thickness. The reference gauge-length strain rate for the oxidized and unoxidized samples is 0.018%/second.

*Work supported by the U.S. Department of Energy, Office of Fusion Energy Research, under contract W-31-109-Eng-38.

The terminology and the methodology for analyzing tensile data from strip-chart recordings is established in ASTM Designation E 6 and E 8, respectively.[1] It is worthwhile to review these terms and methods. For monotonically increasing load vs. displacement curves up to the maximum load, YS is the load (divided by the initial gauge cross-sectional area) corresponding to an offset strain of 0.2% (displacement at zero load divided by the initial gauge length). The offset value of 0.2% has no intrinsic significance. It is based on practicality and experience in analyzing tensile curves. The offset strain is determined by "analytically" or "graphically" unloading the specimen at a linear load-displacement slope corresponding to the effective linear portion of the load-displacement curve. The intersection of this line with the horizontal axis determines the offset displacement and strain. While various methods (e.g., initial tangent modulus, tangent modulus, secant modulus and chord modulus) are given in the ASTM standards, the methodology used in the current work corresponds more closely to the tangent modulus approach. With most of the load-displacement curves for vanadium alloys tested in the ANL Instron machines exhibiting an elongated "S" shape during the low-strain rise in load, the modulus is determined by the tangent line coinciding with the most number of points in the elongated part of the S-shape. Some of the load-displacement curves analyzed exhibit discontinuous yielding which consists of a rise to a high load (upper yield point, UYP) followed by a drop in load to a minimum value (lower yield point, LYP) followed by a rise in load with displacement up to the maximum load. For these cases, the 0.2% offset stress has little meaning. For consistency, the stress corresponding to the minimum yield point is designated as YS in the current work for samples which exhibit discontinuous yielding.

The UTS is relatively straightforward to determine. For monotonically increasing load with displacement up to the maximum load, the UTS is simply the maximum load divided by the initial gauge cross-sectional area. In the case of discontinuous yielding, the UYP may represent a higher load than for the continuous part of the curve after the discontinuous yielding. In such cases, the UYP is not to be used in determining UTS. The offset displacement (or strain) corresponding to the peak load (or UTS) is called the uniform elongation (UE). While UTS can be uniquely determined, more uncertainty is involved in determining UE, particularly for cases for which the maximum load is nearly constant over a displacement (or strain) range. While the ASTM standards imply that the midpoint of this flat region should be used to determine UE, the maximum offset strain corresponding to the maximum load is used in the current work. This decision is based on detailed analyses of stainless steel stress-strain curves and the criteria for necking. The maximum strain at peak load is more characteristic of the uniform elongation of the gauge section prior to necking.

The total elongation (TE) corresponds to the offset strain just prior to failure. The same slope as is used in the determinations of YS and UE is used to determine the offset displacement and strain at failure.

Results

About 100 tensile-test strip chart recordings have been re-analyzed for V-Ti and V-Cr-Ti alloys irradiated in FFTF. An additional four recordings have been re-analyzed for V-Cr-Ti alloys irradiated in HFIR. The difference between revised and previously-reported values of YS is on the order of ±10%. Much of this difference lies within the uncertainty of interpreting YS from load-displacement curves which exhibit discontinuous yielding. Some of the difference arises from the use of a different slope to determine the offset strain. The remaining differences have to do with uncertainty in interpreting results with changes in the strip-chart load scale. In any case, the ±10% is well within the uncertainties involved in determining YS and within the heat-to-heat variation for most structural alloys. The agreement between revised and previously reported values for UTS is even better (±1% deviation). This is not surprising given the relative simplicity and lack of ambiguity in determining the peak load and dividing it by the initial cross-sectional area. With regard to the uniform and total elongations, the average slope of the linearized-portion of the

load-displacement curve is about 1.6 kN/mm, giving an average effective modulus of about 115 MPa/%. When the effective modulus for each load/displacement or stress/strain trace is used to determine the permanent offset UE and TE values, the revised values for UE and TE are lower by 4 - 9% strain for UE and 1 - 7% strain for TE than the previously reported values. The significance of these corrections increases as the irradiation/test temperature decreases and the ductility (UE and TE) of the vanadium alloys decreases.

The vanadium alloys in the unirradiated condition have higher ductilities (UE and TE) than those in the irradiated condition. Data from about 200 tensile-tested, unirradiated vanadium alloys have been reported previously in the literature. During the current reporting period, about 30 of the original tensile strip-chart recordings were located and re-analyzed. Based on the 30 cases analyzed, similar differences between revised and previously-reported YS, UTS, UE and TE values have been observed for the unirradiated cases as were observed for the irradiated cases. However, for the 30 cases analyzed. the vanadium alloys retain significant ductility even after the corrections have been made to UE and TE.

Discussion

Tensile properties of structural materials are significantly different than inherent material properties such as Young's modulus and Poisson's ratio. The test results for YS, UTS, UE and TE are dependent on sample size and shape, sample preparation, strain rate, test environment, as well as the methodology used to interpret the test data. The tensile properties generated within this R&D program do not constitute a "design data base" because of the small gauge length (7.62 mm) and the lack of repetition of tests under the same nominal conditions. For example, ASME specifications for pressure vessel material establish minimum values of YS, UTS and TE based on a two-inch (51 mm) gauge length for the shape of samples used in this R&D program. For most ductile materials which fail by local necking, TE decreases as the gauge length increases. Rather, the tensile data base is intended to be used in conjunction with other mechanical properties tests (e.g., Charpy, fracture-toughness, creep, fatigue, etc.) to compare the performance of different vanadium alloys, as well as the differences among the same nominal chemical composition with different impurity levels and microstructures. In order for the comparison to be meaningful, however, it is important that each party generating tensile data use the same terminology and methodology with regard to determining and reporting values for YS, UTS, UE, and TE. This is essential to the selection and optimization efforts within the vanadium alloy R&D program. Consistent with this rationale, the tensile properties reported by ANL for all irradiated samples and some unirradiated samples have been critically reviewed, and revised as needed, based on a combination of ASTM standards and knowledge of material performance. While standards such as those established in ASTM do not give a unique method for determining tensile properties and are somewhat naive with regard to material science considerations, the important aspect of a comparative program is to select and use a consistent and physically-realistic methodology. This implies using some common sense in applying standards, rather than blindly appling such standards. The following example illustrates this point.

The following discussion is contained in ASTM Ref. 1 (page 20) under **modulus of elasticity:**

"The stress-strain relations of many materials do not conform to Hooke's law throughout the elastic range, but deviate therefrom even at stresses well below the elastic limit. For such materials the slope of either the tangent to the stress-strain curve at the origin or at a low stress, the secant drawn from the origin to any specified point on the stress-strain curve, or the chord connecting any two specified points on the stress-strain curve is usually taken to be the 'modulus of elasticity.' In these cases, the modulus should be designated as the 'tangent modulus,' the 'secant modulus,' or the 'chord modulus,' and the point or points on the stress-strain curve described...."

This ASTM discussion may have some practical value in interpreting tensile data from strip-chart recordings, but it has little meaning with regard to material science and performance. Many structural materials (e.g., ferritic steels, stainless steels, vanadium alloys) have well-defined elastic moduli and elastic regimes which can be determined by dynamic methods. However, because of a variety of factors associated with the tensile test (e.g., machine stiffness and slip, the manner of gripping, the shape and size of the sample, etc.), the low-strain rise in load is more "S" shaped than linear and the effective modulus used to determine YS, UE and TE has little to do with the elastic modulus of the material. It is often at least an order of magnitude less than Young's modulus.

FUTURE WORK

Complete the re-analysis of the original load-displacement strip-chart recordings for unirradiated samples of vanadium alloys.

Issue a detailed report containing YS, UTS, UE and TE (and RA where available) tensile results for unirradiated and irradiated vanadium alloys tested at ANL, including sample identification number, neutron damage level, helium content, irradiation temperature and test temperature.

Re-evaluate trends in tensile data for vanadium alloys, particularly decrease in ductility with increase in strength due to increased Cr, Ti and Si levels, impurity levels, microstructure, and neutron-damage/helium-content.

REFERENCE

1. 1996 Annual Book of ASTM Standards, Section 3: Metals Test Methods and Analytical Procedures, Volume 03.01: Metals -- Mechanical Testing; Elevated and Low-Temperature Tests; Metallography; Designation E 6 (Standard Terminology Relating to Methods of Mechanical Testing, pp 17-26) and Designation E 8 (Standard Test Methods for Tension Testing of Metallic Materials, pp 55-96), ASTM, West Conshohocken, PA.

TENSILE PROPERTIES OF VANADIUM ALLOYS IRRADIATED AT 390°C in EBR-II*

H. M. Chung, H.-C. Tsai, L. J. Nowicki, and D. L. Smith (Argonne National Laboratory)

SUMMARY

Vanadium alloys were irradiated in Li-bonded stainless steel capsules to ≈4 dpa at ≈390°C in the EBR-II X-530 experiment. This report presents results of postirradiation tests of tensile properties of two large-scale (100 and 500 kg) heats of V-4Cr-Ti and laboratory (15-30 kg) heats of boron-doped V-4Cr-4Ti, V-8Cr-6Ti, V-5Ti, and V-3Ti-1Si alloys. Tensile specimens, divided into two groups, were irradiated in two different capsules under nominally similar conditions. The 500-kg heat (#832665) and the 100-kg heat (VX-8) of V-4Cr-4Ti irradiated in one of the subcapsules exhibited complete loss of work-hardening capability, which was manifested by very low uniform plastic strain. In contrast, the 100-kg heat of V-4Cr-4Ti irradiated in another subcapsule exhibited good tensile properties (uniform plastic strain 2.8-4.0 %). A laboratory heat of V-3Ti-1Si irradiated in the latter subcapsule also exhibited good tensile properties. These results indicate that work-hardening capability at low irradiation temperatures varies significantly from heat to heat and is influenced by nominally small differences in irradiation conditions.

INTRODUCTION

Recent attention to vanadium alloys has focused on low-temperature irradiation performance of V-4Cr-4Ti, especially the phenomenon of loss of work-hardening capability. This phenomenon, usually manifested by low uniform elongation (<1%), was not observed for irradiation temperature ≥ 500°C. Under conditions of conventional neutron irradiation (i.e., negligible helium generation), complete loss of work-hardening capability has been reported for a 500-kg heat of V-4Cr-4Ti (heat #832665) irradiated to ≈0.4 dpa at 100-275°C in the High Flux Beam Reactor (HFBR)[1] and for a 30-kg heat of V-4Cr-4Ti (BL-47) irradiated to ≈10 dpa at ≈200°C in the High Flux Isotope Reactor (HFIR).[2]

In contrast, the 30-kg laboratory heat (BL-47) has been reported to retain a significant level of work-hardening capability (uniform elongation ≈3%) after irradiation to ≈10 dpa at ≈400°C in the HFIR.[3] Despite the low uniform elongation, total elongation appears to be significant, and fracture surface morphology is typically ductile dimple fracture. This report presents results of postirradiation testing of tensile properties of large-scale and laboratory heats of several vanadium alloys irradiated in Li-bonded stainless steel subcapsules to ≈4 dpa at ≈390°C in the EBR-II X530 experiment.

MATERIALS AND TESTING PROCEDURES

The elemental composition of the alloys, determined prior to irradiation, is given in Table 1. Tensile specimens with a gauge length of 7.62 mm and a gauge width of 1.52 mm (SS-3 geometry) were machined from ≈1.0-mm-thick sheets that had been produced by rolling a ≈3.8-mm-thick plate at 25 or 400°C. Specimens from the V-Cr-Ti alloys were annealed at 950-1125°C for 1 h in an ion-pumped vacuum system, whereas specimens from V-Ti and V-Ti-Si alloys were annealed at 1050°C for 1 h. Following irradiation and specimen retrieval, the specimens were cleaned ultrasonically in alcohol and tested without the customary degassing treatment at 400°C (used to expel hydrogen). Tensile properties were measured at 390°C (same irradiation temperature) in flowing argon at a strain rate of 0.001 s^{-1}.

IRRADIATION CONDITIONS

Details of the X-530 experiments, the last irradiation experiment in EBR-II before its shutdown, are described elsewhere.[4] The tensile specimens were irradiated at ≈390-394°C to ≈4 dpa in

* Work supported by U.S. Department of Energy, Office of Fusion Energy Research, under Contract W-31-109-Eng-38.

Table 1. Chemical composition of vanadium alloys irradiated to ≈4 dpa at ≈390°C in lithium in the EBR-II X530 experiment

Heat ID	Irradiated in Subcapsule	Nominal Compo. (wt.%)	Impurity Concentration (wt. ppm) O	N	C	Si
BL-45	S8	2.5Ti-1Si	345	125	90	9900
BL-62	S8	3.1Ti	320	86	109	660
BL-46	S8	4.6Ti	305	53	85	160
QN74[a]	S9	4.0Cr–4.1Ti-B	480	79	54	350
BL-63	S8	4.6Cr-5.1Ti	440	28	73	310
VX-8[b]	S8 and S9	3.73Cr-3.93Ti	350	70	300	500
832665[c]	S9	3.8Cr–3.9Ti	310	85	80	783

[a]Contains ≈250 appm boron–10.

[b]100-kg heat, obtained from Russian Federation, contains (in wppm) 1120 Al, 280 Fe, 500 Co, 270 Mo, 1280 Nb, 19 Zr.

[c]500–kg heat produced by Teledyne Wah Chang Albany, OR.

[d]All others are 15– to 30–kg laboratory heats.

Li-bonded Type 304 stainless steel subcapsules. They were divided into two groups and irradiated in two different subcapsules under nominally similar conditions (see Table 1).

RESULTS AND DISCUSSION

Uniform and total plastic strains of the specimens irradiated in the Subcapsule S8 (loaded in Capsule AH-2) are shown in Figs. 1A and 1B, respectively. Similar results measured on specimens irradiated in the Subcapsule S9 (loaded in Capsule AH-1) are shown in Fig. 2. According to the original plan, all heats of V-4Cr-4Ti were irradiated in the same subcapsule, i.e., S9. Specimens from other alloys were irradiated in the S8 subcapsule under nominally the same conditions. Only the specimens from the 100-kg heat of V-4Cr-4Ti (VX-8) were irradiated in both subcapsules.

A surprising observation is the contrasting work-hardening behavior of Heat VX-8 (V-4Cr-4Ti) after irradiation and retrieval from Subcapsules S8 and S9. That is, uniform plastic strain of the heat irradiated in Subcapsule S8 was as high as 2.8-4.0 %, whereas specimens irradiated in the counterpart subcapsule S9 exhibited uniform strains of only ≈0.6-0.8 %. All four specimens were double-checked and it was confirmed that specimen identity was correct.

At this time, it is difficult to understand the contrasting behavior of the VX-8 specimens under nominally similar irradiation conditions. One factor being investigated, however, is possible contamination of Li in Subcapsule S9, either during fabrication or disassembly. In contrast to the TZM subcapsules used in the past irradiation experiments at 420-600°C in the FFTF-MOTA, Type 304 stainless steel subcapsules were used in this experiment. It cannot be unequivocally ruled out at this time that impurity (such as N) transfer from stainless steel wall was more pronounced in Subcapsule S9 than in S8.

The specimens from the 500-kg heat of V-4Cr-4Ti (#832665) that were irradiated in Subcapsule S9 exhibited minimal work-hardening capability, and uniform plastic strain was <0.6% regardless of annealing conditions. Compared to the VX-8 specimens irradiated in Subcapsule S8 (uniform elongation 2.8-4.0 %), the specimens from Heat #832665 irradiated in Subcapsule S9 (uniform elongation 0.4-0.6 %) exhibited a higher degree of localized wall thinning at the fracture tip, indicating that the latter heat suffered more from loss of work-hardening capability and strain localization than did the former heat.

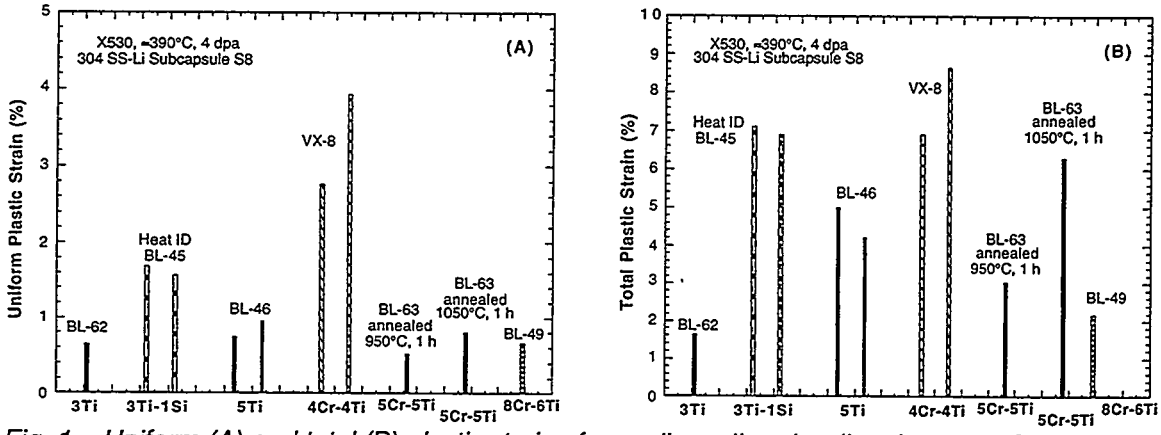

Fig. 1. Uniform (A) and total (B) plastic strain of vanadium alloys irradiated at ≈390°C to ≈4 dpa in lithium in S8 subcapsule.

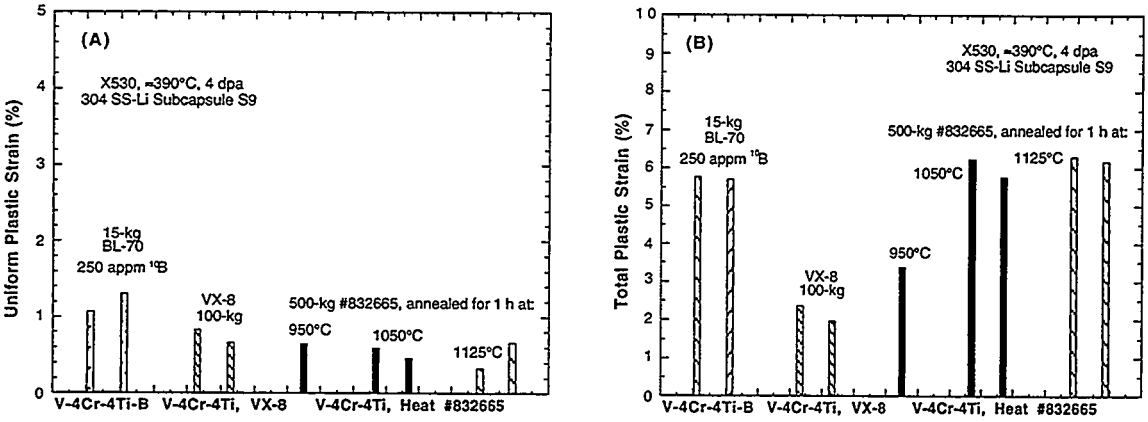

Fig. 2. Uniform (A) and total (B) plastic strain of vanadium alloys irradiated at ≈390°C to ≈4 dpa in lithium in S9 subcapsule.

However, specimens from Heat 832665 were not loaded in Subcapsule S8, nor were any tensile specimens from the 30-kg heat of V-4Cr-4Ti (BL-47), which exhibited good tensile behavior at 400°C in HFIR,[3] included in this experiment. Nevertheless, it seems that the tensile properties of V-4Cr-4Ti during conventional neutron irradiation near 400°C vary strongly from heat to heat, and possibly, due to subtle differences in irradiation conditions. This behavior was, however, not observed at irradiation temperatures ≥ 500°C.

Figure 3 shows yield and ultimate tensile strengths of BL-45 (V-3Ti-1Si) and VX-8 (V-4Cr-4Ti) irradiated in Subcapsule S8, the two heats that exhibited good tensile properties in this experiment.

CONCLUSIONS

1. Vanadium alloys were irradiated in two Li-bonded Type 304 stainless steel subcapsules to ≈4 dpa at ≈390°C in the X530 experiment in EBR-II. A 500-kg heat (Heat ID 832665) and a 100-kg heat (Heat ID VX-8) of V-4Cr-4Ti irradiated in one of the subcapsules suffered from complete loss of work-hardening capability, which was manifested by very low uniform plastic strains.

2. In contrast, the 100-kg heat (Heat VX-8) irradiated in another subcapsule exhibited good tensile properties (uniform plastic strain 2.8-4.0 %), although the irradiation conditions were

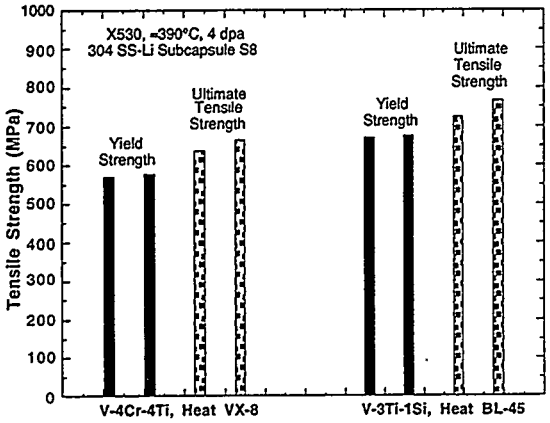

Fig. 3.
Yield and ultimate tensile strength of Heat BL-45, V-3Ti-1Si and Heat VX-8, V-4Cr-4Ti irradiated in S8 subcapsule.

nominally the same. The contrasting work-hardening behavior of this heat in the two subcapsules is not understood.

3. Susceptibility of V-4Cr-4Ti to low-temperature (<430°C) loss of work-hardening capability varies strongly from heat to heat. This phenomenon, not observed at irradiation temperatures ≥ 500°C, is probably associated with synergistic interaction between minor nonmetallic impurities and displacement damages produced at low irradiation temperatures.

4. A 15-kg heat of V-3Ti-1Si (Heat ID BL-45) irradiated in one subcapsule exhibited relatively good tensile properties (uniform plastic strain 1.6-1.7 %). Heat-to-heat sensitivity of the alloy to susceptibility to low-temperature loss of work-hardening capability, similar to that observed for V-4Cr-4Ti, is not known yet.

5. Elimination of the culprit nonmetallic impurity or impurities, or doping of an alloy (e.g., V-4Cr-4Ti and V-3Ti-1Si) with certain metallic elements, is believed to be effective in suppressing susceptibility to low-temperature loss of work-hardening capability.

FUTURE WORK

Chemical analysis and microstructural characterization will be conducted, with a focus on specimens from V-3Ti-1Si (Heat BL-45) and V-4Cr-4Ti (Heats VX-8 and #832665) to provide an understanding of the contrasting work-hardening behavior of these heats.

REFERENCES

1. D. J. Alexander, L. L. Snead, S. J. Zinkle, A. N. Gubbi, A. F. Rowcliffe, and E. E. Bloom, "Effects of Irradiation at Low Temperature on V-4Cr-4Ti," in Fusion Reactor Materials, Semiannual Prog. Rep. DOE/ER-0313/20, Oak Ridge National Laboratory, Oak Ridge, TN (1996), pp. 87-95.

2. H. M. Chung, L. Nowicki, and D. L. Smith, "Tensile Properties of Vanadium Alloys Irradiated at 200°C in the HFIR," in this report.

3. H. M. Chung, L. Nowicki, and D. L. Smith, "Tensile Properties of Vanadium Alloys Irradiated at 400°C in the HFIR," in Fusion Reactor Materials, Semiannual Prog. Rep. DOE/ER-0313/20, Oak Ridge National Laboratory, Oak Ridge, TN (1996), pp. 84-86.

4. H.-C. Tsai, R. V. Strain, A. G. Hins, H. M. Chung, L. Nowicki, and D. L. Smith, "Vanadium Alloy Irradiation Experiment X530 in EBR-II," in Fusion Reactor Materials, Semiannual Prog. Rep. DOE/ER-0313/17, Oak Ridge National Laboratory, Oak Ridge, TN (1994), pp. 8-14.

EFFECT OF HELIUM ON TENSILE PROPERTIES OF VANADIUM ALLOYS*

H. M. Chung, M. C. Billone, and D. L. Smith (Argonne National Laboratory)

SUMMARY

Tensile properties of V-4Cr-4Ti (Heat BL-47), 3Ti-1Si (BL-45), and V-5Ti (BL-46) alloys after irradiation in a conventional irradiation experiment and in the Dynamic Helium Charging Experiment (DHCE) were reported previously.[1] This paper presents revised tensile properties of these alloys, with a focus on the effects of dynamically generated helium on ductility and work-hardening capability at <500°C. After conventional irradiation (negligible helium generation) at ≈427°C, a 30-kg heat of V-4Cr-4Ti (BL-47) exhibited very low uniform elongation, manifesting a strong susceptibility to loss of work-hardening capability. In contrast, a 15-kg heat of V-3Ti-1Si (BL-45) exhibited relatively high uniform elongation (≈4%) during conventional irradiation at ≈427°C, showing that the heat is resistant to loss of work-hardening capability.

Helium atoms produced at ≈430°C in dynamic helium charging irradiation seem to be conducive to higher ductility (compared to that under conventional irradiation) and relatively lower yield strength. This seemingly beneficial effect of helium is believed to be important in evaluating the performance of V-4Cr-4Ti and V-3Ti-1Si alloys, because susceptibility to loss of work-hardening capability at low temperatures under fusion-relevant helium-generating conditions is considered to be a major factor in governing the minimum operating temperature for fusion applications. In this respect, V-3Ti-1Si appears to be more advantageous than V-4Cr-4Ti, although other factors such as creep strength could be inferior. Tensile data from conventional irradiation experiments (i.e., negligible helium generation), especially the data for <500°C, appear to differ significantly from the results obtained with simultaneous helium generated by the DHCE. Therefore, a dynamic helium charging irradiation experiment is strongly recommended with a focus on determining tensile and fracture properties of V-4Cr-4Ti and V-3Ti-1Si alloys at 300-470°C at doses of 10-20 dpa with high helium/dpa ratios of ≈4-5 appm He/dpa.

INTRODUCTION

An investigation of the effects of conventional neutron irradiation (at 420-600°C, 30-84 dpa in fast fission spectrum) on tensile properties of V-Ti, V-Ti-Si, and V-Cr-Ti alloys was reported previously.[1] Following that investigation, effects of simultaneous neutron irradiation and helium generation in these alloys were investigated in the DHCE, and results of postirradiation examination of swelling, tensile properties, and fracture behavior were reported for damage levels of up to ≈30 dpa and helium generation rates of 0.4-4.2 appm He/dpa.[2] To determine the effects of helium, tensile properties measured and analyzed for the same heats by the same procedure were compared for the conventional irradiation (negligible helium generated, referred to as "non-DHCE") and DHCE for similar irradiation temperature and damage level.

Subsequently, it was learned that values for uniform and total strains and yield strength reported in Refs. 1 and 2 were determined incorrectly. Also, revised data on neutron fluence and displacement damage accumulated in the DHCE have been since reported in Ref. 3. This paper presents revised tensile properties and irradiation parameters, with a focus on the effects of dynamically generated helium in V-4Cr-4Ti, V-3Ti-1Si, and V-5Ti alloys.

MATERIALS AND PROCEDURES

The elemental composition of the alloys, determined prior to irradiation, is given in Table 1. Tensile specimens, machined from ≈1-mm-thick cold-worked sheets, were annealed in high vacuum for 1 h at 1125°C (V-4Cr-4Ti) or 1050°C (V-3Ti-1Si and V-5Ti).

---

* Work supported by U.S. Department of Energy, Office of Fusion Energy Research, under Contract W-31-109-Eng-38.

Table 1. Chemical composition of alloys investigated

Alloy ANL ID	Ingot Size (kg)	Nominal Composition (wt.%)	Impurity Composition (wppm)			
			O	N	C	Si
BL–45	15	V–2.5Ti–1Si	345	125	90	9900
BL–46	15	V–4.6Ti	305	53	85	160
BL-47	30	V–4.1Cr–4.3Ti	350	220	200	870

The specimens were irradiated in the DHCE in Li-bonded TZM capsules in the Fast Flux Test Facility (FFTF, in MOTA-2B), a sodium–cooled fast reactor, at 430, 500, and 600°C to neutron fluences (E > 0.1 MeV) ranging from 2.5×10^{22} to 4.8×10^{23} n/cm^2 which correspond to 14-27 dpa in vanadium. Helium in the alloy specimens was produced by utilizing transmutation of controlled amounts of ^{6}Li and predetermined amounts of tritium–doped vanadium mother vanadium immersed in ^{6}Li + ^{7}Li. Table 2 summarizes actual postirradiation parameters determined from tensile and disk specimens of the V–4Cr–4Ti alloy (Heat ID BL-47), i.e., fast neutron fluence, dose, and helium and tritium contents measured shortly after the postirradiation tests. Helium and tritium contents were determined by mass spectrometry at Rockwell International Inc., Canoga Park, CA.

Actual irradiation conditions of the seven DHCE subcapsules are described in Ref. 3, in which detailed information on original loading plan, history of canister exchange, tritium charge, and actual loading of subcapsules has been documented. Note that the actual irradiation conditions of Subcapsules 5E1 and 5E2 are different from those given in Ref. 4.

Table 2. Summary of irradiation parameters of DHCE, and helium and tritium contents measured in V-4Cr-4Ti

Capsule ID No.	Irradiation Temp. (°C)	Total Damage (dpa)	Measured Helium Content (appm)	Actual Helium to dpa Ratio (appm/dpa)	Measured Tritium Content (appm)
4D1	430	25	11.2–13.3	0.48	27
4D2	430	27	22.4–22.7	0.84	39
5E2	430	14	3.3–3.7	0.25	2
5D1	500	14	14.8–15.0	1.07	4.5
5E1	500	16	6.4–6.5	0.40	1.7
5C1	600	14	8.4–11.0	0.69	20
5C2	600	18	74.9–75.3	4.17	63

Tensile properties were measured at 23, 100, 200°C, and at the irradiation temperatures in flowing argon at a strain rate of 0.0011 s^{-1}. The same facility and the same procedures were used in testing the tensile specimens irradiated in the DHCE and non-DHCE.

RESULTS AND DISCUSSION

The 0.2%-offset yield strength, ultimate tensile strength, uniform plastic strain, and total plastic strain measured on tensile specimens of V–4Cr–4Ti irradiated in the DHCE at 430–600°C (14–27 dpa, 4–75 appm He) are summarized in Figs. 1A–1D, respectively. Similar properties measured on specimens irradiated at ≈427°C to 14-33 dpa in non–DHCE (revised from Ref. 1) are also plotted in the figure as function of tensile test temperature. Results measured on specimens of V–3Ti–1Si (14-27 dpa, 6–36 appm He) and V–5Ti (13-27 dpa, 9–20 appm He) are shown in Figs. 2 and 3, respectively.

Helium Effect in DHCE at 500-600°C

After irradiation to ≈13-27 dpa at 500-600°C in either a DHCE or a non–DHCE, the three alloys retained significantly high ductilities, i.e., 3.5-8% uniform elongation and 9-20% total elongation. For this range of irradiation temperature, effects of helium on tensile properties do not seem to be significant.

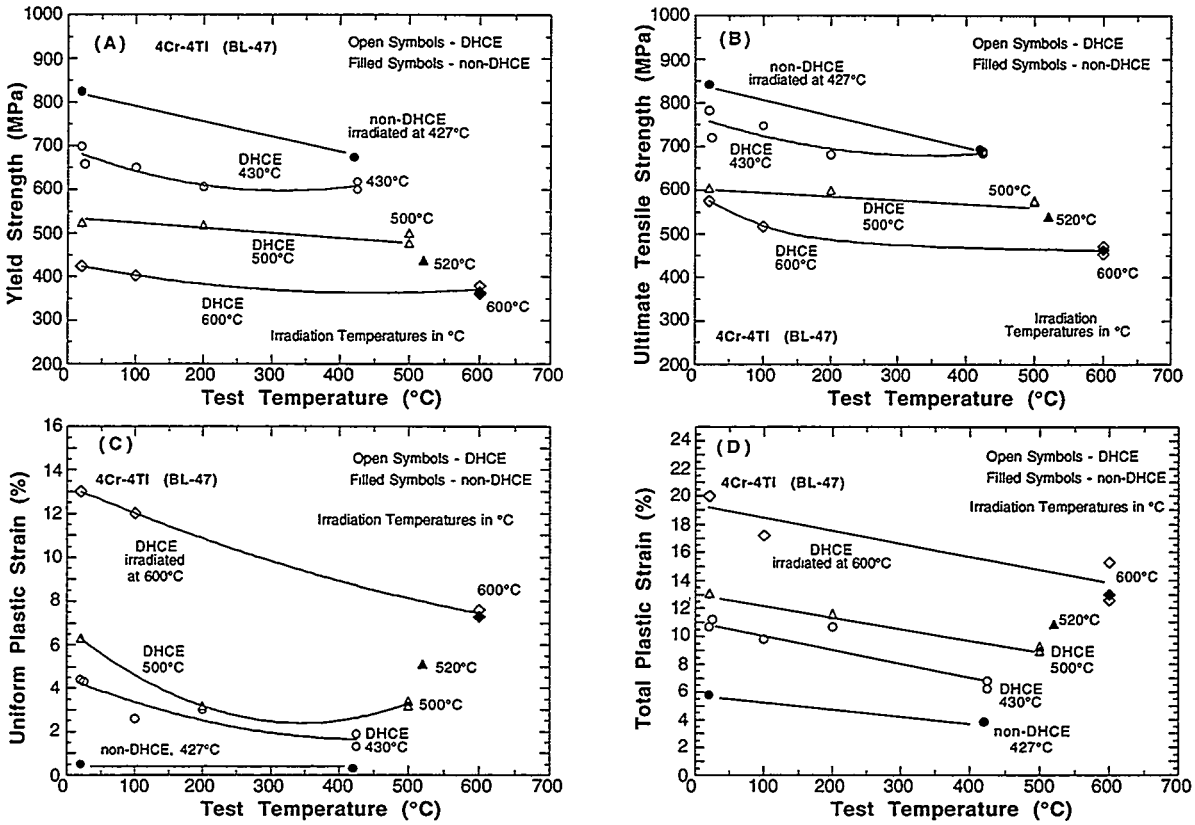

Fig. 1. Yield strength (A), ultimate tensile strength (B), uniform plastic strain (C), and total plastic strain (D) of V–4Cr–4Ti (BL-47) after irradiation at 427–600°C in the DHCE (14–27 dpa, 4–75 appm He) and in non–DHCE (14-33 dpa).

Effects of Test Temperature

Yield strength, ultimate tensile strength, uniform plastic strain, and total plastic strain of the specimens of the three alloys irradiated at 500-600°C appear to increase monotonically for decreasing test temperature (from 500-600°C to 23°C). However, for V-4Cr-4Ti and V-3Ti-1Si specimens irradiated at ≈427°C in a non–DHCE, uniform and total plastic strains appear to be more or less independent of test temperature at 23-420°C. In contrast, similar specimens of V-4Cr-4Ti and V-3Ti-1Si irradiated at ≈430°C in a DHCE exhibit a temperature dependency similar to that of the specimens irradiated at 500-600°C. That is, ductility increases significantly with decreasing test temperature.

Loss of Work-Hardening Capability in V-4Cr-4Ti in non-DHCE at ≈420°C

After irradiation in a non-DHCE at ≈420°C, the 30-kg heat of V-4Cr-4Ti (Heat ID BL-47) exhibited minimal uniform elongation (0.3-0.5%), which is a manifestation of a strong susceptibility to loss of work-hardening capability. The same heat did retain, however, good work-hardening capability with a uniform elongation of ≈3% in a non-DHCE in helium environment in a conventional irradiation experiment in the HFIR to ≈10 dpa at ≈400°C.[3]

A virtual loss of work-hardening capability was observed in a 500-kg heat of V-4Cr-4Ti (Heat ID #832665) in a conventional irradiation experiment (X-530 experiment) in Li-bonded stainless steel capsules in EBR-II to ≈4 dpa at ≈390°C.[4] However, in the same experiment, a 100-kg heat of V-4Cr-4Ti (Heat ID VX-8) exhibited a good work-hardening capability. These results indicate that

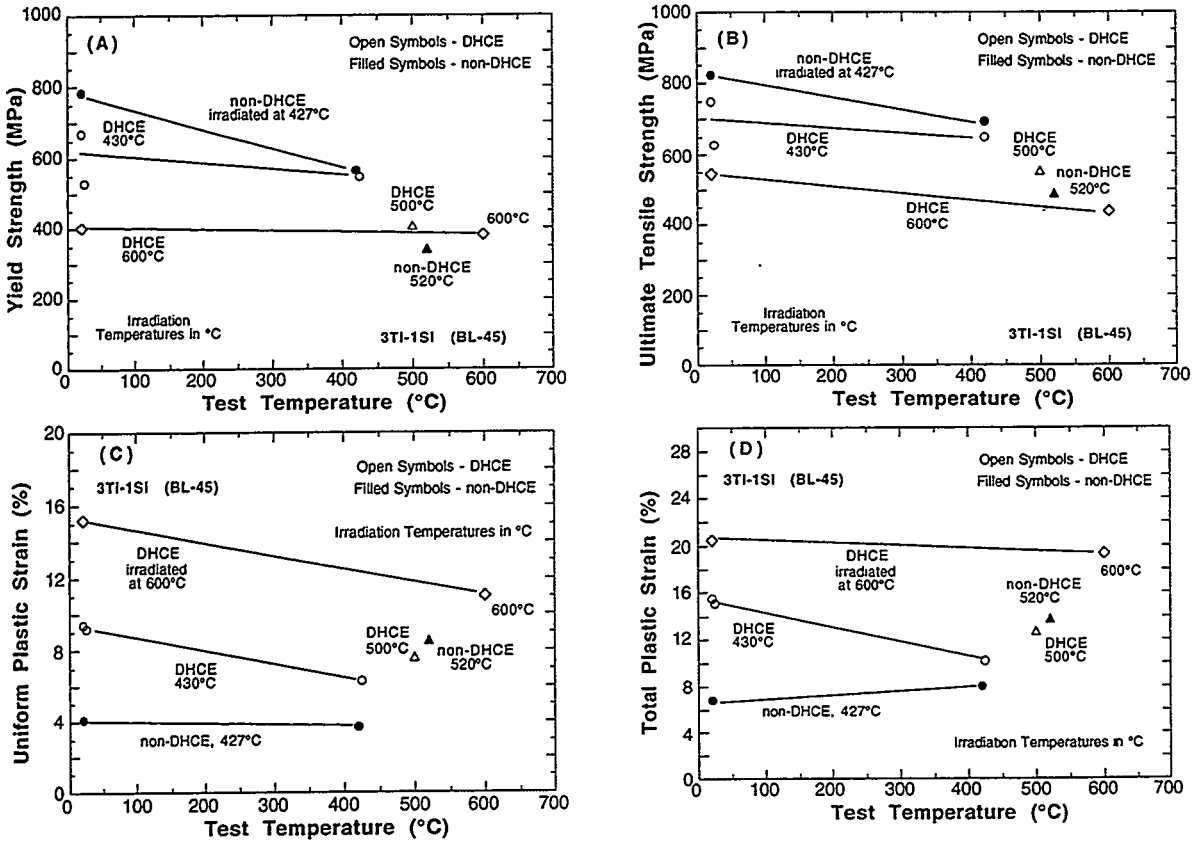

Fig. 2. Yield strength (A), ultimate tensile strength (B), uniform plastic strain (C), and total plastic strain (D) of V–3Ti-1Si (BL-45) after irradiation at 427–600°C in the DHCE (14–27 dpa , 6-36 appm He) and in non–DHCE (14-33 dpa).

loss of work-hardening capability, and hence uniform elongation, in V-4Cr-4Ti class during conventional irradiation experiments at <430°C varies strongly from heat to heat and is influenced by irradiation conditions.

Work-Hardening Capability in V-3Ti-1Si in non-DHCE at ≈430°C

In contrast to V-4Cr-4Ti, the 15-kg V-3Ti-1Si (Heat ID BL-45) exhibited relatively high uniform elongation (≈4 %) under a similar non-DHCE condition, showing that this heat retains good work-hardening capability under neutron irradiation at ≈430°C. Total elongation of the alloy was >7 % for under conditions tested in this study.

Helium Effect at ≈430°C

Interestingly, ductilities of DHCE specimens of V-4Cr-4Ti and V-3Ti-1Si alloys, irradiated at ≈430°C and measured at <430°C, were always higher than those of the similar non–DHCE specimens, whereas strengths were lower. Helium generated during irradiation at ≈430°C appears to promote work-hardening capability in the two alloys. As a result, helium generation seems to be conducive to higher uniform elongation (compared to that in a non-DHCE). This is summarized in Fig. 4. The trend is consistent for all capsules and specimens that were irradiated at ≈430°C, i.e., a total of 13 V-4Cr-4Ti and V-3Ti-1Si specimens irradiated in 3 DHCE and 2 non-DHCE capsules. The trend cannot be explained on the basis of the slightly higher dose level in non-DHCE than in DHCE, i.e., 14-33 versus 14-27 dpa.

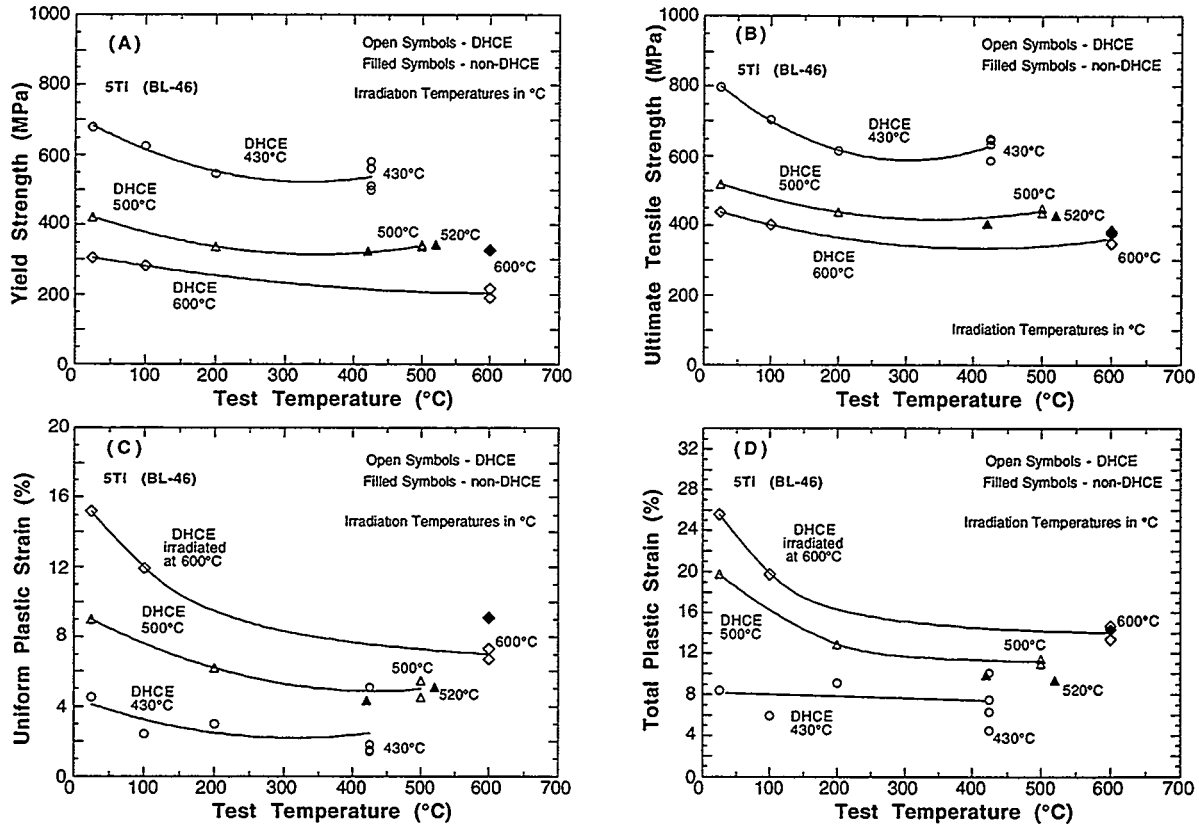

Fig. 3. Yield strength (A), ultimate tensile strength (B), uniform plastic strain (C), and total plastic strain (D) of V–5Ti (BL-46) after irradiation at 427–600°C n the DHCE (14-27 dpa, 9-20 appm He) and non–DHCE.

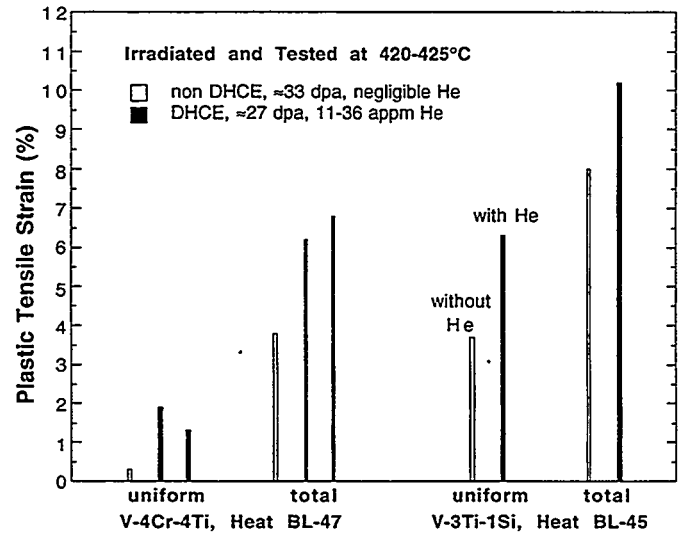

Fig. 4.
Effect of helium on uniform and total plastic strains of V-4Cr-4Ti (BL-47) and V-3Ti-1Si irradiated at ≈430°C.

The seemingly beneficial effect of helium indicates that different type of hardening centers are produced during DHCE. This effect, also reported by Satou et al. for V-5Ti-5Cr-1Si-Y,Al alloy (irradiated at ≈430°C in DHCE to ≈24 dpa, 177 appm He),[5] is believed to be important in evaluating the performance of V-4Cr-4Ti and V-3Ti-1Si alloys, because susceptibility to loss of

work-hardening capability at low temperatures under fusion-relevant helium-generating conditions is considered to be a major factor in governing the minimum operating temperature of a fusion reactor. In this respect, V-3Ti-1Si appears to be more advantageous than V-4Cr-4Ti, although other factors such as creep strength could be disadvantageous.

This finding indicates also that tensile data obtained with negligible helium produced in conventional irradiation experiments are not likely to be applicable, or may even be misleading, for designing and evaluating the performance of first wall structure. Therefore, a dynamic helium charging irradiation experiment is recommended which will focus on determining tensile and fracture properties of V-4Cr-4Ti and V-3Ti-1Si alloys at 300-470°C at higher dose (>30 dpa) and higher helium/dpa ratio (≈4-5 appm He/dpa).

Absence of Intergranular Fracture

No intergranular fracture surface morphology was observed in the present tensile specimens irradiated in the DHCE and non-DHCE and tested at 23–600°C. Even the fracture surface morphology of the specimens of V-4Cr-4Ti irradiated at ≈420°C in non-DHCE and exhibiting uniform elongation of only 0.3-0.5 % was ductile dimple fracture. That is, the low uniform elongation was a result of strong localization of plastic deformation rather than a brittleness. This is in sharp contrast to results reported from tritium-trick experiments, in which dense helium bubbles aggregated on grain boundaries produced intergranular fracture, leading to low uniform and total elongation in the specimen.

CONCLUSIONS

1. After irradiation to ≈14-30 dpa at 500-600°C with (helium generation rate ≈1 appm He/dpa) or without helium generation, V-4Cr-4Ti (Heat BL-47), 3Ti-1Si (BL-45), and V-5Ti (BL-46) retained significantly high ductilities, i.e., 3.5-8% uniform elongation and 9-20% total elongation. Results to date for this range of irradiation temperatures indicate that the effects of helium on tensile properties are insignificant in these alloys. Yield strength, ultimate tensile strength, uniform and total plastic strains of the alloys irradiated at 500-600°C in the DHCE increased monotonically for decreasing test temperature.

2. Uniform and total plastic strains of V-4Cr-4Ti and V-3Ti-1Si irradiated at ≈427°C in a non–DHCE were not influenced significantly by test temperatures at or below the irradiation temperature. In contrast, ductility increased significantly with decreasing test temperature when the specimens are irradiated at similar temperature in a DHCE. This indicates that different types of defect microstructure are produced at ≈430°C during irradiation with and without helium generation, most likely through interaction of impurities and helium atoms with defects or defect clusters.

3. After conventional irradiation in FFTF (negligible helium generation) at ≈427°C, a 30-kg heat of V-4Cr-4Ti (BL-47) exhibited minimal uniform elongation (0.3-0.5%), manifesting a strong susceptibility to loss of work-hardening capability. The same heat, however, did retain relatively good work-hardening capability with a uniform elongation of 1.3-1.9% after irradiation in the DHCE at ≈430°C at helium generation rates of 0.48-0.84 appm He/dpa.

4. No intergranular fracture surface morphology was observed in the tensile specimens after irradiation at 427-600°C either with or without helium generation. The fracture surface morphology of the specimens of V-4Cr-4Ti that exhibited low uniform elongation (0.3-0.5 %) after irradiation at ≈427°C, was ductile dimple fracture, indicating that the low uniform

elongation was a result of strong localization of plastic deformation rather than material brittleness. This is in sharp contrast to results reported from tritium-trick experiments, in which dense helium bubbles aggregated on grain boundaries produced intergranular fracture, leading to low uniform and total elongation in the specimen.

5. In contrast to V-4Cr-4Ti (BL-47), a 15-kg heat of V-3Ti-1Si (BL-45) exhibited relatively higher uniform elongations, i.e., ≈3.7% after conventional irradiation in FFTF at ≈427°C and ≈6.3 % after the dynamic helium charging irradiation in FFTF at ≈430°C. This indicates that this heat is resistant to loss of work-hardening capability.

6. Helium atoms produced at ≈430°C in the dynamic helium charging irradiation seem to be conducive to higher ductility (compared to that under conventional irradiation) and relatively lower tensile strength. This seemingly beneficial effect of helium is believed to be important in evaluating the performance of V-4Cr-4Ti and V-3Ti-1Si alloys, because susceptibility to loss of work-hardening capability at low irradiation temperatures under fusion-relevant helium-generating conditions is considered a major factor in governing the minimum operating temperature of a fusion reactor. In this respect, V-3Ti-1Si appears to be more advantageous than V-4Cr-4Ti, although other factors such as creep strength of the alloy could be inferior.

7. Tensile data obtained from conventional irradiation experiments (i.e., negligible helium generation), especially data for <500°C, appear to be not applicable, or may even be misleading, for designing and evaluating the performance of first wall structure. Therefore, a dynamic helium charging irradiation experiment is strongly recommended with a focus on determining tensile and fracture properties of V-4Cr-4Ti and V-3Ti-1Si alloys at 300-470°C to doses of 10-20 dpa with helium/dpa ratios of ≈4-5 appm He/dpa.

REFERENCES

[1] B. A. Loomis, L. Nowicki, and D. L. Smith, J. Nucl. Mater. 212–215 (1994), 790.

[2] H. M. Chung, B. A. Loomis, and D. L. Smith, J. Nucl. Mater. 233-237 (1996), 466-475.

[3] Memo, H. Matsui to D. L. Smith, "On Actual Loading of Tritium to DHCE Subcapsules," Nov. 22, 1993.

[4] A. M. Ermi, L. R. Greenwood, and H. L. Heinisch, "Irradiation Parameters for the FFTF Materials Open Test Assemblies from 1983 to 1992," WHC-SD-FF-TD-010, Westinghouse Hanford Company, Aug. 1994.

[5] H. M. Chung, L. Nowicki, and D. L. Smith, "Tensile Properties of Vanadium Alloys Irradiated at 200°C in the HFIR," in this report.

[6] H. M. Chung, H.-C. Tsai, L. Nowicki, and D. L. Smith, "Tensile Properties of Vanadium Alloys Irradiated at ≈390°C in EBR-II," in this report.

[7] M. Satou, H. Koide, A. Hasegawa, K. Abe, H. Kayano, H. Matsui, J. Nucl. Mater. 233-237 (1996), 447-451.

TENSILE PROPERTIES OF VANADIUM ALLOYS IRRADIATED AT 200°C IN THE HFIR*

H. M. Chung, L. Nowicki, and D. L. Smith (Argonne National Laboratory)

SUMMARY

Vanadium alloys were irradiated in a helium environment to ≈10 dpa at ≈200°C in the High Flux Isotope Reactor (HFIR). This report presents results of postirradiation tests of tensile properties of laboratory heats of V-(1-18)Ti, V-4Cr-4Ti, V-8Cr-6Ti, V–9Cr–5Ti, V-3Ti-1Si, and V-3Ti-0.1C alloys. Because of significant loss of work-hardening capability, all alloys except V-18Ti exhibited a very low uniform plastic strain of <1%. For V-Ti alloys, work-hardening capability increased with Ti content ≥ 10%, e.g., uniform strain of ≈2.4% for V-18Ti. The mechanism of the loss of work-hardening capability in the other alloys is not understood.

INTRODUCTION

Recently, attention to vanadium alloys has focused on low-temperature irradiation performance, especially tensile properties at <425°C. Under negligible helium generation, a 30-kg laboratory heat of V-4Cr-4Ti (Heat BL-47) was reported to retain a significant level of work-hardening capability (uniform plastic strain ≈3%) after irradiation to ≈10 dpa at ≈400°C in the High Flux Isotope Reactor (HFIR).[1] In contrast, complete loss of work-hardening capability (negligible uniform plastic strain) was reported for a 500-kg heat of V-4Cr-4Ti (Heat #83665) following irradiation to ≈0.4 dpa at 100-275°C in the High Flux Beam Reactor (HFBR).[2] This report presents results of postirradiation tests of tensile properties of V-1Ti, V-5Ti, V-10Ti, V-18Ti, V-4Cr-4Ti, V–8Cr–6Ti, V–9Cr–5Ti, V-3Ti-1Si, and V-3Ti-0.1C irradiated to ≈10 dpa at ≈200°C in a helium environment in the HFIR.

MATERIALS AND PROCEDURES

The elemental composition of the alloys, determined prior to irradiation, is given in Table 1. Tensile specimens with a gauge length of 7.62 mm and a gauge width of 1.52 mm were machined from ≈1.0-mm-thick sheets. Tensile specimens from the V-Cr-Ti alloys were annealed at a nominal temperature of ≈1125°C for 1 h, whereas specimens from the other alloys were annealed at 1050°C for 1 h. Following irradiation and specimen retrieval, the tensile specimens were cleaned ultrasonically in alcohol and tested without the customary degassing treatment at 400°C (used to expel hydrogen). Tensile properties were measured at 200°C in flowing argon at a strain rate of 0.001 s^{-1}.

Table 1. Chemical composition of vanadium alloys irradiated to ≈10 dpa at 200°C in helium in the HFIR

	Nominal Comp.	Impurity Concentration (wt. ppm)			
Heat ID	(wt.%)	O	N	C	Si
BL-50	1.0Ti	230	130	235	1050
BL-46	4.6Ti	305	53	85	160
BL-12	9.8Ti	1670	390	450	245
BL-15	17.7Ti	830	160	380	480
BL-47	4.1Cr-4.3Ti	350	220	200	870
BL-49	7.9Cr-5.7Ti	400	150	127	360
BL-43	9.2Cr-4.9Ti	230	31	100	340
BL-45	2.5Ti-1Si	345	125	90	9900
BL-60	3Ti-0.1C	-	-	-	-

* Work supported by U.S. Department of Energy, Office of Fusion Energy Research, under Contract W-31-109-Eng-38.

The tensile specimens were irradiated in the MFE–RB* 200J–1 capsule in the removable beryllium (RB*) position in the HFIR. The specimens were irradiated at ≈200°C to ≈10 dpa in circulating helium. Details of the capsule design and irradiation conditions are reported in Ref. 3. Helium in the line was purified continuously by a Ti–sponge getter located outside the core region. The specimens were shielded from thermal neutrons by an Hf sleeve located outside the capsule and designed to tailor the neutron spectrum to closely simulate the fusion–relevant helium–to–dpa ratio in stainless steels (i.e., ≈14 appm/dpa). In this experiment, the calculated transmutation rate of V to Cr is ≈0.2 %/dpa, or an increase of ≈2 %, in all alloys at the end of irradiation.

RESULTS AND DISCUSSION

Uniform plastic strain, total plastic strain, 0.2% yield strength, and ultimate tensile strength of the nine alloys are shown in Figs. 1-4, respectively. Except for V-18Ti, tensile properties of V-Cr-Ti alloys irradiated at 200°C in a helium environment in the HFIR were similar to the tensile properties reported for the 500-kg heat of V-4Cr-4Ti after irradiation at 100-275°C in the HFBR.[2] That is, significant or complete loss of work-hardening capability was observed in all alloys except V-18Ti, and as a result, uniform elongation was very low. Uniform plastic strain of the 30-kg heat of V-4Cr-4Ti, irradiated and measured at 200°C, was only 0.40-0.79%; significantly lower than the uniform plastic strain of ≈3% measured at 400°C on counterpart specimens irradiated at 400°C.[1] In contrast to irradiation at 400°C, work-hardening capability of the V-Cr-5Ti alloys during irradiation at 200°C does not appear to be influenced by a variation of Cr content from 4 to 10 wt.%. This is shown in Fig. 5.

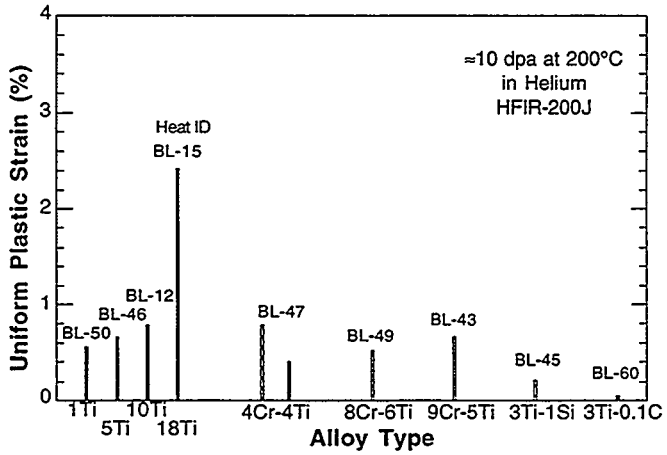

Fig. 1.
Uniform plastic strain of vanadium alloys irradiated at ≈200°C to ≈10 dpa in helium in the HFIR (calculated increase in Cr content of ≈2 % by transmutation).

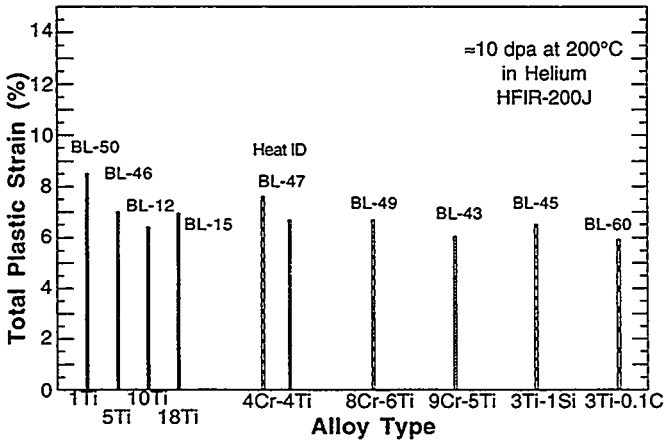

Fig. 2.
Total plastic strain of vanadium alloys irradiated at ≈200°C to ≈10 dpa in helium in the HFIR (calculated increase in Cr content of ≈2 % by transmutation).

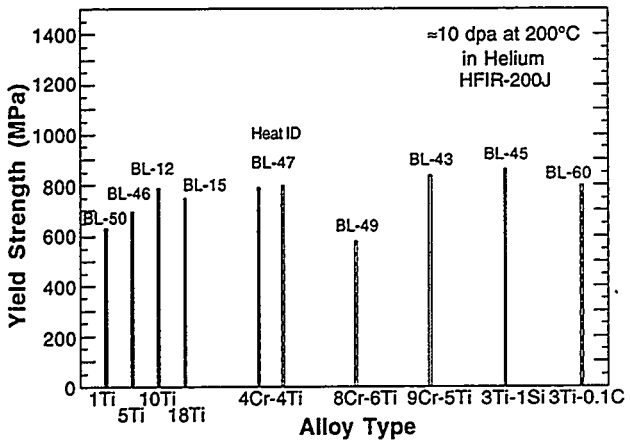

Fig. 3.
0.2%-offset yield strength of vanadium alloys irradiated at ≈200°C to ≈10 dpa in helium in the HFIR (calculated increase in Cr content of ≈2 % by transmutation).

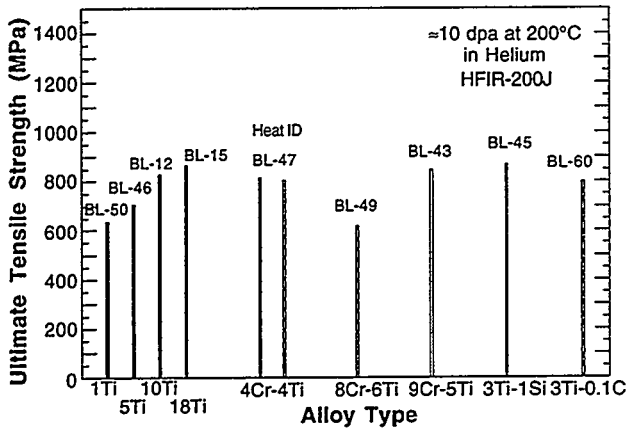

Fig. 4.
Ultimate tensile strength of vanadium alloys irradiated at ≈200°C to ≈10 dpa in helium in the HFIR (calculated increase in Cr content of ≈2 % by transmutation).

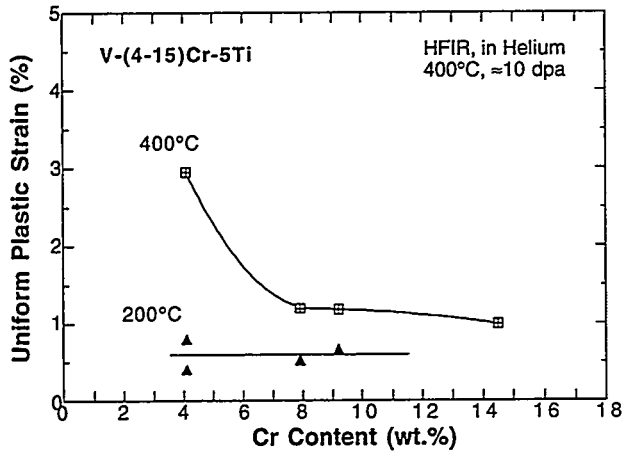

Fig. 5.
Uniform plastic strains of V-Cr-5Ti alloys irradiated at 400 and 200°C as function of starting Cr content (calculated increase in Cr content of ≈2 % by transmutation).

In Fig. 6, effects of Ti on tensile strength and uniform plastic strain are shown for V-Ti alloys (estimated Cr content of ≈2 %). Uniform plastic strain increased significantly for Ti content > 10 wt.%, e.g., to ≈2.4% for Ti ≈ 18 wt.%. This may be interpreted as an indication that loss of work-hardening capability is associated with one or more minor impurities that interact strongly with Ti atoms in solution or on grain boundaries during irradiation at low temperatures. Loss of work-hardening capability through dislocation channeling is also possible. To provide an understanding of the mechanism(s) of loss of work-hardening capability, microstructural characterization is being conducted by means of several metallographic techniques.

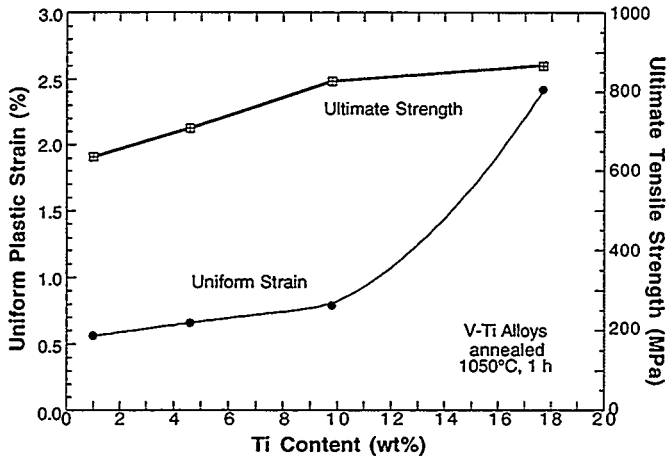

Fig. 6.
Uniform elongation and ultimate tensile strength of V-Ti alloys as function of Ti content (calculated increase in Cr content of ≈2 % by transmutation).

CONCLUSIONS

1. Uniform plastic strain of V-1Ti, V-5Ti, V-10Ti, V-4Cr-4Ti, V–8Cr–6Ti, V–9Cr–5Ti, V-3Ti-1Si, and V-3Ti-0.1C irradiated to ≈10 dpa at 200°C in a helium environment in HFIR were very low (<1%). This is because of significant or complete loss of work-hardening capability in the alloys. Uniform plastic strain of a 30-kg heat of V-4Cr-4Ti, irradiated and measured at 200°C, was only 0.40-0.79%; significantly lower than the uniform plastic strain of ≈3% measured at 400°C on counterpart specimens irradiated at 400°C.

2. In contrast to the above alloys, V-18Ti retained a significant level of work-hardening capability (uniform plastic strain of ≈2.4%). For V-Ti alloys, uniform plastic strain increased significantly for Ti content >10 wt.%. This may be interpreted as an indication that the loss of work-hardening capability is associated with one or more minor impurities that interact strongly with Ti atoms in solution or on grain boundaries during irradiation at low temperatures. Loss of work-hardening capability through dislocation channeling is also a possibility.

3. Loss of work-hardening capability of vanadium alloys at low irradiation temperatures (<430°C) seems to vary strongly from heat to heat, indicating that minor impurities and fabrication procedures are important factors.

ACKNOWLEDGMENT

The authors thank J. Pawel and H.–C. Tsai for the irradiation in HFIR and retrieval of the specimens, respectively.

REFERENCES

1. H. M. Chung, L. Nowicki, and D. L. Smith, "Tensile Properties of Vanadium Alloys Irradiated at 400°C in the HFIR," in Fusion Reactor Materials, Semiannual Prog. Rep. DOE/ER-0313/20, Oak Ridge National Laboratory, Oak Ridge, TN (1996), pp. 84-86.
2. D. J. Alexander, L. L. Snead, S. J. Zinkle, A. N. Gubbi, A. F. Rowcliffe, and E. E. Bloom, "Effects of Irradiation at Low Temperature on V-4Cr-4Ti," in Fusion Reactor Materials, Semiannual Prog. Rep. DOE/ER-0313/20, Oak Ridge National Laboratory, Oak Ridge, TN (1996), pp. 87-95.
3. A. W. Longest, J. E. Pawel, D. W. Heatherly, R. G. Sitterson, and R. L. Wallace, "Fabrication and Operation of HFIR–MFE RB* Spectrally Tailored Irradiation Capsules," in Fusion Reactor Materials, Semiannual Prog. Rep. DOE/ER-0313/14, Oak Ridge National Laboratory, Oak Ridge, TN (1993), pp. 14–40.

TENSILE PROPERTIES OF VANADIUM ALLOYS IRRADIATED AT <430°C*

H. M. Chung and D. L. Smith (Argonne National Laboratory)

SUMMARY

Recent attention to vanadium alloys has focused on significant susceptibility to loss of work-hardening capability in irradiation experiments at <430°C. An evaluation of this phenomenon was conducted on V-Ti, V-Cr-Ti, and V-Ti-Si alloys irradiated in several conventional and helium-charging irradiation experiments in the FFTF-MOTA, HFIR, and EBR-II. Work-hardening capability and uniform tensile elongation appear to vary strongly from alloy to alloy and heat to heat. A strong heat-to-heat variation has been observed in V-4Cr-4Ti alloys tested, i.e., a 500-kg heat (#832665), a 100-kg heat (VX-8), and a 30-kg heat (BL-47). The significant differences in susceptibility to loss of work-hardening capability from one heat to another are estimated to correspond to a difference of ≈100°C or more in minimum allowable operating temperature (e.g., 450 versus 350°C).

INTRODUCTION

Recent attention to vanadium alloys has focused on low-temperature irradiation performance of V-4Cr-4Ti, especially tensile and fracture behavior after irradiation at <450°C. From several irradiation experiments at 80-430°C, it has been reported that some heats of V-4Cr-4Ti exhibited low uniform elongation as a result of complete loss of work-hardening capability.[1-4] Significant susceptibility to loss of work-hardening capability (LWHC) has been not observed at irradiation temperatures ≥500°C, however. Initial assessment indicates that the LWHC phenomenon in V-4Cr-4Ti is strongly dependent not only on heat but also on irradiation variables at <430°C.[2-4] This is important in understanding the phenomenon because susceptibility to LWHC at low temperatures under fusion-relevant conditions is considered to be a major factor in governing the minimum operating temperature of a fusion reactor. Therefore, a systematic evaluation of the phenomenon was conducted on a wider variety of alloys. This report presents results of an analysis of work-hardening behavior and uniform elongation of V-Ti, V-Cr-Ti, and V-Ti-Si alloys irradiated at <430°C in several conventional and helium-charging irradiation experiments in FFTF-MOTA, HFIR, and EBR-II.

MATERIALS AND TESTING PROCEDURES

The elemental composition of the alloys analyzed in this study, determined prior to irradiation, is given in Table 1. Tensile specimens with a gauge length of 7.62 mm and a gauge width of 1.52 mm (SS-3 geometry) were machined from ≈1.0-mm-thick sheets that had been produced by rolling a ≈3.8-mm thick plate at 25 or 400°C. Specimens from the V-Cr-Ti alloys were annealed at 950-1125°C for 1 h in an ion-pumped vacuum system, whereas specimens from V-Ti and V-Ti-Si alloys were annealed at 1000-1050°C for 1 h. Following irradiation, retrieved specimens were cleaned ultrasonically in alcohol and tested without the customary degassing treatment at 400°C (used to expel hydrogen). Tensile properties were measured at the irradiation temperature in flowing argon at a strain rate of 0.0011 s^{-1}.

IRRADIATION CONDITIONS

Details of the conventional and helium-charging irradiation experiments at <430°C in the FFTF-MOTA, HFIR, and EBR-II are summarized in Table 2. In the latter type of experiment (i.e., the Dynamic Helium Charging Experiment, or DHCE), helium atoms were produced during irradiation in the range of 14-76 appm He,[4] whereas in the former type of experiments (referred to as "non-DHCE") helium generation was negligible except for the boron-doped heat QN74 (irradiated in the X530 experiment in EBR-II).

* Work supported by U.S. Department of Energy, Office of Fusion Energy Research, under Contract W-31-109-Eng-38.

Table 1. Chemical composition of vanadium alloys

Heat ID	Nominal Comp. (wt.%)	Impurity Concentration (wt. ppm) O	N	C	Si
BL-50	1.0Ti	230	130	235	1050
BL-62	3.1Ti	320	86	109	660
BL-52	3.1Ti	210	310	300	500
BL-46	4.6Ti	305	53	85	160
BL-12	9.8Ti	1670	390	450	245
BL-15	17.7Ti	830	160	380	480
BL-10	7.2Cr-14.5Ti	1110	250	400	400
BL-24	13.5Cr–5.2Ti	1190	360	500	390
BL-40	10.9Cr-5.0Ti	470	80	90	270
BL-41	14.5Cr-5.0Ti	450	120	93	390
BL-43	9.2Cr-4.9Ti	230	31	100	340
BL-49	7.9Cr-5.7Ti	400	150	127	360
BL-63[a]	4.6Cr-5.1Ti	440	28	73	310
BL-27	3.1Ti–0.25Si	210	310	310	2500
BL-45	2.5Ti-1Si	345	125	90	9900
QN74[b]	4.0Cr–4.1Ti	480	79	54	350
BL-47	4.1Cr-4.3Ti	350	220	200	870
VX-8[c]	3.73Cr–3.93Ti	350	70	300	500
832665[d]	3.8Cr–3.9Ti	310	85	80	783

[a]80-kg heat fabricated with sponge Ti.
[b]Contains ≈250 appm boron–10.
[c]100-kg heat, obtained from Russian Federation, contains (in wppm) 1120 Al, 280 Fe, 500 Co, 270 Mo, 1280 Nb, 19 Zr.
[d]500–kg heat produced in Teledyne Wah Chang Albany, OR.
[e]All others 15– to 30–kg laboratory heats.

Table 2. Summary of irradiation experiments

Experiment ID	Subcapsule	Environment	Temperature (°C)	dpa	He/dpa Ratio
HFIR	200J	He	200	10	-
	400J	He	400	10	-
COBRA-1A2	V499	Li	395	36	-
	V495	Li	379	31	-
EBR-II X530	S8	Li	394	4	-
	S9	Li	390	4	-
FFTF-nonDHCE	many	Li	427-600	14-46	-
FFTF-DHCE	many	Li	430-600	14-27	0.4-4.2

The 30-kg heat BL-47 showed uniform elongation of 1-3% in the temperature range of 380-430°C. This heat appears to exhibit uniform elongation higher than that of #832665, but not as good as that of VX-8, although data that will allow a direct comparison are not available. Understanding the cause of the large heat-to-heat variation of work-hardening capability at <430°C is therefore of major importance. Based on the observation that work-hardening behavior is sensitive to not only heat but also subtle irradiation variations, it is likely that one or more minor impurities are involved. One heat of V-3Ti-1Si (Heat BL-45) exhibited excellent resistance to loss of work-hardening behavior when irradiated at 390-430°C. This heat, like BL-47 of V-4Cr-4Ti, retained a very low ductile-brittle transition temperature (DBTT<-190°C) after conventional irradiation at 420-600°C to 14-33 dpa.

RESULTS AND DISCUSSION

Uniform plastic strains of the alloy specimens irradiated at <430°C are summarized in Table 3. Similar results measured on specimens irradiated at 500-600 were also obtained and compared with those from the low-temperature irradiation. Uniform elongations of four heats of V-4Cr-4Ti and one heat of V-3Ti-1Si determined from the irradiation experiments at 200-430°C are plotted in Fig. 1. For a similar temperature range of 380-425°C, the effect of dpa level appears to be secondary.

It seems from Fig. 1 that work-hardening capability, and hence uniform elongation, of V-4Cr-4Ti class alloys varies strongly from heat to heat and is also influenced significantly by irradiation variations. The 500-kg heat #832665 exhibited the lowest work-hardening capability after irradiation in the X-530 experiment in EBR-II, whereas Heat VX-8 (irradiated in one of the subcapsules) showed excellent work-hardening capability.

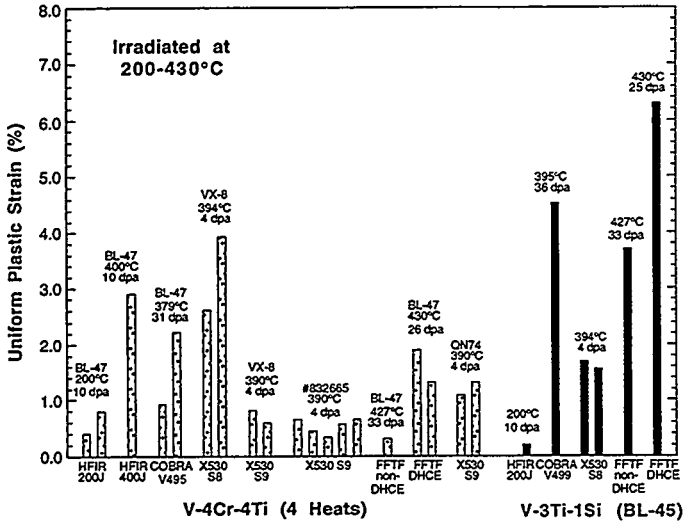

Fig. 1.
Uniform plastic strain of four heats of V-4Cr-4Ti and one heat of V-3Ti-1Si irradiated at 200-430°C to 4-46 dpa in several experiments.

Uniform elongation of all V-Ti, V-Cr-Ti, and V-Ti-Si alloys examined in this study has been plotted in Fig. 2 as a function of irradiation/test temperature. Significant scattering is obvious in this type of plot, probably reflecting the effects of many other factors such as dpa and helium levels and heat-to-heat and alloy-to-alloy variations. However, the plot also serves as an estimate of the approximate threshold temperature above which uniform elongation of these alloys is higher than a threshold level, e.g., 2%. The threshold temperature is considered to be an important consideration in governing the minimum operating temperature of a fusion reactor.

A similar plot for V-Cr-Ti alloys (see Table 3) is shown in Fig. 3. It appears that the threshold temperature to meet a minimum uniform elongation of 2% ($T_{2\%}$) could be anywhere between

Table 3. Uniform plastic strain of vanadium-base alloys irradiated at <430C

	Nominal	Irradiation Experiment							
	Composition	HFIR-200J	HFIR-400J	COBRA-1A2/V499	COBRA-1A2/V495	EBRII-X530-S8	EBRII-X530-S9	FFTF-nonDHCE	FFTF-DHCE
Heat ID	(wt.%)	200°C, 10 dpa	400°C, 10 dpa	395°C, 36 dpa	379°C, 31 dpa	394, 4 dpa	390, 4 dpa	427°C, dpa in (46)	430°C, dpa in (25)
BL-50	1.0Ti	0.56							
BL-62	3.1TI					0.65			
BL-46	4.6Ti	0.66		1.44		0.75, 0.95			1.8, 5.1, 1.4, 1.4 (14-27)
BL-12	9.8Ti	0.79							
BL-15	17.7Ti	2.42						3.7 (46)	
BL-10	7.2Cr-14.5Ti							2.8, 3.0 (46)	
BL-24	13.5Cr-5.2Ti							2.8, 5.0, 3.54, 1.8 (46)	
BL-40	10.9Cr-5.0Ti			1.44					
BL-41	14.5Cr-5.0Ti		0.99						
BL-43	9.2Cr-4.9Ti	0.66	1.18					1.2 (44)	1.0 (25)
BL-49	7.9Cr-5.7Ti	0.52	1.18	1.64		0.65		1.31 (33)	1.8, 1.0 (14-25)
BL-63[a]	4.6Cr-5.1Ti					0.80, 0.52			
BL-27	3.1Ti-0.25Si							1.8, 1.5 (38-46)	
BL-45	2.5Ti-1Si	0.2		4.53		1.68, 1.56		3.7 (33)	6.3 (25)
QN74[b]	4.0Cr-4.1Ti-B						1.07, 1.31		
BL-47	4.1Cr-4.3Ti	0.4, 0.79	2.91		0.92, 2.23 (CW)[c]			0.3 (33)	1.9, 1.3 (25-27)
VX-8[d]	3.7Cr-3.9Ti					2.62, 3.93	0.82, 0.59		
832665[e]	3.8Cr-3.9Ti						0.65, 0.45, 0.34, 0.57, 0.65		

[a]80–kg heat
[b]Contains ≈250 appm boron–10
[c]Coldworked material
[d]100–kg heat obtained from RF
[e]500–kg production–scale heat; all others, 15– to 30–kg laboratory heats unless otherwise noted

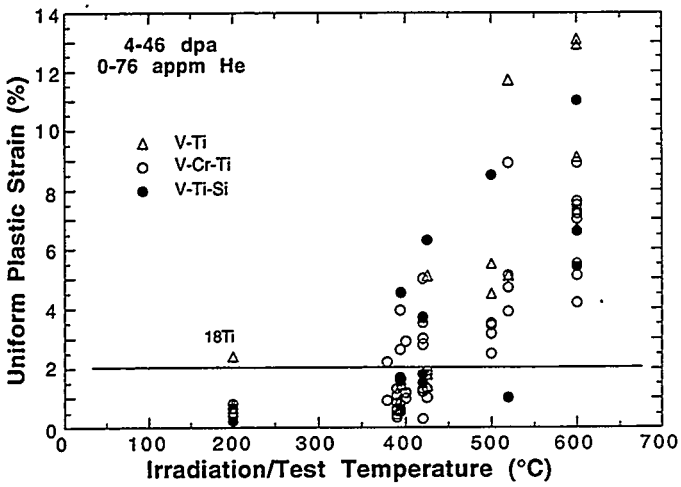

Fig. 2.
Uniform plastic strain of V-Ti, V-Cr-Ti, and V-Ti-Si alloys as function of irradiation temperature (same as test temperature).

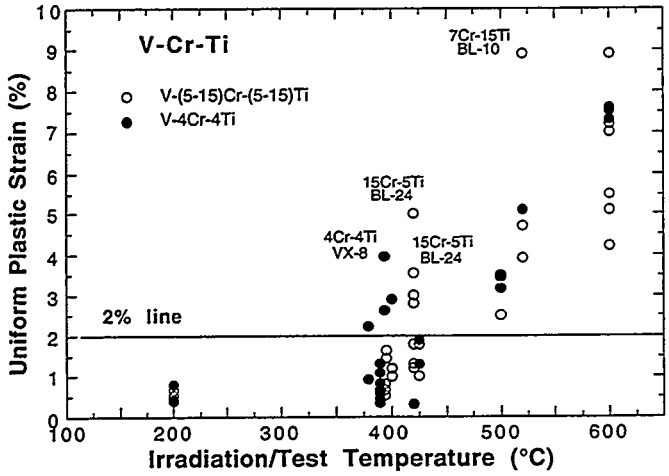

Fig. 3.
Uniform plastic strain of V-Cr-Ti alloys as function of irradiation temperature (same as test temperature).

≈320 and ≈470°C, depending on alloy type, heat, and basis of extrapolation. Interestingly, one heat of V-15Cr-5Ti (BL-24) showed high uniform elongation after irradiation at ≈420°C in the FFTF-MOTA. Similar data limited to V-4Cr-4Ti are shown in Fig. 4. A possible advantage with a resistant heat such as VX-8 is indicated in this figure.

Results in Fig. 5 show that one heat of V-3Ti-1Si (BL-45) exhibits good work-hardening capability at <430°C, whereas one heat of V-3Ti-0.25Si (BL-27) does not. From these data alone, one cannot predict if the heat-to-heat sensitivity of the V-3Ti-1Si class alloys to low-temperature work-hardening capability is inherently less than or similar to that of the V-4Cr-4Ti class.

CONCLUSIONS

1. Work-hardening capability and uniform tensile elongation of V-Ti, V-Cr-Ti, V-Ti-Si alloys during irradiation at 380-430°C appear to vary strongly from alloy to alloy and heat to heat. A strong heat-to-heat variation has been observed in three heats of V-4Cr-4Ti tested, a 500-kg heat (#832665), a 100-kg heat (VX-8), and a 30-kg heat (BL-47).

2. Work-hardening capability of V-4Cr-4Ti alloys appears also to be influenced significantly by variations in irradiation conditions. Based on the observation that work-hardening behavior is sensitive to not only heat but also subtle irradiation variations, it is likely that one or more minor impurities are involved in the process.

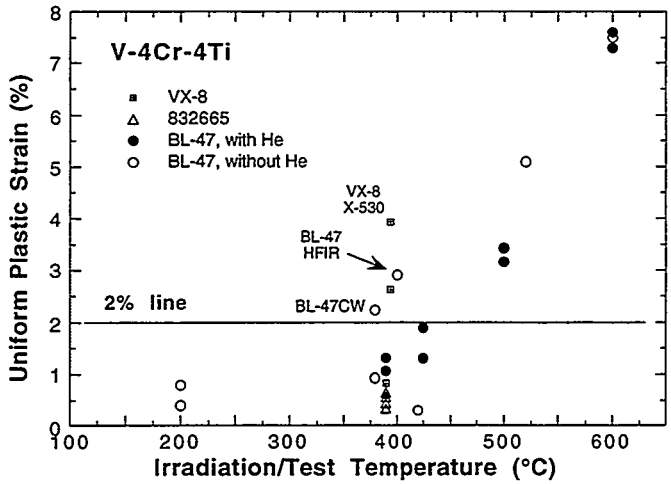

Fig. 4.
Uniform plastic strain of three heats of V-4Cr-4Ti as function of irradiation temperature (same as test temperature).

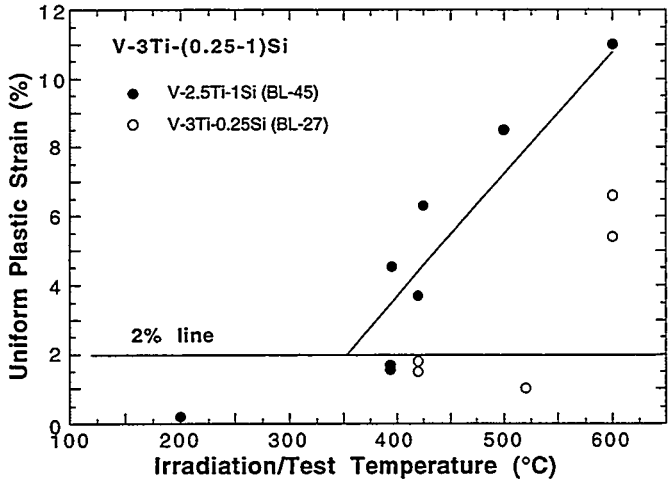

Fig. 5.
Uniform plastic strain of V-Ti-Si alloys as function of irradiation temperature (same as test temperature).

3. Significant differences in susceptibility to loss of work-hardening capability from one heat to another are estimated to correspond to a difference of ≈100°C or more in minimum allowable operating temperature (e.g., 450 vs. 350°C).

REFERENCES

1. D. J. Alexander, L. L. Snead, S. J. Zinkle, A. N. Gubbi, A. F. Rowcliffe, and E. E. Bloom, "Effects of Irradiation at Low Temperature on V-4Cr-4Ti," in Fusion Reactor Materials, Semiannual Prog. Rep. DOE/ER-0313/20, Oak Ridge National Laboratory, Oak Ridge, TN (1996), pp. 87-95.
2. H. M. Chung, L. Nowicki, and D. L. Smith, "Tensile Properties of Vanadium Alloys Irradiated at 400°C in the HFIR," in Fusion Reactor Materials, Semiannual Prog. Rep. DOE/ER-0313/20, Oak Ridge National Laboratory, Oak Ridge, TN (1996), pp. 84-86.
3. H. M. Chung, L. Nowicki, and D. L. Smith, "Tensile Properties of Vanadium Alloys Irradiated at 200°C in the HFIR," in this report.
4. H. M. Chung, M. C. Billone, and D. L. Smith, "Effect of Helium on Tensile Properties of Vanadium Alloys," in this report.

MICROSTRUCTURAL EXAMINATION OF V-(4-5%)Cr-(4-5%)Ti Irradiated in X530 - D. S. Gelles (Pacific Northwest National Laboratory)[a] and H. M. Chung (Argonne National Laboratory)

OBJECTIVE

The objective of this effort is to provide collaborative understanding of microstructural evolution in irradiated vanadium alloys for first wall applications in a fusion reactor.

SUMMARY

Microstructural examination results are reported for two heats of V-(4-5%)Cr-(4-5%)Ti irradiated in the X530 experiment to ~4 dpa at ~400°C to provide an understanding of the microstructural evolution that may be associated with degradation of mechanical properties. Fine precipitates were observed in high density intermixed with small defect clusters for all conditions examined following the irradiation. The irradiation-induced precipitation does not appear to be affected by preirradiation heat treatment at 950-1125°C. There was no evidence for a significant density of large (diameter >10 nm) dislocation loops or network dislocations.

PROGRESS AND STATUS

Introduction

Vanadium-based alloys are being developed for application as a first wall material for magnetic fusion power system. It has been shown that alloys of composition V-(4-5%)Cr-(4-5%)Ti have very promising physical and mechanical properties.[1] Recent attention in this alloy class has focused on several issues, such as the effect of low-temperature irradiation on fracture toughness, the effect of helium generation, the effect of minor impurities, and heat-to-heat variation in work-hardening behavior at low irradiation temperatures. While other classes of alloys are still considered, the V-(4-5%)Cr-(4-5%)Ti alloys are being optimized to suppress their susceptibility to loss of work-hardening capability following irradiation at low temperatures. Susceptibility of the alloy class to this process under fusion-relevant helium-generating conditions is considered to be a major factor in governing the minimum operating temperature of magnetic fusion devices.

Recent irradiation experiments at <430°C have shown that the loss of work-hardening capability and uniform elongation of V-4Cr-4Ti vary strongly from heat to heat and are influenced significantly by helium generated in the alloy.[2] The present effort was initiated to provide an understanding of the microstructural evolution in some heats of the V-(4-5%)Cr-(4-5%)Ti class that correspond to specimens with degradation of mechanical properties.[2] Specifically, two issues were addressed: the microstructural characteristics of a 500-kg heat of V-4Cr-4Ti (Heat #832665, referred to in reference 3 as BL-71) not previously examined following irradiation, and the cause of degraded properties in both an 80-kg heat of V-5Cr-5Ti (Heat BL-63) and the 500-kg heat following irradiation at ~385°C to ~4 dpa in the X530 experiment in EBR-II. In contrast to a 100-kg heat of V-4Cr-4Ti (Heat VX-8), the 500-kg heat did suffer from virtual loss of work-hardening capability during the irradiation.[2]

---

[a]Operated for the U.S. Department of Energy by Battelle Memorial Institute under Contract DE-AC06-76RLO 1830.

Experimental Procedure

Specimens in the form of microscopy disks 3 mm in diameter were included in the X530 experiment. Five samples were selected for examination comprising two heats of material but each with a different preirradiation heat treatment condition. The compositions of the heats are given in Table 1[3,4] and the specimen conditions are shown in Table 2. Specimens of BL-63 had been included in capsule S8 and specimens of BL-71 had been included in capsule S9 of the X530 experiment[5] which achieved an exposure of 35 effective full power days yielding a peak fluence of 7.3×10^{21} n/cm^2 (E>0.1 MeV) corresponding to damage of ~4 dpa.[6] The capsules also contained matching miniature tensile specimens of the same conditions. The bottom of capsule S8 was 9.80 inches from the bottom of the core and the bottom of capsule S9 was 7.35 inches above the bottom of the core upon which actual irradiation temperatures and doses have been estimated and included in Table 2.[7,8] One specimen of each of the BL-71 conditions was electrolytically thinned at ANL following irradiation, and one specimen of each of the BL-63 conditions was thinned at PNNL. Specimen BL-71-WR1050 was briefly repolished at PNNL. Examinations were performed on JEOL 1200EX and 2010F analytical transmission microscopes. Image processing from negatives was entirely by computer, with some minor loss in resolution and contrast range.

Table 1. Composition of Heats Examined

Heat #	Nominal Composition, wt%	Minor Impurities [appm]				
		O	N	C	Si	Other
BL-63	V-4.6Cr-5.1Ti	440	28	73	310	200 Al
832665, BL-71	V-3.8Cr-3.9Ti	310	85	80	783	220 Fe, 190 Al

Table 2. Specimen and Irradiation Conditions for the X530 Experiment.

Specimen Designation	Preirradiation heat treatment	Fluence (n/cm^2)	Dose (dpa)	Temperature (°C)
BL-63-CR950	cold rolled, annealed at 950°C/1h	6.7×10^{21}	4.3	400.5
BL-63-CR1050	cold rolled, annealed at 1050°C/1h	6.7×10^{21}	4.3	400.5
BL-71-WR950	warm rolled, annealed at 950°C/1h	7.3×10^{21}	4.7	399.1
BL-71-WR1050	warm rolled, annealed at 1050°C/1h	7.3×10^{21}	4.7	399.1
BL-71-WR1125	warm rolled, annealed at 1125°C/1h	7.3×10^{21}	4.7	399.1

Results

Despite the limited number of samples available for examination, it was possible to provide useful observations for all sample conditions. Preirradiation heat treatment was verified based on grain size comparison. BL-63-CR950 had a grain size on the order of 10 μm, BL-63-CR1050 much greater than 10 μm, BL-71-WR950 between 2 and 10 μm, BL-71-WR1050 much greater than 5 μm, and BL-71-WR1125 between 20 and 80 μm. The microstructures of all conditions were as expected, showing large and intermediate sized (Ti,V) oxy-carbo-nitride particles randomly distributed, and small particles

decorating grain boundaries in the BL-71-WR1050 and BL-71-WR1125.[9] Evidence for effects of irradiation could only be identified on a fine scale. Examples of each of these microstructures at low magnification are given in Figure 1.

Careful examination of diffraction information indicated enhanced scattering in two regions of reciprocal space: a radial streak in the 200 direction at approximately ¾<200> and a similar tangential streak at approximately ⅔<222>. Dark field imaging with each of these features showed similar but not identical distributions of fine features, assumed to be precipitates. As streaking is in different directions for each of these diffraction features, different populations of precipitates would be expected to be in contrast. Similar attempts to image the dislocation structure using weak beam conditions on matrix reflections gave very complex images with features of similar size to the precipitate features. It is therefore likely that several matrix reflections superimpose on precipitate reflections. It was possible to obtain precipitate dark field images for each sample condition using ¾<200> contrast in stereo by tilting on (200). Stereo model observations demonstrated that the precipitate features tended to form in layers distributed through the foil thickness, verifying that they were not surface artifacts. All specimens gave similar diffraction behavior. Examples of one dark field image for each sample condition using $\vec{g}$ = ¾<200>, and the accompanying bright field image are provided in Figure 2, cropped to show behavior at a grain boundary. Figure 2 also includes an example of the diffraction information, inset.

From Figure 2, it can be demonstrated that precipitation is very fine. For example, particles in Figure 2g are 2 nm long by 1 nm wide, the narrow dimension corresponding to the streaking in <200>. It is surprising that such small particles can be successfully imaged. The precipitate dark field images appear to differ between the two heats, but the size distribution is invariant with respect the preirradiation heat treatment. The exact nature of the differences between the precipitate morphologies for the two heats is difficult to quantify. Although the images of precipitates in BL-63 appear to be larger, careful examination of the negatives suggests that the larger particles are a result of rafts of closely spaced smaller particles, of similar size to those in BL-71. However, it can be argued that the particles are larger in BL-63, and the fine structure appears for other reasons.

Precipitate measurements based on foil thicknesses, measured stereographically, gave particle densities as follows; BL-63-CR950: 6.3 nm mean diameter at $4x10^{17}$ cm^{-3} for a volume fraction of 3.5%, BL-63-CR1050: 4.9 nm mean diameter at $2x10^{17}$ cm^{-3} for a volume fraction of 0.8%, BL-71-WR950: 4.4 nm mean diameter at $1.1x10^{17}$ cm^{-3} for a volume fraction of 0.3%, BL-71-WR1050: 4.8 nm mean diameter at $4x10^{17}$ cm^{-3} for a volume fraction of 1.3%, and BL-71-WR1125: 3.7 nm mean diameter at $3x10^{17}$ cm^{-3} for a volume fraction of 0.4%. These measurements should be considered estimates given the difficulty of the analysis, but they provide further indication that the precipitation found could be responsible for the observed irradiation hardening in BL-71, but do not explain the difference in behavior between the two heats.

Figure 2 also provides insights regarding irradiation response at grain boundaries. The grain boundary images for BL-63-WR950, BL-71-WR950 and BL-71-WR1050 in Figures 2b, f and h appear to show a coating on the boundary. Also, Figure 2g for BL-71-WR1050 shows larger precipitate particles at the grain boundary showing brightly under the same conditions as the fine precipitate, and therefore the two features may be related. Similar larger features can be seen in Figure 2j for BL-71-WR1125, and are expected to be remnants of the preirradiation heat treatment.[8]

Several attempts were made to obtain compositional information from the fine precipitate features. Difficulties were encountered identifying the exact location of a precipitate so that a 1 nm focussed spot could be positioned to obtain characteristic precipitate composition information. Techniques based on ¾<200> dark field imaging and lattice imaging to identify precipitate locations failed to

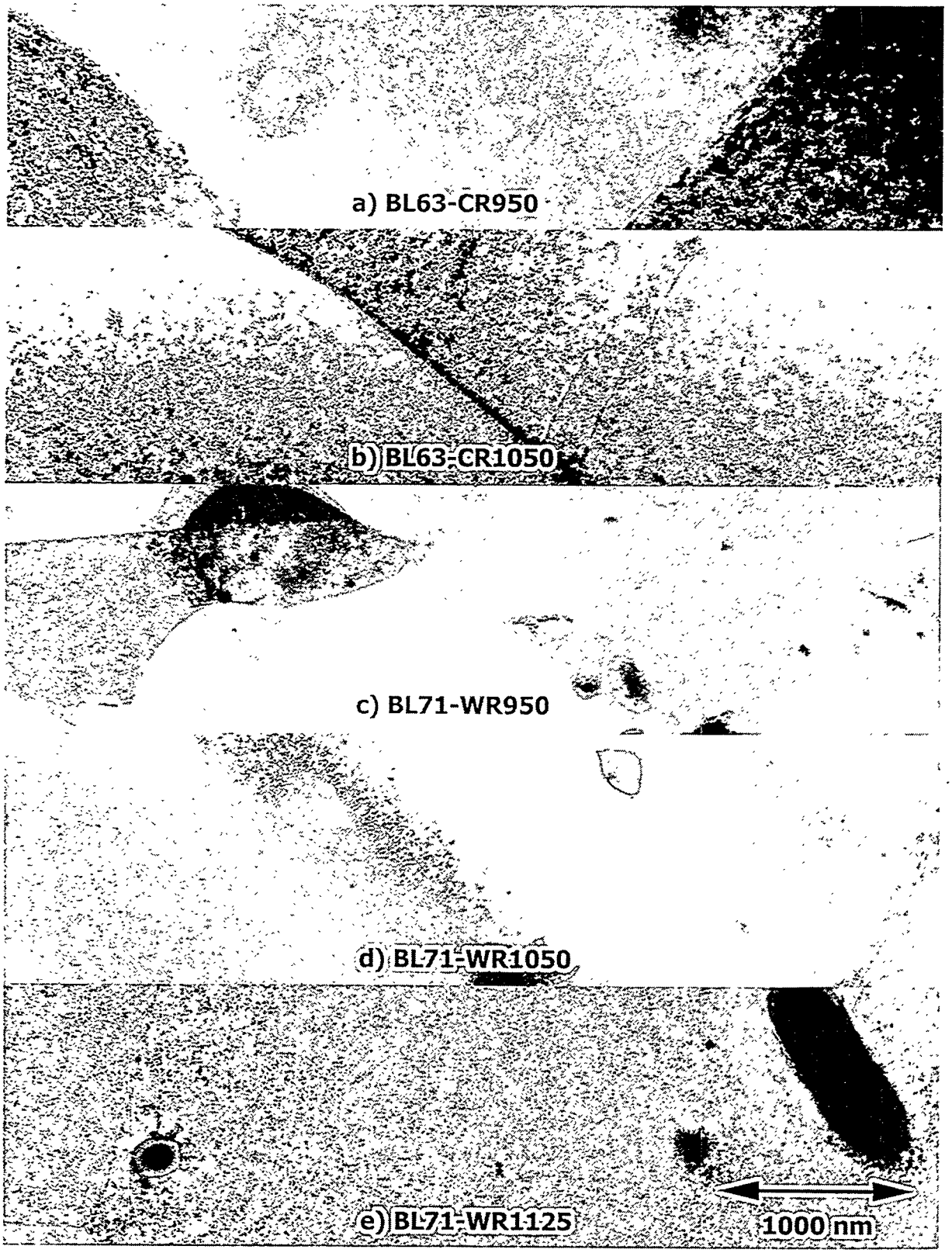

Figure 1. Low magnification examples of microstructures in specimens of V-(4-5%)Cr-(4-5%)Ti irradiated in the X530 experiment.

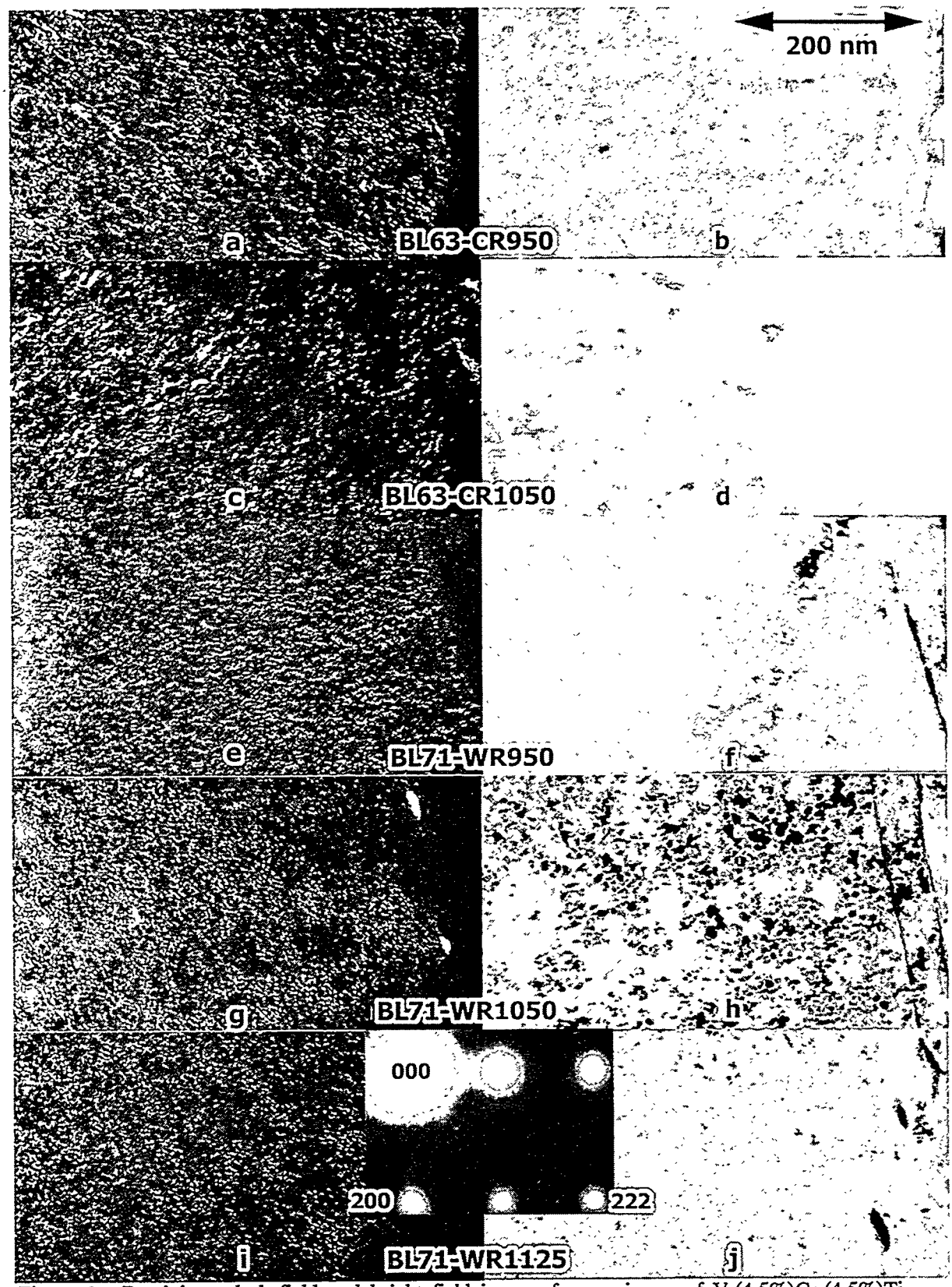

Figure 2. Precipitate dark field and bright field images for specimens of V-(4-5%)Cr-(4-5%)Ti irradiated in the X530 experiment with a (011) diffraction pattern from BL-71-WR1125 inset.

provide any composition dependencies that could be considered characteristic. An effort to identify composition differences at a grain boundary in BL-71-WR1050 were also unsuccessful. Although these efforts will continue within the constraints of available funding, it must be concluded that larger precipitate particles are probably needed to definitively identify the composition of these precipitates.

Discussion

The purpose of this work was to provide an explanation for mechanical property degradation in some heats of V-(4-5%)Cr-(4-5%)Ti. The above results indicate that precipitation during irradiation is probably responsible. Unfortunately, the composition of the precipitate has not yet been established, so that it is not yet possible to provide recommendations for composition modifications for improved properties. This discussion is provided as speculation on the likely causes for the behavior observed.

Several important facts should be first summarized. Table 3 provides postirradiation mechanical properties response[2] for conditions identical to those examined in this study. From Table 3, it can be shown that BL-63 gave lower levels of both yield strength (YS) and ultimate tensile strength (UTS), but uniform elongation (UE) was similar in comparison with BL-71 following annealing at 950°C, whereas higher annealing temperatures for BL-71 produced lower UE. Total elongation (TE) values followed none of these trends. However, comparison of the compositional differences in Table 1 demonstrates that BL-71 contains less chromium and titanium but higher silicon.

Table 3. Postirradiation mechanical properties for selected specimens in the X530 experiment.

Specimen Designation	Preirradiation heat treatment	0.2% YS (MPa)	UTS (MPa)	UE (%)	TE (%)
BL-63-CR950	cold rolled, annealed at 950°C/1h	701	743	0.8	2.8
BL-63-CR1050	cold rolled, annealed at 1050°C/1h	723	765	1.0	7.0
BL-71-WR950	warm rolled, annealed at 950°C/1h	819	847	0.8	4.1
BL-71-WR1050	warm rolled, annealed at 1050°C/1h	809	818	0.4	6.0
BL-71-WR1125	warm rolled, annealed at 1125°C/1h	880	883	0.2	6.0

Therefore, the experimental observations can be summarized as follows. BL-71 develops more hardening and less uniform elongation following irradiation, BL-71 contains significantly more silicon and a little less chromium and titanium, but the irradiation temperatures are expected to be very similar. Based on this, the likely cause for the observed enhanced hardening would be expected to be precipitation of silicide phases. The observed precipitate particles are very finely distributed, and precipitate number density has been measured for each condition. It can be argued that the particles are larger or more non-uniformly distributed in BL-63, and therefore effectively at lower density (although not supported by quantitative microscopy because distribution is not taken into account), in agreement with the observed hardening behavior.

The diffraction information obtained for this fine precipitation does not straightforwardly correspond to precipitation previously identified in this alloy class. Chung and Smith[10] have provided diffraction information for $Ti_5(Si,P)_3$ and Ti_2O that have similar appearance but different diffraction response. One published diffraction pattern in Figure 2 does show a streak at ⅔<222>, but no comment is provided. Chung etal.[11] found similar grain boundary contrast in V-4Cr-4Ti irradiated at 425°C to 31 dpa in the DHCE experiment but ruled out Ti_5Si_3 precipitation. Chung, Loomis, and Smith[12] showed

microstructures in irradiated V-4Cr-4Ti containing Ti_5Si_3, but provided no diffraction information. Satou etal.[13] showed diffraction and dark field images of Ti_5Si_3 precipitates in V-5Ti-5Cr-1Si-Al following irradiation at 520°C, but the diffraction information is not in agreement with the present findings. Gelles and Chung[14] found precipitation in V-5Cr-5Ti following irradiation with a diffraction streak at ¾<200>, but compositional information was not obtained and it was "anticipated that the phase was TiP, but similar morphologies have been identified previously as Ti_5Si_3." Chung etal.[15] again published a grain boundary image in V-4Cr-4Ti irradiated at 425°C to 31 dpa similar to those in Figure 2. Finally, Fukumoto etal.[16] showed dark field images of similar features in V-4Cr-4Ti following irradiation but identify them as titanium oxide, Ti_2O or TiO_x ($x<0.5$) without giving any diffraction information. From these analyses it appears that the precipitate found in the present work cannot be identified as a silicide based on diffraction information, whereas it may be, but has not definitively been shown to be, an oxide or a phosphide. If an oxide is responsible for the hardening found in the X530 experiment, then differences in heat-to-heat response could best be explained by a consequence of variation in irradiation temperature and not composition. However, as noted in Table 2, due to capsule radial positions, negligible differences are expected.[7] A phosphide cause for embrittlement is unlikely because phosphorus levels are low in BL-71.[4] The most critical experiment continues to be identification of the phase in BL-71 that causes the diffraction streaks at ¾<200> and ⅔<222>.

CONCLUSIONS

Five specimen conditions from the X530 experiment, comprising two heats of V-(4-5%)Cr-(4-5%)Ti given different preirradiation heat treatments and directly corresponding to tested mechanical properties specimens, have been examined to identify the cause of irradiation hardening. It is found that hardening is at least in part due to precipitation of a high density of small particles. However, analytical electron microscopy was unable to provide precipitate composition and it is not yet possible to provide and explanation for the differences in response between the heats.

FUTURE WORK

This work will be continued within the confines of funding and specimen availability.

REFERENCES

1. B. A. Loomis, A. B. Hull, and D. L. Smith, J. Nucl. Mater., 179-181 (1992) 148.

2. S. J. Zinkle, D. J. Alexander, J. P. Robinson, L. L. Snead, A. F. Rowcliffe, L. T. Gibson, W. S. Eatherly and H. Tsai, DOE/ER-0313/21, 73.

3. H. M. Chung, J. Gazda, L. J. Nowicki, J. E. Sanecki, and D. L. Smith, DOE/ER-0313/15, 207.

4. H. M. Chung, H. Tsai, D. L. Smith, K. Peterson, C. Curtis, C, Wojcik, and R. Kinney, DOE/ER-0313/17, 178.

5. H. Tsai, V. Strain, A. G. Hins, H. M. Chung, L. J. Nowicki, and D. L. Smith, DOE/ER-0313/17, 8.

6. H. Tsai, V. Strain, A. G. Hins, H. M. Chung, L. J. Nowicki, and D. L. Smith, DOE/ER-0313/18, 85.

7. Personal communication from Bob Strain, ANL: "A more refined thermal analysis of the X530 experiment shows that the centerline temperature for subcapsule S8 to be 400.5°C and that for S9 to be 399.1°C. The subcapsule inside surface temp was ~1.5°C lower, in both cases. S8, at a higher axial elevation, ordinarily would have a higher temperature. But the capsule it was in, AH2, was located at the the center of the hex, thus receiving less heat from the neighboring (hotter) subassemblies. The two countervailing effects essentially cancelled out."

8. Personal communication from L. W. Greenwood, PNNL, recommending that an extra column be added to table 3, DOE/ER-031/21, page 228, headed dpa (vanadium) and reading 14.0, 31.0, 38.1, 29.3, 15.4, 6.36.

9. D. S. Gelles and Huaxin Li, DOE/ER-0313/19, 22.

10. H. M. Chung and D. L. Smith, J. Nucl. Mater., 191-194 (1992) 942.

11. H. M. Chung, L. J. Nowicki, J. Gazda, and D. L. Smith, DOE/ER-0313/17, 211.

12. H. M. Chung, B. A. Loomis, and D. L. Smith, J. Nucl. Mater., 212-215 (1994) 804.

13. M. Satou, K. Abe, and H. Kayano, IBID, 794.

14. D. S. Gelles and H. M. Chung, DOE/ER-0313/21, 79.

15. H. M. Chung, B. A. Loomis, and D. L. Smith, J. Nucl. Mater., 233-237 (1996) 466.

16. K. Fukumoto, H. M. Chung, J. Gazda, D. L. Smith, and H. Matsui, "Helium Behavior in Vanadium-Based Alloys Irradiated in the Dynamic Helium Charging Experiments," presented at the 18th ASTM International Symposium on Effects of Radiation on Materials, held June 1996 in Hyannis, MA, to be published.

OXIDATION KINETICS AND MICROSTRUCTURE OF V-Cr-Ti ALLOYS EXPOSED TO OXYGEN-CONTAINING ENVIRONMENTS*

K. Natesan (Argonne National Laboratory), M. Uz (Lafayette College, Easton, PA), and T. Ulie (Purdue University)

OBJECTIVE

The objectives of this task are to (a) evaluate the oxygen uptake of several V-Cr-Ti alloys as a function of temperature and oxygen partial pressure in the exposure environment, (b) examine the microstructural characteristics of oxide scales and oxygen trapped at the grain boundaries in the substrate alloys, and (c) evaluate the influence of alloy composition on oxygen uptake and develop correlation(s) between alloy composition, exposure environment, and temperature.

SUMMARY

A systematic study is being conducted to determine the effects of time, temperature, and exposure environment on the oxidation behavior and microstructure of V-Cr-Ti alloys. All samples were from 1-mm-thick cold-rolled sheets, and each was annealed in vacuum at 1050°C for 1 h prior to high-temperature exposure. Different samples from each alloy were heated in air and low -oxygen environments at temperatures between 400 and 650°C for times up to a few hundred hours. Some exposures were conducted in a thermogravimetric analysis (TGA) apparatus, in which continuous measurements of weight change were recorded.

EXPERIMENTAL PROGRAM

The alloys selected for evaluation included vanadium, V-10 wt.%Cr, V-4 wt.%Cr-4 wt.%Ti, V-5 wt.%Cr-5 wt.%Ti, V-10 wt.%Cr-5 wt.%Ti, and V-15 wt.%Cr-5 wt.%Ti alloys. The alloys were obtained in 1-mm-thick sheets. Samples measuring about 1 x 10 x 20 mm were cut from each alloy. Before any further treatment or testing, all samples were annealed for 1 h at 1050°C under a pressure of $\approx 10^{-6}$ torr. The samples were wrapped in tantalum foil to protect them from contamination during this heat treatment process. Samples from each alloy were heated in a TGA apparatus in air at different temperatures to determine oxidation kinetics as a function of temperature. The TGA experiments were carried out at temperatures in a range of 320-650°C. Weight gain was recorded continuously on a strip chart throughout each experiment [1,2]. All samples were also weighed separately before and after any high-temperature exposure to determine the resulting total weight change. In addition, specimens of several of the alloys were also exposed to low-pO_2 environments in a vacuum system with a feed and bleed arrangement. Oxygen pressure in the sample exposure chamber was maintained at 0.1, 4×10^{-4}, or 1×10^{-6} torr oxygen. Samples were retrieved periodically, weighed, and re-exposed to obtain kinetic data.

The oxide scales on the samples were identified by X-ray diffraction (XRD) analysis on the surfaces of several samples, as well as on the oxides scraped from their surfaces. Metallographic examination of the longitudinal and transverse cross-sections of the cold-rolled and thermally treated samples used both an optical microscope and a scanning electron microscope (SEM). The metallographic specimens were chemically etched with a solution of lactic-nitric-hydrofluoric acids at a volume ratio of 30-15-5. The grain sizes of each sample exposed to high temperature (annealed or oxidized) are being determined by both lineal and areal analysis methods according to ASTM Standard E112, and the average of the two is reported as the grain size of each sample. Oxygen diffusion depth (or the depth of the hardened layer) of each oxidized sample is being estimated from the microhardness profile along its thickness, which is obtained with a Vickers microhardness tester and a load of 25-50 g.

---

*This work has been supported by the U.S. Department of Energy, Office of Fusion Energy Research, under Contract W-31-109-Eng-38.

RESULTS

Extensive studies were conducted on the oxidation kinetics of V-4Cr-4Ti and V-5Cr-5Ti alloys over a temperature range of 300-650°C; the results were reported earlier [1-3]. The current oxidation study on several of the V-Cr-Ti alloys supplements the data developed earlier on those two alloys. Figure 1 shows normalized weight changes (in mg/mm^2), obtained by TGA, of several V-Cr-Ti alloys in air at temperatures in a range 475-550°C. Additional experiments are in progress at other temperatures and will be used to develop correlations between oxidation kinetics, alloy composition, and exposure temperature.

During this period, experiments were also continued to evaluate the influence of pO_2 on the oxidation kinetics of V-Cr-Ti alloys. Figure 2 shows the weight change data obtained for the two alloys in a pure oxygen environment at pressures of 0.1, 5×10^{-4}, and 5×10^{-6} torr and temperatures of 500, 600, and 700°C. The preliminary indication is that for a given exposure time, oxygen enrichment of the alloys at lower oxygen pressures may be greater due to absence of and/or differences in oxide type and morphology that develop at different pressures. The exposed specimens are being analyzed for oxide type by XRD and oxygen diffusion in the alloy by hardness measurements.

REFERENCES

[1] K. Natesan and W. K. Soppet, "Effect of Oxidation on Tensile Properties of a V-5Cr-5Ti Alloy," Proc. 2nd Intl. Conf. Heat-Resistant Materials, eds. K. Natesan, P. Ganesan, and G. Lai, ASM International, Sept. 11-14, 1995, Gatlinburg, TN, 375.

[2] K. Natesan and W. K. Soppet, "Effect of Oxygen and Oxidation on Tensile Properties of V-5Cr-5Ti Alloy," J. Nucl. Mater., in press, 1997.

[3] K. Natesan and M. Uz, "Oxidation Kinetics and Microstructure of V-(4-5) wt.%Cr-(4-5) wt.%Ti Alloys Exposed to Air at 300-650°C," Fusion Reactor Materials Semiannual Progress Report for Period Ending June 30, 1996, DOE/ER-0313/20, p. 105, Oct.1996.

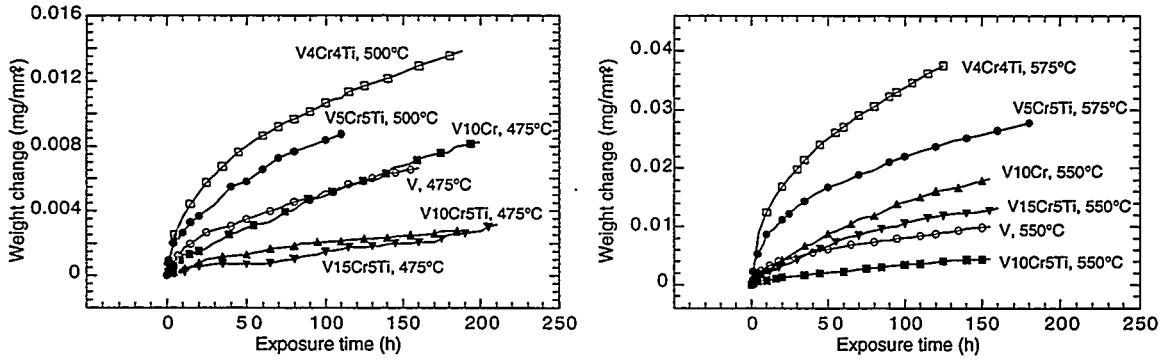

Figure 1. Thermogravimetric weight change data for several V-Cr-Ti alloys exposed to air at 475-550°C.

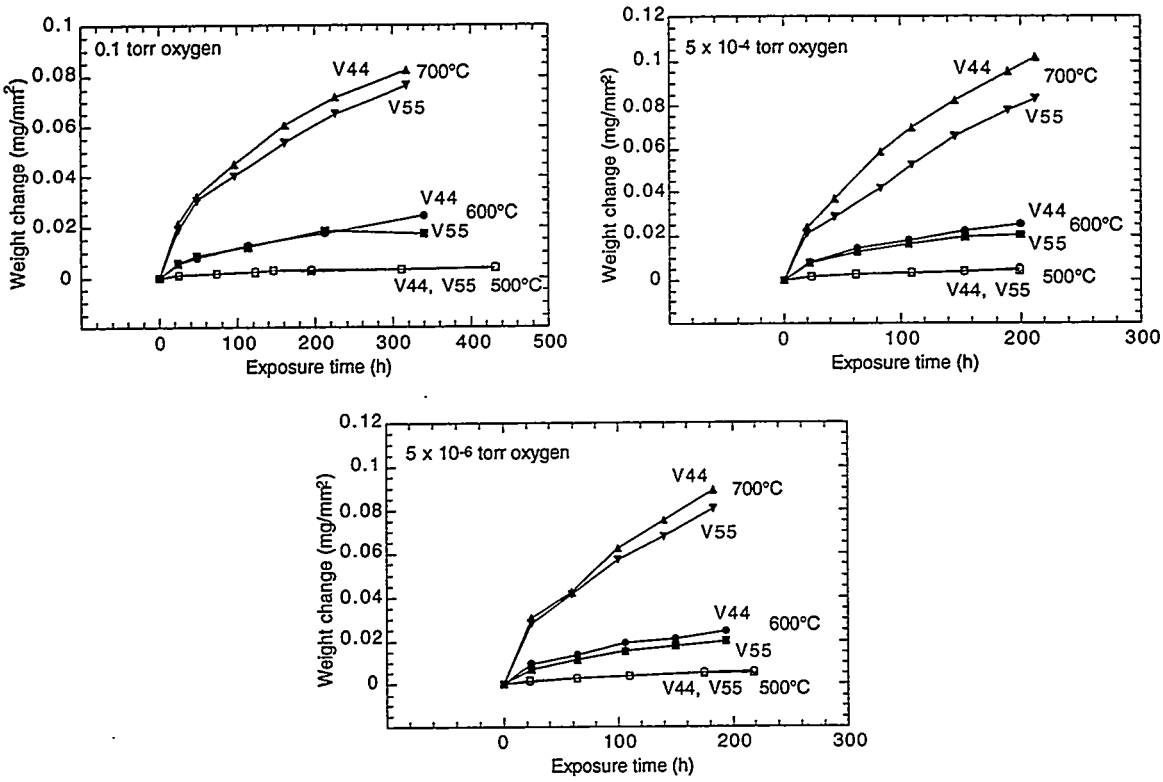

Figure 2. Weight change vs. time data for V-4Cr-4Ti and V-5Cr-5Ti alloys in oxygen environment at pressures of (top) 0.1 torr, (middle) 5 x 10^{-4} torr, and (bottom) 5 x 10^{-6} torr

TENSILE PROPERTIES OF ALUMINIZED V-5Cr-5Ti ALLOY AFTER EXPOSURE IN AIR ENVIRONMENT*

K. Natesan and W. K. Soppet (Argonne National Laboratory)

OBJECTIVE

The objectives of this task are to (a) develop procedures to modify surface regions of V-Cr-Ti alloys in order to minimize oxygen uptake by the alloys when exposed to environments that contain oxygen, (b) evaluate the oxygen uptake of the surface-modified V-Cr-Ti alloys as a function of temperature and oxygen partial pressure in the exposure environment, (c) characterize the microstructures of oxide scales and oxygen trapped at the grain boundaries of the substrate alloys, and (d) evaluate the influence of oxygen uptake on the tensile properties of the modified alloys at room and elevated temperatures.

SUMMARY

A pack diffusion process was used to enrich surface regions of V-5 wt.% Cr-5 wt.% Ti alloy specimens with aluminum, which is a more stable oxide former than vanadium; also, the oxide has a much slower growth rate than that of vanadium oxide. Oxidation studies were conducted on surface-modified V-5Cr-5Ti alloy specimens in an air environment to evaluate the oxygen uptake behavior of the alloy as a function of temperature and exposure time. Uniaxial tensile tests were conducted at 500°C on several preoxidized specimens of the surface-modified alloy to examine the effects of oxidation and oxygen migration on tensile strength and ductility.

EXPERIMENTAL PROGRAM

Detailed studies have been conducted earlier on oxidation and on effect of oxygen ingress on tensile properties of V-Cr-Ti alloys; results have beed reported elsewhere [1-3]. For the development of a surface modification approach to minimize oxidation of the alloy and to retain the mechanical properties of the base alloy, a heat of vanadium alloy with a nominal composition of V-5 wt.% Cr -5 wt.% Ti was selected; this heat was designated BL-63. A sheet of the alloy was annealed for 1 h at 1050°C prior to pack diffusion, oxidation, and tensile testing. Coupon specimens that measured ≈15 x 7.5 x 1 mm were used for the oxidation studies. Tensile specimens were fabricated according to ASTM Standard E8-69 specifications and had a gauge length of ≈19 mm and a gauge width of ≈4.5 mm.

Aluminum oxide is thermodynamically more stable than the oxides of the constituent elements (V, Cr, and Ti) of the vanadium alloy (see Fig. 1). Further, the growth rates of aluminum oxide is much slower than that of the refractory metal oxides such as vanadium or titanium oxide. Therefore, surface enrichment of the alloy with Al to develop aluminum oxide scale in oxidizing environments can protect the underlying alloy from further oxidation.

Surface aluminization of the V alloy was done by a pack-diffusion process in which the V-alloy substrate material was brought into contact with a pack of powders and heated for 4-12 h at ≈900°C. The composition of such powders (e.g., 65 wt.% Al_2O_3, 33 wt.% Al, 2 wt.% NH_4Cl) provided the packing with metallic Al, alumina as filler material, and NH_4Cl as activator. The Al deposited on the substrate surface diffuses into the subsurface regions of the material, where it forms intermetallic phases consisting of Al and V. Because the substrate material is heated to near the annealing range for times sufficient to cause solution processes in the matrix, the material needs a final treatment to optimize the structure. The aluminide layers reach thicknesses of 0.02–0.04 mm, depending on the composition of the substrate material. The high temperature of the formation process creates layers that develop compressive stresses at lower temperatures; thus, the layers do not contain cracks after preparation is complete.

*This work has been supported by the U.S. Department of Energy, Office of Fusion Energy Research, under Contract W-31-109-Eng-38.

Coupon specimens of bare and aluminized V-5Cr-5T alloy were oxidized in air at 400, 500, and 575°C in a thermogravimetric apparatus to evaluate their oxidation behavior. Surface-modified tensile specimens of V-5Cr-5Ti alloy were oxidized in air at 500°C for periods ranging from 164 to 2544 h. The preoxidized specimens were tensile-tested on an Instron machine at a constant crosshead speed of 0.02 cm/min, which corresponds to an initial strain rate of 1.8×10^{-4} s^{-1}. The test temperature was maintained within 2°C in all tests performed in air at 500°C. The specimens were loaded by means of pins that pass through holes in the grips and in the enlarged end sections of the specimen, thus minimizing misalignment. Total elongation was measured with a vernier caliper and by using load/elongation chart records. The fracture surfaces and longitudinal and axial cross sections of the tested specimens were examined by scanning electron microscopy (SEM). In addition, Vickers hardness was examined in several tested specimens.

RESULTS

Oxidation Behavior

Figure 2 shows weight change versus time for both bare and aluminized specimens. Oxidation of the alloys followed parabolic kinetics with respect to time. Detailed SEM analysis (with both energy-dispersive and wavelength-dispersive analysis) of the oxidized samples of bare alloy showed that the outer layer was predominantly vanadium-rich oxide and the inner layer was (V,Ti) oxide. Furthermore, X-ray diffraction of the oxides showed the outer oxide to be V_2O_5; no nitrogen or nitride phases were detected. The aluminized specimens exhibited much lower rates of oxidation at all temperatures in the present study. The oxidation rate at 575°C for the aluminized specimen was lower than that observed for the bare alloy at 575°C. Detailed microscopy and hardness measurements are in progress on the aluminized specimens.

Effect of Oxidation on Tensile Properties

To evaluate the effect of oxide scale formation and oxygen penetration into the substrate alloy, tensile behavior of the aluminized alloy was examined as a function of oxygen ingress and oxide scale formation. Specimens were exposed to air for 164-2544 h at 500°C and then tensile-tested in air at 500°C at a strain rate of 1.8×10^{-4} s^{-1}. Figure 3 shows the engineering stress/engineering strain curves at 500°C for specimens after oxidation for several exposure times up to 2544 h. Stress/strain behavior of the alloy is virtually unaffected by oxidation in air at 500°C.

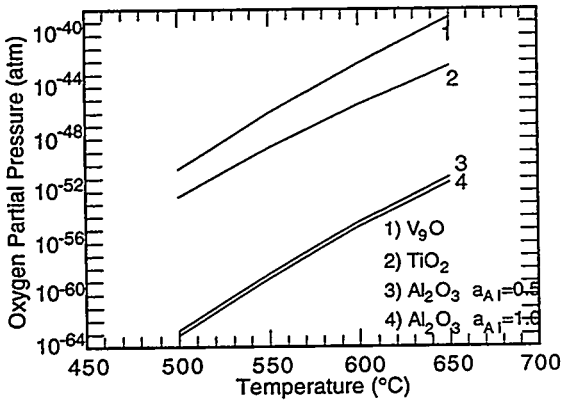

Figure 1. Stability of alumina compared with that of vanadium and titanium oxides. a_{Al} indicates aluminum activity in the alloy.

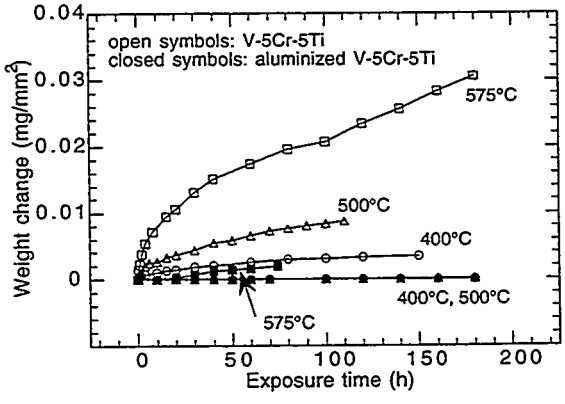

Figure 2. Weight change vs. time for bare and aluminized V-5Cr-5Ti specimens during oxidation in air

The load-displacement curves were analyzed by drawing lines parallel to the initial portion of the loading curve at the points of maximum load and rupture load. The intersects of these lines with the displacement axis are used to calculate the uniform and total elongation for the specimenssubjected to various oxidation treatments. This approach accounts for the stiffness, or lack of it, in the loading fixture of the tensile machine and, as a result, yields elongation values that are more representative of the gauge section of the tensile specimen.

Figures 4 and 5 show the variations in maximum engineering stress and uniform and total elongation as a function of preoxidation time in air at 500°C for tests conducted at 500°C on both bare and aluminized specimens. Figure 4 shows that the maximum tensile stress for the aluminized alloy was essentially the same over the oxidation period of 2544 h and is similar to the values observed for the oxidized V-5Cr-5Ti alloy. Figure 5 shows that total elongation for the

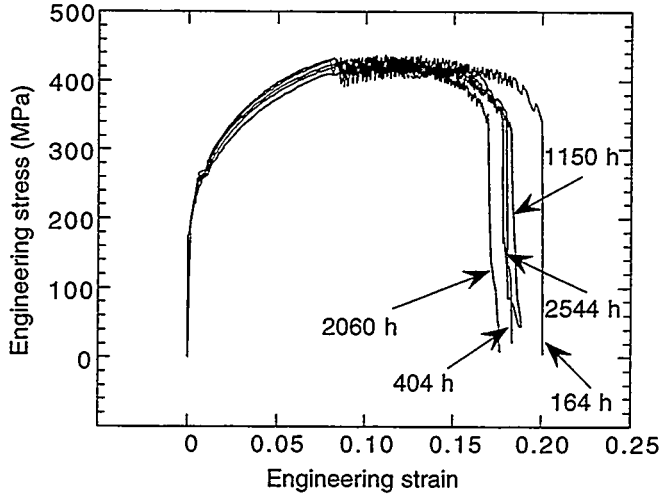

Figure 3. Effect of preoxidation at 500°C on stress/strain behavior of aluminized V-5Cr-5Ti alloy tested at 500°C in air at a strain rate of 1.8×10^{-4} s^{-1}.

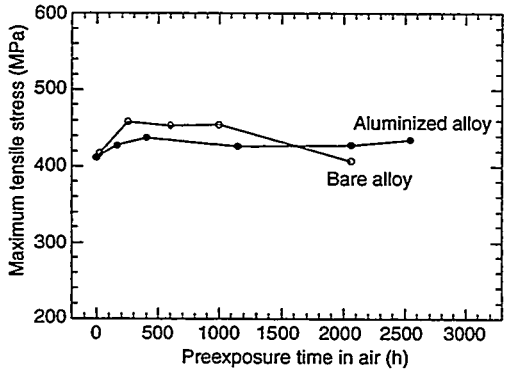

Figure 4. Maximum tensile stress as a function of preexposure time at 500°C in air for aluminized V-5Cr-5Ti alloy tensile-tested at 500°C in air.

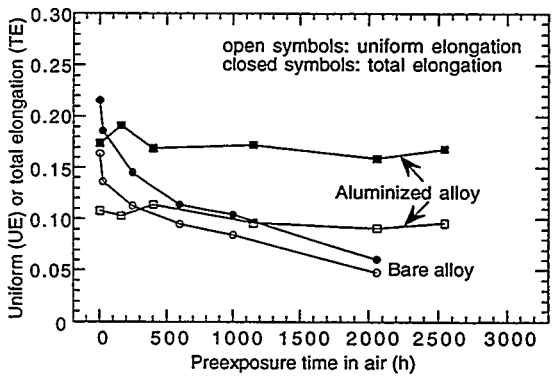

Figure 5. Uniform and total elongation as a function of preexposure time at 500°C in air for aluminized V-5Cr-5Ti alloy tensile- tested at 500°C in air.

aluminized alloys remains fairly high over the oxidation period of 2544 h, while that of the oxidizedbase alloy exhibited decreased total elongation with increase in oxidation time. The uniform elongation for the aluminized specimens was lower (≈0.11) but remained constant over theoxidation period. These results indicate that the drop in uniform elongation occurs during the aluminizing process, which is conducted at 900°C. We believe that the initial drop in uniform elongation can be minimized by optimizing the aluminizing process with regard to time and temperature.

REFERENCES

1. K. Natesan and W. K. Soppet, "Effect of Oxidation on Tensile Behavior of V-Cr-Ti Alloys," Fusion Reactor Materials Progress Report for Period Ending March 31, 1995, Argonne National Laboratory, DOE/ER-0313/18, p. 247, July 1995.

2. K. Natesan and W. K. Soppet, "Effect of Oxidation on Tensile Behavior of a V-Cr-Ti Alloy," Proc. 2nd Intl. Conf. on Heat Resistant Materials, ASM International, Materials Park, OH, p. 375 (1995).

3. K. Natesan and W. K. Soppet, "Effect of Oxygen and Oxidation on Tensile Behavior of V-5Cr-5Ti," Fusion Reactor Materials Progress Report for the Period Ending Dec. 31, 1995, Argonne National Laboratory, DOE/ER-0313/19, p. 50, April 1996.

HEAT TREATMENT EFFECTS ON TENSILE PROPERTIES OF V-(4-5) WT.% Cr-(4-5) WT.% Ti ALLOYS*

K. Natesan and W. K. Soppet (Argonne National Laboratory)

OBJECTIVE

The objectives of this task are to (a) examine the influence of thermomechanical treatments on microstructural development in V-Cr-Ti alloys and (b) assess the impact of changes in microstructures on the mechanical properties of these alloys.

SUMMARY

Effects of thermomechanical treatments on microstructures and mechanical properties are of interest for long term application of V-Cr-Ti alloys in fusion reactor systems. Influence of thermal annealing at 1050°C on stress/strain behavior, maximum engineering strength, and uniform and total elongation were evaluated. The results show that multiple annealing has minimal effect on the tensile properties of V-(4-5)Cr-(4-5)Ti alloys tested at room temperature and at 500°C.

EXPERIMENTAL PROGRAM

Thermomechanical treatments can have a significant effect on the development of microstructures that can lead to changes in the bulk mechanical properties of the materials, especially for refractory alloys such as V-base alloys. As a first step, we are evaluating the role of annealing in the development of microstructures and tensile properties. The heats of the vanadium alloy selected for the study had nominal compositions of V-5 wt.% Cr -5 wt.% Ti (designated BL-63) and V-4 wt.% Cr -4 wt.% Ti (designated BL-71). Sheet tensile specimens were fabricated according to ASTM Standard E8-69 specifications and had a gauge length of ≈19 mm and a gauge width of ≈4.5 mm. Specimens of the two alloys were wrapped in a tantalum foil and given an annealing cycle of heating up to 1050°C in $\approx 10^{-6}$ torr vacuum, a hold for 1 h at 1050°C, and slow-cooling in the furnace. The specimens were given either one, two, or three annealing cycles.

The annealed specimens were tensile-tested in air at room temperature and at 500°C. Crosshead speed in the Instron machine was set to yield a strain rate of 1.8×10^{-4} s^{-1} for all tests. The specimens were loaded by means of pins that pass through holes in the grips and in enlarged end sections of the specimen, thus minimizing misalignment. Total elongation was measured with a vernier caliper and by using load/elongation chart records. The fracture surfaces and longitudinal and axial cross sections of tested specimens were examined by scanning electron microscopy (SEM). In addition, Vickers hardness and grain size of several of tested specimens are being measured.

RESULTS AND DISCUSSION

Engineering stress/engineering strain data for V-Cr-Ti alloys in as-rolled condition and after single anneal treatments were reported earlier [1,2]. Stress/strain behavior of the alloys showed that the as-rolled material possess high tensile strength and low tensile ductility at both test temperatures. Materials subjected to one anneal cycle at 1050°C exhibited substantial reduction in tensile strength with an improvement in tensile ductility. Figure 1 shows the engineering stress/engineering strain curves from tests at room temperature and 500°C, for V-4Cr-4Ti and V-5Cr-5Ti specimens subjected to either two or three anneal treatments. The effect of multiple annealing is negligible on the room temperature tensile properties of either of the alloys. At

*This work has been supported by the U.S. Department of Energy, Office of Fusion Energy Research, under Contract W-31-109-Eng-38.

500°C, the stress/strain curves for both alloys are similar up to the maximum stress value but the rupture strains are somewhat smaller for V-4Cr-4Ti when compared with those for V-5Cr-5Ti alloy. The test at 500°C normally takes about 2 hours of heat up/thermal equilibration in air during which time some oxidation of the alloys occurs. Since V-4Cr-4Ti exhibits a slightly higher oxidation rate than V-5Cr-5Ti alloy [3], this increased oxygen uptake may have contributed to lower values of total elongation for the V-4Cr-4Ti alloy.

The load-displacement curves were analyzed by drawing lines parallel to the initial portion of the loading curve at the points of maximum load and rupture load. The intersects of these lines with the displacement axis are used to calculate the uniform and total elongation for the specimens subjected to different annealing treatments. This approach accounts for the stiffness, or lack of it, in the loading fixture of the tensile machine and, as a result, yields elongation values that are more representative of the gauge section of the tensile specimen.

Figure 2 shows the variations in maximum engineering stress for specimens in as-rolled condition and after single and multiple annealing treatments and tested in air at room temperature and at 500°C. The data indicate that for a given alloy and temperature, multiple anneal has little effect on maximum stress values. The maximum stress values are consistently lower by ≈5-10% for both alloys as the temperature increases from room temperature to 500°C and number of anneals has negligible effect.

Figures 3 and 4 show the variations in uniform and total elongation for the two alloys in as-rolled condition and annealing treatments. Uniform and total elongation values are higher at room temperature than at 500°C, for both alloys used in this study. Multiple anneal has small effect on either uniform or total elongation of both the alloys. Measurements of grain size of V-4Cr-4Ti alloy with different annealing treatments showed virtually no grain growth, which is consistent with grain size data for the alloy up to 2000 h at 1000°C reported earlier[3].

REFERENCES

1. K. Natesan and W. K. Soppet, "Effect of Oxygen and Oxidation on Tensile Behavior of V-5Cr-5Ti," Fusion Reactor Materials Semiannual Progress Report for Period Ending December 31, 1995, Argonne National Laboratory, DOE/ER-0313/19, p. 50, April 1996.

2. K. Natesan and W. K. Soppet, "Tensile properties of V-Cr-Ti alloys after exposure in helium and low-partial-pressure oxygen environments," Fusion Reactor Materials Semiannual Progress Report for Period Ending December 31, 1996, Argonne National Laboratory, DOE/ER-0313/21, p. 40, April 1997.

3. K. Natesan, W. K. Soppet, M. Uz, and T, Ulie, "Corrosion Compatibility," Presented at the Workshop on Vanadium Alloy Development, Argonne National Laboratory, March 11-13, 1997.

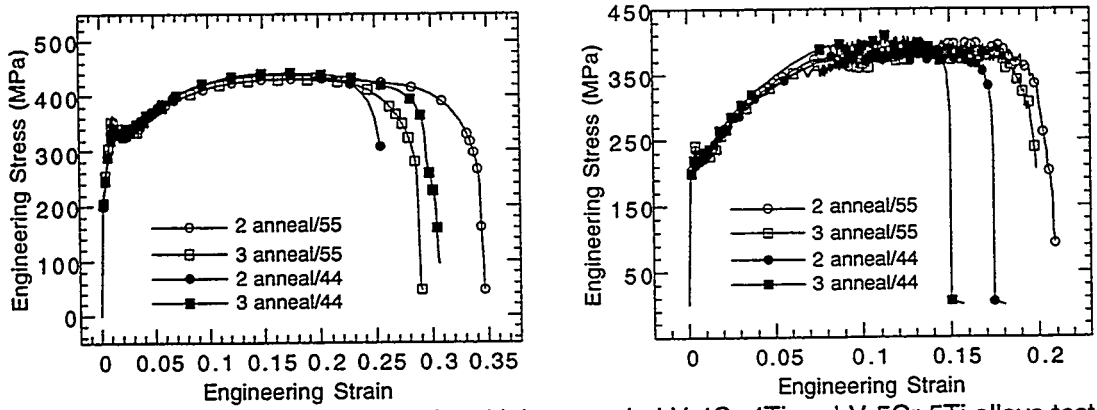

Figure 1. Stress/strain behavior of multiple-annealed V-4Cr-4Ti and V-5Cr-5Ti alloys tested at (left) room temperature and (right) 500°C, in air at a strain rate of 1.8×10^{-4} s^{-1}

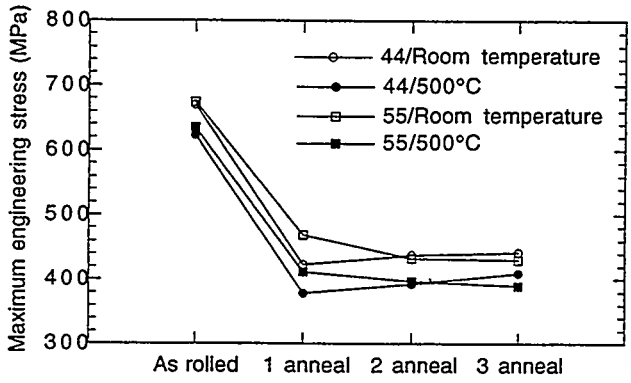

Figure 2. Maximum tensile stress for V-4Cr-4Ti and V-5Cr-5Ti alloys in as-rolled condition and after annealing treatments

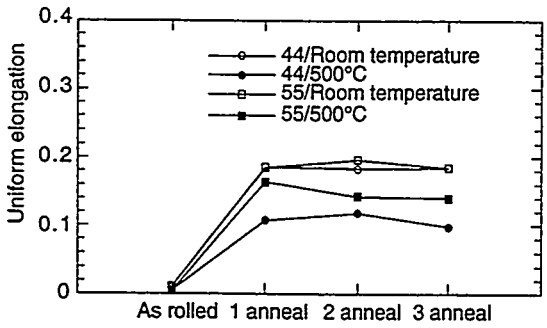

Figure 3. Uniform elongation for V-4Cr-4Ti and V-5Cr-5Ti alloys in as-rolled condition and after annealing treatments

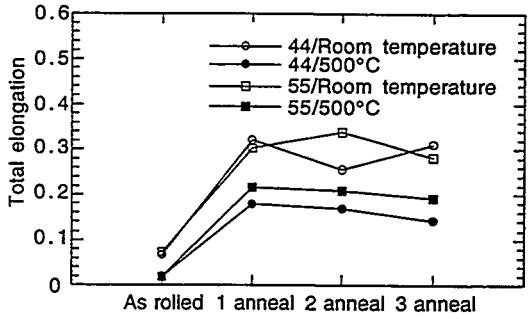

Figure 4. Total elongation for V-4Cr-4Ti and V-5Cr-5Ti alloys in as-rolled condition and after annealing treatments.

Study of Irradiation Creep of Vanadium Alloys* H. Tsai, R. V. Strain, and D. L. Smith (Argonne National Laboratory), and M. L. Grossbeck (Oak Ridge National Laboratory)

Summary

Thin-wall tubing was produced from the 832665 (500 kg) heat of V-4 wt.% Cr-4 wt.% Ti to study its irradiation creep behavior. The specimens, in the form of pressurized capsules, were irradiated in Advanced Test Reactor and High Flux Isotope Reactor experiments (ATR-A1 and HFIR RB-12J, respectively). The ATR-A1 irradiation has been completed and specimens from it will soon be available for postirradiation examination. The RB-12J irradiation is not yet complete.

Objective

Vanadium alloys are candidates for first-wall/blanket structural materials in fusion reactors, because of their attractive high-temperature properties and low activation. Although many of the properties have been extensively studied, irradiation-induced creep has not received much attention. Data on irradiation creep are important because creep is one of the principal contributors to deformation and is potentially performance limiting. The objective of this task to determine the creep rate under various loading and irradiation conditions.

Experimental Procedure

Creep Tube Fabrication

The starting material for fabrication of the tubing was a 28.6-mm-thick plate from the 832665 heat of V-4 wt.% Cr-4 wt.% Ti. Two 28.6 x 28.6 x 200-mm bars, with the long dimension parallel to the rolling direction, were cut from the plate and used in our experiments. An industrial vendor performed the tube fabrication according to specifications provided by Argonne National laboratory.

The two square bars were pressed straight and a 19.1-mm-diam hole was gun drilled through the center. The bars were then turned round to an OD of 27.9 mm concentric to the drilled hole. Following cleaning and vacuum annealing at ≈1025°C for 1 hr, the two pieces were drawn at room temperature in three steps, each producing an areal reduction of 12-15%. After the total areal reduction of ≈40%, the bars were cleaned, annealed and drawn again. This cleaning/annealing/ drawing operation was repeated eight times to produce finished tubing with a nominal 4.57-mm OD, 4.06 mm ID, and ≈45% cold work. To limit the impurity uptake during the process, all annealing was conducted with the pieces wrapped in Ti getter foil. The intermediate tubes were shortened, whenever necessary, to fit them in the vendor's small annealing furnace, which gave a better vacuum (≈7×10^{-5} torr) than their big furnace. Approximately 12 m of tube sections of various lengths was produced in this manner.

Sections of the finished tubing were analyzed for major alloying elements and interstitial impurities according to ASTM testing methods E-663 and E-1019. The results, shown in Table 1, indicate discernible uptake of interstitial impurities. The extent of the uptake, however, is limited and not expected to have a deleterious effect on material performance.

* Work Supported by Office of Fusion Energy, U.S. Department of Energy, under Contract W-31-109-Eng-38.

Table 1. Results of Analysis of Finished Creep Tubing

Element	Finished Tubing	Starting Material
O (wppm)	560	310
N (wppm)	95	85
C (wppm)	300	80
Cr (wt.%)	3.6	3.8
Ti (wt.%)	3.5	3.9
V (wt.%)	92.4	Bal.

Attempts were made to inspect the finished tubes by either ultrasonic or eddy-current methods; however, the trials were unsuccessful because of the small dimensions of the tubing and the demanding specification for flaw detection (<0.025-mm flaw size). Radiography was the only nondestructive method used to evaluate the internal condition of the tubing. The radiographs were taken along with a machined defect standard (0.025-mm-deep longitudinal groove in a creep tube) to establish the sensitivity of every exposure. Tube sections with any questionable mass densities were excluded from use as specimens.

The 25.4-mm-long tube blanks intended for making test specimens were measured for OD, ID, OD roundness, ID roundness, concentricity and wall thickness. These measurements were performed at two axial (8.4 mm from each end) and 8 azimuthal (45° interval) locations with a coordinate measurement machine. The results showed the dimensional attributes, in particular, the standard deviations, of these sections to be excellent. For example, for the 16 tubing sections that were selected for the ATR-A1 experiments, the measurements yielded an average ID of 4.041 ± 0.002, an average OD of 4.569 ± 0.001, ID roundness of 0.007 ±0.003, OD roundness of 0.005 ±0.002, concentricity of 0.007 ± 0.003, and wall thickness of 0.264 ± 0.001 (all in mm).

Creep Specimen Fabrication

The creep specimens are 25.4-mm-long tubes with welded end plugs, as shown in Fig. 1. The end plugs were produced by electro-discharge machining of plate stock. The circumferential plug-to-tube welds were made with an electron-beam welder in vacuum. The specimens were then vacuum annealed at 1000°C for 1.0 h while wrapped in Ti foil. They were then pressurized, through a 0.25-mm-diam hole in the top end plug, in a pressue chamber that contained high-purity helium. The final closure weld of the 0.25-mm-diam hole was made with a laser through the quartz window in the chamber. The calculated hoop stresses in the specimens for the two experiments are shown in Table 2. The specified pressure loading was determined with a code that takes into account the thermal expansion of the creep tubing and the compressibility of the helium gas. Following a leak check, the dimensions of the assembled creep specimens were measured with a precision laser profilometer at five axial and 19 azimuthal locations to an accuracy of 10^{-4}mm.

Fig. 1. Schematic of Creep Specimens

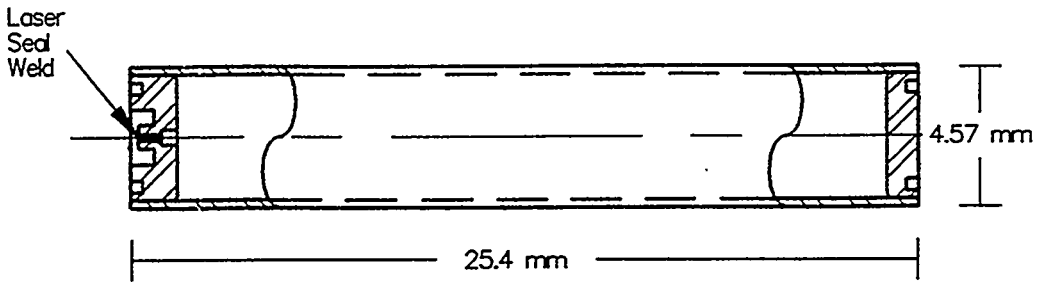

Table 2. Nominal Hoop Stress in the ATR-A1 and HFIR-RB-12J Creep Specimens

Experiment	Target Temp. (°C)	Specimen No.	Nominal Midwall Hoop Stress (MPa)
ATR-A1	200	A5	0
		A4	100
		A2	150
		A3	200
	300	A1	0
		A10	100
		A7	150
		A11	200
HFIR 12J	500	B1	0
		B12	50
		B11	100
		B3	150
		B9	150
		B5	200

Status of Experiments

The irradiation of the ATR-A1 experiment is completed and the creep specimens have been retrieved from the irradiation capsule and subcapsules. Preliminary data from subcapsule gas sampling indicate that all specimens are intact after irradiation. The RB-12J experiment is still ongoing in the HFIR reactor.

Future Activities

The diameters of the irradiated specimens will be measured again, with the same laser profilometer. The stress and temperature dependence of the creep strains will be evaluated. The stress-free swelling of the material from the 0 MPa specimens will also be evaluated. These

results will be compared with the limited previously-published in-reactor creep data on vanadium alloys. The microstructure of the creep tubes, particularly the dislocation morphology, will be evaluated from the stand point of correlating it with the observed creep behavior.

RECENT PROGRESS ON GAS TUNGSTEN ARC WELDING OF VANADIUM ALLOYS — M. L. Grossbeck, J. F. King, D. J. Alexander, and G. M. Goodwin (Oak Ridge National Laboratory)

OBJECTIVE

The goal of this research is to acquire a fundamental understanding of the metallurgical processes in welding vanadium alloys and develop techniques for joining structural components of these alloys.

SUMMARY

Emphasis has been placed on welding 6.4 mm plate, primarily by gas tungsten arc (GTA) welding. The weld properties were tested using blunt notch Charpy testing to determine the ductile to brittle transition temperature (DBTT). Erratic results were attributed to hydrogen and oxygen contamination of the welds. An improved gas clean-up system was installed on the welding glove box and the resulting high purity welds had Charpy impact properties similar to those of electron beam welds with similar grain size. A post-weld heat treatment (PWHT) of 950°C for two hours did not improve the properties of the weld in cases where low concentrations of impurities were attained. Further improvements in the gas clean-up system are needed to control hydrogen contamination.

INTRODUCTION

The susceptibility of vanadium alloys to interstitial embrittlement raises concerns with welding large fusion system components, and the selection of welding methods will have a strong economic impact on component fabrication. The gas tungsten arc (GTA) and electron beam (EB) welding processes are being evaluated in V-4Cr-4Ti with particular emphasis on interstitial contamination.

EXPERIMENTAL RESULTS AND DISCUSSION

It was shown earlier that electron beam welds can be made with satisfactory properties in 6.4 mm plate of V-4Cr-4Ti. A DBTT on the order of -100°C has been achieved. However the technique does not lend itself for use in welding large components because of the requirement for a large vacuum chamber. Other processes such as GTA will be needed, but contamination by impurities in the inert gas atmosphere is a persistent problem. As a result, most of the recent research has focused on the GTA welding process.

A plate of V-4Cr-4Ti, Wah Chang heat 832665, 6.4 mm in thickness was prepared for welding by machining to form a beveled groove between two plates with a 75° included angle. Multi-pass welds with nine passes using filler metal wire fabricated from the same alloy and heat as the base metal were made using GTA welding. This technique was chosen as the standard for the present series of tests. Following welding, Charpy specimens 25.4 mm in length by 3.3 mm square with a notch depth of 0.66 mm and a root radius of 0.076 mm were cut in the L-T direction with respect to the original plate. The notch was cut such that the crack propagated entirely within weld metal, parallel to the weld direction.

Previously reported results indicated that the DBTT for GTA welds could exceed 200°C, and that a PWHT of 950°C for 2 hours could replace the DBTT to around room temperature. However the results were plagued by occasional lower shelf behavior in cases where specimens tested at lower temperatures exhibited upper shelf behavior. Such erratic results were sufficiently frequent to warrant further investigation. Fractography revealed that the

lower shelf fracture was almost entirely by cleavage. Inert gas fusion analysis was used to determine the concentrations of interstitials in the weld and base metal of a random selection of welds.[1] Table 1 presents the results of these analyses. Oxygen concentrations were elevated in several of the welds, as expected. However, hydrogen contamination was indicated in GTA 11, GTA 2, and GTA 3. Hydrogen embrittlement is consistent with the observation of cleavage fracture. However, unpredictable cleavage fractures also occurred in specimens which had been given a PWHT of 950°C for 2 h in vacuum, which should be adequate to remove hydrogen from the specimens. It was therefore concluded that the hydrogen-induced cracks must be present prior to the PWHT, and this was confirmed in the case of GTA 11, which cracked during specimen fabrication. X-ray CAT scans revealed a number of cracks in the as-welded plate.

Table 1. Results of analyses for interstitials in V-4Cr-4Ti welds (Wt. ppm)

Base Metal	Weld Metal	H	O	N	C
	GTA 11	58.5	446	288	
GTA 11		53.5	364	96	
Virgin V-4Cr-4Ti					
Etched		1.2			
Weld Wire			360	109	155
	EBW 11	36.4	327	99	
EBW 11		23.1	323	99	
	GTA 2 (VQ11)	11.2			
	GTA 2 (V909)	10.1			
	GTA 3	20.5			
	GTA 8		410	98	
GTA 8			332	96	
	EB 2	2.8			
	EB 12	7.9			

The elevated hydrogen concentration in GTA 11 could have resulted from an air leak in the glove box since oxygen and nitrogen were also high in this weld. However, this does not explain the elevated concentrations in other welds. The system was leak checked and a small leak repaired. In addition, a purification system was added which consisted of a molecular sieve moisture trap followed by a hot titanium sponge oxygen getter system. Gas was withdrawn from the glove box and recirculated using a sealed bellows pump.

Using the purification system, weld GTA 13 was made in an argon atmosphere of 4 wt. ppm oxygen and 23 wt. ppm water. As shown in Table 2 and Fig. 1, an oxygen concentration of 374 wt. ppm and a nitrogen concentration of 104 wt. ppm were achieved, and the resulting DBTT was at ~57°C, with evidence of erratic fracture behavior. In order to examine further the effect of atmosphere impurities, weld GTA 14 was made with an intentionally contaminated environment containing 14 wt. ppm oxygen and 84 wt. ppm water. These conditions resulted in 352 wt. ppm oxygen, 110 wt. ppm nitrogen, and 21 wt. ppm hydrogen in the fusion zone of the weld. The DBTT was raised slightly to 82°C. Weld GTA 15 was made with higher levels of impurities, 27 wt. ppm oxygen and 260 wt. ppm water, and the weld contained 412 wt. ppm oxygen, 146 wt. ppm nitrogen, and 15 wt. ppm hydrogen. Charpy specimens failed in a brittle mode at ~100°C and the DBTT was raised to ~288°C (Fig. 1).

[1]Analyses were performed by Leco, Inc. of St. Joseph, MI.

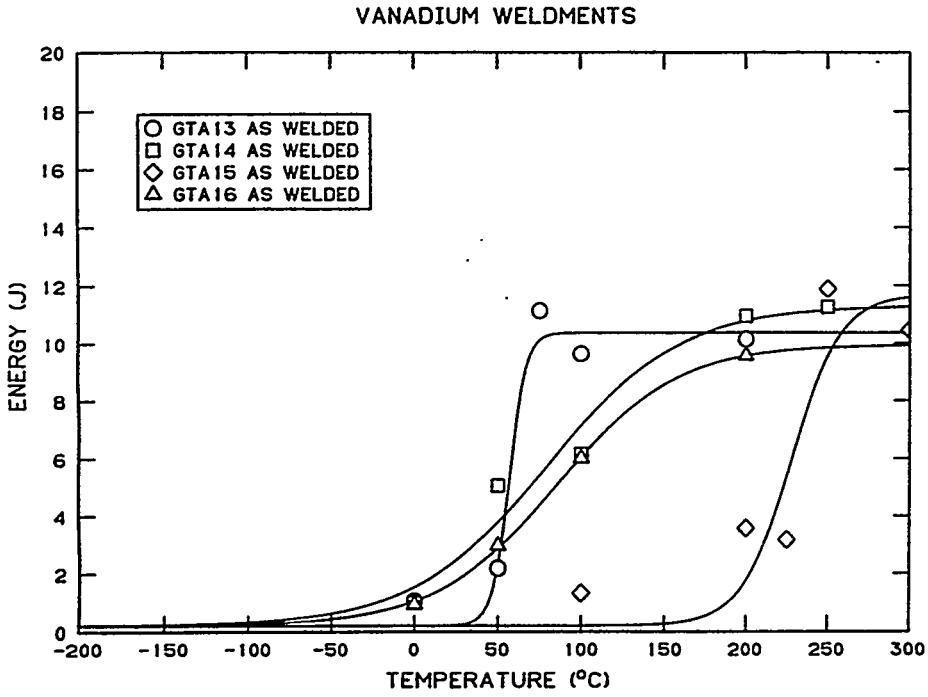

Fig. 1. Charpy impact curves for V-4Cr-4Ti GTA welds in the as welded condition.

A PWHT of 950°C for two hours was applied to all three welds. The results, shown in Fig. 2 and Table 2, demonstrate that little change resulted in GTA 13 and GTA 14, but the high DBTT of GTA 15 was reduced to a level similar to that of the other welds. It appears that the heat treatment, which precipitates oxygen in the form of titanium oxides, improves a contaminated weld, but does little or nothing to an already clean weld, a very significant result considering the difficulty in performing such a high temperature PWHT in the field.

Table 2. Parameters for Impurity Test Series of Welds

		Welding Atmosphere		Fusion Zone Concentration			
Weld	PWHT	Oxygen Wt. ppm	Moisture Wt. ppm	Oxygen Wt. ppm	Nitrogen Wt. ppm	Hydrogen Wt. ppm	DBTT °C
GTA 13	as welded	4	23	374	104		57
GTA 13	950°C/2h						60
GTA 14	as welded	14	84	352	110	21	82
GTA 14	950°C/2h						80
GTA 15	as welded	27	260	412	146	15	228
GTA 15	950°C/2h						86
GTA 16	as welded	0.8	25	370	107		85
GTA 16	950°C/2h						38

To further confirm the effect of contamination on weld properties, GTA 16 was made with atmospheric impurity levels still lower than those for GTA 13. The impurity concentrations and DBTT values are again shown in Table 2. The welding atmosphere had 0.8 wt. ppm oxygen and 25 wt. ppm water in argon which resulted in an oxygen level of 370 wt. ppm and a nitrogen level of 107 wt. ppm in the fusion zone of the weld. The oxygen level in the base metal was 336 wt. ppm, thus the oxygen level increased during welding by only 10%. In spite of the lower levels of oxygen and moisture in the glove box atmosphere, the DBTT for this weld was

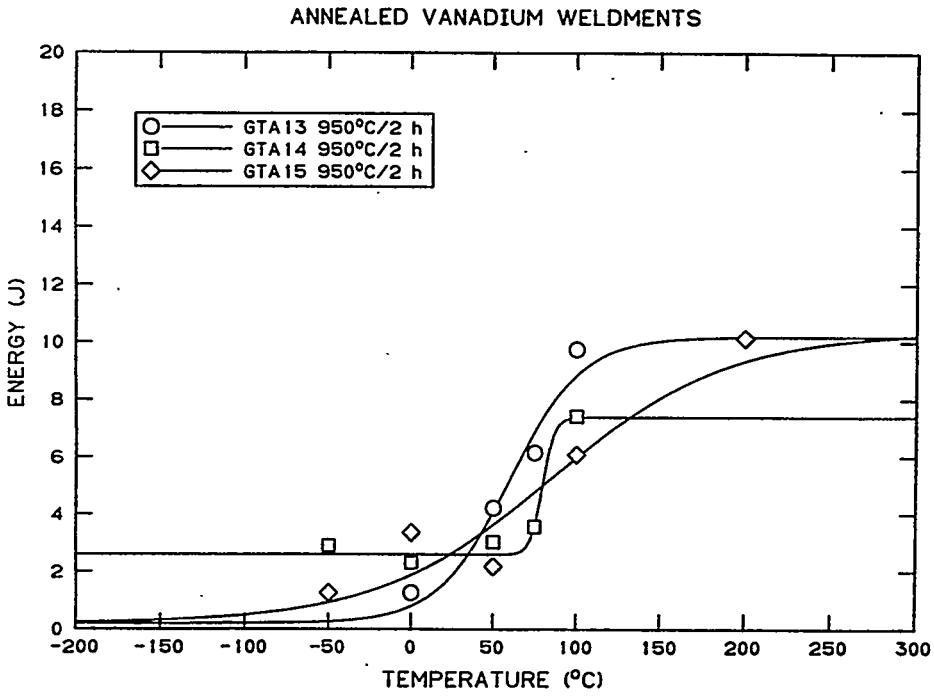

Fig. 2. Charpy impact curves for V-4Cr-4Ti TTA welds following an oxygen precipitation post weld heat treatment of 950°C for two hours.

no better than those for welds GTA 13 and GTA 14. However, the hydrogen concentration in the weld was determined to be unexpectedly high (~63 wt. ppm). An out gassing heat treatment of 400°C for 1 hour was performed and the Charpy tests repeated; the curve shown in Fig. 3 shows an improvement in DBTT to 38°C, but a return of the erratic behavior illustrated by the specimen tested at 100°C, which failed by cleavage. It was concluded that cracking was present prior to the out-gassing treatment at 400°C, indicating that further improvements in the gas purification system are needed.

The titanium sponge in the purification system is held at 600-800°C. At this temperature, water is reduced and oxygen is readily reacted to form titanium oxide, but no hydride of titanium is stable. Hydrogen is, therefore, passed along into the glove box. Clearly the molecular sieve trap is not adequate to remove moisture from the system so that an additional hydrogen trap will be necessary.

These results are significant in that they illustrate that high purity GTA welds can be made and that they may not require a post-weld heat treatment. Further work remains to be done on controlling hydrogen, and grain size refinement remains to be investigated.

CONCLUSIONS

1. Low interstitial content welds can be made by the gas tungsten arc method using a high-purity glove box atmosphere with special purification.

2. A high-temperature post-weld heat treatment for oxygen precipitation may not be necessary if the atmosphere can be made sufficiently pure.

3. Hydrogen is easily incorporated into vanadium alloy welds and can cause cracking.

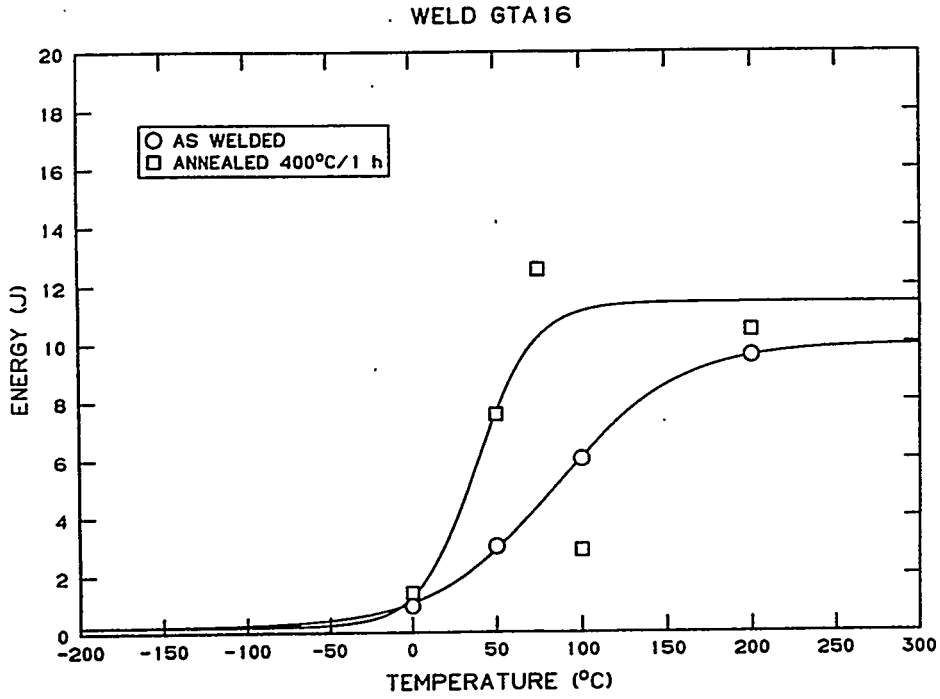

Fig. 3. Charpy impact curves for V-4Cr-4Ti weld GTA 16 in both the as welded condition and following a hydrogen out gassing heat treatment of 400°C for 1 h.

2.0 SILICON CARBIDE COMPOSITE MATERIALS

INVESTIGATION OF REACTIVITY BETWEEN SiC AND Nb-1Zr IN PLANNED IRRADIATION CREEP EXPERIMENTS - C. A. Lewinsohn (Associated Western Universities), M. L. Hamilton, and R. H. Jones (Pacific Northwest National Laboratory)*

OBJECTIVE

The objective of this study is to determine whether detrimental reactions will occur between silicon carbide (SiC) composites and niobium-1wt% zirconium (Nb-1Zr) during experiments intended to measure the irradiation creep properties of the composites. The experiment designed to measure the creep of SiC fiber-reinforced, chemically vapor infiltrated SiC composites under irradiation involves using a Nb-1Zr pressurized bladder in contact with a cylindrical SiC composite. Data regarding the compatibility between Nb-1Zr and SiC are not available. Therefore, the reactivity between Nb-1Zr and SiC is investigated by using a computer program (Chemsage) capable of calculating the Gibbs free energy of formation for all compounds within the program database that can exist for a given thermodynamic state (pressure, temperature, number of moles). The actual reaction that will occur, however, will be limited by the kinetics of the transport mechanisms and the chemical reactions. A series of diffusion couple experiments aimed at gathering information on the kinetic aspects of the reactivity between Nb-1Zr and SiC is described.

SUMMARY

Thermodynamic calculations and diffusion couple experiments showed that SiC and Nb-1Zr were reactive at the upper range of temperatures anticipated in the planned irradiation creep experiment. Sputter-deposited aluminum oxide (Al_2O_3) was selected as a diffusion barrier coating. Experiments showed that although the coating coarsened at high temperature it was an effective barrier for diffusion of silicon from SiC into Nb-1Zr. Therefore, to avoid detrimental reactions between the SiC composite and the Nb-1Zr pressurized bladder during the planned irradiation creep experiment, a coating of Al_2O_3 will be required on the Nb-1Zr bladder.

PROGRESS AND STATUS

Introduction

Silicon carbide fiber-reinforced silicon carbide matrix composites (SiC_f/SiC_m) are attractive materials for fusion energy systems for a variety of reasons[1-6]. The radioactivation of these composite materials is expected to be very low and would in fact be dominated by the activation of impurity elements[1-3]. These impurities most likely can be controlled to produce a truly low-activation material, especially via the chemical vapor infiltration (CVI) forming technique. Toughening mechanisms, such as matrix cracking, crack deflection, interface debonding, crack-wake bridging, and fiber pullout, provide ceramic matrix composites (CMCs) with a greater reliability against catastrophic failure processes than unreinforced ceramics[7]. A fundamental understanding of the mechanisms that control the lifetime of these materials is required.

---

* Pacific Northwest National Laboratory is operated for the U. S. Department of Energy by Battelle Memorial Institute under Contract DE-AC06-76RLO 1830.

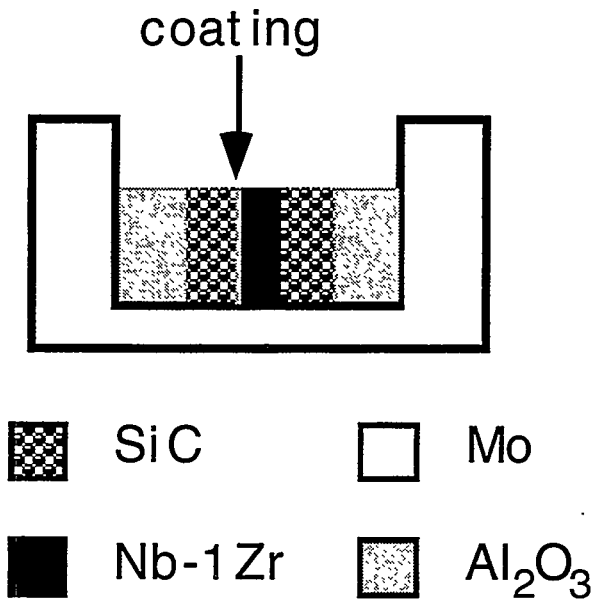

Figure 1. Schematic drawing of the fixture used for diffusion couple experiments.

Very little data for the irradiation creep of SiC is available[8-10]. The data indicates that the creep of SiC is enhanced by radiation and possesses a temperature insensitive regime, similar to many metals. No data exists for the irradiation creep behavior of SiC_f/SiC_m. Irradiation creep is one of the major processes by which the dimensional stability of structural components can be altered by radiation exposure. The thermal creep behavior of SiC_f/SiC_m is not very well understood, either. Therefore, experiments have been designed to measure the irradiation creep response of SiC_f/SiC_m composites.

The experiment designed to measure the creep of SiC_f/SiC_m composites under irradiation involves using a Nb-1Zr pressurized bladder in contact with, and surrounded by, a cylindrical SiC composite[11]. Data regarding the compatibility between Nb-1Zr (Nb-1Zr) and SiC (SiC), at elevated temperatures, are not available. Therefore, efforts were made to investigate the thermodynamic stability of Nb-1Zr and SiC and also to investigate the kinetics of possible reactions. The results of this work are presented in this report.

Experimental Technique

An experimental approach was used to determine the kinetic stability of an Al_2O_3 coating with Nb-1Zr and β-SiC. β-SiC refers to the cubic polytype of SiC, also known as 3C, which composes the matrix of the SiC_f/SiC_m composites of interest to this study. Fixtures, procedures, and analytical methods were designed and verified for these experiments. The fixtures consisted of a molybdenum holder and alumina inserts to hold a sandwich of Nb-1Zr between two pieces of β-SiC (Fig. 1). The Nb-1Zr was the same material as that which will be used to form the pressurized bladders. The β-SiC was fabricated by chemical vapor deposition, so that it would be similar to the matrix of the composite, and supplied by Morton Advanced Materials, Woburn, MA. One side of the Nb-1Zr was coated with a 1 μm thick layer of Al_2O_3. The coating was deposited, at room temperature, by

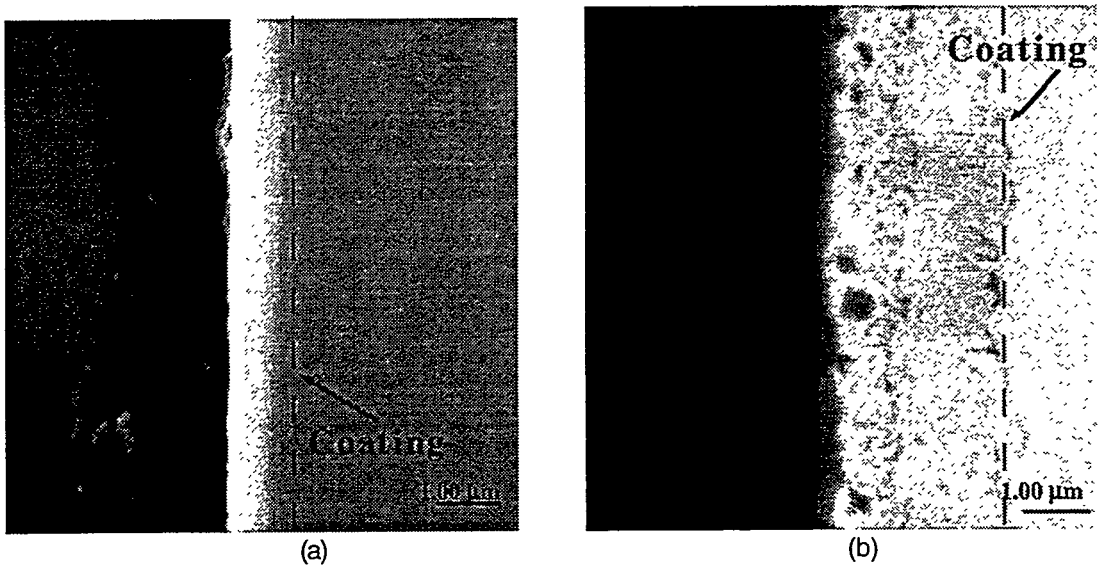

Figure 2. SEM micrograph of the Al_2O_3 coating (a) before and (b) after treatment at 400 h at 1000°C, in flowing argon. Dashed line indicates approximate edge of coating.

electron-beam sputter deposition at PNNL. The purpose of the alumina spacers (Fig. 1) was to obtain a clamping stress on the sandwich, due to differential thermal expansion. The clamping stress was designed to be of the order of 200 MPa, or slightly higher than the maximum stress anticipated in the creep experiment. The samples and fixtures were heated for various times in a resistively heated furnace, under flowing argon gas (< 50 Pa O_2). The diffusion couple specimens were examined via scanning electron microscopy (SEM), energy-dispersive x-ray spectroscopy (EDS), and Auger electron spectroscopy (AES).

Results

Previously[11], the thermodynamic stability of Nb-1Zr and β-SiC was calculated at the lower end of the range of temperature of interest: 800°C, 10^5 Pa total pressure, in pure helium. At this temperature, a niobium carbide (Nb_8C_7) and a silicide ($NbSi_2$) had a negative Gibbs free energy of formation, as did zirconium carbide (ZrC_4), according to the following reaction,

$$Nb\ (s) + Zr\ (s) + \beta\text{-}SiC\ (s) \leftrightarrow Nb_8C_7\ (s) + NbSi_2\ (s) + \beta\text{-}SiC\ (s) + ZrC_4\ (s)$$

The Gibbs Standard Free Energy of Reaction, $\Delta G°$, is -27.2 kJ. These results indicated that a diffusion barrier coating must be placed between the Nb-1Zr and the SiC to prevent a detrimental reaction from occurring during the creep experiments. Based upon the results of additional thermodynamic based calculations, Al_2O_3 was selected as the most suitable coating material.

An experimental approach was used to determine the kinetics of the reactions between Nb-1Zr and SiC and to evaluate a 1µm thick, sputter-deposited coating of Al_2O_3 as a diffusion barrier coating. After heat treatment for 400 h at 1000°C, the alumina coating appeared much coarser, and the width of the coating was approximately 3 µm (Fig 2). Mullite ($3Al_2O_3$-$2SiO_2$, or $2Al_2O_3$-SiO_2) may have formed as a reaction product between the SiC and Al_2O_3 coating, or

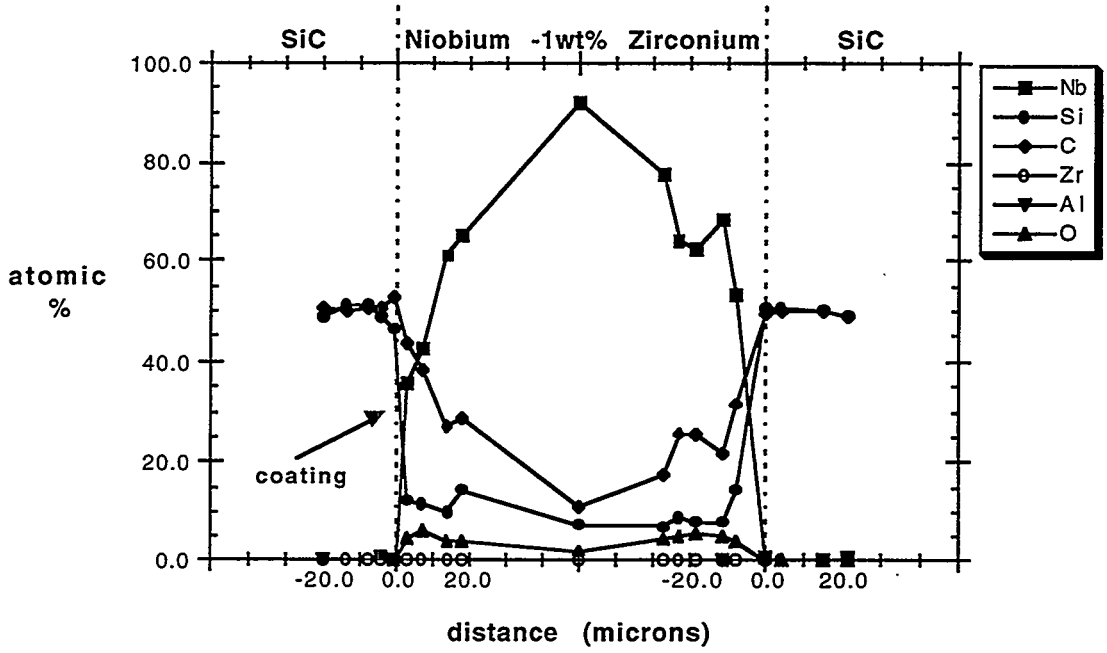

Figure 3. AES profile of a diffusion couple profile after 400 h at 1000°C.

the Al_2O_3 coating may have coarsened by grain growth. Neither hypothesis has been investigated further. The temperature, 1000°C, was chosen to evaluate the highest possible temperature expected in the irradiation creep experiment. Therefore, the results of these studies would actually overestimate the rates at which diffusional processes would occur during the creep experiment.

A detailed investigation of the diffusion couple was performed with AES. Spot scans were conducted along a line crossing the interfaces between the SiC and the Nb-1Zr coated with Al_2O_3 and the SiC and the uncoated Nb-1Zr. The distance between spot scan positions was 4 μm apart. From this analysis a compositional profile was constructed (Fig. 3). The concentrations of each element are not absolute since the data has not been corrected for the various sensitivity coefficients. Nevertheless, the results indicate that there is very little interdiffusion on the side of the specimen with the coating. On the other hand, on the side without the coating silicon appears to have diffused from the SiC into the Nb-1Zr and some niobium may have diffused into the β-SiC. These results suggest that a reaction does take place between the Nb-1Zr and the SiC.

Additional experiments were repeated for 400 h at 1000°C, in flowing argon to confirm the previous results. AES with a distance between analysis points of 0.35-0.60 μm was used to investigate the details of the interface between the Nb-1Zr and the SiC. Although this analysis was also only qualitative, since internal calibration of the signals was not performed, the results indicate that silicon diffuses readily from the SiC to the Nb-1Zr specimen under these conditions (Fig. 4). On the other hand, silicon (or any other element) was not detected

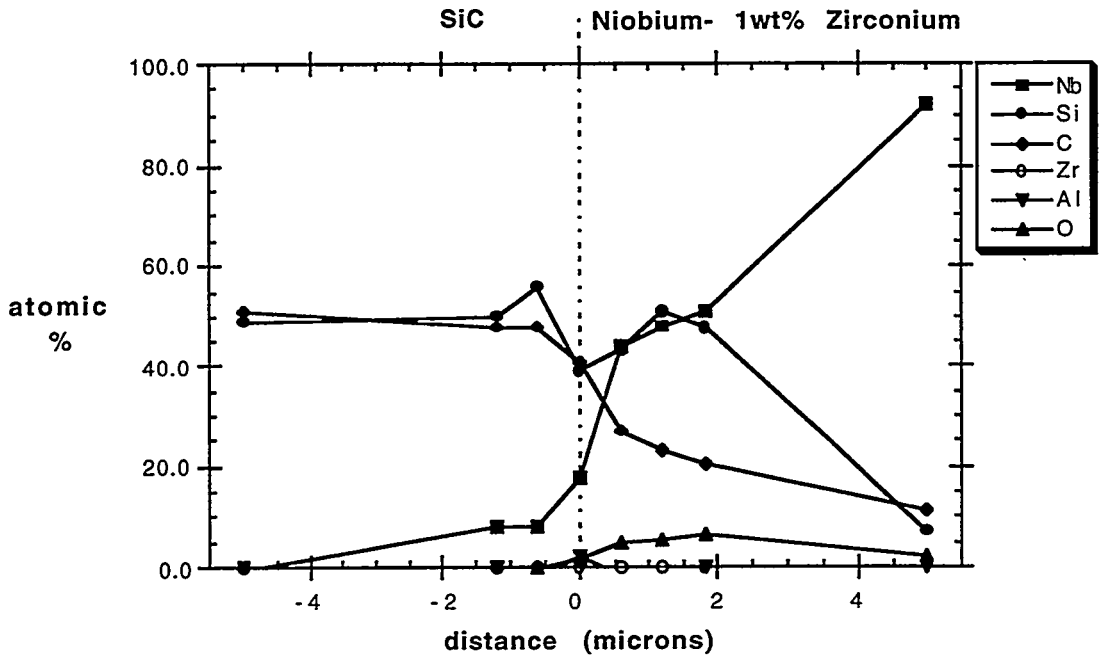

Figure 4. AES profile of a diffusion couple profile after 400 h at 1000°C, in flowing argon, showing that silicon diffuses from the SiC to the uncoated Nb-1Zr.

in higher than average concentrations in the Nb-1Zr sample that had been coated with a 1 μm thick layer of Al_2O_3. These results confirm that SiC and Nb-1Zr are reactive under the conditions studied, and that the Al_2O_3 coating is effective in preventing diffusion between the two materials.

CONCLUSIONS

The thermochemical stability of Nb-1Zr and SiC was analyzed via thermodynamic calculations and diffusion couple experiments. Both techniques showed that the two materials were reactive under the conditions studied. A technique to deposit an Al_2O_3 diffusion barrier coating on Nb-1Zr was developed. Although the coating coarsened, under the conditions investigated, the coating did not allow interdiffusion to occur. On the other hand, it appeared that, under the same conditions, the uncoated Nb-1Zr reacted with SiC. Therefore, a sputter-deposited Al_2O_3 diffusion barrier coating is highly recommended for any irradiation creep experiments involving this design concept.

REFERENCES

1. R.H. Jones, C.H. Henager, Jr., and G.W. Hollenberg, J. Nucl. Mater. 191-194 (1992) 75.
2. P. Fenici, and H.W. Scholz, J. Nucl. Mater. 212-215 (1994) 60.
3. H.W. Scholz, M. Zucchetti, K. Casteleyn, C. Adelhelm, J. Nucl. Mater. 212-215 (1994) 655.
4. R.H. Jones, and C.H. Henager, Jr., J. Nucl. Mater. 212-15 (1994) 830.

5. R.H. Jones, and C.H. Henager, Jr., J. Nucl. Mater. 219 (1995) 55.
6. L.L. Snead, and O.J. Schwarz, J. Nucl. Mater. 219 (1995) 3.
7. D.B. Marshall, and J.E. Ritter, "Reliability of Advanced Structural Ceramics and Ceramic Matrix Composites - A Review," Bull. Am. Ceram. Soc., **66** [2], 309-17 (1987).
8. R.J. Price, in HTGR Base Program Quarterly Progress Report for the Period Ending August 31,1967, General Atomic Division of General Dynamics Report GA-8200, p. 91 (1967).
9. R.J. Price, Nucl. Tech. 35 (1977) 320.
10. R. Scholz, A. Frias Rebelo, and P. Dos Santos, Proc. of the IEA Workshop on Fusion Materials, Ispra, Italy, 1996.
11. M.L. Hamilton, C.A. Lewinsohn, R.H. Jones, G.E. Youngblood, F. A. Garner, and S.L. Hecht, "Progress in the Development of a SiC_f/SiC Creep Test," Fusion Materials Semiannual Progress Report for the Period Ending June 30, 1996, DOE/ER-0313/20.

ANALYSIS OF NEUTRON IRRADIATION EFFECTS ON THERMAL CONDUCTIVITY OF SIC-BASED COMPOSITES AND MONOLITHIC CERAMICS - G. E. Youngblood and D. J. Senor (Pacific Northwest National Laboratory)*

OBJECTIVE

The objective of this work is to examine SiC composites fabricated by various processing methods designed to improve composite thermal conductivity. It is desired to increase the thermal conductivity of these composites to meet requirements for advanced fusion energy systems. Specifically, this paper will analyze data reported by Senor, et al., in Fusion Technology [1] and orally presented at the 1996 American Nuclear Society Annual Meeting, 16-20 June, Reno NV and at the Fifth Symposium on Fabrication and Properties of Ceramics for Fusion Energy and Other High Radiation Environments, American Ceramic Society 99th Annual Meeting, 5-7 May, 1997, Cincinnati OH.

SUMMARY

After irradiation of a variety of SiC-based materials to 33 or 43 dpa-SiC at 1000°C, their thermal conductivity values were degraded and became relatively temperature independent, which indicates that the thermal resistivity was dominated by point defect scattering. The magnitude of irradiation-induced conductivity degradation was greater at lower temperatures and typically was larger for materials with higher unirradiated conductivity. From these data, a K_{irr}/K_{unirr} ratio map which predicts the expected equilibrium thermal conductivity for most SiC-based materials as a function of irradiation temperature was derived. Due to a short-term EOC irradiation at 575° ± 60°C, a duplex irradiation defect structure was established. Based on an analysis of the conductivity and swelling recovery after post-irradiation anneals for these materials with the duplex defect structure, several consequences for irradiating SiC at temperatures of 1000°C or above are given. In particular, the thermal conductivity degradation in the fusion relevant 800°-1000°C temperature range may be more severe than inferred from SiC swelling behavior.

REVIEW

The performance of a variety of SiC-based composites and monolithic ceramics in the unirradiated, thermal annealed and irradiated conditions was characterized by determining their thermal conductivity values. The irradiation was conducted in the EBR-II reactor to doses of 33 and 43 dpa-SiC (185 EFPD) in an uninstrumented capsule designed to operate at 1000°C. Thermal annealed control specimens were held at 1010°C for 165 days to approximately duplicate the thermal exposure of the irradiated specimens. Through-the-thickness thermal diffusivity was measured generally over the temperature range 400° to 1150°C using the laser flash method, and converted to thermal conductivity using density data and calculated specific heat values. Table 1 presents a summary of the materials tested in this study.

The listed densities were determined by measuring the dimensions and weighing the

*Pacific Northwest National Laboratory is operated for the U. S. Department of Energy by Battelle Memorial Institute under Contract DE-AC06-76RLO 1830.

unirradiated material. The baseline composite consisted of a Nicalon CG fiber reinforced matrix, nominally fully crystalline ß-SiC. Two alternate matrix materials, polymer impregnation with a 150 nm thick pyrolytic carbon (PyC) interface and a chemical vapor infiltrated (CVI) SiC and pyrolysis (PIP) and Blackglas SiC, were tested in combination with Nicalon CG fiber reinforcement. The resulting matrices were carbon- and oxygen-rich and at least partially amorphous. Two alternate fiber reinforcements (Tyranno and HPZ) and two alternate interfaces (15 nm PyC and 150 nm BN) also were tested in combination with the PIP SiC matrix. Two SiC-based particulate reinforced composites, SiC whisker (SiC_w) and SiC particulate (SiC_p) in combination with forced CVI and Blackglas matrices respectively, were tested. The monolithic ceramics included chemical vapor deposited (CVD) ß-SiC and two types of sintered α-SiC, Hexoloy SA and SX.

Table 1. SiC-based materials included in the test matrix.

Reinforce-ment	Fiber Architec-ture	Interface	Matrix	Measured Density (g/cm^3)	Vendor
Nicalon CG	0°/90°	150 nm PyC	CVI SiC	2.48 to 2.63	DuPont
Nicalon CG	0°/±86°	150 nm PyC	CVI SiC	2.68	DuPont
Nicalon CG	0°/90°	150 nm PyC	PIP SiC	2.20	Dow Corning
Nicalon CG	0°/90°	150 nm PyC	Blackglas	2.04	Allied Signal
Nicalon CG	0°/90°	15 nm PyC	PIP SiC	2.18	Dow Corning
Nicalon CG	0°/90°	150 nm BN	PIP SiC	2.21	Dow Corning
Tyranno	0°/90°	150 nm PyC	PIP SiC	2.10	Dow Corning
HPZ	0°/90°	150 nm PyC	PIP SiC	2.12	Dow Corning
SiC_w	-	-	CVI SiC	2.72	ORNL
SiC_p	-	-	Blackglas	2.73	Allied Signal
-	-	-	CVD ß-SiC	3.25	Morton
-	-	-	Hexoloy SA	3.16	Carborundum
-	-	-	Hexoloy SX	3.19	Carborundum

In general, the thermal conductivity values decreased with increasing temperature as expected for phonon conduction. Composites with higher bulk densities had higher thermal conductivity values. Composites with the more crystalline CVI matrix had thermal conductivity

values roughly a factor of five greater than composites with the less crystalline and less pure PIP SiC matrix, and a factor of ten greater than composites with the amorphous Blackglas matrix. Fiber architecture and coating variations had no discernible influence on the thermal conductivity for these materials, and the long-term thermal annealing at 1010°C had little influence. The thermal conductivity values of the dense and high purity CVD ß-SiC exhibited the steepest temperature dependence and, depending upon temperature, were 8-15 times greater than the values for the CVI composites. The thermal conductivity values for the Hexoloy SA and SX sintered SiC were intermediate to that for the CVD ß-SiC and the CVI composites, with the SA material exhibiting conductivity values a consistent 10-20% higher than the SX material. The higher conductivity of the Hexoloy SA is attributed to the use of a boron sintering aid, whereas Hexoloy SX uses Y_2O_3.

Due to the irradiation doses, which were well above saturation doses, thermal conductivity values and their temperature dependences for all the monolithic materials and for the more crystalline CVI matrix composites were reduced significantly as expected. In contrast, the thermal conductivity values for the more amorphous PIP and Blackglas composites actually increased about 35% due to the irradiation at 1000°C which presumably caused partial crystallization and densification of the amorphous matrix. Details for each material listed in Table 1 are given in Reference 1.

In Figure 1, the thermal conductivity degradation for crystalline SiC and CVI SiC matrix composites, expressed as a ratio of the irradiated to the unirradiated thermal conductivity values (k_{irr}/k_{unirr}), is presented as a function of the irradiation/test temperature. To construct this map, data from Thorne, et al., Price, Rhode and Hollenberg, et al., were added to the data at 575° and 1000°C from this work.

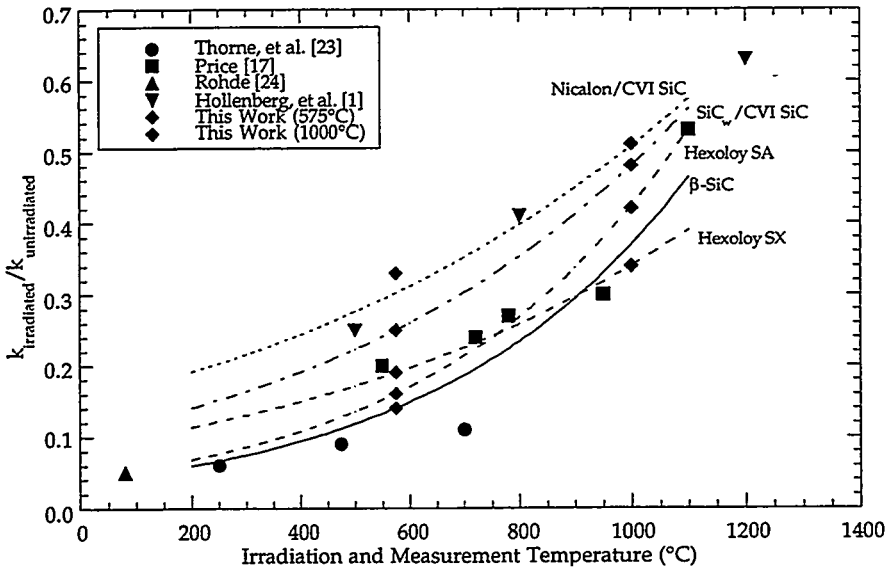

Figure 1. Thermal conductivity degradation as a function of irradiation/test temperature for crystalline SiC and CVI SiC matrix composites.

The general trend is for the k_{irr}/k_{unirr} ratio to increase as the irradiation/test temperature increases. For example, this ratio for ß-SiC ranges from 0.05 to 0.32 at 100°C and 1000°C, respectively. This trend reflects the relative dominance of the temperature independent irradiation point defect phonon scattering in the lower temperature range, while the temperature dependent intrinsic phonon-phonon scattering becomes relatively more important as the irradiation temperature increases. Significantly, the ratios can be separated into a family of roughly parallel best-fit curves which apparently depend upon purity, density and probably microstructural features. In this separation, the curve for CVD ß-SiC has the lowest ratio and represents the intrinsic irradiation behavior of SiC. In order of increasing ratios are curves for the sintered Hexoloy materials, the SiC_w particulate composite, and the continuous fiber reinforced CVI SiC matrix composite. From these curves, the thermal conductivity for irradiated crystalline SiC-based materials at any temperature can be predicted from measured values for unirradiated material. Most importantly, these curves establish fundamental limits to processing strategies, such as B-doping or thermal annealing treatments, which are designed to enhance the thermal conductivity of irradiated SiC-based materials. No thermal conductivity values greater than those predicted for irradiated CVD ß-SiC should be expected. As a general rule, the larger the thermal conductivity enhancement achieved through a processing strategy, the larger the relative degradation due to irradiation effects. The thermal conductivity degradation for irradiated SiC will always be dominated by the phonon scattering of radiation-induced point defects, primarily the vacancies.

The latter supposition is supported by the results from two different annealing studies given to the irradiated CVD ß-SiC material. In one study, a pair of passive CVD ß-SiC temperature monitor bars indicated that the capsule had been irradiated at a temperature much lower than the design temperature of 1000°C. In fact, the temperature monitor bars indicated via an isochronal annealing method that the irradiation temperature was 575° ± 60°C. In this method, bar lengths were measured after one-hour annealing times at successively higher temperatures. No length changes were observed to occur for annealing temperatures below 575°C; while the bar lengths decreased uniformly for the successively higher annealing temperatures once they exceeded the apparent 575°C irradiation temperature. After the final anneal at 1450°C (3 hours), the length recovery was only 50%. In similar annealing tests, others have observed at least 85% swelling recovery for irradiations at 800°C, so the limited 50% recovery was unexpected. This high level of residual swelling even after the 1450°C anneal is indicative of a substantial quantity of remaining stable irradiation defects, presumably due to the long-term 1000°C portion of the irradiation cycle. The approximately 50% swelling that actually recovered must have been primarily due to recovery of the short-term EOC 575°C irradiation defect structure. Thus, due to the operation of the reactor at reduced power for less than a day at the end of the normal 185 EFPD cycle, a duplex defect structure was induced in these CVD ß-SiC bars. One part of the duplex structure was characteristic of a long-term 1000°C irradiation; the other part was characteristic of a short-term 575°C irradiation, estimated to be representative of about a 0.1 dpa-SiC dose. This type of duplex defect structure also should have been present in all of the similarly irradiated SiC-based materials tested in this experiment.

In the second annealing study, the thermal conductivity degradation and recovery for one of the irradiated CVD ß-SiC diffusivity specimens was examined after a series of post-irradiation one hour anneals at 1150°, 1250°, 1350° and 1450°C. The effects on the thermal conductivity for this specimen are shown in Fig. 2.

The upper curve depicts the unirradiated thermal conductivity values as a function of

temperature for high purity and dense ß-SiC; the lowest curve depicts the as-irradiated values. Note that the k_{irr}/k_{unirr} ratio at 575°C would be about 0.15 and would correspond to the data point shown for this material at that temperature in Fig. 1. The intermediate curves show the thermal conductivity temperature dependence for partially recovered ß-SiC since the thermal diffusivity was measured as a function of decreasing temperature after the one hour anneals. However, even after the 1450°C anneal about 50% of the thermal conductivity degradation remained. If the only defect structures generated during the irradiation were vacancies and small interstitial clusters, the 1450°C anneal should have been sufficient to restore the conductivity to near unirradiated values.

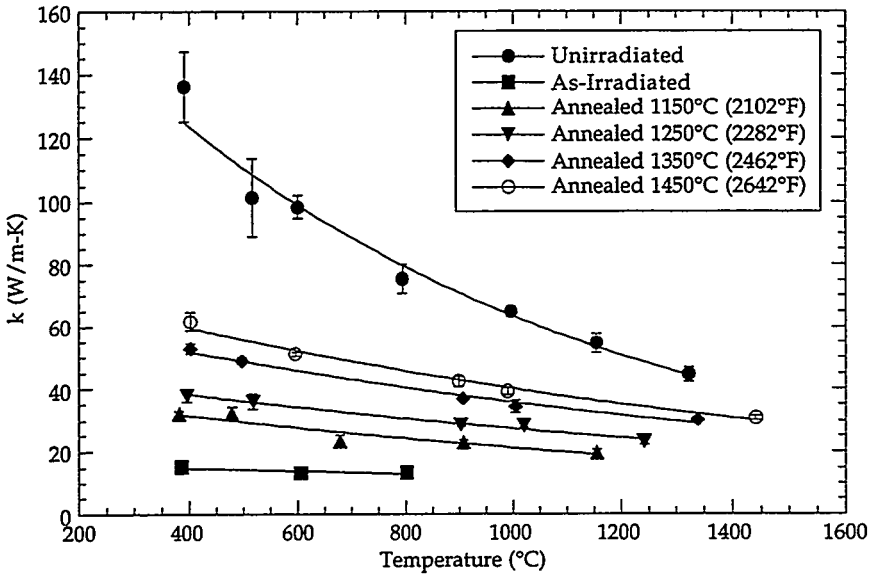

Figure 2. Effects of irradiation and multiple post-irradiation anneals on thermal conductivity of CVD ß-SiC.

The duplex irradiation defect structure proposed to explain 50% swelling recovery in the temperature monitor bars explains these thermal conductivity recovery data as well. The long-term 1000°C irradiation established a relatively stable network of interstitial dislocation loops, while the short-term 575°C irradiation established a defect structure characterized by smaller, less stable interstitial clusters. The vacancies for both types of interstitial configurations remain relatively isolated and distributed throughout the SiC lattice. The interstitial dislocation loops themselves are expected to be relatively coherent with the SiC crystal structure and are not expected to significantly degrade the thermal conductivity. The thermal conductivity and swelling recovery that occurred after anneals from 575°C up to about 1000°C was the result of interstitials not bound in the stable dislocation loops recombining with vacancies. With continued irradiation above about 1000°C, many interstitials would accumulate and stabilize into the dislocation loops which means that a corresponding number of the generated vacancies also would continue to accumulate. Eventually the vacancies become mobile at temperatures above about 1250°C. Nevertheless, the significant residual thermal conductivity degradation must be caused primarily by vacancies, either isolated or as small clusters scattered throughout the lattice,

which provide the most effective phonon scattering sites.

The fact that only a small amount of recovery apparently occurred for that portion of the thermal conductivity degradation or of the swelling induced in SiC by the 1000°C irradiation has important consequences. Normally, the swelling versus irradiation temperature curve, which has decreasing values with increasing irradiation temperature and an extremely low minimum linear swelling of about 0.1% at 1000°C, is thought to saturate at a relatively low dose. Hence, after an initial small amount of swelling, ß-SiC has exhibited remarkable dimensional stability, especially during continued irradiation in the fusion relevant 800° to 1000°C temperature range. Above 1000°C the swelling should increase with further increase in irradiation temperature and should exhibit a dose dependent swelling maximum at about 1250°C, where vacancy mobility becomes important. However, the dose independence of the swelling minimum must be reconsidered in light of these recovery data. Based on the hypothesis that a stable interstitial defect structure can be formed in ß-SiC for a 1000°C irradiation, the dose dependent swelling maximum at 1250°C should shift to lower temperatures because of the continual buildup of the more stable interstitial dislocation loops. More importantly, the thermal conductivity degradation may not exhibit the same type of irradiation temperature dependence as the swelling with a dose independent minimum at 1000°C. Since in irradiated SiC the thermal conductivity degradation depends more upon the residual vacancy concentration than the interstitial defect configuration, the thermal conductivity degradation in the fusion relevant 800°-1000°C temperature range may be more severe than inferred from SiC swelling behavior.

FUTURE WORK

The irradiation and recovery effects for SiC-based materials irradiated in the COBRA 1A2 tests at 800°C will be analyzed.

REFERENCES

1. D.J. Senor, G.E. Youngblood, C.E. Moore, D.J. Trimble, G.A. Newsome and J.J. Woods, "Effects of Neutron Irradiation on Thermal Conductivity of SiC-Based Composites and Monolithic Ceramics," Fusion Technology 30(3), 943-955 (1996). Other pertinent references are given in this reference.

CREEP BEHAVIOR FOR ADVANCED POLYCRYSTALLINE SIC FIBERS - G. E. Youngblood and R. H. Jones (Pacific Northwest National Laboratory),* G. N. Morscher (Case Western Reserve University) and Akira Kohyama (Institute of Advanced Energy, Kyoto University, Japan)

OBJECTIVE

The objective of this work is to examine irradiation enhanced creep behavior in advanced polycrystalline SiC fibers.

SUMMARY

A bend stress relaxation (BSR) test is planned to examine irradiation enhanced creep in polycrystalline SiC fibers which are under development for use as fiber reinforcement in SiC/SiC composite. Baseline 1 hr and 100 hr BSR thermal creep "m" curves have been obtained for five selected advanced SiC fiber types and for standard Nicalon CG fiber. The transition temperature, that temperature where the S-shaped m-curve has a value 0.5, is a measure of fiber creep resistance. In order of decreasing thermal creep resistance, with the 100 hr BSR transition temperature given in parenthesis, the fibers ranked: Sylramic (1261°C), Nicalon S (1256°C), annealed Hi Nicalon (1215°C), Hi Nicalon (1078°C), Nicalon CG (1003°C) and Tyranno E (932°C). The thermal creep for Sylramic, Nicalon S, Hi Nicalon and Nicalon CG fibers in a 5000 hr irradiation creep BSR test is projected from the temperature dependence of the m-curves determined during 1 and 100 hr BSR control tests.

PROGRESS AND STATUS

Introduction

As part of the Joint DOE/Monbusho Program to support materials development for fusion energy, PNNL has initiated a systematic study of the potential effects of irradiation creep in SiC/SiC composites and SiC fibers. A previous report described a simple bend stress relaxation test designed to examine the creep behavior of irradiated and unirradiated SiC fibers [1]. A second report presented 1 hr BSR thermal creep results for selected advanced fibers, namely Nicalon S™ and Hi Nicalon™ manufactured by Nippon Carbon Co. and Sylramic™ manufactured by Dow Corning Corp [2]. This report presents 100 hr BSR thermal creep results for these same fibers plus results for annealed Hi Nicalon and Hi Nicalon S fibers and the newly introduced Tyranno™ Lox E fiber, the latter fiber being manufactured by Ubekosansha, Japan. The properties for the selected fibers are given in Table 1. Measured lot specific properties are italicized; otherwise manufacturer's values are given.

All the fibers listed in Table 1 are polymer-derived, small diameter fibers suitable for weaving into fabric for composite fabrication. They were received as fiber tows from which single fiber strands were selected for the BSR and tensile strength tests. The measured tensile strengths were made at ambient using a Micropul™ device designed for this purpose. They represent the average strength values from a Weibull analysis for 20-25 individual

*Pacific Northwest National Laboratory is operated for the U. S. Department of Energy by Battelle Memorial Institute under Contract DE-AC06-76RLO 1830.

Table 1. Properties of SiC Fibers Selected for the Irradiation Creep Tests.

Property	Nic CG	Hi Nic	Nic S	Sylramic	Hi Nic*	Nic S*	Tyranno E
Diam, μm	*14*	*12*	*11*	10	*12*	*11*	*11*
Density, g/cm^3	*2.55*	*2.74*	*2.98*	3.0	2.8	3.1	*2.40*
Tens. Stren., GPa	*2.6*	*3.4*	2.6	2.8	*2.4*	*1.0*	3.3
Tens. Mod., GPa	190	270	420	400	320	440	220
Composition-Si	56	62	69	66			55
(wt %) -C	32	37	31	28			37
-O	12	0.5	0.2	0.9 +2 (B)			6 + 2 (Ti)
(atomic) - C/Si	1.31	1.39	1.05	1.0			1.6
Xstallite G. S., nm	*<2*	*5*	10	75	8	10	18
Transition Temp.,°C (1 hr, m = 0.5)	*1110*	*1230*	*1450*	*1420*			

*Annealed one hour in argon at 1500°C.

measurements for each fiber type. Two of the fibers, Hi Nicalon and Nicalon S, were annealed simultaneously at 1500°C in argon to improve their creep resistance. For these two fibers, the strengths were determined using a "bit" strength test in which single strands were bent around drill bit shanks of diminishing diameters until the fiber failed. By this test, the strengths of annealed Hi Nicalon (Hi Nic*) and Nicalon S (Nic S*) were determined to have decreased to values of 2.4 ± 0.5 and 1.0 ± 0.3 GPa, respectively. The Hi Nic* strength decrease was similar to that observed by Ichikawa, et al. [7] for annealed Hi Nicalon. On the other hand, the Nic S* strength decreased by an amount much larger than expected. SEM inspection of the Nic S* fiber surface revealed numerous, but unexplained pore "blowout" type flaws. For this reason, the Nic S* fibers were eliminated from further consideration in this BSR test series. The 1 hr BSR transition temperatures were taken from the one hour BSR creep results given in Ref. [2].

Theoretical and Experimental Review

Theoretical and experimental details of the BSR test were presented previously [1,2]. Briefly, an initial elastic bend strain is applied to a single fiber by wrapping several coiled loops onto a SiC mandrel of radius R_o. The loops are captured by a SiC sleeve that slips over the fiber-wrapped mandrel. For the test designed to examine the potential effects of irradiation enhanced creep, the fiber loops will be subjected to a specific time (t), temperature (T), and irradiation dose (ϕ) at the fixture imposed strain ($\varepsilon_o = r_f/R_o$), where ε_o represents the maximum strain at the outer edge of the coiled fibers and r_f is the fiber radius. The BSR parameter "m" quantifies the stress relaxation that occurs during treatment and is determined from:

$$m = 1 - R_o/R_a \qquad (1)$$

where R_a is the arc radius of the relaxed fiber measured after treatment. In BSR tests, values of m range from 1 to 0 with m = 1 or 0 indicating the occurrence of no relaxation or complete relaxation by creep, respectively. Intermediate values of m indicate partial relaxation. To

separate thermal from irradiation creep effects, the irradiation dependent strain increment $\Delta\varepsilon$ can be defined as

$$\Delta\varepsilon = \varepsilon_o\{1/m(\phi,T,t,\varepsilon_o) - 1/m(T,t,\varepsilon_o)\} \quad (2)$$

The term in brackets is the difference in reciprocal m-values for the irradiation and the thermal control BSR tests, respectively. Results for the 1 hr thermal control BSR tests were given in Ref. [2]; the results for the 100 hr control tests are given in this report.

A good approximation for the tensile creep strain (ε_c) that would result from a constant stress creep test for equivalent BSR test temperatures and times can be estimated from measured m-values via [2]:

$$\varepsilon_c/\varepsilon_o \approx m^{-1} - 1 \quad (3)$$

In particular, ε_c predicted by Eq. (3) has been shown to approximately give the same time and temperature dependence as conventional tensile creep data [5].

Primary creep in fibers can be modelled by the semi-empirical creep equation [6]:

$$\varepsilon_c = A_o\sigma^n[t\,exp(-Q/RT)]^p \quad (4)$$

In this expression A_o, n and p are empirically determined creep parameters, σ is stress in GPa, t is time in hours, Q is the controlling creep energy in kJ/mol, R is the gas constant (8.31 J/mol-K) and T is temperature in Kelvin. Using Eqs. (3) and (4), for Nicalon fiber DiCarlo obtained close agreement between converted BSR m-data and actual tensile creep data. From DiCarlo's analysis the creep parameters for Nicalon fiber were: $A_o = 2.2 \times 10^5$, n = 1.2, p = 0.40, and Q = 500 ± 65 kJ/mol.

The effective creep energy Q can be estimated directly from m-data by the cross-cut method using the expression $Q = 2.3R/\Delta(1/T)$ where $\Delta(1/T)$ is the spacing between one order of magnitude change in time at a constant m-value [3]. The numerical factor 2.3 must be replaced by 4.6 for two orders of magnitude time change. Alternately, Eq. (3) can be employed to convert measured m-data to normalized creep strains which are then used with Eq. (4) to calculate the best-fit empirical parameters and the Q-values by linear regression. The latter approach is fairly accurate for the condition $0.9 > m > 0.1$. Once the Q-value is obtained, normalized thermal creep strains (or m-values) can be estimated for any stress, time and temperature assuming that Eq. (4) continues to describe the creep process.

Results and Discussion

In Figure 1, the 100 hr BSR m-values for the SiC fibers listed in Table 1 (except for Nic S*) are plotted as a function of reciprocal temperature.

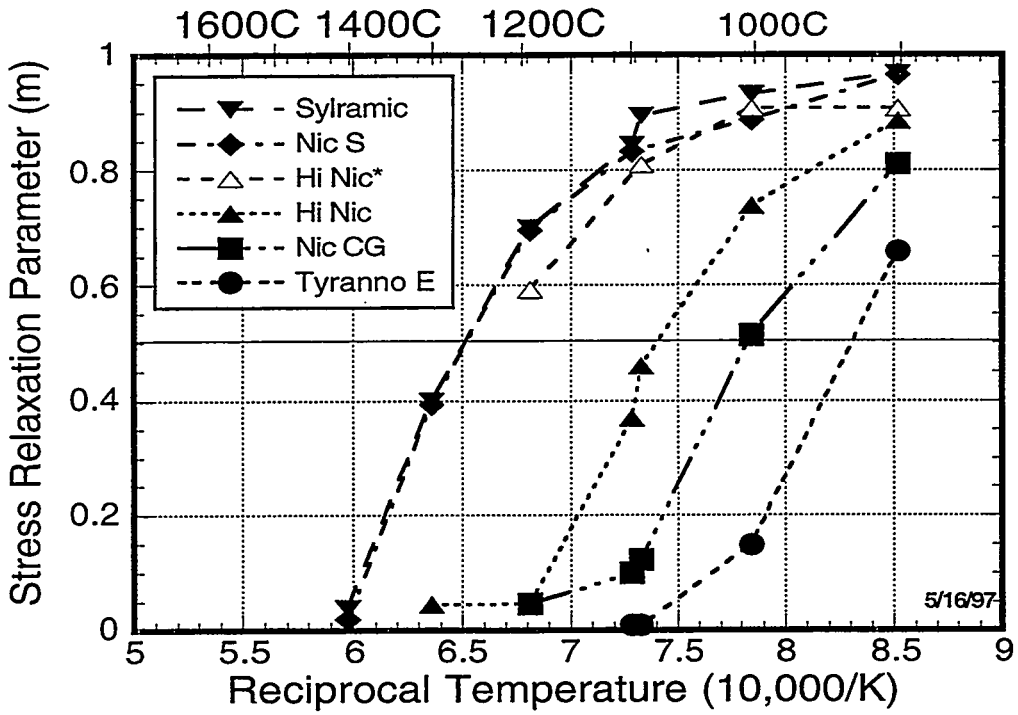

Fig. 1. Comparison of 100 hour BSR thermal creep results for advanced SiC and Nicalon CG fibers (ε_o = 0.1 to 0.3%).

In order of decreasing 100 hr transition temperatures (in parenthesis) or thermal creep resistance, the fibers ranked: Sylramic (1261°C), Nicalon S (1256°C), annealed Hi Nicalon (1215°C), Hi Nicalon (1078°C), Nicalon CG (1003°C) and Tyranno E (932°C). By comparison with the 1 hr BSR thermal creep results given in Ref. [2], the S-shaped curves have shifted right for the Nicalon S, Sylramic, Hi Nicalon and Nicalon CG fibers. The controlling creep "activation" energies were calculated for these four fiber types by the temperature shift cross-cut method and by linear regression using Eqs. (3) and (4). The results are given in Table 2.

Table 2. Thermal creep energy and projected m-values for 5000 hr , 800 or 1000°C tests.

Fiber Type	Q* (kJ/mol)	Q^ (kJ/mol)	m(800°C)#	m(1000°C)#
Nicalon CG	607	500 ± 65	0.88	0.18
Hi Nicalon	503	505 ± 40	0.95	0.37
Nicalon S	517	530 ± 60	0.99	0.65
Sylramic	622	650 ± 40	0.99	0.74

*Estimated using the temperature shift cross-cut method.
^Estimated using linear regression and Eqs. (3) and (4).
#Based on projections from the 100 hr m-values and using Eqs. (3) and (4).

Fair agreement was obtained using either the temperature shift cross-cut method or using Eqs. (3) and (4) to estimate the controlling thermal creep energy. The thermal creep energies for these polymer-derived SiC fibers lie in the 500-650 kJ/mol range. Creep energies in this range appear to correspond to the activation energies for carbon and silicon diffusion in SiC grain boundaries which have been reported as 563 and 550-611 kJ/mol, respectively [4]. For comparison, activation energies for C or Si lattice diffusion in ß-SiC are 840 and 912 kJ/mol, respectively. By inference then, thermal creep in the polymer-derived SiC fibers probably is controlled by a grain boundary mechanism, presumably grain boundary sliding.

To be able to discern any enhancement of creep by irradiation, it is desirable for the thermal creep contribution to be relatively small, i.e., $m(T,t,\varepsilon_o) \geq 0.8$ in Eq. (2). Using Eqs. (3) and (4), example thermal 5000 hr m-values were projected from the 100 hr m-values. The 5000 hr time period is typical of an irradiation cycle, and the 800 and 1000°C temperatures are fusion relevant. The thermal BSR m-value projections for these conditions also are given in Table 2.

For a BSR fiber creep test at 1000°C during a 5000 hr irradiation cycle, thermal creep would probably dominate any irradiation enhanced creep and make it unobservable except possibly for the Nicalon S and Sylramic fibers. However, for an irradiation temperature of 800°C the m-value projections for all the fibers are > 0.8. Therefore, a temperature of 800°C or lower is recommended for a 5000 hr (208 EFPD) fiber BSR irradiation creep test.

CONCLUSIONS

1. The thermal creep behavior for five advanced SiC fiber types and Nicalon CG was examined by using a 100 hr BSR fiber creep test. In order of decreasing creep resistance, the fibers ranked as follows: Sylramic, Nicalon S, annealed Hi Nicalon, Hi Nicalon, Nicalon CG and Tyranno E.

2. A methodology for predicting the thermal creep contribution during a BSR test of irradiated fibers was developed. To be able to separate thermal from irradiation creep, a temperature of 800°C or lower is recommended for a typical 5000 hr irradiation test cycle.

FUTURE WORK

Due to a scheduling conflict in the ATR reactor, the startup of the first BSR test on irradiated fibers has been delayed from January to August, 1997. This test will be carried out at 260°C to a 5 dpa dose. Expected completion of the irradiation cycle is May, 1998. A second test at 800°C is planned for the HFIR reactor as part of the Jupiter P3-4 experiment tentatively scheduled to commence mid-1998.

REFERENCES

1. G. E. Youngblood, M. L. Hamilton and R. H. Jones, "Technique for Measuring Irradiation Creep in Polycrystalline SiC Fibers," p. 146 in Fusion Materials Semiannual Progress Report for Period Ending June 30, 1996. DOE/ER--0313/20.

2. G. E. Youngblood, R. H. Jones, G. N. Morscher and Akira Kohyama, "Creep Behavior for Advanced Polycrystalline SiC fibers," p. 89 in Fusion Materials Semiannual Progress Report for Period Ending December 31, 1996. DOE/ER--0313/21.

3. Gregory N. Morscher and James A. DiCarlo, "A Simple Test for Thermomechanical Evaluation of Ceramic Fibers," J. Amer. Ceram. Soc.,75(1),136-40 (1992).

4. G. N. Morscher, J. A. DiCarlo, X. J. Ning and P. Pirouz, "Effect of Heat Treatment on the Stress Relaxation and Microstructure of CVD SiC Fibers," Advances in Ceramic-Matrix Composites, 679-90 (1995).

5. Gregory N. Morscher, Hee Man Yun and Jon C. Goldsby, "Viscoelastic Analysis of Bend Stress Relaxation and Tensile Creep of a Polycrystalline α-SiC Fiber," Plastic Deformation of Ceramics III (1995).

6. James A. DiCarlo, "Creep Limitations of Current Polycrystalline Ceramic Fibers," Composites Science and Technology 51, 213-222 (1994).

7. Hiroshi Ichikawa, Kiyohito Okamura and Tadao Seguchi, "Oxygen-Free Ceramic Fibers from Organosilicon Precursors and E-Beam Curing," p. 65 in High-Temperature Ceramic-Matrix Composites II, edited by A. G. Evans and R. Naslain, Ceramic Transactions, 58 (1995).

DESIGN OF A CREEP EXPERIMENT FOR SiC/SiC COMPOSITES IN HFIR - S. L. Hecht (Duke Engineering Hanford), M. L. Hamilton, R. H. Jones, G. E. Youngblood, and R. A. Schwartz (Pacific Northwest National Laboratory), and C. A. Lewinsohn (Associated Western Universities)

OBJECTIVE

The purpose of this work is to design an in-reactor creep experiment for composite materials.

SUMMARY

A new specimen was designed for performing in-reactor creep tests on composite materials, specifically on SiC/SiC composites. The design was tailored for irradiation at 800°C in a HFIR RB* position. The specimen comprises a composite cylinder loaded by a pressurized internal bladder that is made of Nb1Zr. The experiment was designed for approximately a one year irradiation.

INTRODUCTION

This report describes the pressurized cylinder experiment design and supporting analysis for in-reactor creep testing of silicon carbide (SiC/SiC) composites, which are under consideration for structural applications in proposed magnetic fusion reactor systems. Recent qualitative and estimated quantitative data suggest that there is a significant effect of irradiation on the creep of SiC/SiC, and hence it is an issue which needs to be addressed in the design of such structures. This experiment is designed to obtain "engineering" creep data which can be utilized in the design process.

A number of design concepts were considered and analyzed in the preliminary design phase. Some of these concepts were rejected on the basis of programmatic constraints, and others were rejected because of technical issues. The result of this "screening process" was a design (referred to as the "reference design") which has a high degree of confidence of success. A second alternative design also holds some promise and is briefly addressed.

This report describes the experiment, and provides supporting performance predictions. Nuclear physics (shielding-heat deposition), thermal and structural analyses which provide design support are provided.

EXPERIMENTAL OBJECTIVES AND METHODS

The goal of the experiment is to obtain irradiation creep data which is representative of design needs for the fusion reactor system. These are specimen irradiation doses of 5 to 10 dpa and irradiation temperatures of 500 to 1000°C. Stresses were chosen to best study mechanistic effects. Here, hoop stresses in the specimen are expected to be initially chosen below, near and above the matrix cracking strength.

The experiment is designed to go in the High Flux Isotope Reactor (HFIR) in a Large Removable Beryllium (RB*) mid-core location. The HIFR is assumed to be operating at 100 MW power at the time of the irradiation. The experiment is expected to remain in the reactor for approximately one year, i.e., 300 effective full power days (EFPD), to obtain the desired dose.

The design is based on an assumed irradiation at the most severe conditions, i.e., 300 EFPD at 1000°C and a specimen hoop stress of 150 MPa. Hence a considerable design margin is expected to exist in experiments with a less severe environment.

The experimental system, because of available space, also provides an irradiation testing environment for other passive SiC specimens, such as bend bars and fibers.

DESIGN

The reference design of the SiC creep experiment system consists of a SiC/SiC cylinder specimen with an associated specimen loading subsystem, passive SiC creep specimens, and a subcapsule (RB*) whose main function is to provide mechanical support and temperature control. The experimental components, which are not specimens, i.e., the RB* subcapsule and the specimen-loading subsystem, are referred to herein as the "test assembly." There are three sets of specimens in each RB* subcapsule, as shown in Figure 1. The RB* subcapsule fits inside a stainless steel HIFR RB* Irradiation Capsule (at power ID = 1.364 in., OD = 1.504 in.), with the radial clearance between these two capsules set to provide the desired temperature range (see thermal analysis section).

The RB* subcapsule has the function of positioning the specimen systems, and providing the thermal environment and backup structural restraint for the specimen loading system (see structural analysis section). This subcapsule is fabricated of Nb1Zr refractory alloy, and is of welded construction. The Nb1Zr was chosen for the combined high-temperature strength and ductility, and ease of fabricability (see alternative design section). This capsule has a central thermocouple tube and gas line feed through a tube welded to the end caps. The end caps provide positioning holes for the specimen systems and centering and temperature control of the capsule via a scallop ledge. The RB* subcapsule is filled with helium gas at atmospheric pressure.

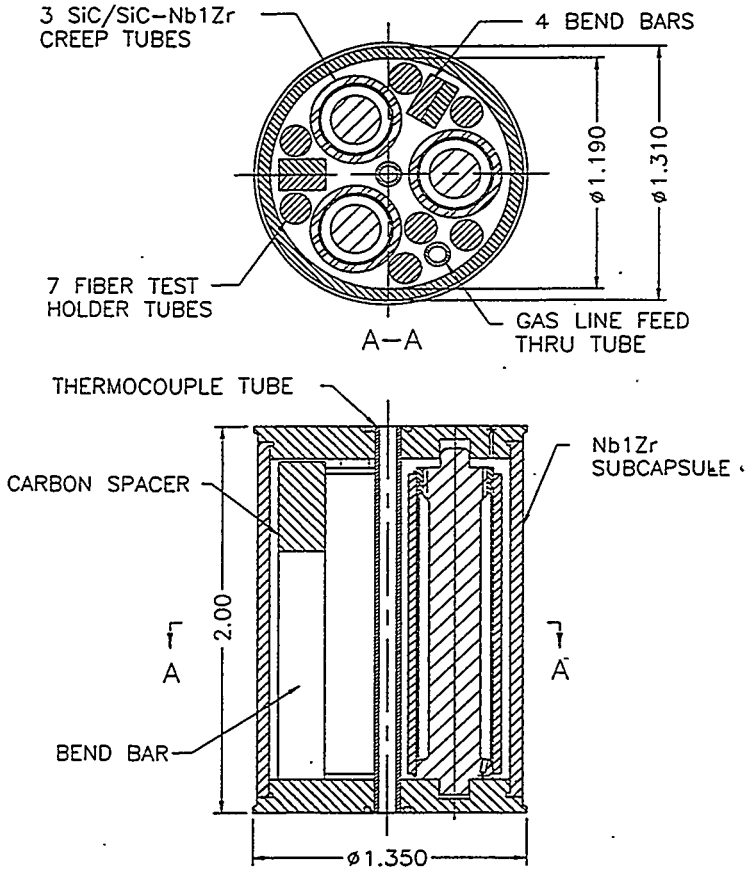

Figure 1 Layout of the RB* subcapsule. Dimensions given in inches.

The specimen loading system, also referred to as the SiC/SiC-Nb1Zr creep subcapsule, is shown along with the specimen cylinder in Figure 2. The main function of this system is to provide a fairly constant radial loading (pressure) to the SiC cylinder, which in turn, gives rise to a constant hoop stress in the specimen. The cylindrical specimen fits tightly on the loading subsystem (secured by pins) and is loaded from the thin-walled tubing (0.010 in. "bladder"). The outside of the bladder tube may be coated with a thin film (approximately 1 μm) of alumina to minimize any adverse chemical interactions between the Nb1Zr tube and the SiC cylinder. The center core and end cap components (with a threaded and welded ring at one end) minimize the axial deformation and axial load transmitted to the RB* subcapsule (see structural analysis section). This subsystem is constructed of all Nb1Zr. This material was chosen for the same reasons given above, plus it is the only refractory material for which irradiation creep data exist for the high temperatures of interest (see section on performance predictions). The gas space is filled with pressurized He gas. This pressure is set at room temperature so that at the operating temperature, the pressure is such that the desired hoop stress is produced in the specimen.

In addition to the test design described above, the experiment requires that a photon shield, most likely fabricated of depleted uranium, be inserted in the HFIR RB* location. This shield (ID = 1.66 in., OD = 1.92 in.) is an RB* position liner that fits around the RB* coolant channel, and reduces the gamma heating rates, as well as associated temperatures and temperature gradients in the specimen.

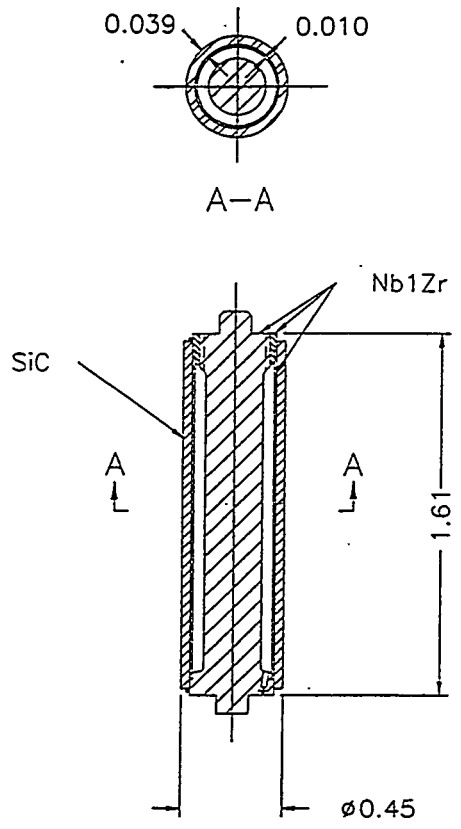

Figure 2 Schematic of creep specimen.

The experiment functions as follows:

1. As the reactor comes to power, gamma and neutron heating are generated within the RB* capsules.

2. This heat flows to the reactor coolant (outside the HFIR RB* irradiation capsule) via convection, conduction and radiation, creating temperature gradients within the capsules. To obtain the desired specimen temperature range, the annular control gas gap between the RB* capsule and the HFIR RB* irradiation capsule is set to a value determined in the design analysis. To compensate for uncertainties, the temperature can be "fined tuned" by adjusting the composition of the He/Ne gas mixture (RB* temperature control system) in the small annular temperature control gap.

3. Because of the increase in temperature over ambient conditions with the onset of irradiation, the preset pressure within the specimen loading system capsule increases (nominally according to the ideal gas law), which in turn imposes a radial pressure on the specimen cylinder. This radial pressure is reacting internally by a hoop stress within the

specimen. Differential thermal expansion causes an interference between the specimen and the bladder, but this is a secondary effect which relaxes out readily with irradiation.

4. The creep compliance in the thin Nb1Zr bladder tube is several orders of magnitude greater than that in the specimen, and in effect this tube "flows" with the specimen allowing the gas pressure to be transmitted radially to the specimen, with a minimum resistance of its own. Hence, during irradiation, a fairly constant hoop stress is maintained on the specimen, providing creep data at constant stress.

5. This thin-walled bladder tube is restrained in the axial direction both internally by the Nb1Zr core in the specimen loading subsystem and externally by the RB* subcapsule. This restraint mitigates the potential for stress rupture failure due to axial creep.

PERFORMANCE PREDICTIONS

Performance predictions were made to determine the time-dependent structural behavior of the pressurized cylinder specimen. The focus here was to get assurance that the objectives of the experiment could be met, and to provide a model which could be used in post-test data analysis. In the preliminary design phase, parametric studies were performed to improve the design and to assess sensitivities.

Finite element analysis (FEA) of the proposed experiment design modeled the pressurized Nb1Zr thin wall bladder tube, the SiC/SiC specimen cylinder (tube), and the interaction between the two tubes, at regions away from the end caps. The ANSYS FEA program (Swanson) was used for the two-dimensional (2-D) axisymmetric (R-Z) model using axisymmetric shell elements (SHELL51) for the tubes and gap elements (CONTAC12) for the frictionless interaction mechanics. The finite element model (FEM) only considers radial deformations, as axial friction between the bladder and the specimen is assumed to be nonexistent (see below). The model schematic is shown in Figure 3, giving element and node numbers.

The model considered internal gas pressure loading on the bladder tube, thermal expansion of both tubes, irradiation creep of both tubes, and irradiation swelling of the Nb1Zr tube. Irradiation swelling the SiC/SiC cylinder was ignored as it is expected to be negligible. Because irradiation creep and swelling correlations did not exist for the Nb1Zr material at the temperatures of interest, relationships were developed using regression analysis on data given in the space power program literature (Paxton). Irradiation creep rates for the SiC composite were taken from Garner, et al., 1996. Other Nb1Zr material properties were taken from Carter, Hayes et al., and Garner et al., 1994. Neutron fluxes were assumed to be those for the HFIR reactor RB* location as given by Hobbs and Hicks. Analysis was made for the two main temperatures of interest, 800 and 1000°C. The corresponding room temperature pressures within the bladder tube were 8.95 and 7.26 MPa,[1] respectively, and were determined using an iterative procedure to produce a nominal initial 150 MPa specimen hoop stress at power.

Analysis of the reference design at 800 and 1000°C, in which there was an assumed small initial room temperature diametral gap of 0.02 mm (0.0008 in.), showed a small permanent increase in diameter of approximately 4.6 μm (a measurable value using existing equipment) at the end of 300 EFPD. The predicted deformations are comparable for both cases as the hoop stresses are equal and the creep rate is temperature independent for temperatures

---

[1]SI and English units for pressure/stress are used interchangeably in this report. Both unit systems are not always cited; to convert psi to MPa multiply by 0.006896

below 1000°C. Figure 4 shows the calculated hoop stresses in both the SiC/SiC specimen and the bladder tube during the irradiation, for both temperature conditions analyzed. As shown, the hoop stress in the specimen remains nearly constant over the life of the experiment, a design goal.

At 1000°C, the calculated hoop stress in the specimen decreases 0.7% over 300 EFPD; for the 800°C case, the stress increases 3.1%. These differences can be explained, and are mainly due to the difference in thermal expansion interference (the Nb1Zr expands into the SiC/SiC). For irradiation at 1000°C, the hoop stress on the bladder tube is compressive, due to the combined effect of differential thermal expansion and internal pressure loading. As the interference compressive hoop stress on the bladder tube relaxes due to creep (the SiC/SiC specimen is dominant as its creep resistance is orders of magnitude greater then the Nb1Zr), the tube contracts, and hence, it causes a reduction of the interface pressure and the hoop stress in the specimen. As there is less interference at the 800°C conditions, the combined thermal and pressure effect produce a tensile hoop stress on the bladder, and hence has an opposite effect on the specimen. The hoop stress in the bladder in both cases significantly relaxes, and hence the bladder tube effectively transmits the internal pressure loading radially to the specimen with little internal resistance, as intended. This is confirmed as there is close agreement with the calculated hoop stress in the specimen using the thin wall treatment (pr/t) with the bladder pressure at power.

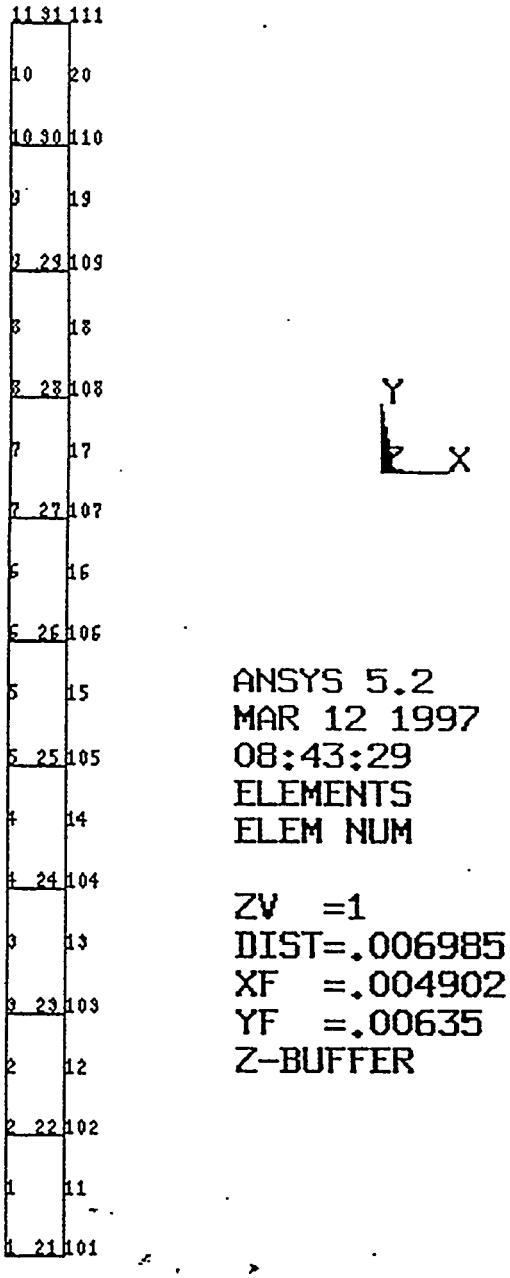

Figure 3 Schematic of FEM model, showing element and node numbers.

The uncertainty in friction between the coated Nb1Zr tube and the SiC/SiC specimen leads to an uncertainty in the stress state, and hence the effect on predictions versus measurement. The predictions assume a stress state which is uniaxial (hoop, θ). If friction exists along with negligible tangential creep in the bladder tube, then a biaxial stress state would exist in the specimen. The upper bound would be near a stress state for a pressurized closed tube, i.e., 2:1 (hoop to axial). Reality is likely to be a biaxial stress state somewhere in-between. This stress state should remain constant, unless

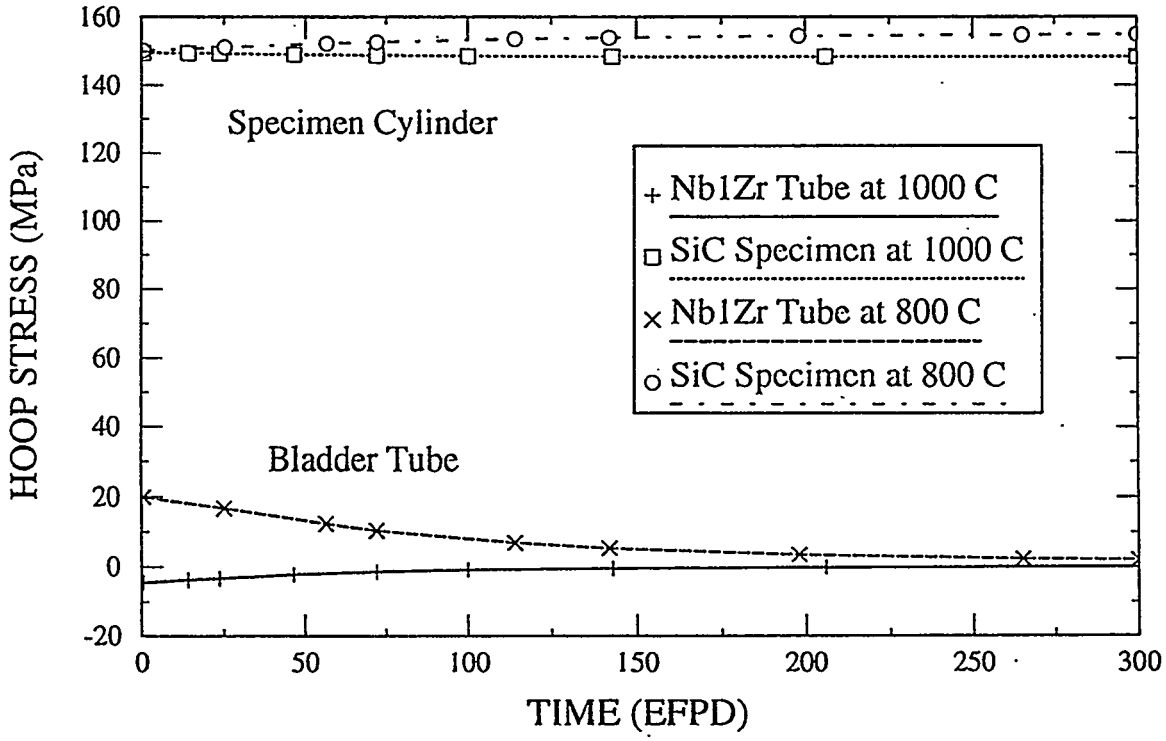

Figure 4 Calculated hoop stresses in SiC/SiC specimen and bladder tube during irradiation at 800 and 1000°C.

loading system "bottoms out" on the RB* capsule, in which case the axial strain increment is zero.

This uncertainty is expected to introduce at worst only a small error. Multiaxial stress state creep is based on the equivalent, or effective, stress and conservation of volume. The effective stress for this biaxial case is defined as:

$$\sigma_e = [(\sigma_\theta^2 + \sigma_a^2 + (\sigma_\theta - \sigma_a)^2) / 2]^{1/2}$$

For the case where the axial stress is ½ of the hoop stress, then:

$$\sigma_e = 0.866\ \sigma_\theta$$

This says that there is an uncertainty range of creep deformation due to friction effects of no more than 13% (only the radial deformation is measured).

Sensitivity study cases were run for variations in Nb1Zr tube thickness, and irradiation creep and swelling rates to account for uncertainties. Calculations showed that reasonable uncertainties in the Nb1Zr material properties, including those due to irradiation swelling, did not have a significant effect on the resulting specimen stress and deformation. Small changes in the bladder wall thickness also did not have a significant effect on the specimen performance.

PHYSICS ANALYSIS

The purpose of this analysis was to determine the gamma ray heating rates for the material used in the SiC/SiC experiment and adjacent reactor components in a mid-core RB* location. The effects of different photon shield materials were also evaluated. These heating rates are used in subsequent thermal analysis.

The MCNP computer code (Breismeister, Carter) was used for the heat deposition calculations. The calculation was made by modeling a cylinder containing regions for each of the different elements, i.e., concentric cylinders, as shown in Table 1. This model represents the photon shield (if included), the RB* coolant channel (water), the HFIR irradiation capsule, and the RB* subcapsule and internals. For this analysis it was assumed that the RB* subcapsule was constructed of TZM (see alternative design).

Table 1. MCNP Model Dimensions and Materials.

Radius (in.)	Shield	Density (g/cc)
0.25	Inner Void	0.0
0.28	Niobium	8.55
0.319	Carbon	2.62
0.358	Silicon	2.33
0.59	Helium	0.1787
0.625	Molybdenum	10.2
0.68	Helium	0.1787
0.75	Iron	7.86
0.83	Water	1.0
0.96	Shield (W/U)	19.3/18.9

The input files include an f6 heating tally to calculate the gamma heating. Because MCNP calculates the heat deposition as MeV/g, the heating tally was multiplied by 1.6022E-13 W/MeV to convert to units of W/g.

The energy dependent gamma ray flux distribution used for these calculations is given in Table 2. The source was modeled in the MCNP calculation as four planes surrounding the metal element model. The source particles were emitted perpendicular to the different source planes. The total particle weight for the MCNP calculation was set equal to the total flux multiplied by the surface area of the four planes.

Table 3 summarizes the calculated heating rates for the various elements for cases of no shield, a uranium shield and a tungsten shield. As shown, the depleted uranium shield is the most effective in minimizing the heating rates, and hence was chosen as for the reference design.

Table 2. Gamma Ray Flux.*

Energy (MeV)	Flux (photons/cm^{2}s^{-1})	
	PTP	RB*
0.00	0.00e+00	0.00e+00
0.50	7.80e+15	3.54e+15
1.00	1.85e+15	5.12e+14
1.50	8.52e+14	2.23e+14
2.00	3.72e+14	1.16e+14
2.50	3.39e+14	8.75e+13
3.00	1.51e+14	4.65e+13
4.00	1.55e+14	5.69e+13
5.00	1.14e+14	2.43e+13
20.00	9.27e+13	4.58e+13
Total	1.15e+16	4.65E+15

*From J. Gekin, ORNL.

Table 3. Heating Rates with Different Shields.

Element	No Shield (W/g)	Tungsten Shield (W/g)	Uranium Shield (W/g)
Nb	17.4	8.40	7.12
C	9.63	6.07	5.31
Si	10.5	6.50	5.71
He	9.42	5.78	5.04
Mo	18.6	8.13	6.90
He	9.43	5.57	4.84
Fe	13.1	6.47	5.63
Average (above)	12.6	6.70	5.79
Water	11.5	6.12	5.30
Shield		15.1	16.8

THERMAL ANALYSIS

The goal of the thermal design is to provide a design temperature (or temperature range) for the specimens. A secondary goal is to assure that the temperatures of structural members of the test assembly are acceptable. The thermal design includes the sizing of wall thicknesses, sizing of the control gas gap, and sizing of the scalloped centering rings on the RB* subcapsule end caps where much of the gamma heating occurs due to their thickness. The reduced gap at the end caps, in addition to providing a centering function, allows much of the heat to flow out of the RB* capsule without adversely affecting the temperature of the specimen.

Two 2-D finite element thermal analyses, an R-Z axisymmetric and a 2-D sector analysis, were made to determine the temperature distribution in the SiC/SiC specimens and test assembly. Both models use the ANSYS (Rev. 5.2) Finite element analysis program. These analyses considered internal heat generation due to gamma heating, conduction/convection within the specimen/bladder and capsule, thermal radiation across gas gaps, and convection to the reactor coolant. Material properties for these analyses were taken from Carter, CRC, Hayes et al., and Touloukin.

It is desirable, but not necessarily required, that all contents within the RB* subcapsule are at approximately the same test temperature (800 or 1000°C). The subcapsule is filled with helium gas for maximum heat transfer and uniformity in temperature. The Nb1Zr capsule wall and end caps provide much of the gamma heating to the subcapsule. The annular gas gap (Ne/He mixture) is used for temperature control. For design purposes, a nominal 50/50 mix of He and Ne is assumed. It is assumed that the ability to vary the gas mixture will compensate for any uncertainties in the analysis and reactor operations. Converging on a design, i.e., desired temperatures, was an iterative process involving varying the thickness of the subcapsule wall (within stress constraints), the annular gas gaps and the gas mixture.

The first thermal FEM, i.e., the R-Z axisymmetric model, is used primarily to size gas gaps and wall thicknesses. Resulting temperatures within the RB* subcapsule represent homogenized, or smeared, values only. One-dimensional models were not considered because of the axial effects (end cap gap and adjacent capsules). This R-Z axisymmetric FEM represents a one-half (axial symmetric centerline) axisymmetric section of the RB* subcapsule within the HFIR RB* irradiation capsule. Radially the model spans the RB* centerline to the reactor coolant. The FEM also simulates axial heat transfer to an adjacent cooler RB* subcapsule, which is expected to be the initial case, via pseudo axial gas gaps. The ANSYS model comprises axisymmetric ring conduction (PLANE55) elements, and radiation link (LINK31) elements which connect nodes on both side of the control gas gap.

This first FEM is shown schematically in Figure 5 (showing materials). The light blue color (#1) elements represent stainless steel components, e.g., the HFIR RB* irradiation capsule. The magenta color (#8) elements represent the He/Ne gas mixture in the temperature control gap. The red (#3) elements represent the Nb1Zr RB* subcapsule wall and end cap. The green (#6) elements represent the homogenized contents inside the RB* subcapsule. Here, volume weighted average properties and heat generation rates are used where the volume fractions are 54.1% He; 26.4% SiC; and 19.5% Nb1Zr. It was expected that the temperatures in the pressurized cylinder specimen and the specimen loading subsystem would likely be hotter than the maximum temperature predicted for homogenized treatment, and hence the design goal was set for a lower maximum predicted temperature (approximately 50°C). Material properties (thermal conductivity) are taken as temperature independent at an expected temperature range, and are given in Table 4. The effective emissivity used for the thermal radiation between the concentric stainless steel and Nb1Zr cylinders is 0.125. The convective heat transfer coefficient used for convection from the

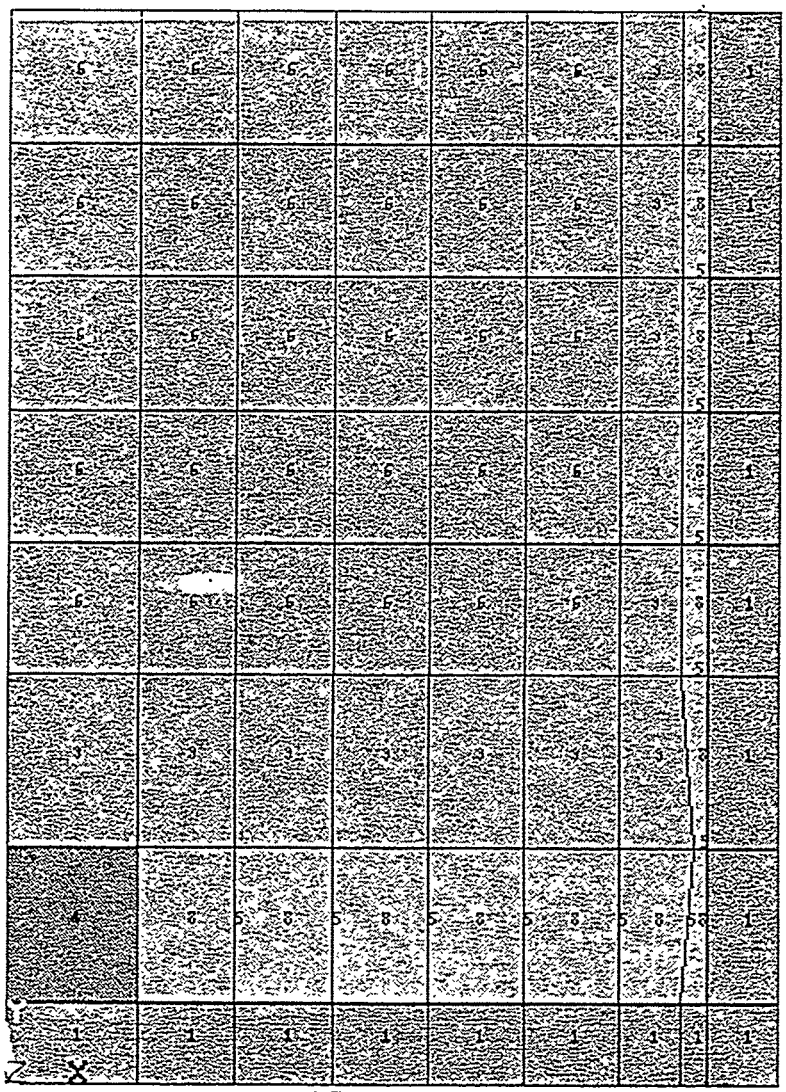

Figure 5 R-Z thermal FEM: materials/conductivity elements

convective heat transfer coefficient used for convection from the HFIR RB* irradiation capsule to reactor coolant (at 66°C) is 1935 Btu/hr-ft^2-°C. This was determined via empirical relationships (Rohsenow, et al.) for forced convection for reactor coolant (water) flowing at 0.85 ft/s.

Figure 6 shows the resulting temperature profile for the 1000°C case. Here the maximum temperature in the HFIR RB* irradiation capsule is less than 200°C. The temperature drop across the control gas gap is approximately 650°C. The RB* capsule wall is at temperatures in the range of 870 to 890°C. An average 80°C temperature gradient is calculated within the RB* capsule, with a maximum average temperature of 950°C. The SiC/SiC cylinder specimen is expected to be at an average 1000°C. Similar trends were predicted for the 800°C design.

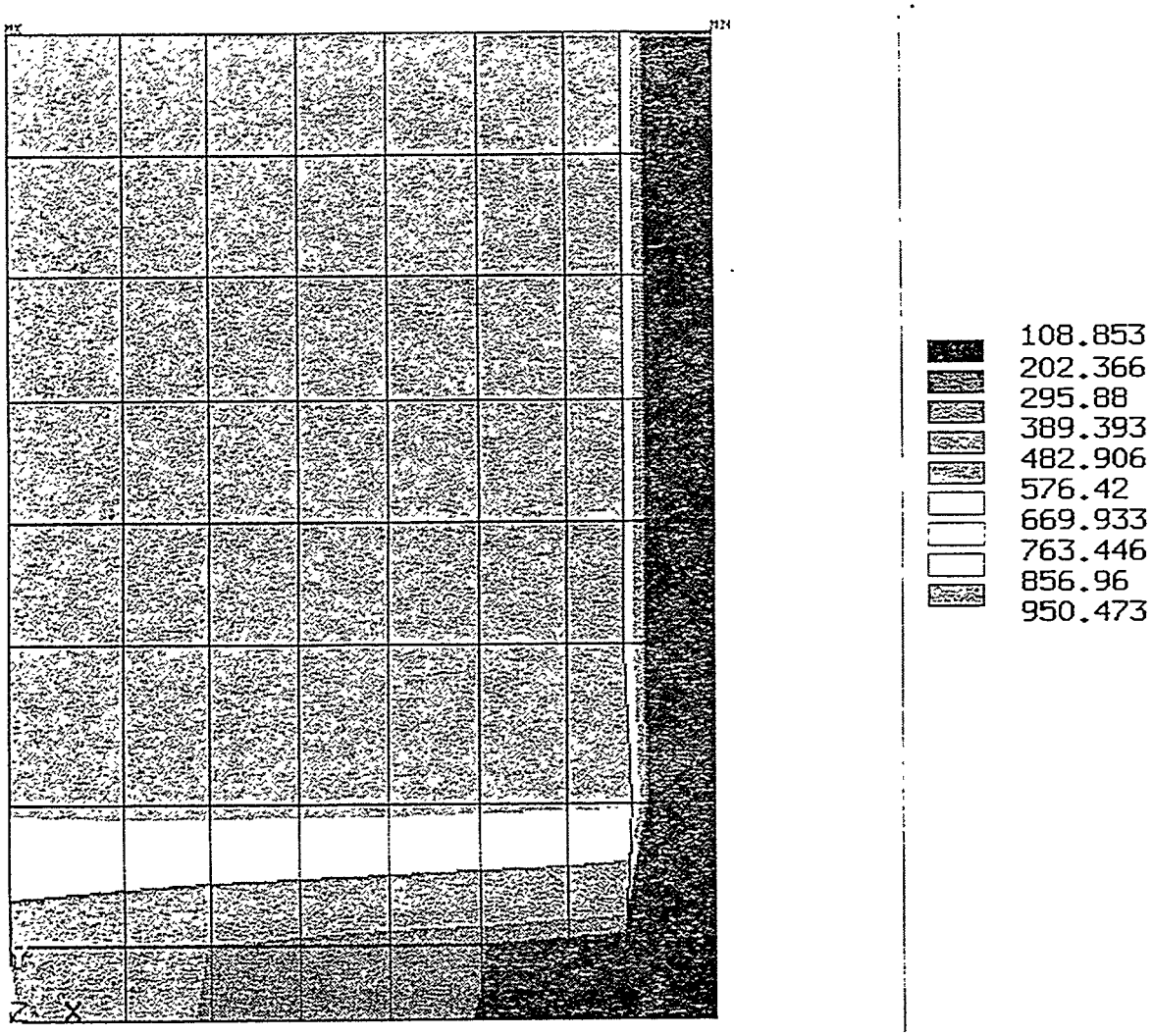

Figure 6 R-Z thermal FEM: temperature profile (1000°C case).

To obtain the desired temperature ranges, the following radial temperature control gaps (inches at power) are required:

	800°C case	1000°C case
Tube-to-tube:	0.019	0.027
Effective[1] end cap to tube:	0.010	0.018

The second thermal FEM is designed to calculate more detail temperatures within the RB* subcapsule. This model (see Figures 7 and 8) is a 2-D 60° sector model (minimum section of symmetry) representing a slice through the axial center of the experiment. Regions from the thermocouple tube to the reactor coolant are modeled. As this model does not consider heat

[1]As modeled minimum clearance; the actual geometry, i.e., the scalloped ridge, should have an equivalent thermal conduction characteristics.

flow in the axial directions, and is based on the tube-to-tube gaps, the resulting temperatures are expected to be higher than actual.

The model comprises ANSYS 2-D plane thermal conduction (PLANE55) elements and radiation link (LINK31) elements. Figure 7 shows the conduction elements with material numbering (colors and numbers). The light blue (#1) elements represent the stainless steel HFIR RB* Irradiation Capsule. The purple (#2) elements represent He gas in the bladder tube. The red (#3) elements represent the Nb1Zr components, which include the RB* Capsule tube, the thermocouple tube, and the bladder tube and core. The dark blue (#4) elements represent the SiC specimens and components. The magenta (#8) elements represent the control gas Ne/He 50/50 mixture. The yellow-green (#9) elements represent the He gas fill within the RB* subcapsule. The thermal conductivity, k, for this gas is an effective conductivity, k_{eff}, as it includes the effects of natural convection. This is considered reasonable as the gap is large enough for the existence of convection currents. K_{eff} is determined from empirical relationship summarized by Irwin, and effectively is 1.8 times larger than the normal conductivity of the gas itself. Radiation link elements are shown in Figure 8. Material properties (some of which are temperature dependent) are given in Table 5. Effective emissivities for material couples (assumes concentric cylinders with small annular gap for geometry) were 0.125 for Nb1Zr to Nb1Zr and Nb1Zr to stainless steel; and 0.14 for SiC to

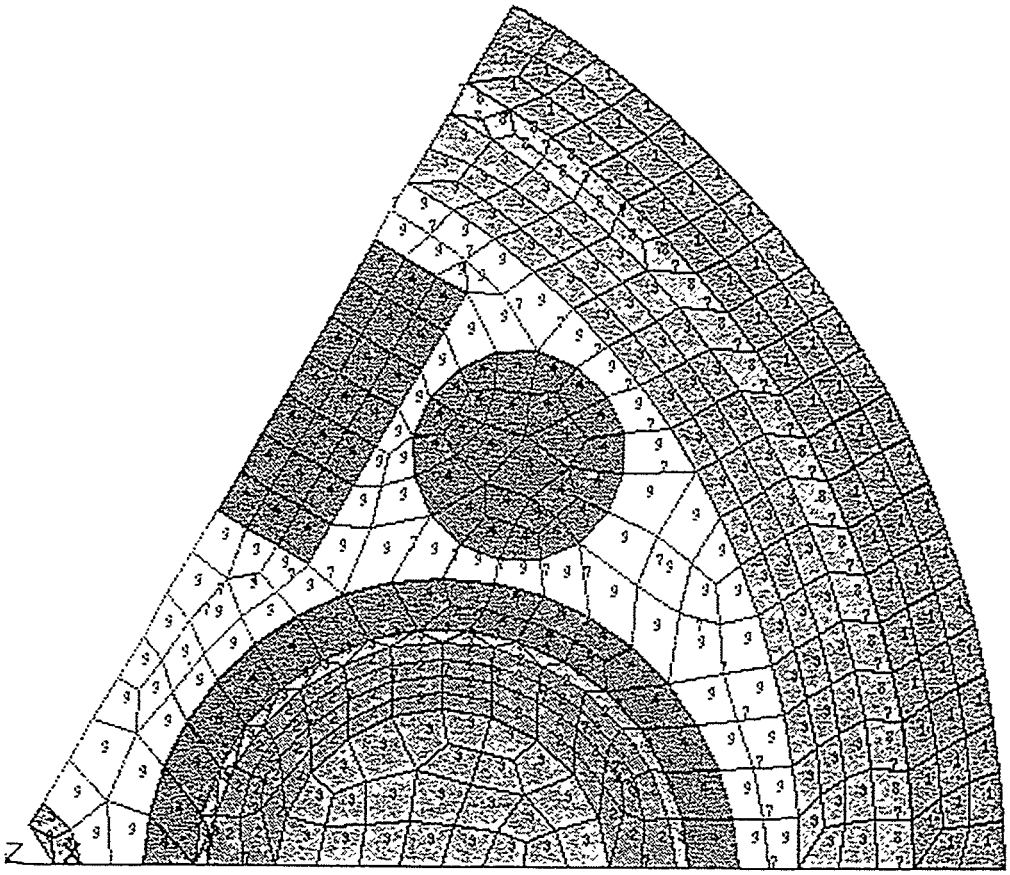

Figure 7 Sector thermal FEM: materials/conductivity elements.

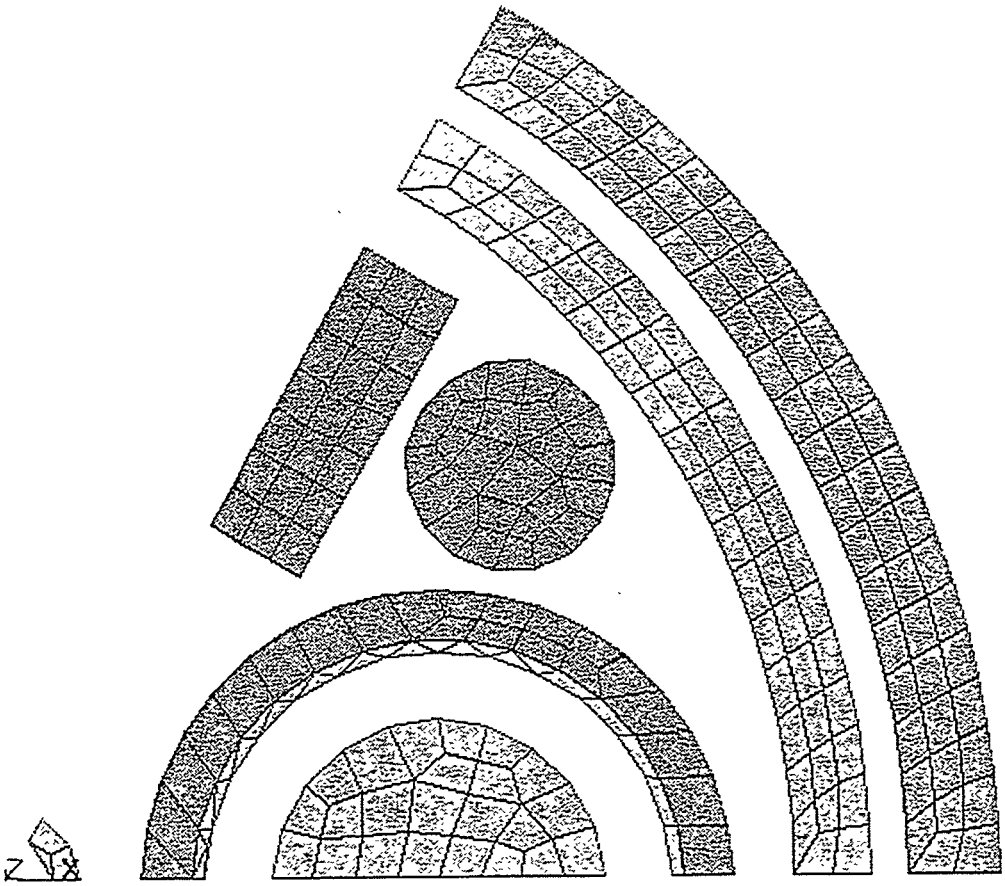

Figure 8 Sector thermal FEM: radiation link elements

SiC and SiC to Nb1Zr (Rohsenow, Touloukin). Predictions were made for the 1000°C case only, using the same annular control gap as was used in the R-Z analysis. Resulting temperature profiles are given in Figure 9 (overall profile) and 10 (internal RB* subcapsule). The overall profile shows that the temperature of the RB* subcapsule wall is about 170°C cooler than that predicted in the R-Z analysis, and that the gradient across the RB* capsule is 490°C, considerably more (as expected) than that predicted for the case with homogenized properties. When comparing the two cases, it is apparent that this sector model, which neglects the axial heat transfer effects, will overstate temperature gradients (axial effects and the thick end caps should mitigate the large ΔTs). It is likely that the RB* subcapsule wall will be hotter and that the specimen be cooler than is shown in Figures 9 and 10. Nevertheless, several conclusions can be drawn from these results. The thermocouple measurement may be as much as 80°C higher than the average cylinder specimen temperature. The temperature gradient around the circumference of the cylinder specimen may be as high as 150°C. The average temperature in the passive SiC specimens may be as much as 100°C cooler than the cylinder specimen. Temperature gradients across the bend bar and fiber test holder specimens may be up to 130 and 90°C, respectively.

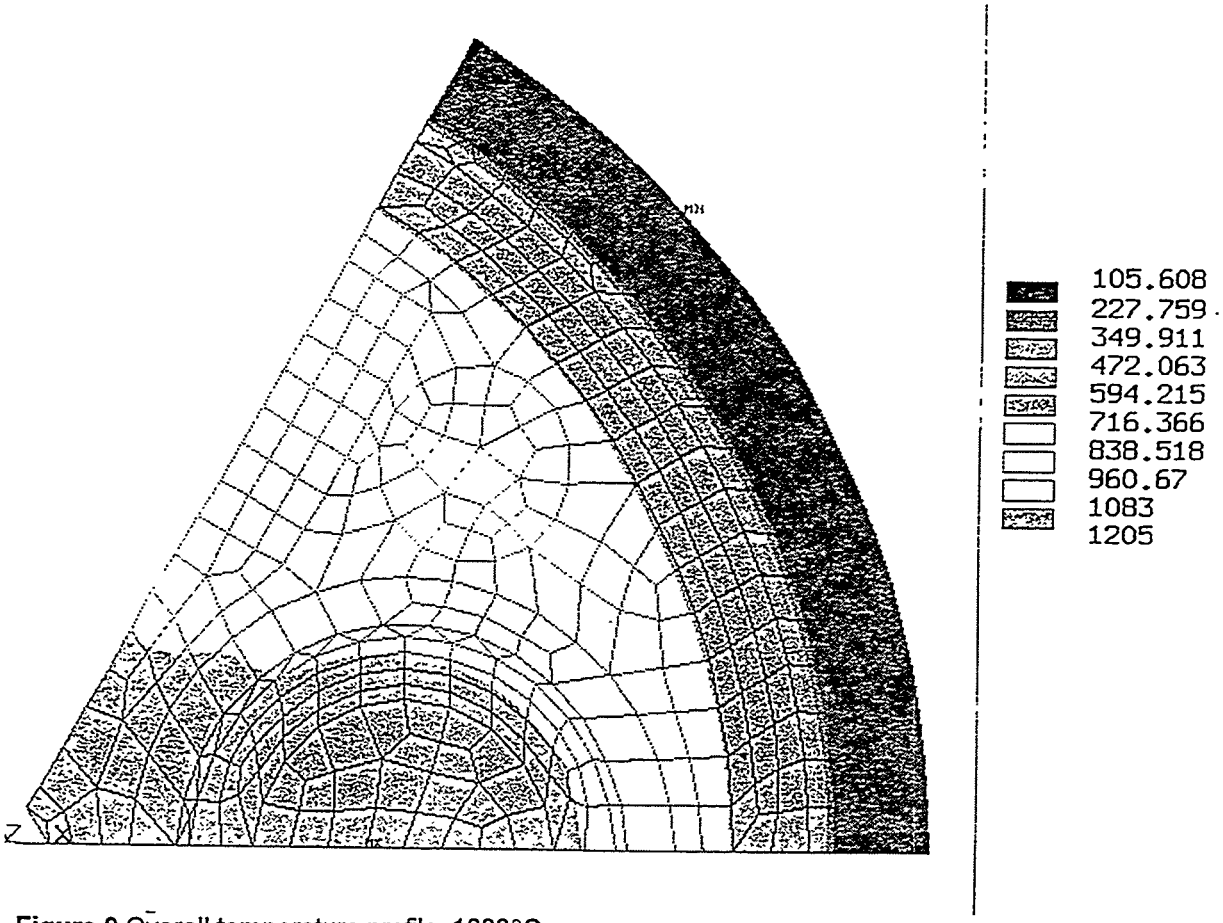

Figure 9 Overall temperature profile, 1000°C case.

Additional 2-D sector analyses were made to determine the effect of design options. One analysis assessed the control temperature range by varying the gas mixture. Here, pure He was used instead of the 50/50 Ne-He gas in the annular control gap. The results showed an 80°C change in average specimen temperature. Hence, the expected control range is 160°C or ± 80°C. Another design option (see alternative design section) considered a specimen loading system without a center core section. Here, the calculated circumferential temperature gradient was 100°C, as compared to 150°C in the reference design.

STRUCTURAL ANALYSIS

The structural analysis addresses the mechanical behavior and the structural integrity of the key components of the test assembly. This involves the calculation of stresses, strains, and deformations and their comparisons with failure criteria. The primary load on the system is from the internal gas pressure in specimen loading subsystem. Other loadings, which are secondary, are those due to differential thermal expansion. Loading due to differential swelling is not considered as the swelling gradients in the Nb1Zr are expected to be small (Garner et al., 1994, Wiffen).

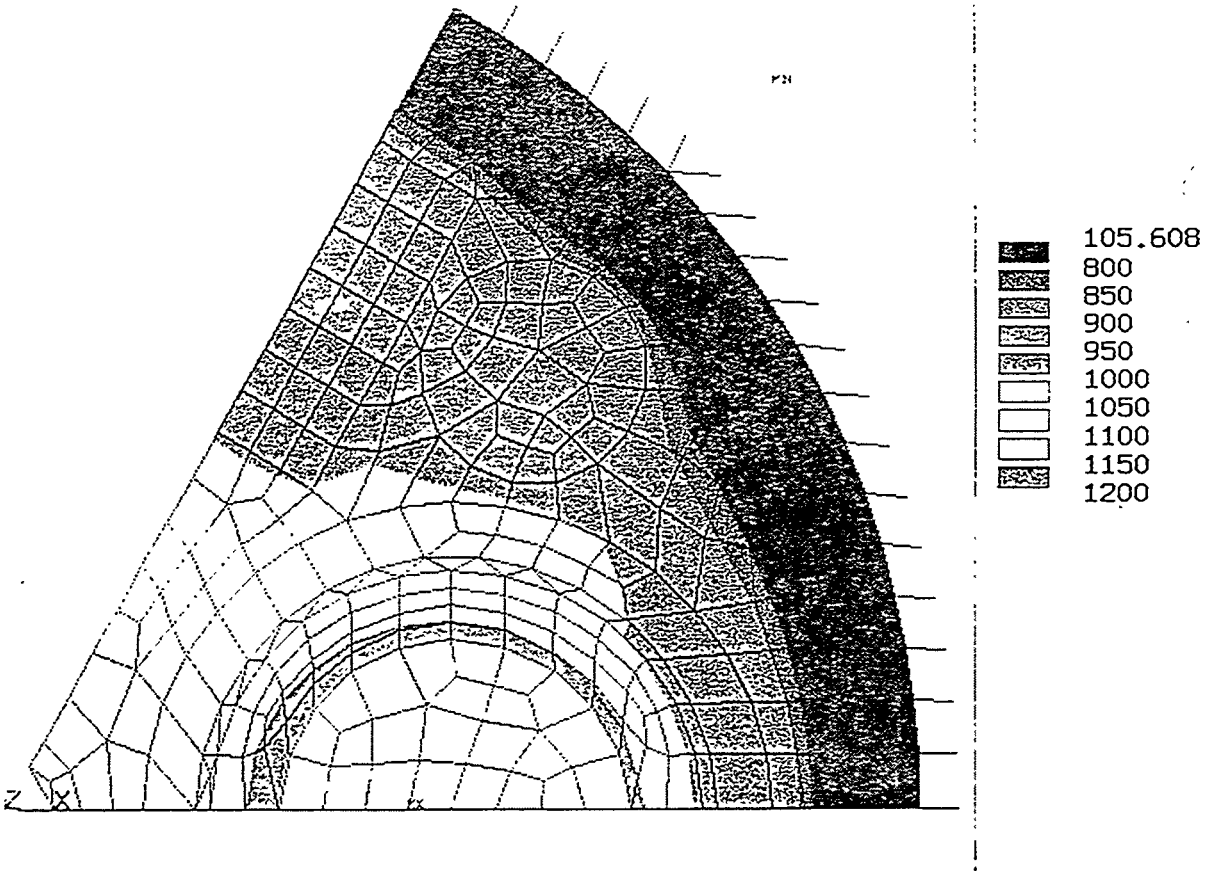

Figure 10 Internal subcapsule temperature profile for 1000°C case.

The specimen loading system is designed to resist the load from internal pressure on its own, i.e., without external support. For the 1000°C case, on which the design is based, the internal gas pressure increases from the room temperature value due to the increased temperature (the gas temperature is approximately 75 °C higher than the specimen) by a factor of (1075 + 273)/(21 + 273) = 4.59, to a pressure of 33.34 MPa. This pressure causes an axial force which is equal to this pressure multiplied by the cross-sectional area in the annular space between the bladder tube and the core. This force is reacted by the cross-sectional area of the bladder tube and the core, to produce an axial stress (F/A) of 26.59 MPa (note: this calculation conservatively neglects any resistance in the axial direction due to friction with the specimen). The radial force is reacted by the tube/specimen, which caused a secondary hoop stress in the bladder tube; these are given in the performance predictions section. As these hoop stresses are secondary (relax out) and are lower than the axial component, they need not be evaluated further, i.e., they are bounded. Discontinuity stresses in the bladder tube to end cap junction are not an issue as the deformations are restrained by the specimen.

The main concern for this component is that the axial stress will cause a stress rupture failure in the bladder tube/core. Stress rupture is evaluated via a Larson-Miller Parameter rupture curve as given in Figure 11 (Conway). For the estimated maximum temperature of the

bladder tube/core, 1100°C (2,472°R) and 300 EFPD (7,200 hr), the parameter P = 2,472*[15 + log (7,200)] = 4.66 x 10^4. From the curve in Figure 11 for the lower bound of the Nb1Zr data, the minimum stress to rupture is 29.5 MPa, which is greater than the operating stress of 26.6 MPa, and hence failure from stress rupture is not expected. Furthermore, for the 1000°C case, it is expected (see below) that the specimen loading system axially interacts with the RB* subcapsule due to creep, and hence the axial stress and corresponding creep damage on the bladder/core will be reduced.

The axial creep deformation in the specimen loading subsystem was also calculated. The analysis used a simple single element ANSYS model as ANSYS input data was previously set up for irradiation creep of Nb1Zr. Here a single ANSYS 2-D spar (LINK1) element of unit length and cross-sectional area was employed, so that the axial stress (26.6 MPa) is input as an axial force and the creep strain is calculated directly. Two cases were run: 1000 and 1100°C (the estimated temperature for the 1000°C specimen case). Creep strains of 0.98% and 5.2% were calculated at 300 EFPD for the 1000°C and 1100°C cases respectively. As the bladder tube length is 1.35 in., the creep deformations are 0.013 and 0.070 in. for the two respective temperature cases.

The axial clearance between the specimen loading system and the RB* subcapsule is 0.050 in., and hence for the 1000°C specimen case, axial interaction can be expected after approximately 210 EFPD (differential thermal expansion, with a 250°C ΔT, would close an additional 0.003 in.). For specimen temperatures lower than 1000°C, interaction is not expected.

Other secondary stresses in the specimen loading subsystem, which will relax out from creep, arise from the 100°C temperature difference between the hotter core and the bladder tube. To determine this thermal stress, we apply the conditions of equilibrium and compatibility and get the equation:

$$\alpha \Delta T_t l + F/k_t = \alpha \Delta T_c + F/k_c$$

where k (stiffness) = AE/l; (l is length, A is cross-sectional area, E is the modulus of elasticity, α is the coefficient of thermal expansion, and the subscripts c and t refer to core and tube, respectively)

As l is equal, and assuming E and α are equal for the core and tube, we can solve for the interaction force (F). Here,

$$F = \alpha E \Delta T_{c\text{-}t} /(1/A_c + 1/A_t)$$

$$= (7.6 \times 10^6)(4.3 \times 10^6)(100)/(1/0.049 + 1/0.0113) = 30.0 \text{ lb}$$

The corresponding stresses are:

$$\sigma_t = 30.0/0.0113 = 2{,}660 \text{ psi;}$$

and

$$\sigma_c = -30.0/0.049 = -612 \text{ psi}$$

Primary loading and associated stresses on the RB* subcapsule arise from the above-mentioned interaction. The force produced by the bladder internal pressure is now reacted by the specimen loading system and the RB* subcapsule (in parallel). To determine the time-

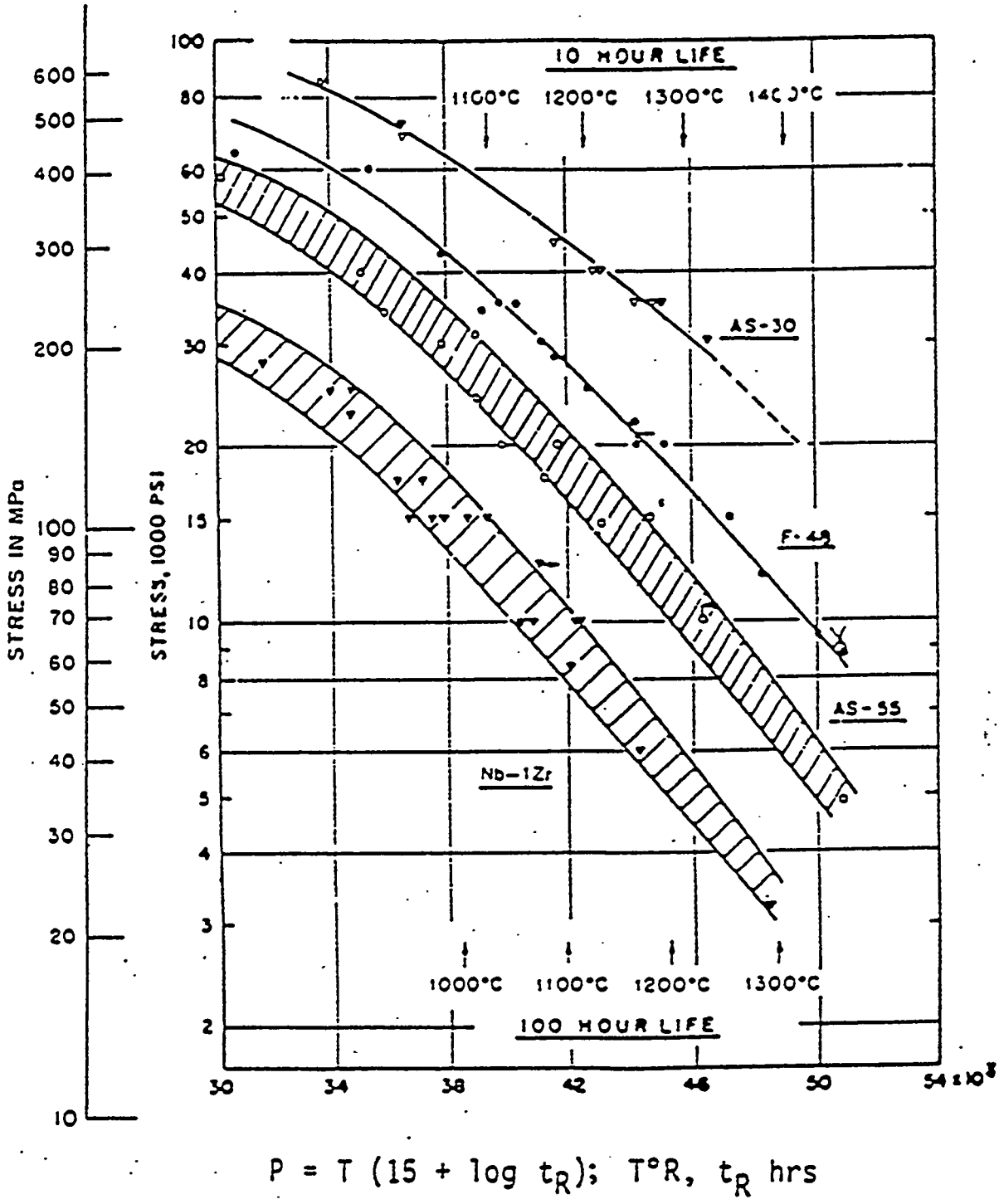

Figure 11 Stress rupture strength of Nb-1Zr.

independent loading distribution, the relative stiffness, k, of these two load paths needs to be determined. This time-independent treatment shows that approximately 65% of the load is carried by the RB* subcapsule. When creep is involved, comparison of the inverse of the creep compliance needs to be addressed. For conservatism, it is assumed that all the load of 3,110 N (700 lb) from the three specimen loading systems is reacted by the RB* subcapsule. Assuming the stress is uniformly distributed to the end plates (see below), the axial primary membrane stress in the RB* capsule (A = 0.235 in.^{2}) tube wall is F/A = 700/0.235 = 2,980 psi (this conservatively assumes that the thermocouple tube does not carry any of the load (see below). The primary (bending) principal stress in the end caps circular plate (thickness = 0.170 in.) as given by Griffel for a case where the outer edge is fixed and supported and the inner edge (thermocouple tube) is fixed, is:

at the center: $\sigma_{r,t} = K_1 W/t^2 = (0.192)(700)/(0.17)^2 = 4{,}650$ psi

at the edge: $\sigma_r = K_2 W/t^2 = (0.221)(700)/(0.17)^2 = 5{,}350$ psi

This closed form theoretical solution is conservative in that the thermocouple tube is free to float (rotation fixed). To better assess the stresses here and also to determine the load distribution on the circumference, which is needed for subsequent discontinuity analysis, and to address the actual loading, an FEA was performed. The ALGOR FEA program (Algor, Hecht) using three and four node Plate/Shell (Type 6) elements were used. This 60° sector (minimum section of symmetry) model is shown is Figure 12. Loading was applied as a pressure load on the region where the specimen loading system interacts with the RB* subcapsule. Both the full thickness of 0.170 in. and the reduced section, where the peg from the specimen loading system fits in the end cap, are modeled. Displacement boundary conditions were used for the fixed condition at the edge and the thermocouple joint. Appropriate boundary conditions, along with the use of boundary elements (on the 60° line) were employed to give symmetry conditions.

The calculated stress intensity profile(maximum difference of principal stresses) on the end cap is shown in Figure 12 (deformed shape stress plot). The maximum stress intensity at the center and edge are 1,790 and 1,420 psi, respectively. On the outer edge the bending stress varies by ± 43% from an average value.

To determine this discontinuity stress including effects of stress concentrations (peak stress) an elastic FEA was used. Here, one-half symmetrical section of the RB* subcapsule (end cap and tube) was modeled. The model also included the central thermocouple tube, as it also provides axial support. The weld regions (weld preps) were modeled in detail to accurately treat stress concentrations, and calculate peak stresses. This FEM is an R-Z axisymmetric model as shown in Figure 13. Here the ALGOR program using both triangular and quadrilateral 2-D axisymmetric Solid Elasticity Elements (Type 4) was used. A very fine mesh was used in regions of stress concentrations. Loading was input as a constant pressure on the inside surface of the end cap.

Figure 13 shows the maximum principal stress (very close to stress intensity values) profile. The maximum peak principal stress of 16,800 psi is calculated at the root of the weld for the thermocouple. When considering the effect of the circumferential loading distribution, as determined on the end cap load analysis, the maximum peak principal stress in the root of the weld between the tube and the end caps is (1.43)(12,400) = 17,700 psi. The maximum

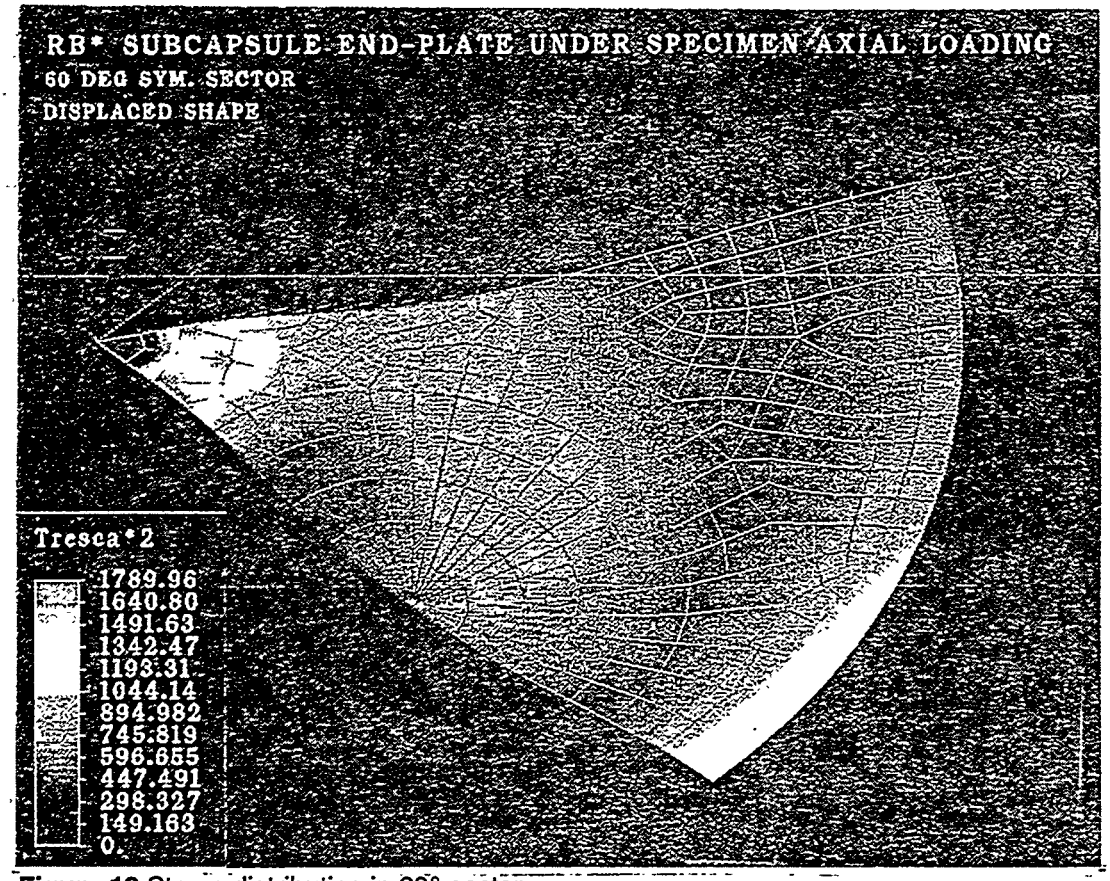

Figure 12 Stress distributino in 60° sector.

stress intensity, not considering stress concentrations, due to structural discontinuity is approximately (2,340)(1.43) = 3,350 psi at the junction of the tube and end cap.

The results show that the maximum axial membrane primary stress in the thermocouple tube is 10,200 psi (70.3 MPa). This is fairly high stress when considering stress rupture at the 1080°C thermocouple tube temperature. For the 90 EFPD time when the primary stress is expected to occur, the Larson-Miller parameter, P, is equal to 4.46×10^4 (see Figure 11). Stress rupture failures would not be expected at effective stress values below 6,000 psi (lower bound of the curve), and hence the current design is not acceptable. However some simple design fixes would provide an acceptable design. For example, increasing the thermocouple tube wall thickness from the current 0.040 to 0.065 in., will reduce the axial stress to 5,200 psi, an acceptable value. Additional design changes, such as increasing the axial clearance between the specimen load system and the RB* subcapsules, from the current 0.050 in., will also mitigate the above concern.

Secondary stresses are also produced from differential thermal expansion. Two areas need to be addressed here. The first is a temperature gradient across the RB* subcapsule tube

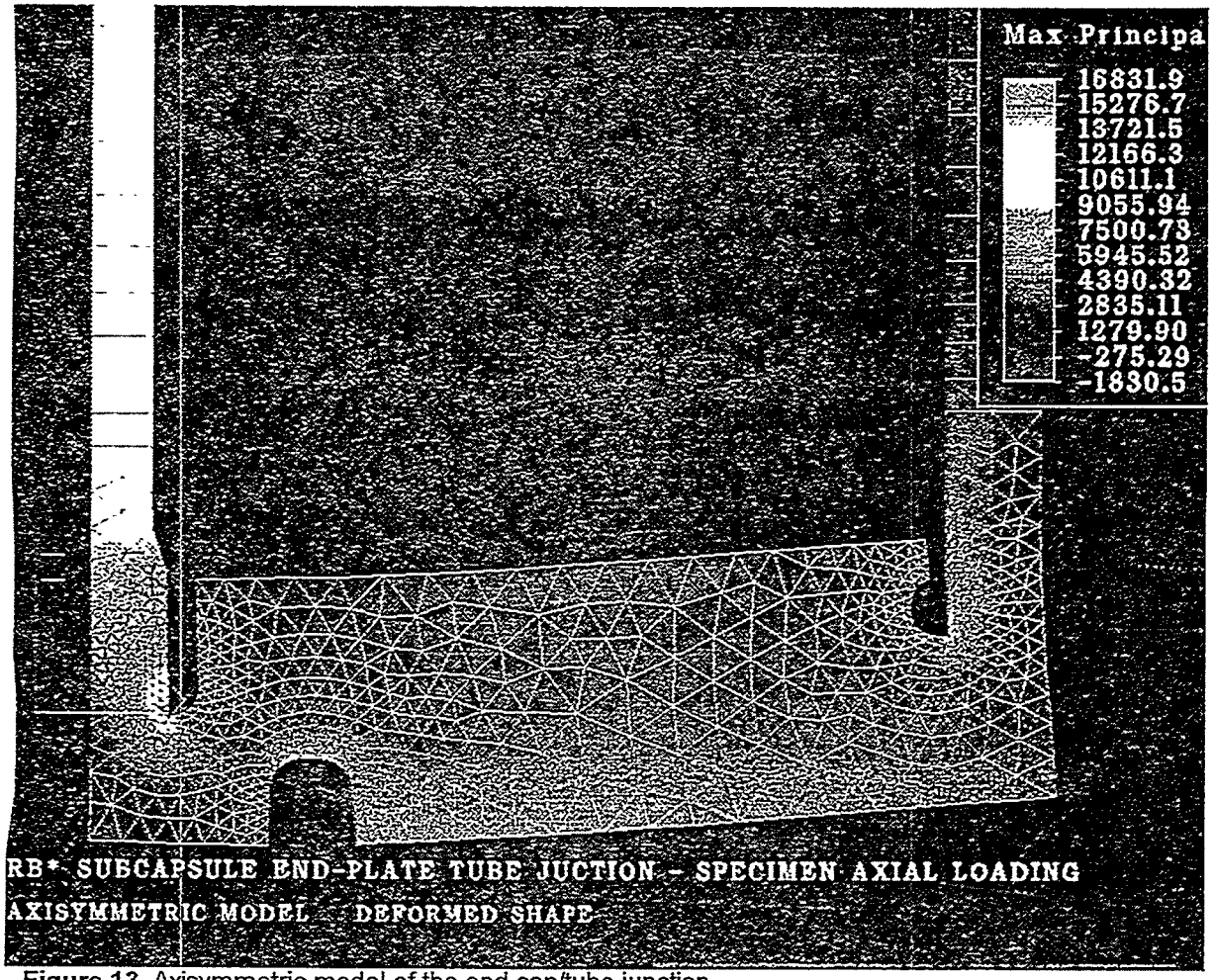

Figure 13 Axisymmetric model of the end cap/tube junction.

wall, where the maximum ΔT was calculated at 1000°C. The elastic bending stress due to the temperature gradient across the wall is:

$$\sigma = E\alpha\Delta T/[2(1-\nu)] = 0.857 \text{ MPa (125 psi)}.$$

Other thermal stresses are those due to temperature differential between the thermocouple tube (1080°C), the end cap and the capsule tube (850°C). To determine these stresses, nodal temperatures were specified on the FEM used in the discontinuity stress evaluation (approximate temperature in the end cap). Two load steps were evaluated: thermal loading only; and thermal plus axial pressure loading.

The results of this analysis show that the thermal load tends to counteract the axial pressure load, with the combined effect being lower stresses than calculated for just the axial loading. The combined loading is only in existence for the 90 EFPD, or less, when axial contact from the specimen loading system occurs. The thermal loading has the effect of closing the weld prep gaps (inherent crack), whereas the pressure load tends to open the gaps. For this combined primary plus secondary load case the maximum stress on the thermocouple tube

is reduced to 5,900 psi. For the welds the peak principal stresses reduce to approximately 1,000 psi at the root of thermocouple weld, and to (1.43)(10,800) = 15,400 psi at the end cap to tube junction. The combined axial plus bending (due to end cap expansion) stress in the capsule tube is less than 1,000 psi. These thermal stresses will tend to relax due to creep. However upon thermal unloading these stress ranges will exist in an opposite sense, and are considered in fatigue evaluations.

Evaluation of the structural integrity of the specimen loading system (at 1050 to 1100°C) and the RB* subcapsule (at 850 to 1080°C) need also be considered for failure modes other than the stress rupture evaluation as given above. Here failure modes such as ductile rupture, fatigue, and ratchetting are considered.

The unirradiated yield strength, S_y, and ultimate strength, S_u, of Nb1Zr at the 850°C are 22,000 and 30,000 psi, respectively (Conway). Wiffen has shown that HFIR irradiation to 14 to 28 dpa (higher than the reference EOL conditions) increases S_y to 28,000 psi and S_u to 40,000 psi. Irradiated uniform and total elongations of 3 and 5% were reported by Wiffen for 800°C, indicating some ductile behavior.

At 1050 to 1100°C, irradiated Nb1Zr showed good ductility with total elongations approaching 10% and with irradiated strengths of 30,000 and 37,700 psi for yield and ultimate, respectively (Hoark, et al., 1994). The unirradiated strengths of 20,000 and 23,000 psi were reported by Conway.

For the specimen loading subsystem, the maximum primary membrane stress of 26.6 MPa (3,860 psi) is well below either the irradiated or unirradiated yield strength of Nb1Zr. Using the rule of the ASME Boiler and Pressure Vessel Code: Section III for Class 1 Nuclear Power Plant Components, this stress should not exceed the minimum of $S_u/3$ or $S_y/2$, or 7,670 psi (using the conservative unirradiated values). The maximum secondary stress of 2,600 psi combined with the primary stress of 3,860 or 6,460 psi, should not exceed three times the primary stress intensity limit, or 23,000 psi. As both these conditions are met, the structural integrity of the specimen loading system is assured to a high degree of confidence.

For the RB* subcapsule, the maximum primary stress intensity of 5,200 psi in the redesigned thermocouple tube (at 1080°C) is less than the 7,670 psi allowable. The maximum primary membrane plus bending stress intensity of 1,790 psi in the end cap (conservatively assumes a temperature of 1080°C) does not exceed the code allowable of 1.5 times the primary membrane stress intensity limit, or 11,500 psi. The RB* subcapsules maximum primary plus secondary stress intensity is the 4,900 psi stress on the thermocouple tube. As this value is less than that evaluated for the primary stress intensity, it need not be further evaluated. As the peak stress intensity of 17,700 psi at the end cap to tube junction weld is less than the yield strength of the weld material and the number of cycles are low (reactor start-ups and shut-downs), fatigue failure is not a concern. Hence, as all conditions are satisfied, there is a high degree of confidence of maintaining structural integrity of the RB* subcapsule.

DISCUSSION

The analysis given here shows that with a few minor changes, the reference design experiment meets the design objectives. There is a high probability for success of the experiment as the design margins related to structural integrity and uncertainties associated with environmental conditions and performance are acceptable. The main disadvantage of the reference design is that the temperature gradient in the cylinder specimen is larger than desired. It is expected that variations to the reference design would mitigate this undesirable condition. Design changes, such as using a thicker bladder tube (high thermal conductivity to

even out temperatures), and making the fiber tube holder out of Nb1Zr (higher heating in a region where the temperature needs to be higher) would reduce this temperature gradient.

It is recognized that there is uncertainty in the thermal analysis results due to both the modeling assumptions (as demonstrated by different results for different 2-D analysis), and the uncertainties in material thermophysical properties, particular emissivities. No attempt has been made here to quantify the uncertainties, however it is expected the flexibility in the temperature control system is sufficient to compensate for these. If greater assurance of meeting the desired temperature is needed, an argon-helium gas mixture could be used instead of the neon-helium mixture considered here. This change would significantly increase the control range. However, the use of argon gas, while feasible, is discouraged as argon activates during irradiation, and presents problems to HFIR reactor operation.

ALTERNATIVE DESIGN

An alternative test assembly design was also evaluated in this design process. This design uses an RB* subcapsule that was made entirely of TZM, and a Nb1Zr specimen loading subsystem without a core. The test assembly functions basically the same way. However, the mechanics of the test assembly are somewhat different. Here, the axial load from the pressurized specimen loading subsystem is resisted by the RB* subcapsule. This axial load is approximately a factor of two higher than in the reference design. The RB* subcapsule is stronger here than in the reference design as TZM has high temperature strength significantly greater than Nb1Zr (approximately 3.5 times stronger, Wiffen).

The main advantage of this design is that there is less gamma heating in the subcapsule, without a core in the loading subsystem, and hence the temperature gradient in the specimen is lower (~100°C). Another advantage is the design and fabrication of the specimen loading subsystem is simpler. The main disadvantage of this design is that the irradiated TZM weld material has been shown to have very low ductility at temperatures below the irradiation temperature, following irradiation; such conditions could occur during the creep test, e.g., when HFIR is shut down between reactor cycles. The design was such that peak stresses (at stress concentrations) were kept to approximately 70% of the yield strength. The consensus on this issue is that the inherent margin of safety in this design is not sufficient. Other disadvantages are that the fabrication of TZM (welding and machining) is both difficult and costly.

COMPUTER RUNS

ANSYS input and output computer files are temporarily stored on the Hanford Scientific and Engineering Computational Center (SECC) in the /home/v92627/ansys/SiC directory. The ALGOR data files are temporarily stored on machine nucdes2.rl.gov in the /home/v92627/fem2/sic directory. At the program conclusion or termination the relevant files are anticipated to be archived in an compressed UNIX TAR file sic.tar.Z on the Hanford Common File System (bluegate.rl.gov) in directory /v92627/fem.

REFERENCES

1. American Society of Mechanical Engineers, *ASME Boiler and Pressure Vessel Code - Section III: Rules for Construction of Nuclear Power Plant Components*, 1971 Edition.

2. Algor, Inc., 1994, *ALGOR Reference Manuals*, P/N 6000.401, 4300.405, Pittsburgh, Pennsylvania.

3. Breismeister, J. F., Editor, 1993, *MCNP - A General Monte carlo Code N Particle Transport Code*, Version 4a, LA-12625, Los Alamos National Laboratory, Los Alamos, New Mexico.

4. Carter, L. L., 1996, *Certification of MCNP Version 4A for WHC Computer Platforms*, WHC-SD-MP-SWD-30001, Rev. 7, Westinghouse Hanford Company, Richland, Washington.

5. Carter, R. J., 1989, *Ceramic Matrix Composites: Physical Properties for SiC/SiC Laminates*, Du Pont, Newark, Delaware.

6. Conway, J. B., 1984, *Mechanical and Physical Properties of Refractory Metals and Alloys*, Proceeding from Symposium on Refractory Alloy Technology for Space Nuclear Power Applications, Oak Ridge, Tennessee, August 1983, CONF-8308130.

7. CRC, 1970, *Handbook and Tables for Applied Engineering Science*, Chemical Rubber Company, Cleveland, Ohio.

8. Garner, F. A., Youngblood, G. E. and Hamilton, M. L., 1996, "Review of Data on Irradiation Creep of Monolithic SiC," Fusion Material Semiannual Report.

9. Garner, F. A., L. R. Greenwood, and D. J. Edwards, 1994, *The Influence of Starting State on Neutron Induced Density Change Observed in Nb-1Zr and Mo-41Re at High Exposures*, Journal of Nuclear Materials 212-215 426-430.

10. Griffel, W., 1966, *Handbook of Formulas for Stress and Strain*, Ungar Publishing Co., New York, New York.

11. Hayes, S. L., D. J. Senor, J. K. Thomas, and K. L. Peddicord, 1989, *Properties Library for Space Nuclear Reactors, Version 1.0*, Advanced Nuclear Fuel Laboratory, Texas A&M University, ANFL-10-R.

12. Hecht, S. L., 1991, *ALGOR Computer Code QA*, WHC-SD-GN-CSWD-321, Rev. 0, Westinghouse Hanford Company, Richland, Washington.

13. Hoark, J. A., M. M. Paxton, and L. K., Egner, 1991, *Third Interim Report on the Mechanical Properties of Nb-1Zr*, ORNL/TM-11430.

14. Horak, J. A., M. L. Grossbeck, and M. M Paxton, 1994, *Effects of High-Temperature Exposure to Vacuum, Lithium and Fast Neutron Radiation on the Tensile Properties of Nb-1Zr*, ORNL-6810.

15. Hobbs, R. W., 1994, *High Flux Isotope Reactor Experimenter's Guide*, Oak Ridge National Laboratory, ORNL/M-2303.

16. Hicks, G. R., B. H. Montgomery, K. R. Thoms, and C. D. West, 1986, *HFIR Irradiation Facilities Improvements - The HIFI Project*, Journal of Nuclear Materials 141-143 (1986) 1018-1024.

17. Irwin, J. J., 1995, *Thermal Analysis Methods for Safety Analysis Reports for Packaging*, WHC-SD-TP-RPT-005, Rev. 1, Westinghouse Hanford Company, Richland, Washington.

18. Paxton, M. M., 1993, *Nb-1Zr Pressurized Tube Creep Correlation at SP-100 Service Conditions*, WHC-SP-1014, Westinghouse Hanford Company, Richland, Washington.

19. Rohsenow, W. M., and J. P. Hartnett, 1973, *Handbook of Heat Transfer*, McGraw-Hill, New York, New York.

20. Swanson Analysis System, Inc, 1994, *ANSYS User's Manual, Rev. 5.1*, DN-R300:51, Houston, Pennsylvania.

21. Touloukin Y. S., and D. P. Dewitt, 1972, *Thermophysical Properties of Matter*, Plenum, New York, New York.

22. Wiffen, F. W., 1994, *Effects of Irradiation on Properties of Refractory Alloys with Emphasis on Space Power Reactor Applications*, Proceeding from Symposium on Refractory Alloy Technology for Space Nuclear Power Applications, Oak Ridge, Tennessee, August 1983, CONF-8308130.

THERMOCHEMICAL INSTABILITY EFFECTS IN SiC-BASED FIBERS AND SiC_f/SiC COMPOSITES -- G. E. Youngblood, C. H. Henager and R. H. Jones (Pacific Northwest National Laboratory)*

OBJECTIVE

The objective of this work is to assess the development and the performance of continuous fiber SiC_f/SiC composites as structural material for advanced fusion energy systems.

SUMMARY

Thermochemical instability in irradiated SiC-based fibers with an amorphous silicon oxycarbide phase leads to shrinkage and mass loss. SiC_f/SiC composites made with these fibers also exhibit mass loss as well as severe mechanical property degradation when irradiated at 800°C, a temperature much below the generally accepted 1100°C threshold for thermochemical degradation alone. The mass loss is due to an internal oxidation mechanism within these fibers which likely degrades the carbon interphase as well as the fibers in SiC_f/SiC composites even in so-called "inert" gas environments. Furthermore, the mechanism must be accelerated by the irradiation environment.

PROGRESS AND STATUS

Introduction

The thermochemical stability of continuous SiC fiber-reinforced/SiC matrix composites (SiC_f/SiC) can be compromised at high temperatures even in "inert" environments such as argon or helium. Usually composite degradation is related to the instability of the fibers, which for Nicalon™ CG fiber occurs when temperatures exceed about 1100°C and is primarily connected to the instability of the silicon oxycarbide phase ($SiO_{2x}C_{1-x}$) in this fiber [1]. According to Labrugere, et al, the mass of Nicalon CG fiber will decrease as the oxygen and free carbon in the bulk fiber decrease following primary and secondary processes [2]:

$$SiO_{2x}C_{1-x} \rightarrow SiO(g) + (2x-1)CO(g) + (2-3x)C(s) \qquad (1)$$

$$SiO(g) + 2C(s) \rightarrow SiC(s) + CO(g) \qquad (2)$$

where CO is the main gaseous species formed during the fiber decomposition. Fiber shrinkage, SiC grain growth and tensile strength loss generally accompany such mass loss in Nicalon CG fiber. In a SiC_f/SiC composite, the carbon present in the left-hand side of Eq. (2) could also include carbon used as fiber coating [2]. Since the mechanical behavior of the composite is so dependent on the interphase performance, potential reactions at the fiber-carbon interface due to this secondary process will profoundly contribute to the degradation of the composite properties. Notably, this degradation mechanism does not depend directly upon the surrounding oxygen partial

---

*Pacific Northwest National Laboratory is operated for the U. S. Department of Energy by Battelle Memorial Institute under Contract DE-AC06-76RLO 1830.

pressure, but depends on the local activities established by the constituents, usually the fiber and the fiber coating compositions, and perhaps upon structural diffusion restrictions.

Development efforts devoted to improving fiber stability and composite performance have met with considerable success with the recent commercial introduction of the low oxygen Hi Nicalon^{TM} fiber. Likewise, the developmental fibers, S type Hi Nicalon^{TM} and Sylramic^{TM}, have compositions very near stoichiometric SiC and should be considerably more stable than Nicalon CG. Nevertheless, for fusion or other applications involving an irradiation environment, experiments that test composite or fiber stability must be carefully planned and carried out because an irradiation environment will surely accelerate degradation mechanisms. Even though the operation temperature may be considered low enough to ensure thermal stability, proper consideration must be given to the effects of longer exposure times, enhanced kinetics, and the actual gaseous environment encountered in an irradiation experiment (or in service).

As an example, consider a typical irradiation subcapsule loaded with SiC_f/SiC bend bars made with Nicalon CG fiber. The fiber has the following composition in weight percent: Si (56.5), C (31.2), O (12.3) and a C/Si atomic ratio of 1.3. The samples usually will take up about 70% of the subcapsule volume, while the remaining space is back-filled with helium gas (at one atm.). Assuming that the bars contain 40 volume percent fiber, oxygen represents about 4.8% of the mass loading. Free carbon, carbon not associated with the SiC phase balance, also represents about 4.8% of the mass loading, while a 0.15 μm thick pyrocarbon fiber coating would contribute another 1.4%. If all of the oxygen were consumed via the internal oxidation process described by Eqs. (1) and (2), CO(g) would be generated and the composite mass loss would be about 8.4% due to mass loss in the fibers and of the carbon interphase. In a closed system, such as in an irradiation subcapsule, the CO gas pressure buildup would retard completion of the reactions and the mass loss would be less than the 8.4% for complete oxygen loss [3]. Nevertheless, fiber and probably coating mass loss could occur with attendant degradation of fiber and composite properties when the fibers (or matrix) contain unstable oxycarbide phases.

In this report, results from two experiments will be explained by using this internal oxidation mechanism. In the first experiment, the irradiation temperature was 800°C, a low enough temperature where SiC_f/SiC composite mass loss was thought not to be a consideration. In a second experiment, an unusual fiber shrinkage behavior will be explained according to the mass loss mechanism. Since the composites in the first experiment were fabricated using the same fibers examined in the second experiment, the fiber shrinkage results and the composite property degradation are correlated through the mass loss mechanism.

Experimental

For the first experiment, composite SiC_f/SiC was obtained from three sources: Dupont, General Atomics (GA) and Ubekosansha (Ube, Japan). The material was cut into bend bars whose descriptions are given in Table 1. The Dupont material, so-called reference CVI SiC_f/SiC made with 0.15 μm pyrocarbon (PyC) coated Nicalon CG fiber, was described in detail in the previous Semiannual Report [4]. The composite made by GA was similar to the Dupont material, except that the PyC coating on the Nicalon CG fiber

was slightly thicker (0.2 μm). The Ube composite was made with Tyranno fiber, but the coating was unspecified. Both the Dupont and GA bend bars were cut orthogonal to the 2D-0/90° plain weave, while the Ube bend bars were a 2D-0/90° or -45/45° pattern.

Table 1. Composite SiC_f/SiC irradiated in COBRA 1A2

Source	Fiber	Coating (μm)	Weave (°/°)	L x W x H (mm)	Density (g/cc)	Number
Dupont	Nic CG	0.15 PyC	0/90	38x6.3x3.5	2.50	6
GA	Nic CG	0.2 PyC	0/90	38x6.1x3.0	2.60	7
GA	Nic CG	0.2 PyC	0/90	38x3.3x1.7	2.45	8
Ube	Tyranno	?	0/90	25x3.8x1.9	2.50	6
Ube	Tyranno	?	45/45	25x3.8x1.9	2.50	6

Half of the samples were inserted into a TZM subcapsule (D05) and irradiated in the EBR II reactor Runs 162-170 for 337 EFPD as part of the COBRA 1A2 test series. The other half were preserved for comparative purposes. Subcapsule D05 received a fast fluence of 6.58 x 10^{26} n/m^2 (E>0.1 MeV), equivalent to a calculated dose of about 80 dpa-SiC [5]. The gas-gapped, but uninstrumented subcapsule was designed to operate at 800°C; however two passive SiC temperature monitors in subcapsule D05 indicated that the end of cycle (EOC) temperature actually was 550 ± 50°C. Similar bars inserted into subcapsules F06 and G03 during the same test indicated EOC irradiation temperatures within 25°C of their design temperatures, 500 and 615°C, respectively. It is assumed that the beginning of cycle (BOC) irradiation temperature was 800°C, as designed. Because of possible gas-gap changes during the long-term reactor operation, it also is assumed that the EOC temperature truly was 550 ± 50°C.

The samples were weighed and dimensioned before and after irradiation. Four-point flexure stress-strain curves were acquired for both the unirradiated and irradiated samples. The flexure tests were carried out at the BOC irradiation temperature of 800°C by a procedure described previously [6]. SiC fixtures with outer/inner spans of 30/15 or 20/10 mm were used with the 38 and 25 mm length bars, respectively. Fracture surfaces were examined by SEM for representative samples.

For the second experiment, Nicalon CG and Tyranno fibers also were irradiated in the EBR II reactor, but at 1000°C for 165 EFPD [7]. The effective dose was 43 dpa-SiC. The fiber properties are given in Table 2. The Tyranno fiber contains even more oxygen and free carbon in an amorphous oxycarbide phase than does the Nicalon CG fiber.

Table 2. Properties of SiC-based fibers selected for mass loss analysis.

Fiber Type	Composition (w/o)	Density (g/cc)	Strength (GPa)	Modulus (GPa)	Microstructure
Nicalon CG	Si-31C-12O	2.55	2.6	190	2 nm ß-SiC grains, free C in amorphous Si-O-C matrix
Tyranno	Si-28C-17O-3Ti	2.37	2.5	190	2 nm ß-SiC grains, free C in amorphous Si-O-C-Ti matrix

In the experiment, bare and coated fiber bundles (63 or 32 mm lengths, respectively) were irradiated and fiber bundle length and density changes were determined.

Results

Composite average 4-pt. bend strengths (BStren), strains at maximum strength (BStrain), initial modulus (IMod) values, proportional limits (PropLim), and relative mass losses after irradiation are given in Table 3. For comparison, the unirradiated values are listed above the irradiated values for each composite type with the standard deviations given in parenthesis. Representative flexure stress-strain curves are given in Figure 1 for the unirradiated and irradiated composites. Representative SEM fracture surfaces are depicted for unirradiated and irradiated SiC_f/SiC composite in Figure 2.

Table 3. Composite mechanical properties before and after irradiation.*

Bar Type/ Fiber Type	BStren (MPa)	BStrain (%)	IMod (GPa)	PropLim (MPa)	Mass Loss (%)
Dupont/	369 (29)	0.43 (0.06)	102 (17)	210 (30)	
Nic CG	207 (29)	0.38 (0.08)	111 (42)	117 (20)	0.15 (0.02)
GA-3.0/	329 (30)	0.94 (0.13)	146 (18)	120 (10)	
Nic CG	129 (46)	0.57 (0.17)	130 (30)	67 (17)	0.37 (0.06)
GA-1.7/	374 (42)	0.76 (0.08)	150 (35)	163 (21)	
Nic CG	88 (6)	0.10 (0.03)	140 (12)	82 (2)	0.74 (0.26)
Ube-0/90	120 (30)	0.13 (0.05)	97 (5)	120 (30)	
Tyranno	148 (30)	0.12 (0.02)	117 (7)	148 (brittle)	0.75
Ube-45/45	215 (55)	0.31 (0.05)	102 (5)	150 (30)	
Tyranno				too brittle	0.63

* Calculated from flexure tests at 800°C in argon.

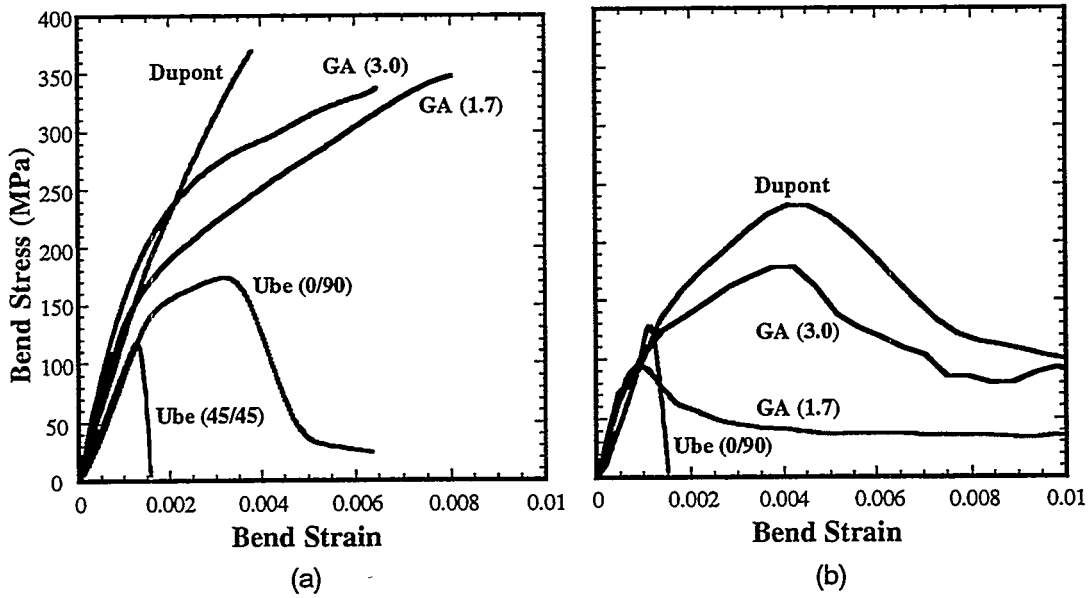

Figure 1. Representative 4-pt. bend stress-strain curves for (a) unirradiated and (b) irradiated SiC_f/SiC composites. The flexure tests were performed at 800°C in argon.

The bend strengths, strains and proportional limits (an indicator of the matrix cracking strengths) decreased roughly 50% or more after the irradiation for the Dupont and GA

composites made with Nicalon CG fiber. The mechanical property degradation was greater for the GA composites compared to the Dupont composite, and for the thin (1.7 mm) GA bars compared to the thick (3.0 mm) GA bars. A similar trend is observed when the composite mass losses are compared, i.e., the mass loss for the GA composites were larger than for the Dupont composite, and the thin GA bars exhibited a

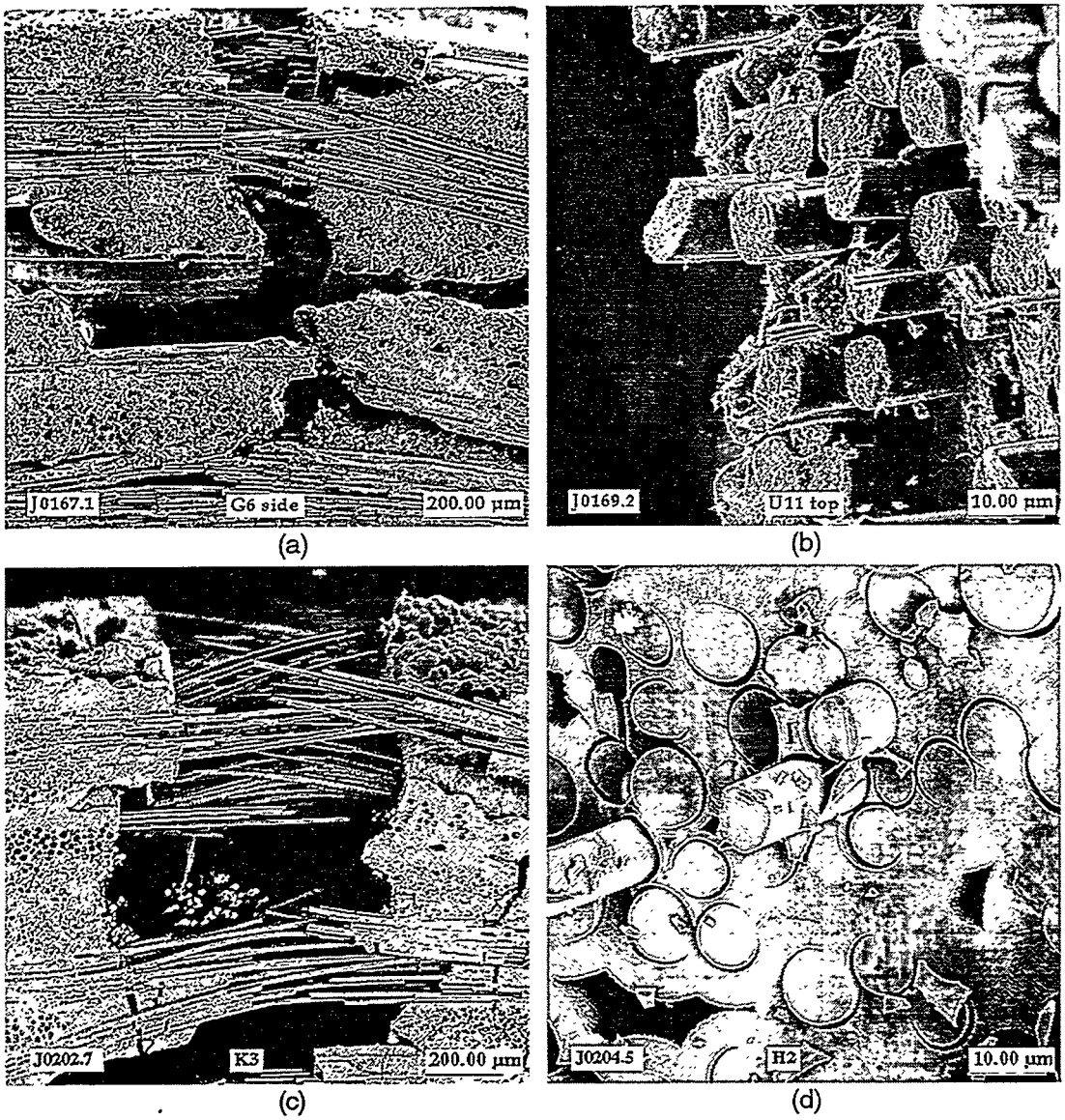

Figure 2. Representative SEM fracture surfaces near the tensile surface for unirradiated (a) GA/Nic CG and (b) Ube/Tyranno composites and for irradiated (c) Dupont/Nic CG and (d) GA/Nic CG composites. Fig. 2(a) illustrates desirable random fiber pull-out for the GA/Nic CG material, while Fig. 2(b) illustrates limited fiber bundle pull-out characteristic of brittle fracture for the Ube/Tyranno material. Fig. 2(c) illustrates more extensive fiber pull-out for the irradiated Dupont/Nic CG material, while Fig. 2(d) illustrates a brittle fracture surface for the irradiated GA/Nic CG material with limited fiber pull-out and large gaps around the individual fibers.

larger mass loss than the thick GA bars. For example, the thin irradiated GA bars, with an average mass loss of 0.74%, exhibited a severely degraded stress-strain curve (see Fig. 1b). The curves for all of the irradiated composites indicate greatly reduced toughness. The mechanical properties for the unirradiated Ube composites were characteristic of brittle fracture, however, the irradiated Ube composites also exhibited significant mass loss.

In Table 4, the measured irradiation-induced relative density ($\Delta\rho/\rho_o$) and length ($\Delta L/L_o$) changes reported for coated and uncoated Nicalon CG and Tyranno fibers are presented along with relative mass loss ($\Delta m/m_o$) predictions. The ratios of the carbon coating mass to the fiber mass (m_c/m_f) also are listed for each fiber. This ratio was estimated using the expression $m_c/m_f = 4t\rho_c/\rho_f D_f$ where t, ρ_c, ρ_f and D_f are the carbon coating thickness and density and the fiber density and mean diameter, respectively.

Table 4. Irradiated fiber mass loss predicted from measured length and density changes.

Fiber	PyC Coat (μm)	$\Delta\rho/\rho_o$ (%)*	$\Delta L/L_o$ (%)*	$\Delta m/m_o$ (%)^	m_c/m_f (%)
Nic CG1	bare	+8.5 (0.4)	-2.9 (0.5)	-0.2	0
Nic CG2	bare	+10.3 (1.3)	-3.8 (0.4)	-1.1	0
Nic CG1	0.15	+10.1 (0.4)	-7.1 (0.8)	-11	3.2
Nic CG2	0.15	+9.4 (0.5)	-7.1 (0.5)	-12	3.2
Nic CG2	0.15 (BN)	+12.4 (0.4)	-3.0 (2.4)	+3	0
Tyranno	bare	+12.7 (0.7)	-5.6 (1.3)	-4	0
Tyranno	0.15	+12.9 (0.5)	-16.6 (0.5)	-37	3.4

* Measured values from Ref. [7], standard deviations given in parenthesis.
^ Calculated using Eq. (3)

The irradiated Nicalon CG and Tyranno fibers both exhibited significant instability with density increases near 9 and 13% and linear shrinkage from 3-7% and 6-17%, respectively. The irradiated fibers that were coated with 0.15 μm PyC shrunk significantly more than the uncoated fibers. The same trend was noted for uncoated and coated HPZ type fibers which also have a high oxygen content. In contrast, Hi Nicalon fiber with a low 0.5% oxygen content exhibited only a 0.7% density increase (data reported in Ref. [7]).

DISCUSSION

It is proposed that the thermochemical instability of the oxycarbide phase in Nicalon CG and Tyranno fibers, which apparently is enhanced by irradiation even at 800°C or below, leads to mass loss and mechanical property degradation in the composites made with these fibers.

For fibers, a good approximation for $\Delta m/m_o$ is given in terms of $\Delta\rho/\rho_o$ and $\Delta L/L_o$ by:

$$\Delta m/m_o = 3(\Delta L/L_o) + \Delta\rho/\rho_o \qquad (3)$$

In deriving Eq. (3), differentials of the mass density ($\rho = 4m/\pi D^2 L$) were taken and isotropic shrinkage ($\Delta D/D = \Delta L/L_o$) was assumed.

Equation (3) was used to predict the $\Delta m/m_o$ values from the measured density and length change measurements in Table 4. The $\Delta L/L_o$ measurements sometimes have rather large uncertainties due to the difficulty in demarcating the ends of a fiber bundle. Nevertheless, the predictions listed in Table 4 consistently indicate mass losses for all cases except for the BN-coated Nicalon fiber. The predicted mass losses for the uncoated and coated Nicalon CG fibers average about -0.6% and -12%, respectively. The predicted mass losses for the uncoated and coated Tyranno fibers are much larger, -4% and -37%, respectively. Apparently, the carbon coating enhances the mass loss mechanism in these two irradiated fibers.

By inspection, the relative mass loss is a factor of 4 to 10 larger than the m_c/m_f ratio for the coated Nicalon CG or Tyranno fibers, respectively. For the Nicalon fibers with 0.15 μm thick PyC coating, the ratio of the bulk free carbon mass to the carbon coating mass also is about four. This implies that nearly all of the free carbon in the Nicalon fiber as well as the fiber coating was oxidized and lost as CO(g) via the internal oxidation mechanism. Likewise, for the Tyranno fiber with a factor of 10 larger all the bulk free carbon and the carbon coating must have been oxidized.

Since the irradiation temperature was 1000°C in the fiber experiment, a larger fiber mass loss and more severe degradation would be expected than if the temperature were 800°C, the BOC irradiation temperature of the SiC_f/SiC composites containing these same fibers. The irradiated SiC_f/SiC composite mechanical property degradation follows the behavior expected for composite made with fiber exhibiting thermochemical instability, except that the degradation occurs even at 800°C or lower due to the irradiation. For the irradiated Dupont and GA composites, the larger mass loss correlates with more severe degradation. The flexural strengths for the irradiated GA composites were lower than for the irradiated Dupont composites. Apparently, the fiber mass loss mechanism is retarded somewhat by the composite structure as the thinner GA samples lost significantly more mass than the thicker GA samples. All the observed composite mass losses were lower than 0.75%, much below the 8.4% limit which is possible only if all the oxygen were to react. The diminished composite mass losses probably occurred as a result of temperatures lower than 1000°C, buildup of a retarding CO partial pressure in the subcapsule and the CVI matrix structure acting as a gas diffusion barrier. Nevertheless, the mechanical property degradation exhibited by these two types of SiC_f/SiC composites was severe and would be unacceptable for fusion structural components.

CONCLUSIONS

1. SiC_f/SiC composite made with SiC-based fibers that contain an amorphous silicon oxycarbide phase may exhibit mass loss due to an internal oxidation mechanism.

2. The mass loss is correlated to fiber and interphase degradation, and perhaps to severe composite mechanical property degradation.

3. The internal oxidation mass loss mechanism can occur at temperatures of 800°C or lower in an irradiation environment, much below the 1100°C thermal stability threshold generally accepted for these materials.

4. The internal oxidation mechanism can be retarded in a closed system due to buildup of CO gas. However in an open or large gas volume system, the reactions could proceed unrestricted and the mass loss and mechanical property degradation probably would be worse than observed in a closed system.

FUTURE WORK

Future work will emphasize testing composites made with low oxygen content fibers to avoid the internal oxidation mass loss mechanism. Careful attention will be given to assessing mass loss behavior in fibers or in composites in future irradiation experiments.

REFERENCES

1. P. Greil, "Thermodynamic Calculations of Si-C-O Fiber Stability in Ceramic Matrix Composites," J. of the European Ceram. Soc., 6, 53-64 (1990).

2. C. Labrugere, A. Guette and R. Naslain, "Effect of Ageing Treatments at High Temperatures on the Microstructure and Mechanical Behavior of 2D Nicalon/C/SiC Composites. 1: Ageing under Vacuum or Argon," J. of the European Ceramic Soc., 17, 623-640 (1997).

3. M. H. Jaskowiak and J. A. DiCarlo, "Pressure Effects on the Thermal Stability of Silicon Carbide Fibers," J. Am. Ceram. Soc., 72 (2), 192-97 (1989).

4. G. E. Youngblood, C. H. Henager, Jr., and R. H. Jones, "Effects of Neutron Irradiation on the Strength of Continuous Fiber Reinforced SiC/SiC Composites," p. 117 in Fusion Materials Semiannual Progress Report, DOE/ER-0313/21, 1996.

5. L. R. Greenwood and R. T. Ratner, "Neutron Dosimetry and Damage Calculations for the EBR-II COBRA-1A Irradiations." ibid., p. 225.

6. G. E. Youngblood, C. H. Henager, Jr., D. J. Senor and G. W. Hollenberg, "Effects of Neutron Irradiation on Dimensional Stability and on Mechanical Properties of SiC/SiC Composites," p. 321 in Fusion Materials Semiannual Progress Report, DOE/ER-0313/17.

7. D. J. Senor, G. E. Youngblood, J. L. Brimhall, D. J. Trimble, G. A. Newsome and J. J. Woods, "Dimensional Stability and Strength of Neutron-Irradiated SiC-Based Fibers," Fusion Technol., 30 (3), 956-68 (1996).

3.0 FERRITIC/MARTENSITIC STEELS

HEAT TREATMENT EFFECTS ON IMPACT TOUGHNESS OF 9Cr-1MoVNb AND 12Cr-1MoVW STEELS IRRADIATED TO 100 dpa—R. L. Klueh and D. J. Alexander (Oak Ridge National Laboratory)

OBJECTIVE

The goal of this study is to evaluate the impact behavior of irradiated ferritic steels and relate the changes in properties to the heat treatment of the steel.

SUMMARY

Plates of 9Cr-1MoVNb and 12Cr-1MoVW steels were given four different heat treatments: two normalizing treatments were used and for each normalizing treatment two tempers were used. Miniature Charpy specimens from each heat treatment were irradiated to ≈19.5 dpa at 365°C and to ≈100 dpa at 420°C in the Fast Flux Test Facility (FFTF). In previous work, the same materials were irradiated to 4-5 dpa at 365°C and 35-36 dpa at 420°C in FFTF. The tests indicated that prior austenite grain size, which was varied by the different normalizing treatments, had a significant effect on impact behavior of the 9Cr-1MoVNb but not on the 12Cr-1MoVW. Tempering treatment had relatively little effect on the shift in DBTT for both steels. Conclusions are presented on how heat treatment can be used to optimize impact properties.

PROGRESS AND STATUS

Introduction

Neutron irradiation effects on the toughness of ferritic/martensitic steels is a prime concern for steels considered for fusion reactor applications. Irradiation at temperatures up to ≈450°C can cause increases in the ductile-brittle transition temperature (DBTT) and decreases in the upper shelf energy (USE), as determined by a Charpy impact test. Heat treatment variations affect the kind of microstructure (e.g., prior austenite grain size, dislocation structure, and the character of the precipitates) developed in the steels, and microstructure affects the mechanical properties, such as the impact behavior.

This paper examines how heat treatment and irradiation to high doses affect the Charpy impact behavior of the 9Cr-1MoVNb (modified 9Cr-1Mo) and 12Cr-1MoVW (Sandvik HT9) steels that have been considered in the past as candidate alloys for fusion reactor applications. Although these two steels are no longer prime candidates for fusion applications, the results are important, because similar behavior should occur in the ferritic/martensitic reduced-activation steels that are now being considered for fusion. Results for these steels with similar heat treatments were previously presented after 4-5 dpa at 365°C and 35-36 dpa at 420°C [1]. In this paper the results are extended to irradiation of ≈20 dpa at 365°C and ≈100 dpa at 420°C.

Experimental Procedure

The 9Cr-1MoVNb steel was from an argon-oxygen decarburized (AOD) and electroslag-remelted (ESR) heat (heat 30176) processed by Carpenter Technology into 25.4-mm-thick plate. The 12Cr-1MoVW steel (Sandvik HT9 composition) was from an AOD/ESR melt that was processed into hot-rolled plate (heat 9607-R2) by Universal Cyclops. Compositions for the test materials fall within the specifications for the steels and have been published [1]. Sections of the 25.4-mm plate were rolled to 9.5-mm thickness, and pieces of these plates measuring 88.9 by 152 by 9.5 mm were normalized and tempered. Two plates of 9Cr-1MoVNb and two plates of 12Cr-1MoVW were austenitized 1 h at 1040°C in air and air cooled; two plates of each steel were also austenitized 1 h at 1100°C and air cooled. Then one plate with each normalization treatment was tempered 1 h at 760°C or 2.5 h at 780°C.

Subsize Charpy specimens measuring 3.3 by 3.3 by 25.4 mm with a 0.51-mm-deep 30° V-notch and a 0.05-to 0.08-mm-root radius were taken from the center of the normalized-and-tempered plates along the rolling direction with the notch running transverse to the rolling direction (L-T orientation). Specimens were irradiated in the Fast Flux Test Facility (FFTF) in the Materials Open Test Assembly (MOTA).

For the 420°C irradiations, specimens austenitized at 1040°C and tempered at 760 and 780°C were used. Six Charpy specimens from each heat-treated condition were irradiated to nominal fluences of 2.26×10^{27} n/m^2 for the 12Cr-1MoVW steel to produce ≈99.5 dpa and 2.28×10^{27} n/m^2 for the 9Cr-1MoVNb steel to produce ≈100.4 dpa (the doses of both will be referred to as 100 dpa). Irradiations at 365°C were on specimens austenitized at 1040 and 1100°C and tempered at 760 and 780°C; they were irradiated to a nominal fluence of 5.12×10^{22} n/m^2, ≈19.5 dpa (referred to as 20 dpa).

Details on the test equipment and the procedure for testing the subsize Charpy specimens have been published [2]. Individual Charpy data sets were fitted with a hyperbolic tangent function to obtain transition temperatures and upper shelf energies. Transition temperatures were determined at half the upper shelf energy.

Results

Specimens with all four heat treatments were irradiated at 365°C, but only specimens austenitized at 1040°C were irradiated at 420°C. Irradiation caused an increase in DBTT and a decrease in USE for all heat-treated conditions (Table 1). Only relatively minor differences were observed between the properties of the steels irradiated at 365°C to 4-5 dpa [1] and 20 dpa (Fig. 1) and between those irradiated at 420°C to 35-36 dpa[1] and 100 dpa (Fig. 2). For all heat treatments, the shift in DBTT (ΔDBTT) for the 12Cr-1MoVW steel was over twice that for the 9Cr-1MoVNb steel (Fig. 3).

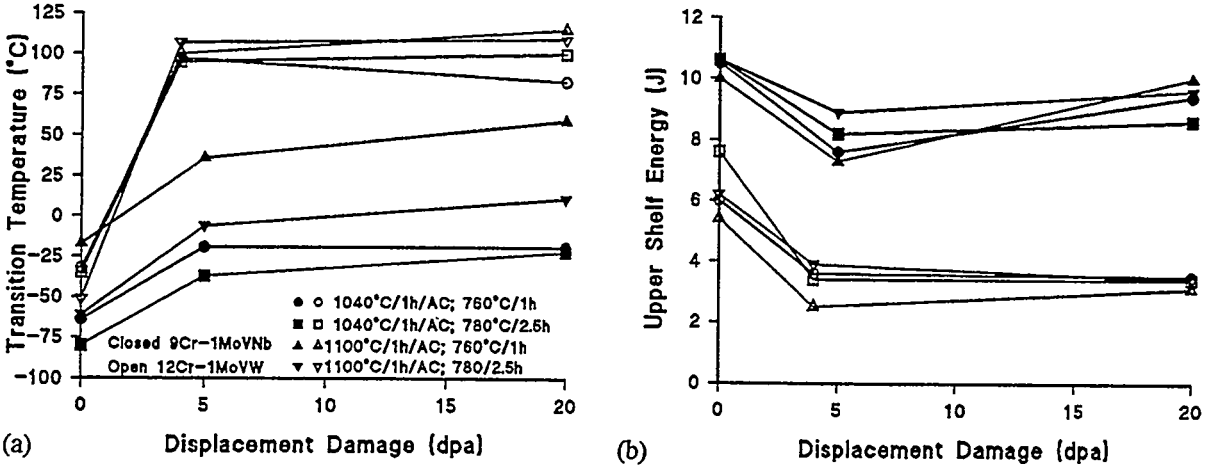

Fig. 1 (a) DBTT and (b) USE as a function of displacement damage for 9Cr-1MoVNb and 12Cr-1MoVW steels with four different heat treatments after irradiation at 365°C in FFTF.

Table 1. Impact properties of 9Cr-1MoVNb and 12Cr-1MoVW irradiated at 365 and 420°C

Heat Treatment[a]	DBTT[b], °C			USE, J		
	Unirr	4/5 dpa	20 dpa	Unirr	4/5 dpa	20 dpa
9Cr-1MoVNb Steel—365°C						
1040/1h/;760/1h	-64	-19	-19	10.5	7.6	9.4
1040/1h;780/2.5h	-80	-37	-22	10.6	8.2	8.6
1100/1h;760/1h	-17	36	59	10.0	7.3	10.0
1100/1h;780/2.5h	-61	-6	11	10.6	8.9	9.6
12Cr-1MoVW Steel—365°C						
1040/1h/;760/1h	-32	97	83	6.0	3.6	3.5
1040/1h;780/2.5h	-35	95	100	7.6	3.4	3.4
1100/1h;760/1h	-34	100	115	5.4	2.5	3.1
1100/1h;780/2.5h	-51	107	109	6.2	3.9	3.4
	Unirr	35/36 dpa	100 dpa	Unirr	35/36 dpa	100 dpa
9Cr-1MoVNb Steel—420°C						
1040/1h/;760/1h	-64	-25	-30	10.5	8.2	7.9
1040/1h;780/2.5h	-80	-35	-32	10.6	7.8	9.0
12Cr-1MoVW—420°C						
1040/1h/;760/1h	-32	55	54	6.0	4.1	5.3
1040/1h;780/2.5h	-35	72	42	7.6	4.1	4.2

[a] Steels were air cooled after the 1040 and 1100°C austenitization; temperatures are in °C.
[b] DBTT was determined at ½ the upper shelf energy.

The largest variation caused by the heat treatment occurred for the 9Cr-1MoVNb steel irradiated at 365°C. The plates of 9Cr-1MoVNb austenitized at 1100°C had the highest DBTT before irradiation [Fig 1(a)] and developed the largest ΔDBTT [Fig. 3(a)] after irradiation to 5 and 20 dpa at 365°C. Of the two 9Cr-1MoVNb plates austenitized at 1100°C, the one tempered at 780°C had the lowest transition temperature before and after irradiation. The two plates austenitized at 1040°C had lower transition temperatures than after the 1100°C heat treatment. Tempering at 780°C gave a slight advantage in the unirradiated condition and after 5 dpa, but there was no difference after 20 dpa. Fig. 3(a) shows that the ΔDBTT for the 9Cr-1MoVNb steel irradiated at 365°C was different for the two different austenitization treatments, but there was little effect of the tempering treatment.

Much less difference in the transition temperatures was observed for the 12Cr-1MoVW steel irradiated at 365°C [Fig 1(a)]. The plate given the 1100°C austenitization and the 780°C temper

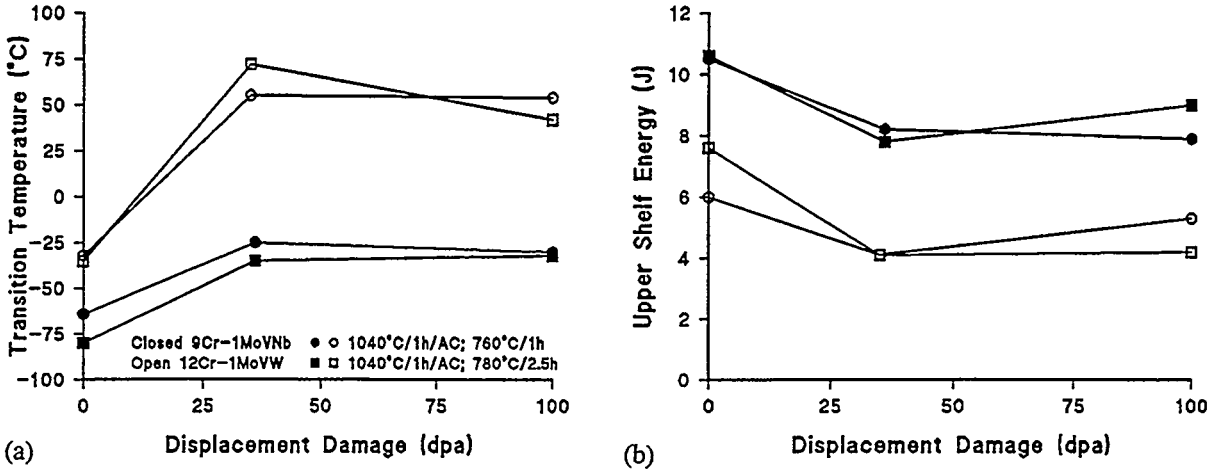

Fig. 2 (a) DBTT and (b) USE as a function of displacement damage for 9Cr-1MoVNb and 12Cr-1MoVW steels with two different heat treatments after irradiation at 420°C in FFTF.

had the lowest transition temperature before irradiation, with little difference being observed for the transition temperatures for the other three heat treatments. After irradiation to 20 dpa at 365°C, specimens with the 1100°C austenitization treatment had the highest transition temperatures, with the plate austenitized at 1040°C and tempered at 760°C having the lowest transition temperature. The variation in transition temperatures was greatest for the 12Cr-1MoVW steel plates after irradiating to 20 dpa at 365°C. This greater variation in properties with heat treatment is also evident for the shift in transition temperature [Fig. 3(a)].

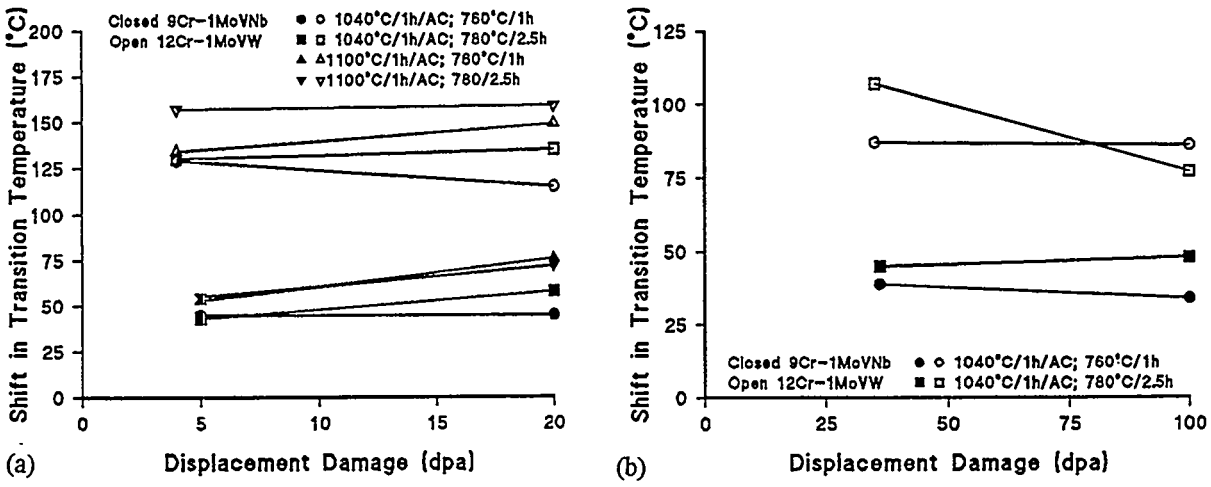

Fig. 3 Shift in DBTT as a function of displacement damage for 9Cr-1MoVNb and 12Cr-1MoVW steels (a) with four different heat treatments after irradiation at 365°C in FFTF and (b) with two different heat treatments after irradiation at 420°C in FFTF.

Both before and after irradiation at 365°C, the USE for the 9Cr-1MoVNb steel was much less dependent on heat treatment than was the DBTT, although there was somewhat more variation after irradiation than before [Fig. 1(b)]. After 20 dpa, the 9Cr-1MoVNb plates austenitized at 1040°C showed the smallest ΔDBTT. In the case of the 12Cr-1MoVW steel, there was a relatively large variation in USE before irradiation and after 5 dpa, but much less variation after 20 dpa at 365°C [Fig. 1(b)].

Only plates austenitized at 1040°C were irradiated at 420°C (Fig. 2). Irradiation at 420°C caused an increase in the transition temperature for both the 9Cr-1MoVNb and 12Cr-1MoVW steels, with the ΔDBTT for the 12Cr-1MoVW steel being about twice that for the 9Cr-1MoVNb steel [Fig. 3(b)]. For neither steel was there a large effect of tempering temperature on the transition temperature, either in the unirradiated condition or after 35-36 dpa and 100 dpa [Fig. 2(a)]. Likewise, tempering temperature caused little difference on the USE for the steels in the unirradiated and irradiated conditions [Fig. 2(b)]. Although the differences were not great, the ΔDBTT for the 9Cr-1MoVNb tempered at 780°C was slightly greater than after tempering at 760°C [Fig. 3(b)]. Slightly more scatter occurred for the ΔDBTT of the 12Cr-1MoVW steel with the different tempering conditions [Fig. 3(b)].

Discussion

The new higher fluence results presented in this report generally confirm the conclusions reached previously [1] that heat treatment can affect properties after irradiation—especially the transition temperature and the shift in transition temperature. In the previous paper [1], the results were compared to results from other investigators who investigated the effect of heat treatment in the normalized-and-tempered [3] and irradiated [4] conditions. Those comparisons will not be repeated, since the conclusions reached previously are not changed by the results presented here.

The objective of using different austenitizing temperatures was to change the prior-austenite grain size. Heat treatment had a relatively small effect on the prior-austenite grain size of the 9Cr-1MoVNb steel, but it had a larger effect on the 12Cr-1MoVW steel: the average grain size after austenitizing at 1040 and 1100°C was estimated at 16 and 22 μm, respectively, for the 9Cr-1MoVNb and 22-45 and 90-124 μm, respectively, for the 12Cr-1MoVW [1]. The smaller prior austenite grain size variation with heat treatment for the 9Cr-1MoVNb steel was attributed to the strong effect of niobium on restricting grain growth of the austenite during the austenitization treatment [5]. Despite the relatively small variation in grain size for the 9Cr-1MoVNb, it still showed a larger variation in transition temperature than the 12Cr-1MoVW [Table 1 and Fig. 1(a)].

Austenite grain size can affect the transition temperature: transition temperature generally increases with increasing grain size [6], which was observed for the 9Cr-1MoVNb. For a given grain size (austenitization temperature), tempering at the higher temperature gave a lower transition temperature, which is also expected, because the higher tempering temperature lowers the strength.

In the previous paper, impact properties for the steels thermally aged at 400°C for 5000, 10000, and 20000 h were presented [1]. Charpy properties were little changed after thermal aging for 20000 h [1]. Although the exposure in the reactor at 420°C was somewhat greater than 20000 h, the most significant changes caused by aging were slight decreases in DBTT and increases in USE for the 9Cr-1MoVNb steel austenitized at 1100°C and tempered at 760°C [1]. These changes are opposite to the effects observed during irradiation. Thus, any properties degradation observed following irradiation cannot be attributed to the thermal aging that occurred simultaneously with irradiation.

The relative differences in DBTT of the 9Cr-1MoVNb steel that were present in the normalized-and-tempered condition remained after 5 dpa [Fig. 1(a)]. After 20 dpa, the difference for the plates

austenitized at 1100°C remained, but there was little difference in the DBTT for the two plates austenitized at 1040°C [Fig. 1(a)]. Thus, grain size eventually determined the DBTT for the steel austenitized at 1040°C. In the case of the 9Cr-1MoVNb plate austenitized at 1100°C, the properties did not converge for the two different tempering treatments. However, the ΔDBTT for the different tempering conditions did show convergence [Fig. 3(a)]. These results indicate that, at least for the 9Cr-1MoVNb and steels like it, it may be possible to improve the irradiation resistance of the impact properties by the thermo-mechanical treatment. For the 9Cr-1MoVNb steel, the 1h at 760°C temper was the optimum temper determined when the steel was developed [7]. As this work indicates, raising that temperature, which would lower the strength, would not improve the impact properties after irradiation. It would be interesting to determine whether a further reduction in the prior-austenite grain size would improve the post-irradiation impact properties.

Although the 12Cr-1MoVW steel showed a somewhat larger variation in prior-austenite grain size than the 9Cr-1MoVNb steel, it showed a smaller variation in transition temperature for the four heat treated conditions in both the normalized-and-tempered condition and after irradiation at 365°C. It showed the most variation after 20 dpa, where the specimens with the smallest prior-austenite grain size again had the lowest transition temperature [Fig. 1(a)]. The ΔDBTT had a similar, though larger, variation [Fig. 3(a)].

Previously the difference in fracture behavior of the 12Cr-1MoVW steel relative to the 9Cr-1MoVNb steel was attributed to the larger volume of carbide precipitates, mainly $M_{23}C_6$ [1]. The 12Cr-1MoVW contains 0.2% C, compared to 0.1% C for the 9Cr-1MoVNb, and thus, the 12Cr-1MoVW contains over twice as much precipitate [8]. Precipitates were postulated to minimize the role of the grain boundaries for the 12Cr-1MoVW [1], and these precipitates could affect the fracture process because the larger, brittle precipitate particles in the 12Cr-1MoVW steel could cause a larger initial crack size for crack initiation during fracture. Carbide particles are believed to be a source of cracks in steels [9,10]. Possible confirmation of this is the relative behavior of the DBTT [Fig. 1(a)] and ΔDBTT [Fig. 3(a)] with different heat treatments. Although the 12Cr-1MoVW plates with the smallest grain size had the lowest DBTT after 20 dpa, the effect of tempering temperature was different from what was expected: the steel tempered at 780°C had the higher DBTT and ΔDBTT. The opposite is expected, because under most conditions, a higher tempering temperature reduces the strength, which should improve fracture properties [5,6]. However, the higher tempering temperature will also produce larger precipitate particles, thus enhancing fracture. Note that the opposite effect occurs for the 9Cr-1MoVNb steel [Fig. 1(a)], which contains the smaller particles [1,8]. The results indicate that the tempering treatment of 2 h at 780°C that is often used for the 12Cr-1MoVW steel could be replaced by shorter times at a lower temperature, thus providing an improved strength without a reduction in toughness.

The observations on the transition temperature after irradiation at 420°C indicate that for the 9Cr-1MoVNb steel, the saturation with fluence that occurs is independent of the tempering conditions [Fig. 2(a)]. A somewhat similar conclusion follows for the 12Cr-1MoVW steel. Here, it appears that after 35 dpa, and the steel tempered at 780°C with the larger precipitate particles has the highest DBTT. However, after 100 dpa, the two converge. This probably means that the particles in the plate tempered at 760°C reached a size where the further irradiation-enhanced growth does not affect fracture properties, thus giving the plates tempered at 760 and 780°C a similar DBTT.

The change in the USE with respect to heat treatment and irradiation appears more random than the transition temperature. In most cases, the USE values after 20 dpa at 365°C or 100 dpa at 420°C irradiations were equal to or greater than those after the previous irradiations. The relatively small change in USE for the 9Cr-1MoVNb steel up to 100 dpa at 420°C and 20 dpa at 365°C shows the superior behavior of this steel. The 9Cr-1MoVNb steel has a higher USE than that for the 12Cr-1MoVW steel in the normalized-and-tempered condition, thus making the relative change considerably less. After all irradiations, the USE of the 9Cr-1MoVNb steel remained higher than the USE of the 12Cr-1MoVW steel in the unirradiated condition.

The superiority of the 9Cr-1MoVNb steel is probably a reflection of the larger carbon concentration of the 12Cr-1MoVW steel. A high carbon concentration is required in the 12Cr-1MoVW steel to avoid δ-ferrite formation during normalization. This was alluded to in the previous paper [1] when the 12Cr-1MoVW was compared to a 12Cr-0.9Mo-0.3V-0.14C steel of Little et al. [3], which showed a significant effect of austenitizing temperature on impact properties. The main difference between the steel of Little et al. and the 12Cr-1MoVW steel of the present study involves the carbon. Based on the microstructural studies described by Little et al. [3], it was concluded [1] that their steel showed a much larger prior austenite grain size effect than the 12Cr-1MoVW steel because of the lower carbon content in the steel of Little et al.[3], which caused a much finer precipitate distribution to form. This implies that the DBTT of the 12Cr-1MoVW could be affected significantly by lowering the carbon content, but to accomplish this, other alloying modifications would be required to avoid δ-ferrite formation during normalization.

The results indicate that the change in Charpy properties with irradiation dose saturates, and saturation is achieved by the lower dose used in these experiments. The shift in DBTT is related to hardening, which is measured as an increase in yield stress. Hardening is also generally thought to saturate with fluence. For 9Cr-1MoVNb and 12Cr-1MoVW steel irradiated in the Experimental Breeder Reactor (EBR-II), little or no change in strength occurred between specimens irradiated to 9-13 and 23-25 dpa [11]. Likewise, a saturation in DBTT occurred for these two steels irradiated to 13 and 26 dpa in EBR-II [12]. However, for a series of Cr-W-V-Ta steels with 2.25, 7, 9, and 12 % Cr irradiated to 25, 35 and 60 dpa at 400°C in FFTF, hardening went through a maximum [13]. A similar observation was made on an 8Cr-2WVTa steel (F82H) irradiated at 400°C to 12, 21, and 34 dpa in the High Flux Isotope Reactor (HFIR) [14]. Khabarov et al. [15] observed a peak in strength for the Russian steel 13Cr2MoNbVB after irradiation in the BN-350 reactor over the range 4 to 85 dpa at 350-365°C.

One explanation for the maximum in strength with fluence is that irradiation-enhanced softening offsets part of the irradiation hardening [13-15]. This would not be completely unexpected, since thermal aging will cause a reduction of strength due to carbide coarsening and dislocation recovery. However, this should only occur after extremely long aging times at a temperature as low as 400°C [16], although it could be accelerated by irradiation.

The shift in DBTT is related to the hardening, but there do not appear to be any results that show a maximum in the DBTT or shift in DBTT with fluence. In the same experiment where Khabarov et al. [15] found a maximum in yield stress with dose for the 13Cr1MoNbVB irradiated in BN-350, no maximum was observed for the DBTT. Likewise, there was no indication of a maximum in the shift in DBTT for the 9Cr-1MoVNb and 12Cr-1MoVW steels irradiated in the present experiment, even after 100 dpa.

SUMMARY AND CONCLUSIONS

Different normalizing-and-tempering treatments were used on 9Cr-1MoVNb and 12Cr-1MoVW steels to study the effect of heat treatment on Charpy impact toughness before and after irradiation. Plates of the steels were austenitized at two temperatures (1040 and 1100°C) to vary the prior austenite grain size, and two tempering treatments (1 h at 760 and 2 h at 780°C) were used for each austenitizing temperature. Subsize Charpy specimens were tested in each heat treated condition before irradiation and after irradiation in FFTF at 365°C to ≈20 dpa; two heat-treated conditions were also tested after irradiation in FFTF at 420°C to ≈100 dpa. Previously these same materials had been irradiated to 4-5 dpa at 365°C and 35-36 dpa at 420°C.

As normalized and tempered, the DBTT of the 9Cr-1MoVNb steel depended on the austenitizing temperature (prior austenite grain size) and on the tempering conditions. The shift in DBTT caused by irradiation for this steel was relatively independent of heat treatment, which meant that after irradiation the relative difference in DBTT for the steel given the different heat treatments was similar to what it was before irradiation. These observations suggest that to insure a low DBTT for 9Cr-1MoVNb after irradiation, it

should be heat treated to produce a low DBTT before irradiation. The best method to do this is by reducing the prior austenite grain size.

Austenitization temperature, and thus prior austenite grain size, had less effect on the transition temperature of the normalized-and-tempered and the irradiated 12Cr-1MoVW steel than the 9Cr-1MoVNb steel. Tempering treatment also had a small effect. The shift in DBTT was relatively independent of heat treatment, but the shifts for the 12Cr-1MoVW steel were over twice those for 9Cr-1MoVNb steel. Therefore, it does not appear possible to use heat treatment to reduce the effect of irradiation on the DBTT of 12Cr-1MoVW. Because of the lack of a heat treatment effect on DBTT, however, it may be possible to use this steel without tempering to the low strength levels at which the steel is usually used.

REFERENCES

[1] R. L. Klueh and D. J. Alexander, in: Effects of Radiation on Materials: 16th International Symposium, ASTM STP 1175, Eds. A. S. Kumar, D. S. Gelles, R. K. Nanstad, and E. A. Little (American Society for Testing and Materials, Philadelphia, 1993) p. 591.
[2] D.J. Alexander, R.K. Nanstad, W.R. Corwin, and J.T. Hutton, in: Applications of Automation Technology to Fatigue and Fracture Testing, ASTM STP 1092, Eds. A. A. Braun, N. E. Ashbaugh, and F. M. Smith, (American Society for Testing and Materials, Philadelphia, 1990) p. 83.
[3] E.A. Little, D.R. Harries, F.B. Pickering, and S.R. Keown, Metals Technology 4 (1977) 205.
[4] C. Wassilew and K. J. Ehrlich, J. Nucl. Mater. 191-194 (1992) 850.
[5] G. Krauss, Steels: Heat Treatment and Processing Principles (ASM International, Materials Park, OH, 1989).
[6] G. E. Dieter, Mechanical Metallurgy (McGraw-Hill, 1976) p. 499.
[7] V. K. Sikka, C. T. Ward, and K. C. Thomas, in: Ferritic Steels for High-Temperature Applications, Ed. A. K. Khare (American Society for Metals, 1983) p. 65.
[8] J. M. Vitek and R. L. Klueh, Met. Trans. 14A (1983) 1047.
[9] R. W. Hertzberg, Deformation and Fracture Mechanics of Engineering Materials, 3rd Edition (John Wiley & Sons, New York, 1989) p. 253.
[10] C. J. McMahon, Jr., Fundamental Phenomena in the Materials Sciences, Vol. 4, L. J. Bonis, J. J. Duga, and J. J. Gilman, Eds. (Plenum Press, New York, 1967) p. 247.
[11] R. L. Klueh and J. M. Vitek, "Tensile Properties of 9Cr-1MoVNb and 12Cr-1MoVW Steels Irradiated to 23 dpa at 390 to 550°C," J. Nucl. Mater. 182 (1991) 230.
[12] W. L. Hu and D. S. Gelles, Influence of Radiation on Material Properties: 13th International Symposium (Part II), ASTM STP 956, ed. F. A. Garner, C. H. Henager, Jr., and N. Igata, (American Society for Testing Materials, Philadelphia, 1987), 83.
[13] A. Kohyama, A. Hishinuma, D. S. Gelles, R. L. Klueh, W. Dietz, and K. Ehrlich, J. Nucl. Mater. 233-237 (1996) 138.
[14] K. Shiba, M. Suzuki, A. Hishinuma, and J. E. Pawel, et al., in: Effects of Radiation on Materials: 17th International Symposium, ASTM STP 1270 (American Society for Testing and Materials, Philadelphia, 1996) 753.
[15] V. S. Khabarov, A. M. Dvoriashin, and S. I. Porollo, J. Nucl. Mater. 233-237 (1996) 236.
[16] P. J. Maziasz and R. L. Klueh, in: Effects of Radiation on Materials: 16th International Symposium, ASTM STP 1125 (American Society for Testing and Materials, Philadelphia, 1992) 1135.

NEUTRON IRRADIATION EFFECTS ON THE DUCTILE-BRITTLE TRANSITION OF FERRITIC/ MARTENSITIC STEELS—R. L. Klueh and D. J. Alexander (Oak Ridge National Laboratory)

Published in: *Recent Advances in Fracture*, Editors, R. K. Mahidhara, A. B. Geltmacher, P. Matic, and K. Sadanana (TMS, Warrendale, PA, 1997) p. 339 and presented at Symposium on Recent Advances in Fracture, Annual Meeting of the Minerals, Metals, and Materials Society, Orlando, FL, February 10-13, 1997.

EXTENDED ABSTRACT

Ferritic/martensitic steels such as the conventional 9Cr-1MoVNb (Fe-9Cr-1Mo-0.25V-0.06Nb-0.1C) and 12Cr-1MoVW (Fe-12Cr-1Mo-0.25V-0.5W-0.5Ni-0.2C) steels have been considered potential structural materials for future fusion power plants. The major obstacle to their use is embrittlement caused by neutron irradiation. Observations on this irradiation embrittlement is reviewed.

Below 425-450°C, neutron irradiation hardens the steels. Hardening reduces ductility, but the major effect is an increase in the ductile-brittle transition temperature (DBTT) and a decrease in the upper-shelf energy, as measured by a Charpy impact test. After irradiation, DBTT values can increase to well above room temperature, thus increasing the chances of brittle rather than ductile fracture.

Neutron irradiation of the conventional 9Cr-1MoVNb and 12Cr-1MoVW steels in a fast reactor over the temperature range 365-550°C has shown that these steels harden below ≈425°C; at higher temperatures there is little change in strength. The steels show an increase in the DBTT and decrease in the USE at the temperatures where the hardening occurs. Increases in DBTT of 54°C for the 9Cr-1MoVNb steel and 124-144°C for the 12Cr-1MoVW steel were observed when the steels were irradiated in a fast reactor. In addition to irradiation hardening, neutrons from the fusion reaction will produce large amounts of helium in the steels used to construct fusion power plant components. Little helium is produced in fast reactor irradiation, but tests to simulate the fusion environment indicate that helium can also affect the toughness.

Irradiation of a structural steel by neutrons generated in the fusion reaction will activate (transmute to radioactive isotopes) elements of the steel. Reduced-activation steels that contain elements that transmute to short-lived isotopes are being developed, thus simplifying the disposal of the radioactive structure after its service lifetime. Common alloying elements that must be eliminated or minimized in reduced-activation steels include Mo, Ni, Nb, Cu, and N. A reduced-activation 9Cr-2WVTa steel was developed that had a much lower DBTT than the conventional steels and showed a shift in DBTT that was about half that of the best conventional steels after fast reactor irradiation.

MICROSTRUCTURAL CHARACTERIZATION OF 5-9% CHROMIUM REDUCED-ACTIVATION STEELS—R. Jayaram (University of Pittsburgh) and R. L. Klueh (Oak Ridge National Laboratory)

OBJECTIVE

The goal of this study is to characterize the microstructures of the reduced-activation ferritic steels and relate the microstructure to the mechanical properties.

SUMMARY

The microstructures of a 9Cr-2W-0.25V-0.1C (9Cr-2WV), a 9Cr-2W-0.25V-0.07Ta-0.1C (9Cr-2WVTa), a 7Cr-2W-0.25V-0.07Ta-0.1C (7Cr-2WVTa), and a 5Cr-2W-0.25V-0.07Ta-0.1C (5Cr-2WVTa) steel (all compositions are in weight percent) have been characterized by Analytical Electron Microscopy (AEM) and Atom Probe Field Ion Microscopy (APFIM). The matrix in all four reduced-activation steels was 100% martensite. In the two 9Cr steels, the stable precipitates were blocky $M_{23}C_6$ and small spherical MC. The two lower-chromium steels contained blocky M_7C_3 and small needle-shaped carbonitrides in addition to $M_{23}C_6$. AEM and APFIM analysis revealed that in the steels containing tantalum, the majority of the tantalum was in solid solution. The experimental observations were in good agreement with phases and compositions predicted by phase equilibria calculations.

PROGRESS AND STATUS

Introduction

First wall and blanket structure materials of fusion power plants are expected to become highly radioactive during service. The ferritic steels first considered for fusion applications in the United States were commercial Cr-Mo steels: 2¼Cr-1Mo (2.25 Cr-1.0Mo-0.1 C), 9Cr-1MoVNb (9 Cr-1.0Mo-0.2V-0.06Nb-0.1C) and 12Cr-1MoVW (12Cr-1.0Mo-0.25V-0.5W-0.5Ni-0.2C). Unless stated otherwise, compositions are in weight percent. Since the disposal of radioactive waste materials poses serious problems, an important consideration in the design of the first wall and blanket structure is to minimize the induced radioactive decay times of the radioisotopes that would be formed during service [1,2]. The alloying elements that result in radioisotopes with long decay times are nickel, molybdenum, nitrogen, copper and niobium.

Reduced-activation steels were developed that were variations of the conventional ferritic/martensitic steels, with molybdenum replaced by tungsten and niobium replaced by tantalum [3]. Previous studies of such steels have indicated that a 9Cr-2WV steel with a nominal composition of 9Cr-2W-0.25V-0.1C had tensile and impact toughness properties similar to the 9Cr-1MoVNb steel that it would replace [3]. The addition of tantalum to the same nominal composition(9Cr-2WVTa) resulted in a steel with superior impact properties [4]. Neutron irradiation of ferritic steels generally causes an increase in the ductile-brittle transition temperature (DBTT) and a decrease in upper shelf energy (USE) as determined in a Charpy impact test. The low DBTT of the unirradiated 9Cr-2WVTa translated into a small shift in DBTT after irradiation. The 9Cr-2WVTa steel had the smallest change in DBTT and USE ever observed for this type of steel (conventional or reduced-activation) after irradiation in a fast reactor [3].

The objective of this study is to characterize the microstructure and chemistry of the matrix and precipitates in unirradiated 5-9% Cr reduced-activation steels using a combination of Transmission Electron Microscopy (TEM) and Atom Probe Field Ion Microscopy (APFIM). It is also of interest to gain a better understanding of these steels by comparing the experimental analytical results obtained from microanalytical techniques with phase equilibria calculations based on the ThermoCalc™ software [5].

Experimental Procedure

The steels chosen for this study were the 9Cr-2WV and 9Cr-2WVTa previously examined [3], along with a 7Cr-2WVTa and a 5Cr-2WVTa steel. The nominal compositions of the steels are given in Table 1 atom percent. Atom percent is used because it is more convenient for the calculations to be discussed later. Tensile specimens were fabricated from 0.76 mm-thick sheet and normalized by austenitizing 0.5 h at 1050°C in flowing helium and cooling in rapidly flowing helium. The steels were tempered 1 h at 750°C [6]. Thin foils were prepared from the shoulders of tensile specimens and examined in a Philips CM30 transmission electron microscope (TEM) at an operating voltage of 300 kV. X-ray energy dispersive spectrometry (XEDS) was performed in a Philips EM 400 TEM equipped with a field emission gun at an operating voltage of 100 kV. Atom probe specimens of the 9Cr-2WVTa and 7Cr-2WVTa steels were fabricated using standard techniques. The analyses were performed at 60 K and a pulse fraction of 20% in the Oak Ridge National Laboratory energy-compensated atom probe [7,8].

Table I. Bulk compositions of the steels in atomic percent (balance iron).

Alloy	Cr	Mn	V	W	Ta	C	Si	N
9Cr-2WV	9.6	0.5	0.2	0.6		0.5	0.5	0.1
9Cr-2WVTa	9.5	0.4	0.2	0.6	0.02	0.5	0.5	0.09
7Cr-2WVTa	7.5	0.4	0.3	0.6	0.01	0.5	0.4	0.05
5Cr-2WVTa	5.0	0.5	0.3	0.6	0.01	0.5	0.4	0.03

Results and Discussion

The four steels were analyzed by TEM and XEDS, and the results will be discussed in the following sections. Results on morphology, size, and number densities of the precipitates and other microstructural features of the four steels are summarized in Table 2, along with selected mechanical properties to which the microstructural changes will be related in a later section.

Table 2. Mechanical properties and quantitative TEM estimates of microstructural features.

	9Cr-2WV	9Cr-2WVTa	7Cr-2WVTa	5Cr-2WVTa
DBTT	-60°C	-88°C	-84°C	-118°C
Yield (MPa)	597	645	583	629
lath size (μm)	0.5-0.7	0.1-0.3	0.1-0.3	0.09-0.2
grain size (μm)	65	32	11	16
$M_{23}C_6$ (blocky) N_v (m^{-3}) Diameter (nm)	$1.0x10^{19}$-10^{20} 100-200	$1.0x10^{19}$-10^{20} 100-200	$1.0x10^{19}$-10^{20} 100-200	$1.0x10^{18}$-10^{19} 200-400
M_7C_3 (faulted) N_v (m^{-3}) Diameter (nm)	n.d.[a]	n.d.	$1.0x10^{19}$-10^{20} 100 - 300	$1.0x10^{20}$-10^{21} 100 - 300
MC (spherical) N_v (m^{-3}) Diameter (nm)	$1.0x10^{17}$-10^{18} 40-50	$1.0x10^{17}$-10^{18} 20-40	n.d.	n.d.
$M(CN)_{1-x}$ (needle) N_v (m^{-3}) Size (nm)	n.d.	n.d.	1.0×10^{23} 5-30	1.0×10^{21} 5-30

[a] n.d.—not detected

Microstructure of Matrix

In a previous study, optical metallography of the 9Cr-2WV and 9Cr-2WVTa steels revealed that these materials were 100% tempered martensite [9]. The microstructures of the 7Cr-2WVTa and the 5Cr-2WVTa were also 100% martensite [10]. Previous studies also revealed that the 9Cr-2WVTa steel had a finer prior austenite grain size than the 9Cr-2WV steel [9]. TEM examinations in this study revealed that the 9Cr-2WVTa steel had a well developed and finer lath structure than the 9Cr-2WV steel (Figs. 1a and 1b), which agrees with a previous study [3]. Similar fine-sized laths were found in the 7Cr-2WVTa and 5Cr-2WVTa steels (Figs. 1c and 1d). The average grain sizes and lath sizes observed in the four steels are listed in Table 2.

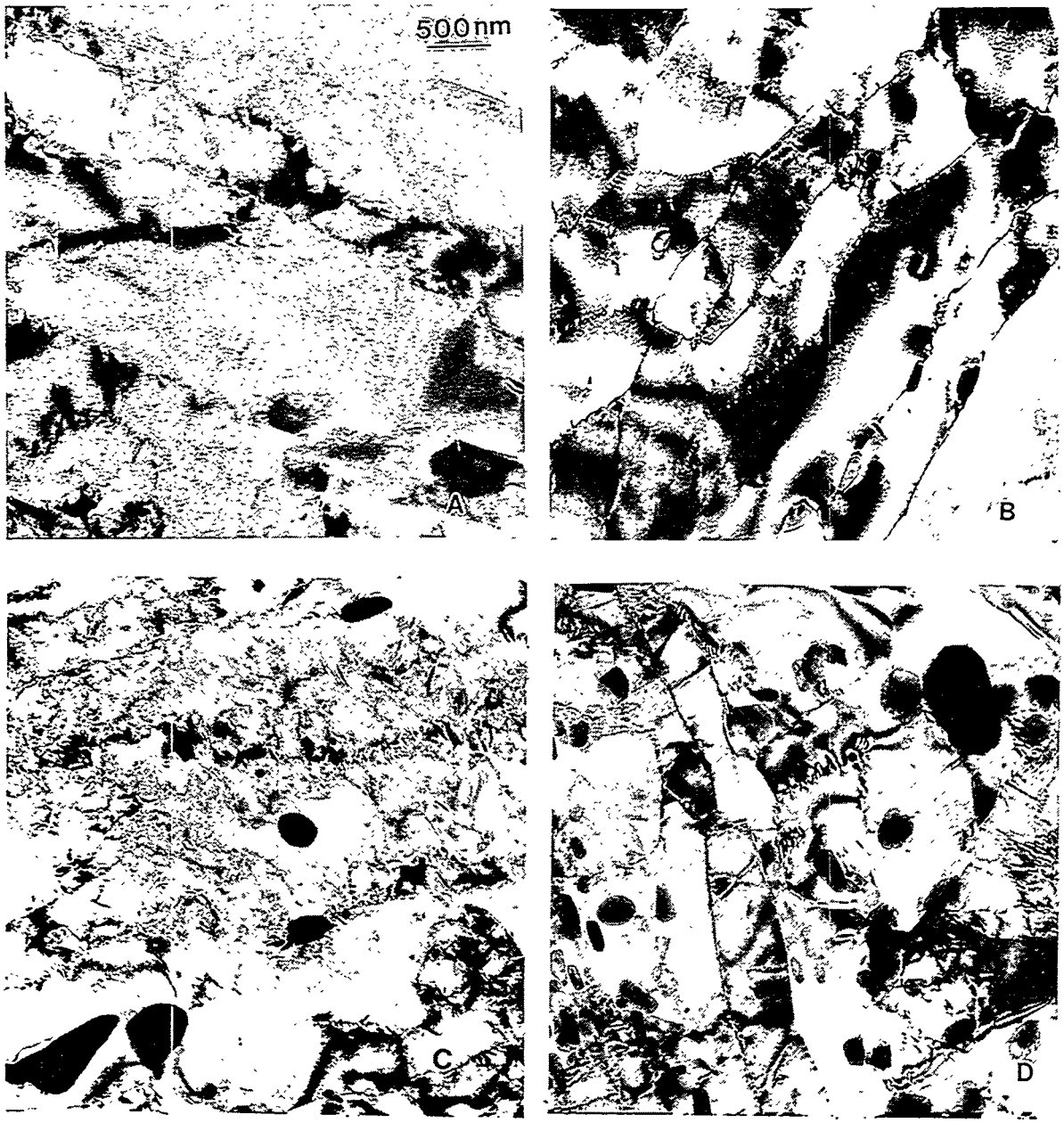

Fig. 1. Micrographs of the normalized-and-tempered (A) 9Cr-2WV, (B) 9Cr-2WVTa, (C) 7Cr-2WVTa and (D) 5Cr-2WVTa steels.

Precipitates in 9Cr-2WV

Transmission electron microscopy of the 9Cr-2WV steel revealed blocky precipitates that were identified as $M_{23}C_6$ based on selected area diffraction patterns. These precipitates displayed a cube-on-cube orientation relationship with the matrix; they were also detected at lath boundaries and prior austenite grain boundaries. Small spherical precipitates (30-50 nm in diameter) at number densities approximately two orders of magnitude lower than those of the $M_{23}C_6$ precipitates were also encountered. These precipitates have been previously observed in both 9Cr steels and have been reported to be V-rich MC precipitates in the 9Cr-2WV steel and V-rich or Ta-rich MC precipitates in the 9Cr-2WVTa steel [9]. The blocky $M_{23}C_6$ precipitates and the small spherical precipitates (arrows) are shown in Fig. 2.

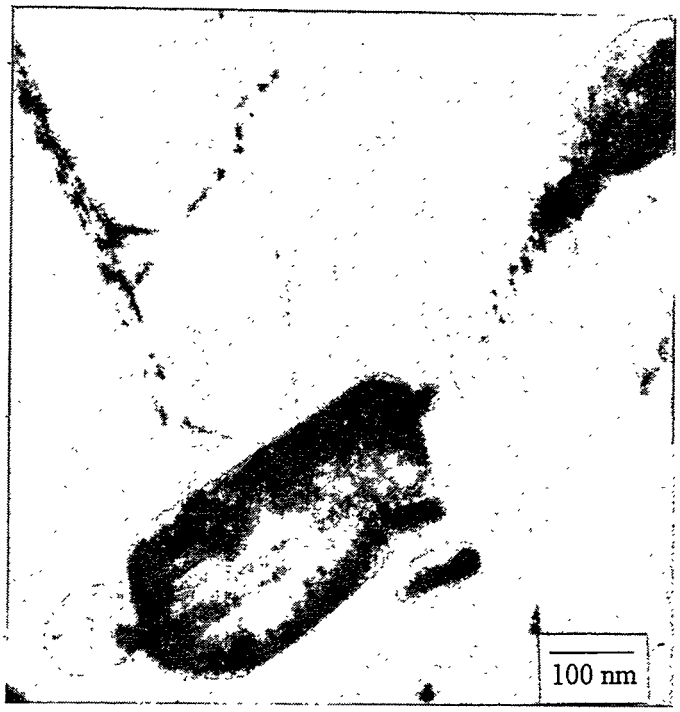

Fig. 2. Transmission electron micrograph of the 9Cr-2WVTa steel showing blocky $M_{23}C_6$ and small spherical MC (arrows) precipitates.

Precipitates in 9Cr-2WVTa

The precipitates in the 9Cr-2WVTa steel were similar to those in the 9Cr-2WV steel. Blocky $M_{23}C_6$ and the small spherical precipitates previously identified as MC [9] were detected in the matrix and at lath boundaries. Precipitate sizes and number densities were comparable to those in the 9Cr-2WV steel, although the small spherical precipitates in the 9Cr-2WVTa steel, most of which were vanadium rich with a few being tantalum rich, appeared to be somewhat smaller than those in the 9Cr-2WV steel.

Precipitates in 7Cr-2WVTa

Blocky $M_{23}C_6$ precipitates were observed in the 7Cr-2WVTa with a similar size and number density range as in the two 9Cr steels (Table 2). In addition, blocky faulted M_7C_3 precipitates (Fig.3) and small needle-shaped precipitates approximately 5 nm in diameter and 30 nm long (Fig. 4) were detected in high number densities in the 7Cr-2WVTa steel. Neither the M_7C_3 nor the needle-shaped precipitates were detected in the 9Cr steels. As discussed later, the needle-shaped precipitates

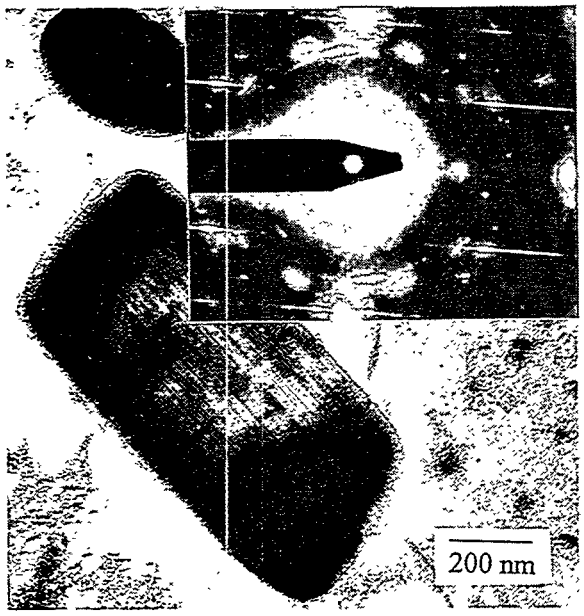

Fig. 3. Micrograph of faulted M_7C_3 precipitates in the in the 7Cr-2WVTa steel. Inset shows typical selected area diffraction pattern.

Fig. 4. Micrograph of needle-like carbonitrides in the 7Cr-2WVTa steel.

were concluded to be vanadium carbonitrides. The needle-shaped precipitates were imaged in the field ion microscope (FIM) as brightly-imaging regions approximately 2-5 nm in diameter (Fig. 5). The small spherical precipitates detected in the 9Cr steels were not detected in 7Cr-2WVTa steel.

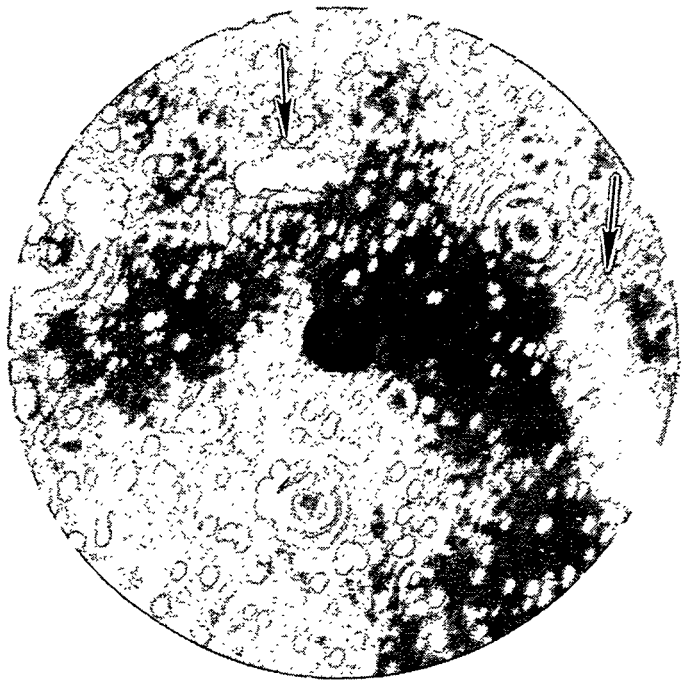

Fig. 5. Field ion micrograph of a specimen of the 7Cr-2WVTa steel showing brightly-imaging needle-like $M(CN)_{1-x}$ precipitates (arrows).

Precipitates in 5Cr-2WVTa

Precipitates in the 5Cr-2WVTa steel were $M_{23}C_6$, M_7C_3 and the needle-shaped particles. The number density of the M_7C_3 precipitates was somewhat higher than in the 7Cr-2WVTa steel, and the needle-shaped particles occurred in approximately two orders of magnitude lower number densities compared to the 7Cr-2WVTa steel. As in the 7Cr-2WVTa steel, the small spherical precipitates found in the 9Cr steels were absent (Table 2).

Microchemistry of Matrix

Atom probe analyses of the 9Cr-2WV, 9Cr-2WVTa, and 7Cr-2WVTa steels revealed that the matrix was depleted of the solutes Cr, W, V, and C. Analysis of the 9Cr-2WVTa and 7Cr-2WVTa steels indicated that a substantial portion of the tantalum was in solution, as shown in Table 3. The fragile nature of these steel specimens precluded the atom probe analysis of the large data blocks (>100,000 ions) necessary to obtain improved statistics on the matrix concentration of tantalum. However, the atom probe estimate of the matrix concentration of tantalum is consistent with the previous AEM observation on 9Cr-2WVTa [9], which indicated that tantalum is present only in the small spherical particles which occurred in low number densities.

Table 3. Atom probe analysis and ThermoCalc™ predictions of matrix composition atom percent of the 7Cr and 9Cr steels (balance iron).

Alloy		Cr	V	W	Ta	C	Si
9Cr-2WV	AP[a]	8.0 ± 0.2	0.1 ± 0.02	0.3 ± 0.03		0.01 ± 0.01	0.4 ± 0.04
	TC[b]	8.3	0.2	0.50		0.01	0.5
9Cr-2WVTa	AP	7.8 ± 0.2	0.2 ± 0.04	0.4 ± 0.04	0.02 ± 0.01	0.02 ± 0.01	0.6 ± 0.05
	TC	8.5	0.2	0.5	0.02	0.01	0.5
7Cr-2WVTa	AP	6.4 ± 0.2	0.07 ± 0.02	0.5 ± 0.06	0.02 ± 0.01	0.01 ± 0.01	0.3 ± 0.04
	TC	6.5	0.2	0.5	0.02	0.01	0.4

[a] AP—Determined by the atom probe.
[b] TC—Calculated with the ThermoCalc software.

Phase predictions for the compositions under discussion were made with the ThermoCalc software; detailed discussions of the calculations are given below. In Table 3, the matrix concentration of alloying elements in 9Cr-2WVTa and 7Cr-2WVTa steels determined by atom probe are compared with the predictions of ThermoCalc. There appears to be reasonably good agreement between the experimental results and ThermoCalc with regard to the 9Cr-2WV and 9Cr-2WVTa steels, although the Cr concentration, as estimated by ThermoCalc, is slightly higher than the experimental value in the two 9Cr steels. An possible explanation for the lower atom probe concentrations of Cr is the that the region of analysis in the matrix was in a Cr-depleted region in close proximity to a large $M_{23}C_6$ or M_7C_3 precipitate. However, it is important to note that the trends predicted by ThermoCalc are in broad agreement with experimental results. The calculations predict that tantalum, at these concentrations, does not partition to any of the carbide phases but is present in the tempered martensite matrix. The severe depletion of carbon and to a lesser extent the depletion of W and V are also consistent with the observation of various carbide phases in these steels.

Microchemistry of Precipitates—General

A comparison of the precipitate compositions determined by XEDS and APFIM with predicted compositions obtained from phase equilibria calculations using ThermoCalc is depicted in Table 4. The

Table 4. Compositions of carbides in atomic percent (balance iron) determined by XEDS and calculated with ThermoCalc™. The XEDS compositions are normalized to the overall stoichiometry based on experimental values, which indicate only the metallic content.

Alloy		Carbide	Cr	W	Ta	V	C	N
9Cr-2WV	Expt[a]	$M_{23}C_6$	46.7	4.6		0.9		
		MC[b]	8.3	0.5		44.2		
	TC[c]	$M_{23}C_6$	50.4	4.8		0.0	20.7	0.0
		$M(CN)_{1-x}$	0.2	0.02		53.0	10.3	36.4
9Cr-2WVTa	Expt[a]	$M_{23}C_6$	42.1	4.6				
		MC[a]	2.9	0.5	41.2	5.7		
	TC	$M_{23}C_6$	50.6	4.8	0.0	0.02	20.7	0.0
		$M(CN)_{1-x}$	0.1	0.02	0.0	52.9	8.5	38.2
7Cr-2WVTa	Expt[d]	$M_{23}C_6$	41.7	1.8				
		M_7C_3	39.2	4.0		3.2		
		$M(CN)_{1-x}$	8.3	9.0		42.9	27.4	12.4
	TC	$M_{23}C_6$	47.0	4.8	0.0	0.03	20.7	0.0
		M_7C_3	53.4	0.5	0.0	5.5	30.0	0.0
		$M(CN)_{1-x}$	0.7	0.2	0.0	52.4	24.3	22.4

[a]Experimental determination of $M_{23}C_6$ and M_7C_3 was by XEDS.
[b]Data taken from Ref. 13.
[c]Calculated with ThermoCalc.
[d]Experimental determination of $M_{23}C_6$ and M_7C_3 was by XEDS and $M(CN)_{1-x}$ was by Atom Probe.

results of atom probe analyses performed on the 9Cr-2WV, 9Cr-2WVTa and 7Cr-2WVTa steels reveal that the experimentally observed phases and their compositions follow the trend predicted by ThermoCalc, with the exception of the identity of the small spherical precipitates in the 9Cr steels. This discrepancy will be discussed in a later section.

Microchemistry of Precipitates in 9Cr-2WV

The compositions of the $M_{23}C_6$ precipitates in the 9Cr-2WV as determined by XEDS revealed them to be chromium rich with smaller amounts of tungsten and vanadium, with the balance of the metallic component being iron (Table 4). Previous XEDS studies on carbon film replicas of 9Cr-1MoVNb-2Ni [11] and atom probe analyzes of 12% Cr steel weld metals [12] indicated that the iron content is close to 25%. The number densities of the small spherical precipitates were not high enough to be detected in the atom probe. Carbon film replica analyses from a previous study indicated that these were MC precipitates that were vanadium rich [13].

Microchemistry of Precipitates in 9Cr-2WVTa

The composition of $M_{23}C_6$ precipitates in the 9Cr-2WVTa was similar to that in the 9Cr-2WV steel. Analyses of foil specimens by XEDS indicated that some of the small spherical precipitates contained tantalum. Previous analyses of carbon film replicas revealed two kinds of these MC precipitates in this steel [13]: some were rich in vanadium, similar to those in the 9Cr-2WV steel, and others were rich in tantalum. The Ta-rich precipitates contained up to 41 at. % Ta [13].

A rough calculation of the amount of tantalum in the spherical precipitates was made based on the TEM estimates of number density, mean precipitate diameter, and the tantalum content of the precipitates as determined by XEDS. It was assumed that the spherical particles had a similar structure and unit cell as TaC. The calculation revealed that approximately 2% of the total tantalum concentration in the bulk went into the precipitates. Since tantalum was not detected in any of the other precipitates, the implication is that the majority of the tantalum (98%) must remain in solid solution, consistent with the atom probe results in Table 3.

Microchemistry of Precipitates in 7Cr-2WVTa

In addition to $M_{23}C_6$, M_7C_3 precipitates were also analyzed in the 7Cr-2WVTa. Although these precipitates are also chromium rich, the Cr, W and V concentrations are higher compared to the $M_{23}C_6$ precipitates (Table 4). The small size of the needle-shaped precipitates in the 7Cr-2WVTa alloy precluded reasonable XEDS compositional measurements in thin foil specimens. However, the number densities of the needle-shaped precipitates were high enough to be detected in the FIM images, and atom probe analyses revealed these precipitates to be predominantly vanadium rich with high concentrations of carbon and nitrogen, leading to the conclusion that they are carbonitrides with the composition given in Table 4. The four steels used in this study contained 100-200 wppm N.

Phase Equilibria Calculations

Phase equilibria calculations with ThermoCalc were performed to gain a better understanding of the phases that are experimentally observed in these multicomponent alloy systems. The temperature used in the calculations was 750°C which was the temperature at which the steels were tempered. Significant carbon depletion was observed in the three steels investigated in the atom probe, and this was consistent with the TEM results, which revealed the formation of three distinct carbides in the matrix and at lath boundaries. The vanadium depletion was significantly higher in the 7Cr-2WVTa steel compared to the two 9Cr steels. This observation was consistent with the atom probe and TEM results which indicated V-rich carbonitrides [$M(CN)_{1-x}$] precipitated in a significant number density in the 7Cr-2WVTa steel.

The ThermoCalc calculations predict that in the two 9Cr steels the most stable phases are the body-centered cubic (bcc) matrix, the $M_{23}C_6$ precipitate, and the face-centered cubic (fcc) phase, which is a predominantly V-rich carbonitride. The predicted matrix phase and its composition are in full agreement with experimental results, which revealed a 100% tempered martensite matrix depleted in Cr, W, V and C. The metallic component of the precipitates, determined by XEDS, were normalized with respect to the overall stoichiometry of the phase and appear to be in broad agreement with the values predicted by ThermoCalc. The predictions of ThermoCalc with regard to the V-rich fcc carbonitrides could not be verified experimentally because the number density of the small spherical precipitates in the 9Cr steels (observed in the TEM) were not high enough to be detected in the apex region of the APFIM specimens, and therefore, accurate elemental compositions of these small spherical precipitates could not be determined directly. However, it is likely that these precipitates are carbonitrides because XEDS measurements revealed them to be rich in vanadium, similar to those predicted by ThermoCalc [13].

The agreement between experimental results and the calculations is better for the 7Cr-2WVTa steel. ThermoCalc predicts that M_7C_3 will form in addition to $M_{23}C_6$, and the calculated compositions are in rough agreement with the experimentally determined values. The high number density of the small needle-shaped precipitates enabled their elemental compositions to be determined directly by atom probe analysis (Table 4), which revealed them to be M(CN)-type precipitates with the metallic component consisting of vanadium with some contribution from chromium and tungsten. The atom probe composition is in general agreement with the M(CN) predicted by ThermoCalc, although the concentrations of chromium and tungsten are somewhat higher than

predicted. It is possible that some matrix ions (Cr and W) were sampled by the probe hole during analysis due to the small diameter (2-5 nm) of the precipitates. The largest metallic component of the precipitates is vanadium (42.9 at. %) with nitrogen accounting for a significant portion of the non-metallic component (12.4 at. %). The direct experimental confirmation of the presence of V-rich carbonitrides in the 7Cr-2WVTa steel lends further support to the suggestion that the small spherical vanadium-rich precipitates observed in the 9Cr steels might be the carbonitrides predicted by ThermoCalc and not MC precipitates, as often referred to in the literature.

The fact that these precipitates contain nitrogen is not unexpected for two reasons. First, accurate quantitative estimates of carbon and nitrogen by XEDS are difficult to obtain and require the use of a light element detector. Secondly, it is known that nitrogen can dissolve in carbides. Honeycomb states [14]: "...there are a few elements which enter predominantly the carbide phase. Nitrogen is the most important element, and it forms carbonitrides with iron and many alloying elements." Microalloyed steels containing stable carbide and nitride formers such as vanadium and niobium are known to form carbonitrides, often designated as V(C,N), Nb(C,N), or (V,Nb)(C,N)[15]. When Tupholme et al. [16] examined a series of 9Cr-WVTa and 12Cr-WVTa reduced-activation steels with 0.75 and 3% W, 0.25-0.4% V, 0.1% Ta, 0.1% C, and 100-400 wppm N, they found small spheroidal intragranular precipitates with a cubic structure in addition to $M_{23}C_6$. The small precipitates contained tantalum and vanadium, and the authors concluded were probably carbonitrides, which they designated (V,Ta) (C,N) [16].

An interesting aspect of the phase equilibrium calculations was that ThermoCalc does not predict the fcc phase if nitrogen is totally removed as a component in the thermodynamic system in the two 9Cr steels and the 7Cr-2WVTa steel. However, when nitrogen is included in amounts as small as 20 appm, the fcc phase appears as a V-rich carbonitride containing significant amounts of nitrogen (20-30 at. %). Moreover, if nitrogen is totally absent as a component and the carbon concentration is increased above the levels in these steels (0.5 at. %), ThermoCalc predicts that the MC phase will still not form. Instead, in the 9Cr steels, the M_7C_3 phase will begin to form, in addition to $M_{23}C_6$ phase. Increasing the carbon level of the 7Cr steel merely increases the molar fraction of the M_7C_3 phase. ThermoCalc rules out the possibility of an MC phase in which carbon is the only non-metallic species for the steel compositions used in this work.

The phase equilibria calculations applied to the steels in this work clearly reveal the important role of the trace impurity nitrogen. The formation of the stable carbonitrides has implications for mechanical properties, not only in the steels in this study, but also in the much broader context of various other types of steels which contain V, Ti or Nb, all of which are known to be potent carbonitride formers.

The formation of the various phases in the 9Cr-2WV, 9Cr-2WVTa, 7Cr-2WVTa and 5Cr-2WVTa steels is related to the interplay of the relative levels of Cr, V, C and N. In the two 9Cr steels and the 7Cr-2WVTa steel, it is reasonable to assume that the addition of trace quantities of nitrogen stabilizes the fcc phase sufficiently to allow for the formation of $M(CN)_{1-x}$ along with the $M_{23}C_6$ phase. After tempering at 750°C when the chromium level is reduced to 7.5 at. %, ThermoCalc predicts that M_7C_3 begins to form as a stable phase in addition to the bcc matrix, $M_{23}C_6$, and the fcc carbonitride phases, which agrees with the observations.

At chromium levels of 5 at. %, the phase field is unchanged from that of the 7Cr-2WVTa system and the stable phases predicted by ThermoCalc are the bcc matrix, the $M_{23}C_6$ and M_7C_3 carbides, and the fcc V-rich $M(CN)_{1-x}$. All four phases were observed in TEM in the 5Cr-2WVTa steel. The number density of the M_7C_3 was higher and that of the needle-shaped precipitates lower than in the 7Cr-2WVTa steel (Table 2). The number density of the $M_{23}C_6$ precipitates was also somewhat lower than in the 7Cr-2WVTa steel. An interesting aspect of the phase equilibria calculations in this steel is that ThermoCalc predicts the formation of the fcc V-rich carbide in the absence of nitrogen. Although an atom probe analysis was not performed on the 5Cr-2WVTa steel to confirm this

prediction, ThermoCalc results revealed that with 300 appm N present in the bulk, the fcc phase has the composition 47.2 at. % V-2.9% Cr-3.3% W-0.1% Fe-40.9% C-5.6% N. This result indicates that even with nitrogen present in the alloy the fcc precipitate is predominantly carbon rich with a nitrogen concentration of only 5%.

Mechanical Properties

Since mechanical properties are influenced by microstructural features, it is important to consider how the microstructures of the four steels relate to the mechanical properties. A comparison of the Charpy impact properties of the 9Cr-2WV and 9Cr-2WVTa steel revealed significant differences (Table 2). The DBTT of the 9Cr-2WV and 9Cr-2WVTa in the normalized-and-tempered condition was -60 and -88 °C, respectively, while the USE was 8.4 and 11.2 J, respectively [3]. These results were taken to indicate the effect of tantalum on the properties [3].

A significant difference between the microstructure of the 9Cr-2WVTa steel and the 9Cr-2WV steel was in the finer prior austenite grain size [10] and smaller lath size of the steel containing tantalum. Although atom probe analysis revealed that the majority of the tantalum is in solid solution in the Ta-containing alloys, some small fraction could conceivably segregate to grain and lath boundaries and thereby provide a mechanism for grain refinement. Further experimental work is needed to verify this suggestion. Previous work concluded that tantalum in solution has a significant effect on the Charpy properties of the 9Cr-2WVTa steel relative to the 9Cr-2WV steel, perhaps by increasing the fracture stress of the 9Cr-2WVTa [17]. The atom probe results that indicate that most of the tantalum remains in solution reinforces that conclusion.

It has been suggested in the literature that better fracture toughness correlates with lower Cr content in a steel [18]. Superficially, this suggestion seems to be supported by experimental data for the reduced-activation steels of this study (Table 4) and previous studies [4,10]. The USE of a 9Cr-2WV and a 5Cr-2WV steels were 9.5 and 11.7 J, respectively [4]; the USE of the 9Cr-2WVTa, 7Cr-2WVTa and 5Cr-2WVTa steels were 10.1, 11.4, and 14.3 J, respectively [10]. Likewise, although the 9Cr-2WVTa and 7Cr-2WVTa steels have similar DBTTs, the DBTT for 5Cr-2WVTa is considerably lower than those of the other steels (Table 2), again indicating the possible effect of chromium. As pointed out above, tantalum affects the DBTT [3,4], but its effect on the USE is not as obvious.

The size and number density of the $M_{23}C_6$ precipitates were nearly the same in all four steels, and $M_{23}C_6$ probably does not influence the differences in the mechanical behavior of these steels. Similar arguments apply to the large M_7C_3 precipitates in the 7Cr-2WVTa and 5Cr-2WVTa steels. The small $M(CN)_{1-x}$ precipitates might be expected to contribute to an increase in the yield stress through precipitate hardening in the 7Cr-2WVTa steel, where they occur in significant number densities. This argument is not, however, borne out by yield stress data (Table 2). The room temperature yield stress of the 7Cr-2WVTa steel was 583 MPa compared to 645 MPa for the 9Cr-2WVTa, 629 MPa for the 5Cr-2WVTa, and 597 MPa for the 9Cr-2WV steels [10], thus giving no indication of a discernible trend, even though the Charpy properties appear to be sensitive to the microstructural differences.

SUMMARY AND CONCLUSIONS

The microanalytical characterization of four reduced activation 5-9% Cr steels revealed that the matrix was 100% tempered martensite. Blocky (100-200 nm) Cr-rich $M_{23}C_6$ formed in all four steels. The 9Cr-2WV and 9Cr-2WVTa steels also contained small spherical V-rich and V- or Ta-rich precipitates, respectively. Analysis of the 7Cr-2WVTa and 5Cr-2WVTa alloys revealed Cr-rich blocky faulted M_7C_3 in the matrix and at lath boundaries. Small V-rich needle-shaped $M(CN)_{1-x}$ in high number densities were also detected in the 7Cr-2WVTa and 5Cr-2WVTa steels. The XEDS and atom probe analysis revealed that with the exception of a few of the small spherical precipitates, no tantalum was detected in any of the other precipitates. Atom probe analysis of the matrix

indicated a depletion of Cr, W, V, and C and that nearly all the tantalum was in solid solution in the tantalum-containing steels.

The experimentally observed stable phases and their compositions are in general agreement with phase equilibria calculations using the ThermoCalc software. The thermodynamic calculations revealed the important role of trace amounts of nitrogen in these alloys. ThermoCalc predicts the absence of the V-rich fcc carbide as a stable phase in the 9Cr-2WVTa and 7Cr-2WVTa steels unless nitrogen is present in the system as a trace impurity in quantities as low as 20 appm. Atom probe analysis of the needle-shaped precipitates in the 7Cr-2WVTa steel directly confirmed the presence of these carbonitrides and revealed that these precipitates contained significant levels of nitrogen (12 at. %). These results support the argument that the small spherical precipitates in the 9Cr-2WV and 9Cr-2WVTa steels are also V-rich carbonitrides and not MC.

REFERENCES

1. R.L. Klueh and E.E. Bloom, *Nucl. Eng. Design/Fusion*, 1985, vol. 2, pp. 383-89.
2. R.W. Honeycombe, *Structure and Strength of Alloy Steels*, Climax Molybdenum Company, London 1974.
3. R.L. Klueh, *JOM*, 1992, vol. 44, p. 20-24.
4. R.L. Klueh, D.J. Alexander and P.J. Maziasz, *J. Nucl. Mater.,* 1992, vol. 186, p. 185-195.
5. B. Sundman, B. Jansson and J.O Andersson, *Calphad* , vol. 9,1985, 153.
6. R.L. Klueh and P.J. Maziasz, *Reduced Activation Materials for Fusion Reactors*, ASTM STP 1047, edited by R.L. Klueh, D.S. Gelles, M. Okada and N.H. Packan, American Society for Testing and Materials, Philadelphia, 1990, pp.140.
7. M.K. Miller and G.D.W. Smith, *Atom Probe Microanalysis: Principles and Applications to Materials Problems*, Materials Research Society, Pittsburgh, PA, 1989.
8. M.K. Miller, *J. de Physique*, vol. 47-C2, 1986, pp. 493.
9. R.L. Klueh and P.J. Maziasz, *Metall. Trans. A*, vol. 20A , 1989, pp. 373-382.
10. R.L. Klueh, Oak Ridge National Laboratory, unpublished research, 1995.
11. P.J. Maziasz and R.L. Klueh, *Effects of Radiation on Materials: 14th International Symposium*, vol. 1, ASTM, STP 1046, edited by N.H. Packan, R.E. Stoller and A.S. Kumar, American Society for Testing Materials, Philadelphia, 1989, pp.35.
12. G. J. Cai, L. Lundin, H. O. Andrén and L. E. Svensson, *App.Surf. Sci.*, vol. 76/77, 1994, pp. 248.
13. R.L. Klueh, P.J. Maziasz and W.R. Corwin, *Development of Ferritic Steels for Fusion Reactor Applications*, Report No.6472, ORNL,1988.
14. R. W. K. Honeycomb, *Steels: Microstructure and Properties*, Edward Arnold, London, 1981, pp. 61.
15. M. J. Crooks, A. J. Garratt-Reed, J. B. Vander Sande, and W. S. Owen, *Met. Trans. A.,* vol. 12A, 1981, pp. 1999.
16. K. W. Tupholme, D. Dulieu, and G. J. Butterworth, *J. Nucl. Mater.*, vol. 179-181, 1991, pp.684.
17. R.L. Klueh, D.J. Alexander and P.J. Maziasz, *J. Nucl. Mater.,* 1996, vol. 233-237, pp. 336.
18. H. O. Andrén, G. Cai and L. E. Svensson, *App. Surf. Sci.*, vol. 87/88, 1995, pp. 200.

4.0 COPPER ALLOYS AND HIGH HEAT FLUX MATERIALS

EFFECT OF HEAT TREATMENTS ON THE TENSILE AND ELECTRICAL PROPERTIES OF HIGH-STRENGTH, HIGH-CONDUCTIVITY COPPER ALLOYS —

S. J. Zinkle and W. S. Eatherly (Oak Ridge National Laboratory)

OBJECTIVE

The objective of this report is to summarize recent tensile and electrical resistivity measurements on several different unirradiated commercial high-strength, high-conductivity copper alloys that are being considered for the divertor structure and first wall heat sink in ITER.

SUMMARY

The unirradiated tensile properties of CuCrZr produced by two different vendors have been measured following different heat treatments. Room temperature electrical resistivity measurements were also performed in order to estimate the thermal conductivity of these specimens. The thermomechanical conditions studied included solution quenched, solution quenched and aged (ITER reference heat treatment), simulated slow HIP thermal cycle (~1°C/min cooling from solutionizing temperature) and simulated fast HIP thermal cycle (~100°C/min cooling from solutionizing temperature). Specimens from the last two heat treatments were tested in both the solution-cooled condition and after subsequent precipitate aging at 475°C for 2 h. Both of the simulated HIP thermal cycles caused a pronounced decrease in the strength and electrical conductivity of CuCrZr. The tensile and electrical properties were unchanged by subsequent aging in the slow HIP thermal cycle specimens, whereas the strength and conductivity following aging in the fast HIP thermal cycle improved to ~65% of the solution quenched and aged CuCrZr values. Limited tensile and electrical resistivity measurements were also made on two new heats of Hycon 3HP CuNiBe. High strength but poor uniform and total elongations were observed at 500°C on one of these new heats of CuNiBe, similar to that observed in other heats.

PROGRESS AND STATUS

Introduction

In a previous semiannual report [1], data from room temperature electrical resistivity measurements and elevated tensile test measurements at several different strain rates were summarized for wrought dispersion strengthened copper (Cu-Al_2O_3) and solutionized and aged CuCrZr and CuNiBe. Since the mechanical and electrical properties of precipitation strengthened alloys such as CuCrZr and CuNiBe are known to be sensitive to heat treatment conditions [1-5], the objective of the present study was to quantify the degradation in electrical conductivity and tensile strength which may occur under some heat treatment conditions. In particular, this study focuses on CuCrZr subjected to several different heat treatment cycles. The current reference design for the International Thermonuclear Experimental Reactor (ITER) utilizes a hot isostatic press (HIP) technique to join the Cu alloy heat sink to the stainless steel structure in the first wall [6]. The joining is performed at a temperature of ~950°C, and the cooling time to reach ~400°C after joining is estimated to be ~1 h due to the large size of the first wall panels. A similar HIP technique is envisioned for fabricating the Cu/W/carbon-carbon composite monoblocks for the divertor. However, higher cooling rates of ~100 to 200°C/min may be achievable with gas cooling on the inside of the Cu tube for these components [6]. The effect of two different HIP thermal cycle heat treatments (furnace cool and gas cool) on the properties of CuCrZr are summarized in this report. The effects of subsequent precipitate aging heat treatments were also studied. Finally, the results of limited tests on two new heats of Hycon 3HP™ CuNiBe are reported and compared to previous results obtained on other CuNiBe heats.

Table 1. Summary of Heat Treatments for CuCrZr Specimens

Alloy and heat treatment	Solutionizing treatment	Aging treatment
Zollern CuCrZr, heat Z822		
solution quenched (as-received)	970°C, 20 min./water quench	---
solution quenched & aged	970°C, 20 min./water quench	475°C, 2 h
HIP furnace cool	980°C, 1 h/ furnace cool (~6 h to cool to 400°C)	---
HIP furnace cool & aged	980°C, 1 h/ furnace cool	475°C, 2 h
HIP fast cool	980°C, 1 h/ gas cool (~100°C/min cooling rate)	---
HIP fast cool & aged	980°C, 1 h/ gas cool	475°C, 2 h
Kabelmetal CuCrZr,heat AN4946		
ITER solution quenched & aged	980°C, 1 h/ water quench	475°C, 2 h

Experimental Procedure

Most of the work reported here was performed on bar stock of CuCrZr that was received in a solution quenched condition. The bar was manufactured by Zollern GmbH, Laucherthal, Germany (heat Z822) with a reported composition of 0.85 wt%Cr, 0.09 wt%Zr and <0.001 wt%P. The bar was solutionized for 20 minutes at 970°C and water quenched. The short solutionizing time and slightly lower solutionizing temperature compared to typical CuCrZr solutionizing conditions was specified by Joint European Tokamak (JET) designers in order to minimize the grain size of the final product. Miniature SS-3 sheet tensile specimens with nominal gage dimensions 0.76 mm × 1.5 mm × 7.6 mm were electro-discharge machined from the bar and subsequently heat treated at several different conditions which are summarized in Table 1. The HIP solutionizing treatments were performed in flowing Ar, and all of the aging treatments were performed in flowing He.

The Kabelmetal Cu-0.65%Cr-0.10%Zr specimens were obtained from a 2 cm thick plate that was originally fabricated under the trade name of Elbrodur G by KM-Kabelmetal, Osnabrück, Germany as an F37 (cold-worked and aged) temper, heat #AN4946. A 2 × 3 × 5 cm piece from this plate was solution annealed in flowing argon for 1 hour at 980°C, water quenched, then aged in flowing helium at 475°C for 2 hours (furnace cool) at ORNL, in accordance with the draft ITER heat treatment specifications. Miniature SS-3 sheet tensile specimens were subsequently machined from the solutionized and aged plate.

Two different heats of Hycon 3HP™ CuNiBe produced by Brush-Wellman were investigated. Heat #35562 was fabricated as 3.2 mm thick strip in a cold-worked and aged (TH04 temper) condition. The reported solute composition for this heat was 1.56%Ni, 0.25%Be, 0.1%P. Heat #28626 was supplied in two different heat treatments, and had a reported solute composition of 1.90%Ni, 0.32%Be, 0.1%P. The HT (TH04 temper) material from heat #28626 was supplied as 0.89 mm thick strip. A thicker plate of HT temper material from this heat was reprocessed by Brush-Wellman to the AT (solutionized, air-quenched and aged) condition. The AT heat treatment consisted of solutionizing at 932°C for 1 h (gas quench) followed by aging at 510°C for 3 h. The AT material was fabricated into sheet tensile specimens with an overall length of 12.2 cm and a thickness of 3.2 mm. Miniature SS-3 sheet tensile specimens were cut from the grip regions of these large tensile specimens after they had been tensile tested by McDonnell-Douglas in an induction furnace system at 500°C. Since the 8 min. hold time at 500°C for the tensile tests on the large sheet tensile specimens was much less than the aging time of 3.5 h at 510°C, the precipitate structure in the grip regions should be similar to that of the as-fabricated AT material.

Four-point probe electrical resistivity measurements were performed at room temperature on a total of 2 to 5 different SS-3 sheet tensile specimens for each of the heat treatment conditions, using procedures summarized elsewhere [7]. The temperature was recorded for each measurement and the resistivity data were corrected to a reference temperature of 20°C using the copper resistivity temperature coefficient of $d\rho/dT = 6.7 \times 10^{-11}$ Ω-m/K. Nonuniformities in the width and thickness in the specimen gage region caused the typical experimental uncertainty of individual resistivity measurements to be ±0.5%. The relation 17.241 nΩ-m = 100% IACS (international annealed copper standard) was used to convert the resistivity measurements to electrical conductivity values.

The tensile properties of the SS-3 sheet tensile specimens were measured at room temperature or 500°C at a crosshead speed of 0.0085 mm/s (with the exception of the Kabelmetal CuCrZr specimen which was tested at 0.017 mm/s), which corresponds to initial strain rates of 1.1×10^{-3} and $2.2 \times 1\ 0^{-3}$ in the gage region, respectively. The room temperature tests were performed in air, and the elevated temperature tests on CuNiBe were performed in vacuum (10^{-6} to 10^{-5} torr). Two different heating cycles were used for the 500°C tests on CuNiBe in order to determine if the tensile properties degraded after holding at the test temperature. One specimen was rapidly heated to 500°C (heating time <8 minutes) and tensile tested as soon as it reached the test temperature. A second specimen was heated to 500°C over a period of ~0.5 h and subsequently held at the test temperature for 0.25 h prior to the start of each tensile test. One specimen was tested in an Instron servohydraulic machine for each experimental condition. The tensile properties were determined from graphical analysis of the chart recorder curves. A plastic deformation offset of 0.2% was used for measuring the yield strength.

Results

Table 2 summarizes the results of the room temperature electrical resistivity measurements. All three of the CuNiBe thermomechanical conditions had electrical conductivities near 67% IACS. This conductivity is comparable to that previously measured [1,7] in other heats of Hycon CuNiBe (64-72% IACS). As expected, the solution quenched CuCrZr had a low conductivity of ~36% IACS. The Kabelmetal solution quenched and aged CuCrZr had a superior electrical conductivity compared to that of Zollern solution quenched and aged CuCrZr (83% vs. 76% IACS), presumably due to the short solutionizing time and lower solutionizing temperature along with the higher Cr concentration for the Zollern material. The HIP slow furnace cool condition produced a modest degradation in the electrical conductivity of the Zollern CuCrZr compared to the solution quenched and aged condition (~68% vs. 76% IACS). The conductivity remained slightly degraded following aging.

The tensile properties obtained in the present study are summarized in Table 3. Previous tensile tests on the AT CuNiBe (heat 28626) material performed at 500°C using large sheet tensile specimens indicated that the uniform and total elongations were 3.1 to 6.1% [8]. The present tensile tests, performed at 500°C with miniature SS-3 type sheet tensile specimens, produced yield strengths that were in good agreement with the large sheet tensile specimen results. However, the measured uniform and total elongations were significantly smaller than that reported for the larger specimens. This indicates that the small size of the SS-3 sheet tensile specimens (~10 to 20 grains across the gage thickness) accentuates the intergranular deformation mode that occurs in CuNiBe [1,7] for elevated test temperatures. There did not appear to be a pronounced effect of hold time at 500°C on the tensile properties. Although the tensile test performed with the shorter hold time had a somewhat higher elongation, in both cases the total elongation was well below 2%.

Table 2. Room Temperature Electrical Properties Measured in the Present Study (see Table 1 and text for detailed heat treatments)

Alloy and heat treatment	Meas. resistivity at 20°C	Electrical conductivity
Zollern CuCrZr, heat Z822		
solution quenched	48.29 nΩ-m	35.7% IACS
solution quenched & aged	22.55 nΩ-m	76.4% IACS
HIP furnace cool	25.41 nΩ-m	67.9% IACS
HIP furnace cool & aged	24.94 nΩ-m	69.1% IACS
HIP fast cool	39.57 nΩ-m	43.6% IACS
HIP fast cool & aged	25.91 nΩ-m	66.5% IACS
Kabelmetal CuCrZr, heat AN4946		
ITER solution quenched & aged	20.67 nΩ-m	83.4% IACS
Hycon 3HP CuNiBe		
solution quenched & aged (AT), heat 28626	25.62 nΩ-m	67.3% IACS
cold-worked & aged (HT), heat 28626	25.45 nΩ-m	67.7% IACS
cold-worked & aged (HT), heat 35562	25.41 nΩ-m	67.9% IACS

Table 3. Summary of Tensile Properties Measured in the Present Study (see Table 1 and text for detailed heat treatments)

Alloy and heat treatment	Temperature	σ_y (MPa)	UTS (MPa)	e_u (%)	e_{tot} (%)
Zollern CuCrZr					
solution quenched	20°C	118	243	42	52
solution quenched & aged	20°C	310	418	17	25
HIP furnace cool	20°C	—	—	—	—
HIP furnace cool & aged	20°C	68	217	23	29
HIP fast cool	20°C	37	216	56	61
HIP fast cool & aged	20°C	206	328	18	23
Kabelmetal CuCrZr					
solution quenched & aged	20°C	316	414	16	24
Hycon CuNiBe, heat 28626					
solution quenched & aged (AT)	500°C*	399	414	0.6	0.6
solution quenched & aged (AT)	500°C**	414	445	1.3	1.3

*heated to 500°C within ~30 min. and held at temperature for 15 min. prior to starting tensile test
**heated to 500°C within ~ 8 min.; tensile test started immediately after reaching 500°C.

The solution quenched and aged heat treatments for the Zollern and Kabelmetal CuCrZr produced comparable room temperature tensile properties, with yield strengths of ~310 MPa, ultimate strengths of ~420 MPa and uniform elongations of ~16%. The slow cooling rate associated with the HIP furnace cool treatment resulted in a very low yield strength even after subsequent aging. It is interesting to note that the yield strength for the HIP furnace cool and aged condition was even lower than that for the solution quenched condition. A very low yield strength was also obtained in the HIP fast cooled specimens. In this case, however, the room temperature strength could be increased to 200-210 MPa (i.e., ~65% of the solution quenched and aged yield strength) by subsequent aging.

Discussion

Table 4 compares the room temperature thermal stress figures of merit, $M=\sigma_y k_{th}(1-\nu)/\alpha E$, for CuCrZr in various heat treatment conditions with other high-strength, high conductivity copper

alloys. The M values were calculated using pure copper data [9] for Young's modulus (E), Poisson's ratio (ν) and the coefficient of thermal expansion (α), and by utilizing the Wiedemann-Franz relation to convert the electrical conductivity measurements to thermal conductivity (k_{th}). The HIP furnace cool and aged specimens exhibited a very low thermal stress figure of merit, although this parameter may not be the most appropriate guidepost if moderate amounts of deformation can be tolerated in the design. The CuCrZr thermal stress figure of merit for the HIP fast cool and aged condition is ~60% of the solutionized and aged value. This degradation in strength and thermal conductivity must be considered in designs for the divertor structure that use CuCrZr. A similar moderate degradation in strength has been reported for CuNiBe following a HIP furnace cool heat treatment [5]. The electrical conductivity was not changed within the accuracy of the experimental measurement in the study by Singh, et al. Dispersion strengthened copper did not appear to be degraded by a HIP furnace cool heat treatment [5].

Table 4. Thermal Stress Figures of Merit for High-Strength, High Conductivity Copper Alloys

Alloy and thermomechanical condition	M at 20°C (kW/m)
Kabelmetal CuCrZr (ITER solution quenched & aged)	33
Zollern CuCrZr (solution quenched & aged)	30
Zollern CuCrZr (HIP furnace cool & aged)	6
Zollern CuCrZr (HIP fast cool & aged)	17
GlidCop Al25 (IG0)	36
Hycon 3HP CuNiBe (AT, heat 46546)	45
Hycon 3HP CuNiBe (HT, heat 46546)	60

Several relevant studies on the time-temperature-transformation (TTT) kinetics of precipitation in Cu-Cr alloys have been published [2-4]. The key finding from these studies is that cooling rates >20°C/s are necessary to fully quench the Cu-Cr solid solution. Additional relevant studies such as quenching to intermediate temperatures, followed by conventional aging heat treatments were also performed. Considering the estimated cooling rates following HIP joining procedures for ITER first wall and divertor components of ~0.1-0.2°C/s and ~2°C/s, respectively [6], it may be concluded that the Cr solute will not be quenched and therefore inferior properties compared to water-quenched and aged specimens will occur (as observed in the present study).

As demonstrated in Tables 2 and 3, the degradation in conductivity and strength is particularly severe in the as-cooled CuCrZr specimens that have been subjected to the HIP thermal cycle. Subsequent aging does not have a significant effect on the properties of the HIP furnace cooled specimens, whereas a substantial improvement in strength and conductivity occurs in the HIP fast cooled specimens. Therefore, a post-joining heat treatment at ~475°C should be used for CuCrZr alloys fabricated into divertor monoblocks, where the cooling rate after HIPping is relatively fast. On the other hand, a post-joining heat treatment is not recommended for the large first wall HIPped components, since no improvement in properties is expected.

A recent study on CuCrZr subjected to a HIP furnace cool and aged heat treatments reported a modest degradation in the yield strength and no significant change in electrical conductivity compared to solution quenched and aged specimens [5]. A much larger strength degradation for HIP furnace cooled + aged CuCrZr specimens was observed in the present study (Table 3). The source of this discrepancy can be understood by noting that the room temperature yield strength of the solutionized and aged specimens in the previous study [10] was only ~30% that of the solutionized and aged specimens in the present study.

The effect of neutron irradiation on the tensile and electrical properties of these CuCrZr alloys in different heat treatment conditions will be studied in a series of 3 reactor irradiation experiments that are scheduled to begin in the summer of 1997. Further details on this irradiation experiment will be given in the next semiannual report volume.

ACKNOWLEDGEMENTS

The Zollern CuCrZr bar used in this study was supplied by George Kalinin (ITER-Garching joint work site) via Kevin Slattery (McDonnell-Douglas). The Kabelmetal CuCrZr plate was supplied in the F37 temper condition by K. Slattery, McDonnell-Douglas. The two Hycon 3HP™ CuNiBe heats were supplied by K. Slattery, McDonnell-Douglas.

REFERENCES

1. S.J. Zinkle and W.S. Eatherly, in Fusion Materials Semiannual Progress Report for Period ending Dec. 31, 1996, DOE/ER-0313/21 (Oak Ridge National Lab, 1996) p. 165.
2. T. Toda, Transactions of the Japan Institute of Metals 11 (1970) 24.
3. T. Toda, Transactions of the Japan Institute of Metals 11 (1970) 30.
4. H. Suzuki and M. Kanno, Journal of the Japan Institute of Metals 35 (1971) 434.
5. B.N. Singh, D.J. Edwards, M. Eldrup and P. Toft, Risø National Lab, Roskilde, Denmark Report Risø-R-937(EN) (1997); see also D.J. Edwards et al., in Fusion Materials Semiannual Progress Report for Period ending Dec. 31, 1996, DOE/ER-0313/21 (Oak Ridge National Lab, 1996) p. 183.
6. G. Kalinin, personal communication, May, 1997.
7. S.J. Zinkle and W.S. Eatherly, in Fusion Materials Semiannual Progress Report for Period ending June 30, 1996, DOE/ER-0313/20 (Oak Ridge National Lab, 1996) p. 207.
8. K. Slattery, personal communication, March, 1997.
9. S.J. Zinkle and S.A. Fabritsiev, Atomic and Plasma-Material Interaction Data for Fusion (supplement to Nuclear Fusion) 5 (1994) 163.
10. B.N. Singh, D.J. Edwards and P. Toft, J. Nucl. Mater. 238 (1996) 244.

INVESTIGATION OF THE INFLUENCE OF GRAIN BOUNDARY CHEMISTRY, TEST TEMPERATURE, AND STRAIN RATE ON THE FRACTURE BEHAVIOR OF ITER COPPER ALLOYS, K. Leedy and J.F. Stubbins (Univ. of Illinois), D.J. Edwards (Pacific Northwest National Laboratory), * R.R. Solomon (OMG Americas) and D. Krus (Brush Wellman)

OBJECTIVE

The objective of this work is determine how the changes in grain boundary chemistry, temperature, and strain rate affect the tensile and fracture behavior of GlidCop™ Al25, Hycon 3HP™ CuNiBe, and Elbrodur CuCrZr.

SUMMARY

In an effort to understand the mechanical behavior at elevated temperatures (>200°C) of the various copper alloys being considered for use in the ITER first wall, divertor, and limiter, a collaborative study has been initiated by the University of Illinois and PNNL with two industrial producers of copper alloys, Brush Wellman and OMG Americas. Details of the experimental matrix and test plans have been finalized and the appropriate specimens have already been fabricated and delivered to the University of Illinois and PNNL for testing and analysis. The experimental matrix and testing details are described in this report.

PROGRESS AND STATUS

Introduction

Although the microstructure and processing are significantly different for the following three alloys, oxide dispersion strengthened (DS) GlidCop™ Al25, and Hycon 3HP™ CuNiBe and Elbrodur CuCrZr (two precipitation strengthened alloys), the general trend for each alloy is that the tensile properties and fracture toughness decrease with increasing test temperature, and in the case of the CuAl25 and Hycon, the fracture toughness drops very rapidly at $T_{test} \geq$ 200°C [1-8]. Along with the decrease in strength and toughness is a concomitant loss of ductility characterized by a large decrease in uniform and total elongation. The decrease in toughness is much more rapid than for the tensile properties, and it has been speculated that the poor toughness and possibly the strength are related to either an environmental and/or an impurity effect that alters the flow and fracture properties of these materials. The GlidCop™ alloys are now known to possess a strain rate dependence as the temperature increases, which may also affect their fracture toughness [6].

Literature surveys [9-11] suggest that the zirconium additions may act as a sulfur or oxygen scavenger, thereby reducing the effect of these elements on the fracture and flow properties. While tests at ORNL have indeed shown that CuCrZr does not exhibit as rapid a decrease in toughness as the other two alloys [4,5], the reason for this behavior still remains unclear. There is no evidence to support the idea that an environmental effect is solely responsible for the poor fracture toughness of the CuAl25 since tests conducted in vacuum at ORNL showed a marked decrease in fracture toughness with increasing temperature, though not quite as severe as that measured when tested in air.

---

* Pacific Northwest National Laboratory is operated for the U.S. Department of Energy by Battelle Memorial Institute under Contract DE-AC06-76RLO 1830.

One large uncertainty that needs to be resolved is whether more than one mechanism may be responsible for the observed behavior in these three alloys, or if a different mechanism is operating in each alloy. Factors that complicate the analyses of these alloys and their behavior are the differences in grain size, strengthening phase, and composition. For example, the grains range in size and shape from 1μm x 20 μm (elongated shape) in the DS copper to over 30 μm (equiaxed shape) in the Hycon and CuCrZr. In addition, the precipitate density in the CuNiBe alloys is typically 100-1000 times higher than that present in the oxide dispersion strengthened GlidCop™ alloy, and is accompanied by large coherency strains around the γ"-phase in the CuNiBe alloys.

These microstructural variables and the testing parameters are known to influence the behavior of the alloys, however their respective roles are not clearly understood. Consequently, a study has been undertaken to begin looking at the influence of test temperature and strain rate on the mechanical properties and how the grain boundary chemistry and microstructure are related. This work is a collaboration between four parties: University of Illinois-UC, Pacific Northwest National Laboratory, OMG Americas, and Brush Wellman, Inc.

Experimental Procedure

Three different copper alloys are to be tested and analyzed. The GlidCop™ Al25 (Heat #C-8064) is in the cross-rolled and annealed condition and boron deoxidized, which is currently considered as the ITER Grade 0 (IG0) condition. The material was purchased from OMG Americas as 1 inch thick plates with a pure copper cladding. The Hycon 3HP CuNiBe (Heat #46546) was supplied by Brush Wellman, Inc. as four 1.25 inch thick plates. All four of the plates were originally in the HT temper (cold worked and aged), however, two of the plates were heat treated again to produce an AT tempered condition (solutionized, quenched, and aged). For this experiment only specimens from the AT temper are to be used. A small piece of Elbrodur G CuCrZr (Heat # AN4946) in the cold worked and aged condition (F37 temper) was used as the third alloy. Specimens from the CuCrZr are to be heat treated according to ITER draft specifications (solutionized 1 hour at 980°C, quenched, aged at 475°C for 2 hours, then furnace cooled). The compositions for the three materials are listed in Table 1.

Fracture toughness tests (J-integral) over a range of three temperatures (RT, 200°C and 300°C) will be conducted to determine the effect of test temperature. Test temperature will be limited to 300°C since the rapid decrease in strength already occurs at lower temperatures. Three-point bend bars will be used for the fracture toughness tests, as well as notched tensile specimens to allow more flexibility in the test matrix. The geometry of the specimens is provided in Figures 1 and 2. Representative fracture surfaces will be thoroughly analyzed to establish the nature of the microstructure, surface and near surface chemistry of the two alloys following fracture using optical metallography/SEM and Auger analysis.

Annealing experiments will also be conducted and subsequent Auger/TEM analysis used to determine if there are changes in grain boundary chemistry resulting from the high temperature exposure. Auger analysis of the specimens may require hydrogen charging and subsequent fracture inside the Auger microscope to eliminate oxidation on the fracture surface.

To better understand the material flow behavior near yield, interrupted tensile tests will be analyzed for microstructural development just past the point of yield, again at a number of representative temperatures (i.e. RT, 200°C and 300°C) at a minimum of two deformation

rates. This will indicate the extent to which flow is initiated and distributed during the initial stages of post-yield deformation. The tensile geometry to be used is the same as that used in previous and ongoing experiments in the Russian Federation as part of a collaboration with the United States, the European Community, and Japan. The details of the tensile specimen geometry are provided in Figure 3.

These three complementary studies should clarify the major contributors to the limited elevated temperature flow and fracture behavior of the two alloys. They will provide a means to differentiate between flow limitations during initial plastic deformation which leads to early localized flow or to localized flow stemming from the influence of grain boundaries or other microstructural features.

FUTURE WORK

In a separate but related study PNNL will perform Auger analysis on samples of the same three materials that have been held under load at the 350°C to see if any changes in grain boundary chemistry occur. Hydrogen charging may be necessary to initiate failure within the Auger microscope, however, the exact details remain to be worked out.

Depending on the outcome of the above studies, possible minor alterations in alloy chemistry or microstructure could lead to improvements in flow and fracture behavior. Such alloy alterations would be suggested by the current study (e.g. adding deoxidants - Zr - to alter grain boundary oxide levels, or inducing a precipitate sizes which would enhance cross-slip and flow distribution). These possibilities could be examined as a next logical step based on the outcome of the current work.

ACKNOWLEDGEMENTS

D.J. Edwards' participation was supported by the U.S. Department of Energy under contract DE-AC06-76RLO 1830 with the Battelle Memorial Institute at the Pacific Northwest National Laboratory.

REFERENCES

1. R.R. Solomon, J.D. Troxell, A.V. Nadkarni, J. Nucl. Mater., **233-237** (1996) p. 542.
2. S.J. Zinkle and W.S. Eatherly, Fusion Materials Semiannual Progress Report for the Period ending June 30, 1996, DOE/ER-0313/20 (ORNL, 1996), p. 207.
3. S.A. Fabritsiev, S.J. Zinkle, and B.N. Singh, J. Nucl. Mater., **233-237**, (1996) p. 127.
4. D.J. Alexander, Fusion Materials Semiannual Progress Report for the Period ending June 30, 1996, DOE/ER-0313/20 (ORNL, 1996), p. 217.
5. D.J. Alexander, Fusion Materials Semiannual Progress Report for the Period ending Dec. 31, 1996, DOE/ER-0313/21 (ORNL, 1996), p. 175.
6. S.J. Zinkle and W.S. Eatherly, Fusion Materials Semiannual Progress Report for the Period ending Dec. 31, 1996, DOE/ER-0313/21 (ORNL, 1996), p. 165.
7. B.N. Singh, D.J. Edwards, M. Eldrup and P. Toft, Risø-R-937 (EN), (Jan. 1997), (also accepted for publication in the J. Nucl. Mater.)

8. B.N. Singh, D.J. Edwards, M. Eldrup and P. Toft, Risø-R-971 (EN), (Feb. 1997), (also submitted to the J,. Nucl. Mater.)

9. R.D.K. Misra, C.J. McMahon, Jr. and A. Guha, Scripta Metall., **31** (1994), p. 1471.

10. R. Muthiah, A. Guha and C.J. McMahon, Jr., Materials Science Forum, **207-209** (1996), p. 585.

11. M. Kanno, Z. Metallkde, **79** (1988), p. 684.

Table 1 Compositions (wt% unless otherwise noted) of the three alloys being investigated in this study.

Material					
GlidCop™ Al25*	0.25 Al	23 ppm Fe	6 ppm Pb	~250 ppm B	10 ppm S *typical*
Hycon 3HP™ CuNiBe**	0.35 Be	1.92 Ni	<0.01 Co	<0.01 Fe	<0.03 Cr
Elbrodur G CuCrZr***	0.65 Cr	0.10 Zr	------	-------	--------

* Heat # C-8064, OMG Americas Inc.

** Heat # 46546, Brush Wellman Inc.

*** Heat # AN4946, KM-Kabelmetal

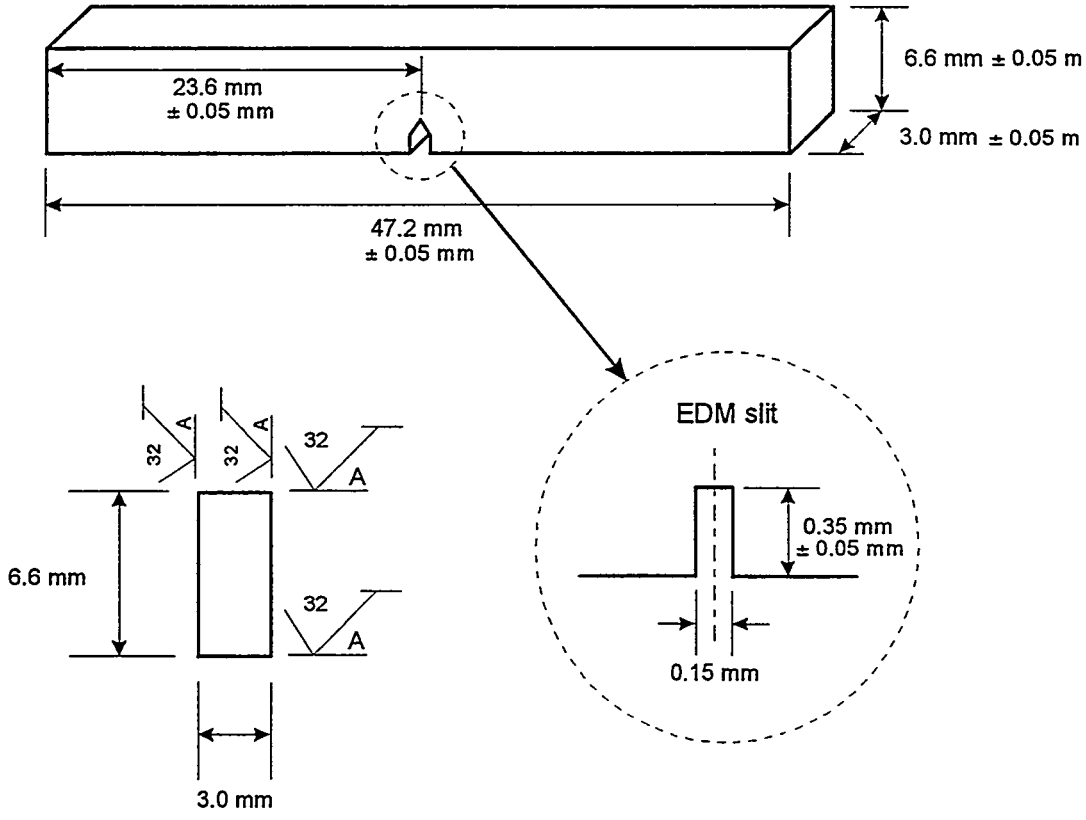

Fig. 1. Geometry and size of bend bars for fracture toughness testing.

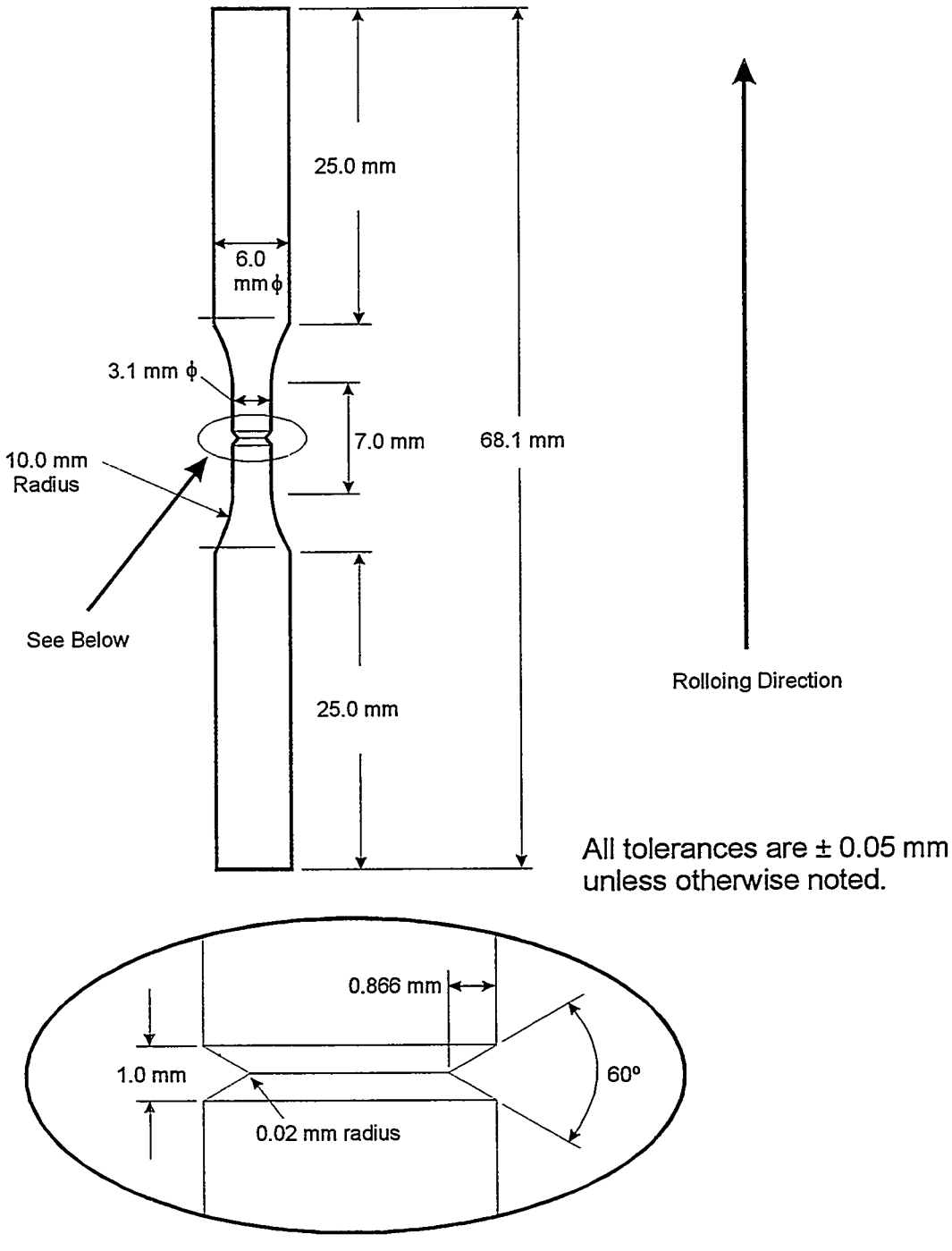

Fig. 2. Geometry and size of notched tensile specimens.

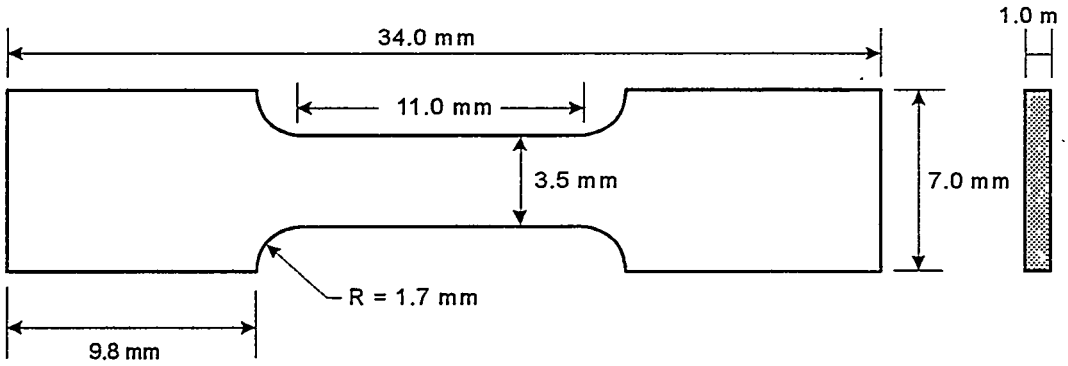

Fig. 3 Geometry and size for tensile specimens.

5.0 AUSTENITIC STAINLESS STEELS

MICROSTRUCTURAL EVOLUTION OF AUSTENITIC STAINLESS STEELS IRRADIATED TO 17 DPA IN SPECTRALLY TAILORED EXPERIMENT OF THE ORR AND HFIR AT 400°C — E. Wakai (Japan Atomic Energy Research Institute), N. Hashimoto (Oak Ridge National Laboratory), T. Sawai (JAERI), J. P. Robertson and L. T. Gibson (ORNL), I. Ioka, and A. Hishinuma (JAERI)

OBJECTIVE

The purpose of this work is to summarize the microstructural evolution of six austenitic steels irradiated at 400°C to 17.3 dpa in the spectrally tailored experiments of the ORR and HFIR.

SUMMARY

The microstructural evolution of austenitic JPCA aged and solution annealed JPCA, 316R, C, K, and HP steels irradiated at 400°C in spectrally tailored experiments of the ORR and HFIR has been investigated. The helium generation rates were about 12-16 appm He/dpa on the average up to 17.3 dpa. The number densities and average diameters of dislocation loops in the steels have ranges of 3.3×10^{21}- 9.5×10^{21} m^{-3} and 15.2- 26.3 nm, respectively, except for HP steel for which they are 1.1×10^{23} m^{-3} and 8.0 nm. Precipitates are formed in all steels except for HP steel, and the number densities and average diameters have ranges of 5.2×10^{20}- 7.7×10^{21} m^{-3} and 3.4- 19.3 nm, respectively. In the 316R, C, and K steels, the precipitates are also formed at grain boundaries, and the mean sizes of these are about 110, 50, and 50 nm, respectively. The number densities of cavities are about 1×10^{22} m^{-3} in all the steels. The swelling is low in the steels which form the precipitates.

PROGRESS AND STATUS

1. Introduction

One of the favored first wall and blanket concepts for near term fusion systems such as the International Thermonuclear Experimental Reactor (ITER) is a low pressure water-cooled austenitic stainless steel structure [1]. The neutron sources with a maximum energy of 14 MeV in the D-T fusion reactor create displacement damage in the wall, and produce hydrogen and helium atoms from (n, p) and (n, α) reactions. In the absence of operating fusion reactors, the necessary irradiation experience has to be gained from a partial simulation of the fusion environment using water-cooled mixed-spectrum fission reactors. For austenitic stainless steels, it is possible to reproduce the damage rate, neutron fluence, and helium generation rate typical of the fusion environment using spectral tailoring [2-5]. Spectral tailoring involves progressively changing the ratio of thermal to fast neutron flux through the use of removable shields surrounding the experimental assembly [2]. In this way the two-step thermal neutron reaction with 58Ni [6] can be manipulated so that the ratio of helium generation rate to displacement rate (He/dpa ratio) approximates that for fusion throughout the irradiation. In this study the microstructural evolution of six types of austenitic stainless steels have been examined under the controlled He/dpa ratio. This experiment is being conducted under the DOE/JAERI Collaborative Agreement.

2. Experimental Procedure

The spectrally tailored experiments were performed in two stages. The first stage of the irradiation was carried out in the Oak Ridge Research Reactor (ORR) in capsule ORR-MFE-7J [7-12]. After accumulating approximately 7.4 dpa in the ORR, the specimens were transferred to the High Flux Isotope Reactor (HFIR) in capsule HFIR-RB-400J-1 for the second stage [13-15]. In each reactor, the specimens were irradiated at 400°C.

Table 1. Damage levels, helium concentrations, and the ratios of He/dpa of type 316 and JPCA stainless steels irradiated in the spectrally tailored experiments of the ORR and HFIR

	316 (13wt%Ni)			JPCA (16wt%Ni)		
	Damage (dpa)	He (atppm)	He/dpa	Damage (dpa)	He (atppm)	He/dpa
ORR (MFE-7J)	7.4	100	14	7.4	155	21
HFIR (RB-400J-1)	9.9	100	10	9.9	125	13
ORR + HFIR	17.3	200	12	17.3	280	16

Table 2. Chemical compositions of austenitic stainless steels used in this study (wt%)

Alloy	Fe	Cr	Ni	B	C	N	P	S	Si	Ti	Mn	Nb	Mo
JPCA	Bal.	14.2	15.6	0.003	0.06	0.0039	0.027	0.005	0.50	0.24	1.77	-	2.3
316R	Bal.	16.8	13.5	-	0.06	-	0.028	0.003	0.61	0.005	1.80	-	2.5
C	Bal.	15.4	15.6	-	0.02	0.0018	0.017	0.007	0.51	0.25	1.56	0.08	2.4
K	Bal.	18.0	17.6	-	0.02	0.004	0.015	0.005	0.48	0.29	1.46	-	2.6
HP	Bal.	17.1	11.8	-	0.005	0.020	-	-	0.005	-	-	-	-

Temperatures were continuously measured and controlled in these experiments during irradiation. The thermal and fast (E >0.1 MeV) neutron fluences in the ORR were 8.1×10^{25} and 9.5×10^{25} n/m^2 [13], and those of the HFIR were 4.0×10^{25} and 1.6×10^{26} n/m^2[5, 7], respectively. The experiments achieved a total peak damage level of 17.3 dpa. The helium concentration generated in type 316 and JPCA stainless steel were 200 and 280 He appm, respectively, and the controlled average ratios of He/dpa were 12 and 16 appm for the 316 and JPCA, respectively, in this irradiation. The details are listed in Table 1.

Transmission electron microscopy (TEM) disks of six different austenitic stainless steels were irradiated in these capsules. The steels are the JPCA-aged, JPCA, 316R, C, K, and HP (a high-purity ternary austenite) . Chemical compositions of these alloys are given in Table 1. The JPCA steel contains boron, phosphorus, and titanium. The 316R is a standard of type 316 stainless steel. The C and K stainless steels have low carbon concentration, and they are modified exploratory alloys with titanium and/or niobium. The HP steel is a standard ternary alloy with iron, chromium, and nickel contents similar to those of type 316. The JPCA, 316R, C, K, and HP alloys were solution annealed (SA), and the JPCA aged steel was aged for 1 hr at 800 °C after 20 % cold work prior to irradiation.

Microstructures of these specimens were examined using a JEM-2000FX transmission electron microscope with a LaB_6 gun operated at 200 kV. In order to evaluate defect density the foil thickness of each TEM specimen was measured by thickness fringes or by the improved CSS method [16, 17].

3. Results and Discussion

3.1 Precipitate Formation

Precipitates are formed in all the steels, except for the HP steel, and are observed as particles with a fringe contrast as seen in Figure 1. One of the micrographs is taken by a weak beam dark-field condition, and the others are taken by a bright-field, using **g**=200, as noted in the figure. The moire fringes observed in the steels are parallel type. The precipitates are identified, from the spacing of the moire fringe, as MC type for the JPCA aged and 316R steels, $M_{23}C_6$ type for JPCA-SA and C steels, and M_6C or $M_{23}C_6$ for the K steel, respectively, as summarized in Table 3. The mean sizes and number densities of the precipitates are given in Table 4. The JPCA and 316R steels have a highest and lowest number density of precipitates, respectively. The mean size of precipitates is relatively small in steels with high number density.

The precipitates are also observed at grain boundaries in the 316R, C, and K steels as shown in Figure 2. The mean sizes of grain boundary precipitates are 110, 50, and 50 nm for the three steels, respectively, and the number density of precipitates on grain boundaries in the 316R steel is lower than that of the C and K steels. In other steels, the precipitates at grain boundaries were not observed.

Although the titanium concentration of 316R steel is low, i.e., 0.005%, MC type precipitates are formed. In the previous report [5] for the specimens from this experiment examined after the ORR irradiation to 7.4 dpa, the formation of precipitates was only in the steels with titanium

Table 3. Identification of the precipitates formed in the steels irradiated at 400°C to 17.3 dpa with a helium generation rate of about 12 -16 appm He/dpa on the average throughout this experiment

	JPCA aged	JPCA SA	316R SA	C SA	K SA
Measured the spacings of the moire fringe (nm)	1.3	1.7	1.4	1.7	2.7
Precipitate type	MC	$M_{23}C_6$	MC	$M_{23}C_6$	M_6C or $M_{23}C_6$
Lattice parameter (nm)	0.41 [18]	1.06 [19]	0.41	1.06	1.11 [19] or 1.06
The corresponding plane of the precipitates	(002)	(335)	(002)	(335)	(335) or (026)
Calculated the moire spacing (nm)	1.43	1.68	1.43	1.68	2.94 or 2.64

Table 4. Mean sizes and densities of precipitates formed in six austenitic steels irradiated at 400°C to 17.3 dpa

Alloy	Type of Precipitates	Mean Size (nm)	Number Density (m^{-3})
JPCA aged	MC	11.5	1.3×10^{21}
JPCA SA	$M_{23}C_6$	3.4	7.7×10^{21}
316R SA	MC	15.1	5.2×10^{20}
C SA	$M_{23}C_6$	5.3	5.8×10^{21}
K SA	M_6C or $M_{23}C_6$	19.3	9.5×10^{20}
HP SA	-	-	-

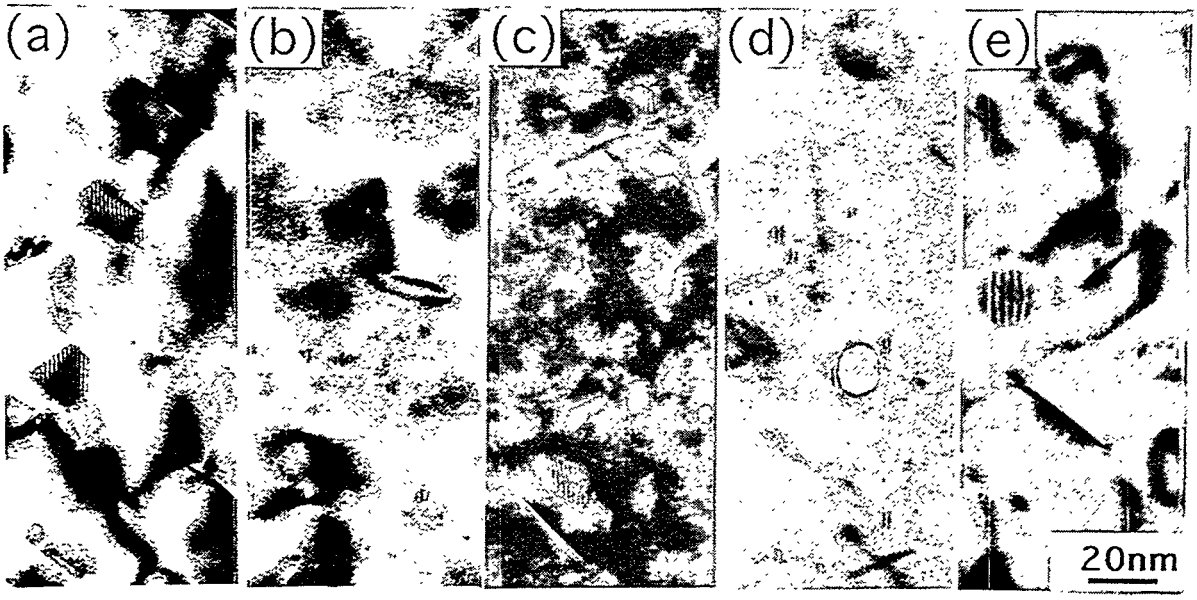

Figure 1. Precipitates formed in (a) JPCA-aged , (b) JPCA-SA, (c) 316R-SA, (d) C-SA, and (e) K-SA after irradiation at 400 °C to 17.3 dpa with a helium generation rate of about 12 -16 appm He/dpa on the average throughout this experiment. The micrographs of (a), (b), (d), and (e) are taken with bright-field image conditions, and of (c) is a weak beam dark-field condition, using **g**=200 near (011) orientation, respectively.

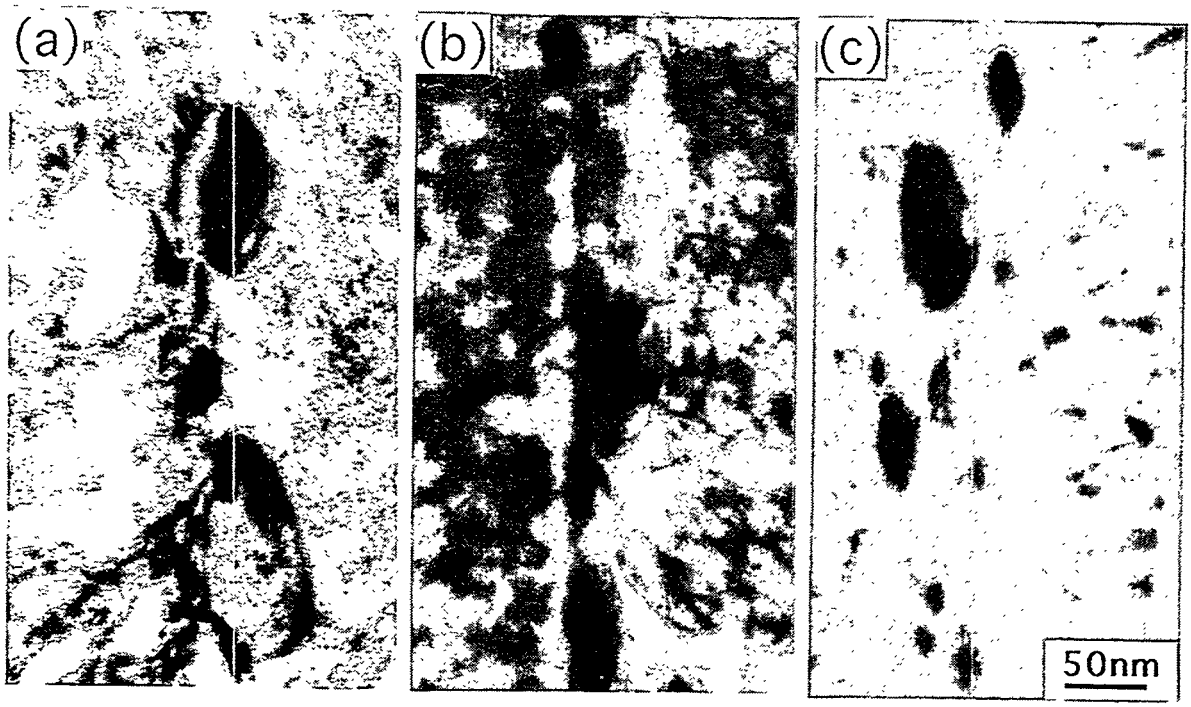

Figure 2. Precipitates at grain boundaries in (a) 316R-SA, (b) C-SA, and (c) K-SA after irradiation at 400 °C to 17.3 dpa.

Table 5. Mean sizes, number densities, and total line lengths of dislocation loops formed in six austenitic steels irradiated at 400°C to 17.3 dpa with a helium generation rate of about 12 -16 appm He/dpa on the average throughout this experiment

Alloy	Mean Size (nm)	Number Density (m^3)	Total line length of the loops (m/m^3)
JPCA aged	15.2	7.3×10^{21}	3.5×10^{14}
JPCA SA	18.7	7.0×10^{21}	4.1×10^{14}
316R SA	20.2	9.5×10^{21}	6.0×10^{14}
C SA	26.3	3.3×10^{21}	2.7×10^{14}
K SA	22.1	4.5×10^{21}	3.1×10^{14}
HP SA	8.2	1.1×10^{23}	2.8×10^{15}

contents of more than 0.01 %, i.e., JPCA-SA, C, and K steels [5]. This fact appears to imply that the precipitates are still developing up to of the irradiation of 17.3 dpa. In low carbon C and K steels, the precipitates of $M_{23}C_6$ or M_6C types are formed, while in the high carbon 316R and JPCA steels the precipitates of MC or $M_{23}C_6$ are formed. Therefore, the formation of these carbides is likely intimately related with the titanium and carbon concentration.

3.2 Dislocation Loop Formation

Figure 3 shows dislocation loops formed in the six austenitic steels irradiated at 400°C to 17.3 dpa. The electron micrographs are taken with beam direction **B** close to <110>, and are dark-field images which are formed using a streak due to stacking faults in the diffraction pattern. The loops observed are Frank loops on {111} planes in all steels, but in the K steels there are some loops which have a large size and are perfect loops; these are identified by the weak beam dark-field image. The mean sizes, number densities, and total line lengths of these loops are given in Table 5.

The mean size of the loops is the smallest in the HP steel and that of the C steel is the largest. Conversely, the number density of the loops in the HP steel is the highest and that of the C steel is the lowest. The growth of dislocation loops has a tendency to be faster in the steels with low number density of loops. The total line length of the loops is the highest in the HP. The total line lengths and the type of loops are discussed for the cavity growth in next section.

The number density of loops in HP steel is more than one order higher than those of the others as shown in Table 5. The elemental contents of the HP steel are iron, chromium, and nickel with low impurity levels as given in Table 2. However, the nitrogen concentration in the HP steel is especially higher than that of the other steels. The C steel with the lowest number density of loops contains lower carbon and nitrogen concentrations than those of the other steels. Interstitial impurities such as nitrogen and carbon may enhance the formation of dislocation loops [20]. Thus, the cause of the loop formation with a high number density may be due to be the high nitrogen concentration, and the idea is supported by the fact that the number densities of the loops in the HP and C steels are the highest and lowest, respectively.

3.3 Cavity Formation

The micrographs of cavities in the steels are as shown in Figure 4, and in the C steel the precipitates are seen on the surfaces of some cavities. The size distribution of these cavities

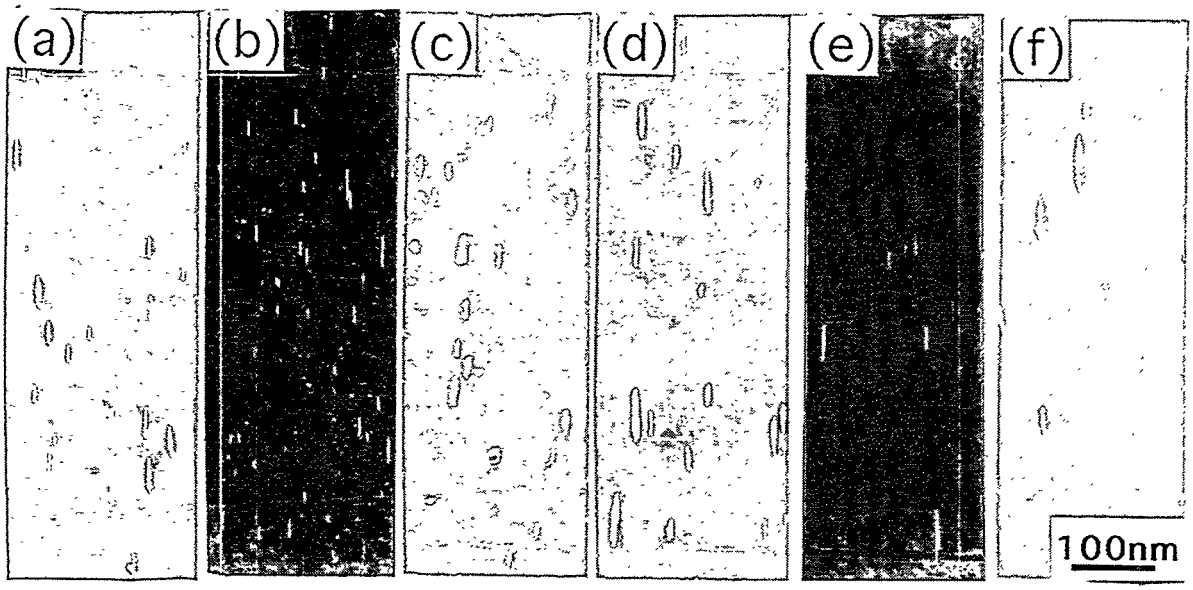

Figure 3. Dislocation loops formed in (a) JPCA -aged, (b) JPCA-SA, (c) 316R-SA, (d) C-SA, (e) K-SA, and (f) HP-SA after irradiation at 400 °C to 17.3 dpa with a helium generation rate of about 12 -16 appm He/dpa on the average throughout this experiment.

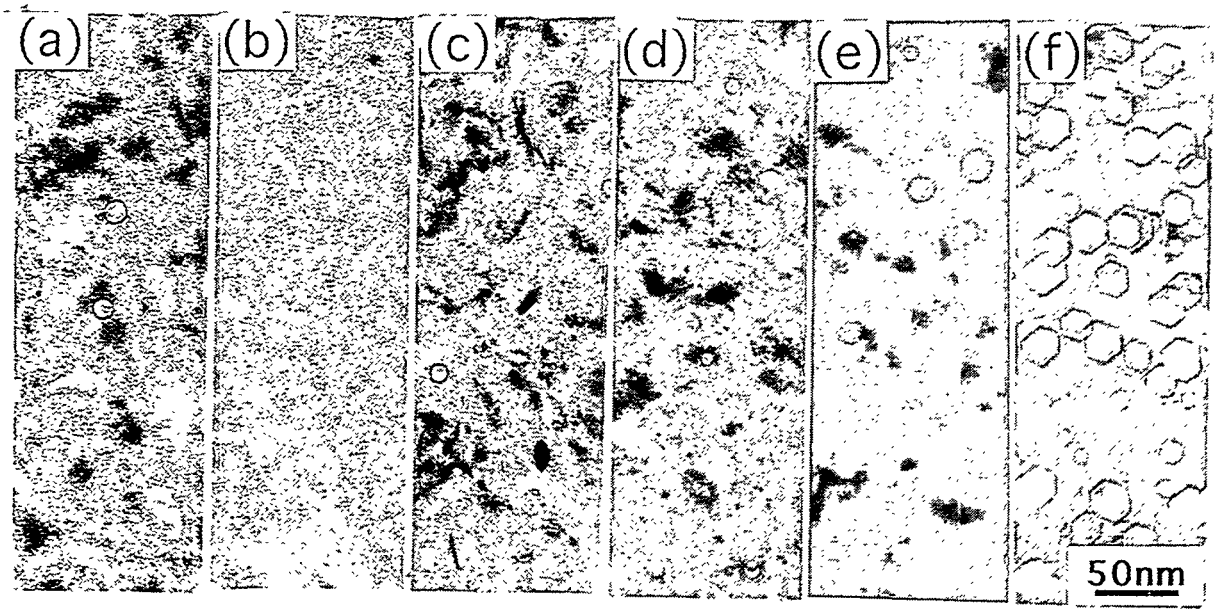

Figure 4. Cavities formed in (a) JPCA-aged, (b) JPCA-SA, (c) 316R-SA, (d) C-SA, (e) K-SA, and (f) HP-SA after irradiation at 400 °C to 17.3 dpa with a helium generation rate of about 12 -16 appm He/dpa on the average throughout this experiment.

Table 6. Swelling data of the cavities formed in six austenitic steels irradiated at 400°C to 17.3 dpa with a helium generation rate of about 12 -16 appm He/dpa on the average throughout this experiment

Alloy	Root Mean Cube of Cavity Radius (nm)	Number Density (m^{-3})	Swelling (%)
JPCA aged	1.4	1.7×10^{22}	0.020
JPCA SA	1.5	1.1×10^{22}	0.016
316R SA	1.8	6.2×10^{21}	0.015
C SA	2.5	1.1×10^{22}	0.079
K SA	4.0	1.0×10^{22}	0.27
HP SA	7.2	1.9×10^{22}	2.9

is given in Figure 5, and the distributions of cavities are bi-modal. The swelling, S, is described as:

$$S = (V'/V) \times 100\ (\%) = (400\pi/3)\ R_r^3 \times N,$$

where V' is total volume of all cavities per unit volume, V; N is a total number of cavities per unit volume; and R_r is the root mean cube of cavity radius (RMC radius).
The RMC radius is described as;

$$R_r = (\Sigma R_i^3/N)^{1/3},$$

where R_i is a cavity radius i. The RMC radius, number density, and swelling are summarized in Table 6 for each steel.

In HP steel the RMC radius is the largest and the number density is also the highest of all steels, and therefore the value of swelling is the highest. The number densities of the cavities are about 1×10^{22} m^{-3} in all the steels. However, the swelling has a large alloy dependence, i.e., except for the K and HP steels the swelling is very low. In this experiment, the steels which formed the precipitates have relatively low swelling values.

In this experiment the HP steel has no precipitate formation and a high number density of the loops, while the other steels have many precipitates and relatively low number density of the loops. Thus, there appears to be a relationship between the precipitate development and cavity growth. The cause of cavity growth suppression in steels which form the precipitates is thought to be due to two effects. One is the decrease of vacancy oversaturation concentration due to dislocations with shorter total line lengths [21, 22] as given in Table 5. Another is the increase of recombination for vacancy and interstitial atoms at the precipitates, which are in high density. Therefore, the vacancy concentration in the other steels under irradiation may be lower than that of the HP steels, leading to a high swelling value.

The K steel has a relatively large swelling, but the line length of the loops of K steel is nearly the same as those of the other steels which form the precipitates as given in Tables 5 and 6. The K steel has not only Frank loops but also perfect loops, which have a strong bias factor [21, 22], compared with that of the Frank loops. Therefore, the larger swelling of the K steel may be due to a strong bias factor of the perfect loops.

Finally, the comparison of the reference data [23, 24] for the non-spectrally tailored experiments (non-ST experiments) of the HFIR irradiation and the present data of the spectrally tailored one for the same steels is listed in Table 7. The number densities of dislocation loops of the non-ST ones are higher than those of the present work, and the total

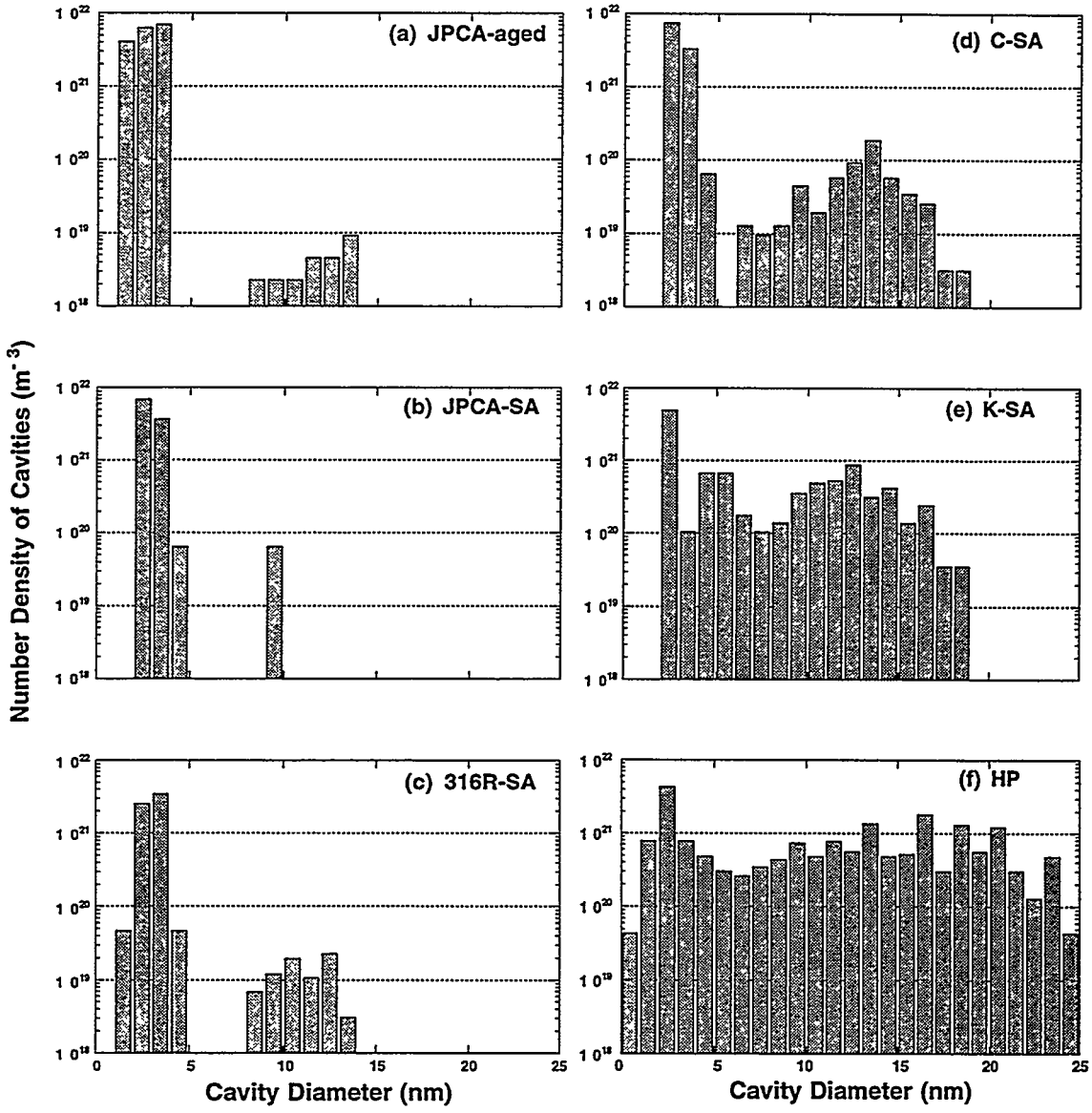

Figure 5 Size distribution of cavities in (a) JPCA-aged, (b) JPCA-SA, (c) 316R-SA, (d) C-SA, (e) K-SA, and (f) HP after irradiation at 400 °C to 17.3 dpa.

Table. 7. Comparison of the reference data of the non-spectrally tailored experiments (non-ST) of the HFIR irradiation [21, 22] and this spectrally tailored one (ST) for the same steels

	Irradiations			Cavities			Loops			Precipitates	
	Temp. (°C)	Damage (dpa)	He (atppm)	Mean size (nm)	Number density (m^{-3})	Swelling (%)	Mean size (nm)	Number density (m^{-3})	Total line length (m/m^3)	Mean size (nm)	Number density (m^{-3})
Reference data (non-ST)											
JPCA-SA	400	10.2	530	1.8	2.9×10^{23}	0.08	12.0	2.0×10^{22}	7.5×10^{14}	0	0
JPCA-SA	400	33.6	2470	2.6	2.9×10^{23}	0.25	12.3	2.4×10^{22}	9.3×10^{14}	3.1	1.9×10^{22}
316R-SA	400	33.4	2140	2.3	3.4×10^{22}	0.22	16.0	2.5×10^{22}	1.3×10^{15}	-	-
Present data (ST)											
JPCA-SA	400	17.3	280	1.5	1.1×10^{22}	0.016	18.7	7.0×10^{21}	4.1×10^{14}	3.4	7.7×10^{21}
316R-SA	400	17.3	200	1.8	6.2×10^{21}	0.015	20.2	9.5×10^{21}	6.0×10^{14}	15.1	5.2×10^{20}

line length of the loops is longer. In the non ST experiments, the helium generation, the mean size, number density, and the swelling of the cavities are higher than those of the present work.

FUTURE WORK

Comparisons of these data with those from the first stage of the experiment (7.4 dpa in the ORR) as well as the microstructural analyses of cold worked specimens in the HFIR-400J-1 capsule are still in progress. Void swelling measurement by immersion densitometry will be also performed for the same specimens.

ACKNOWLEDGMENTS

The authors are grateful to Messrs. A. T. Fisher, J. W. Jones, J. J. Duff, and members of hot laboratory of ORNL for the technical support.

REFERENCES

1. G. L. Kulcinski, J. Nucl. Mater., **122&123**(1984)457.
2. M. L. Grossbeck et al., in: Proc. Conf. on Fast, Thermal, and Fusion Reactor Experiments, Salt Lake. City, Utah, April 1985, Vol. 1, pp. 199-210.
3. A. F. Rowcliffe, A. Hishinuma, M. L. Grossbeck, and S. Jitsukawa, J. Nucl. Mater., **179-181** (1991)125.
4. R. E. Stoller, P. J. Maziasz, A. F. Rowcliffe, and M. P. Tanaka, J. Nucl. Mater., **155-157** (1988)1328.
5. T. Sawai, P. J. Maziasz, H. Kanazawa, and A. Hishinuma, J. Nucl. Mater., **191-194** (1992) 712.
6. A. A. Bauer and M. Kangilaski, J. Nucl. Mater., **42**(1972)91.
7. J. P. Robertson, I. Ioka, A. F. Rowcliffe, M. L. Grossbeck, and S. Jitsukawa, Effects of Radiation on Materials: 1 8th International Symposium, ASTM STP 1325, R. K. Nastad, et. al., Eds., American Society for Testing and Materials, Philadelphia, 1997.
8. I. I. Siman-Tov, Fusion Reactor Materials Semiannual Progress Report for Period Ending September 30, 1987, Office of Fusion Energy, DOE/ER-0313/3, 1988, p. 7.
9. L. R. Greenwood, Fusion Reactor Materials Semiannual Progress Report for Period Ending March 31, 1989, Office of Fusion Energy, DOE/ER-0313/6, 1989, p. 23.

10. L. R. Greenwood and D. V. Steidl, Fusion Reactor Materials Semiannual Progress Report for Period Ending March 31, 1990, Office of Fusion Energy, DOE/ER-0313/8, 1990, p. 34.
11. L. R. Greenwood, Alloy Development for Irradiation Performance Semiannual Progress Report for Period Ending March 31, 1989, Office of Fusion Energy, DOE/ER-0045/16,1986, p. 17.
12. T. Sawai, P. J. Maziasz, H. Kanazawa and A. Hishinuma, Fusion Reactor Materials Semiannual Progress Report for Period Ending September 30, 1990, Office of Fusion Energy, DOE/ER-0313/9, 1990, p. 152.
13. L. R. Greenwood, C. A. Baldwin and B. M. Oliver, Fusion Reactor Materials Semiannual Progress Report for Period Ending September 30, 1994, Office of Fusion Energy, DOE/ER-0313/17, 1995, p. 28.
14. A. W. Longest, J. E. Pawel, D. W. Heatherly, R. G. Sitterson, and R. L. Wallace, Fusion Reactor Materials Semiannual Progress Report for Period Ending March 31, 1993, Office of Fusion Energy, DOE/ER-0313/14, 1993, p. 14.
15. A. W. Longest, D. W. Heatherly, E. D. Clemmer, and J. E. Corum, Fusion Reactor Materials Semiannual Progress Report for Period Ending March 31, 1993, Office of Fusion Energy, DOE/ER-0313/14, 1993, p. 14.
16. T. Sawai, M. Suzuki, P. J. Maziasz, and A. Hishinuma, J. Nucl. Mater., **187**(1992)146.
17. T. Sawai, and M. Suzuki, Scripta Metall., **24**(1990)2047.
18. E. H. Lee, P. J. Maziasz, and A. F. Rowcliffe, in: Phase Stability During Irradiation, Eds. J. R. Holland, L. K. Mansur, and D. I. Potter (TMS-AIME, Warrendale, PA, 1981)pp. 191-218.
19. K. W. Andrews, D. J. Dyson, and S. R. Keown, in: Interpretation of Electron Diffraction Patterns (Plenum Press, New York), p172.
20. E. Wakai, A. Hishinuma, Y. Kato, S. Takaki, and K. Abiko, Proc. Ultra High Purity Base Metals, Ed. K. Abiko, K. Hirakawa, and S. Takaki, The Japan Institute of Metals, Sendai (Japan) 1994 p. 522.
21. W. G. Wolfer and M. Ashkin, J. Applied Phys., **47**(1976)791.
22. W. G. Wolfer, L. K. Mansur, and J. A. Sprague, Proc. Intern. Conf. on Radiation Effects in Breeder Reactor Structural Materials. Scottsdale, Az (1977) eds. M. L. Bleiberg and J. W. Bennett, p. 841.
23. M. P. Tanaka, P. J. Maziasz, A. Hishinuma, and S. Hamada, J. Nucl. Mater., **141-143** (1986) 943.
24. S. Hamada, P. J. Maziasz, M. P. Tanaka, M. Suzuki, and A. Hishinuma, J. Nucl. Mater., **155- 157** (1988) 838.

THE DEVELOPMENT OF A TENSILE-SHEAR PUNCH CORRELATION FOR YIELD PROPERTIES OF MODEL AUSTENITIC ALLOYS – G.L.Hankin, (I.P.T.M.E, Loughborough University, UK), M.L.Hamilton, F.A.Garner (Pacific National Northwest Laboratory)* and R.G.Faulkner (I.P.T.M.E, Loughborough University, UK)

OBJECTIVE

To refine an existing tensile-shear punch correlation using a large data base from three neutron-irradiated model austenitic alloys and to provide fundamental support for the empirical correlation.

SUMMARY

The effective shear yield and maximum strengths of a set of neutron-irradiated, isotopically tailored austenitic alloys were evaluated using the shear punch test. The dependence on composition and neutron dose showed the same trends as were observed in the corresponding miniature tensile specimen study conducted earlier [1]. A single tensile-shear punch correlation was developed for the three alloys in which the maximum shear stress or Tresca criterion was successfully applied to predict the slope. The correlation will predict the tensile yield strength of the three different austenitic alloys tested to within ±53 MPa. The accuracy of the correlation improves with increasing material strength, to within ±43 MPa for predicting tensile yield strengths in the range of 400 - 800 MPa.

PROGRESS AND STATUS

Introduction

A number of experiments have been done recently [2-5] to facilitate development of a tensile-shear punch correlation, i.e., a relationship between uniaxial tensile strength and effective shear strength that would allow the use of shear punch data to predict tensile data. In order to validate the proposed tensile-shear punch correlation it is desirable to test a variety of materials exhibiting a wide range of microstructures and mechanical properties. The ^{59}Ni isotopic tailoring experiment [6], originally designed to elucidate the effect of fusion-relevant amounts of helium on austenitic structures, produced such a specimen matrix. The experiment used an isotopic tailoring approach to evaluate the effect of helium generation rates typical of a fusion reactor environment on the tensile properties of three neutron-irradiated model austenitic alloys (Fe-25Ni-15Cr, Fe-25Ni-15Cr-0.04P and Fe-45Ni-15Cr). Helium generation rates relevant to a fusion reactor were produced by an (n,α) reaction involving the decay of ^{59}Ni, an isotope which is not found in natural nickel. Nickel enriched in the ^{59}Ni isotope was extracted from Inconel 600 fracture toughness specimens, which were originally irradiated in the Engineering Test Reactor (ETR). The enriched nickel contained 2% of the ^{59}Ni isotope. The helium to dpa (displacements per atom) ratios obtained were of the order of 0.5 appm He/dpa for the undoped alloys and up to 20 appm He/dpa for the ^{59}Ni-doped alloys.

Transmission electron microscope (TEM) disks of the three Fe-Ni-Cr alloys were irradiated side-by-side with the miniature tensile specimens as part of the ^{59}Ni experiment in the Fast Flux Test Facility's Materials Open Test Assembly (FFTF-MOTA). Each alloy was

---

* Pacific Northwest National Laboratory is operated for the U. S. Department of Energy by Battelle Memorial Institute under Contract DE-AC06-76RLO 1830.

irradiated both with and without ^{59}Ni content, and were prepared in both the cold worked (CW) and solution annealed (SA) conditions. The twelve alloy combinations were irradiated at three different temperatures and were available from up to four discharges of the FFTF-MOTA. The TEM discs were originally intended for TEM examination only but many of them were never used since 3 to 6 specimens were available at each set of irradiation conditions. The remaining TEM discs were therefore available to generate effective shear strength data, which when coupled with the original tensile data, resulted in a large database for further refining the existing tensile-shear punch correlation.

Experimental Procedure

The shear punch test is essentially a blanking operation in which a 1 mm diameter punch is driven at a constant rate of 0.127 mm/min. (0.005 in./min.) through a TEM-sized disk (nominally 0.25 mm thick and 2.8 mm in diameter). The disk is constrained along both its upper and lower surfaces in a test fixture, which also guides the punch. The load on the punch is measured as a function of specimen displacement, which is taken to be equivalent to the crosshead displacement [3]. The yield and maximum loads are taken from a plot of punch load versus punch displacement. Effective shear yield strength (τ_{sy}) and maximum shear strength (τ_{sm}) are evaluated from these values, respectively, by the following equation [4]:

$$\tau_{sy,sm} = \frac{P}{(2\pi rt)} \tag{1}$$

where P is the appropriate load, r is the average of the bore and punch radii, and t is the specimen thickness. An earlier report [7] provides more details of the shear punch test and the facility in which the irradiated materials were tested.

Previous work has shown that shear yield and maximum strengths obtained by shear punch test methods can be correlated to tensile yield and ultimate properties. When corresponding sets of τ and σ are plotted they fall along a straight line. A linear regression is performed to obtain the constants *m* and *K* in:

$$\sigma = m\tau + K \tag{2}$$

The y-axis intercept, *K*, was originally ascribed to punch-die-specimen friction [8] and the regression slope previously appeared to be somewhat material-dependent [4]. For the purpose of this study, equation (3) will be used, in which $\tau_0 = -K/m$ from equation (2).

$$\sigma = m(\tau_{meas} - \tau_0) \tag{3}$$

The offset parameter τ_0 (the x-axis intercept of the regression line) is used to indicate that the offset is some frictional characteristic which is associated with the shear punch test and not the tensile test.

Two TEM specimens were available for each irradiated condition and five specimens for each unirradiated starting state. The shear punch data were first evaluated for consistency with the corresponding tensile data [1]. The tensile shear-punch database was then used to refine the existing correlation coefficients.

Results

From the results of shear punch tests on the unirradiated material it was established that the effective shear yield and maximum strengths of duplicate specimens typically exhibited a scatter of ±15 MPa. Figure 1 shows the variation of effective shear yield strengths of each of the alloys with increasing dpa for specimens irradiated at 365 and 490°C. As expected, the results of the shear punch test were in good agreement with those from the original miniature tensile specimen study [1]. It can be seen that helium/dpa ratios typical of a fusion reactor environment (~15-20 appm He/dpa) have no significant effect on the yield properties of the materials when compared to the scatter in the data from their respective

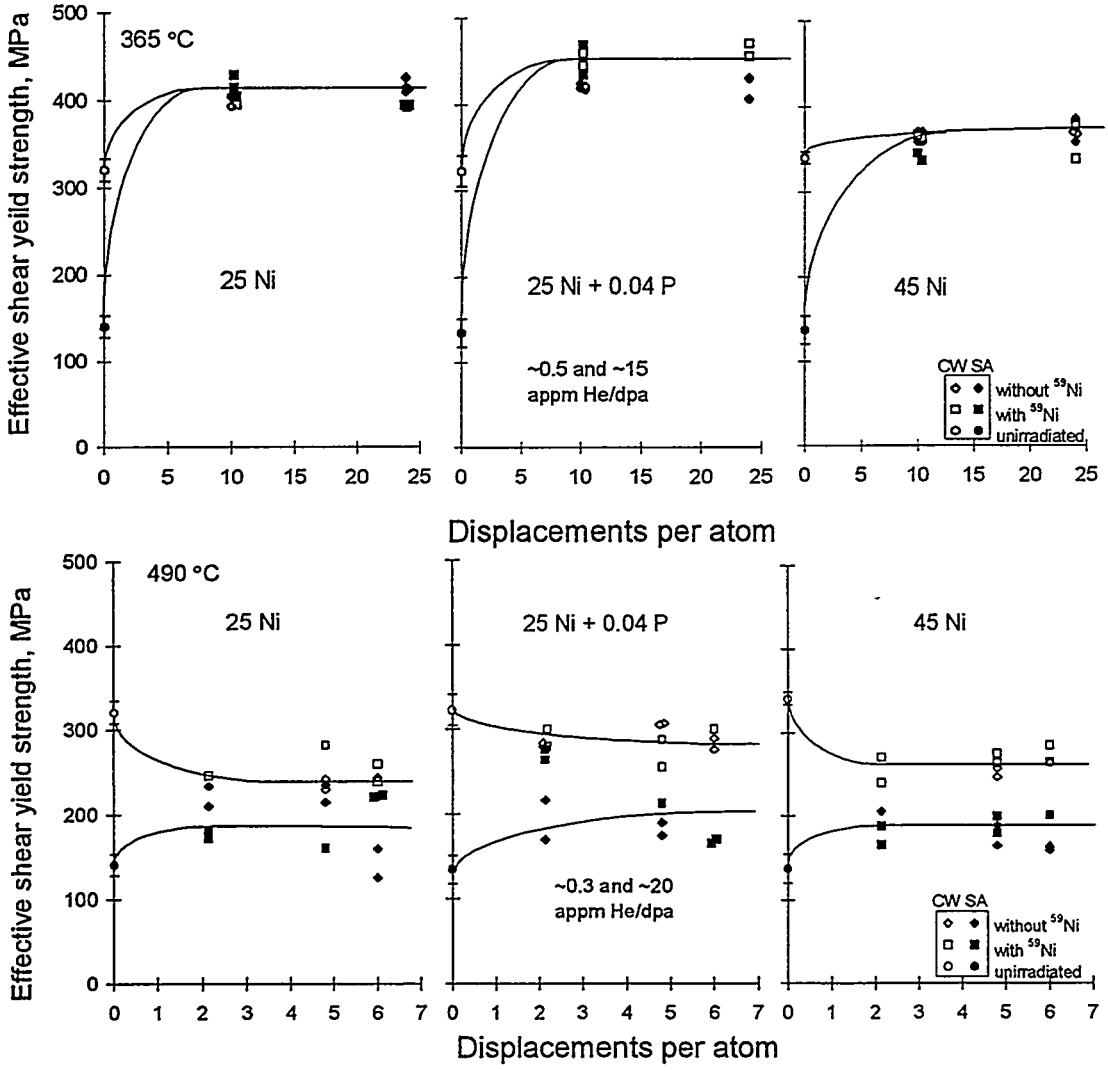

Figure 1. The influence of thermomechanical starting state and different He/dpa ratios on the effective shear yield strength of three austenitic alloys irradiated below core at 365°C and above core at 490°C. The average helium generation rates for undoped and doped specimens are shown on each figure.

controls. The value of τ_{sy} of each of the irradiated materials approaches a saturation level that is dependent on the irradiation temperature, but independent of the thermomechanical starting state. Convergence in material strength with increasing dpa is very clear for the material irradiated at 365°C (Fig.1), but has not been completed at 490°C due to the low dpa levels achieved.

The tensile-shear punch relationship was first produced for the yield properties of the three materials individually. A linear regression on each data set yielded slopes that were ~2 (Table 1). On the basis of the maximum shear stress or Tresca yield criterion, the slope was fixed at 2 (Fig. 2). Each correlation was then adjusted by the appropriate offset parameter, τ_0, and all three were combined to form a single correlation (Fig. 3). A practical measure of the accuracy of the final correlation was calculated as the standard deviation of σ_y (±53 MPa). Thus in practice, it would be expected that shear punch yield data would be used to predict tensile yield strength to within 53 MPa, or to within 43 MPa for σ_y between 400 and 800 MPa (Fig. 4).

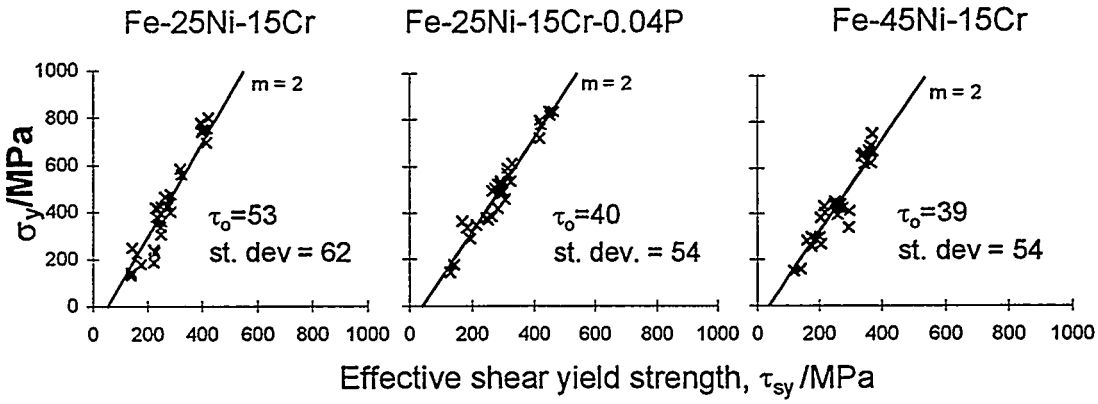

Figure 2. Tensile-shear punch correlation for three austenitic alloys with regression slopes defined as 2 by the Tresca criterion.

Discussion

It was noted that when the regression was applied to the three austenitics individually, the slopes were all ~2 (Table 1). Earlier work summarised by Hamilton [4] shows the value of the slope to be somewhat variable for individual material systems using smaller data sets. For example stainless steels appear to have a slope of ~1.7 and values of 2.8 and 2.6 were seen for vanadium and aluminium respectively. When the austenitic material data sets were adjusted for τ_0 and combined, the slope of the final regression was almost exactly equal to 2. The wide range of material strength data available in the current study was considered to increase the confidence in the accuracy of the correlation and so the question arose whether there was some fundamental reason for the regression slopes to tend to this value. The ratio of shear to uniaxial stress in the maximum shear stress or Tresca yield criterion is 2, i.e.,

$$\sigma_y = 2\tau_{max} \tag{4}$$

This result would only be expected if a state of pure shear can be assumed in the process zone of the specimen during a shear punch test. This is not necessarily the case since there is a small clearance (~0.02 mm) between the punch and die, which would lead to other stress components being present in the TEM specimen under test.

Table 1. Regression constants for tensile-shear punch correlation of three austenitic alloys.

Material	Linear regression of yield data		Tresca criterion applied to yield data (slope of 2)	
	m (slope)	τ_0	*m* (slope)	τ_0
Fe-25Ni-15Cr	2.3	84	2.0	53
Fe-25Ni-15Cr-0.04P	2.0	38	2.0	40
Fe-45Ni-15Cr	2.1	49	2.0	39

Kullen [9], however, previously applied the Tresca yield criterion with some success to predict the tensile yield strengths of a number of materials after conducting a series of 3 mm punch tests to produce TEM discs. Lucas [2] noted that the regression coefficient in a tensile-shear punch correlation for yield data from a variety of materials when combined was close to $\sqrt{3}$ = 1.73. This is the ratio of shear to uniaxial stress in the von Mises yield criterion. Attempts at fitting the current data to the von Mises criterion were unsuccessful. The individual material regressions were calculated for a slope of 2 (Fig. 2) to investigate the suitability of applying the Tresca criterion. The resulting values of τ_0 are displayed along side those for the individual data sets in Table 1. It can be seen that the values of τ_0 appear to be converging, which indicates that a single value may be assigned to this alloy class. The three correlation were adjusted by their respective values of τ_0 and combined to form a single correlation (Fig. 3).

The effectiveness of the correlation is measured by the standard deviation of the measured tensile data from the value that the correlation predicts from the shear punch yield strength. It can be seen from Figure 3 that the majority of the data lie within ± 53 MPa (a 68% confidence limit). It is likely that if multiple shear punch tests could be carried out for a particular material

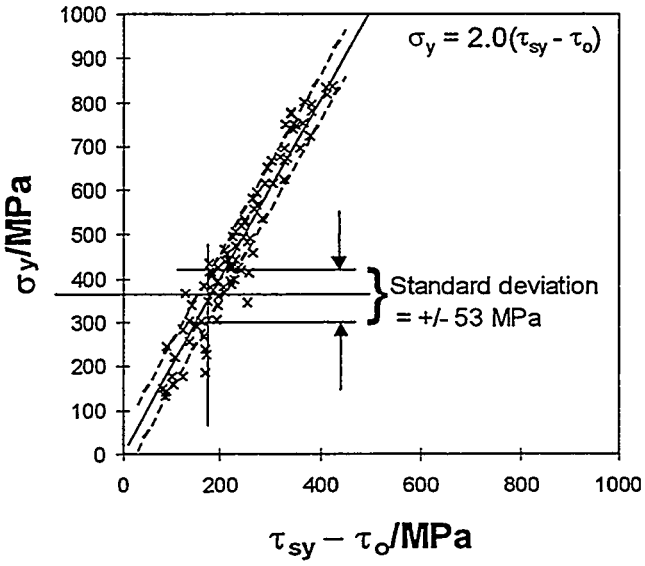

Figure 3. Single correlation developed from all three austenitic alloys.

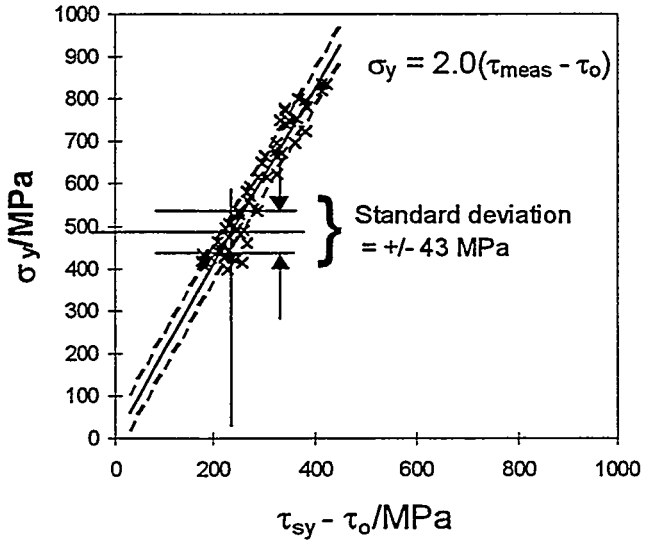

Figure 4. Single correlation for all three austenitic alloys for $\sigma_y > 400$ MPa.

condition, the standard deviation observed in the correlation would be reduced since the average of data from only two shear punch tests and one or two miniature tensile test were used for each correlation point. The difficulty of defining a common practice for determining the yield point for a shear punch test also contributes to the prediction accuracy. The 2% strain offset used to determine the tensile yield strength cannot be applied to the shear punch test. It is therefore difficult, especially for softer materials, to extract effective shear yield strength data. This is evident in Figure 3 where the scatter is clearly greatest for the data from the lower strength materials. It was for this reason that Figure 4 was constructed for only those materials having a measured tensile yield strength greater than 400 MPa, where the standard deviation was reduced to ± 43 MPa.

CONCLUSIONS

The shear punch test will reliably replicate the trends obtained in tensile test data. This is an important result since tensile specimens are not always available. A reliable correlation has been developed which can be used to predict yield properties over a wide range of material strengths to an acceptable level of accuracy. Applying the Tresca criterion would appear to be valid, but further qualification of this theory is required. The Tresca criterion is superior to von Mises' for this data set. The offset parameter requires further investigation before definitive conclusions can be drawn as to its origin and nature.

FUTURE WORK

Similar analysis will be applied to the shear maximum strength data from this study. Additional testing on both TEM and miniature tensile specimens will be performed on a set of 316 austenitic stainless steel variations irradiated over a wide range of conditions in FFTF-MOTA and the validity of the correlation will be further assessed with these data.

REFERENCES

1. Garner, F.A., Hamilton, M.L. Greenwood, L.R., Stubbins, J.F. and Oliver, B.M., "Isotopic Tailoring with ^{59}Ni to Study Helium Generation Rates and Their Effect on Tensile Properties of Neutron-Irradiated Fe-Cr-Ni Alloys," Effects of Radiation on Materials: Sixteenth International Symposium, ASTM STP 1175, Arvind S. Kumar, David S. Gelles, Randy K. Nanstad, Edward S. Little, Eds., American Society for Testing and Materials, Philadelphia, 1993.
2. Lucas, G.E., Sheckherd, J.W., Odette, G.R. and Panchandeeswaran, S, "Shear Punch Tests for Mechanical Property Measurements in TEM Disc-Sized Specimen," p. 429 in J. of Nucl. Matl., (122-123), 1984.
3. Lucas, G.E., Odette, G.R. and Sheckherd, J.W., "Shear Punch and Microhardness Tests for Strength and Ductility Measurements," p. 112 in The Use of Small Scale Specimens for Testing Irradiated Material, ASTM STP 888, Philadelphia, 1986.
4. Hamilton, M.L., Toloczko, M.B., Lucas, G.E., "Recent Progress in Shear Punch Testing," p. 46 in Miniaturized Specimens for Testing of Irradiated Materials, Hans Ullmaier and Peter Jung, Eds., Forschungszentrum Jülich GmbH, January, 1995.
5. Hamilton, M.L., Toloczko, M.B., Edwards, D.J., Sommer, W.F., Borden, M.J., Dunlap, J.A., Stubbins, J.F., Lucas, G.E., "Correlation Between Shear Punch and Tensile Data for Neutron Irradiated Aluminium Alloys," Effects of Radiation on Materials: Seventeenth International Symposium, ASTM STP 1270, David S. Gelles, Randy K. Nanstad, Arvind S. Kumar and Edward S. Little, Eds., American Society for Testing and Materials, Philadelphia, 1996, in press.

6. Simons, R.L., Brager, H.R. and Matsumoto, W.Y., "Design of a Single Variable Helium Effects Experiment for Irradiation in FFTF Using Alloys Enriched in Nickel-59," p. 1057-1060 in J. of Nucl. Matl., (141-143), 1986.
7. Hankin, G.L., Hamilton, M.L., Gelles, D.S. and Toloczko, M.B., "The effect of fusion-relevant helium levels on the mechanical properties of isotopically tailored ferritic alloys," p.156 in Fusion Reactor Materials Semiannual Progress Report for the period ending 31 December 1996, DOE/ER-0313/21.
8. Lucas, G.E., "The development of small specimen mechanical test techniques," p. 327 in J. of Nucl. Matl., (117), 1983.
9. Kullen, P.S., Smith, H.H. and Michel, D.J., "The Shear Punch Measurement of the Mechanical Properties of Selected Unirradiated and Irradiated Alloys," p. 57 in J. of Nucl. Matl., (158), 1988.

6.0 INSULATING CERAMICS AND OPTICAL MATERIALS

SUMMARY OF THE 9TH IEA WORKSHOP ON RADIATION EFFECTS IN CERAMIC INSULATORS — S. J. Zinkle (Oak Ridge National Laboratory), E. R. Hodgson (CIEMAT), and T. Shikama (Tohoku Univiversity)

OBJECTIVE

The objective of this report is to summarize the discussions held at the IEA workshop on Radiation Effects in Ceramic Insulators.

SUMMARY

Twenty one scientists attended an IEA workshop in Cincinnati, Ohio on May 8-9, 1997, which was mainly devoted to reviewing the current knowledge base on the phenonenon of radiation induced electrical degradation in ceramic insulators. Whereas convincing evidence for bulk RIED behavior has been observed by two research groups in sapphire after electron irradiation, definitive levels of bulk RIED have not been observed in high purity Al_2O_3 by several research groups during energetic ion or fission neutron irradiation. Possible reasons for the conflicting RIED results obtained by different research groups were discussed. It was concluded that RIED does not appear to be of immediate concern for near-term fusion devices such as ITER. However, continued research on the RIED phenomenon with particular emphasis on electron irradiations of single crystal alumina was recommended in order to determine the underlying physical mechanisms. This will allow a better determination of whether RIED might occur under any of the widely varying experimental conditions in a fusion energy device. Several critical issues which are recommended for future study were outlined by the workshop attendees.

PROGRESS AND STATUS

Introduction

Several IEA workshops have been held over the past few years to discuss the growing number of experimental studies on the intriguing phenomenon of radiation induced electrical degradation (RIED). The experimental evidence for RIED is primarily based on electron irradiation studies performed by Eric Hodgson and coworkers on single and polycrystal forms of Al_2O_3 [1-6]. Additional evidence for RIED has been reported by several research groups for electron-, light ion- and neutron-irradiated Al_2O_3 [7-11]. These studies suggest that the electrical conductivity of Al_2O_3 may exceed 10^{-5} S/m after doses as low as ~10^{-3} displacements per atom (dpa) if an electric field >100 V/mm is applied during irradiation in the temperature range of ~200 to 550°C. On the other hand several other research groups have failed to observe catastrophic RIED in Al_2O_3 following electron [12,13], light ion [14-16], or neutron irradiation [17-20]. Some published results for electron [3,5,21] and light ion [22] irradiation have suggested that the initiation of RIED may be influenced by the purity or quality of the insulator.

Due to the difficulties associated with performing in-situ electrical conductivity measurements on irradiated insulators, considerable attention has recently been focused on measurement methods. The essential experimental techniques for accurate in-situ measurement of the electrical conductivity of ceramic insulators were discussed in detail at an IEA workshop held in Stresa, Italy in September 1993. It was concluded that the experimental techniques used by the investigators which had observed RIED were generally appropriate, but additional recommendations for future experimental studies were formulated. A round robin RIED experiment on Wesgo AL995 alumina (the IEA reference insulator) was initiated following the Stresa workshop, and the results were reported at an IEA workshop held in Obninsk, Russia in

September 1995. No evidence for bulk RIED in this material was observed by 5 different research groups using electron, light ion, and neutron irradiation sources [23].

In the past year, several new RIED irradiation experiments have been performed which have a significant impact on the understanding of the RIED phenomenon. These experiments include a HFIR neutron irradiation experiment on 12 different grades of single- and poly-crystal alumina (450°C, ~3 dpa, 200 V/mm) and several additional electron and light ion irradiation experiments. The primary objective of the IEA workshop was to review the available RIED studies on ceramic insulators. Some discussion of recent work in other areas such as loss tangent measurements, mechanical strength, etc. occurred on the final afternoon of the workshop. The workshop was held immediately after a related symposium on "Fabrication and Properties of Ceramics for Fusion Energy and Other High Radiation Environments," which was convened on May 5-7, 1997, as part of the American Ceramic Society annual meeting in Cincinnati, Ohio. Copies of the viewgraphs presented at the IEA workshop and abstracts of the presentations were collected for distribution to the attendees as a bound booklet (ORNL/M-6068).

Workshop Presentations

The agenda for the workshop is given in Table 1, and the list of attendees is given in Table 2. In the opening talk, Eric Hodgson summarized the experimental evidence generated in his laboratory for bulk RIED in ceramic insulators. A clear increase in the volume current was measured using guard ring techniques in several specimens irradiated with electrons. Small surface currents were observed in sapphire and Vitox alumina, whereas large surface and bulk currents were measured in MgO and spinel. Optically visible features could be observed in the bulk of electrically degraded sapphire specimens, which are apparently clusters of gamma alumina precipitates according to TEM analysis. He presented results which support the importance of point defect production in the degradation process, and then outlined a theoretical model which may explain the RIED process. The model assumes that the degradation is due to the formation and clustering of oxygen vacancies via the following sequence: F (oxygen vacancy with two trapped electrons) ->F^+ (one trapped electron, enhanced mobility compared to F center) ->F_2 ->colloids (Al metal precipitate due to deficiency of oxygen). The colloids are assumed to promote gamma alumina precipitation in neighboring regions, since the gamma alumina (spinel) structure can be formed by introducing cation vacancies on octahedral sites [24].

Tatsuo Shikama summarized evidence for long-term increases in the electrical conductivity of ceramic insulators irradiated in fission reactors. The presence of an offset current which has been attributed to "radiation induced electro-motive forces" (RIEMFs) was observed in essentially all cases, although the physical mechanism responsible for this offset current remains unclear. He proposed that the premature failure (electrical shorting) observed in several of the specimens irradiated in the HFIR-TRIST-ER1 experiment may be correlated with specimen type, although there was no evidence for an increase in electrical conductivity prior to the shorting. A pronounced increase in the electrical conductivity of a 0.05%Cr-doped sapphire (ruby) specimen was observed in the HFIR experiment at low doses (~0.1 dpa). The conductivity slowly decreased with increasing dose for the remainder of the irradiation.

Chiken Kinoshita presented in-situ electrical conductivity data obtained on sapphire specimens with thicknesses of 0.27 and 0.75 mm irradiated with 1 MeV electrons in an HVEM. The temperature dependence of the bulk radiation induced conductivity was found to be dependent on the specimen electrode type (vacuum deposited Ti or Au versus sputter deposited Pt). Permanent RIED was not detected for irradiation up to ~9×10^{-5} dpa at 420°C with an applied electric field of 93 V/mm. It was proposed that previous reports of RIED may be due to the effect of electrode materials and/or the measuring system.

Table 1. Agenda for IEA Workshop on Radiation Effects in Ceramic Insulators

Wednesday afternoon (May 7):

1:00 pm Introductory Comments--Workshop organizers

1:10 pm Evidence for bulk RIED in ceramics
E.R. Hodgson (CIEMAT)
T. Shikama (Tohoku Univ.)

1:50 pm Recent RIED experiments
1:50 pm Electron irradiations
C. Kinoshita (Kyushu Univ.)
T. Terai (U. Tokyo)
Y. Chen (DOE)
E.R. Hodgson (CIEMAT)

2:50 pm Ion irradiations
W. Kesternich (KFA-Jülich)
A. Möslang (Forschungszentrum Karlsruhe)
V.M. Chernov (IPPE-Obninsk)

3:50 pm Neutron irradiations
S.J. Zinkle/HFIR-TRIST-ER1 (ORNL)
T. Shikama/JMTR (Tohoku Univ.)
K. Noda/JRR (JAERI)
V.M. Chernov (IPPE-Obninsk)
E.R. Hodgson/Mol (CIEMAT)

Thursday (May 8):

8:30 am Possible explanations for conflicting results on bulk RIED
Effects of dose rate, temperature, electric field, material, and test environment
E.R. Hodgson (CIEMAT)

Electron beam straggling and implanted charge effects
A. Möslang (Forschungszentrum Karlsruhe)
S.J. Zinkle (ORNL)

Irradiation spectrum effects on F/F^+/colloid formation
S.J. Zinkle (ORNL)

1:00 pm Overview of recent work on ceramic insulators (non-RIED)
E.R. Hodgson (CIEMAT)
R. Vila (CIEMAT)
V.M. Chernov (IPPE-Obninsk)
K. Noda (JAERI)
C. Kinoshita (Kyushu Univ.)
T. Shikama (Tohoku Univ.)
S.J. Zinkle (ORNL)

3:00 pm Discussion of critical issues, workshop statement on RIED, recommendations for future work (including proposed collaborations/ round-robin experiments)

Table 2. Attendees at IEA Fusion Ceramics Workshop.

Anton Möslang, Forschunszentrum Karlsruhe, Germany

Wilto Kesternich, Forschunszentrum Jülich, Germany

Rafael Vila, CIEMAT, Spain

Eric Hodgson, CIEMAT, Spain

Tatyana Bazilevskaya, Kharkov State University, Ukraine

Vyacheslav M. Chernov, SSC RF-IPPE, Obninsk, Russia

Chusei Namba, National Institute for Fusion Science, Japan

Akira Kohyama, Kyoto University, Japan

Tatsuo Shikama, Tohoku University, Japan

Akira Hasegawa, Tohoku University, Japan

Kenichi Shiiyama, Kyushu University, Japan

Chiken Kinoshita, Kyushu University, Japan

Toyohiko Yano, Tokyo Institute of Technology, Japan

Takayuki Terai, University of Tokyo, Japan

Kenji Noda, Japan Atomic Energy Research Institute, Japan

Lance Snead, Oak Ridge National Laboratory, USA

Steve Zinkle, Oak Ridge National Laboratory, USA

Kenneth Young, Princeton Plasma Physics Laboratory, USA

Yok Chen, U.S. Department of Energy, USA

F. W. Wiffen, Office of Fusion Energy Sciences, U.S. Department of Energy, USA

J. Y. Park, Korean Atomic Energy Research Institute, Korea

Yok Chen summarized electron irradiation RIED results on unguarded sapphire specimens reported in two recent publications [10,11]. He concluded that the mechanisms leading to RIED in Al_2O_3 appear to be similar to those for thermal dielectric breakdown. In particular, a moderately high dislocation density (~$10^{12}/m^2$) was present in both irradiated and thermally degraded oxide specimens. Precipitates were not observed in the irradiated specimens. A theoretical model based on carrier injection from the electrodes was outlined which appeared to describe the main features of the RIED process in his experimental studies. RIED was observed to be inhibited when the electric field was reversed, in contrast to an earlier study by Hodgson [3]. According to the carrier injection model, the electrical conductivity should decrease immediately after the electric field is reversed.

Eric Hodgson reported his recent work on Wesgo AL995 surface/bulk conductivity. He observed that irradiation in vacuum causes severe surface degradation, but irradiation in air or He does not. In further irradiations it was observed that collimation of the electron beam to irradiate only the central electrode drastically reduces the surface degradation (i.e. the surface degradation is radiation induced or enhanced) He noted that this observation helps to explain the conflicting results of Kesternich and Möslang. Further experiments were carried out with a collimated beam

to study the volume degradation in vacuum. Up to 500 kV/m no volume degradation was observed (> 200 h irradiation). However at 1 MV/m a clear volume degradation was observed. The process is complicated by radiation enhanced impurity segregation (electrolysis) at the negative electrode, which caused saturation in the observed RIED. However polishing off < 0.1 mm indicated severe volume degradation. At 1.5 MV/m (AC 50 Hz) a clear volume degradation was observed with no saturation.

Wilto Kesternich summarized RIED data obtained on several different grades of alumina, including Rubalit, Wesgo AL995 and Deranox (Vitox) irradiated with energetic protons or alpha particles. Bulk RIED was not observed in any of these specimens. In one case, specimen microcracking produced an increase in the current measured by the center electrode. After an initial increase in the measured current, the crack appeared to slowly heal (or else the surface conducting layer oxidized and became poorly conducting) with further increases in dose. He reiterated the importance of adhering to all of the measurement techniques approved at the Stresa IEA workshop in 1993, and added that the possibility of surface microcracking must be investigated (using SEM) in all specimens which show an apparent increase in bulk conductivity.

Anton Möslang presented the results of RIED studies on 104 MeV He^+ ion irradiated Al_2O_3 (Vitox/Deranox, Wesgo AL995) and AlN specimens. A previously reported [22] observation of pronounced RIED in a Vitox alumina specimen was attributed to specimen cracking effects in his presentation; a nominally identical grade of alumina (Deranox) produced by the same manufacturer did not exhibit any permanent electrical degradation following irradiation to similar conditions as the Vitox specimen. In addition, RIED was not observed in Wesgo AL995 alumina or AlN specimens. He concurred with Kesternich's conclusion that specimen cracking must be investigated in specimens which exhibit apparent bulk RIED.

Vyacheslav Chernov reported that neither RIC nor RIED was observed in alumina irradiated with 10 MeV protons at room temperature or with fission neutrons at ~580°C, 70 Gy/s. These irradiation conditions are outside of the temperature range where previous studies have reported RIED (~250-530°C). The lack of observable RIC in the neutron irradiated specimen may be attributable to the relatively high temperature and low ionizing dose rate. On the other hand, the absence of observable RIC in the proton-irradiated specimen is unexpected based on previous RIC studies near room temperature by other research groups. He also reported observation of dielectric breakdown and cracking within ~0.8 mm of the incident surface of a 2.7 mm thick sapphire specimen irradiated with 1 MeV electrons.

Steve Zinkle summarized the results of a recently completed DOE/Monbusho in-situ electrical conductivity experiment on several different grades of alumina that was performed at 450-500°C in the HFIR fission reactor. A total of 15 specimens (3 without dc bias) were irradiated to a maximum dose of ~3 dpa. The bulk conductivity measured during full-power irradiation (10-16 kGy/s) remained below 1×10^{-6} S/m in all of the pure alumina specimens. The only specimen which exhibited an apparent bulk conductivity higher than 1×10^{-6} S/m was a 0.05% Cr-doped sapphire specimen, which showed a rapid initial increase in conductivity to ~$2 \times 1 \times 10^{-4}$ S/m after ~0.1 dpa, followed by a gradual decrease to <1×10^{-6} S/m after 2 dpa. Nonohmic electrical behavior was observed in all of the specimens, and was attributed to preferential attraction of ionized electrons in the capsule gas to the unshielded low-side bare electrical leads emanating from the subcapsules. The electrical conductivity was determined from the slope of the specimen current vs. voltage curve at negative voltages, where the gas ionization effect was minimized. More than half of the coaxial cables shorted during the 3 month irradiation. Dielectric breakdown tests performed on nonirradiated coaxial cables indicated that the shorting was associated with breakdown in the glass used to seal the ends of the cables. Postirradiation measurements of the temperature-dependent electrical conductivity of all specimens are planned, along with examination of the shorted coaxial cables. Measurements made on two high purity sapphire specimens which were irradiated for the full 3 reactor cycles indicate that the electrical conductivity did not exceed the normal RIC value of ~1×10^{-6} S/m at any point during the irradiation.

Tatsuo Shikama reported results of a JMTR fission neutron experiment carried out under the US/Japan collaboration in conjuction with the recent HFIR experiment (performed under the same collaboration framework, and reported at the workshop by Steve Zinkle). He pointed out some interesting but mysterious phenomena obtained in fission reactor experiments. These results were first recognized in JMTR and clearly and confidently confirmed in HFIR. These results may infer problems associated with fusion reactor developments. He implied that they may have some correlation with a long term degradation of electrical insulation of ceramics. He proposed to continue international collaborations which focus on studying the fundamental nature of these phenomena in inexpensive and easily accessible reactors such as JMTR.

Kenji Noda described a recently completed in-situ electrical conductivity experiment on MgO and Al_2O_3 performed at 300 to 450°C in the JRR-3 reactor. The RIC values appeared to be in good agreement with previous studies. It was concluded that RIED did not occur to any significant degree up to the maximum damage level of 0.2 dpa. The session was concluded by Eric Hodgson with a brief description of a neutron irradiation experiment in the Mol reactor that is scheduled to begin in the summer of 1997.

On the second day of the workshop, the morning session was devoted to discussion of possible reasons for the apparent conflicting results regarding the presence of RIED in irradiated specimens. Eric Hodgson noted that most of the observations of RIED were obtained using electrons at low dose rates ($<10^{-9}$ dpa/s), whereas most of the ion and neutron irradiation experiments were performed at 3 orders of magnitude higher dose rate. Assuming that the incubation dose for RIED is proportional to the square root of dose rate (in analogy with void swelling and colloid processes), then RIED for typical ion and neutron conditions would become evident at doses ~10 to 100 times higher than that for the electron irradiations. However, the reported absence of RIED at doses above 0.01 to 0.1 dpa in several ion and neutron irradiation studies cannot be explained by dose rate effects. Hodgson also noted that several experiments which reported the absence of RIED were performed at temperatures outside the RIED temperature regime of ~250-530°C. The electric field threshold for initiation of RIED is expected to be material dependent, and it is possible that low-purity materials may have higher threshold electric fields than the ~50 kV/m threshold reported for high-purity sapphire. Similarly, impurities may increase the incubation dose for initiation of RIED. Hodgson also suggested that additional work is needed to understand the role of test environment (air vs. vacuum, etc.) on the electrical degradation process.

Anton Möslang and Steve Zinkle discussed aspects associated with electron irradiation which might promote the RIED process in electron-irradiated specimens compared to neutron-irradiated specimens. Both presentations pointed out that, due to the large range straggling for electrons, greater than 20% of the charge from a 1.8 MeV electron beam incident on a 1 mm-thick Al_2O_3 specimen would be deposited in the specimen. This implanted charge might produce high localized electric fields under certain circumstances, which could lead to internal dielectric breakdown (similar to the well-known Lichtenberg avalanche breakdown patterns in electron-implanted insulators). A further consideration for near-threshold irradiation sources such as electron beams is the nonstoichiometric defect production rate on the anion and cation sublattices, which may contribute to localized polarization effects. It was noted that the internal electric field is generally not related to the applied electric field in a simple manner; however, it was interesting to note that the macroscopic electric field due to the injected charge from the electron beam in a 1 mm-thick specimen was comparable to the threshold electric field for rapid RIED obtained in electron irradiation studies. Another effect worth considering is that the relatively high ionization/ displacement ratio for electron irradiation may enhance the F^+/F center ratio compared to neutron irradiations, which could have an impact on the microstructural evolution of irradiated specimens (particularly if colloid formation is responsible for the initiation of RIED).

Several additional details associated with RIED were brought up in the ensuing general discussion. Yok Chen expressed concern about F^+ center identification and recommended cathodoluminescence instead of radioluminescence/ photoluminescence. However Hodgson

insisted that the optical characteristics of the F, F^+ and F_2 reported were in excellent agreement with literature values and could be adequately identified by absorption and radioluminescence.

Two preliminary models were proposed to describe the RIED process, based on charge injection form the electrodes and colloid/gamma alumina precipitation, respectively. Both models appear to successfully explain some aspects of the electrical degradation observed in electron irradiated specimens, but do not explain other aspects. For example, pronounced electrical degradation would have been predicted by the charge injection model for the long-term (2 days to 3 months) ion and neutron irradiation experiments where RIED was not detected. There also appeared to be a discrepancy between the results of two research groups [3,11] on whether RIED is suppressed when the electric field is periodically reversed during electron irradiation. Further work is clearly required to address this discrepancy.

There was general agreement by the workshop participants that, with the possible exception of ion irradiation results by Pells [7] (which might be attributable to specimen cracking similar to that observed by Möslang and Kesternich), definitive levels of bulk RIED have not been observed for ion or neutron irradiations. This raises the possibility that perhaps some aspect of electron irradiation promotes RIED more vigorously than ion or neutron irradiation sources. Even for the case of electron irradiation, several studies have failed to detect RIED under conditions where pronounced electrical degradation was found by Hodgson and coworkers and Zong et al. Therefore, the workshop participants concluded that the most fruitful research area for future RIED studies would be to develop an improved understanding of the electron irradiation conditions which enhance RIED (e.g., effect of specimen thickness, reversed electric fields, etc.). Eric Hodgson agreed to distribute virgin specimens of the Union Carbide sapphire used in his electron irradiation studies to W. Kesternich and T. Terai for a round-robin electron irradiation study.

Concerning fission reactor experiments, there was a general consensus that the recent HFIR experiment gave conclusive results in a helium environment. To confirm the results, postirradiation examination of irradiated specimens, including the temperature dependence of the conductivity of irradiated specimens and examination of the mineral insulated cables, and if possible microstructure (TEM) examination, was recommended. Eric Hodgson's planned reactor experiment in Mol will be a useful complement to the HFIR experiment, since it will provide information on the effect of environment (inert gas vs. vacuum) and dose rate dependence. Tatsuo Shikama's proposal of a JMTR experiment will enlighten fundamental aspects of electrical conductivity of ceramic insulators under fission reactor iradiation (which is the closest high-intensity approximation to the fusion irradiation environment presently available).

Brief summaries of recent non-RIED work on ceramic insulators were presented by the workshop participants in the final afternoon session. Copies of the presented viewgraphs are contained in the bound volume (ORNL/M-6068) to be distributed to the workshop participants.

Workshop Summary Statement

Volumetric defects (gamma-alumina and/or dislocations) and evidence for bulk RIED-like behavior have been observed in sapphire by two research groups during electron irradiation near 450°C with applied E fields >100 V/mm [5,10,11,24]. However, 2 other research groups did not observe pronounced RIED in sapphire after electron irradiation [12,13]. Evidence for bulk RIED has been found in only one new experiment [24] since the Stresa IEA workshop in September 1993, where revised standard experimental conditions were defined. However, very few electron irradiations have been performed on sapphire since that time.

Definitive levels of bulk RIED have not been observed in high purity Al_2O_3 by several research groups during energetic ion or fission neutron irradiation. All ion and neutron irradiation experiments performed since the Stresa workshop have not observed bulk RIED. Some

previous reports of RIED in ion and neutron irradiated specimens are due to surface leakage currents or specimen cracking. Postirradiation examination of the HFIR-TRIST-ER1 specimens should be performed to determine if any low-level RIED (i.e., below ~$5x10^{-7}$ S/m at 450°C) exists in the irradiated specimens. To aid in the interpretation of the HFIR and other reactor experimental results, some radiation-induced phenomena such as RIEMF and non-ohmic behavior should be studied using smaller reactors. The planned BR-1 and BR-10 reactor experiments (with vacuum environment) will provide additional important information concerning RIED under fission reactor irradiation.

Two models have been proposed to explain the RIED phenomenon under electron irradiation, based on Al colloid/gamma alumina formation and electrode charge injection, respectively. Neither model fully explains all of the available electron irradiation data on RIED.

RIED does not appear to be of immediate concern for near-term fusion devices such as ITER. However, continued research on the RIED phenomenon with particular emphasis on electron irradiations of single crystal alumina is warranted in order to determine the underlying physical mechanisms. This will allow a better determination of whether RIED might occur under any of the widely varying experimental conditions in a fusion energy device. Future studies on RIED should continue to follow the Stresa IEA workshop recommendations regarding essential features of the experimental technique [23], including careful measurement of surface and contact resistances. In addition, detailed postirradiation microstructural examination (SEM for cracks and TEM for bulk defects) should be performed and reported on all specimens exhibiting apparent RIED. Research is particularly recommended in two areas: (1) effects of AC or periodically reversed DC electric fields on the RIED process, and (2) vacuum/gas environmental effects (strong effects have been reported for the surface conductivity, but it is uncertain whether any effect on the bulk conductivity may occur).

Although RIED does not appear to be an issue for near-term fusion devices such as ITER, numerous experiments have highlighted technological problems which need to be considered in the reactor design. These issues include enhanced surface conductivity, crack propagation, and issues associated with the best way to terminate mineral insulated cables. Additional work is needed to determine if acceptable engineering designs can be made to accommodate these problem areas.

CRITICAL ISSUES AND RECOMMENDED FUTURE WORK

- The priority for future RIED studies should be on electron irradiation experiments on UV-grade sapphire
  — air vs. vacuum
  — field reversal effects (flipped sample and ac electric field)
  (Eric Hodgson agreed to supply unirradiated Union Carbide sapphire specimens to W. Kesternich and T. Terai for electron irradiation studies)

- Attention should be given to the various experimental problems which have been identified in recent RIED studies (specimen cracking, surface conductivity, MI cable terminations, etc.)
  — any relation to bulk RIED?
  — significance of these problems for ITER and future devices?

- Concerning the increase in electrical conductivity due to RIC, the most recent results have a tendency to give lower values of RIC. This could be interpreted that the more improved techniques will give more appropriate and lower values of RIC. Considering that the accumulated values of RIC do not always satisfy the ITER magnetic coil critera for ceramic insulators, namely conductivity lower than 10^{-6} S/m at 10 kGy/s, confident evaluation of RIC values by the most accurate experimental technique is recommended.

- Standardized dpa calculations for ceramics are urgently needed
- R&D on blanket insulator coatings is needed, although recent results were not discussed in the workshop
- The value of IFMIF was recognized, but details regarding effective utilization of such an irradiation source were not discussed in the workshop

REFERENCES

[1] E.R. Hodgson, Cryst. Latt. Def. Amorph. Mater. 18 (1989) 169.
[2] E.R. Hodgson, J. Nucl. Mater. 179-181 (1991) 383.
[3] E.R. Hodgson, J. Nucl. Mater. 191-194 (1992) 552.
[4] E.R. Hodgson, in Int. Conf. on Defects in Insulating Materials vol. 2, eds. O. Kanert and J.-M. Spaeth (World Scientific, 1993) p. 332.
[5] E.R. Hodgson, J. Nucl. Mater. 212-215 (1994) 1123.
[6] A. Moroño and E.R. Hodgson, J. Nucl. Mater. 212-215 (1994) 1119.
[7] G.P. Pells, J. Nucl. Mater. 184 (1991) 177.
[8] T. Shikama et al., J. Nucl. Mater. 191-194 (1992) 575.
[9] T. Shikama, M. Narui, H. Kayano and T. Sagawa, J. Nucl. Mater. 212-215 (1994) 1133.
[10] X.-F. Zong et al., Phys. Rev. B 49 (1994) 15514.
[11] X.-F. Zong et al., Phys. Rev. B 54 (1996) 139.
[12] T. Terai, T. Kobayashi and S. Tanaka, Nucl. Instr. Meth. B 116 (1996) 294.
[13] K. Shiiyama, T. Izu, C. Kinoshita and M. Kutsuwada, J. Nucl. Mater. 233-237 (1996) 1332.
[14] W. Kesternich, F. Scheuermann and S.J. Zinkle, J. Nucl. Mater. 219 (1995) 190.
[15] C. Patuwathavithane, W.Y. Wu and R.H. Zee, J. Nucl. Mater. 225 (1995) 328.
[16] P. Jung, Z. Zhu and H. Klein, J. Nucl. Mater. 206 (1993) 72.
[17] L.L. Snead, D.P. White and S.J. Zinkle, J. Nucl. Mater. 226 (1995) 58.
[18] L.L. Snead, D.P. White, W.S. Eatherly and S.J. Zinkle, in Fusion Materials Semiannual Progress Report for Period ending December 31, 1995, DOE/ER-0313/19 (Oak Ridge National Lab, 1995) p. 249.
[19] E.H. Farnum and F.W. Clinard, Jr., J. Nucl. Mater. 219 (1995) 161.
[20] E.H. Farnum et al., J. Nucl. Mater. 228 (1996) 117.
[21] A. Moroño and E.R. Hodgson, J. Nucl. Mater. 233-237 (1996) 1299.
[22] A. Möslang, E. Daum and R. Lindau, in Proc. 18th Symp. on Fusion Technology, eds. K. Herschbach, W. Naurer and J.E. Vetter (North-Holland, Amsterdam, 1994) p. 1313.
[23] S.J. Zinkle, in Fusion Materials Semiannual Progress Report for Period ending December 31, 1995, DOE/ER-0313/19 (Oak Ridge National Lab, 1995) p. 258.
[24] G.P. Pells and E.R. Hodgson, J. Nucl. Mater. 226 (1995) 286.

ANALYSIS OF IN-SITU ELECTRICAL CONDUCTIVITY DATA FROM THE HFIR TRIST-ER1 EXPERIMENT — S. J. Zinkle, W. S. Eatherly, L. L. Snead (Oak Ridge National Laboratory), T. Shikama (Tohoku University), and K. Shiiyama (Kyushu University)

OBJECTIVE

The objective of this work is to determine the existence or absence of bulk radiation induced electrical degradation (RIED) in neutron-irradiated Al_2O_3.

SUMMARY

The current vs. applied voltage data generated from the HFIR TRIST-ER1 experiment have been analyzed to determine the electrical conductivity of the 15 aluminum oxide specimens and the MgO-insulated electrical cables as a function of irradiation dose. With the exception of the 0.05%Cr-doped sapphire (ruby) specimen, the electrical conductivity of the alumina specimens remained at the expected radiation induced conductivity (RIC) level of $<10^{-6}$ S/m during full-power reactor irradiation (10-16 kGy/s) at 450-500°C up to a maximum dose of ~3 dpa. The ruby specimen showed a rapid initial increase in conductivity to $\sim 2 \times 10^{-4}$ S/m after ~0.1 dpa, followed by a gradual decrease to $<1 \times 10^{-6}$ S/m after 2 dpa. Nonohmic electrical behavior was observed in all of the specimens, and was attributed to preferential attraction of ionized electrons in the capsule gas to the unshielded low-side bare electrical leads emanating from the subcapsules. The electrical conductivity was determined from the slope of the specimen current vs. voltage curve at negative voltages, where the gas ionization effect was minimized. Dielectric breakdown tests performed on unirradiated mineral-insulated coaxial cables identical to those used in the HFIR TRIST-ER1 experiment indicate that the electrical shorting which occurred in many of the high voltage coaxial cables during the 3-month irradiation is attributable to thermal dielectric breakdown in the glass seals at the end of the cables, as opposed to a radiation-induced electrical degradation (RIED) effect.

PROGRESS AND STATUS

Introduction

As reported in a preceding semiannual progress report [1] a collaborative DOE/Monbusho irradiation experiment has been completed which measured the in-situ electrical resistivity of 12 different grades of aluminum oxide during HFIR neutron irradiation at 450-500°C. The main objective of the Temperature Regulated In-Situ Test - Electrical Resistivity (TRIST-ER1) experiment was to determine if radiation induced electrical degradation (RIED) occurred in several different grades of aluminum oxide during irradiation in a fusion-relevant irradiation environment up to relatively high doses. According to previous studies performed primarily with 1.8 MeV electrons, RIED is expected to be most pronounced at temperatures between 300 and 600°C and at applied voltages >100 V/mm, with an apparent maximum degradation rate occurring near 450°C [2,3]. The HFIR TRIST-ER1 experiment was performed at an irradiation temperature of 450-500°C with a dc electric field of 200 V/mm.

The preliminary analysis of the electrical data reported previously [1] did not show any evidence for bulk RIED in the high-purity alumina specimens above the expected RIC level of $\sim 1 \times 10^{-6}$ S/m during full-power irradiation up to a maximum dose of 3 dpa. However, there were several issues which were not satisfactorily addressed in this preliminary analysis: (1) only a limited analysis of the electrical conductivity of the specimens at selected times was performed for the previous report, (2) the cause of the eventual failure of 10 of the 15 coaxial cables during the 3-1/2 month irradiation was uncertain (it was speculated in the preceding report to be due to dielectric breakdown in the glass seals at the cable termination), and (3) the physical mechanism(s) responsible for the observed nonohmic electrical behavior were uncertain. Recent progress toward resolution of these issues is summarized in this report.

Experimental Procedure

The experiments were performed in the Temperature-Regulated In-Situ Test (TRIST) facility located in a Removable Beryllium position of the High Flux Isotope Reactor (HFIR) at Oak Ridge National Laboratory (ORNL). A total of 15 specimens were irradiated in the in-situ electrical conductivity capsule. The specimen matrix included 12 different grades of polycrystal and single crystal alumina (Table 1) in order to confirm published studies which suggested that the threshold dose for initiation of RIED depends on specimen purity [3,4]. The TRIST-ER1 experiment was performed following the guidelines outlined in ASTM Standard Test Method for DC Resistance or Conductance of Insulating Materials (ASTM D257-91), and in accordance with the stringent experimental technique conditions adopted by the participants to an IEA ceramic insulator workshop held in Stresa, Italy in September 1993 [5]. In particular, the electrical contacts were brazed onto the specimen surface so that contact resistances were negligible, and the leakage resistances between the back (high voltage) and low voltage guard and center electrodes was measured periodically throughout the irradiation. The specimen temperatures were monitored continuously by two thermocouples located in each subcapsule. The sample temperatures were controlled by adjusting the composition of a flowing mixture of helium and neon in the control gas gap between the subcapsules and the holder sleeve [1,6]. The measured irradiation temperatures for the 15 subcapsules ranged from ~440 to 500°C, depending on the subcapsule position. Details of the irradiation temperature history are described elsewhere [6]. All of the subcapsules were sealed to minimize the amount of surface contamination buildup during irradiation.

The specimen matrix included 7 high-purity single crystal alumina specimens produced by two different manufacturers with different crystallographic orientations (Table 2). Seven polycrystalline alumina specimens with impurity contents ranging from 0.1 to 3% were included in the capsule, along with a 0.05% Cr-doped single crystal alumina (ruby) specimen. Two of the single crystal specimens and one of the polycrystal specimens (subcapsules 11, 12 and 15) were irradiated without dc bias and served as control specimens for the RIED experiment. The alumina specimens were irradiated as disks with dimensions of 8.5 mm diameter by 0.75 mm thick. A 1.1 mm OD triaxial MgO powder-insulated cable with a copper center wire and a braided copper sheath was used as the low-side data lead from each subcapsule. A 1.6 mm OD coaxial MgO powder-insulated cable with a copper center conductor was used as the power lead. The leads for the coax and triax cables were torch-brazed and spot welded to the appropriate Ni wires from each subcapsule. The mineral insulated (MI) cables were connected to polymer-insulated coax and triax cables near the top of the HFIR pressure vessel. The series line resistances of the coaxial and triaxial cables were all ~3-5 Ω. Further experimental details are given elsewhere [1].

Data acquisition and control was performed using a National Instruments Labview III program running on a Macintosh computer. A Keithley 7002 matrix switch system (containing Keithley 7169A switch cards on the high side and 7058 switch cards on the low side) was used to switch the specimen leads to the appropriate electrical instruments. A dc potential of 150 V was continuously supplied to the brazed base surface of 12 of the specimens (except for brief periods when electrical measurements were taken) by two HP 6035A power supplies, producing an electric field of 200 V/mm in the specimens. As described elsewhere [1], several different types of electrical measurements were performed on the specimens in order to differentiate between bulk conductivities and surface conductances. These tests included frequent measurement of the specimen and guard ring currents at 100 V and periodic measurement of the ohmic nature of the electrical currents in the alumina samples and coaxial MI cables over a typical potential range of +100 V to -100V. Diagnostic measurements were also performed periodically which allowed the surface resistance and cable insulation conductivities to be measured. For each electrical measurement, a settling time of 10 to 30 seconds was typically used from the time the specimen was switched to the power supply until an electrical current was measured in order to eliminate signal noise associated with the cable and specimen capacitance. During the reactor startup and shutdown, a settling time of 5 to 10 seconds was typically used in order to obtain data more rapidly.

The irradiation was accomplished over a time period of about three and one half months, and involved three irradiation cycles (cycles 344-346, each ~26 days long) of the HFIR reactor operating at 85 MW. The electrical conductivity of the specimens was measured before, during and following each of the three HFIR irradiation cycles. The specimen temperatures ranged from 30 to 50°C when the reactor was off, and between 50 and 170°C (depending on the control gas mixture) when the reactor was at 10% power. The irradiation temperature was maintained at 440 to 500°C for all 15 specimens during full-power irradiation. The full-power reactor ionizing dose rate [6] was 10 to 16 kGy/s and the average displacement damage rate was ~2.4 to 4.3×10^{-7} dpa/s, with the lowest dose rates obtained for subcapsules 1 and 15 and the highest dose rate for subcapsule 8 (Table 2). The ionizing dose rate in the core with the reactor turned off (spent fuel removed) was ~10 Gy/s.

During the first five days of the irradiation, all of the biased specimens which were not undergoing an electrical measurement were left connected to the 150 V dc bias from the HP power supplies. This was performed in order to minimize the amount of time that the "biased" samples were exposed to irradiation with the electric field turned off. However, this arrangement had a disadvantage of producing large (~0.1-1 A) transient electrical current spikes in the coax cables during the switching operations, particularly when specimens were switched from an ohmic check measurement at -100 V back into the bias circuit at +150 V. Several of the coaxial cables failed (electrical short) during the first few days of irradiation, presumably due to these high transient currents. The Labview program was modified after five days of irradiation to shut off the 150 V bias during electrical measurements, and to slowly ramp the power supply from 0 to 150 V when the bias was reapplied following completion of a set of electrical measurements. The frequency of electrical measurements was reduced to ~ two per day when this change was implemented in order to minimize the amount of time that specimens were irradiated without the 150 V bias. The 150 V potential was applied to the biased specimens ~98% of the total irradiation time. Several additional coaxial cables shorted during the subsequent 3 months of irradiation, although the frequency of failure was much lower compared to the first 5 days of irradiation.

In order to evaluate whether the coaxial cable shorting was associated with normal dielectric breakdown effects versus a radiation-induced phenomenon, the dielectric breakdown strength was measured on 6 spare unirradiated coaxial cables that were produced by the vendor in the same batch as the HFIR cables. These electrical breakdown measurements were performed at either room temperature or at 200°C in an open-air furnace with a Keithley 237 Source-Measure Unit as the power supply. The temperature of 200°C corresponds to the maximum expected operating temperature of the coaxial cables in the TRIST-ER1 capsule during full-power irradiation.

Results

Nonohmic electrical behavior

Figure 1 shows the result of an ohmic check performed on a UV-grade sapphire specimen (sample #1) during full-power HFIR irradiation. The electrical current for positive applied potentials was significantly higher than the magnitude of the electrical current for negative applied potentials. Variation of the settling time between voltage application and current measurement (τ_{RC}) from 5 s to 180 s had no effect on the shape of the current vs. voltage curve. The calculated RC time constant for the HFIR electrical circuit was mainly determined by the capacitance of the coaxial cable (7 nF) which was three orders of magnitude larger than the capacitance of the alumina specimens (~7 pF). Using the typical measured resistances of the coaxial cables and alumina specimens during full-power irradiation, the calculated RC time constant for the HFIR circuit was ~10 ms, which is orders of magnitude smaller than the settling times used for the HFIR measurements. The ohmic check measurements were generally obtained by first applying a positive voltage, followed by progressively decreasing voltages. However, a similar current vs. voltage curve was also obtained when the voltage application sequence was reversed (i.e., initially applying negative voltages, followed by progressively more positive voltages). The asymptotic slope of the ohmic check curve at the highest positive voltages was typically between two and ten times larger than the slope measured at negative voltages.

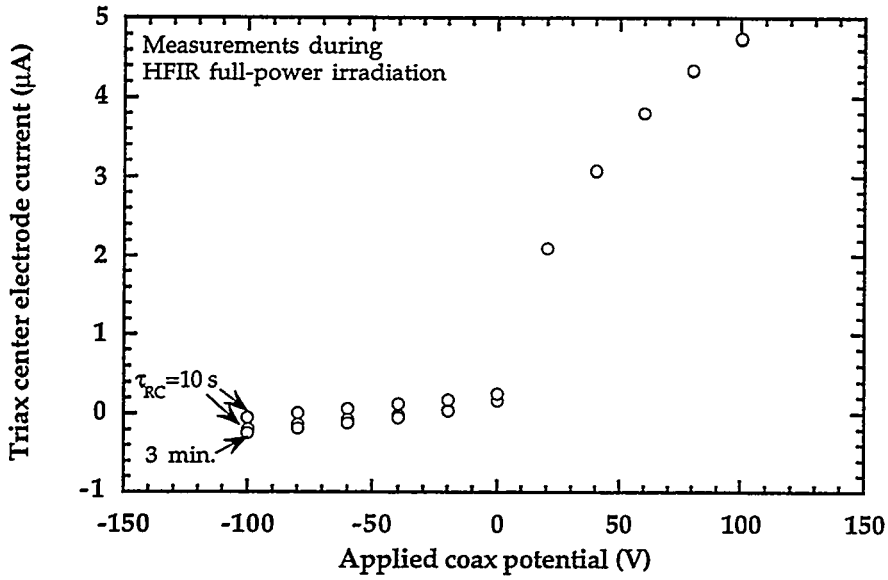

Fig. 1. Effect of RC wait time (τ_{RC}) on the electrical response of Crystal Systems sapphire (UV grade, a-axis orientation) during full-power HFIR irradiation at ~450°C. The τ_{RC}=10 s measurements were performed immediately before and after the τ_{RC}=3 min measurements.

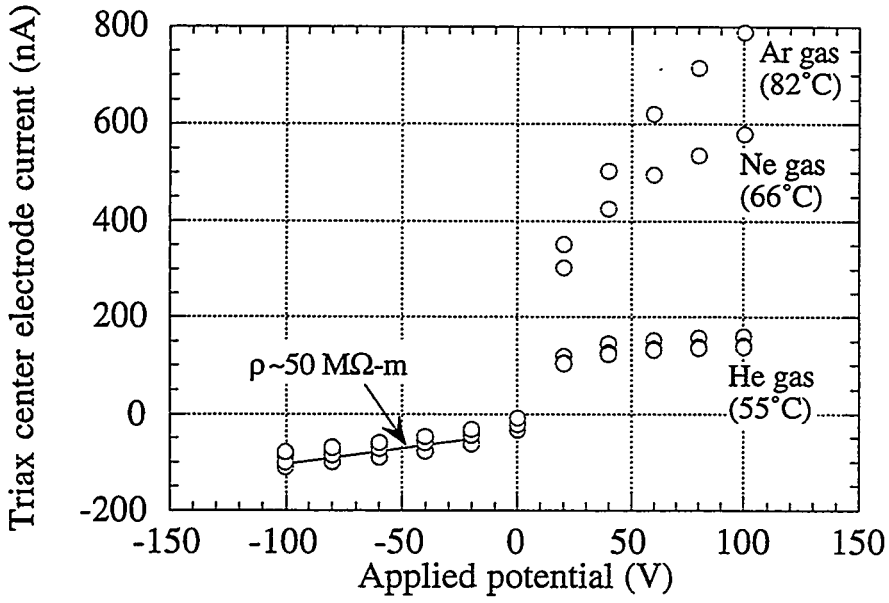

Fig. 2. Electrical response of Crystal Systems UV grade sapphire (c-axis orientation, sample #2) approximately 1 h after completion of the first HFIR irradiation cycle.

Table 1. Ion pair production rates for several gases [7]

Gas	K (ion pairs/cm^3-Gy)
He	2.3×10^{10}
Ne	7.0×10^{10}
Ar	17.7×10^{10}
air	21.5×10^{10}

As noted in our previous semiannual report [1], a pronounced increase in the measured current for positive applied voltages (but not for negative voltages) was observed in all samples on several occasions prior to the initial startup of the HFIR reactor. From a comparison with the operating history of the TRIST-ER1 capsule gas handling system, it was determined that this increase in current for positive voltages coincided with switching from the default He gas mixture to an Ar/He gas mixture. Figure 2 shows the results of several ohmic check measurements that were performed on a UV-grade sapphire specimen following the end of the first HFIR cycle (~1 dpa). The capsule gas mixture (used to control the specimen temperatures during full-power irradiation) was changed in the sequence He->Ne->Ar in an attempt to increase the specimen temperature and thereby measure the temperature-dependent electrical conductivity of the irradiated specimens in a relatively low ionizing radiation field compared to full-power reactor operation. Only a small elevation in temperature was achieved by this change in gas mixture, due to the low residual nuclear heating rate after reactor shutdown and the relatively small gas gaps (~20-100 μm) in the HFIR TRIST-ER1 design. The radiation induced conductivity obtained from the slope in the negative quadrant of the current vs. voltage curves was ~2×10^{-8} S/m for all three gas mixtures. On the other hand, the slope of the current vs. voltage curve in the positive quadrant was dependent on the gas environment, with the highest slope occurring for Ar and the lowest slope occurring for He.

The conductivity of an ionized gas is given by $\sigma = n_e e \mu_e + n_i e \mu_i$, where n_e and n_i are the density of ionized electrons and ions (assumed singularly charged), respectively, e is the electron charge, and μ_e and μ_i are the electron and ion mobilities, respectively [8]. Since the ion mobility is much smaller than the electron mobility, $\mu_i \sim 10^{-3}\ \mu_e$ [7,8], the ion contribution to the current can be neglected. Therefore, the gaseous current should be mainly evident for positive applied voltages (due to preferential attraction of electrons) and should be orders of magnitude smaller for negative voltages. The electrical conductivity in most gases has been found to be proportional to ionizing dose rate up to ~10^{10} Gy/s, due to the high electron reattachment rate (typical free electron lifetimes are ~10 ns) [9]. The electrical conductivity of the ionized gas can be described by the following equation [10].

$$\sigma_e = n_e e \mu_e = KDe\mu_e/\alpha \qquad (1)$$

where K is the production rate for ion pairs, D is the ionizing dose rate and α is the electron attachment rate. The electrical conductivity of air for dose rates relevant to full-power HFIR irradiation (16 kGy/s) is $\sigma_e = 3.7 \times 10^{-6}$ S/m, which is comparable to the RIC in Al_2O_3. Table 1 summarizes the ion pair production rate for different gases [7]. It can be seen that Ar would produce the highest gas conductivity and He would produce the lowest gas conductivity among the 3 noble gases, which is similar to the experimental results for positive voltages shown in Fig. 2. Therefore, the observations that the nonohmic behavior occurs mainly for positive applied voltages and that the relative magnitude of the current agrees with the expected RIC values for different gas species both suggest that the observed non-ohmic electrical behavior during HFIR irradiation is due to preferential attraction of ionized electrons in the capsule gas to the unshielded portion of the "low-side" electrical leads.

Whereas gas conductivity effects appear to qualitatively explain much of the observed nonohmic behavior in the TRIST-ER1 experiment, quantitative agreement is more difficult to obtain. It should be noted that the specimen electrical currents were measured on the low side (i.e., near electrical ground). The voltage change in the low-side triaxial cable was on the order of 0.1 mV as the coaxial voltage was changed between 100 V and -100 V. Furthermore, only ~1 to 2 cm of the

triaxial electrical lead from each subcapsule was unshielded. Considering the ~6 orders of magnitude smaller electric field for the gas compared to the alumina specimen and the comparable areas of the bare triaxial center lead and the alumina specimen electrodes, the calculated current in the triaxial cable center lead would be expected to be dominated by the alumina specimen rather than gas conductivity effects.

The shape of the current vs. voltage plots shown in Figs. 1 and 2 are qualitatively very similar to Langmuir probe current-voltage plots obtained in plasma physics studies of ionized gases [11]. Since a gas ionized by radiation is essentially a weakly ionized plasma, this plasma physics approach may be useful for the analysis of the nonohmic TRIST-ER1 electrical data. The nonohmic behavior in the Langmuir probe plots has been shown to be due to the difference in the electron and ion fluxes incident on the wire probe, the ratio of which is proportional to $(m_i/m_e)^{1/2}$ where m_i and m_e are the ion and electron masses. Further analysis is necessary to determine whether the plasma physics equations developed for Langmuir probes can quantitatively describe the HFIR TRIST-ER1 electrical data.

In the following sections, the electrical conductivity was calculated from the slope of the current vs. voltage plots for applied coaxial cable voltages less than -20 V. The surface leakage resistances between the center, guard and back electrodes were routinely measured and compared with the apparent bulk resistance to determine if surface leakage currents were affecting the conductivity measurements, using the equations given by Kesternich et al. [12].

Time-dependent electrical conductivity

Figure 3 shows the electrical conductivity measured on UV grade Crystal Systems sapphire before and during the first few days of the first HFIR cycle. The measured electrical conductivity outside of the reactor core was $<10^{-10}$ S/m, which is at the resolution limit of the electrical equipment used for the HFIR TRIST-ER1 experiment (due to the ~1 TΩ leakage resistance of the scanner cards in the matrix switch system). The electrical conductivity increased to $\sim 4 \times 10^{-9}$ S/m when the capsule was inserted into the HFIR core prior to the start of the radiation (residual background radiation dose rate of ~10 Gy/s). The electrical conductivity was $\sim 4 \times 10^{-8}$ S/m and $\sim 1.2 \times 10^{-7}$ S/m for 10% power and full power irradiation conditions. Figure 4 shows the electrical conductivity of a regular grade of Crystal Systems sapphire measured before, during and after the three HFIR reactor cycles. It can be seen that the electrical conductivity of the specimen never exceeded $\sim 3 \times 10^{-7}$ S/m during full-power irradiation at an ionizing dose rate of ~12 kGy/s during the 3 HFIR irradiation cycles. Following the irradiation, the electrical conductivity of the specimen returned to a value that was similar to the preirradiation value (limited by the leakage resistance in the TRIST-ER1 electrical equipment).

Table 2 summarizes the electrical conductivity measurements for the 15 alumina specimens before and during the initial stages of the first HFIR irradiation cycle. The preirradiation in-core electrical conductivity ranged from $\sim 3 \times 10^{-10}$ S/m to 4×10^{-9} S/m for the different specimens. The electrical conductivity at 10% reactor power (1.0-1.6 kGy/s) ranged from 4×10^{-8} S/m to 2×10^{-7} S/m. The high-purity single crystal specimens generally had higher RIC values than the polycrystal specimens for both of these irradiation conditions. The RIC values for full-power irradiation ranged from 1.2×10^{-7} to 1×10^{-6} S/m, with no consistent difference between the single crystal and polycrystal specimens.

Table 3 shows the corresponding electrical conductivity values measured for the 15 MgO-insulated coaxial cables. The electrical conductivity was determined from the slope of the power supply current vs. voltage plots at voltages less than -20 V. The well-known geometry factor for coaxial cables, $R/\rho = \ln(b/a)/2\pi L$, was used to convert the measured resistance (R) to resistivity (ρ) values, where b and a are the outer and inner diameters of the MgO insulation and L is the length of the coaxial cable that was in the HFIR core region. The value of L used for the conductivity calculation ranged from 5 cm for cable #1 to 45 cm for cable #15. The RIC values for the coaxial

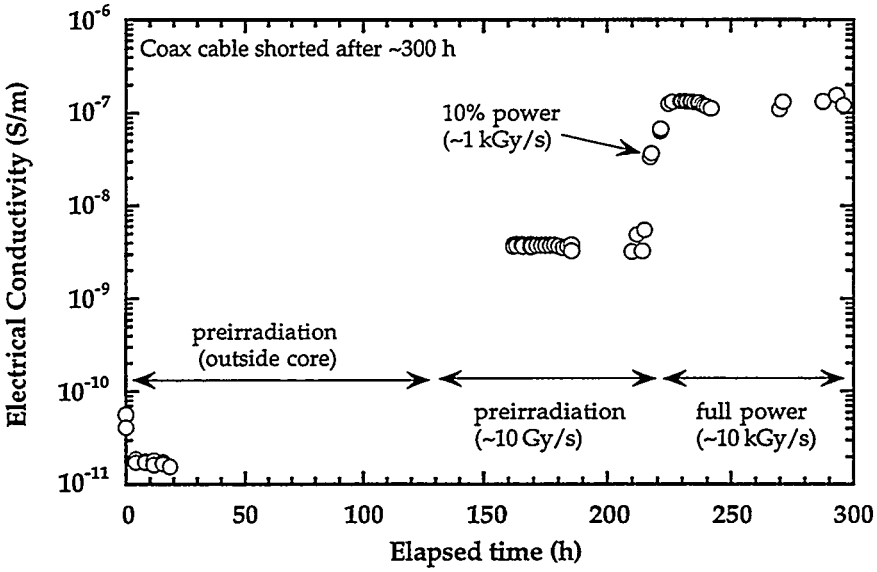

Fig. 3. Electrical conductivity of Crystal Systems sapphire (UV grade, a-axis orientation, specimen position #1) prior to and during the first HFIR irradiation cycle.

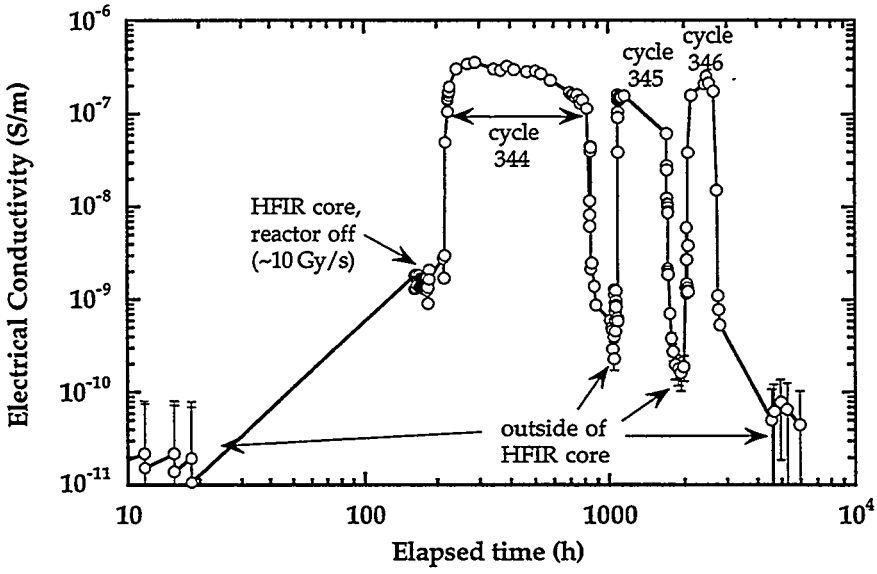

Fig. 4. Electrical conductivity of Crystal Systems sapphire (regular grade, c-axis orientation, specimen position #3) prior to, during and following the three HFIR irradiation cycles.

Table 2. Summary of HFIR TRIST-ER1 electrical conductivity measurements at startup

Position # and material	Electrical Conductivity (S/m)		
	In-core, reactor off (10 Gy/s, 60°C)	10% power (1-1.6 kGy/s, 170°C)	100% power (10-16 kGy/s,450°C)
1. CSI sapphire,UV, a-axis	4×10^{-9}	4×10^{-8}	1.2×10^{-7}
2. CSI sapphire,UV, c-axis	3×10^{-9}	6×10^{-8}	3×10^{-7}
3. CSI sapphire,regular, c-axis	2×10^{-9}	5×10^{-8}	3×10^{-7}
4. CSI sapphire,regular, a-axis	1.5×10^{-9}	9×10^{-8}	4×10^{-7}
5. Vitox (99.9% purity)	$(<7 \times 10^{-8})$*	$(\leq 4 \times 10^{-7})$*	1×10^{-6}
6. Kyocera A480 (99.9% purity)	3×10^{-10}	1×10^{-7}	1×10^{-6}
7. Wesgo AL300 (97% purity)	5×10^{-10}	2×10^{-7}	5×10^{-7}
8. Kyocera A479 (99.0% purity)	3×10^{-10}	6×10^{-8}	3×10^{-7}
9. Coors AD998 (99.8% purity)	3×10^{-10}	1×10^{-7}	—
10. Wesgo AL995 (99.5% purity)	3×10^{-10}	6×10^{-8}	8×10^{-7}
11. Wesgo AL995 (99.5% purity)	4×10^{-10}	4.5×10^{-8}	2×10^{-7}
12. CSI sapphire,regular, c-axis	2×10^{-9}	6×10^{-8}	3×10^{-7}
13. Un. Carbide Cr-doped sapphire	1×10^{-9}	7×10^{-8}	2×10^{-7}
14. Kyocera SA100, [1102]	3×10^{-9}	7×10^{-8}	2×10^{-7}
15. Kyocera SA100, [1102]	$(<1 \times 10^{-7})$*	$(<1 \times 10^{-6})$*	$(<3 \times 10^{-6})$*

*values in parenthesis denote upper limits to bulk conductivity due to high surface leakage currents

Table 3. Summary of measured in-core conductivities (S/m) for the coax cables at the start of the HFIR irradiation (from the negative quadrant of the ohmic check plots). The data marked with an asterisk denote values that are a upper limit to the bulk conductivity due to low (<1 MΩ) surface leakage resistances (measured with the reactor turned off)

HFIR position	Preirradiation (10 Gy/s,50°C)	10% power, 0 dpa (1-1.6 kGy/s, 170°C)	Full power, 0 dpa (10-16 kGy/s, 440-500°C)	Full power, 1st cycle avg. (10-16 kGy/s, 440-500°C)
1.	$(<1.5 \times 10^{-6})$*	$\sim 6 \times 10^{-6}$	$\sim 6 \times 10^{-6}$	$\sim 6 \times 10^{-6}$
2.	$(<2 \times 10^{-7})$*	$\sim 1x \times 10^{-6}$	$\sim 4 \times 10^{-6}$	$\sim 2 \times 10^{-5}$
3.	$\sim 2 \times 10^{-9}$	$\sim 2 \times 10^{-7}$	$\sim 5 \times 10^{-7}$	$\sim 2 \times 10^{-6}$
4.	$(<5 \times 10^{-8})$*	$\sim 4 \times 10^{-7}$	$\sim 3 \times 10^{-6}$	—
5.	$(<4 \times 10^{-5})$*	$(<2 \times 10^{-5})$*	$(<5 \times 10^{-5})$*	$(<5 \times 10^{-5})$*
6.	$(<1.5 \times 10^{-8})$*	$\sim 2.5 \times 10^{-7}$	$\sim 2 \times 10^{-6}$	—
7.	$\sim 2 \times 10^{-10}$	$\sim 8 \times 10^{-8}$	$\sim 5 \times 10^{-7}$	$\sim 5 \times 10^{-7}$
8.	$(<1 \times 10^{-7})$*	$\sim 4 \times 10^{-7}$	$\sim 8 \times 10^{-7}$	$\sim 4 \times 10^{-7}$
9.	$(<3 \times 10^{-7})$*	$\sim 2 \times 10^{-7}$	$\sim 5 \times 10^{-7}$	$\sim 4 \times 10^{-7}$
10.	$(<1 \times 10^{-7})$*	$\sim 1 \times 10^{-7}$	$\sim 1 \times 10^{-5}$	—
11.	$\sim 1.5 \times 10^{-9}$	$\sim 5 \times 10^{-8}$	$\sim 5 \times 10^{-7}$	$\sim 2 \times 10^{-7}$
12.	$\sim 1 \times 10^{-9}$	$\sim 7 \times 10^{-8}$	$\sim 1 \times 10^{-6}$	$\sim 2 \times 10^{-6}$
13.	$(<2 \times 10^{-8})$*	$\sim 2 \times 10^{-7}$	$\sim 5 \times 10^{-7}$	$\sim 2 \times 10^{-6}$
14.	$\sim 5 \times 10^{-10}$	$\sim 5 \times 10^{-8}$	$\sim 3 \times 10^{-7}$	—
15.	$(<5 \times 10^{-5})$*	$(<7 \times 10^{-5})$*	$(<1 \times 10^{-4})$*	$(<3 \times 10^{-5})$*

cables were comparable or somewhat higher than that measured for the alumina specimens. The measured RIC values for the coaxial cables are an upper limit to the bulk conductivity, since possible effects associated with surface leakage currents were not measured for the cables. Figure 5 shows the time-dependent electrical conductivity of the coaxial cable for sample #3. The apparent electrical conductivities measured with the reactor off were much higher than the corresponding values for the Al_2O_3 specimens, most likely because of surface leakage currents at the cable termination. Anomalously high leakage currents were observed in coax cable #3 during most of the shutdown period between HFIR cycles 345 and 346, suggesting that some degradation (surface or bulk) may have occurred in the MgO insulation or glass seal. However, measurements made several months following the completion of the third irradiation cycle produced apparent conductivities similar to the preirradiation value.

Figure 6 shows the time dependent electrical conductivities for two polycrystalline alumina specimens whose coaxial cables shorted during the second HFIR irradiation cycle. In both specimens, the electrical conductivity was essentially constant during full-power irradiation with values near 2 to 6×10^{-7} S/m. There was no evidence of degradation of the bulk conductivity of either specimen prior to the shorting in the electrical cables. The cable for the Wesgo AL300 specimen shorted during an ohmic check measurement with an applied voltage of -100 V. The electrical measurements made at +100 to -80 V in this measurement sequence did not indicate any unusual behavior in either the coaxial cable or the alumina specimen.

Figures 7-12 show electrical conductivity vs. displacement damage dose plots for several of the alumina specimens irradiated in the HFIR TRIST-ER1 experiment. The dose level was obtained by using the following conversion from neutron fluence: 1 dpa = 1×10^{25} n/m^2 (E>0.1 MeV). Only measurements made during full-power reactor operation are plotted in these figures in order to maintain roughly constant dose rates. In several cases (e.g., Figs. 7,8), the electrical conductivity increased slightly by a factor of 2 to 5 during the first few days of HFIR irradiation (up to ~0.1 dpa), and this was followed by a gradual decrease in electrical conductivity at higher doses. None of the polycrystalline alumina or high-purity sapphire specimens irradiated with a dc electric field of 200 V/mm exhibited a full-power electrical conductivity above ~10^{-6} S/m during this experiment, despite the fact that several specimens achieved damage levels of nearly 3 dpa. Pronounced RIED (σ_e>10^{-5} S/m) occurred for doses of less than 10^{-4} dpa in several previous electron irradiation studies performed on high-purity sapphire and Vitox polycrystalline alumina [3]. When corrections for the high dose rate in the HFIR irradiation compared to the electron irradiations are taken into account, pronounced RIED would have been predicted to occur at HFIR doses above ~0.01 dpa according to extrapolations from the electron irradiation data base [3]. Therefore, it appears that the as-yet uncertain physical mechanisms responsible for RIED during electron irradiation may not be present during neutron irradiation up to relatively high doses.

As shown in Fig. 12, a large increase in the electrical conductivity of the 0.05% Cr-doped sapphire (ruby) specimen occurred during the first three days of HFIR irradiation. The electrical conductivity reached a peak value of ~2×10^{-4} S/m at a dose of ~0.1 dpa. Diagnostic measurements of the surface leakage resistances between the center, guard and back electrodes showed that this high apparent conductivity was not due to high surface leakage currents. The rapid increase in electrical conductivity of this specimen is very similar to the RIED behavior reported in several electron and ion irradiation studies [3,4,13-15]. However, continued irradiation to doses above 0.1 dpa resulted in a monotonic decrease in the electrical conductivity. The electrical conductivity decreased to <10^{-6} S/m by the middle of the third HFIR irradiation cycle (~2 dpa), which is only slightly larger than the initial RIC value for this specimen measured at the start of the first HFIR irradiation cycle. This "healing" of the high electrical degradation suggests that a physical process such as specimen microcracking [16] might have been responsible for the initial increase in conductivity. If microcracking were responsible for the initial conductivity increase, oxidation of the conducting layer in the crack could produce a subsequent decrease in conductivity. Postirradiation microstructural examination of this specimen is planned to provide further insight into possible physical mechanisms responsible for the initial increase and subsequent decrease in electrical conductivity.

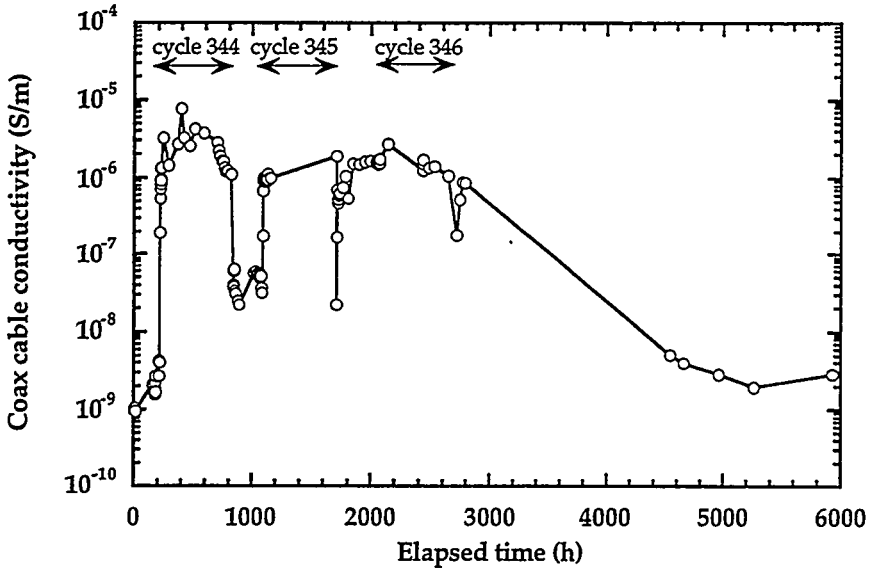

Fig. 5. Electrical conductivity of the MgO insulation in the coaxial cable for subcapsule #3 prior to, during and following the three HFIR irradiation cycles.

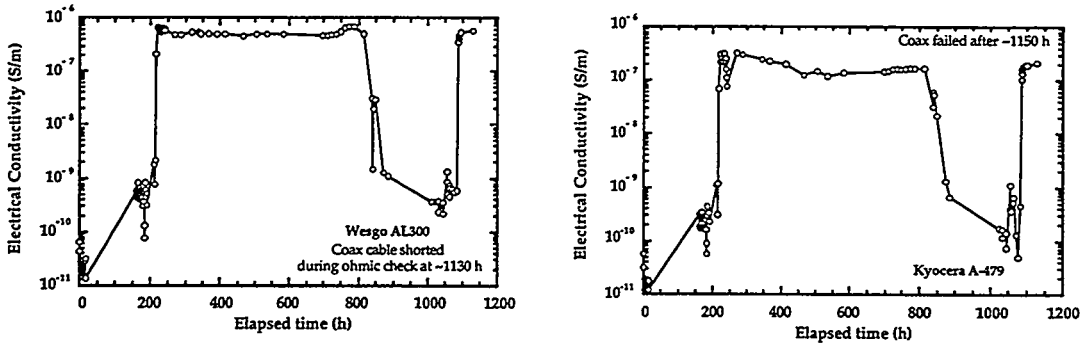

Fig. 6. Electrical conductivity of two polycrystalline alumina specimens (positions #7 and #8) before and during the first two HFIR irradiation cycles. Cycle 344 started at ~200 h and the reactor was shut down between 800 and 1100 h for normal core replacement operations.

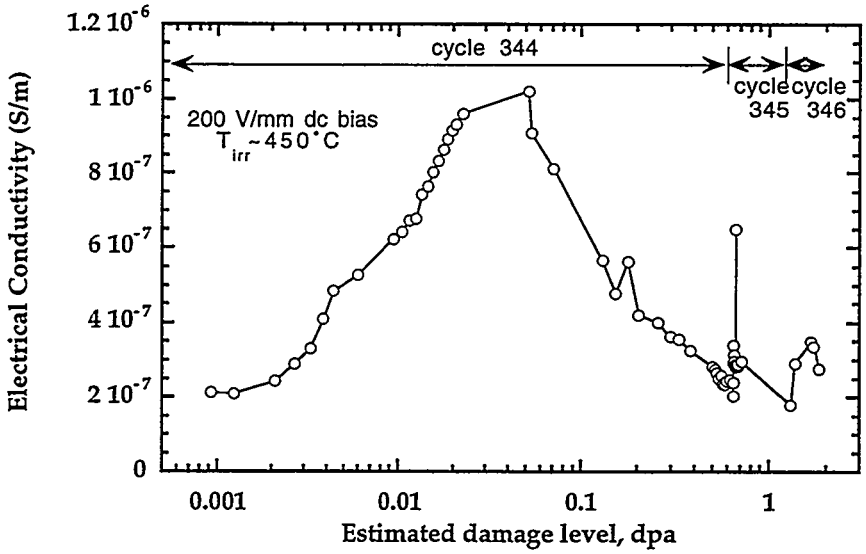

Fig. 7. Dose dependent electrical conductivity of UV grade Crystal Systems sapphire (position #2) during full-power HFIR irradiation.

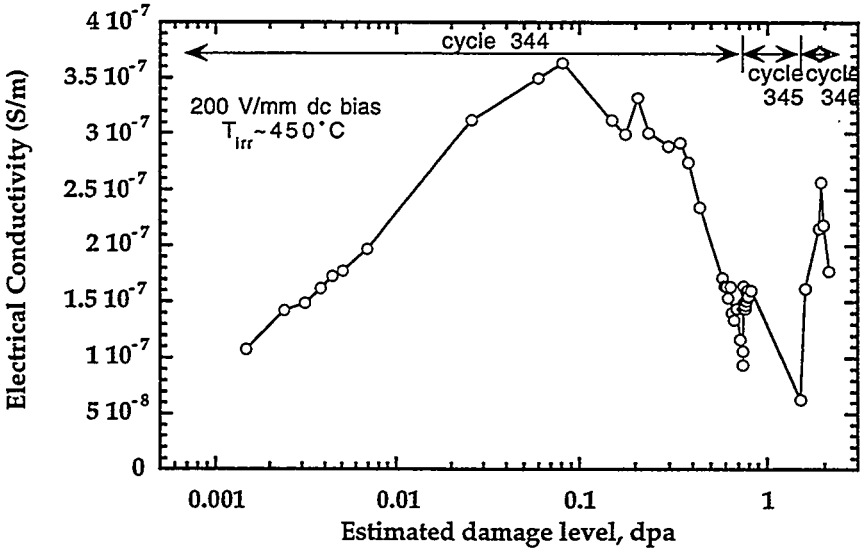

Fig. 8. Dose dependent electrical conductivity of regular grade Crystal Systems sapphire (position #3) during full-power HFIR irradiation.

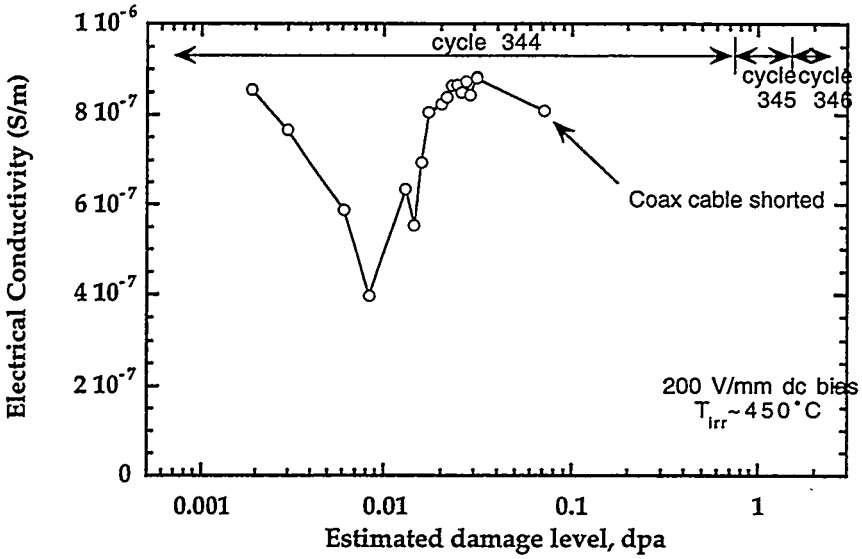

Fig. 9. Dose dependent electrical conductivity of Vitox alumina (position #5) during full-power HFIR irradiation.

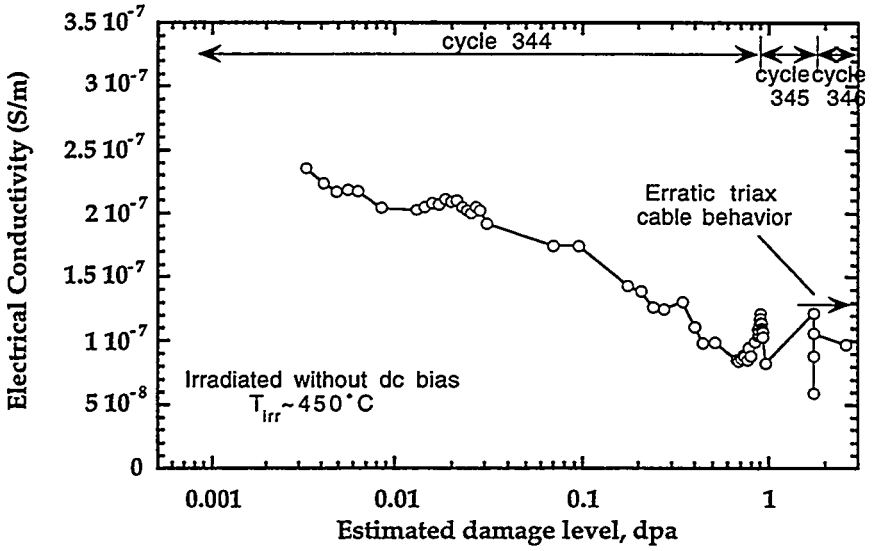

Fig. 10. Dose dependent electrical conductivity of Wesgo AL995 (position #11) during full-power HFIR irradiation. The specimen was irradiated without dc bias.

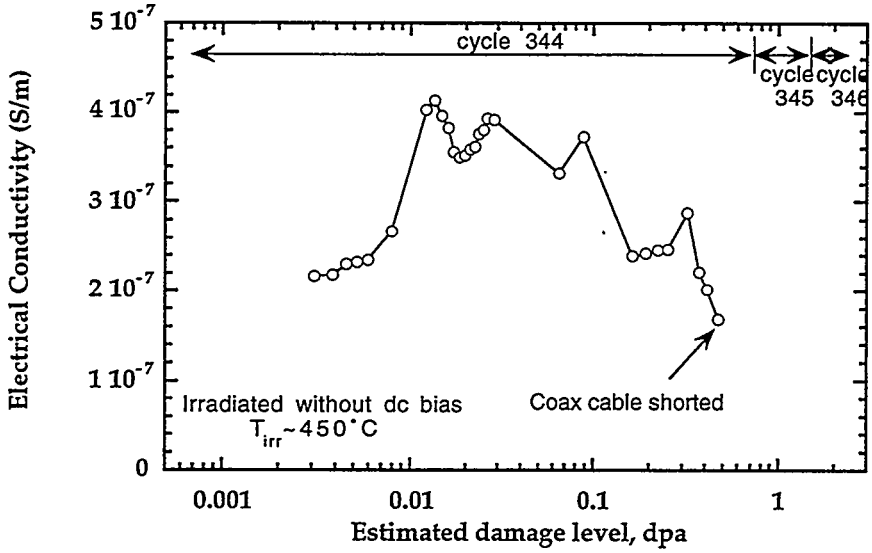

Fig. 11. Dose dependent electrical conductivity of regular grade Crystal Systems sapphire (position #12) during full-power HFIR irradiation. The coaxial cable failed near the end of the first HFIR irradiation cycle despite the fact that the specimen was irradiated without dc bias.

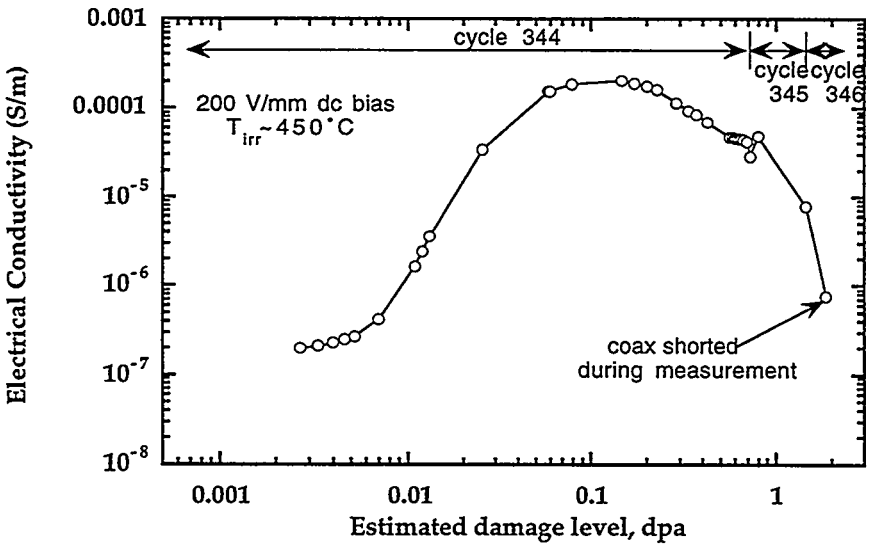

Fig. 12. Dose dependent electrical conductivity of 0.05% Cr-doped sapphire (position #13) during full-power HFIR irradiation.

Investigation of the dielectric breakdown strength of the HFIR TRIST-ER1 coaxial cables

A total of ten of the 15 coaxial cables in the HFIR TRIST-ER1 capsule failed by partial or full electrical short during the 3 1/2 month irradiation. It is worth noting that two of the electrical shorts in the coaxial cables occurred in unbiased specimens (cables for subcapsules 12 and 15, e.g., Fig. 10). This suggests that the cable failure was not associated with some type of RIED phenomenon. The biased coaxial cables were subjected to a dc potential of 150 V during the HFIR irradiation, which produced a maximum electric field of ~400 kV/m near the center conductor. All of the HFIR cables (biased and unbiased) were subjected to periodic electric measurements with potentials ranging from +100 V to -100 V (+150 V to -150 V in some cases).

The dielectric breakdown strength (DBS) of the MgO powder insulation used in the HFIR coaxial cables is expected to be comparable to the DBS for monolithic MgO, which has been measured to be ~100 MV/m at ~500°C and ~0.1 MV/m at 1200°C [17]. On the other hand, the dielectric breakdown strength of glass decreases from a typical value of ~100 MV/m at room temperature to <1 MV/m at temperatures above 200°C (depending on the particular grade of glass) [18]. The HFIR coaxial cables were sealed with Ferro 7556 lead borosilicate glass, which has a softening temperature of 330°C. The temperature-dependent dielectric breakdown strength of this grade of glass was not available from the glass manufacturer.

Experimental tests were performed on six unirradiated control coaxial MI cables from the HFIR TRIST-ER1 experiment in order to measure the dielectric breakdown strength of the cables. Since the dielectric breakdown strength of glass depends on both test temperature and the duration of the applied electric field, several different types of tests were performed. Most of the tests were performed at 200°C, which corresponds to the maximum expected operating temperature of the coaxial cables during full-power HFIR irradiation. For short term tests of the DBS, the voltage was applied for a time period of 0.5-1 min. If no shorting occurred, the voltage was increased by 50 V and the test was repeated. Table 4 summarizes the results of the dielectric breakdown tests. The DBS measured from short-term application of a constant-polarity voltage ranged from >1100 V (the maximum voltage for the Keithley 237 power supply) at room temperature to 850 V at 200°C. The DBS decreased to 500 V when the polarity of the applied potential alternated from positive to negative in short term tests. The DBS was approximately 300 V when the voltage was applied for several hours at a given potential. The dielectric breakdown was confirmed to occur in the glass seal region of the MI cables in all of these tests.

The measured dielectric breakdown strength of the glass seals in the control MI cables for the long term (>5 h) tests) is within a factor of two of the dc potential continuously applied to the 12 biased specimens in the HFIR TRIST-ER1 capsule. In addition, the measured DBS for the short term tests with alternating polarity is only about a factor of 5 larger than the voltages applied to all (biased and unbiased) of the HFIR specimens during ohmic check measurements. Therefore, it seems reasonable to assume that the shorting of the HFIR coaxial cables may be due to conventional dielectric breakdown in the glass seals (possibly assisted by some radiation-induced degradation in the glass). Postirradiation examination of the coaxial cables from the HFIR TRIST-ER1 experiment is planned in order to verify the cause of the shorting of the cables.

Table 4. Dielectric breakdown strength measurements on unirradiated HFIR coaxial MI cables.

T_{test}	Test condition	Dielectric breakdown strength
20°C	short term tests (≤1 min.), constant polarity	>1100 V (>2.8 MV/m)
200°C	"	850 V (2.2 MV/m)
200°C	short term tests, alternating polarity	~500 V (1.3 MV/m)
200°C	long term tests (>5 h), constant polarity	300 V (0.8 MV/m)
200°C	long term tests, alternating polarity	~300 V (0.8 MV/m)

Discussion and summary

Catastrophic radiation-induced electrical degradation (σ_e>10^{-4} S/m) was not observed in any of the HFIR-irradiated polycrystalline or high-purity sapphire specimens (~3 dpa maximum dose). As shown in Fig. 13, the measured RIC values for alumina are in good agreement with previous studies [2]. The quantitative level of RIC decreased slightly following irradiation in several of the specimens, in agreement with previous irradiation studies performed without an applied electric field during irradiation [19]. The decrease in conductivity has generally been attributed to increased electron-hole trapping at radiation-produced defects.

Previous studies of the RIED phenomenon have either used irradiation sources with very high ionizing radiation/dpa environments (electron and light ion irradiations) and/or were only performed to relatively low doses (e.g., less than ~0.5 dpa for JMTR fission reactor studies) [2]. The electron irradiation studies indicated that RIED would be most pronounced in high-purity single crystal specimens, and would be the least pronounced in low-purity polycrystal specimens [3]. In the TRIST-ER1 experiment, two single crystal specimens of alumina were successfully irradiated to the highest doses ever studied in an RIED experiment (>2 dpa). Previous RIED studies on single crystal alumina were limited to a maximum dose of 0.01 dpa [2]. The electrical conductivity of all specimens except for the Cr-doped sapphire (ruby) remained less than ~1×10^6 S/m (i.e., at the normal RIC level) during extended full-power irradiation in HFIR. As discussed at a recent IEA workshop [20], there are several possible explanations for the discrepancy between the electron RIED studies and the present work. One possibility is that the large amount of implanted charge associated with electron irradiation may somehow trigger the initiation of RIED. Further work is needed to understand the physical mechanism(s) responsible for producing RIED in electron-irradiated samples.

A moderate amount of RIED that apparently is not due to surface leakage currents was observed in the Cr-doped sapphire specimen; the full-power conductivity increased by nearly 3 orders of magnitude after the first few days of irradiation and then gradually decreased over the ensuing 3 months. Further work is needed to determine the cause of the high apparent bulk conductivity of the ruby specimen which occurred at a dose of ~0.1 dpa.

Simple calculations suggest that the observed non-ohmic electrical behavior during HFIR irradiation is due to preferential attraction of ionized electrons in the capsule gas to the unshielded "low-side" electrical leads, but further analysis is needed to determine if this process can quantitatively explain the observed experimental data.

Shorting of many of the coax cables in the HFIR TRIST-ER1 capsule is attributed to dielectric breakdown of the glass used to seal the ends of the cables, based on tests performed on several non-irradiated control coax cables at 200°C. The dielectric breakdown strength (DBS) decreased with increasing temperature, and the breakdown was confirmed to occur in the glass terminations.

Disassembly of the HFIR TRIST-ER1 capsule is currently in progress. Several different post-irradiation measurements are planned, including electrical resistivity vs. temperature for all 15 alumina specimens and examination of the shorted coaxial cables. Microstructural examination of selected alumina specimens may also be performed.

REFERENCES

[1] S.J. Zinkle et al., in Fusion Materials Semiannual Progress Report for Period ending June 30, 1996, DOE/ER-0313/20 (Oak Ridge National Lab, 1996) p. 257.
[2] C. Kinoshita and S.J. Zinkle, J. Nucl. Mater. 233-237 (1996) 100.
[3] E.R. Hodgson, J. Nucl. Mater. 212-215 (1994) 1123.
[4] A. Möslang, E. Daum and R. Lindau, in Proc. 18th Symp. on Fusion Technology, eds. K. Herschbach, W. Naurer and J.E. Vetter (North-Holland, Amsterdam, 1994) p. 1313.

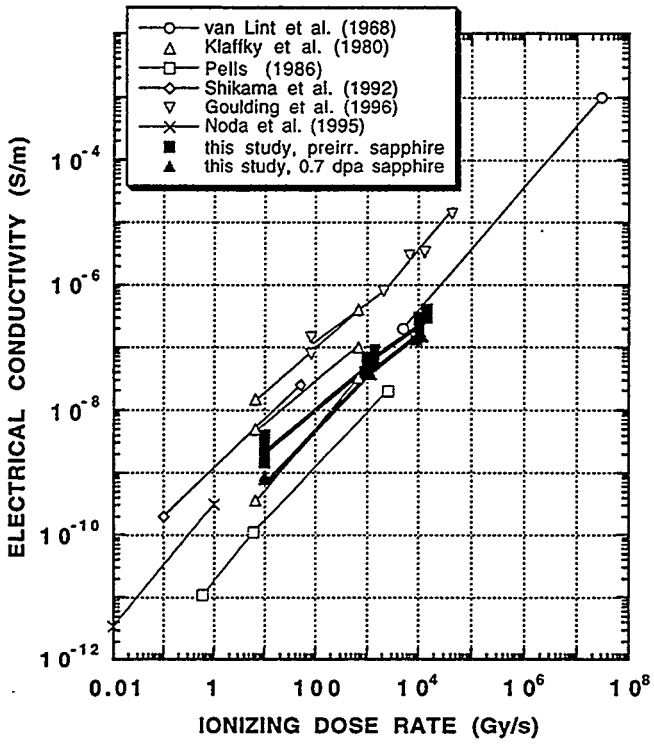

Fig. 13. Comparison of the electrical conductivity of high purity sapphire measured in the present study with previous studies on RIC in alumina.

[5] S. J. Zinkle, in Fusion Materials Semiannual Progress Report for Period ending December 31, 1995, DOE/ER-0313/19 (Oak Ridge National Lab, 1995) p. 258.
[6] A. L. Qualls et al., in Fusion Materials Semiannual Progress Report for Period ending June 30, 1996, DOE/ER-0313/20 (Oak Ridge National Lab, 1996) p. 267.
[7] V.A.J. van Lint et al., Mechanisms of Radiation Effects in Electronic Materials, Vol. 1 (John Wiley & Sons, New York, 1980) p. 359.
[8] F. J. Blatt, Physics of Electronic Conduction in Solids (McGraw-Hill, New York, 1968) p. 446.
[9] J. G. Chervenak and V.A.J. van Lint, IEEE Trans. Nucl. Sci. NS-32 (1985) 4308.
[10] J. G. Chervenak and V.A.J. van Lint, IEEE Trans. Nucl. Sci. NS-29 (1982) 1880.
[11] F. F. Chen, in Plasma Diagnostic Techniques, eds. R. H. Huddlestone and S. L. Leonard (Academic Press, New York, 1965) p. 113.
[12] W. Kesternich, F. Scheuermann and S. J. Zinkle, J. Nucl. Mater. 219 (1995) 190.
[13] E. R. Hodgson, J. Nucl. Mater. 179-181 (1991) 383.
[14] G. P. Pells, J. Nucl. Mater. 184 (1991) 177.
[15] X.-F. Zong et al., Phys. Rev. B 49 (1994) 15514.
[16] S. J. Zinkle, J. D. Hunn and R. E. Stoller, in Microstructure of Irradiated Materials, MRS Symp. Proc. vol. 373, eds. I.M. Robertson et al. (Materials Research Soc., Pittsburgh, 1995) p. 299.
[17] K. L. Tsang, Y. Chen and J. J. O'Dwyer, Phys. Rev. B 26 (1982) 6909.
[18] J. J. O'Dwyer, The Theory of Dielectric Breakdown of Solids (Oxford Univ. Press, 1964)
[19] S. J. Zinkle and E. R. Hodgson, J. Nucl. Mater. 191-194 (1992) 58.
[20] S. J. Zinkle, E. R. Hodgson and T. Shikama, in Fusion Materials Semiannual Progress Report for Period ending June 30, 1997, DOE/ER-0313/22, in press.

IRRADIATION SPECTRUM AND IONIZATION-INDUCED DIFFUSION EFFECTS IN CERAMICS — S. J. Zinkle (Oak Ridge National Laboratory)

SUMMARY

There are two main components to the irradiation spectrum which need to be considered in radiation effects studies on nonmetals, namely the primary knock-on atom energy spectrum and ionizing radiation. The published low-temperature studies on Al_2O_3 and MgO suggest that the defect production is nearly independent of the average primary knock-on atom energy, in sharp contrast to the situation for metals. On the other hand, ionizing radiation has been shown to exert a pronounced influence on the microstructural evolution of both semiconductors and insulators under certain conditions. Recent work on the microstructure of ion-irradiated ceramics is summarized, which provides evidence for significant ionization-induced diffusion. Polycrystalline samples of MgO, Al_2O_3, and $MgAl_2O_4$ were irradiated with various ions ranging from 1 MeV H^+ to 4 MeV Zr^+ ions at temperatures between 25 and 650°C. Cross-section transmission electron microscopy was used to investigate the depth-dependent microstructure of the irradiated specimens. Dislocation loop nucleation was effectively suppressed in specimens irradiated with light ions, whereas the growth rate of dislocation loops was enhanced. The sensitivity to irradiation spectrum is attributed to ionization-induced diffusion. The interstitial migration energies in $MgAl_2O_4$ and Al_2O_3 are estimated to be $\leq$0.4 eV and $\leq$0.8 eV, respectively for irradiation conditions where ionization-induced diffusion effects are expected to be negligible.

RESULTS AND DISCUSSION

Numerous microstructural studies of radiation effects in ceramics have been performed over the past 35 years, utilizing a variety of irradiation sources including electrons, ions and neutrons [1-3]. In order to make quantitative comparisons between data obtained with different irradiation sources, the effects of irradiation spectrum (along with other important experimental variables such as temperature and dose rate) need to be considered. Two main components of the irradiation spectrum must be considered for nonmetals. First, the energy spectrum of primary knock-on atoms (PKAs) produced by elastic collisions can affect the efficiency of point defect production, in a manner analogous to that commonly observed in metals. Second, inelastic collisions (electronic ionization and subthreshold atomic collisions) may affect point defect recombination and diffusion. As noted later in this paper, ionization effects often appear to be more important than PKA spectrum effects in irradiated ceramics.

Figure 1 compares measurements of the surviving defect fraction (displacement damage efficiency) in Al_2O_3 and Al as a function of the average PKA energy [4-9]. The data have been normalized to the calculated displacements per atom (dpa) according to the Norgett-Robinson-Torrens (NRT) modified Kinchin-Pease formula. Most of the data on Al_2O_3 were obtained from optical absorption measurements of oxygen monovacancy (F center) concentrations, and therefore are a lower limit to the total surviving defect fraction. Further details are discussed elsewhere [10]. The data for Al show a monotonic decrease in surviving defect fraction with increasing PKA energy, which is similar to the behavior observed in numerous other metals. Considerable scatter exists in the corresponding Al_2O_3 data, but the measurements do not exhibit any apparent dependence on PKA energy. As reviewed elsewhere, the surviving defect fraction data for MgO also appear to be insensitive to PKA energy, with an average value of ~30% [10]. There are several possible explanations for the weak dependence of the surviving defect fraction of PKA energy in MgO and Al_2O_3. Some studies suggest that the spontaneous recombination volume for close Frenkel pairs in these materials may be much larger than typical values in metals [11,12]. This would produce efficient recombination of point defects produced by low

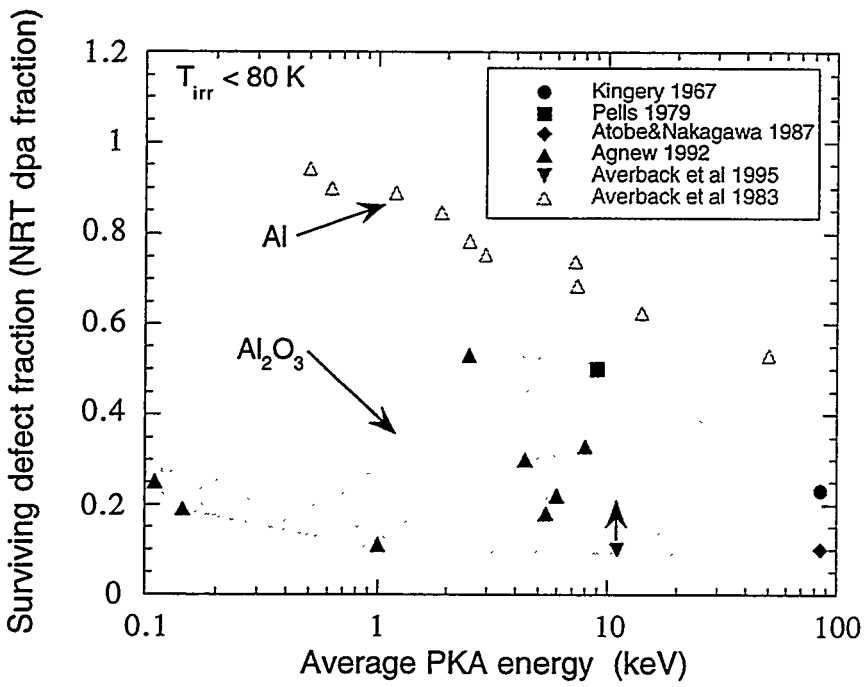

Fig. 1. Comparison of the defect production efficiency in Al_2O_3 [4-7] and Al [9].

energy PKAs, since their average separation distance could be comparable to the spontaneous recombination distance. However, molecular dynamics calculations on MgO indicate that the spontaneous recombination volume is only slightly larger than typical values for metals [13]. It has also been noted that the low atomic mass and high melting point of Al_2O_3 would inhibit the formation of the dense displacement cascades which are responsible for the decrease in displacement damage efficiency in metals at high PKA energies [7]. Rigorous analysis of the experimental data base is hampered by a lack of information on interstitial migration energies in MgO and Al_2O_3 [10]. Several studies suggest that interstitials in Al_2O_3 may be mobile at temperatures below 80 K (corresponding to migration energies of 0.2 to 0.8 eV) [4,14], whereas other authors have concluded that interstitial migration only occurs at temperatures above 300 K with migration energies as high as 1.8 eV [7,15]. All of the Al_2O_3 data in Fig. 1 at PKA energies <10 keV are from Agnew [7], who performed irradiations at ~80 K. If interstitials in Al_2O_3 are mobile at 80 K, point defect recombination could explain the low measured values of the surviving defect fraction in Al_2O_3 compared to the Al data. The Al data were obtained at temperatures <10 K, where interstitials are immobile.

Another possible explanation for the low measured surviving defect fractions in MgO and Al_2O_3 at low PKA energies is associated with ionization-induced migration and recombination of point defects [16-18]. It is worth noting that typical low-PKA energy irradiation sources such as electrons and light ions produce high amounts of ionization per dpa. Therefore, if ionization-induced diffusion processes are operating, the relative importance of ionization-induced point defect recombination would be highest for the irradiation sources which were used to generate the low-PKA energy data.

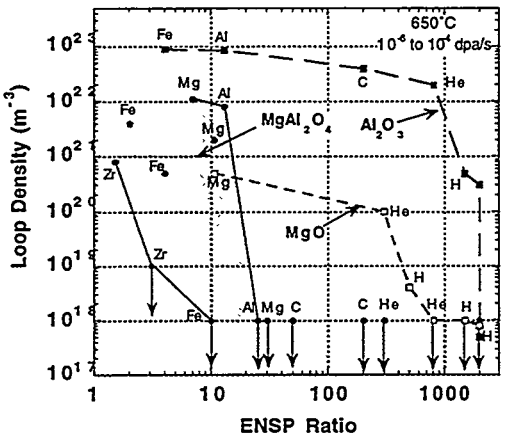

Fig. 3. Effect of ENSP ratio on the loop density in ion-irradiated ceramics.

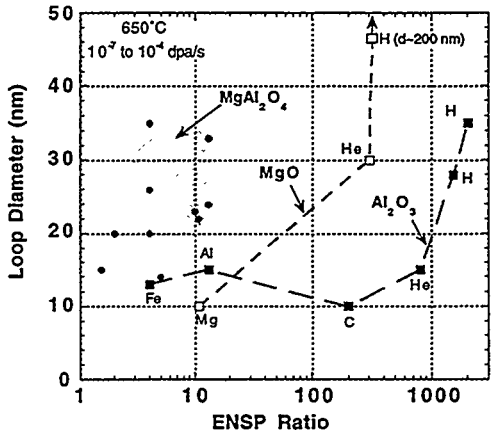

Fig. 4. Effect of ENSP ratio on the loop size in ion-irradiated ceramics.

Measurements of the dislocation loop size and density were performed on cross-section TEM specimens of $MgAl_2O_4$, Al_2O_3 and MgO following ion irradiation at 650°C. Quantitative measurements were typically obtained at one or two depths in regions that were at least 0.3 μm from the irradiated surface and implanted ion region. Both MgO and Al_2O_3 were found to be relatively insensitive to variations in the ion mass for ions heavier than He. However, dramatic decreases in the midrange dislocation loop density occurred in MgO and Al_2O_3 for helium ion and proton irradiations, respectively. Figures 3 and 4 summarize the loop density and size measurements as a function of the ENSP ratio for the 3 ceramics irradiated with different MeV ions at 650°C at damage rates between 10^{-6} and 10^{-3} dpa/s. Measurements were typically obtained at several depths (with corresponding different ENSP ratios) for each type of ion, as labeled in Figs. 3 and 4. A sharp decrease in the loop density occurred in $MgAl_2O_4$ for ENSP ratios greater than ~10. The corresponding critical ENSP ratios for MgO and Al_2O_3 were ~500 and ~1500, respectively. Further work is needed to establish the effect of temperature and dose rate on these critical ENSP values. The loop density and size were only weakly dependent on the ENSP ratio below the critical value. It is noteworthy that the loop size increases significantly in the same position where the loop density sharply decreases. The decrease in loop density and concomitant increase in loop size (coarsening) above a critical ENSP ratio is indicative of enhanced point defect diffusion, according to standard chemical rate theory. The increase in loop size associated with the decrease in loop density indicates that ionization-induced diffusion is the principle mechanism responsible for the irradiation spectrum effect. However, it is also possible that ionization-enhanced point defect recombination may be contributing to the observed sensitivity to irradiation spectrum.

The dislocation loop data for spinel exhibits a transition from a high density of small loops to a low density of large loops for ENSP ratios of ~2 to ~20 for different ions, suggesting that there may be an underlying PKA spectrum effect. However, most of the scatter in the spinel data disappears if the loop parameters are plotted vs. the ratio of the total ionization per unit damage energy (TI-DE). An analysis of the data plotted in Figs. 3 and 4 indicates that the critical TI-DE ratio for spinel is ~15, corresponding to ~60 electron-hole pairs per dpa. The corresponding critical TI-DE ratios for MgO and Al_2O_3 are ~1000 and 2000, respectively (~4000 and ~10^4 electron-hole pairs per dpa).

In summary, it appears that the observed irradiation spectrum effect on the microstructure of ion irradiated oxide insulators is primarily associated with ionization-induced diffusion processes. Both vacancy and interstitial diffusion appear to be promoted by ionizing radiation. However, the possibility that PKA energy spectrum and ionization-enhanced point defect recombination processes may be exerting some influence on the microstructural evolution cannot be discounted. A brief overview of ionization-induced point defect diffusion processes is given in the following section.

As discussed elsewhere, very little is known about the interstitial migration energies in Al_2O_3 and $MgAl_2O_4$ [10]. Several radiation effects studies on Al_2O_3 have suggested that interstitial migration does not occur until temperatures of ~300 and 700 K for the oxygen and aluminum sublattices, respectively [7,19], which corresponds to an activation energy of ~1.6 eV for the slower defect (Al in this case). Conversely, Kingery [4] concluded that interstitial migration occurred in Al_2O_3 with a range of activation energies between 0.2 and 0.8 eV. A rough estimate of the migration energy of the rate-determining (slower) interstitial for the cation and anion sublattices can be determined from measurements of the width of the denuded zone adjacent to internal sinks such as grain boundaries in irradiated materials. As shown elsewhere [20], the width of the loop denuded zone (L) adjacent to a point defect sink can be derived from simple chemical rate theory equations in the limiting case of high sink densities ($C_s > 10^{14}/m^2$) to be

$$L = \frac{D_i C_i^{crit} \sqrt{C_s}}{P} \qquad (2)$$

where P is the displacement damage rate, D_i is the interstitial diffusivity, and C_i^{crit} is the threshold matrix interstitial concentration to produce observable dislocation loop nucleation. Chemical rate theory models for metals have found that $C_i^{crit} \sim 10^{-14}$/atom [21]. In this simple analysis, it is assumed that the presence of a denuded zone is indicative of an insufficient interstitial concentration on both the anion and cation sublattices (i.e., it is assumed that the increased sink strength associated with cluster nucleation by the slower-moving interstitial species would lead to capture of the faster-moving interstitial species and subsequent stoichiometric interstitial loop formation). Using this assumption, the interstitial diffusivity in Eq. 2 is associated with the slower-moving interstitial species. Based on microstructural measurements [20,22] of the midrange loop sink strength and the grain boundary denuded zone width of 15 nm for Al_2O_3 irradiated with 2-MeV Al^+ ions at 650°C, the estimated interstitial diffusivity is $\sim 10^{-10}$ m^2/s. This corresponds to a migration energy of ~0.8 eV, assuming typical values for the pre-exponential factor (Eq. 1). It should be noted that impurity trapping effects may have reduced the effective interstitial mobility in the denuded zone width measurements. Therefore, the migration energy of ~0.8 eV is likely an upper limit to the intrinsic (impurity-free) value in Al_2O_3. This estimate of the interstitial migration energy is subject to considerable uncertainty, particularly since the value of C_i^{crit} is not reliably known. However, the migration energy of $\leq$0.8 eV for the slower-moving interstitial species appears to be in reasonable agreement with the measurement by Kingery [4]. Further support that the migration energy for the slower-moving anion or cation interstitial is ~0.5-1 eV in Al_2O_3 comes from TEM observations that faulted interstitial dislocation loops were readily formed during 4 MeV Ar^+ ion irradiation at 300 K, whereas resolvable loops were not detected in specimens irradiated at 200 K to the same dose of 10 dpa [23,24].

The migration energy for the slowest interstitial species in $MgAl_2O_4$ can be estimated using the same technique. For example, using the measured loop sink strength and the grain boundary denuded zone width of 250 nm [20] for spinel irradiated with 2-MeV Al^+ ions under identical conditions to that used for the alumina specimen, the estimated diffusivity is

~10^{-8} m^2/s. This corresponds to a migration energy of ~0.4 eV. Once again, this is likely an upper limit to the intrinsic migration energy of the slowest interstitial species, since impurity trapping effects may have reduced the effective interstitial mobility in the experimental measurements. There are no known measurements of interstitial migration energies in spinel with which this estimate can be compared.

Summary of Ionization-Induced Diffusion Processes

The pronounced coarsening in the dislocation loop microstructure above a critical value of the ENSP ratio, along with the absence of dislocation loops in ionization-rich irradiation environments, suggest that the observed irradiation spectrum dependence in the three oxide ceramics (Figs. 3,4) may be primarily associated with ionization-induced diffusion effects. According to simple chemical rate theory, the steady state concentration of point defects ($C_{i,v}$) is proportional to $P/(D_vC_s)$ and $P/(D_iC_s)$ for vacancies and interstitials, respectively for sink-dominant conditions, where C_s is the sink strength and P is the displacement damage rate [25,26]. The corresponding steady state concentrations for point defect recombination-dominant conditions are proportional to $(P/D_v)^{1/2}$ and $(PD_v/D_i^2)^{1/2}$ for vacancies and interstitials, respectively. Therefore, for both sink- and recombination-dominant conditions, the matrix point defect concentrations are reduced for high diffusivities. If the point defect concentration falls below the critical level needed to produce significant loop nucleation (~10^{-14}/atom for interstitials), then dislocation loops would not be observed in the irradiated region.

Several different mechanisms for enhanced point defect diffusion associated with ionizing radiation have been proposed for nonmetals [16,17,27,28]. The "electrostriction" mechanism is based on the possibility that a high concentration of electron-hole pairs in the conduction band may alter the bond lengths (local lattice parameter) and consequently the point defect migration energy. The "energy release" mechanism assumes that electron-hole pair recombination (or energy released by de-excitation of an excited state) may provide sufficient thermal energy to induce point defect migration. These two diffusion mechanisms are discussed in detail elsewhere [16,17,27,28] and will not be considered further. The "normal ionization-enhanced diffusion" mechanism (more appropriately called "normal IID") is based on the concept that a point defect in an ionized charge state may have a significantly lower migration energy compared to a non-ionized defect. A final intriguing diffusion mechanism is the "Bourgoin-Corbett" (bistable defect) mechanism. In this mechanism, athermal point defect migration is possible if the stable site for the ionized charge state corresponds to the migration saddle point for the non-ionized defect charge state, and vice versa.

The bistable defect configuration has been reported for Si and Ge interstitials [17]. Recent calculations for oxygen interstitial migration in MgO indicate that the ground state lattice position is (111) dumbbell and the O^{2-} lattice position is the cube centered site, with the lowest energy saddle point for the O^{2-} interstitial being the (111) dumbbell [29]. Therefore, ionization-induced athermal migration via the Bourgoin-Corbett mechanism appears to be possible for the MgO oxygen interstitial. Corresponding calculations for the Mg sublattice in MgO or for the point defects in Al_2O_3 or $MgAl_2O_4$ are not available. Oxygen vacancy migration in MgO or Al_2O_3 via the Bourgoin-Corbett mechanism does not appear to be possible, since quantum chemical calculations indicate that non-ionized and ionized vacancies occupy the same lattice site in these materials [30,31]. A simple estimate of the magnitude of point defect diffusion possible via the Bourgoin-Corbett mechanism can be obtained by assuming that the rate-limiting step is ionization of the point defect (i.e., by assuming that the time for the ionized defect to reacquire a free electron and return to the ground state is negligible) and by assuming that point defect ionization by capture of migrating holes is negligible. Assuming random-walk diffusion in a simple cubic lattice, the

diffusion coefficient can be written as $D \sim 1/6\ a^2\ \Gamma$, where Γ is the jump frequency (point defect ionization frequency) and a is the jump distance associated with the two hops by the ionized and ground state defect (roughly equal to the lattice parameter). The atomic ionization frequency in MgO for a typical medium-mass ion beam current of ~1 $\mu A/cm^2$ (~1 MGy/s ionizing dose rate) is $\Gamma \sim 0.01$ ionizations/atom-s, assuming a bandgap energy of 10 eV. The resultant diffusion coefficient for this ionizing dose rate is $D \sim 2 \times 10^{-22}$ m^2/s, which would produce a minuscule random-walk diffusion distance of ~1 nm in 1 hour.

From this simple calculation, it appears that the Bourgoin-Corbett bistable defect mechanism would generally produce negligible amounts of long-range interstitial migration in MgO for most experimental irradiation conditions. On the other hand, this athermal defect migration mechanism would be an efficient method for correlated "close-pair" point defect recombination. This IID mechanism also offers a possible explanation for the observed amorphization resistance of irradiated MgO at low temperatures, since it is unlikely that the critical levels of atomic disordering (chemical mixing) necessary to induce amorphization could be achieved if close-pair point defect recombination occurred readily. This mechanism may also be responsible for the observed sublinear accumulation rate of oxygen vacancies (F centers) in MgO irradiated at 4 K with 2.2 MeV electrons [12]. Since the maximum irradiation dose of <0.001 dpa was too low for saturation of the defect density to occur, the sublinear accumulation rate suggests that athermal impurity or oxygen interstitial migration (with resultant uncorrelated point defect recombination) may have occurred.

Several studies have obtained evidence that ionized point defects in semiconductors [16,17] and insulators [29] may have a lower migration energy than non-ionized defects, as proposed by the "normal IID" mechanism. The calculations for MgO indicate that the migration energies for ionized oxygen interstitials and vacancies may be 40 to 80% of the ground state migration energies [29,30]. A key uncertainty for quantification of the amount of diffusion possible via this mechanism is the lifetime of the ionized point defect. If the point defect rapidly reacquires an electron during migration through the lattice then, by analogy with the preceding Bourgoin-Corbett mechanism calculation, the "normal IID" mechanism would not produce a significant contribution to long-range diffusion. Ionized point defect lifetimes of >1 μs would generally be necessary to produce significant long-range diffusion for typical ion irradiation conditions in ceramic insulators.

CONCLUSIONS

Published surviving defect fraction (production efficiency) measurements for MgO and Al_2O_3 show a surprisingly weak dependence on PKA energy, with a typical value of ~30% of the modified Kinchin-Pease displacements for PKA energies between ~0.1 and 100 keV. It is possible that ionization-induced diffusion processes associated with the ionization-rich low PKA energy irradiations (electrons, light ions) may have caused correlated (and uncorrelated) point defect recombination and thereby produced an underestimate of the "intrinsic" stable defect production rate at low PKA energies.

Significant irradiation spectrum effects have been observed in dislocation loop microstructures of ion-irradiated MgO, Al_2O_3 and $MgAl_2O_4$. Loop formation is inhibited for irradiation with light ions. The sensitivity to irradiation spectrum appears to be primarily associated with ionization-induced diffusion effects, although PKA spectrum and ionization-enhanced point defect recombination effects may also be playing a role. Additional data obtained at different temperatures and dose rates, along with rate theory modeling, are needed in order to better understand the physical processes responsible for the observed dependence of the microstructure on irradiation spectrum.

The rate-limiting interstitial migration energies for Al_2O_3 and $MgAl_2O_4$ are estimated to be ~0.8 eV and ~0.4 eV, respectively for irradiation conditions where ionization-induced diffusion should not have a strong influence. Ionization-induced diffusion is expected to reduce these migration energies, but calculated values for the migration energies of ionized point defects are not available for either of these two materials.

REFERENCES

[1] L.W. Hobbs, J. Amer. Ceram. Soc. 62 (1979) 267.
[2] F.W. Clinard, Jr. and L.W. Hobbs, in Physics of Radiation Effects in Crystals, eds. R.A. Johnson and A.N. Orlov (Elsevier Science Publishers, Amsterdam, 1986) p. 387.
[3] L.W. Hobbs, F.W. Clinard, Jr., S.J. Zinkle and R.C. Ewing, J. Nucl. Mater. 216 (1994) 291.
[4] W.D. Kingery, J. Nucl. Mater. 24 (1967) 21.
[5] G.P. Pells, A.E.R.E. Harwell Report AERE-R9359 (1979).
[6] K. Atobe and M. Nakagawa, Cryst. Latt. Def. Amorph. Mater. 17 (1987) 229.
[7] P. Agnew, Nucl. Instr. Meth. B 65 (1992) 305.
[8] R.S. Averback, P. Ehrhart, A.I. Popov and A.v. Sambeek, Rad. Effects Def. Solids 136 (1995) 169.
[9] R.S. Averback et al., J. Nucl. Mater. 113 (1983) 211.
[10] S.J. Zinkle and C. Kinoshita, J. Nucl. Mater. (1997) in press.
[11] A.E. Hughes, J. Physique 34, Colloque C9 (1973) 515.
[12] C. Scholz and P. Ehrhart, in Beam Solid Interactions: Fundamentals and Applications, MRS Symposium Proceedings vol. 279, eds. M. Nastasi et al. (Materials Research Society, Pittsburgh, 1993) p. 427.
[13] T. Sonoda, C. Kinoshita and Y. Isobe, Annales de Physique 20, Colloque C3 (1995) 33.
[14] R.T. Cox, Phys. Lett. 21 (1966) 503.
[15] T.D. Gulden, Philos. Mag. 15 (1967) 453.
[16] J.C. Bourgoin and J.W. Corbett, Rad. Effects 36 (1978) 157.
[17] J.C. Bourgoin, Rad. Effects Def. Solids 111&112 (1989) 29.
[18] L.C. Kimerling, Solid-State Electronics 21 (1978) 1391.
[19] G.P. Pells, Rad. Phys. Chemisty 22 (1983) 1053.
[20] S.J. Zinkle, in 15th Int. Symp. on Effects of Radiation on Materials, ASTM STP 1125, eds. R.E. Stoller, A.S. Kumar and D.S. Gelles (American Society for Testing and Materials, Philadelphia, 1992) p. 749.
[21] R.E. Stoller, 1996.
[22] S.J. Zinkle, in Microstructure of Irradiated Materials, MRS Symposium Proceedings vol. 373, eds. I.M. Robertson et al. (Materials Research Society, Pittsburgh, 1995) p. 287.
[23] S.J. Zinkle and L.L. Snead, Nucl. Instr. Meth. B 116 (1996) 92.
[24] S.J. Zinkle and G.P. Pells, J. Nucl. Mater. (1997) to be publ.
[25] R. Sizmann, J. Nucl. Mater. 69&70 (1978) 386.
[26] L.K. Mansur, J. Nucl. Mater. 206 (1993) 306.
[27] J.W. Corbett and J.C. Bourgoin, IEEE Trans. Nucl. Sci. NS-18 (1971) 11.
[28] J.C. Bourgoin and J.W. Corbett, J. Chem. Phys. 59 (1973) 4042.
[29] T. Brudevoll, E.A. Kotomin and N.E. Christensen, Phys. Rev. B 53 (1996) 7731.
[30] E.A. Kotomin, M.M. Kuklja, R.I. Eglitis and A.I. Popov, Mater. Sci. Eng. B 37 (1996) 212.
[31] A. Stashans, E.A. Kotomin and J.-L. Calais, Phys. Rev. B 49 (1994) 14854.

DEFECT PRODUCTION IN CERAMICS* — S.J. Zinkle (Oak Ridge National Laboratory) and C. Kinoshita (Kyushu University)

Extended Abstract

A review is given of several important defect production and accumulation parameters for irradiated ceramics. Materials covered in this review include alumina, magnesia, spinel, silicon carbide, silicon nitride, aluminum nitride and diamond. Whereas threshold displacement energies for many ceramics are known within a reasonable level of uncertainty (with notable exceptions being AlN and Si_3N_4), relatively little information exists on the equally important parameters of surviving defect fraction (defect production efficiency) and point defect migration energies for most ceramics. Very little fundamental displacement damage information is available for nitride ceramics. The role of subthreshold irradiation on defect migration and microstructural evolution is also briefly discussed.

Based on a review of published experimental measurements, the threshold displacement energies for SiC, diamond and alumina (oxygen sublattice) should be revised downward from previously recommended values (cf. Table 1). Additional E_d measurements on BeO, $MgAl_2O_4$ and SiC are needed to supplement the existing data base. Furthermore, experimental E_d measurements are particularly needed for AlN and Si_3N_4, where no data currently exist.

Considerable uncertainty exists regarding the quantitative values of point defect migration enthalpies in ceramics. Some of this uncertainty is likely associated with ever-present impurity trapping effects, which increase the apparent migration energy. On the other hand, radiation induced diffusion processes such as ionization induced diffusion or subthreshold elastic collisions may produce low apparent migration energies during irradiation. The available data (Table 2) indicate that interstitials are mobile in MgO and Al_2O_3 at temperatures well below room temperature, whereas vacancies become mobile above ~200°C in both materials. The significant interstitial mobility at room temperature has not been taken into account in numerous published radiation effects studies on Al_2O_3 and MgO. Further experimental radiation effects studies at liquid helium temperatures (combined with isochronal annealing) would be valuable in determining the interstitial migration energies for all ceramic materials.

Very few reliable measurements of the surviving defect fraction (displacement damage efficiency) exist for ceramics. Most of the published work was performed at room temperature, and the data analysis did not account for likely correlated and uncorrelated recombination of point defects. Therefore, the reported values are typically an underestimate of the surviving defect fraction. The limited number of cryogenic irradiation studies on MgO and Al_2O_3 suggest that the surviving defect fraction is ~0.3 for both materials over a wide range of PKA energies (0.1-100 keV). This apparent independence on PKA energy is in sharp contrast to work performed on light metals such as aluminum, where the surviving defect fraction (relative to the NRT calculated displacements) varies from ~1 to ~0.5 as the PKA energy increases from ~0.1 to ~50 keV. Additional experimental work is needed to evaluate the importance of correlated and uncorrelated point defect recombination effects (in conjunction with ionization induced diffusion) on the measured defect production rates in ceramics.

There is considerable evidence that the irradiation spectrum (particularly ionizing radiation) can have a pronounced effect on the microstructural evolution in ceramics and semiconductors. Recent work on MgO, Al_2O_3 and $MgAl_2O_4$ suggests that a dramatic transition in the microstructural

*Extended abstract of paper to be published in Journal of Nuclear Materials (proceedings of the International Workshop on Defect Production, Accumulation and Materials Performance in Irradiation Environment, Davos, Switzerland, October 2-8, 1996).

evolution occurs at a certain ratio of the electronic to nuclear stopping power. The observed microstructure in these materials also appears to be sensitive to the magnitude of the ionizing radiation dose rate. On the other hand, ionizing radiation does not appear to have a pronounced influence on the microstructure of some ceramics such as SiC. Further work is needed to quantify the role of ionizing dose rate and PKA spectrum on the microstructural evolution of ceramics.

Table 1. Recommended threshold displacement energies in ceramics

Material	Threshold displacement energy	Comments
Al_2O_3	E_d^{Al}~20 eV, E_d^O=50 eV	previous "standard" value for E_d^O was 76 eV
MgO	E_d^{Mg}=55 eV, E_d^O=55 eV	good agreement among 5 studies
CaO	E_d^O=60 eV	only 1 known measurement
$MgAl_2O_4$	E_d^O=60 eV	only 1 known measurement
ZnO	E_d^{Zn}~50 eV, E_d^O=55 eV	moderate uncertainty in E_d^{Zn}
BeO	E_d^{Be}~25 eV, E_d^O~70 eV?	large uncertainty in data
UO_2	E_d^U=40 eV, E_d^O=20 eV	only 1 known measurement
SiC	E_d^{Si}~40 eV?, E_d^C=20 eV	large uncertainty in E_d^{Si}
graphite	E_d^C=30 eV	extensive data base
diamond	E_d^C=40 eV	4 known measurements

Table 2. Summary of experimental and calculated point defect migration energies in MgO and Al_2O_3

Material	Point defect	Migration energy
MgO	Mg vacancy	2.0-2.3 eV
"	O vacancy	2.0-2.5 eV
"	Mg, O interstitials	0.5-1.5 eV
"	Mg, O interstitials	≤0.2 eV
Al_2O_3	Al vacancy	1.8-2.1 eV (<1 eV)
"	O vacancy	1.8-2 eV (1.1 eV)
"	Al, O interstitials	0.2-0.8 eV

7.0 SOLID BREEDING MATERIALS

No contributions.

8.0 RADIATION EFFECTS, MECHANISTIC STUDIES, AND EXPERIMENTAL METHODS

EFFECTS OF IN-CASCADE DEFECT CLUSTERING ON NEAR-TERM DEFECT EVOLUTION -
H.L. Heinisch (Pacific Northwest National Laboratory)*

OBJECTIVE

The objective of this work is to determine the energy and temperature dependence of defect production and microstructure evolution for the development of fission-fusion correlations.

SUMMARY

The effects of in-cascade defect clustering on the nature of the subsequent defect population are being studied using stochastic annealing simulations applied to cascades generated in molecular dynamics (MD) simulations. The results of the simulations illustrate the strong influence of the defect configuration existing in the primary damage state on subsequent defect evolution. The large differences in mobility and stability of vacancy and interstitial defects and the rapid one-dimensional diffusion of small, glissile interstitial loops produced directly in cascades have been shown to be significant factors affecting the evolution of the defect distribution. In recent work, the effects of initial cluster sizes appear to be extremely important.

PROGRESS AND STATUS

Introduction

The production of defect clusters directly in cascades in copper is well established, both in atomic-scale MD computer simulations [1,2] and experimentally in results of diffuse x-ray scattering experiments [3]. The consequences of intracascade clustering of self-interstitial atoms (SIAs) and vacancies, and of the thermal stability of these clusters, have been specifically addressed in the recently proposed "Production Bias Model" (PBM) [4]. The PBM has been further developed to account for the very important consequences of one-dimensional transport of small, glissile SIA clusters [5,6] and of the continuous transformation of larger sessile SIA clusters into glissile ones due to their interactions with single vacancies[7]. The PBM or any other such model can predict the global behavior of the system over macroscopic sizes and times. However, it has the limitation of not being able to deal explicitly with the problem of temporal and spatial fluctuations in the defect cluster production and size distributions occurring continuously under cascade damage conditions. At present, these cascade phenomena are dealt with by assuming some global average values for the relevant parameters. Clearly, accurate and reliable predictions from the PBM or other such models are possible only if physically realistic values for their input parameters can be obtained either experimentally (unlikely) or from atomic-scale models that include explicit temporal and spatial information. The determination of parameters for PBM from results of these models is, therefore, of crucial importance.

---

*Pacific Northwest National Laboratory is operated for the U.S. Department of Energy by Battelle Memorial Institute under Contract DE-AC06-76RLO 1830.

Even after the longest practical MD simulation, the defect clusters of a single cascade remain spatially localized in a "metastable" state far from the spatial and temporal uniformity required for the global picture to which rate theory may be applied. Atomic scale stochastic annealing simulation provides the necessary link between the localized, short-term, atomistic view of individual MD cascades and the spatially averaged global view required for the application of rate theory. In the present work, stochastic annealing simulations are being done on individual, isolated cascades, as well as on simulated irradiations represented by continuous introduction of new cascades into an annealing volume with periodic boundaries. Preliminary results of the effects of clustering are presented here.

Clusters of Self-interstitial Atoms

Self-interstitial atoms form small clusters in cascades, with size up to n = 14 SIAs observed in x-ray scattering experiments [3]. In MD simulations, SIA clusters up to about size n = 15 are observed [1], and small (n = 4-6) clusters have been observed to form initially sessile loop configurations that unfault to glissile loops on (110) planes within picoseconds after the cascade occurs [2]. In earlier annealing simulations performed in the present program [8], it was assumed that SIA clusters up to n = 9 spontaneously become glissile loops, while larger clusters become sessile loops requiring greater energy to unfault. Little is known about the kinetics and energetics of SIA loops in copper, but MD-based studies are in progress elsewhere. The consequences of changing the assumptions of the earlier annealing simulations are being determined to study the effects of defect cluster properties.

In earlier work [8], cascades in copper generated with MD at 25 keV [1] were annealed as individual, isolated cascades as a function of temperature. Even at temperatures above 0.3 T_m (melting temperature), where all vacancy clusters dissociate, the SIA clusters with n > 9, which were assumed sessile, remained essentially intact in the cascade region, unaffected by the dissipation of the local vacancy concentration. In recent annealing simulations using lower energy cascades of 5-10 keV [2], which have no clusters/loops larger than n = 9, all SIA clusters escape the cascade region, except for a very few cases where clusters coalesce to form sessile clusters. Thus, with the present model (SIA loops up to n = 9 being glissile), there is a significant energy dependence in the annealing stage of cascades that is manifested at relatively high cascade energy. If the maximum allowable size of glissile SIA loops is increased in the model, all SIA loops escape the cascade region at all energies, as expected. Clearly, more details of loop formation are needed.

Defect evolution during irradiation is being studied by performing annealing simulations on fluxes of recoils represented by cascades of various energies placed randomly in space and time into a large, periodic volume. Dose rates and total doses are well below where cascade overlap would be expected. A very low sink density is represented by absorption of mobile defects that have traveled at least several microns, which is simulated by their wrapping around the periodic boundaries a limiting number of times. Using 5-25 keV cascades in the approximate ratios representing a fast reactor irradiation, and with the present n = 9 glissile SIA loop limit, the net vacancy population initially dominates at 400 K. However, during the simulation the population of large sessile SIA clusters eventually builds to become quite dominant. Reduction of large sessile loops to glissile size by absorption of vacancies does not occur under the conditions studied. To achieve a

vacancy super saturation, it is probably necessary to let SIA clusters much larger than n=9 be glissile or easily become glissile.

Vacancy Clusters

Vacancy clustering is observed in MD simulations [1,2] usually as somewhat organized agglomerations of vacancies. The very stable stacking fault tetrahedra (SFT) have not been observed to form during the time that can be followed by MD simulations. At temperatures well above 0.3 T_m the amount of vacancy clustering in cascades is not particularly important, since clusters are quite unstable at those temperatures. At lower temperatures, the vacancy cluster distribution in cascades can have an effect on the fraction of vacancies that escape from the cascades. Figure 1 shows the fractions of escaping vacancies as a function of temperature for cascades of various energies. The 25 keV cascades, containing some larger, more stable vacancy clusters, display a different temperature dependence than the lower energy cascades, which contain only a few small clusters that easily dissociate at lower temperatures. Thus, the clustering behavior of vacancies in cascades also results in a recoil energy dependence. However, when the potential formation of more stable vacancy configurations (e.g. SFT) is taken into account, the effect may be somewhat different from that displayed in Fig. 1.

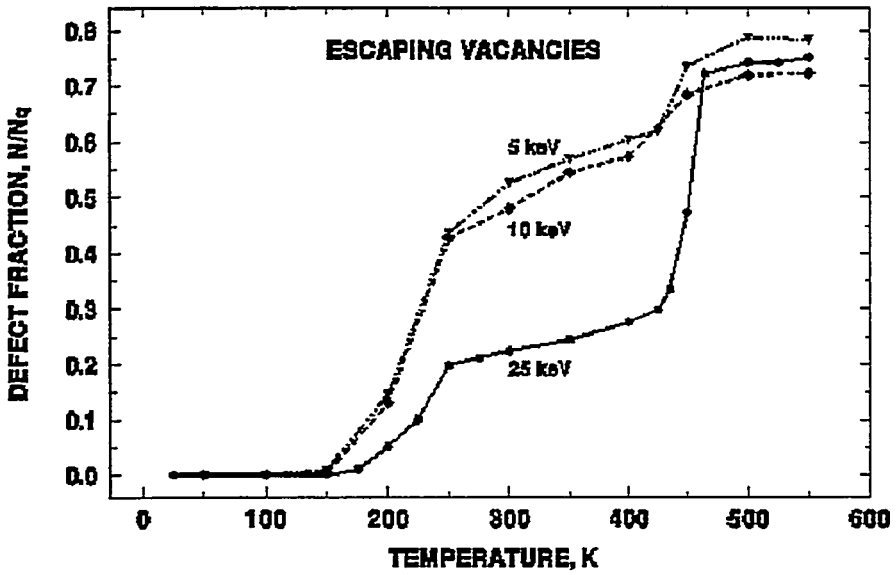

Figure 1. The fractions of vacancies escaping from the cascades during annealing as a function of annealing temperature. The fractions are relative to the initial number of vacancies at the end of the MD simulation in each cascade.

CONCLUSIONS

The preliminary results in this study indicate that defect evolution beyond the primary damage state modeled by MD simulations is sensitive to the characteristics of cluster formation in cascades. To make models more realistic, it is necessary to know more details about the production, migration and interaction of both SIA and vacancy clusters. More MD cascades are needed to get good statistics on cluster production. MD studies are needed to determine the characteristics of loop formation, especially sessile-glissile transformations, migration energies, glide direction changes and loop interaction characteristics. In the absence of this information, stochastic annealing simulations will be used to explore the consequences of variation in the relevant parameters.

FUTURE WORK

The effects of glissile SIA loop migration characteristics are being investigated in annealing simulations. Thermally-activated and interaction-stimulated changes in glide direction are being incorporated into the model along with sessile-glissile transformations. This work will be reported on at ICFRM-8.

REFERENCES

1. T. Diaz de la Rubia and M.W. Guinan, Mat. Sci. Forum 97-99 (1992) 23.

2. A.J.E. Foreman, W.J. Phythian and C.A. English, Philos. Mag. A66 (1992) 671.

3. R. Rauch, J. Peisl, A. Schmalzbauer and G. Wallner, J. Nucl. Mater. 168 (1989) 101.

4. C.H. Woo and B.N. Singh, Phys.Stat. Sol. (b) 159 (1990) 609; Philos. Mag. A65 (1992) 889.

5. H. Trinkaus, B.N. Singh and A.J.E. Foreman, J. Nucl. Mater. 199 (1992) 1; J. Nucl. Mater. 206 (1993) 200.

6. H. Trinkaus, B.N. Singh and A.J.E. Foreman, J. Nucl. Mater. 212-215 (1994) 18.

7. B.N. Singh, S.I. Golubov, H. Trinkaus, A. Serra, Yu.N. Osetsky and A.V. Barashev, J. Nucl. Mater. in press.

8. H.L. Heinisch and B.N. Singh, J. Nucl. Mater., in press.

INFLUENCE OF SUBCASCADE FORMATION ON DISPLACEMENT DAMAGE AT HIGH PKA ENERGIES — R. E. Stoller (Oak Ridge National Laboratory) and L. R. Greenwood (Pacific Northwest National Laboratory)

(Summary of a paper presented at 1997 TMS Symposium on Materials for Spallation Neutron Sources, submitted for publication to TMS)

Extended Abstract

The design of first generation fusion reactors will have to be rely on radiation effects data obtained from experiments conducted in fission reactors. Two issues must be addressed to use this data with confidence. The first is differences in the neutron energy spectrum, and the second is differences in nuclear transmutation rates. Differences in the neutron energy spectra are reflected in the energy spectra of the primary knockon atoms (PKA). The issue of PKA energy effects has been addressed through the use of displacement cascade simulations using the method of molecular dynamics (MD). Although MD simulations can provide a detailed picture of the formation and evolution of displacement cascades, they impose a substantial computational burden. However, recent advances in computing equipment permit the simulation of high energy displacement events involving more than one-million atoms [1-3]; the results presented here encompass MD cascade simulation energies from near the displacement threshold to as high as 40 keV. Two parameters have been extracted from the MD simulations: the number of point defects that remain after the displacement event is completed and the fraction of the surviving interstitials that are contained in clusters. The MD values have been normalized to the number of atomic displacements calculated with the secondary displacement model by Norgett, Robinson, and Torrens (NRT) [4].

The energy dependence of the two MD defect parameters was used to evaluate the effects of neutron energy spectrum. Simple, energy-dependent functional fits to the MD results were obtained, and the SPECOMP and SPECTER codes [5,6] were used to compute effective cross sections for point defect survival and point defect clustering. PKA spectra for iron obtained from SPECTER were then used to weight these effective cross sections in order to calculate spectrum-averaged values. In order to provide a broad comparison, values were obtained for several irradiation sites. These include: the 1/4-thickness position in the pressure vessel of a typical commercial pressurized water reactor (PWR), the peripheral target position (PTP) and a removable beryllium reflector position (RB*) of the HFIR, a midcore and below-core position (BC) in the FFTF, the first wall spectrum of Starfire [7], and the radiation effects facility in the intense pulsed neutron source (IPNS REF) in the Argonne National Laboratory [8,9]. Since the IPNS is a spallation neutron source with neutron energies up to the proton beam energy of 450 MeV, it produces PKA with even higher energies than does DT fusion.

The primary results of these calculations are summarized in Fig. 1. The PKA-spectrum-averaged defect survival fraction is shown in Fig. 1a, and the interstitial clustering fraction in Fig. 1b. In both cases, the effective production cross section has been divided by the NRT dpa cross section. The lowest point defect survival fraction is obtained in the Starfire FW as a result of the 14.1 MeV source term. However, the defect survival fractions shown in Fig. 1a are not simply determined by how hard the initial neutron energy spectrum is. For example, the survival fractions for IPNS and both FFTF sites are greater than any of the water moderated fission reactor spectra. An examination of the PKA spectra indicates that the results shown in Fig. 1a and 1b are generally dominated by PKA below 100 keV. Thus, average behavior is controlled by the details of the spectra in the low to intermediate energy region. Here the differences between the fission and Starfire PKA spectra are greater than those between fission and IPNS. Similarly, the average interstitial clustering fraction shown in Fig. 1b is only weakly dependent on the initial neutron energy spectrum. The average clustering fraction tracks the defect survival fraction (since only defects that survive can cluster), but the differences among the various environments are reduced because the energy dependence of interstitial clustering is opposite to that of defect survival [1-3].

Although the values shown in Fig. 1a and 1b for the Starfire first wall lie at the lower limit of all the sites illustrated, these results suggest that the nature of the displacement damage formed in a DT fusion reactor first wall should not be significantly different from that obtained in fission reactors. The average defect survival fraction is about 0.20 to 0.30 and the interstitial clustering fraction is about 0.10 to 0.15 for all the cases shown. In this case, the primary uncertainty regarding the use of such data is the impact of differences in transmutation production rates between the two environments.

References

1. R. E. Stoller, J. Nucl. Mater. 233-237 (1996) 999-1003.

2. R. E. Stoller, JOM 48 (1996) 23-27.

3. R. E. Stoller, G. R. Odette, and B. D. Wirth, "Primary Defect Formation in bcc Iron," presented at the International Workshop on Defect Production, Accumulation, and Materials Performance in Irradiation Environments, Davos, Switzerland, October 2-8, 1996, accepted for publication in J. Nucl. Mater.

4. M. J. Norgett, M. T. Robinson, and I. M. Torrens, Nucl. Eng. and Des. 33 (1975) 50-54.

5. L. R. Greenwood, "SPECOMP Calculations of Radiation Damage in Compounds," Reactor Dosimetry: Methods, Applications, and Standardization, ASTM STP 1001, H. Farrar IV and E. P. Lippincott, Eds., American Society of Testing and Materials, West Conshohocken, PA, 1989, pp. 598-602.

6. L. R. Greenwood and R. K. Smither, "SPECTER: Neutron Damage Calculations for Materials Irradiations," ANL/FPP/TM-197, Argonne National Laboratory, Argonne, IL, January 1985.

7. "STARFIRE - A Commercial Tokomak Fusion Reactor Power Plant Study," ANL/FPP-80-1, Argonne National Laboratory, Argonne, IL, September, 1980.

8. M. A. Kirk, R. C. Birtcher, T. H. Blewitt, L. R. Greenwood, R. J. Popek, and R. R. Heinrich, J. Nucl. Mater. 96 (1981) 37-50.

9. R. C. Birtcher, T. H. Blewitt, M. A. Kirk, T. L. Scott, B. S. Brown, and L. R. Greenwood, J. Nucl. Mater. 108 & 109 (1982) 3-9.

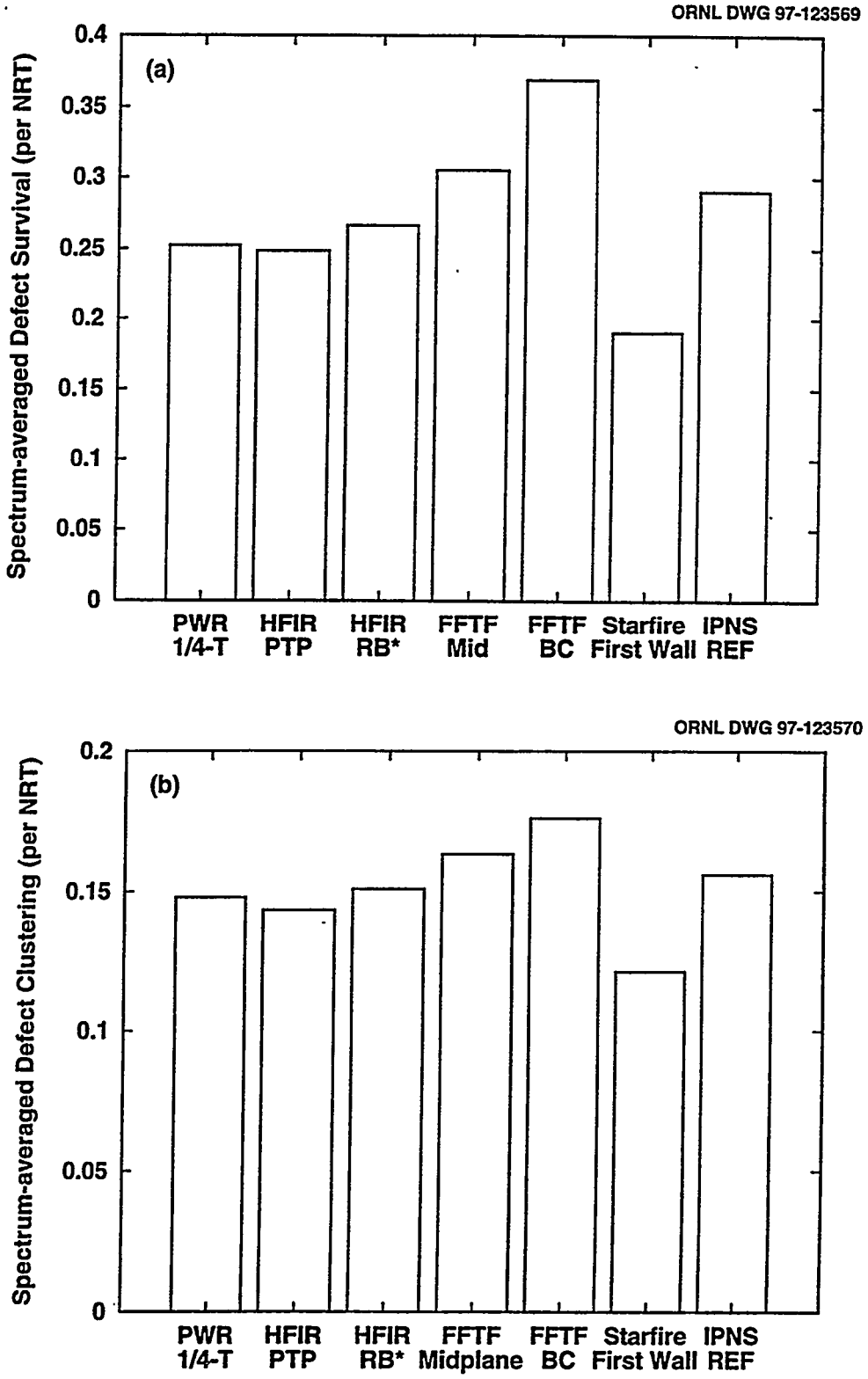

Figure 1. Comparison of spectrally-averaged damage production cross sections (per NRT dpa) for various irradiation environments; defect survival ratio is shown in (a) and the interstitial clustering fraction is shown in (b).

9.0 DOSIMETRY, DAMAGE PARAMETERS, AND ACTIVATION CALCULATIONS

ANALYSIS OF THE DHCE EXPERIMENT IN THE POSITION A10 OF THE ATR REACTOR*

I.C.Gomes, D. L. Smith, and H. Tsai, (Argonne National Laboratory)

OBJECTIVE

The objective of this work was to assess the suitability of the neutron flux spectrum of the A-10 irradiation position of the ATR reactor for a DHCE (Dynamic Helium Charging Experiment) experiment using Eu_2O_3 thermal neutron filter. The amount of tritium leaking from the capsule and the initial tritium charge to a reference capsule was calculated as well as the helium to dpa ratio during irradiation.

SUMMARY

Calculations were performed to assess the possibility of performing DHCE experiments in mixed spectrum fission reactors. Calculated values of key parameters were compared with limit values for each quantity. The values calculated were: He-4 production from the $^{6}Li(n,t)^{4}He$ reaction, tritium leakage, required tritium concentration in lithium, initial tritium charge per capsule, and helium to dpa ratio after 10 dpa of irradiation.

INTRODUCTION

In DHCE experiment the helium production induced by high energy neutrons from a fusion environment is simulated by the use of the decay of tritium to ^{3}He. Tritium is charged to a mother alloy at a level that after the diffusion during the irradiation due the temperature increase, the amount of tritium inside the vanadium samples are such that the correct amount of ^{3}He is produced at the same time that atomic displacements take place.

One aspect of having ^{3}He instead of ^{4}He is the high $^{3}He(n,p)^{3}H$ cross section. Figure 1 shows the cross section of that reaction. As can be seen the cross section has a 1/E behavior and it is as high as 5,000 barns in the thermal region. This fact implies that in a thermal neutron rich environment the produced ^{3}He would be burned and the helium production could not be simulated by the DHCE experiment. Then, the requirement of eliminating the thermal and as much as possible of the epithermal neutron flux is an imperative for the success of a DHCE experiment in a mixed spectrum fission reactor.

Another aspect that can be a limiting factor for the success of a DHCE experiment is the solubility limit of tritium in lithium or other thermal bonding material. This limitation comes from the fact that the distribution of tritium atoms between the thermal bonding material and the vanadium samples only applies for free atoms and when the tritium concentration is below the saturation limit.

In terms of helium production in the lithium due to the $^{6}Li(n,t)^{4}He$ reaction, there is the pressure limitation inside the capsule. The pressure inside for a typical irradiation capsule has to stay below roughly 20 atm. Then, the lithium enrichment has to stay below some limiting number to avoid excessive gas production inside the capsule and the excessive build-up of pressure.

The analysis of the tritium leakage becomes important because of reductions in available tritium for decay and possible restrictions associated with tritium contamination in the reactor.

---

*Work supported by Office of Fusion Energy, U.S. Department of Energy, under Contract W-31-109-Eng-38.

Relative to the transport of the DHCE capsules, a large tritium inventory inside the capsule creates problems for transporting the capsule and it may result in significative cost impact for the experiment. Then, the assessment of the required tritium inventory per capsule is an important issue.

Finally, a DHCE experiment must be designed to simulate the helium production in a fusion environment, which is roughly constant with the irradiation time. Then, the helium to dpa rate profile must be roughly constant during the irradiation.

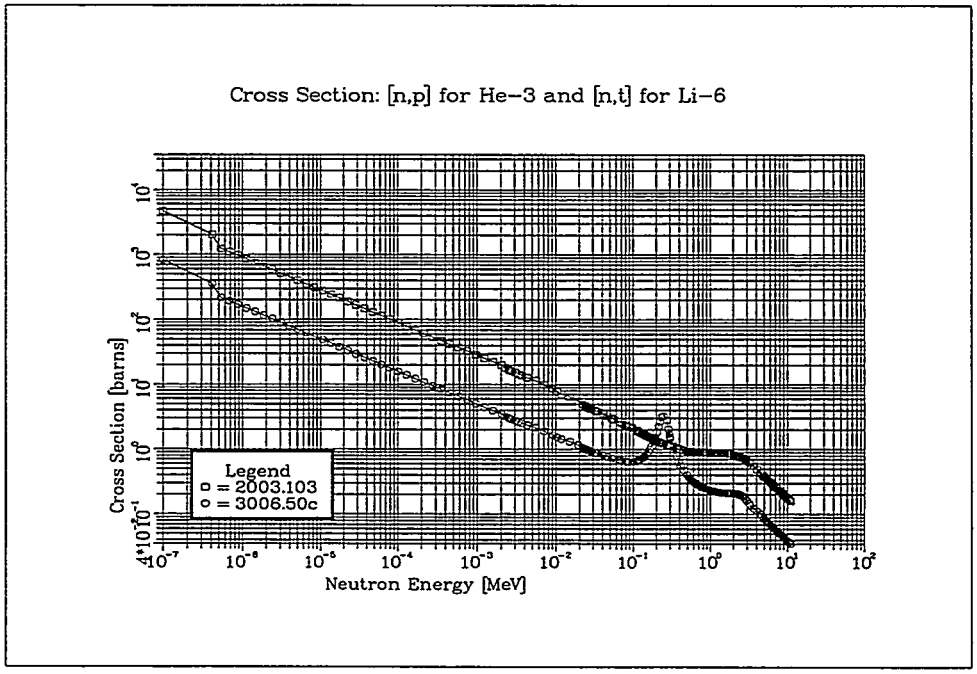

Figure 1. $^{3}He(n,p)^{3}H$ and $^{6}Li(n,t)^{4}He$ cross sections as a function of the incident neutron.

RESULTS AND DISCUSSION

Following are the aspects analyzed and the conclusion obtained from the calculations performed to assess a few parameters of a DHCE experiment in the position A-10 of the Advanced Test Reactor (ATR).

A- Total Helium production in Lithium below the equivalent maximum pressure inside the capsule.

The first part of the calculation was to define the maximum lithium enrichment that would produce a pressure inside the capsule below the 20 atm limit. The assumption assumed was conservative by nature, since it is considered that all ^{4}He produced would be in gas phase and as such contributing for the pressure build-up inside the capsule.

Assuming a gas plenum volume inside the capsule of 6 cm^3 (if this volume is reduced to 3 cm^3 the maximum number of helium atoms is reduced by a half) the maximum number of helium atoms that can be generated from the $^6Li(n, \alpha)\ ^3H$ reaction is:

Temp = 400°C => $N_{he} = 1.31x10^{21}$ ^4He atoms in the gas phase inside the capsule.

Temp = 425°C => $N_{he} = 1.26x10^{21}$ ^4He atoms in the gas phase inside the capsule.

Temp = 500°C => $N_{he} = 1.14x10^{21}$ ^4He atoms in the gas phase inside the capsule.

Temp = 600°C => $N_{he} = 1.01x10^{21}$ ^4He atoms in the gas phase inside the capsule.

The ^4He production rate from ^6Li inside the capsule, for a fixed irradiation facility and position, is basically dependent only on the neutron flux spectrum and intensity. For a mixed-spectrum reactor such as ATR the use of thermal neutron absorber to filter the neutrons is an imperative. Then, the ^4He production rate will basically depend on the filter material and its thickness. Table 1 presents the maximum ^6Li enrichment for a 2.9cm^3 volume of lithium inside the capsule, to keep the pressure below 20 atm. after 10 dpa in the A-10 position of ATR, for a few filter materials and thicknesses analyzed. It can be noted that the Eu_2O_3 filter (50% density) has a superior performance compared to other filter materials analyzed. The fact that a higher enrichment can be allowed indicates that a lower ^3He burn-up is also achieved.

Table 1. Maximum allowable ^6Li enrichment to maintain the pressure inside the capsule below 20 atm for a gas plenum volume of 6 cm^3.

	Temp=400°C	Temp=425°C	Temp=500°C	Temp=600°C
3 mm thick Eu_2O_3	12.2 %	11.8%	10.6%	9.5%
1 mm thick Eu_2O_3	6.85%	6.6%	6.0%	5.3%
3 mm thick Gd-nat	4.75%	4.6%	4.1%	3.6%
0.8mm thick Eu_2O_3 + 0.2 mm thick Gd	7.2%	6.9%	6.25%	5.5%
2 mm thick Gd-nat + 1 mm thick Hf-nat	5.9%	5.7%	5.2%	4.6%
2 mm thick Eu_2O_3 + 1 mm thick Hf-nat	7.6%	7.4%	6.7%	5.9%

B- Acceptable helium to dpa ratio.

The helium to dpa ratio that can be obtained using Eu_2O_3 filter with 50% density (in powder form) and the maximum ^6Li enrichment shown in Table 1 is dependent on the distribution coefficient (weight per cent of tritium in vanadium divided by the weight per cent of tritium in lithium) and on the irradiation temperature. Table 1 presents, for the cases considered (Eu_2O_3 filter with 3 and 1 mm thickness and TZM capsule walls with 1 and 2.5 mm, respectively), the helium to dpa ratios after 10 dpa of irradiation. These values are calculated considering an initial tritium charge equivalent to a tritium concentration in the vanadium samples of 1500 appm. It can be noted that although the helium to dpa ratio is not exactly 5, values relatively close to the target values can be obtained. The cause for the decrease in the helium to dpa ratio for high temperature irradiation is the increase in the tritium leakage from the capsule. A way to reduce the leakage is to increase the thickness of the TZM capsule wall or using other means to reduce the hydrogen permeability of the capsule walls.

Table 2. Estimated helium to dpa ratio after 10 dpa's of irradiation in the position A-10 of the ATR reactor using Eu_2O_3 thermal neutron filter.

3 mm thick Eu_2O_3 filter with 1 mm TZM capsule wall.

Distribution Coeff.	Temp=400°C	Temp=500°C	Temp=600°C
0.0200	7.4	6.8	4.3
0.0100	6.4	5.9	3.7
0.0050	5.9	5.5	3.5
0.0033	5.7	5.4	3.4
0.0020	5.6	5.3	3.3

1 mm thick Eu_2O_3 filter with 2.5 mm TZM capsule wall.

Distribution Coeff.	Temp=400°C	Temp=500°C	Temp=600°C
0.0200	6.2	5.9	4.7
0.0100	5.3	5.1	4.1
0.0050	4.9	4.8	3.9
0.0033	4.8	4.6	3.8
0.0020	4.7	4.6	3.7

C- Total amount of tritium dissolved in Lithium below the solubility limit.

The maximum calculated amount of tritium (in atom percent) dissolved in lithium during irradiation for a 10 dpa's irradiation campaign is presented in Table 3. These values are calculated considering the maximum allowable enrichment and as such do not depend on the filter material used.

Table 3. Maximum amount of tritium (in atom percent) dissolved in lithium during irradiation.

Distribution Coeff.	Temp=400°C	Temp=500°C	Temp=600°C
0.0200	2.4%	2.2%	*1.6%*
0.0100	4.0%	3.6%	*3.1%*
0.0050	7.0%	6.3%	*6.3%*
0.0033	10.%	*9.4%*	*9.4%*
0.0020	16.%	*15.7%*	*15.7%*

*Distribution coefficient is defined as the weight fraction of tritium in Vanadium divided by the weight fraction of tritium dissolved in Lithium.

The values in italic in the above table indicate that the initial concentration of tritium in lithium is larger in the beginning of the life and as such is tabulated as the constraint value. These values can be compared with the solubility limit of tritium in lithium.

D- Tritium leakage rate below the acceptable limits.

Finally, concerning the leakage term. The amount of tritium to be released from the capsules during a continuos 10 dpa irradiation campaign (considering the 1-week/40days shut-down periods) is shown in Table 4 in Curies for a Lithium volume inside the capsule of 2.9 cm^3.

Table 4. Tritium leakage from the DHCE capsule (in Curies) during the an irradiation campaign of 10 dpa's.

3 mm thick Eu_2O_3 filter with 1 mm TZM capsule wall.

Distribution Coeff.	Temp=400°C	Temp=500°C	Temp=600°C	Initial Charge
0.0200	0.9	16.	100.	117.
0.0100	1.5	26.	165.	218.
0.0050	2.7	48.	297.	422.
0.0033	3.8	69.	430.	625.
0.0020	6.2	111.	695.	1032.

1 mm thick Eu_2O_3 filter with 2.5 mm TZM capsule wall.

Distribution Coeff.	Temp=400°C	Temp=500°C	Temp=600°C	Initial Charge
0.0200	0.8	6.5	52.	117.
0.0100	1.3	10.8	86.	218.
0.0050	2.4	19.6	157.	422.
0.0033	3.5	28.4	227.	625.
0.0020	5.6	45.6	371.	1032.

CONCLUSION

The values calculated tend to indicate that is possible to perform a DHCE experiment in the ATR A-10 position and to expect reasonable helium to dpa ratios during the irradiation.

FUTURE WORK

To perform a more detailed analysis of the parameters of the experiment and to compare the values obtained with other limiting values.

NEUTRONICS ANALYSIS OF THE DHCE EXPERIMENT IN ATR-ITV*, I.C.Gomes, D.L. Smith, and H.Tsai (Argonne National Laboratory)

OBJECTIVE

The object of this analysis was to assess the suitability of the irradiation test vehicle (ITV), under design, for Dynamic Helium Charging Experiment (DHCE) with vanadium alloys. To achieve this goal a preliminary analysis of the irradiation conditions inside the vehicle, reaction rates, tritium leakage, among others have to be calculated. The objective is to calculate the helium to dpa ratio and analyze its range of variation and stability during a given irradiation period.

SUMMARY

The preliminary analysis of the DHCE experiment in the ITV of ATR was performed and its was concluded that such a vehicle is suitable for this kind of experiment. It is recommended to place an extra filter material in the thermocouple sleeve (such as B-10), to improve the helium to dpa ratio profile during irradiation. Also, it was concluded that a preliminary estimation of period of time for replacement of the external filter would be around 5 dpa's.

INTRODUCTION

The DHCE irradiation experiment was conceived to simulate Helium production due to neutron interaction in a fusion environment through the tritium decay to Helium-3. The experiment consists in charging a mother alloy with tritium at a concentration that after diffusion into vanadium alloy specimens produces a net build-up of helium in the samples compatible with the helium to dpa ratio of a fusion environment. The use of lithium as thermal bonding in the experiment allows an extra production of tritium during irradiation.

The analysis of such an experiment is complex in nature due to the large number of intervening variables. For example, the net build-up of helium-3 is a function of neutron flux intensity, neutron flux spectrum, tritium leakage rate from the capsule, initial tritium charge, the distribution coefficient of tritium atoms between samples, thermal bonding material, and capsule walls. Also, the tritium concentration inside any of the component materials (mainly in the lithium bonding) has to be below saturation otherwise chemical compounds are created and the distribution of the atoms among the material regions would not follow the theoretical distribution coefficient.

From a neutronics point-of-view the characterization of the thermal and epithermal neutron flux is very important in this analysis because of the very high cross section of the $^{3}He(n,p)\ ^{3}H$ reaction in those energy regions. Despite the lithium thermal bonding producing tritium through the $^{6}Li(n, \alpha)\ ^{3}H$ reaction, the cross section for the $^{3}He(n,p)\ ^{3}H$ is between 5 and 10 times larger for almost all neutron energies. This indicates that the reaction rate for both reactions should be reduced to a minimum to allow a reasonable growth of the ^{3}He concentration in the sample.

Another factor that is very important in the balance for the net ^{3}He production is the tritium leakage from the capsule. A large leakage rate means that a large fraction of the initial and produced ^{3}H is going to leak out of the capsule reducing the ^{3}H inventory and the ^{3}He generation rate.

---

*Work supported by Office of Fusion Energy, U.S. Department of Energy, under Contract W-31-109-Eng-38.

This paper presents a brief summary of the analysis performed for a DHCE experiment in the ATR (Advanced Test Reactor). The calculations are based on the current design of the ITV (Irradiation Test Vehicle) to be placed in the central flux trap of the reactor.

RESULTS AND DISCUSSION

Results of analyses conducted include neutron filtering, filter depletion, tritium leakage, and distribution coefficient. Results and discussions for each of these areas are presented.

1. Neutron Filtering.

The large thermal/epithermal neutron interaction cross section of the ^{3}He makes the use of thermal neutron absorbers, an imperative for DHCE experiments performed in mixed spectrum fission reactors. ATR is among the available mixed spectrum reactors suitable for fusion materials irradiation that can provide a relatively large fast to thermal neutron flux ratio. Despite this favorable characteristic, the requirement for the use of an effective thermal neutron filter is essential.

The current design of the ITV calls for a replaceable external neutron filter 2.6mm thick made of borated aluminum. The boron concentration in the aluminum is about 4.3% by weight and 100% B-10 is used instead of natural boron. The diameter of the region inside the filter is about 7.4cm. Three holes drilled in an aluminum filler of this region contain the irradiation capsules, temperature control gas lines and thermocouple leads. A small water annulus is used as a coolant outside each of the irradiation capsules. The combination of the filling material, samples, and cooling water provides a potential for attenuating neutrons and producing an increase in the thermal and epithermal components of the flux inside the filter region. As an option for enhancing the filter performance the possibility of borating the thermocouple sleeves is also being considered. Since the thermocouple sleeves are a semi-permanent component of the irradiation vehicle, the depletion of the boron in this component has to be kept as low as possible. This is achieved by replacing the external filter periodically.

Figure 1 displays a comparison of the different filter configurations. These results are for a 400°C irradiation, which implies that the tritium leakage is small. The curve labeled "filter1" represents the configuration where only the outside filter is used, the curve "filter2" represents a configuration that both, outside filter and borated thermocouple sleeve is used, and the curve "no depl" represents that case that the depletion of the external filter is not accounted. The results shown are for natural lithium, initial tritium charge equivalent to 1500 appm in the vanadium sample, temperature of irradiation 400°C, and distribution coefficient between the lithium and vanadium samples of 100 (in weight percent - weight per cent of tritium in lithium over weight per cent of tritium in vanadium). As can be seen, the helium to dpa ratio is maintained within an acceptable range. The performance of the configuration with outside and inside filter has a fairly good performance. The results indicate that using inside and outside filter the outside filter can be replaced after 5 dpa is reached without much of an impact to the helium to dpa ratio. The configuration with only outside filter suffers a clear reduction of performance above 5dpa, indicating the need for replacement of the external filter above this level.

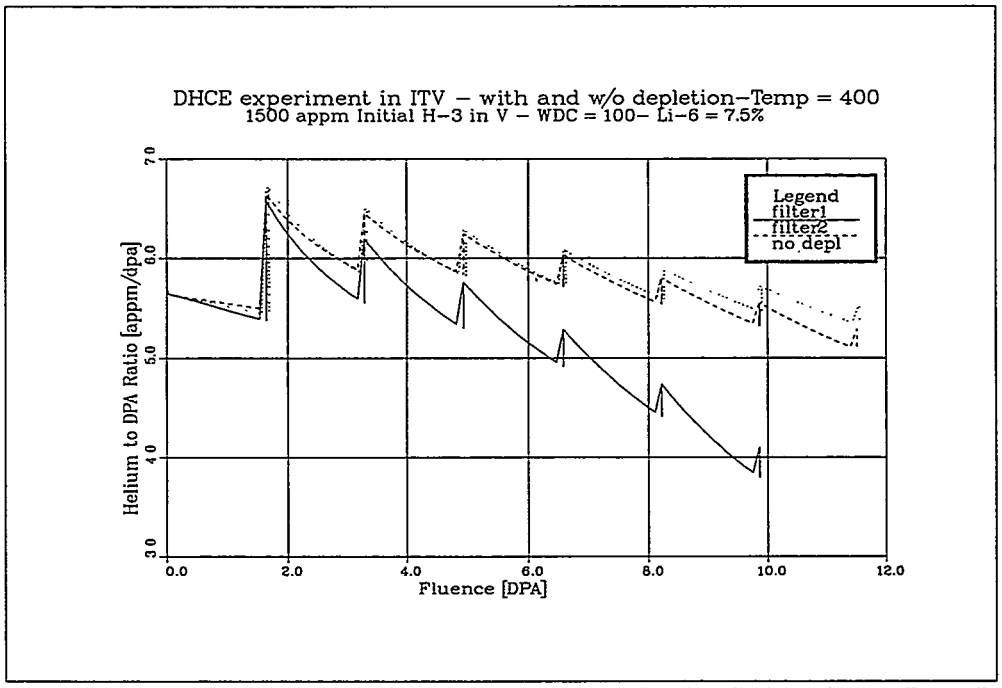

Figure 1. Calculated evolution of the helium to dpa ratio during irradiation of vanadium alloys in a DHCE experiment in the ITV position of ATR. The values plotted are for a temperature of 400°C, a weight distribution coefficient of 100, and lithium thermal bonding with natural enrichment.

2. Filter Depletion.

The depletion of the thermal neutron absorbing atoms of the filter material is an important parameter to be analyzed in the design of an experiment. During irradiation the number of absorbing atoms is reduced and the effectiveness of the filter decreases. As indicated in Figure 1, the filter depletion was taken into account and the neutron flux, at the sample position, was calculated each cycle to reflect the new filter atomic composition. Except for small local variations the neutron flux represents fairly well what would be expected during the irradiation length of an experiment.

3. Tritium Leakage

The permeation of tritium through the subcapsule wall is a function of the tritium concentration inside the capsule and the leakage coefficient. An equation that describes the variation of the number of tritium atoms inside the capsule as a function of the time can be written as follows:

$$dN_T/dt = -L\, N_t \qquad (1)$$

where N_T is the number of tritium atoms at the time t and L the leakage coefficient. The leakage coefficient is a function of the diffusion coefficient of tritium in the capsule material, distribution coefficient of tritium between capsule material and lithium, surface area of the capsule in contact with lithium, among others. A way to represent this coefficient is given as follows:

$$L = D^c K^c_a (\Omega_L/\Omega_c) (S/ dV_L) \qquad (2)$$

where D^c is the diffusion coefficient of tritium in the capsule material, K^c_a the distribution coefficient of tritium between the capsule and lithium (in atomic percent), Ω_L the atomic volume of lithium, Ω_c the atomic volume of the capsule material, S the surface area of the capsule, "d" the capsule wall thickness, and V_L the volume of lithium in the capsule. This formulation is basically theoretical and does not take in account the effects of the surface, this means that the tritium is considered to be free to leak out of the surface. The diffusion coefficient of tritium is strongly dependent on the temperature, which makes the leakage coefficient also strongly dependent on the temperature. It is well known that a thin oxide (or other compound) layer can have a strong effect in inhibiting the tritium leakage. Also, desorption of tritium at low pressures was not considered in this calculation. In the analysis performed, the leakage coefficient was assumed to be diffusion controlled, without taking credit for the possible improvements represented by the use of surface barriers for the tritium.

Figure 2 displays a comparison of the helium to dpa ratio for different temperatures considering all other variables constant. The results presented are for the configuration with only outside filter, for a distribution coefficient of 100, natural lithium enrichment, and initial tritium charge equivalent to 1500 appm in the vanadium samples. The values presented in this plot are calculated based on the diffusion controlled leakage, without any credit for the use of some kind of auxiliary tritium barrier or for H desorption rate control. As can be seen, for 600°C the helium to dpa ratio decreases considerably over the irradiation time, being at 5 dpa roughly 4 and at 10 dpa roughly 2. In this case filter replacement would not improve the performance. The possible solution is to have a more effective filter associated with a higher lithium enrichment, to reduce the leakage through the use of a tritium barrier in the outside capsule wall, or to include possible benefits of disorption controlled permeation.

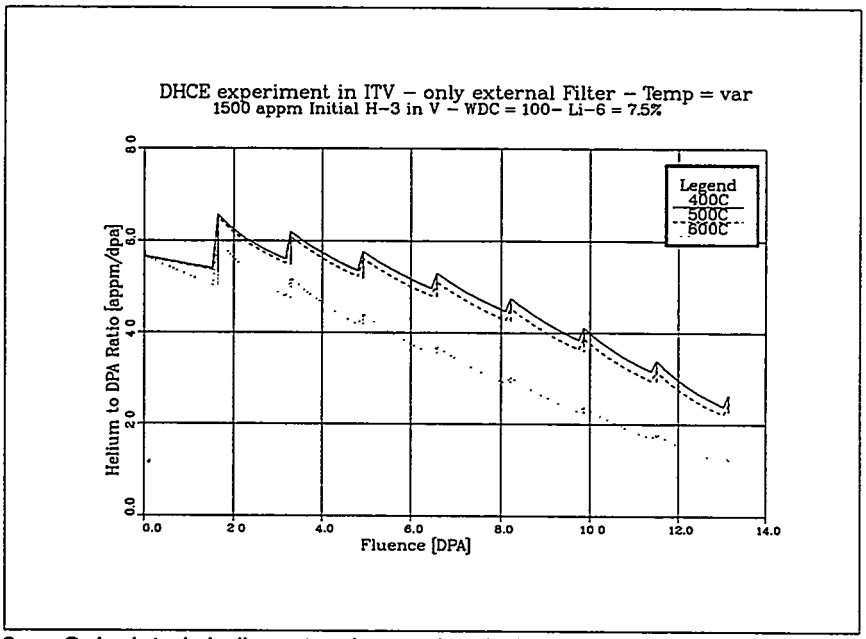

Figure 2. Calculated helium to dpa ratio during the irradiation for different irradiation temperatures. The lithium thermal bonding has natural enrichment, only outside filter is used, and initial tritium concentration is equivalent to an equilibrium tritium concentration in the vanadium samples of 1500 appm.

4. Distribution Coefficient

Distribution coefficient is defined as the ratio of the equilibrium concentration of an element able to diffuse through two media that are in contact. In this case the term distribution coefficient is used to represent the ratio of the tritium concentration in lithium to that in vanadium. This quantity is given the symbol WDC (weight distribution coefficient) or ADC (atomic distribution coefficient). The quantity which is the inverse (concentration of tritium in vanadium over concentration in lithium) is given the symbol K_w or K_a, depending on being weight or atomic distribution coefficient, respectively.

In this analysis the WDC was let to vary from 50 to 500. Studies performed by Park et.al. [1] indicated that this value should be in the range of roughly 100-150 depending on temperature and alloy composition.

Figure 3 and 4 show a comparison of the estimated helium to dpa values for a 500°C irradiation, with natural lithium. Figure 3 displays calculated values using only outside filter and Figure 4 using inside and outside filter. Figure 3 presents the worst scenario where only outside filter is used and the filter is not replaced for the full length of the irradiation. As it was shown in Figure 4, the use of inside and outside filter improves considerably the overall performance of the configuration. Important information that can be extracted from these plots is that the distribution coefficient has some impact on the helium to dpa profile during the irradiation but its impact is not as large as the temperature.

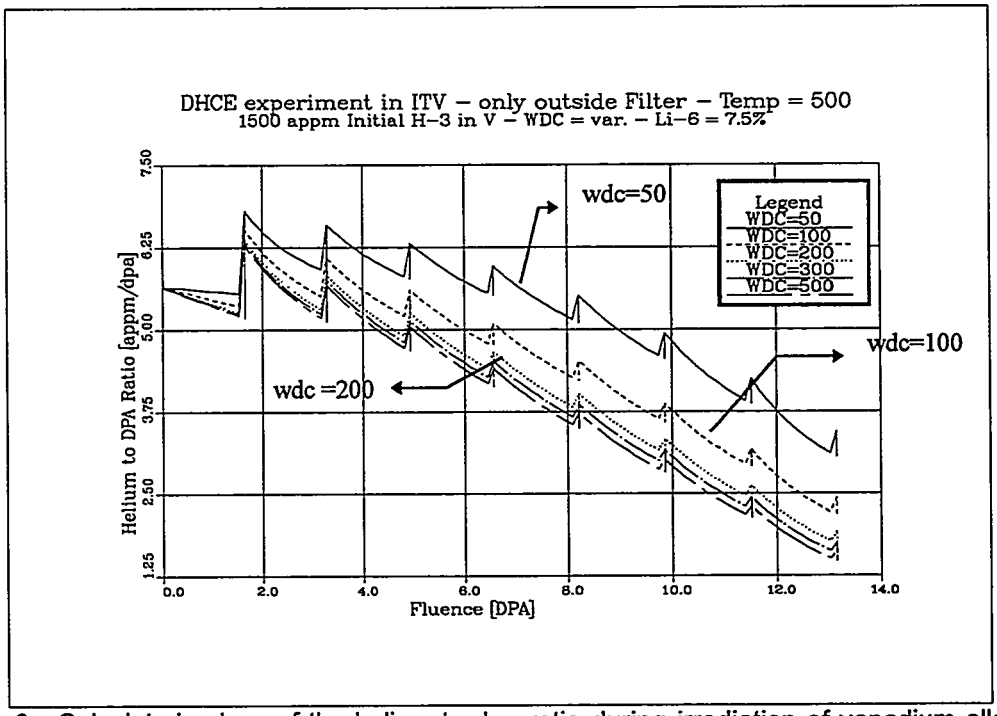

Figure 3. Calculated values of the helium to dpa ratio during irradiation of vanadium alloys in the ITV position of ATR. The temperature of irradiation is 500°C, the lithium thermal bounding has natural enrichment, only outside filter is used, and initial tritium concentration is equivalent to an equilibrium tritium concentration in the vanadium samples of 1500 appm.

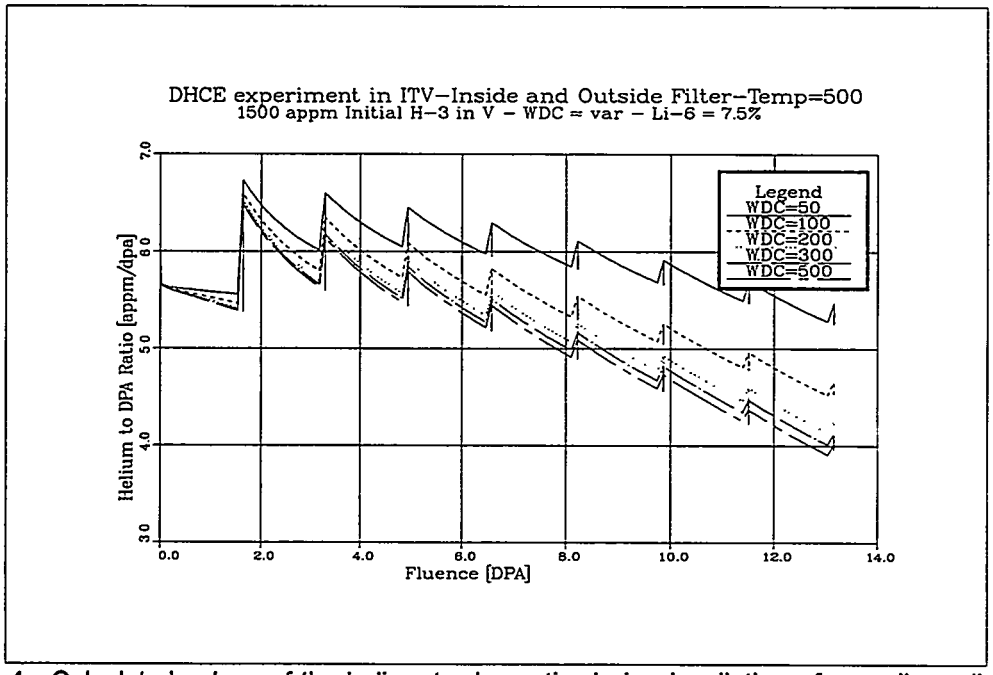

Figure 4. Calculated values of the helium to dpa ratio during irradiation of vanadium alloys in the ITV position of ATR. The temperature of irradiation is 500°C, the lithium thermal bounding has natural enrichment, outside and inside filter is used, and initial tritium concentration is equivalent to an equilibrium tritium concentration in the vanadium samples of 1500 appm.

FUTURE WORK

The future activities in the analysis of the DHCE experiment in the ITV include refinement of the current geometric module of the irradiation train, inclusion of the axial profile of the neutron flux into the model with, if possible, the use of the full model of the ATR core to better represent local and global variations of the neutron flux, interaction with the ITV designers to achieve the design goals of developing an operational vehicle suitable for fusion materials irradiation. Also, calculations for the total tritium charge for each capsule (as soon as a final design of the capsule is available), the total tritium inventory and estimated tritium leakage, as well as other parameters of the experiment are to be performed to support the design of a DHCE experiment in the ITV position of ATR.

REFERENCES

[1] J.-H. Park, R. Erck, S. Crossley and F. Deleglise, Fusion Materials Semiannual Progress Report for ending period December 31, 1996, DOE/ER-0313/21, April 1997, pp. 45-51.

10.0 MATERIALS ENGINEERING AND DESIGN REQUIREMENTS

No contributions.

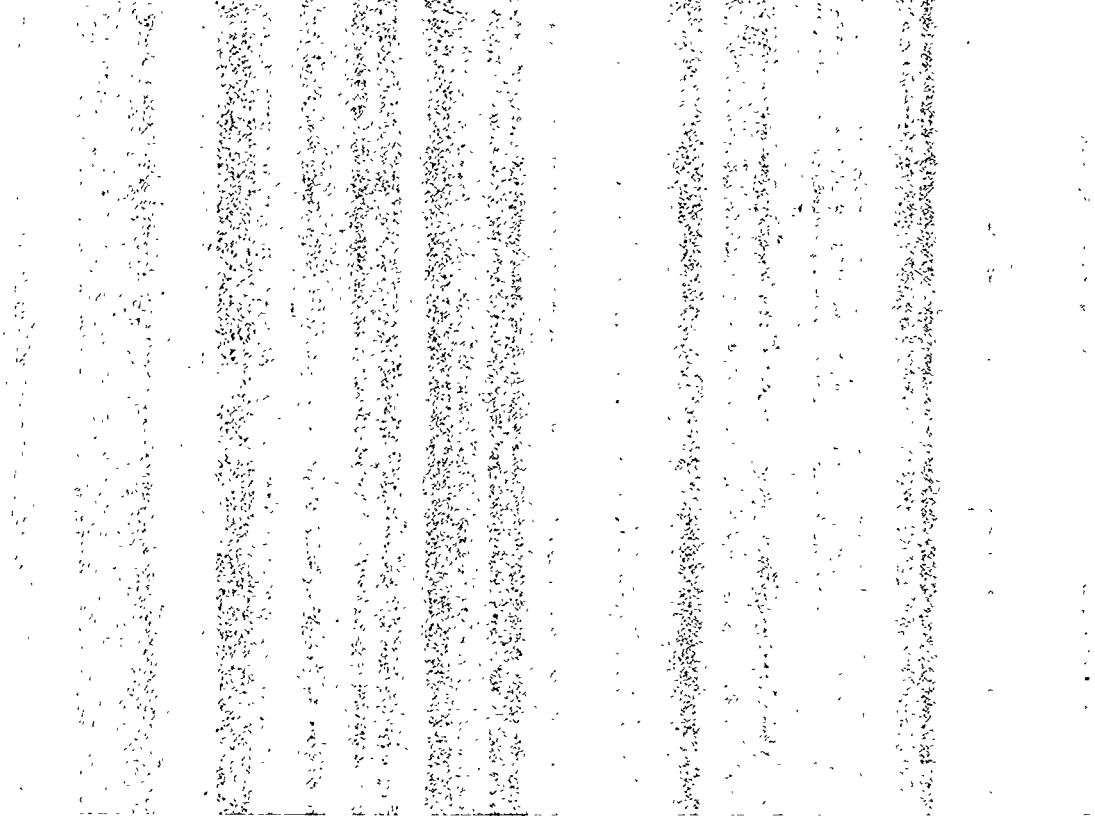

11.0 IRRADIATION FACILITIES, TEST MATRICES, AND EXPERIMENTAL METHODS

PROGRESS REPORT ON THE VARYING TEMPERATURE EXPERIMENT

A. L. Qualls, M. T. Hurst, D. G. Raby, D. W. Sparks (Oak Ridge National Laboratory), and T. Muroga (National Institute for Fusion Science, Japan)

OBJECTIVE

The purpose of this experiment is to determine the effects of temperature variation during irradiation on microstructure and mechanical properties of potential fusion reactor structural materials.

INTRODUCTION

A capsule has been designed that permits four specimen sets to be irradiated in an RB☆ location in the High Flux Isotope reactor (HFIR) with distinct temperature histories. During the reporting period critical component prototyping was completed. The results have lead to some design and operational changes from that previously reported. The primary design changes are 1) compression seals in the specimen holes of the beryllium holders, and 2) oxide-dispersion strengthened aluminum alloy (DISPAL) specimen sleeves in all holders.

Details of the capsule design are presented in the previous issue of this publication[1]. Four, axially displaced temperature zones are independently controlled. Holder temperatures are monitored by thermocouples and controlled by a combination of adjustable temperature control gas mixtures and auxiliary heaters. The high temperature holders are located in the center of the experimental region, which is centered on the reactor mid-plane, and the low temperature holders are located at the ends of the experimental region. The zones are to operate as follows:

A) low temperature, steady temperature zone (350°C),
B) high temperature, steady temperature zone (500°C),
C) high temperature, variable temperature zone (300-500°C),
D) low temperature, variable temperature zone (200-350°C).

Specimens will be irradiated to 5 to 10 dpa (depending on material and location). Specimen temperatures are controlled whenever the reactor is greater than a low power limit, tentatively set at 8.5 MW in order to reduce the exposure levels at improper temperature to below 10^{-4} dpa. The four zones are essentially identical. The primary differences in zones are 1) the amount of heat generated within them due to neutron and gamma heating, 2) the temperature at which they operate, and 3) the material of which they are made. The high temperature holders are made of a structural grade beryllium alloy (Brush Wellman S-200F), and the low temperature holders are made of 6061-T6 aluminum alloy.

Identical specimen sets are contained in corresponding steady and variable temperature zones (the high temperature and low temperature sets are different). The temperatures of the variable temperature zones are maintained at their respective low value for 10% of the total fluence, and then increased to match that of the corresponding steady temperature zones.

PROTOTYPE TESTING

A prototype capsule containing a single temperature zone was fabricated and operated. The gas flows, temperature control gas gaps, and heater arrangement within the prototype were similar to that of the Low-Temperature, Variable Temperature (LTVT) holder. The gas gap was set to produce a holder temperature of 165°C when the heat produced within the holder equals that expected in the LTVT holder during irradiation in an RB☆ position of HFIR.

The questions to be addressed by the prototype were:

1) what are the operational limits of the heaters, and are they adequate to properly control the experiment,

2) will the proposed mixing of the temperature control gas provide adequate time response to prevent specimen over-temperature as the reactor power is increased,

3) what are the end loss effects of the stainless steel separation pieces, and how does that affect the achievable temperature range of the holder, and

4) is the response time of the proposed heater controllers suitable for the application.

Issues 1 and 2 were addressed and reported on during the previous reporting period. The dual element heaters used for temperature control can operate safely with 9 amps of current passing through both elements or 15 amps passing through only one of the elements, before reaching a limiting sheath temperature of 1000°C in the section of the heater directly above the holder. Mixing the temperature control gases inside the capsule results in adequate temperature response to gas flow adjustments to prevent specimen over temperature during typical reactor power increases. The purpose of the final phase of testing was: 1) to test heater controllers, 2) verify the thermal models used in the design of the holders, and 3) verify that the heaters can meet the requirements of the experiment.

Heater Controllers

A software based, temperature control loop was developed to control the temperature of the prototype holder by issuing a demand for heater current based on holder temperature. Phase angle fired, silicon rectified controllers (SRC) were selected for heater control because phase angle firing results in a lower element temperature for a given heat output and reduces the temperature oscillations within an element compared to burst firing SRC controllers or ON-OFF controllers. The effect of which is longer heater lifetime.

Phase angle fired controllers regulate the point in each AC voltage sine wave at which the current is allowed to pass to the heaters. If 100% of the heater power is demanded, the full sine wave passes through the heaters. As less power is demanded, the controller delays the passing of the current until the phase angle corresponds to the demanded power percentage.

Estimate of holder heat loss

The thermal characteristics of the holder and separation piece assembly were tested to determine parasitic heat losses. A quick comparison of the potential heat loss paths from the holder suggests that no more than 25 watts out of 1450 watts should be lost across the separation pieces of the LTVT holder in the actual capsule. To test heat loss from the prototype, a known amount of heat was added to the holders and the temperature was monitored. The flow rate of argon through the temperature control gas gaps was scanned and the resulting temperature was recorded.

The thermal conductivity of the temperature control gas mixture is calculated from the relative flow rates of helium and argon through the system, and the average temperature of the holder and housing tube. The calculated thermal conductivity is very sensitive to the percentage of helium in the gas mixture. The measured helium flow rate through capsule during the experiment was 10 standard cubic centimeters per minute (sccm). The experimentally measured temperatures are higher than the predicted temperatures if a flow rate of 10 sccm of helium is assumed through the temperature control gas gap. This implies that the actual helium flow through the gas gap was less than the measured helium flow rate through the experiment. The flow rate instrumentation was calibrated for air and a factor was used to correct for the use of helium, and the flow rate measurement was made at 10% of the full scale reading of the instrument, where the accuracy is reduced.

Also, the prototype capsule had some leakage out of a temporary top seal, the affect of which on the gas mixture is not exactly known. So it is reasonable to assume that the helium flow rate through the gas gap was lower than the measured flow rate through the experiment. It is also probable that the flow rate of helium through the gas gap was reduced as the argon flow was increased. There is, therefore, a degree of uncertainty associated the calculation of the thermal conductivity of the control gas mixture.

A correction must be made to the helium flow rate in order for the experimentally measured data to have a reasonable fit to the predicted data. The assumed flow rate of helium was reduced until acceptable agreement was achieved between the predicted and measured temperatures at the low temperatures, where parasitic heat loss should be small and the gas mixture was mostly helium. There is a degree of subjectiveness in determining the fit, however the best results are obtained for assumed helium flow rates of 4 to 5 sccm.

With the low temperature data corrected by assuming a reduced helium flow, the measured temperature deviates from the flow-corrected, predicted temperatures at higher temperatures. This deviation is assumed to be due to parasitic heat loss from the ends of the holder. The magnitude of the parasitic heat loss is estimated by assuming that it is proportional to the temperature of the holder. The value of the proportionality constant is determined by adjusting it until the experimental data has reasonable agreement with the predicted temperature over the entire temperature range.

Figure 1 shows the measured data, the predicted temperature assuming the measured helium flow (10 sccm), the predicted temperature assuming the reduced helium flow (4 sccm), and the predicted temperature assuming reduced helium flow and corrected for parasitic heat loss. The required parasitic heat loss factor increases as the assumed helium flow is reduced. For an assumed flow of 4 sccm to 5 sccm, the required values of the proportionality constant suggests that over 80% to 90% of the heat loss will occur across the temperature control gas gap in the prototype when the temperature difference between the holder and the housing tube is 270°C.

The parasitic losses in the capsule are expected to be lower than that of the prototype due primarily to the use of thinner-walled separation pieces and increased gap between the separation piece and the I.D. of the housing tube. For the LTVT holder the upper separation piece is a heat source instead a heat sink. The heaters and TCATs are also a heat source, but the heat conducted through them is expected to be negligible.

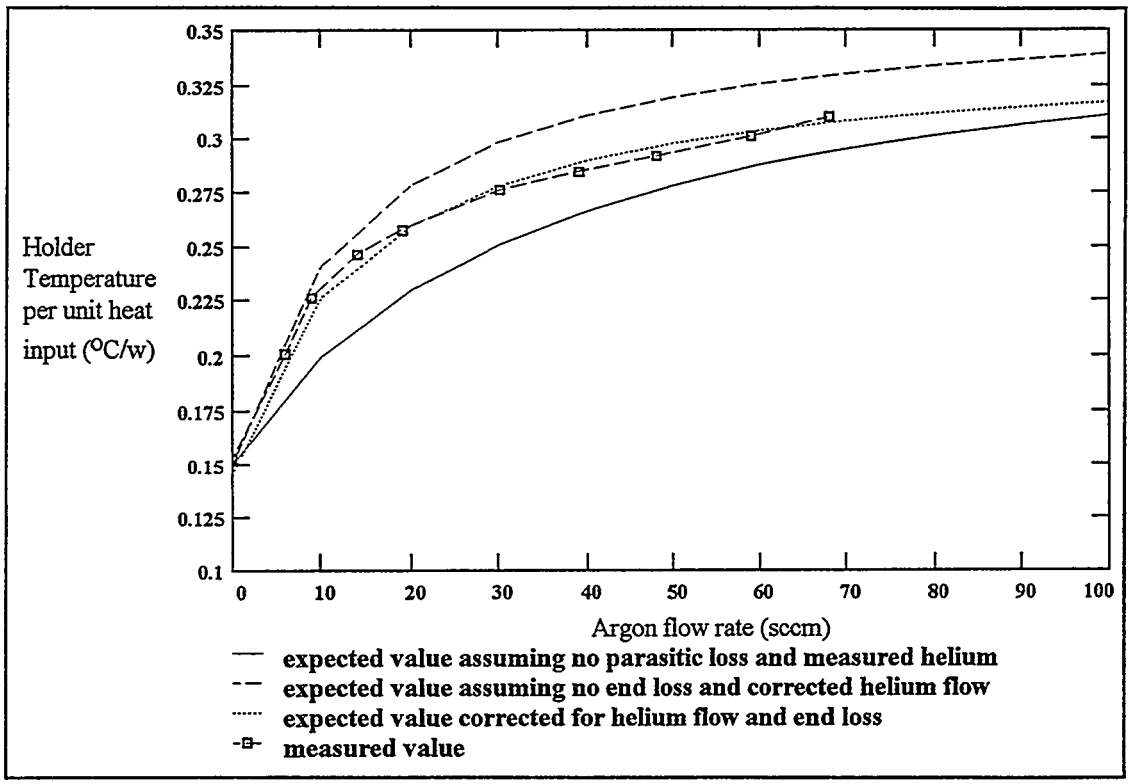

Fig. 1. Temperature of the holders as a function of argon flow compared to the expected value.

Holder Temperature Range

With the parasitic losses from the capsule conservatively estimated, the expected temperature range of holders can be calculated. The gas mixing scheme used in the capsule does not allow pure argon to flow through the gas gaps of the holders without turning off the helium purge flow. This limits the minimal thermal conductivity in the temperature control gas gap to below that which could be produced by flowing pure argon in the gaps. This, in addition to parasitic heat losses limits the achievable temperature range of a holder.

Figure 2 shows: 1) the expected temperature range for the LTVT holder (designed to operate at 165°C when the temperature control gas is pure helium and 1450 watts are generated within the holder) as a function of heat generated within the holder, if pure argon can be input into the gas gaps and there were no parasitic heat losses, and 2) the expected temperature range if parasitic heat losses are assumed equal to the largest value estimated in the prototype experiment (helium flow = 4 sccm) and the gas mixture is assumed to vary from pure helium to a 95% argon-5% helium mixture.

The achievable temperature range of the LTVT holder with parasitic losses and 5% helium content is very close to required temperature range of 165°C to 330°C. If the parasitic heat loss is higher than expected or the heat generated in the holder due to nuclear interactions is lower than expected, auxiliary heat from the heaters could be required to elevate specimen temperatures to the desired high temperatures.

The losses assumed for this calculation are larger than those expected in the capsule, and the helium purge can be terminated when high power is not being demanded from the heaters if needed. It is expected that the required high temperature in the LTVT holder can be achieved without the use of auxiliary heat. Because of

the location of the LTVT, the heat generated within it will increase as the reactor cycle progresses, making it easier to maintain temperature.

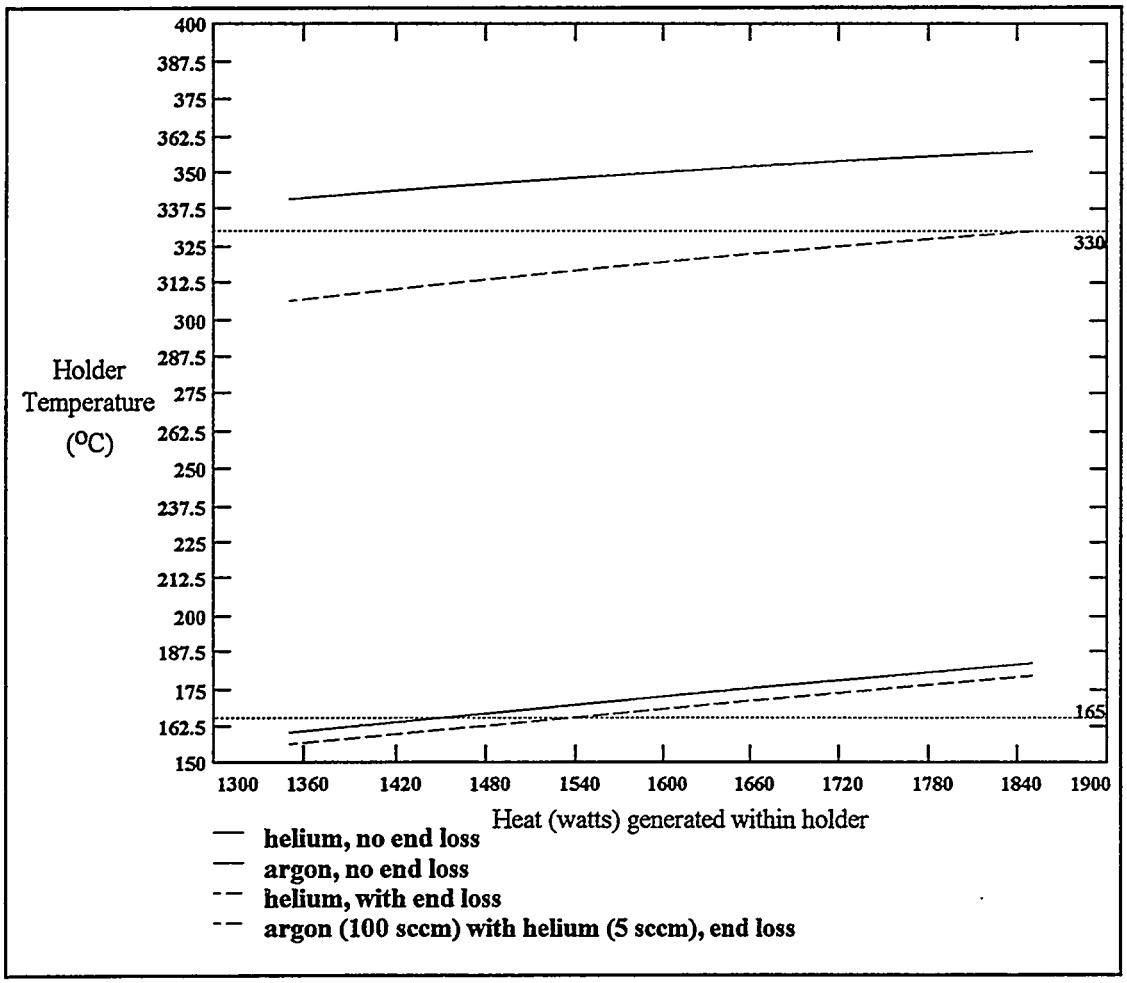

Fig. 2. Predicted temperature range of the LTVT holder.

Heater Performance

The maximum heat output from the heaters is dependent on the design temperature of the holder. In order to have a margin for error, holders are designed to operate below the required temperature. If more heat is generated within the holders than anticipated, the specimens can still be controlled at the desired temperature. Increasing the margin for error (lowering the design temperature) increases auxiliary heat requirements when the reactor is operating at reduced power. The maximum heat requirements will occur if a large margin for error is assumed, and 1) the actual heat generated is less than anticipated, and 2) parasitic heat losses are larger than expected.

The design temperature of each holder is set to limit the maximum credible auxiliary heat requirement to less than that produced when 9 amps pass through the nine elements in each holder. The estimated heat required to maintain specimen temperature in each of the four holders as a function of argon flow through the gas gaps (along with an assumed helium flow rate of 3 sccm) is shown in Fig. 3. This calculation assumes the parasitic heat loss implied by an assumed flow of 4 sccm of helium through the gas gap of the prototype holder.

The maximum required heat input is estimated to be 1200 watts, to maintain a temperature of 350°C in the LTST holder if it is designed to operate at 235°C at EOC with pure helium as the temperature control gas. At 10% power, approximately 220 watts will be generated in the LTST holder due to neutron and gamma interactions. To maintain the desired specimen temperature, 980 watts of auxiliary heat must be added to the holder when 70 sccm of argon and 3 sccm of helium is flowing through the gas gap. If the 980 watts are evenly distributed over the 9 heaters in the holder (average element resistance is 1.35 ohms), then 9 amps will be required through each heater element.

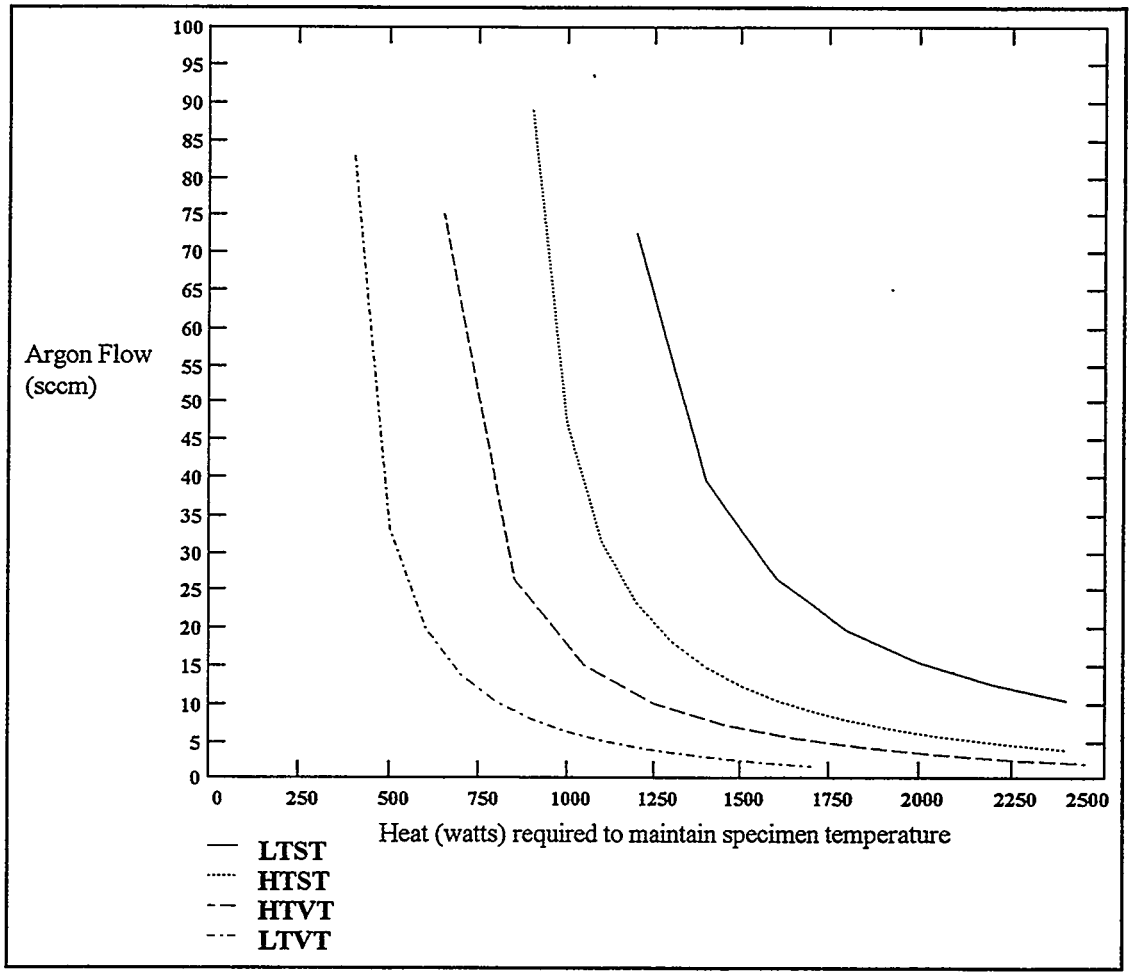

Fig. 3. The estimated heat required to maintain specimen temperature in each of the four holders as a function of argon flow through the gas gaps. A constant helium flow rate is assumed.

The maximum current requirement of 9 amps through the heater elements is the limit established during prototype testing as the operating limit. The 9 amp limit was set to limit sheath temperature to 1000°C in the region between holders, because melting of the sheath at this location was the predominant form of heater failure during testing. The melting temperature of the sheath material (304 stainless steel) however, is > 1450°C, and dual-element heaters have been operated at > 12 amps through both elements in steady state, and > 15 amps through only one of the elements without failure. If four of the original nine elements in a holder are operational, specimen temperatures can be elevated and controlled in the LTST whenever the reactor power is above 10% of full power, even if parasitic heat loss in the capsule holders are as high as the most conservative estimate of the heat losses from the prototype holder.

Heater element lifetime for mineral insulated heaters is limited by wire oxidation, which occurs at a rate proportional to temperature. To ensure a lifetime of at least one year, it is recommended that the element temperature be limited to 870°C. The temperature of a heater element when 9 amps are passing through it, while it is operating in a 500°C holder is estimated to be below 800°C, however, the temperature of the extension wire in the region directly above the holder is known to be >1000°C when 9 amps are passed through both elements. This is an important reason for limiting the current through the heaters. While it is possible to operate at higher power output, doing so will reduce heater lifetime.

During a typical startup, reactor power is increased to approximately 10% of full power and held for 15-20 minutes for instrumentation checks. Specimen temperatures will be elevated and controlled during this period. The heaters will be required to operate at the highest power for approximately 150 minutes over the course of the entire 10-cycle experiment, if all start-ups proceed smoothly. The prototype heaters were operated at 9 amps through both elements longer than the total time expected to be required during the experiment, and were cycled to >9 amps many times more than the 10 cycles required during the experiment. If the current to the heaters can be limited to 9 amps, heater failure due to wire oxidation or melting of the sheath is unlikely.

The effects of transmutations in heater elements and extension wire are not precisely known. While heaters have been irradiated at higher temperatures, the linear power output from those heaters was not as high as the heaters used in this experiment, and heaters have never been operated at ORNL to the fluence that will be encountered in this experiment. These unknown factors provide added incentive for minimizing the heat demanded from the heaters.

Based on the measured resistances across sections of the (shortened) prototype heaters, the total resistance of a full length capsule heater is estimated to be 4.5 ohms. Three elements in series will produce a total loop resistance of approximately 13.5 ohms. A 110 VAC controller could only pass approximately 8 amps through a series of three heaters. Therefore, while a 110 VAC controller was used to test the prototypes, a 208 VAC controller, capable of outputting over 15 amps through three heaters, will be used for capsule operation.

CAPSULE CONTROL

Controller Response

To test the response of the control loop, the system was allowed to equilibrate and then was perturbed by changing operating conditions. The response of the controller for the control heaters and the temperature deviation from the set point temperature to a series of perturbations is shown in Fig. 4. The temperature set point is 175°C, and the helium flow rate and heat output from a secondary set of heaters were held constant during the experiment. Initially, the controller output is limited by the control computer even though holder temperature is below the set point temperature of 175°C. The argon flow is increased and the temperature increases. Upon the detection of increasing temperatures, the demanded current to the heaters is reduced. This is followed by a series of small argon flow increases, which result in small oscillations in holder temperature. At approximately 12:23, the coolant flow past the capsule is terminated and the holder temperature increases. The control heater output is reduced to zero, which reduces the holder temperature. (For operation in the actual capsule, a temperature deviation of this magnitude would result in an automatic reduction in the argon flow rate and termination of current to all heaters in the holder.) Coolant flow is resumed, and the controller returns the holder to the proper temperature after slightly overshooting the set point temperature. The final perturbations are large changes in the argon flow rate, which are designed to simulate changes in reactor power. The largest increase is estimated to simulate a reactor power increase of 10%. The resulting increase in holder temperature is approximately 5°C.

The controllers must respond quickly enough to compensate for expected reactor power increases of 20% of full reactor power (18 MW), and gas mixture adjustments will be made to keep heater outputs within

acceptable limits. Reactor power will be increasing as gas mixture adjustments are made. Some temperature deviation is unavoidable during these transitions. Because reactor power increases are usually limited to 20% of full power (< 18 MW) and settling time is allowed between steps, the temperature deviations are expected to be < 10°C.

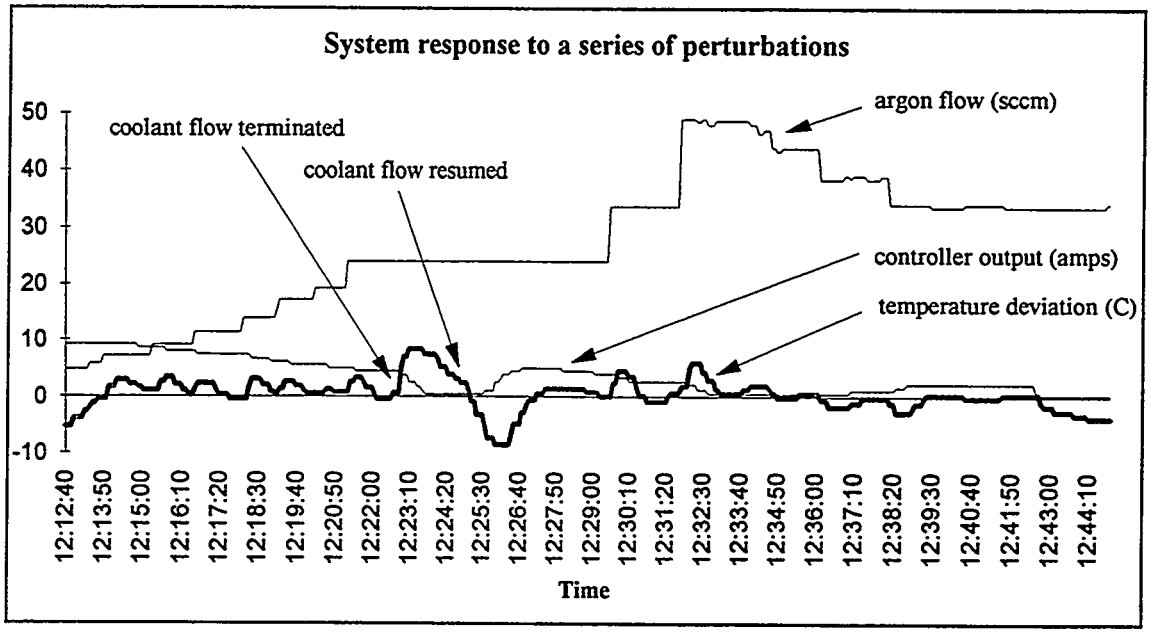

Fig. 4. System response to a series of perturbations.

Automated Control During Start-ups

Gas mixture adjustments will be controlled automatically during a reactor startup. Before startup, the experiment operator will input values into a "setout" table that specifies the argon flow and set point temperature for each zone as a function of reactor power. The flow rates are set to allow the control heaters to operate within a defined power range while maintaining the specified specimen temperatures.

The inputs to this table will be determined during the start-up of the first cycle of operation, which will be strictly specified and monitored. Reactor power levels are either input to the system by the experiment operator or read by the control computer from an on-line database containing real-time reactor conditions. When the reactor power exceeds the power limit for which a temperature set point above ambient coolant temperature (50°C) is specified, temperature control begins automatically. As the reactor power exceeds the values in the setout table, the argon is reduced to the value listed in the table.

By the time the reactor reaches 90% of full power, essentially all of the argon will be removed from the system. At full reactor power, the experiment operator will manually adjust the flow of neon or argon to each temperature zone until the power output of the control heaters falls between the upper and lower alarm limits if required. Once this is done, the capsule can be operated automatically without operator supervision.

The capsule will remain in this configuration until it is time to increase the temperatures in the variable temperature zones (about 2 days). Before the transition, the operator will gradually eliminate the neon or argon from the steady temperature zones, increasing the current demand to the heaters in those zones. The purpose of this is to provide additional adjustment capability in those zones in the event that some of the argon added to the variable temperature zones leaks into the steady temperature zones.

At the time of the transition, the operator will increase the temperature control set points and the argon flow rates of the varying temperature zones. If the change of gas mixtures or temperatures in the variable temperature zones causes an increase in the temperature of the steady temperature zones, the control heater output for those zones will automatically compensate. After the transition, the operator will again manually adjust the neon or argon flow rates to all zones in order to force the control heater outputs between the alarm limits.

Heater Failure

If all three heater zones in a holder were to fail (power failure to control cabinet, for example), the temperature of the specimens would be temporarily reduced to the value dictated by the gas mixture, which is approximately 5°C below set point temperature. The capsule could then be controlled with automated gas mixture adjustments as is routinely done in instrumented RB☆ capsules.

Reactor Power Reduction or Unscheduled Shutdown

If the reactor must be operated at a reduced power level, the control heaters will attempt to compensate with increased heater output. However, once the control heater output from more than one zone exceeds a specified upper value (that is, once the reactor power falls below a certain level), the computer will turn off all heaters and allow the temperature of the specimens to fall below the setpoint value, activating the low temperature alarms. The control system is assuming that the reactor has shutdown and is attempting to prevent holding the specimens at elevated temperatures when they are not being irradiated. Reactor operators will be instructed to shutdown the reactor. If the reactor must be operated at reduced power levels, the experiment operator can manually reset the setout table to accommodate.

WELDING MOCK-UP

The specimens will be sealed in a static helium environment. The required seal was to be accomplished by laser welding a cap into the tops of the specimen holders after the specimens have been loaded. Testing of this sealing method was done for both aluminum and beryllium. An acceptable welding procedure was developed for the aluminum holder, but leak tight seals could not consistently be produced in the beryllium mock-ups with the available equipment, time and resources.

A mechanical seal was designed to facilitate seals in the beryllium holders. The specimen holes are threaded, and threaded, copper-beryllium alloy caps compress a titanium sealing disk between the polished base of the cap and a polished surface inside the specimen hole, as shown in Fig. 5. Titanium was selected as the gasket material because it will act as an oxygen getter in the event that a small amount of leakage does occur. Mock-ups of the mechanical seal are being fabricated and will be tested before the design is finalized.

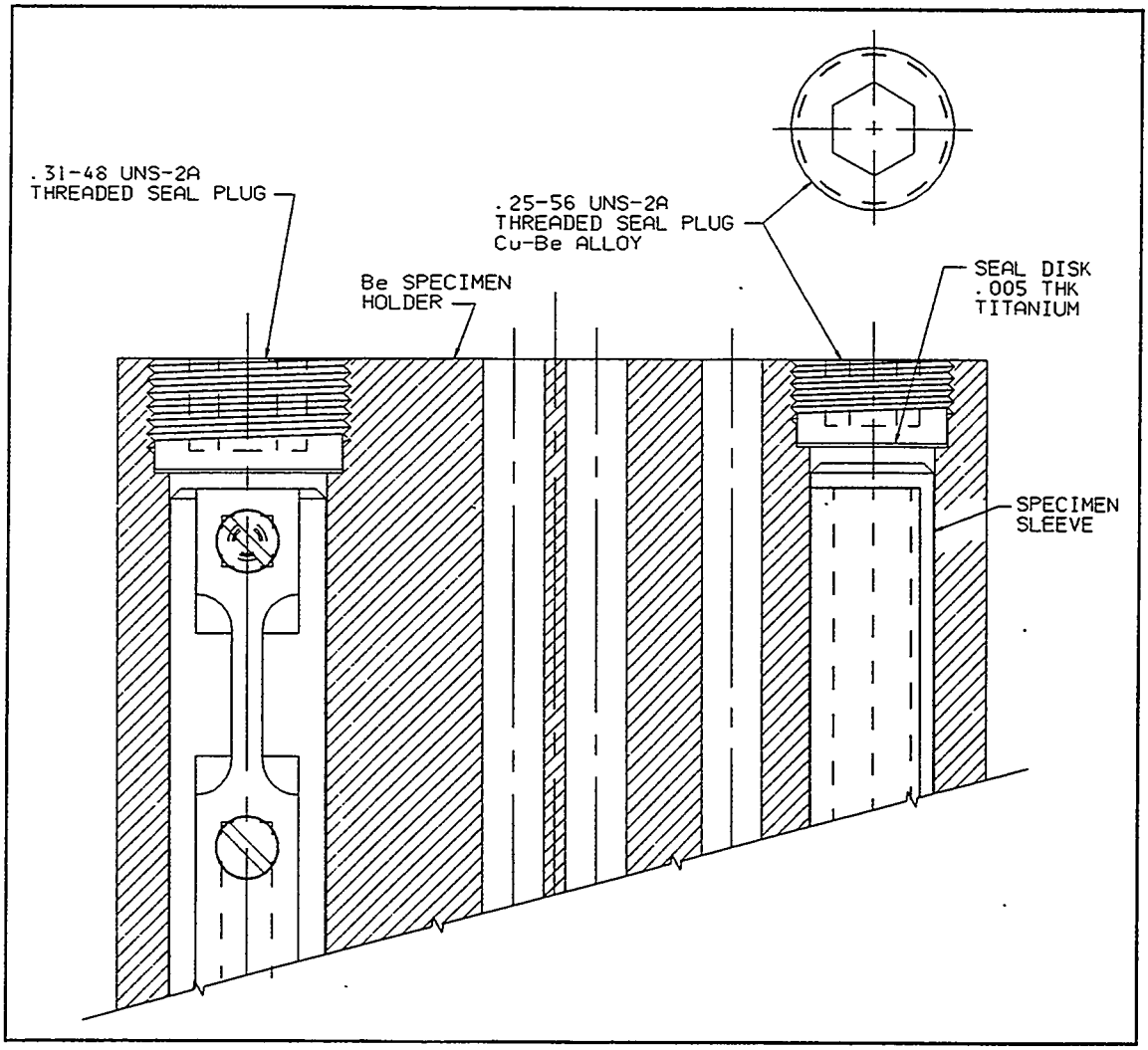

Fig. 5. Detail of the sealing caps to be used in the beryllium (high temperature holders).

MATERIAL CHANGE

The specimen sleeves were changed to DISPAL in both holders to reduce the expense associated with making identical sets out of different materials, and making and handling a large number of beryllium components. The DISPAL can be used at temperatures up to 500°C, and is therefore acceptable for use in all four holders. It will also prevent the specimens from being in direct contact with beryllium.

SCHEDULE

Fabrication of the capsule housing components and the heaters and thermometry has begun. The holders will be fabricated as soon as the mechanical sealing technique has been verified. Specimens are scheduled for delivery to ORNL in August 1997. Capsule assembly is scheduled for July - October. The control hardware is scheduled for completion by October 1997, and the assembled capsule will be connected to the control system in December 1997. Irradiation is scheduled to begin after the irradiation of RB-11J and RB-12J is complete, in February or March 1998.

REFERENCES

1) A. L. Qualls, T. Muroga, "Progress Report on the Design of a Varying Temperature Irradiation Experiment for Operation in HFIR," Fusion Materials, Semiannual Progress Report for Period Ending December 31, 1996, pp 255-262.

THE MONBUSHO/U.S. SHIELDED HFIR IRRADIATION EXPERIMENT: HFIR-MFE-RB-11J AND 12J (P3-2 AND P3-3) — M. L. Grossbeck, K. E. Lenox, and M. A. Janney (Oak Ridge National Laboratory), T. Muroga (National Institute for Fusion Science), D. W. Heatherly and K. R. Thoms (Oak Ridge National Laboratory)

SUMMARY

This experiment is a joint project between the Japanese Monbusho, the Japan Atomic Energy Research Institute, and the U.S. Fusion Energy Sciences Program. It is the first of a series of experiments using europium oxide as a thermal neutron shield to minimize transmutations in vanadium alloys and ferritic/martensitic steels. The europium oxide shields were developed using ceramic processing techniques culminating in cold pressing and sintering. This experiment, which is a prototype for future fast neutron experiments in the HFIR, contains approximately 3200 specimens of 18 different types. The experiment began operating at 300 and 500°C in February 1997 and is projected to attain its goal fluence of ~5 dpa in February 1998.

PROGRESS AND STATUS

Introduction

This experiment is a low exposure irradiation containing a large variety of specimens primarily for microstructural analysis and mechanical properties of a wide variety of materials. It consists of two irradiation vehicles, one at 300°C (HFIR-MFE-RB-11J) and the other at 500°C (HFIR-MFE-RB-12J). Vanadium transmutes to chromium by thermal neutron absorption with an absorption cross section of 80 barns. As a result, initially pure vanadium will contain 10% Cr after an exposure of 5 dpa in a HFIR reflector position. For the low activation ferritic-martensitic steels, transmutation of tantalum and tungsten, which have thermal absorption cross-sections of 25 and 19 barns, respectively, could significantly perturb alloy composition. To minimize these transmutation effects, a europium oxide shield was developed for this experiment that reduces the thermal flux by a factor of about 100.

To maintain controlled specimen temperatures and minimize radiative heat transfer, the specimens are held in carefully designed racks of aluminum alloy. The specimens had to be machined to close tolerances in order to fit into the racks and to achieve good thermal contact. Twenty-one thermocouples are positioned along the length of each capsule, some near the centerline, and the remainder toward the periphery of the holders. Temperature is maintained by surrounding the specimen chamber with an annulus of inert gas which can be varied in composition from pure helium to neon or argon, or a mixture of helium and one of the other gases. An automatic computer-controlled system uses an average thermocouple temperature for control and adjusts the gas mixture to maintain the design temperature.

Experiment Goals

The irradiation vehicles contain many varied experiments for fusion materials research. Only a few examples will be stated. Pressurized tubes of low Cr-Ti-vanadium alloys are being irradiated for the first time to evaluate irradiation creep in this alloy class. Pressurized tubes of ferritic/martensitic alloys are also included to evaluate the newer low-activation ferritic/martensitic steels. A large portion of the space is devoted to ceramic materials, including ceramic/metallic braze joints. Advanced SiC/SiC fiber composites using low-oxygen SiC are being irradiated to study irradiation-induced densification. Alumina and silicon nitride bend bars of different thicknesses are included to study size effects on fracture of irradiated ceramics. There is also a series of TEM disks with varying minor element chemistry to study the effects of transmutation on microstructure. Mechanical test samples of tensile, compact tension, and Charpy bars as well as bend bars are included to evaluate mechanical properties of several classes of alloys and ceramics. Table 1 presents the specimen loading by material and type of specimen.

Table 1. Specimen Loading for HFIR-MFE-RB-11J (300°C)

Alloy	PRZ Tubes JP/US	1.5 mm CVN (JP)	SS-J (JP)	DCT (JP/ US)	TEM (JP/ US)	U.S. SS-3	U.S. CVN	U.S. PCVN	Bend Bar 1 2x2x15mm (JP)	Bend Bar 2 1x2x15 (JP)	Bend Bar 3 0.5x2x15 (JP)	Bend Bar 4 .25x2x15 (JP)	Bend Bar 5 .6x1.4x9 (JP)	Bend Bar 7 0.7x1x10 (JP)	Bend Bar 8 3x2.5x25 (ORNL)	Fiber Bundle Tube 2od x 50mm	Thermal Diffusivity 10dx2mm (US)
JLF-1	5	9	8	5/2	15/0	10	5	5									
JLF-1B	4	9	5		6/0												
JLF-1Mn1	4	8	5		6/0												
JLF-1Mn2	4	8	5		6/0												
JLF-1LS			5														
JLF-1LM			5														
JLF-1LSM			5														
F82H	5	9	5		10/0												
Kimura (ferritic)					30/0												
ODSHK (ferritic)		9	5		6/0												
9Cr-2WVTa																	
V-4Cr-4Ti-.1Si(JP)			7		10/0												
V-4Cr-4Ti(JP)			7		10/0												
V-5Cr-4Ti(JP)			7		10/0												
V-4Cr-3Ti(JP)			7		10/0												
V-5Cr-3Ti(JP)			7		10/0												
V-5Cr-5Ti(JP)			7		10/0												
V-4Fe-4Ti-.1Si			7		10/0												
V-4Fe-4Ti			7		10/0												
V-4Fe-3Ti			7		10/0												
V-4Cr-4Ti-.1SiR			7		10/0												
V-4Cr-4Ti-SiAlY-x			40		50/0												
V-4Cr-4Ti 832665 (Partial rxl)					0/3	3		4									
V-4Cr-4Ti 832665 (Full rxl)					0/3	3											
V-5Cr-5Ti					0/4	3											
V-4Cr-4Ti-Si					0/4	3											
V-3Cr-3Ti					0/4	3											
V-6Cr-3Ti					0/4	3											
V-6Cr-6Ti					0/4	3											
V-4Cr-4Ti-B					0/4	3											
SiC/SiC					0/4	3									20		
SiC (B,Be,N)					6/0				3								
Al_2O_3					6/0				7	7	7	6					
AlN					6/0				4								
MgO/xAl_2O_3					6/0				3								
SiO_2									3								
TiCx					9/0												

Table 1. Specimen Loading for HFIR-MFE-RB-11J (cont'd)
(300°C)

Alloy	PRZ Tubes (JP)	1.5 mm CVN (JP)	SS-J (JP)	DCT (JP/ US)	TEM (JP/ US)	U.S. SS-3	U.S. CVN	U.S. PCVN	Bend Bar 1 2x2x15mm (JP)	Bend Bar 2 1x2x15 (JP)	Bend Bar 3 0.5x2x15 (JP)	Bend Bar 4 .25x2x15 (JP)	Bend Bar 5 .6x1.4x9 (JP)	Bend Bar 7 0.7x1x10 (JP)	Bend Bar 8 3x2.5x25 (ORNL)	Fiber Bundle Tube 2od x 50mm	Thermal Diffusivity 10dx2mm (US)
C/Cu Joints									8								
V/ceramics					6/0								6				
SiC Fiber																	
Transmutation Series																	
V			6		30/15												
V-xCr			6		40/20												
V-4Ti-4Cr			6		40/20												
Cu			4		20/20												
Cu-xNi-yZn			4		40/20												
Cu-xNi-yZnNi			4		40/20												
Fe			6		40/20												
Fe-W&Mn			6		30/15												
ODS			6		20/10												
Fe-Cr-Ni			6		30/15												
Fe-Cr-Ni-x			6		40/20												
316/TiN			6		30/15												
TiAl					10/5												
SiC					20/10												
Al, Al-Si					20/10												
Mo alloys					20/10									46			
Irradiated Cu alloys					9/0												

JAERI/U.S.				
F82H (HT-1)	6	10	12	6	5
F82H (HT-2)	2	10	8	5	5
F82H Ni doped	2	10	5	5	
F82H weld	2	10	4	5	
F82H weldment	2		4	5	
F82H HAZ			4		
9Cr-2WVTa	2	10	6	5	5
Ferritic Alloys TBD		50			

2 Temp Monitors
(Same as Ti)

Table 1. Specimen Loading for HFIR-MFE-RB-12J
500°C

Alloy	PRZ Tubes JP/US	1.5 mm CVN (JP)	SS-J (JP)	DCT (JP/ US)	TEM (JP/ US)	U.S. SS-3	U.S. CVN	U.S. PCVN	Bend Bar 1 2x2x15mm (JP)	Bend Bar 2 1x2x15 (JP)	Bend Bar 3 0.5x2x15 (JP)	Bend Bar 4 .25x2x15 (JP)	Bend Bar 5 .6x1.4x9 (JP)	Bend Bar 6 2x4x25 (PNL/ORNL)	Bend Bar 7 0.7x1x10 (JP)	Bend Bar 8 3x2.5x25 (ORNL)	Fiber Bundle Tube 2od x 50mm	Thermal Diffusivity 10dx2mm (US)
JLF-1	5/0	6	3	3/3	15/0	10	5	5										
JLF-1B	3/0	6	3		6/0													
JLF-1Mn1	3/0	6	2		6/0													
JLF-1Mn2	3/0	6	2		6/0													
JLF-1LS																		
JLF-1LM																		
JLF-1LSM																		
F82H	5/0	6	2		10/0													
Kimura (ferritic)					30/0													
ODSHK (ferritic)		6	2		6/0													
9Cr-2WVTa																		
V-4Cr-4Ti-.1Si(JP)			9		10/0													
V-4Cr-4Ti(JP)			9		10/0													
V-5Cr-4Ti(JP)			9		10/0													
V-4Cr-3Ti(JP)			9		10/0													
V-5Cr-3Ti(JP)			9		10/0													
V-5Cr-5Ti(JP)			9		10/0													
V-4Fe-4Ti-.1Si			9		10/0													
V-4Fe-4Ti			9		10/0													
V-4Fe-3Ti			9		10/0													
V-4Cr-4Ti-.1SiR			9		10/0													
V-4Cr-4Ti-SiAlY-x			40		50/0													
V-4Cr-4Ti 832665 (Partial rxl)	0/6				0/3	3	5											
V-4Cr-4Ti 832665 (Full rxl)					0/3	3												
V-5Cr-5Ti					0/4	1												
V-4Cr-4Ti-Si					0/4	1												
V-3Cr-3Ti					0/4	2												
V-6Cr-3Ti					0/4	2												
V-6Cr-6Ti					0/4													
V-4Cr-4Ti-B					0/4	2												
SiC/SiC														24		10		7
SiC (B,Be,N)					6/6				9									
Al_2O_3					6/0				10	8	10	10	1					
AlN					6/0				16									
MgO/xAl_2O_3					6/0				9									
SiO_2									3									
TiCx					9/0													

1 Temp Monitors
(Same as Ti)

Table 1. Specimen Loading for HFIR-MFE-RB-12J (cont'd)
500°C

Alloy	PRZ Tubes (JP)	1.5 mm CVN (JP)	SS-J (JP)	DCT (JP/ US)	TEM (JP/ US)	U.S. SS-3	U.S. CVN	U.S. PCVN	Bend Bar 1 2x2x15mm (JP)	Bend Bar 2 1x2x15 (JP)	Bend Bar 3 0.5x2x15 (JP)	Bend Bar 4 .25x2x15 (JP)	Bend Bar 5 .6x1.4x9 (JP)	Bend Bar 6 2x4x25 (PNL/ORNL)	Bend Bar 7 0.7x1x10 (JP)	Bend Bar 8 3x2.5x25 (ORNL)	Fiber Bundle Tube 2od x 50mm	Thermal Diffusivity 10dx2mm (US)
C/Cu Joints									8									
V/ceramics					6/0								19					
SiC Fiber																	10	
Transmutation Series																		
V			6		30/0													
V-xCr			4		40/0													
V-4Ti-4Cr			4		40/0													
Cu			4		20/0													
Cu-xNi-yZn			4		40/0													
Cu-xNi-yZnNi			4		40/0													
Fe			6		40/0													
Fe-W&Mn			6		30/0													
ODS			6		20/0													
Fe-Cr-Ni			12		30/0													
Fe-Cr-Ni-x			12		40/0													
316/TiN			12		30/0													
TiAl					10/0													
SiC					20/0													
Al, Al-Si																		
Mo alloys					20/0										59			
Irradiated Cu alloys					18/0													
JAERI/U.S.																		
F82H (HT-1)	8			6	10	11	6	5										
F82H (HT-2)				2	10	5	6	5										
F82H Ni doped				2	10	4	5											
F82H weld				2	10	4	5											
F82H weldment						4												
F82H HAZ						4												
9Cr-2WVTa				2	10	4	6	5										
Ferritic Alloys TBD					50													

Specimen Loading Configuration

The specimens are loaded into round holes and square or rectangular slots along the longitudinal axes of the capsules. Figure 1 shows the center sections of the capsules identifying the holes and slots. The upper and lower sections of each capsule are shown in Fig. 2. In HFIR-MFE-RB-11J, which will be referred to as 11J, the upper and lower sections contain disc compact tension specimens (DCT). In HFIR-MFE-RB-12J, which will be referred to as 12J, the upper and lower sections contain Charpy v-notch specimens (CVN), bend bar specimens (BB), and DCT specimens. The overall geometry of the specimens is shown in Table 2.

Table 2. Specimen Types and Overall Sizes
(The experimenter is the person who may be contacted to obtain drawings.)

Specimen Type	Designation	Overall Dimensions (mm)	Experimenter
Trans. Elect. Micros.	TEM	3 x 0.15-0.25	
Tensile	SSJ	16 x 4 x 0.25	Kohno
Tensile	SS-3	25 x 4.95 x 0.76	Grossbeck
Pressurized Tube		22.4 x 4.57 dia	Kohno
Compact Tension	DCT	9.6 dia x 3.93	Kimura
Compact Tension	DCT	12.5 dia x 4.62	Grossbeck
Charpy	1.5 CVN	20 x 1.5 x 1.5	Kohno
Charpy	CVN	25 x 3.33	Grossbeck
Bend Bar	BB1	15 x 2 x 2	Satou
Bend Bar	BB2	15 x 2 x 1	Satou
Bend Bar	BB3	15 x 2 x 0.5	Satou
Bend Bar	BB4	15 x 2 x 0.25	Satou
Bend Bar	BB5	9.0 x 1.4 x 0.6	Satou
Bend Bar	BB6	25 x 4 x 2	Satou
Bend Bar	BB7	10 x 1 x 0.7	Satou
Bend Bar	BB8	25 x 3 x 2.5	Snead
Fiber Tube	SiC Tube	48 x 2 dia	Satou
Thermal Cond.	TD	10 dia x 2	Satou

The specimen loading for the upper and lower sections of 11J is shown in Table 3. Tables 4 and 5 contain the specimen loading for 12J. Since specimens are loaded side by side in a given slot, two columns are allotted for each row (slot). As can be seen in Fig. 1, there is an inner and an outer specimen holder in the center section of each capsule. The two holders are separate and fit concentrically together very tightly so as not to impede radial heat transfer. The specimen loading for the 11J inner holder is given in Table 6. The specimens are listed top to bottom as

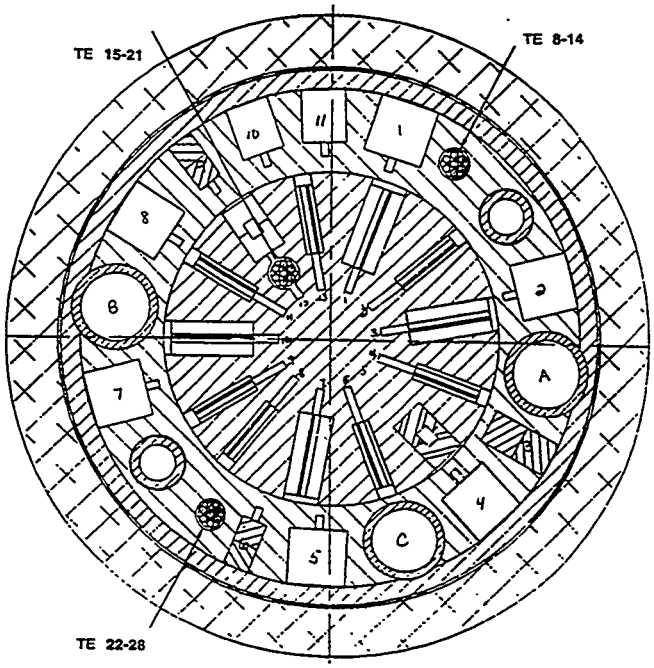

(A) HFIR-MFE-RB-11J

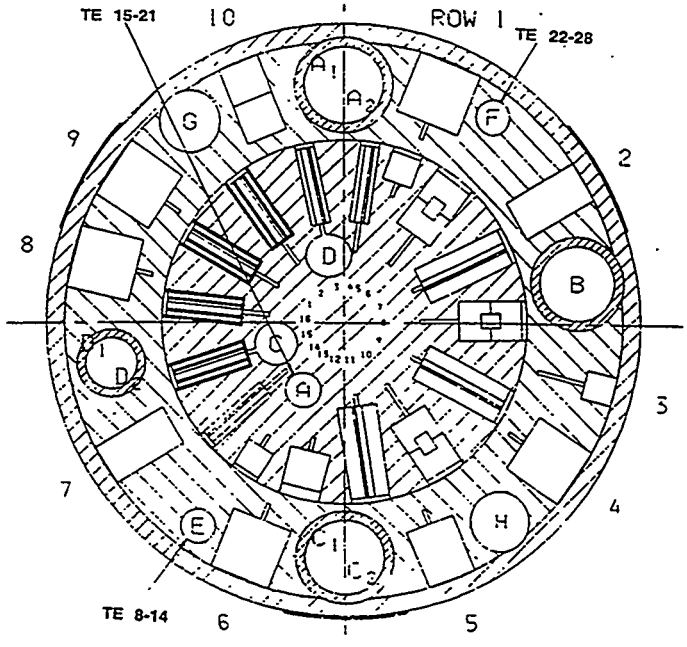

(B) HFIR-MFE-RB-12J

Fig. 1. Cross section through the central portion of the irradiation capsules indicating the designations for the holes and slots.

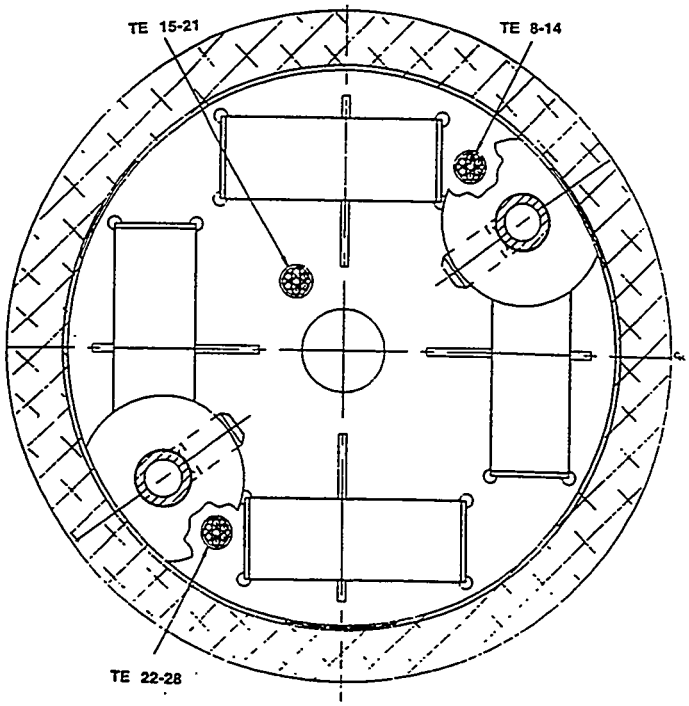

(A) HFIR-MFE-RB-11J

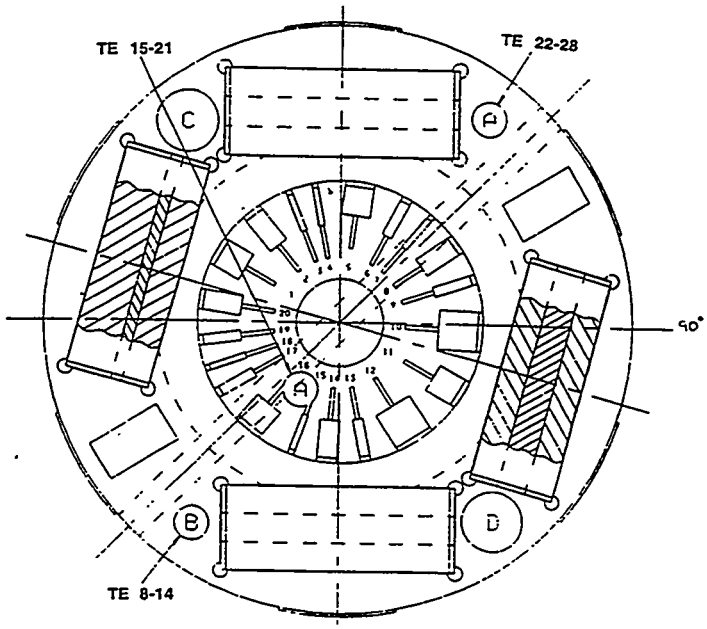

(B) HFIR-MFE-RB-12J

Fig. 2. Cross section through the end sections of the irradiation capsules.

Table 3. Specimen Loading for the End Sections of HFIR-MFE-RB-11J				
Upper Section				
Specimen Type	**DCT**	**DCT**	**DCT**	**DCT**
Row	**1**	**2**	**3**	**4**
	Z106	LFV5	N202	FA13
	FA01	LFV4	TJO2	FA12
	M1	LFV3	TWO2	FA11
Lower Section				
	TWO1	LFW2	LFV2	FA10
	TJ01	LFW1	LFV1	FA09
	N201	FA00	Z105	FA08

Table 4. Specimen Loading for the Upper Section of HFIR-MFE-RB-12J									
Upper Section									
Specimen Type	**DCT**		**DCT, DT**	**TD**	**DCT, TD**	**TD**	**DCT, TD**		**1.5 CVN, BB1, BB2, BB3, BB4**
Row	**1**		**2**		**3**		**4**		**Inner**
	M2	Spacer	B1	D2	P1	D1	P2	Spacer	LDW6
	TWO4		Z108		FA03		N204		DY59
	TW03		Z107		FA02		N203		DY73
									DY78
									LDW5
									DY92
									DY72
									DY56
									DY70
									DY41
									LHW2
									DY50
									DY71
									DY57
									DY35
									LDW4
									DY69
									DY36
									DY68
									DY58

Table 5. Specimen Loading for the Lower Section of HFIR-MFE-RB-12J

Lower Section									
	DCT	BB6	DCT		DCT		DCT	BB6	1.5 CVN, BB1-BB4
Row	1		2		3		4		Inner
	LFTF	D3	LFTH	Spacer	FA16	Spacer	FA19	D4	LHW1
	LFTD		LFTG		FA15		FA18		DY60
	LFTA		LFTB		FA14		FA17		DY74
									DY75
									LDW1
									DY28
									DY79
									DY63
									DY64
									DY42
									LDW3
									DY51
									DT66
									DY61
									DY76
									LDW2
									DY67
									DY65
									DY62

Table 6. Specimen Loading for the Central Inner Holder for HFIR-MFE-RB-11J

Center Section													
Inner Holder													
Row	1		2		3		4		5	6		7	
Specimen Type	SS-3		SS-J		SS-3		SS-4		BB5, BB7	SS-J		SS-3	
	FA12	FA11	AV52	AV46	70	70	LFV6	LFV7	D--5	F5AH	F4AR	TJ03	TJ04
	FA09	FA10	F2AG	F247	UC15	70	LFV4	LFV5	D--4	F5AK	F641	TW03	TW04
	FA07	FA08	AV53	AV44	ST05	ST06	LFV2	LFV3	D--3	TD74	F8AL	TW02	TW01
	FA05	FA06	F34M	F340	ZC13	ZC14	LFV1	LBV5	D--2	F7A9	F5A0	ZH40	ZH41
	A025	A026	AV38	AV41	UC13	UC14	LBV3	LBV4	D--1	TD90	F5A6	Z140	Z141
	A024	A023	AV50	AV48	XC15	ZC15	LBV1	LBV2	C--5	F4AB	TD73	Z142	Z142
	A022	A012	AV51	AV49	XC13	XC14	LDV4	LDV5	C--4	F5AL	F4AH	ST07	N205
	A010	A011	F4A1	F2A2	71	71	LDV2	LDV3	C--3	TD91	TD92	71	72
	A008	A008	AV15	AV43	72	71	LFV8	LDV1	C--2	F8A0	F4A9	ST03	ST04
	A002	A003	F4A3	F34R	72	72	GF38	GF39	C--1	F6AH	F7D0	ST01	STO2
			AV47	AV40			GF30	GF37	FV3	F6AM	TD75		
			AV39	AV37			L1V4	L1V5	FV2	F7AD	F6A6		
			AV54	AV42			L1V2	L1V3	FV1	TD76	F7B0		
			F2A8	FSA1			L1V1	L2V5	FV3	F5A7	F7A6		
			A2AF	F397			L2V3	L2V4	FV2	F6A4	F6A2		
			TD95	TD96			L2V1	L2V2	FV1	F7A1	TD72		
									E--2				
									E--1				
									B--3				
									B--2				
									B--1				
									A--5				
									A--3				
									A--2				
									A--1				
									A--4				
Row	8		9		10		11		12	13			
	SS-J		SS-J		SS-3		SS-J		BB7	SS-J			
	GB38	GB39	AL19	AA47	FK08	FK09	TA03	TD16	H--5	TD55	TD40		
	GA39	GA30	AF87	AL17	FK06	FK07	TD36	TD25	H--4	TD85	TD84		
	LHV1	LHV4	AF85	AF82	FK04	FK05	F8AG	TA00	H--3	TD52	TD65		
	LHV5	YD08	AF84	AF86	FK02	FK03	TD10	TD93	H--2	TD83	TD45		
	GD30	YD09	AF91	AF92	FK00	FK01	TD13	F8A7	H--1	TD54	TD63		
	AA41	YD04	AF90	AA44	TH04	TH05	TA04	TD30	F--3	TD41	TD43		
	AA39	YD10	AA45	AF79	TH02	TH03	TD94	TD23	F--3	TD56	TD82		
	AA37	YD06	AL16	AF81	TJ01	TJ02	F8AR	TD33	F--2	TD70	TD81		
	AA36	YD05	AL20	AA49	N203	N204	TA05	TD32	G--5	TD80	TD53		
	AA40	YD03	AF80	AF77	N201	N202	TA01	TD11	G--4	TD35	TD61		
	AA38	YD07	AA43	AA48			TD21	TA06	G--3	TD82	TD51		
	GD38	YD01	AF83	AA42			TD15	TA02	G--2	TD86	TD71		
	GB37	YD02	AL18	AA46			F8AH	TD26	G--1	TD50	TD64		
	LHV2	LHV3	AF89	AF88			TD12	TD24	J--5	TD46	TD44		
	GA38	GA37	AF78	AL15			TD22	TD14	J--4	TD42	TD66		
	GD37	GD39	AL14	AL13			TD26	TD31	J--3	TD60	TD34		
									J--2				
									J--1				
									F--4				
									E--3				
									F--5				
									I--5				
									I--4				
									I--3				
									I--2				
									I--1				

they are loaded in the capsules. As with the previous tables, specimens loaded side by side appear in adjacent columns under the same row number. Table 7 shows the loading for the outer holder of 11J. In cases where more than one type of specimen is loaded into one slot, all types are listed at the column head. The loadings for the inner and outer central holders for 12J appear in Tables 8 and 9, respectively.

As can be seen in Tables 7 and 9, the TEM specimens are in the outer holders of each capsule, all in one hole in each capsule. The TEM specimens are loaded in tubes with welded end caps and placed into the holes provided. The tubes are of various lengths up to 25 mm in length. Most of the tubes are aluminum with slots for ease of disassembly, but some are zirconium and are completely sealed for protection of vanadium alloys. The loading of the tubes is shown in Tables 10 and 11 for 11J and 12J, respectively. The Zr tubes are indicated below the tube designation. Tubes 1-1 and 2-1 contain radioactive specimens from a previous irradiation in the FFTF. The specimens are listed in the order loaded so that the bottom specimen is listed first. Multiple columns are used simply to accommodate the large number of specimens; all are loaded one on top of the other.

Thermal Neutron Shield

Development of the thermal neutron shield presented the most difficult challenge of the irradiation experiment. The first task was to select the absorber material for the shield. Most available thermal absorbers can be excluded. Hafnium has been used as a thermal neutron shield in flux tailoring experiments in the HFIR,[1] but in the space available, only a factor of ten attenuation can be achieved. Gadolinium and cadmium have such high cross sections that they burn too fast to achieve the required exposure. Boron can be made to last for the duration of the experiment, in this case about one year, especially since it may be enriched in the ^{10}B isotope. However, since the absorption reactions are (n, α), helium will collect in the shield container and produce a gas pressure of about 70 MPa, 10,000 psi, in the duration of the irradiation. This would necessitate using precious space for thick container walls. Europium can be used because the two isotopes initially present transmute into five additional isotopes of Eu and five isotopes of Gd, many of which have cross sections greater than 1000 barns. Thus each initial atom of Eu can ultimately absorb several neutrons.

Having chosen Eu for the absorber, many restrictions involving practicality and reactor safety must be considered. Europium is a very reactive metal necessitating glove box handling. Because of the reactivity and the fact that the atomic density of monoclinic Eu_2O_3 is 30% higher than Eu metal, europium oxide was selected as the absorber material. Europium oxide reacts with water to form a hydroxide which causes disintegration of the physical structure and swelling of about a factor of two. In the case of a leak in the can containing the shield, Eu_2O_3 could escape, and the can could swell and prevent removal from the reactor.

For the first line of defense, a shield can was designed such that two independent welds would have to fail in order to produce a leak. The design of the welds is illustrated in Fig. 3. In the event of a leak, a packed powder of Eu_2O_3 (which could easily be packed to 50% of theoretical density) would allow percolation of water and swelling in a matter of a few days at 70°C. To provide a second line of defense, the Eu_2O_3 was sintered to 92% of theoretical density to reduce percolation of water. In addition, the Eu_2O_3 was coated with aluminum to provide a water resistant coating.

A shield 413 mm in length was required to cover the specimen region of the capsule, but in order to reduce the shield to manageable sections, rings 25 to 50 mm in length were fabricated. The thickness of the rings was 1.85 mm and the outside diameter was 48.3 mm. A step 0.76 mm in length and of half the wall thickness was machined on each end in order to avoid neutron streaming through the cracks between the rings when stacked together. Several completed rings are shown in Fig. 4.

Table 7. Specimen Loading for the Central Outer Holder for HFIR-MFE-RB-11J											
Center Section											
Outer Holder											
Row	1	2	3					4	5	6	
Specimen Type	CVN	CVN	BB1, BB2, BB3, BB4					CVN	CVN	1.5 CVN	
	A001	N201	Y605	Y606				QC61	TWO5	L1V1	L1V2
	A002	N202	DYO7	DY26	DY31	DY32	DY13	FK02	TWO4	L1V3	L1V4
	A003	N203	DY08	DY25	DY29	DY50	DY14	FK03	TWO3	L1V5	L1V6
	A004	N204	DY02	DY91				FK04	TWO2	L2V1	L2V2
	A005	FA42	DY09	DY21	DY22	DY15		A021	TWO1	L2V3	L2V4
	A006	FA49	DT01	DT04				A023	TJ15	L2V5	L2V6
	FA38	FA50	Y601	Y607				A024	TJ14	LFV1	LFV2
	FA39	FA51	DY38	DY40				A025	TJ13	LFV3	LFV4
	FA40	FA54	DY01	DY05				A026	TJ12	LFV6	LFV7
	FA41	FA55	DY37	DY39				QC62	TJ11	LFV8	LFV9
			Y602	Y604						LBV1	LBV2
			DT03	DT06						LBV3	LBV4
			DY10	DY23	DY24	DY16				LBV5	LBV6
			DT05	DY12							
			DY11	DY27	DY33	DY34	DY17				
			DY03	DY18	DY19						
			Y603	Y608							
Row	7	8	9		10	11	A	B	C		
	CVN	CVN	1.5 CVN		BB8	BB8	Pressurized Tubes	Pressurized Tubes	TEM Holders		
	FK34	QC64	LHV1	LHV2	917 T4	919 M2	LFVG	L8VF	1–2		
	FK33	N205	LHV3	LHV4	1–6 SiC	13–18 SiC	LFVF	LBVD	1–1		
	FK32	FK01	LHV5	LHV6	T13	942 T4	LFVD	LBVB	1–8		
	FK31	FK00	LHV7	LHV8	917 M4	19–24 SiC	LFVB	LBVA	1–9		
	FK30	145Z1	LHV5	LHV9	843 M2	942 M4	LFVA	L2VF	1–10		
	130Z1	144Z1	GF31	GF32	T11	917 T3	L2VA	L2VD	1–11		
	129Z1	143Z1	GF33	GF34	843 T4	919 M1	LHVG	L2VB	1–12		
	127Z1	142Z1	GF35	GF36	T7	943 M3	LHVF	L1VF	1–6		
	126Z1	138Z1	LDV1	GF37	7–12 SiC	25–30 SiC	LHVD	L1VD	1–5		
	125Z1	QC63	LDV2	LDV3	843 M1	919 T2	LHVB	L1VB	1–4		
			LDV4	LDV5			LHVA	L1VA			
			LDV6	LDV7							
			LDV8	LDV9							

Table 8. Specimen Loading for the Central Inner Holder for the HFIR-MFE-RB-12J									
Center Section									
Inner Holder									
Row	1		2		3		4		5
	SS-J		SS-J		SS-J		SS-J		1.5 CVN
	TH61	TH56	F7F0	F6A8	AA87	AFJ7	AFL7	AFL2	LFW6
	TH46	TH74	F8AL	F7A5	AF72	AA90	AFL1	AFK5	LFW5
	TH73	TH71	F6AL	F5A4	AA97	AFJ8	AFL3	AFL8	LFW4
	TH58	TH63	F5AG	F4AF	AFK9	AA95	AFK3	AFL9	LFW3
	TH51	TH55	TB06	TB05	AA99	AA92	LDW2	AFL6	LFW2
	TH77	TH75	F4AM	F6A9	AF70	AFK1	LFW1	L2W2	LFW1
	TH66	TH72	TB00	TB03	AA94	AA98	LBW2	LHW2	LHW6
	TH80	TH64	TB07	TB04	AF75	AA96	L1W2	L2W1	L1W6
	TH53	TH62	F7AF	F8AM	AFJ0	AA89	LHW1	LFW3	L1W5
	TH47	TH54	F6A5	F7AA	AF71	AF67	L1W1	LBW1	L1W4
	TH48	TH76	F7G0	F6AD	AF76	AF73	LFW2	LDW1	L1W3
	TH60	TH57	F8AB	F8AD	AA91	AA88	AFK7	AFK8	L1W2
	TH50	TH70	F8A4	F7A2	AF74	AFJ9	AFM2	AFM1	L1W1
	TH81	TH65	TB01	TB02	AF69	AA93	AFL4	AFK6	
	TH67	TH52	F6AK	F8A9	AF68	AA86	AFL5	AFK4	
	TH45	TH78	AV99	AV98	AFK0	AFK2	AFL0	TH38	
Row	6	7		8	9		10	11	
	BB5, BB7	SS-3		BB7	SS-3		BB7	SS-3	
	FY6	N206	N207	G-+5	71	71	H-+3	TH06	TH07
	FY5	FA14	FA15	C-+3	70	70	A-+5	TW07	TW08
	FY4	A056	A055	I-+3	UC16	UC17	E-+4	TJ05	TJ06
	FX7	A038	A039	I-+4	ZC16	ZC17	D-+2	FK18	FK19
	FX6	A036	FA13	H-+5	ST10	ST11	M-+2	FK16	FK17
	FX5	A034	A035	D-+4	ST08	ST09	B--4	FK14	FK15
	FX4	A031	A033	H-+4	XC17	XC16	C-+2	FK12	FK13
	FX3	A029	A030	G-+2	TJ07	TJ08	A-+2	FK10	FK11
	FX2	FA16	FA17	F-+1	Z144	Z145	J-+1	TW05	TW06
	FX1	N208	N209	F-+5	Z146	Z147	D-+5	TH08	TH09
	G-+1			A-+3			B-+4		
	F-+1			H-+2			J-+2		
	E-+1			C-+4			E--4		
	D-+1			F-+2			B-+3		
	C-+1			C-+5			K-+1		
	B-+1			H-+1			E--5		
	A-+1			D-+3			B--5		
	FZ7			E-+5			I-+2		
	FZ6			J-+5			G-+3		
	FZ5			J-+4			M-+1		
	FZ4			G-+4			K-+2		
	FZ3			J-+3			K-+2		
	FZ2			E-+3			K-+3		
	FZ1			A-+4			E-+2		
	FVA			I-+1			B-+2		
	FVD			F-+4			B-+5		

Table 8. Specimen Loading for the Central Inner Holder for the HFIR-MFE-RB-12J (cont'd)										
Center Section										
Inner Holder										
Row	12	13	14		15		16		C	D
	BB1	1.5 CVN	SS-J		SS-J		SS-J		SiC Tubes	SiC Tubes
	Blank	LBW6	TH92	TH88	TH31	TH23	AV92	AV95	J2	J20
	Blank	LBW5	TH84	TH93	TH17	TH35	AVB5	AVB6	J4	J12
	Y624	LBW4	TH98	TH87	TH33	TH41	AV00	AVB1	J6	J14
	Y623	LBW3	TH82	TH96	TH30	TH14	AVB3	AVB9	J8	J16
	Y622	LBW2	TH97	TH91	TH26	TH27	F2A6	F5A4	J10	J18
	Y621	LBW1	TH86	TH95	TH24	TH44	F2A5	F2AM		
	Y620	LHW5	TH90	TH94	TH25	TH20	F5AD	F2AR		
	Y619	L2W6	TH85	TH83	TH36	TH32	F4A5	F4A6		
	Y618	L2W5	YD13	YD12	TH21	TH18	F349	F4A2		
	Y617	L2W4	YD16	YD17	TH11	TH28	F2AK	F4A7		
	Y615	L2W3	YD14	YD18	TH42	TB08	F346	F2A3		
	Y614	L2W2	YD19	YD11	TH13	TH43	F5A2	F5A8		
	Y613	L2W1	YD20	YD15	TH10	TH34	AVB4	AVB7		
	Y612		F343	F344	TH40	TH12	AV96	AVB8		
	Y611		AVC1	AV55	TH15	TH22	AVB2	AV94		
	Y610		AVB0	AV56	TH37	TH16	AV97	AV93		
	Y609									

Table 9. Specimen Loading for the Central Outer Holder for the HFIR-MFE-RB-12J

Center Section											
Outer Holder											
Row	1	2	3	4	5	6	7	8	9	10	
	CVN	B6	1.5 CVN, CVN	CVN	BB8	CVN	BB6	CVN	CVN	BB1	
	QC65	P6	149Z1	QC66	942MI	QC67	S8	QC68	QC69	DY06	DY49
	151Z1	D5	148Z1	FA47	T3	FK09	N3	FK39	N211	DY44	DY45
	A027	H3	147Z1	FA46	942T2	FK06	D7	FK38	N210	DY80	DY83
	A007	G4	135Z1	FA45	942M2	FK05	S7	FK37	N209	DY52	DY54
	A012	P5	134Z1	FA43	942T1	FA48	S3	FK36	N208	DT07	DT11
	A011	G3	133Z1	FA44	917M1	FA64	N2	FK35	TW10	DY02	DY04
	A010	H2	132Z1	A031	917M2	FA62	H5	FK13	TW09	DT14	DT16
	A009	G1	131Z1	A030	917T2	FA61	D6	FK11	TW08	DY93	DY96
	A008	H1	LHW4	A029	917T1	FA59	N1	N207	TWO7	DT10	DT12
		P2	LHW3	A028	T5	FA58	S1	N206	TW06	DY94	DY95
										DY81	DY82
										DY46	DY47
										DT08	DT09
										DT53	DY55
										DT13	DT15
										DY43	DY48
										Y616	Y616

Row	A	B	C	D
	Pressurized Tubes	Pressurized Tubes	Pressurized Tubes	TEM Holders
	3	L2WA	5	2-12
	11	L2WB	9	2-11
	12	L2WD	1	2-10
	LFWA	X6X6	LIWA	2-9
	LFWB	X7X7	LIWB	2-8
	LFWD	X8X8	LBWA	2-1
	LFWF	X9X9	LBWD	2-2
	LHWB	1010	LHWA	2-4
	LIWD	1111	LHWD	2-5
	LBWD	1414	LHWF	2-6
	LHWG	1515	LFWG	

Table 10. Loading of TEM Specimens in HFIR-MFE-RB-11J									
Holder	1–1	1–2		1–4			1–5		
					(Zr)				
Bottom	YS52	G604	KKG1	TE10	TE70	TED0	F2AG	F4D5	F65L
	YS55	G603	KKG2	TE11	TE71	TED1	F2AF	F4D8	F65A
	YS73	G602	KKG3	TE12	TE72	TED2	TEJ0	TEK3	F65F
	YY52	G610	KKB2	TE13	TE73	TED3	F2AM	F4DR	F65H
	YY55	G609	KKH1	TE14	TE74	TED4	F2AS	F4DG	F659
	YY72	G612	KKH2	TE20	TE80	TEE0	TEJ1	TEK4	F657
	YZ55	G611	YD59	TE21	TE81	TEE1	F2A8	F4DD	TEM0
	YZ73	G601	YB38	TE22	TE82	TEE2	F2AK	D4DF	TEM1
	N234	KKA1	KKI1	TE23	TE83	TEE3	TEJ2	TEL0	TEM2
	N235	KKA2	KKI2	TE24	TE84	TEE4	F2AA	F56F	TEM3
	N236	KKA3	KKI3	TE30	TE90	TEG0	F2AH	F56S	F755
		KKB3	KKJ1	TE31	TE91	TEG1	TEJ3	TEL1	F75V
		KKC1	KKJ2	TE32	TE92	TEG2	F374	F565	F75D
		KKC2	KKJ3	TE33	TE93	TEG3	F37X	F56A	F75G
		KKC3	JAR1	TE34	TE94	TEG4	TEJ4	TEL2	F75H
		KKD1	TW36	TE40	TE00	TEH0	F378	F56G	F75S
		KKD2		TE41	TE01	TEH1	F37K	F56D	F75L
		KKD3		TE42	TE02	TEH2	TEK0	TEL3	F754
		KKE2		TE43	TE03	TEH3	F37M	F65R	F868
		KKF1		TE44	TE04	TEH4	F37F	F655	F86T
		KKF2		TE50	TEA0		TEK1	TEL4	F86V
		KKF3		TE51	TEA1		F4D9		F86H
				TE52	TEA2		F4DB		F866
				TE53	TEA3		TEK2		F86L
				TE54	TEA4				
				TE60	TEB1				
				TE61	TEB2				
				TE62	TEB3				
				TE63	TEB4				
				TE64					

Table 10. Loading of TEM Specimens in HFIR-MFE-RB-11J (cont'd)

Holder	1–6				1–8			1–9		
			(Zr)							
Bottom	AV01	AV16	ND16	46	LFV1	GA3B	FML1	YB19	YB58	YB91
	AV02	AV17	ND10	XD25	LFV2	GA3D	FML2	YB20	YB59	YB93
	AV03	AV18	ND18	XD50	LFV3	GA3F	FML3	YB21	YB60	YB93
	AV04	AV19	ND05	XD45	LFV4	GB3A	FR01	YB22	YB61	YB94
	AV05	AV20	ND19	ZD26	LFV5	GB3B	FR02	YB23	YB62	YB95
	AV06	AV21	ND25	ZD50	LFV6	GB3D	FR03	YB24	YB63	A028
	AV07	AV22	XD32	ZD30	LFV7	GB3F	FR04	YB25	YB64	A029
	AV08	AV23	XD48	UD38	LFV8	GG3D	YB01	YB26	YB65	
	AV09	AV24	XD47	UD45	LFV9	GD3A	YB02	YB27	YB66	
	AV10	AV25	XD34	UD25	LFVA	GD3B	YB03	YB28	YB67	
	AV11	AV26	ZD42	ND08	LFVB	GF3A	YB04	YB29	YB68	
	AV12	AV27	ZD36	ND20	LFVD	GF3B	YB05	YB30	YB69	
	AV13	AV28	ZD27	ND27	LFVF	GF3D	YB06	YB31	YB70	
	AV14	AV29	ZD34	ND09	LFVG	GF3F	YB07	YB32	YB71	
	AV15	AV30	UD33	ND02	LFVH	G03A	YB08	YB33	YB72	
		AV31	UD30	UD48	LBV1	G03B	YB09	YB34	YB73	
		AV32	UD46	ZD31	LBV2	G030	YB10	YB35	YB74	
		AV33	UD26	ZD38	LBV3	G03F	YB11	YB36	YB75	
		AV34	71	XD29	LBV4	G13A	YB12	YB37	YB76	
		AV35	71	XD43	LBV5	G13B	YB13	YB39	YB77	
		AV36	71	ND29	LBV6	G13D	YB14	YB40	YB78	
			70	ND28	L1V1	G13F	YB15	YB41	YB79	
			70	UD21	L1V2	FMA1	YB16	YB42	YB80	
			72		L1V3	FMA2	YB17	YB43	YB81	
			72		L1V4	FMA3	AB18	YB44	YB82	
					L1V5	FMD1	A025	YB45	YB83	
					L1V6	FMD2	A026	YB46	YB84	
					L2V1	FMD3		YB47	YB85	
					L2V2	FMF1		YB48	YB86	
					L2V3	FMF2		YB49	YB87	
					L2V4	FMF3		YB50	YB88	
					L2V5	FMH1		YB51	YB89	
					L2V6	FMH2		YB52	YB90	
					LHV1	FMH3		YB53		
					LHV2	FMK1		YB54		
					LHV3	FMK2		YB55		
					LHV4	FMK3		YB56		
					LHV7			YB57		
					LHV8					
					LHV9					
					LHVA					

Table 10. Loading of TEM Specimens In HFIR-MFE-RB-11J (cont'd)

Holder	1–10				1–11		1–12		
Bottom	YB97	XR1T	AF13	AF46	AA07	LDV1	A001	TWO1	SiC
	YB98	XR1X	AF14	AF47	AA08	LDV2	A002	TW02	SiC
	YB99	XR1Y	AF15	AF48	AA09	LDV3	A003	TW03	SiC
	YD50	XR21	AF16	AF49	AA10	LDV4	A004	TW04	SiC
	YD51	XR22	AF17	AF50	AA11	LDV5	A005	TW05	N425
	YD52	XR23	AF18	AH51	AA12	LDV6	A006	TW06	N227
	YD53	XR24	AF19	A030	AL01		A007	TW07	N228
	YD54	XR25	AF20	A031	AL02		A008	TW08	
	YD55	AA01	AF21	A032	AL03		A009	TW09	
	YD56	AA02	AF22	TW25	AL04		A010	TW10	
	YD57	AA03	AF23	CAPA?	AL05		FA14	XI62	
	YD58	AA04	AF24	N232	AL06		FA19	XI67	
	YD60	AA05	AF25		AL07		FA20	XI70	
	YD61	AA06	AF26		AL08		FA10	XI59	
	XR11	AF01	AF27		AL09		FA31	XH63	
	XR12	AF02	AF38		AL10		FA15	HX68	
	XR13	AF03	AF29		AL11		FA12	XH69	
	XR14	AF04	AF30		AL12		N201	XH66	
	XR15	AF05	AF31		AC01		N202		
	XR16	AF06	AF32		AC02		N203		
	XR17	AF07	AF33		AC03		N204		
	XR18	AF08	AF34		AC04		N205		
	XR19	AF09	AF35		AC05		N206		
	XR1A	AF10	AF36		AC06		N207		
	XR1B	AF11	AF37		B000		N208		
	XR1D	AF12	AF38		B001		N209		
	XR1F		AF39		B100		N210		
	XR1G		AF40		B101				
	XR1H		AF41		B200				
	XR1K		AF42		B201				
	XR1L		AF43		B300				
	XR1M		AF44		B301				
	XR1R		AF45						
	XR1S								

Table 11. Loading of TEM Specimens in HFIR-MFE-RB-12J

Holder	2–1	2–2		2–4			2–5			
					(Zr)				(Zr)	
Bottom	YS53	G605	KKE-1	TE15	TE75	TED5	F2AB	FD4A	F65K	AV56
	YS54	G606	KKE-2	TE16	TE76	TED6	F2AB	F4DS	F65D	AV57
	YS56	G607	KKF-1	TE17	TE77	TED7	TEJ5	TEK7	F65G	AV58
	YS57	G608	KKF-2	TE18	TE78	TED8	F2AL	F4DW	F653	AV59
	YY53	G613	KKF-3	TE19	TE79	TED9	F2A4	FRDZ	F65S	AV60
	YY54	G614	KKG-1	TE25	TE85	TEE5	TEJ6	TEK8	F656	AV61
	YY56	G615	KKG-2	TE26	TE86	TEE6	F2AT	F4F1	TEM5	AV62
	YY57	G616	KKG-3	TE27	TE87	TEE7	F2A7	F4F3	TEM6	AV63
	YY74	YC42	KKH-1	TE28	TE88	TEE8	TEJ7	TEK9	TEM7	AV64
	YY75	AFB9	KKH-2	TE29	TE89	TEE9	F2AD	F4F4	TEM8	AV65
	YZ53	KKA-1	KKH-3	TE35	TE95	TEG5	F2AV	F4F5	TEM9	
	YZ54	KKA-2	KKI-1	TE36	TE96	TEG6	TEJ8	TEL5	F75A	
	YZ56	KKA-3	KKI-2	TE37	TE97	TEG7	F379	F563	F758	
	YZ57	KKB-1	KKI-3	TE38	TE98	TEG8	F37A	F565	F756	
	YZ74	KKB-2	KKJ-1	TE39	TE99	TEG9	TEJ9	TEL6	F75K	
	YZ75	KKC-1	KKJ-2	TE45	TE05	TEM5	F37G	F56B	F753	
	YS74	KKC-2		TE46	TE06	TEM6	F37H	F56H	F75R	
	YS75	KKC-3		TE47	TE07	TEM7	TEK5	TEL7	F757	
		KKD-1		TE48	TE08	TEM8	F37W	F56M	F863	
		KKD-2		TE49	TE09	TEH9	F37Y	F56T	F867	
		KKD-3		TE55	TEA5		TEK6	TEL8	F86A	
				TE56	TEA6			F65T	F86G	
				TE57	TEA7			F654	F86M	
				TE58	TEA8			TEL9	F86R	
				TE59	TEA9					
				TE65	TEB5					
				TE66	TEB6					
				TE67	TEB7					
				TE68	TEB8					
				TE69	TEB9					

Table 11. Loading of TEM Specimens in HFIR-MFE-RB-12J (cont'd)

Holder	2-6			2-8				2-9			
		(Zr)									
Bottom	AV66	ND15	71	LFW1	LHW1	G05A	FMB1	FR05	YC12	YC26	LDW1
	AV67	ND14	71	LFW2	LHW2	G05B	FMB2	FR06	YC48	YC62	LDW2
	AV68	ND30	46	LFW3	LHW3	G05D	FMB3	FR07	YC13	YC27	LDW3
	AV69	ND24	46	LFW4	LHW4	G15A	FMG1	F409	YC49	YC63	LDW4
	AV70	ND03	72	LFW5	LHW5	G15B	FMG2	FR0A	YC14	YC28	LDW5
	AV71	ND12	72	LFW6	LHW6	G15B	FMG3	FR0D	YC50	YC64	LDW6
	AV72	XD22	71	LFW7	LHW7	G15D	FMAA	FR0F	YC15	YC29	TW45
	AV73	XD26	71	LFW8	LHW8	G15F	FMAB	YC01	YC51	YC39	TW47
	AV74	XD41	71	LFW9	LHW9	FMA4	FMBA	YC02	YC16	YC30	TW48
	AV75	XD49	46	LFWA	LHWA	FMA6	FMBB	YC03	YC52	YC37	
	AV76	ZD37	46	LFWB	GA5A	FMA7	FMDA	YC59	YC17	XR33	
	AV77	ZD25		LFWD	GA5B	FMD4	FMDB	YC04	YC53	YC88	
	AV78	ZD21		LFWF	GA5D	FMD5	FMFA	YC06	YC18	XR34	
	AV79	ZD40		LFWG	GA5F	FMDG	FMFB	YC07	YC54	YC41	
	AV80	UD43		LFWH	GB5A	FMF4	FMGA	YC43	YC19	XR35	
	AV81	UD20		LBW1	GB5B	FMF5	FMGB	YC08	YC55	YC54	
	AV82	UD40		LBW2	GB5D	FMF6	FMHA	YC44	YC20	XR36	
	AV83	UD32		LBW3	GB5F	FMH4	FMHB	YC09	YC56	XR37	
	AV84	71		LBW4	GG5A	FMH5	FMKA	YC45	YC21	XR38	
	AV85	71		LBW5	GG5D	FMH6	FMKB	YC10	YC57	XR39	
	AV86	71		LBW6	GD5A	FMK4	FMLA	YC46	YC22	XR3A	
	AV87	70		L1W1	GD5B	FMK5	FMLB	YC11	YC58	B002	
	AV88	70		L1W2	GD5F	FMK6		YC47	YC23	B003	
	AV89	70		L1W3	GF5A	FML4			YC24	B102	
	AV90	72		L1W4	GF5B	FML5			YC60	B103	
	AV91	72		L1W5	GF5D	FML6			YC25	B202	
		72		L1W6	GF5F				YC61	B203	
		70		L2W1						B302	
		72		L2W2						B303	
				L2W3							
				L2W4							
				L2W5							
				L2W6							

Table 11. Loading of TEM Specimens in HFIR-MFE-RB-12 (cont'd)									
Holder	2–10				2–11			2–12	
Bottom	YC31	AFA8	AFD1		AFF1	AFG3	AA55	A011	TW11
	YC65	YC78	YC92		YD76	XR26	XR2R	A012	TW12
	YC32	AFA9	AFD2		AFF2	AFG4	AA56	A013	TW13
	YC66	YC79	YC93		YD77	XR27	XR2S	A014	TW14
	YC33	AFA0	AFD3		AFF3	AFG5	AA57	A015	TW15
	YC67	YC80	YC94		YD78	XR28	XR2T	A016	TW16
	YC68	AFB1	AFD4		AFF4	AFG6	AA58	A017	TW18
	YC35	YC81	YC95		YD79	AFG7	XR2X	A018	TW19
	YC69	AFB2	AFD5		AFF5	XR2A	XR2Y	A019	TW20
	YC36	YC82	YC96		YD80	AFG8	AA60	A020	XI66
	YC70	AFB3	AFD6		AFF6	AFG9	XR31	FA17	XI57
	AFA1	YC83	Y097		YD81	XR2D	AA61	FA16	XI65
	YC71	AFB4	AFD7		AFF7	AFG0	XR32	FA13	XI63
	AFA2	YC84	YC98		YD82	XR2G	AA62	FA18	XH60
	YC72	AFB5	AFD8		AFF8	AA51	XR2F	FA22	XH65
	AFA3	YC85	YC99		YD83	XR2H	AC19	FA11	XH56
	YC73	AFB6	AFD9		AFF9	AA52	AC20	FA09	XH58
	AFA4	YC86	AFD0		YD84	XR2K	AC21	N211	
	YC74	AFB7	TW34		AFF0	AA53	AC22	N212	
	AFA5	YC87	TW35		YD85	XR2L	AC23	N213	
	YC75	AFB8	TW37		AFG1	AA54	AC24	N214	
	AFA6	YC88	TW30		YD86		XR2M	N215	
	YC76	YC89	TW44	N231	AFG2		AA59	N216	
	AFA7	AFB0	TW40	N237	YD87			N217	
	YC77	YC90	A037	N243				N218	
			A038	N229				N219	
			A043	N230				N220	
			A027						
			A044						

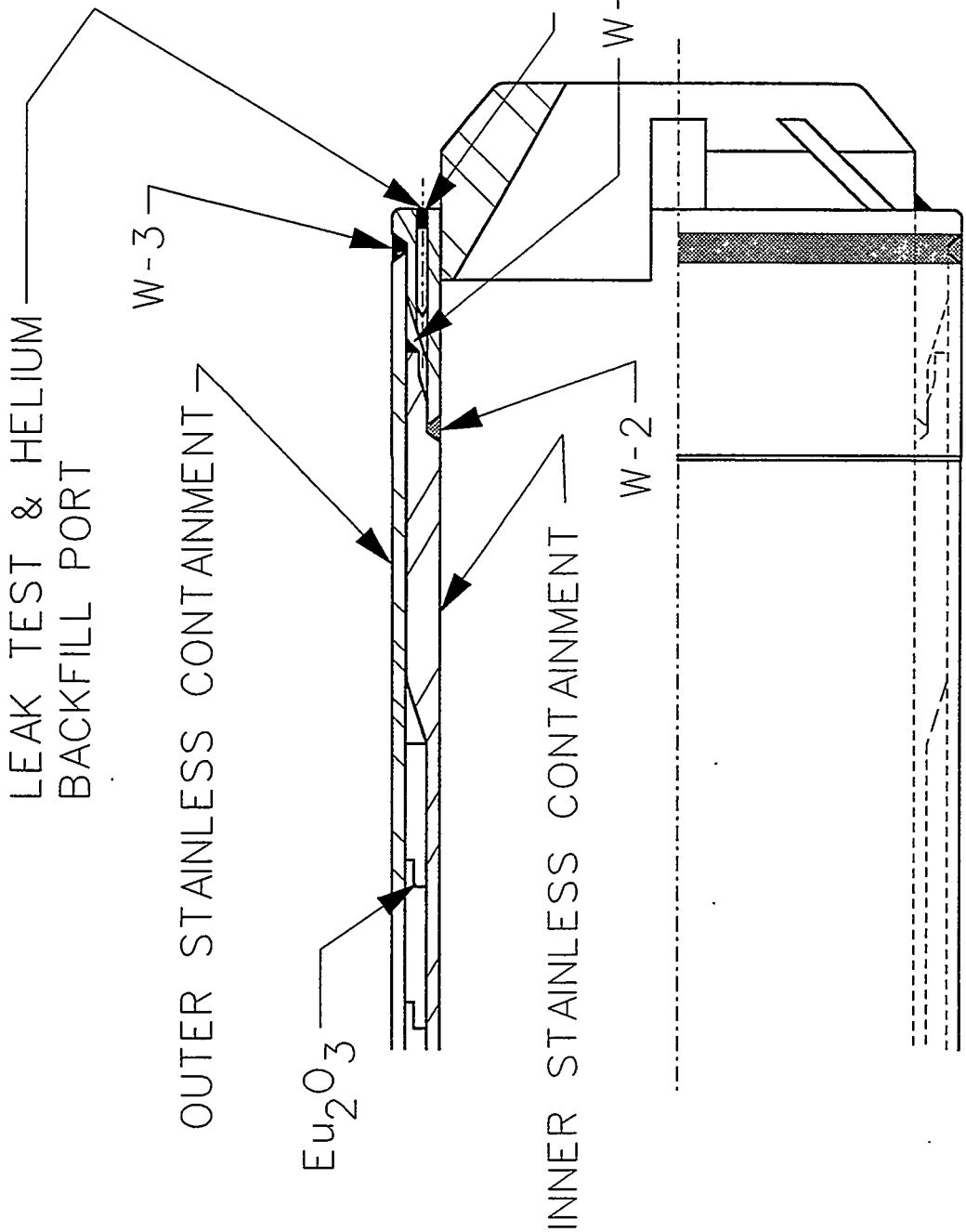

Fig. 3. Bottom section of the shield can showing the details of the seal welds. Weld W-1 and one of W-2, W-3, or W-4 must fail in order to produce a leak. W-4 is the seal for the helium back-fill port to provide a means of leak checking the welds.

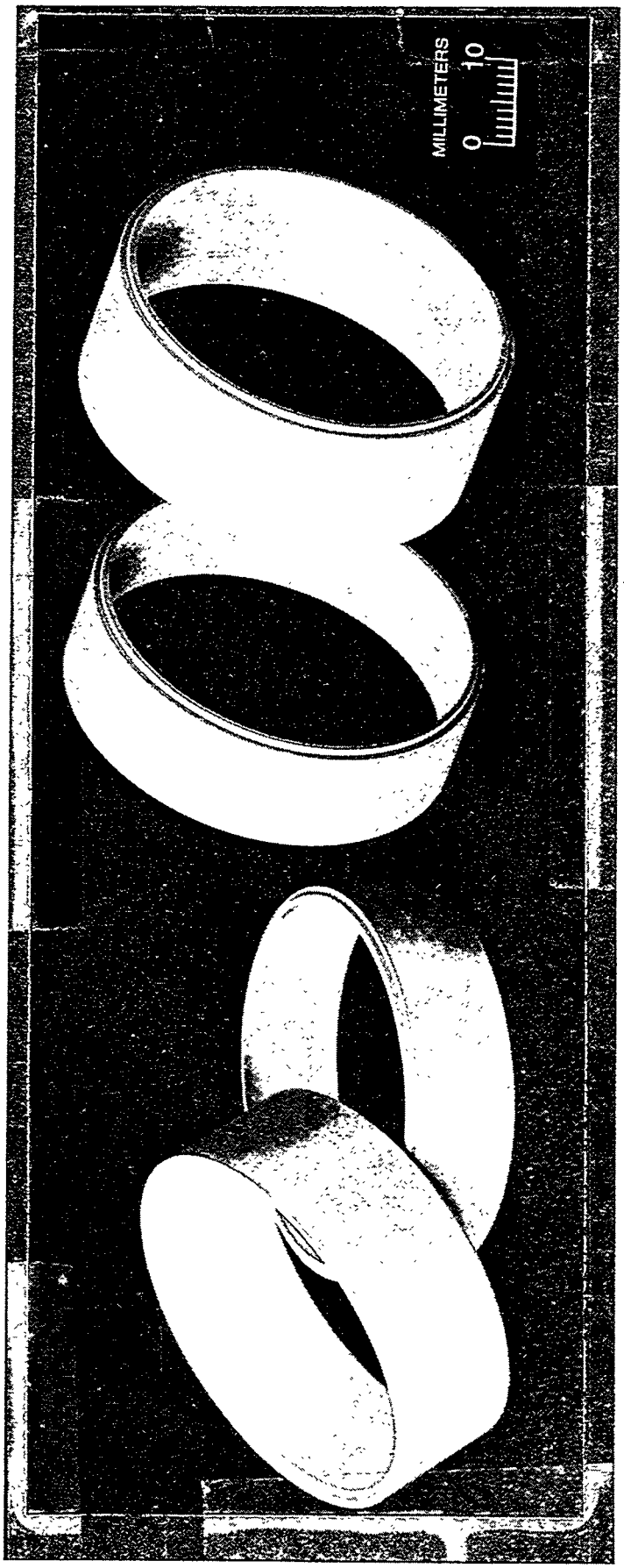

Fig. 4. Rings of europium oxide prior to coating with aluminum and assembling into a shield.

The rings were fabricated by cold pressing and sintering. Cubic Eu_2O_3 powder was isopressed and calcined at 1800°C to transform it to the more dense monoclinic phase. Following crushing, grinding, and milling operations, a binder was introduced to facilitate die pressing. The powder was then pressed in a steel die at 310 MPa, resulting in a compact of 65% of theoretical density. The binder was then burned out at 1300°C in an air atmosphere. The rings were then sintered at 1730°C for one hour in an argon-4%H atmosphere. The final shape was machined to a tolerance of 0.03 mm.* Coating with aluminum was done by plasma sputtering to produce a coating 2-4 μm in thickness. Since the coating produced by this technique was porous, it was sintered in a vacuum at 576°C, 0.9 of the melting point of aluminum, for 4 hours.

The rings were then fitted together on the inner wall of the shield can to form the cylindrical shield pictured in Fig. 5. The ends of the capsules were shielded with sections of a HFIR control plate containing Eu_2O_3 in an Al matrix. Space was not a constraint so that two such 25 mm plates were used and were placed in the specimen chamber which had a monitored containment. In the case of a leak, a high moisture level in the purge gas could be detected within a few minutes.

Thermal Performance

The temperature distribution in the capsules was examined carefully during the first cycle of operation. The temperature distributions are shown in Figs. 6 and 7 for 11J and 12J, respectively. The temperatures plotted are thermocouple temperatures. Specimen temperatures are higher according to heat conduction from the particular specimen and to local nuclear heating, which depends upon axial position and shielding. Calculated corrections to thermocouple temperatures are given in Figs. 6 and 7. It is apparent that the end regions are cooler than expected in both capsules. In 11J, the ends were about 50°C lower than the design temperature, and in 12J the end regions were about 150°C below the design temperature.

It is believed that the low temperatures are the result of two causes: end losses and centering pad losses. A few specimens in the outer middle region are also affected by centering pad losses. Centering pads are used to maintain the position of the specimen holder in the capsule and to maintain the gap needed for the flow of the control gas. However, the centering pads also provide a pathway for heat loss. The localized temperature depression is approximately 20°C (3%) in 11J and 50°C (6%) in 12J. The centering pads affect only those specimens that are near centering pad locations, along with all the upper and lower regions.

The majority of the specimens in both capsules is operating within the desired temperature bands: ±20 C for both the 300 and 500°C capsules. The average of the central thermocouples was chosen for the control temperature in both capsules. The end regions are considered to be at 250 and 350°C for 11J and 12J, respectively. As with any irradiation experiment that does not contain liquid metal, variations between specimens are expected.

Conclusions

Two unique first of a kind irradiation experiments have begun irradiation in the HFIR. The newly developed europium oxide thermal shields permit fast reactor irradiations in the HFIR including, if desired, irradiation at temperatures as low as 60°C. The experiments contain a very large number of specimens of alloys and ceramics of many specimen configurations.

The temperatures at the ends of the capsules were slightly lower than the design temperatures, but this is not unexpected in an experiment of such a new design. The low temperatures are attributed to undesirable heat conduction through centering pads. The design will be modified in future irradiation experiments to alleviate this condition. The experiment will serve as a prototype for other collaborative HFIR experiments between Japan and the U.S.

*Machining was performed by Chand Associated, Inc., Worcester, MA.

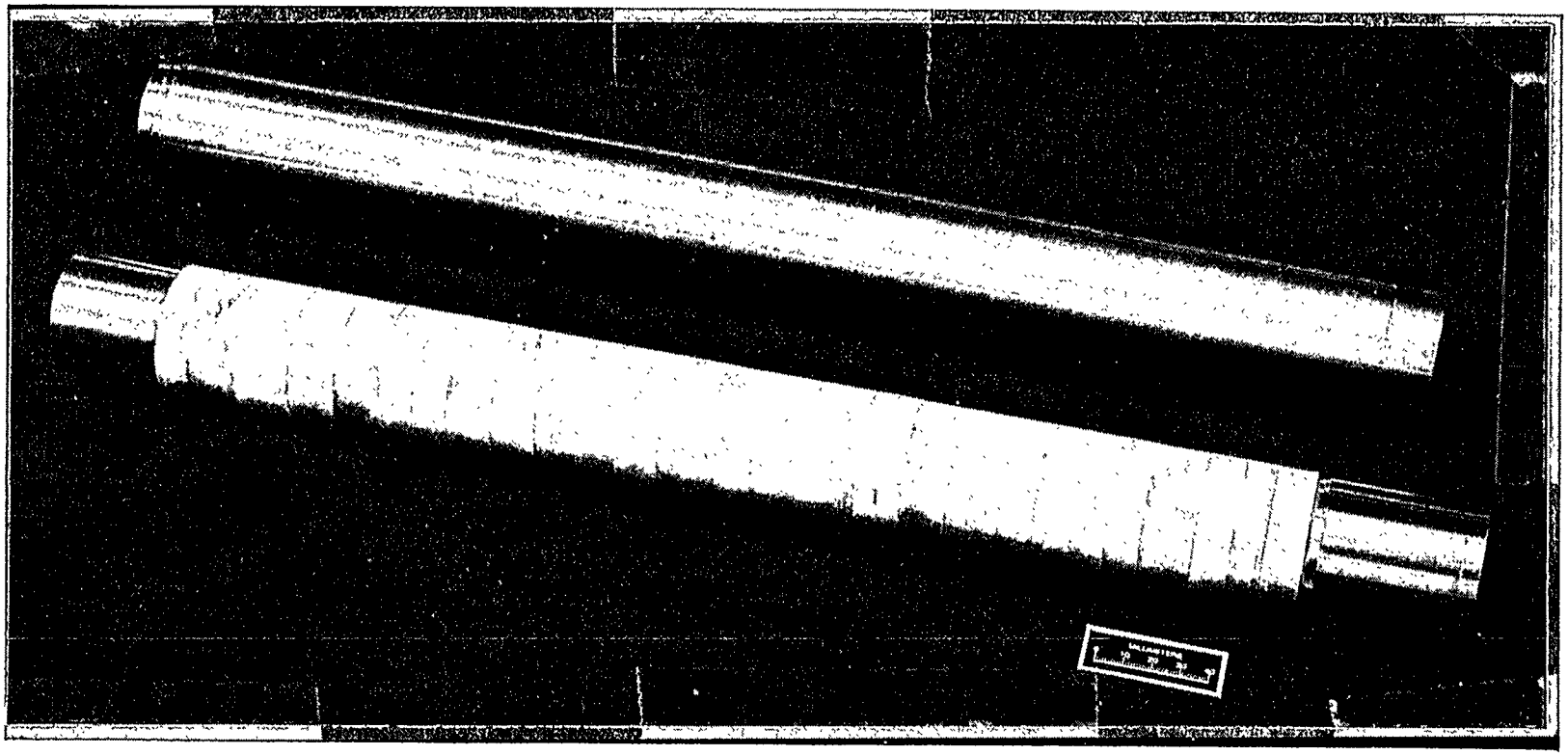

Fig. 5. Europium oxide rings in place on the inner wall of the shield can. The outer wall is at the top in the figure and will be fitted over the europium rings and welded in place.

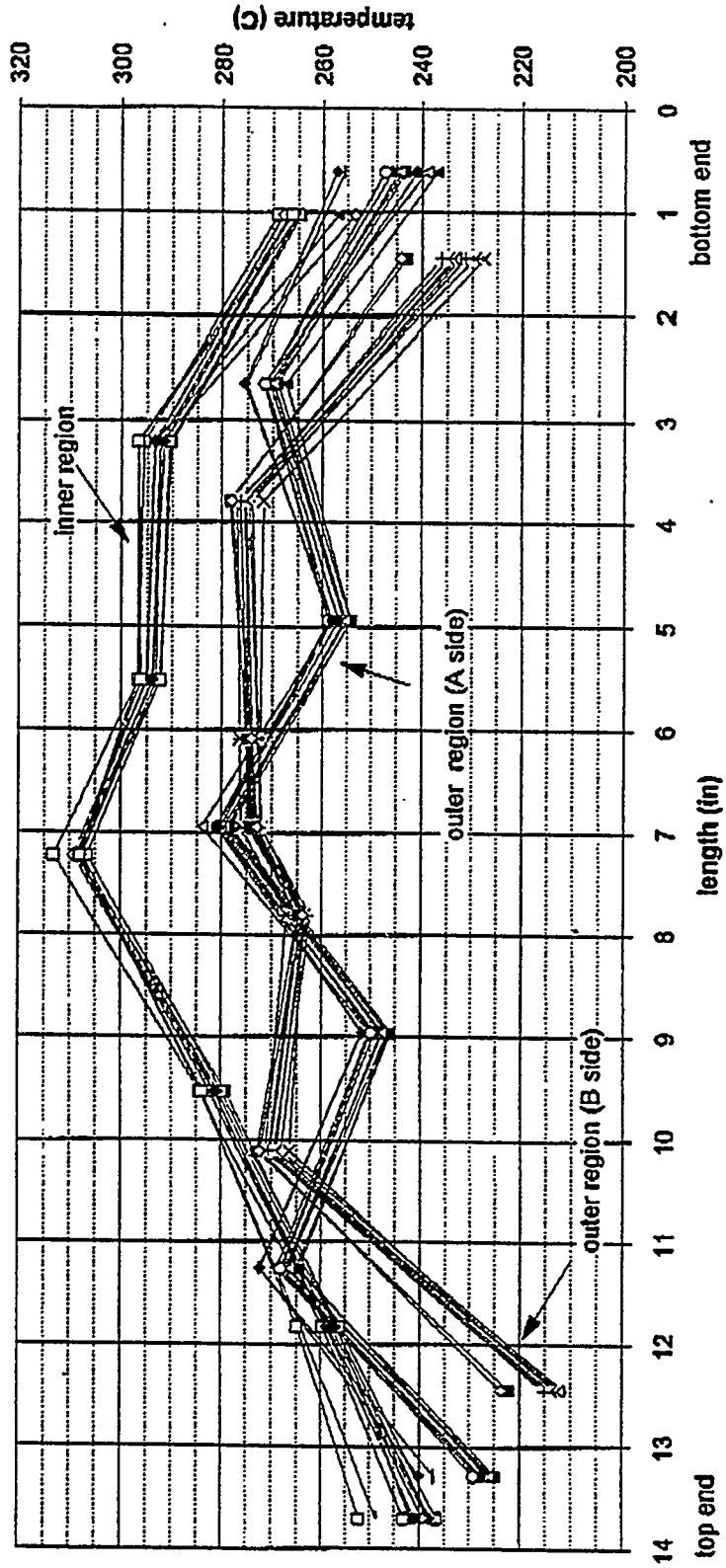

Desired Control Temperature (°C)

Ends	295
Inner	294
Outer	275

Specimen Temperature Corrections

Ends	+5 to 10°C
Inner	+7 to 14°C
Outer	+11 to 29°C

Fig. 6. Temperature data for the first cycle of operation of HFIR-RB-11J.

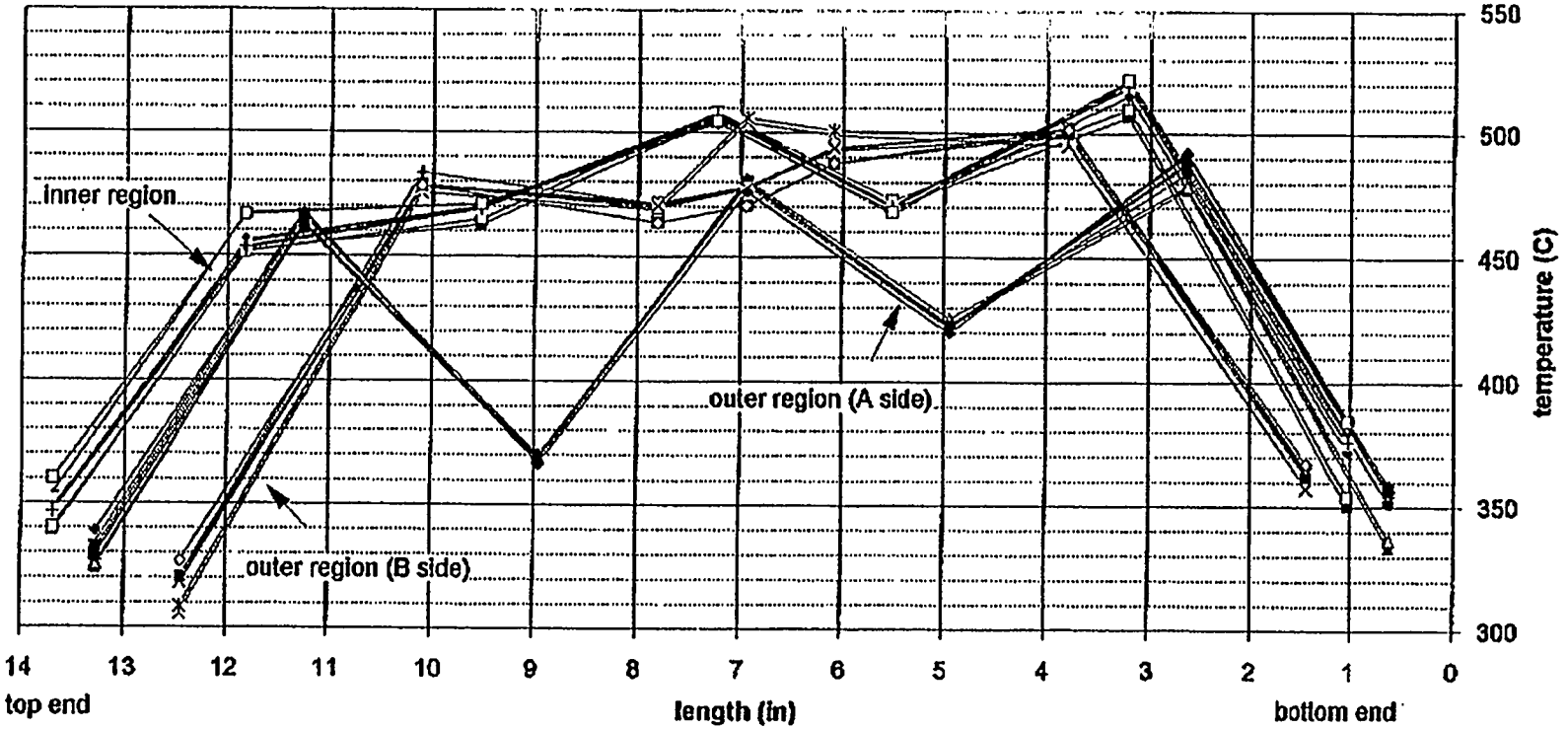

Desired Control Temperature (°C)	
Ends	500
Inner	491
Outer	471

Specimen Temperature Corrections	
Ends	+5 to 10°C
Inner	+7 to 14°C
Outer	+11 to 29°C

Fig. 7. Temperature data for the first cycle of operation of HFIR-RB-12J.

REFERENCES

1. A. W. Longest, J. E. Corum, D. W. Heatherly, and K. R. Thoms, "Design of Spectrally Tailored Fusion Reactor Materials Experiments in the HFIR RB* Capsule Irradiation Facility, *J. Nucl. Mater. 155-157* (1988), 1346.

NEUTRON IRRADIATION OF V-Cr-Ti ALLOYS IN THE BOR-60 FAST REACTOR: DESCRIPTION OF THE FUSION-1 EXPERIMENT — A. F. Rowcliffe (Oak Ridge National Laboratory), H. C. Tsai and D. L. Smith (Argonne National Laboratory), and V. Kazakov, and V. Chakin (RIAR, Dimitrovgrad)

SUMMARY

The FUSION-1 irradiation capsule was inserted in Row 5 of the BOR-60 fast reactor in June 1995. The capsule contains a collaborative RF/U.S. experiment to investigate the irradiation performance of V-Cr-Ti alloys in the temperature range 310 to 350°C. This report describes the capsule layout, specimen fabrication history, and the detailed test matrix for the U.S. specimens. A description of the operating history and neutronics will be presented in the next semiannual report.

INTRODUCTION

Low activation alloys based on the V-Cr-Ti system are the primary option for the first wall and blanket structure for liquid metal-cooled fusion reactor systems. A promising combination of fabricability, strength, ductility, and toughness has been identified within the composition range V-(4-5)Cr-(4-5)Ti. Initial results from fast reactor irradiation experiments conducted over the range 420-600°C indicated very little change in the ductile-to-brittle transition temperature (DBTT) for a V-4Cr-4Ti alloy irradiated to neutron doses in the range 24-36 dpa. However, large upward shifts in DBTT have been reported for a similar alloy irradiated at lower temperatures [1].

This paper describes the construction and operation of a collaborative RF/U.S. irradiation experiment in the BOR-60 reactor designed to investigate the irradiation performance of vanadium alloys in the temperature range 310-350°C for neutron doses in the range 15-20 dpa. The capsule design and specimen fabrication history are described, and details of the specimen test matrix are provided. The operating history, neutronics, and experiment disassembly will be provided in the next semiannual report.

CAPSULE CONSTRUCTION

The layout of the capsule is shown in Fig. 1. The experiment is contained inside a cylindrical tube measuring 41 mm ID × 1 mm thick, which is housed inside a hexagonal duct measuring 44 mm flat-to-flat. The space between the outer duct and inner tube is filled with argon to provide thermal insulation against neighboring fuel assemblies. The experimental capsule is a stainless steel cylindrical tube measuring 36 mm ID × 2 mm thick filled with ^{7}Li of 99.9% purity. The outside of the capsule is in contact with flowing sodium. Both U.S. and RF specimens are supported on a set of 10 tiers with the U.S. specimens occupying the lower six, as shown in Fig. 2. Each of the U.S. tiers has an upper and a lower bulkhead. There are three holes at the periphery of the bulkheads and connecting rods through these three holes join the six tiers together to form an assembly. The connecting rods are welded to the bulkheads at the top and bottom ends and the assembly placed over the bottom end plug of the capsule.

Within each US. tier, the tensile (SS-3), Charpy (CVN), and disk compact tension (DCT) specimens are separated from each other by coil-shaped 0.4-0.5 mm dia molybdenum wires. The TEM disks are contained in perforated stainless steel tubes. The SS-3 and CVN specimens are held upright and bundled into groups with 0.2 mm dia nichrome wires. The DCTs are stacked and aligned with free-standing stainless steel rods through the pull holes. All specimens are tied with nichrome wires around the three connecting rods to form a bundle; this arrangement prevents the specimens from slipping off the edge of the bulkheads.

After loading the specimens, the capsule was shipped to the Institute of Physics and Power Engineering at Obninsk for Li-filling and final weld closure. The ^{7}Li was first purified by distillation and Zr-gettering using the equipment shown in Fig. 3. This process lowered the nitrogen content

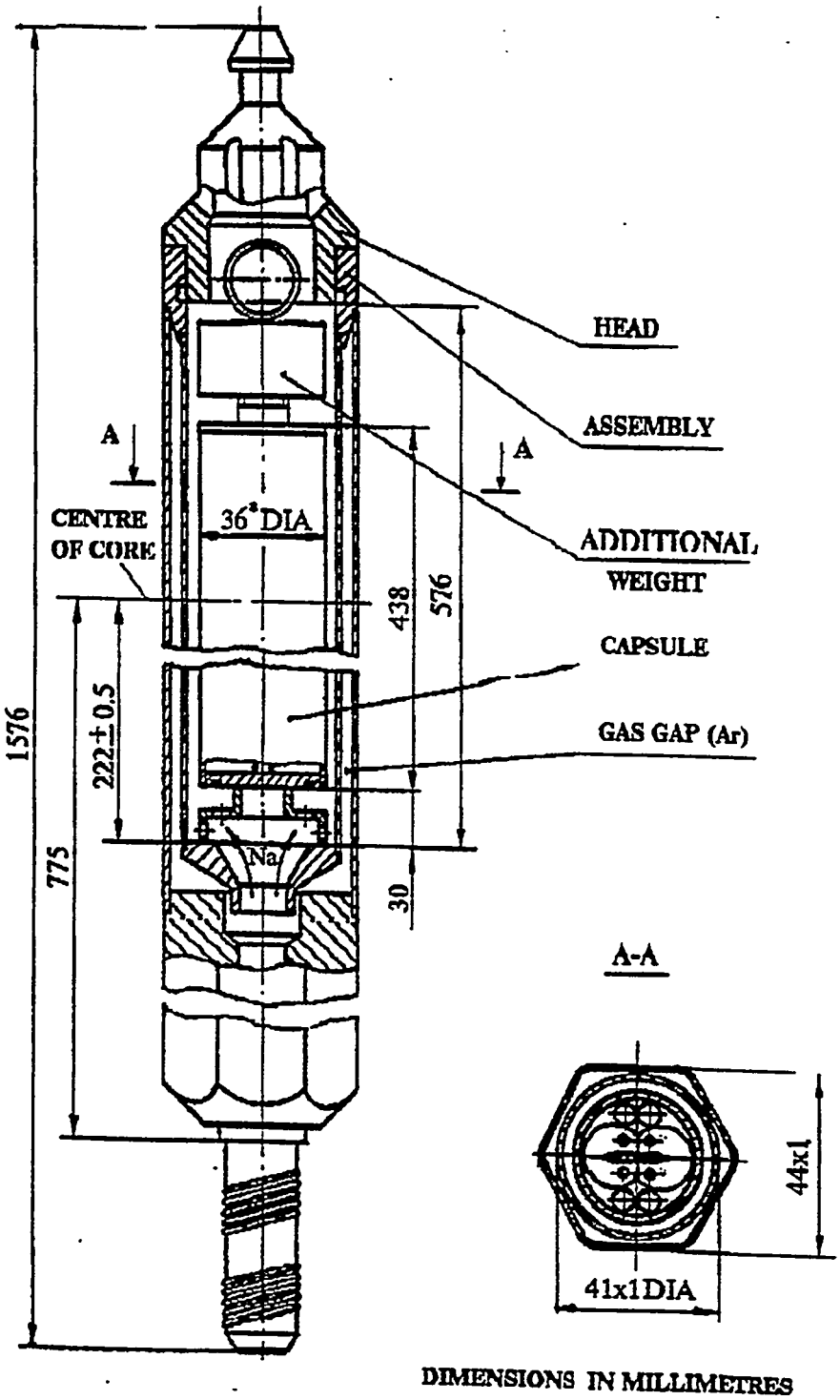

Fig. 1. Schematic of the Fusion-1 Capsule for BOR-60.

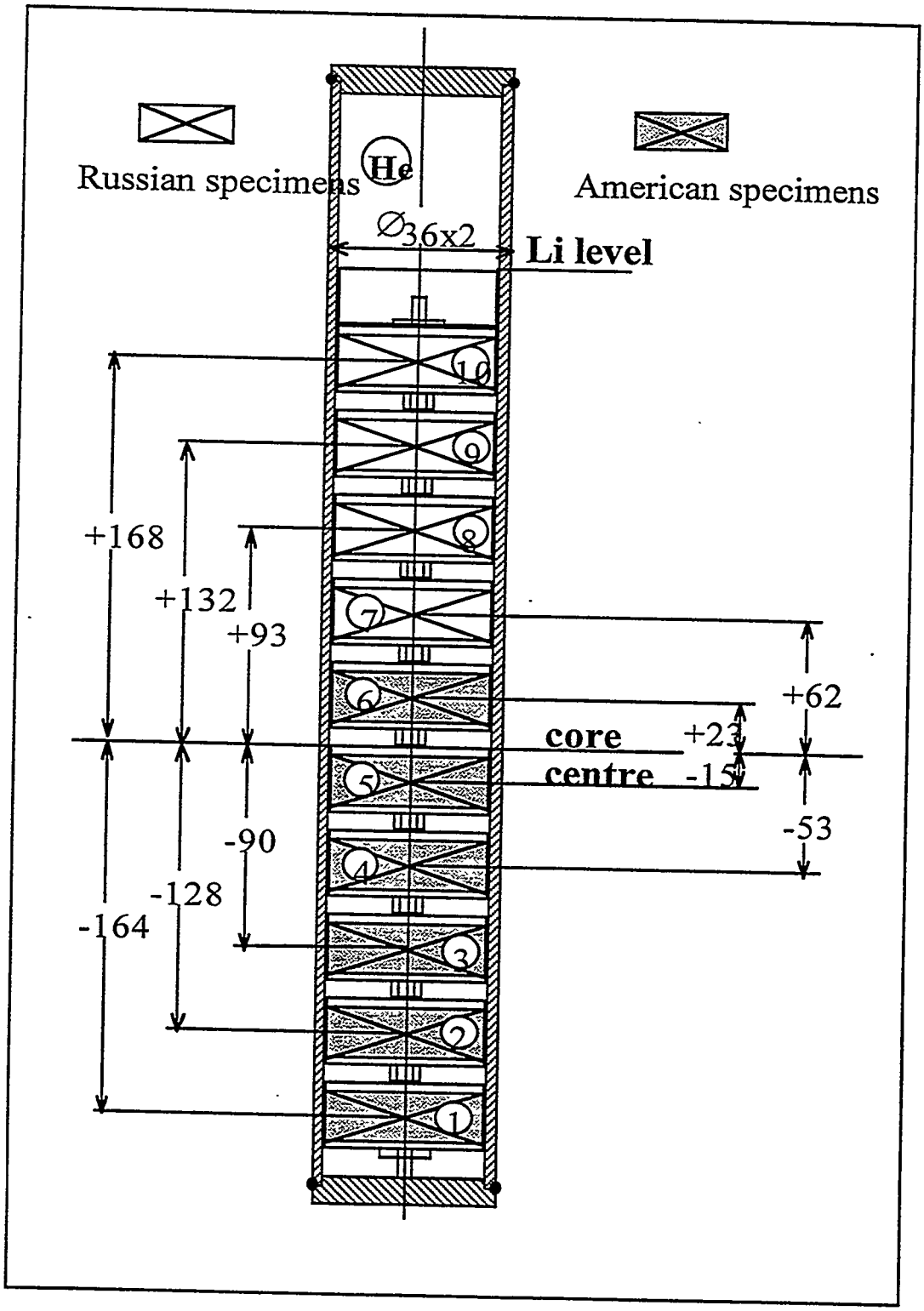

Fig. 2. Distribution of U.S. and RF Specimens within the Fusion-1 Capsule.

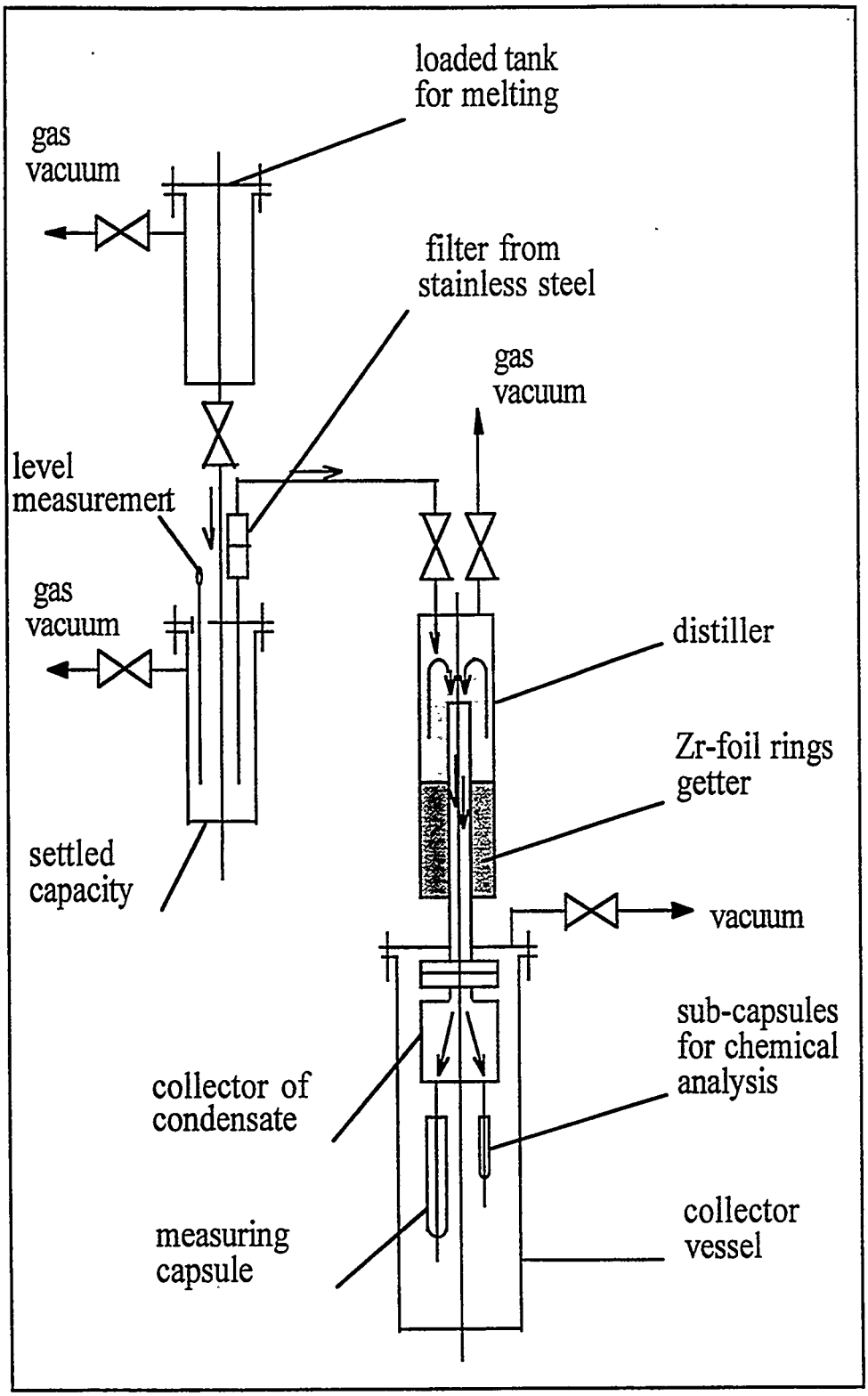

Fig. 3. Li Distillation and Purification System

from 200 to <3 wppm and reduced the carbon content to ~30 wppm. To reduce the probability of forming cavities, the capsule was mechanically vibrated during Li-filling at 250-300°C using the arrangement shown in Fig. 4. Vibration was continued for about 15 min and the vacuum was maintained at better than 10^{-4} torr. Following x-radiography, the capsule was shipped back to RIAR, assembled, and inserted in the G-23 Cell of Row 5 of the BOR-60 reactor on June 27, 1995.

U.S. ALLOYS AND SPECIMEN FABRICATION HISTORY

The primary focus of the U.S. experiment was on the fracture behavior of the 500 kg heat of V-4Cr-4Ti, heat no. 832665. In addition, specimens were also prepared form eight experimental heats with small variations in Cr and Ti concentrations. The chemical analyses of these alloys are presented in Tables 1 and 2. The loading list and specimen identification codes are presented in Tables 3 and 4.

The fabrication histories of the various types of plate supplied by Teledyne Wah Chang, Albany for the 500 kg heat of V-4Cr-4Ti and for the 30 kg heat of compositional variants are summarized in Tables 5 and 6, respectively. Details of the fabrication history of the various sets of specimens are presented in Tables 7, 8, 9, and 10.

FUTURE WORK

The Fusion-1 capsule was successfully disassembled at RIAR and the specimens will be shipped back to the U.S. for postirradiation testing. A report on the operating history and neutronics will be presented in the next semiannual report.

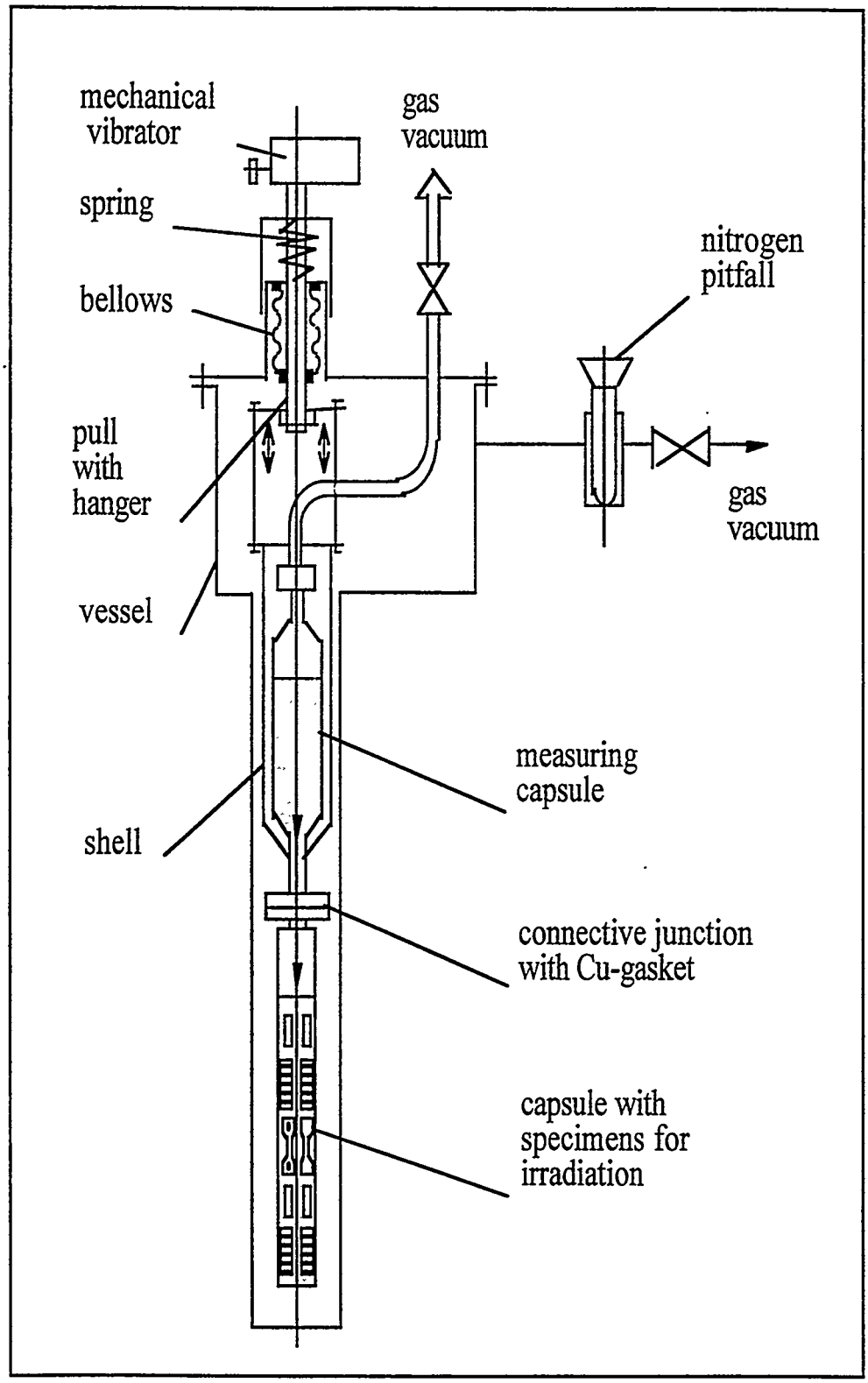

Fig. 4. System for Filling Capsule with Liquid Lithium.

Table 1. Chemical Analyses of 500 kg Heat (832665) of V-4C4-4Ti (wt. ppm)

Element	GDMS Evans	GDMS Evans	GDMS ORNL	ICP-Emission ORNL	Ingot Wah Chang
Ag	0.11	0.045			
Al	450	260	<200		185
As	<1.5	<1.3	<3		
Au	<.059	<.065	<6 int		7
B	4.1	3.3			
Ba	<.23	<.29			
Be	<0.021	<.0017			
Bi	<.0075	<.0061			
Br	<.14	<.092			
C	<260	<140	<310		86
Ca	<.32	<.20			
Cd	<.19	<.13			
Ce	0.017	0.021			
Cl	<.087	<.050			<2
Co	0.31	0.28			
Cr	%3.0	3.5	%3.0	%3.1	%3.77
Cs	<.024	<.013			<10
Cu	0.8	0.88			<50
F	<.081	<0.66			
Fe	210	200	256		220
Ga	1.3	1.5			
Ge	<.030	<.030			
Hf	8.4	8.3	10.8		
Hg	<.045	<.025			
I	<0.18	<.015			
In	0.075	0.057			
Ir	<.0030	<.0032			
K	<.051	<.021			
La	<.00079	<.00064			
Li	<.0017	<.0014			
Mg	0.25	.093			
Mn	0.21	0.21			
Mo	310	320	244		310
N	<200	<84	<4		85
Na	0.016	0.0083			
Nb	<59	<63	<80		60
Nd	<.0077	0.0092			
Ni	9.5	9.7	<12		
O	<610	<320	<190		310
Os	<.0088	<.0072			
P	37	29	<61		<30
Pb	<.0075	<.0061			
Pd	<.13	0.14			
Pt	<.28	<.19			
Rb	<.20	<.22			
Re	<.0037	<.0044			
Rh	<2.3	<2.9			
Ru	<1.4	<1.3	<7		

Table 1. Chemical Analyses of 500 kg Heat (832665) of V-4C4-4Ti (wt. ppm)

Element	GDMS Evans	GDMS Evans	GDMS ORNL	ICP-emission ORNL	Ingot Wah Chang
S	18	15	40		<10
Sb	0.17	0.17			
Sc	<.012	0.011			
Se	<1.7	<.28			
Si	890	680	%0.1	<0.3	780
Sn	0.26	0.22			
Sr	<56	<61	<60		
Ta	<18	<20	<3. int		
Te	<0.86	<.079			
Ti	%4.1	%4.0	%5.3	%4.1	%3.92
Th	0.013	0.0029			
U	0.085	0.082			
V	bal	bal	bal		
W	25	25	22.8		
Y	<3.8	<4.5	<7		
Zn	0.11	0.12			
Zr	<42	<50	<65		

Table 2. Chemical Analyses of T Series 15 kg Heats (wt. ppm)

	V-3Cr-3Ti (Heat T91)		V-4Cr-4Ti-Si (Heat T89)		V-6Cr-3Ti (Heat T92)		V-6Cr-6Ti (Heat T90)		V-5Cr-5Ti (Heat T87)	
Element	Ind.**	TWCA*	Ind.**	TWCA*	Ind.**	TWCA*	Ind.**	TWCA	Ind.**	TWCA*
B	3.8		3.5		3.4		3.9			<5
C	<140	120	<120	112	<92	105	<120	104		109
N	<5.5	62	<1.8	79	<1.8	95	<4.5	85		90
O	<270	230	<270	270	<200	280	<260	250		380
Al	240	200	270	200	300	255	270	235		160
Si	1200	940	1100	1050	1000	950	1400	960		545
P	26	<50	24	<50	22	<50	24	<50		<30
S	27	12	23	10	21	12	20	10		<20
Ti	3.1%	3.02%	5.3%	4.14%	3.0%	2.94%	4.6%	5.98%		5.06%
V	94%	bal.	90%	bal.	91%	bal.	91%	bal.		bal.
Cr	3.0%	2.85%	4.9%	3.7%	6.2%	5.91%	4.3%	5.74%		4.94%
Mn	1.1		1.9		1.7		1.7			
Fe	110	130	140	170	140	165	120	195		160
Ni	7.6		12		8.3		10			
Cu	79	83	50	83	130	140	48	55		67
Zn	5.3		4.7		4.5		4.0			
Ga	3.9		5.9		7.6		5.0			
As	1.7		2.4		1.4		2.0			
Sr	<76		<120		<70		<110			
Y	<5.9		<9.3		<6.1		<8.6			
Zr	<48		<63		<56		<66			
Nb	£55	<50	£56	<50	£50	<50	£54	<50		<100
Mo	380		360		380		340			515
Rh	0.024		0.016		0.02		0.0083			
Ru	0.22		0.18		0.25		0.252			
Hf	0.45		0.12		0.45		0.82			
Ta	<9.7		<5.2		<9.0		<98			<36
W	32		32		32		18			<5

*Teledyne Wah Chang analysis
**Analysis obtained by ORNL from an independent vendor

Table 3. Loading List and Identification Codes for Specimens Prepared at ORNL

Alloy	Specimen Type	Final Heat Treatment	Identification Codes	No. of Specimens
V-4Cr-4Ti 832665	DCT	1000°C/2 h	WC01-WC10	10
	DCT	950°C/2 h	WC16-WC18	3
	PCVN	1000°C/2 h	WB32, WB35-43	10
	PCVN	950°C/2 h	WB61-WB63	3
	MCVN	1000°C/2 h	WB72-WB77	6
	SS-3	1000°C/2 h	WE01-WE12	12
	TEM	1000°C/1 h	WG15-WG24	10
	TEM	950°C/1 h	WG31-WG40	10
	SS-3	1050°C/1 h	WE21-WE25	5
	TEM	1050°C/1h	WG26-WG30	5
GTA Weld V-4Cr-4Ti 832665	DCT	950°C/2 h	WE01-WE04	4
	MCVN	as machined	WD36-WD38	3
	MCVN	950°C/2 h	WD26-WD31	6
	SS-3	as machined	WF08-WF11	4
	SS-3	950°C/2 h	WF01-WF04	4
EB Weld V-4Cr-4Ti 832665	DCT	950°C/2 h	WE11-WE14	4
	MCVN	950°C/2 h	WD51-WD56	6
	SS-3	950°C/2 h	WF16-WF19	4
V-4Cr-4Ti-Si T-89	DCT	1050°C/2 h	YA01	1
	SS-3	1050°C/2 h	YC01-YC03	3
	TEM	1050°C/1 h	YD01-YD10	10
V-3Cr-3Ti T-91	DCT	1050°C/2 h	XA01	1
	SS-3	1050°C/2 h	XC01-XC03	3
	TEM	1050°C/1 h	XD01-XD10	10
V-6Cr-3Ti T-92	DCT	1050°C/2 h	ZA01	1
	SS-3	1050°C/2 h	ZC01-ZC03	3
	TEM	1050°C/1 h	ZD01-ZD10	10
V-6Cr-6Ti T-90	DCT	1050°C/2 h	UA01	1
	SS-3	1050°C/2 h	UC01-UC03	3
	TEM	1050°C/1 h	UD01-UD10	10

Table 4. Loading List and Identification Codes for Specimens Prepared at ANL

Alloy	Specimen Type	Final Heat Treatment	Identification Codes	No. of Specimens
V-4Cr-4Ti 832665	MCVN 30	1000°C/2 h	BL71W: 28, 29, 31, 35	4
	MCVN 30	950°C/2 h	BL71W: 44, 47, 48, 53	4
	PCVN 30	1000°C/2 h	BL71W: 19, 24, 26, 32	4
	SS-3	1000°C/1 h	71	6
	SS-3	1000°C/2 h	71 2H	6
	SS-3	950°C/2 h	71: A-L	12
	TEM	1000°C/2 h	71	10
	TEM	950°C/2 h	71/2	10
V-4Cr-4Ti 832665 Laser Weld	MCVN 30	400°C/1 h	BL71: A01-A05	5
	DCT-A	400°C/1 h	BL71: A12, A14, A15	3
	SS-3	400°C/1 h	71LZ	4
V-5Cr-5Ti T87	MCVN 30	1000°C/1 h	BL72: A, B, C, D	4
	SS-3	1000°C/1 h	72	8
	TEM	1000°C/1 h	72	10
V-4Cr-4Ti BL47	MCVN 30	1000°C/1 h	47: 06, 07, 08	3
	PCVN 45	1000°C/1 h	47: 1-5	5
	DCT-B	1000°C/1 h	47: 07, 08	2
	TEM	1000°C/1 h	47	10
V-4Cr-4Ti-B BL70	MCVN 30	1000°C/1 h	70: A, B, C, D	4
	DCT-A	1000°C/1 h	70	2
	SS-3	1000°C/1 h	70	8
	TEM	1000°C/1 h	70	10
V-4Cr-4Ti-RF BL69	SS-3	1000°C/1 h	69	2
	TEM	1000°C/1 h	69	10

Table 5. Fabrication History for V-4Cr-4Ti Heat 832665: Plate Material

Cast ingot
↓
S.S. jacket/extrude at 1150°C
to 63.5 thick bar
↓
Vacuum anneal, 1050 to 1070°C, 2 h
Cross roll at 400°C in multiple steps to plate thicknesses of
12.7, 6.35, 3.81, and 1.02 mm:
vacuum annealing at 1050 to 1070°C for 2 hr after each 50% reduction
↓
Cold roll 3.81 mm plate to 1.02 mm plate

Plate Identification for ORNL Specimens, V-4Cr-4Ti (832665)

ORNL I.D.	Manufacturers I.D.	Thickness (mm)	Condition
L150	Plate B	3.81	1050°C, 2 h (TWCA)
M150	Plate A	3.81	1050°C, 2 h (TWCA)
P250	Unannealed	6.35	50% warm-rolled
N40	—	1.02	50% cold-rolled

Table 6. Fabrication History for Compositional Variants T89, T90, T91, T92

Cast ingot (11.7 mm dia)
↓
S.S. jacket/extruded at 1175 to 1190°C
↓
Vacuum annealed 1075°C, 2 h
↓
Cross-rolled at 400°C in multiple steps to 6.35, 3.81 mm thick
with vacuum anneals, 1050 to 1075°C, 2 h
after each 50% reduction
↓
Cross-rolled at RT to 1.02 and 0.76 mm thick
with vacuum anneals at ~1060°C, 2 h
after each 50% reduction

Table 7. Fabrication Summary for ORNL Specimens from V-4Cr-4Ti (832665)

Specimen Type	Fabrication Procedure	Identification Code
MCVN PCVN	Plate M150 (TWCA, annealed, 1050°C) Machined L-T orientation Vacuum annealed 1000°C, 2 h Pre-cracked (UCSB)	WB series
DCT	Plate M150 (TWCA, annealed) Machined T-L orientation Vacuum annealed, 1000° or 950°C, 2 h Pre-cracked, side-grooved	WC series
SS-3	Plate N40 (50% C.R., 1.02 mm) Vacuum annealed, 950°C, 2 h Warm-rolled to 0.76 mm (25%) Vacuum annealed, 950°C 2 h Machined Vacuum annealed, 1000 or 1050°C, 2 h	WE series
TEM	Plate N40 (50% C.R., 1.02 mm) Vacuum annealed, 1000°C, 1 h Cold-rolled to 0.46 mm (55%) Vacuum annealed, 1000°C, 1 h Cold-rolled to 0.26 mm Punch disks Vacuum annealed, 1050, 1000, or 950°C for 1 h	WG series

Table 8. Fabrication Summary for V-4Cr-4Ti GTA Weld Specimens

Specimen Type	Fabrication Procedure	Identification Code
DCT	50% warm-rolled plate P250; 6.35 mm Full penetration weld No. GTA 9 Machined notch for crack propagation in fusion zone parallel to weld axis Vacuum annealed 950°C, 2 h Pre-cracked; side-grooved Vacuum annealed, 400°C, 1 h	WE series
MCVN	50% warm-rolled plate P250; 6.35 mm Full penetration weld No. GTA 8 Machined notch for crack propagation in fusion zone parallel to weld axis Vacuum annealed, 950°C, 2 h	WD series
SS-3	50% warm-rolled plate P250; 6.35 mm Full penetration weld No. GTA 8 Machined perpendicular to weld axis with fusion zone in center of gage	WF series

Table 9. Fabrication Summary for V-4Cr-4Ti EB Weld Specimens

Specimen Type	Fabrication Procedure	Identification Code
DCT	50% warm-rolled plate P250; 6.35 mm Full penetration weld No. EBW 9 Machined for crack propagation in weld zone parallel to weld axis Vacuum annealed, 950°C, 2 h Pre-cracked; side-grooved	WE series
MCVN	50% warm-rolled plate P250; 6.35 mm Full penetration weld No. EBW 9 Machined for crack propagation in weld zone parallel to weld axis Vacuum annealed, 950°C, 2 h	WD series
SS-3	50% warm-rolled plate P250; 6.35 mm Full penetration weld No. EBW 9 Machined perpendicular to weld axis with fusion zone in center of gage Vacuum annealed ,950°C, 2 h	WF series

Table 10. Fabrication History for ORNL Specimens from Heats T89, 90, 91, 92

Specimen Type	Fabrication Procedure	Identification Code
DCT	50% warm-rolled plate P250; 6.35 mm Machined T-L orientation Vacuum annealed, 1050°C, 2 h Fatigue pre-cracked; side-grooved	UA, YA, XA, ZA series
SS-3	50% cold-rolled sheet; 0.76 mm Machined L direction Vacuum annealed, 1050, 2h	UC, YC, XC, ZC series
TEM	50% cold-rolled sheet; 0.76 mm Vacuum annealed, 1000°C, 1 h Cold-rolled to 0.25 mm Punched disks Vacuum annealed, 1050°C, 1 h	UD, YD, XD, ZD series

Design Considerations of the Irradiation Test Vehicle for the Advanced Test Reactor* H. Tsai, I. C. Gomes, and D. L. Smith (Argonne National Laboratory), A. J. Palmer, S. J. Hafer, and F. W. Ingram (Lockheed Martin Idaho Technologies Company), M. L. Hamilton (Pacific Northwest National Laboratory), K. R. Thoms (Oak Ridge National Laboratory), and F. W. Wiffen (U.S. Department of Energy)

Summary

An irradiation test vehicle (ITV) for the Advanced Test Reactor (ATR) is being jointly developed by the Lockheed Martin Idaho Technologies Company (LMIT) and the U.S. Fusion Program. The vehicle is intended for neutron irradiation testing of candidate structural materials, including vanadium-based alloys, silicon carbide composites, and low-activation steels. It could possibly be used for U.S./Japanese collaboration in the Jupiter Program. The first test train is scheduled to be completed by September 1998. In this report, we present the functional requirements for the vehicle and a preliminary design that satisfies these requirements.

Objective

With the demise of fast reactors in the U.S., water-cooled mixed-spectrum reactors, such as the High Flux Isotope Reactor and the ATR, are increasingly being relied upon for irradiation testing of fusion structural materials. Because thermal neutrons are largely absent in the first-wall and blanket regions of a fusion reactor, the challenge of using a mixed-spectrum reactor for testing fusion materials lies mainly in curtailing the undesirable side effects of thermal neutrons (e.g., atypical transmutation). The ATR-ITV project is an effort to create a versatile test vehicle in the ATR that would be suitable for a wide range of neutron damage studies of various candidate fusion materials.

ITV Functional Requirements

The following functional requirements were identified by the fusion program and provided to LMIT to guide the vehicle design effort.

1. Thermal Neutron Filtering

   The neutron flux in the test volume shall be hardened to limit the thermally-dominant $V(n,\gamma)Cr$ transmutation in vanadium-based alloys to <0.5wt.% Cr during the irradiation. In addition, the filtered neutron spectrum shall permit the conduct of dynamic helium charging experiments (DHCE)† with vanadium alloys. The thermal neutron filter shall be external and replaceable to maintain a high-quality neutron environment throughout the irradiation.

---

* Work Supported by Office of Fusion Energy, U.S. Department of Energy, under Contract W-31-109-Eng-38.

† The purpose of the DHCE is to study the concurrent effects of neutron damage and helium generation, as they would occur in a fusion reactor. In the experiments, tritium would be precharged in the lithium bond of the specimen capsules. During the irradiation, the tritium would diffuse from the lithium into the specimens and some would decay in-situ into ^3He. The challenge for the DHCE in a mixed-spectrum reactor is to prevent the back conversion of ^3He into ^3H through the (n,p) reactions, which have a high cross-section for thermal neutrons.

2. Multiple Test Temperatures and Active Temperature Control

   The vehicle shall contain multiple specimen capsules each capable of operating at different temperatures. The range of test temperatures will be ≈250-750°C, depending on test material requirements. The temperature of each capsule shall be monitored on a real-time basis; it should be controllable by the blending of two gases (of differing thermal conductivities) in a radial gap that governs the dissipation of heat from the capsule.

3. High Neutron Damage Rate

   The ITV shall be located in a high fast-flux region of the ATR so that a high damage rate, ≈10 dpa in vanadium per calendar year, can be attained.

4. Irradiation Duration

   Except for possible interruption for replacement of the thermal neutron filter, the ITV shall be capable of continuous operation to up to ≈30 dpa. (The fluence requirement for the first test train may be only ≈10 dpa.)

5. Accommodation of Liquid Metal Specimen Bonds

   Capsules that contain vanadium alloy specimens may require lithium or sodium bonding for reasons of heat transfer, impurity control, and the DHCE. Capsules that contain other types of test materials may require helium bonding.

Description of the Preliminary ITV Design

Although the detailed design for the ITV has not yet been finalized, communications between the LMIT designers and the fusion program participants thus far have produced the following generally-agreed-upon design guidelines. These guidelines are consistent with the above functional requirements, based on the results of preliminary calculations.

The vehicle would occupy the ATR's central flux trap, which has a diameter of 81.5 mm and a height of 1219 mm. Three 31-mm-diam. stainless-steel in-pile tubes that contain axially stacked specimen capsules would be located side by side in the flux trap. The tubes would have independent instrumentation and each could be inserted and removed without affecting the other two. Each tube would form its own pressure boundary.

A single, replaceable thermal neutron filter would encompass all three in-pile tubes. An aluminum filler block, to minimize the amount of water inside the filtered volume, would occupy the interstitial space between the three in-pile tubes. With an estimated fast flux of $\approx 1.6 \times 10^{14}$ n/cm^2/s (E > 1.0 MeV) in the central flux trap, the goal fluence rate of 10 dpa/y (vanadium) appears attainable.

The thermal neutron filter would be a cylindrical sleeve made of Al - 4.3% ^{10}B alloy. Because the filter would be on the outside of the in-pile tubes, replacement of the filter sleeve would be possible. Based on results of preliminary analyses [1], and assuming that the sleeve is replaced every ≈5 dpa, the vanadium-to-chromium transmutation would be insignificant and a viable DHCE would be feasible.

Each in-pile tube would contain approximately five stacked specimen capsules. A thermocouple sleeve, extending from the top to the bottom, would separate the specimen capsules from the in-pile tube. Holes in this sleeve would accommodate the thermocouples that extend from the top of the vehicle to each capsule. The sleeve would also form one side of the radial gas gap to control capsule temperature. Channels machined in the in-pile tubes would allow the flow of gap-gas along the length of the capsule. Piston rings would be used to separate the gas flow in individual capsules. The gap gas would be a blend of helium and neon, continuously adjusted on the basis of real-time temperature data, to maintain a constant temperature in the capsule.

Each capsule would have two Type-K (chromel-alumel) thermocouples entering through the top end cap. The capsules would have a stainless steel construction, except those for the DHCE. To minimize tritium permeation loss through the capsule wall, the DHCE capsules would be made of a molybdenum-based alloy, TZM. Alternatively, the DHCE capsules could be made of stainless steel and contain liquid-metal-bonded subcapsules made of TZM.

The usable test volume per in-pile tube depends strongly on the size of the thermocouples that are used. (The size of the thermocouple affects the thickness of the thermocouple sleeve inside the in-pile tube.) Assuming that the diameter of the thermocouples is 2.38 mm, the useable volume per in-pile tube would be ≈200 ml.

Future Activities

Detailed design of the ITV will be finalized. Procurement and construction of the vehicle hardware will begin. Testing of ex-reactor components, such as the temperature control modules and gas analyzers, will continue. A proposal for collaboration will be presented to the Jupiter Program participants.

References

1. I. C. Gomes, H. Tsai, and D. L. Smith, "Neutronic Analysis of the DHCE Experiment in ATR-ITV," this report.

Status of ATR-A1 Irradiation Experiment on Vanadium Alloys and Low-Activation Steels* H. Tsai, R. V. Strain, I. Gomes and D. L. Smith (Argonne National Laboratory), L. R. Greenwood (Pacific Northwest National Laboratory), H. Matsui (Tohoku University, Japan)

Summary

The ATR-A1 irradiation experiment in the Advanced Test Reactor (ATR) was a collaborative U.S./Japan effort to study the effects of neutron damage on vanadium alloys at low temperature. The experiment also contained a limited quantity of low-activation ferritic steel specimens from Japan as part of the collaboration agreement. Irradiation was completed in 1996 after attaining the target exposure of ≈4.7 dpa in vanadium. The irradiated capsule was disassembled in this reporting period, and all specimens and monitors were successfully retrieved.

Objective

The main objective of the experiment was to obtain mechanical property data, including in-reactor creep, on vanadium alloys irradiated at two low temperatures (≈200 and 300°C). The objective of the present task is to receive the irradiated capsule from ATR and to complete the capsule disassembly and specimen retrieval at ANL.

Summary Description of Experiment

The irradiation vehicle was a drop-in capsule consisting of 15 lithium-filled subcapsules in 4 gas-bonded segments, as shown in Fig. 1. The blend of the gas in the gas bond and the width of the bond determined the temperature of the specimens in the subcapsules. The materials for both the capsule and subcapsule components were Type 304 stainless steel. A gadolinium filter set consisting of a tube, a top end disk, and a bottom end disk, was incorporated inside each subcapsule to mitigate transmutations from the thermal neutron flux.

Fig. 1. Schematic Drawing of ATR-A1 Capsule Showing Capsule Segments and Subcapsule Locations

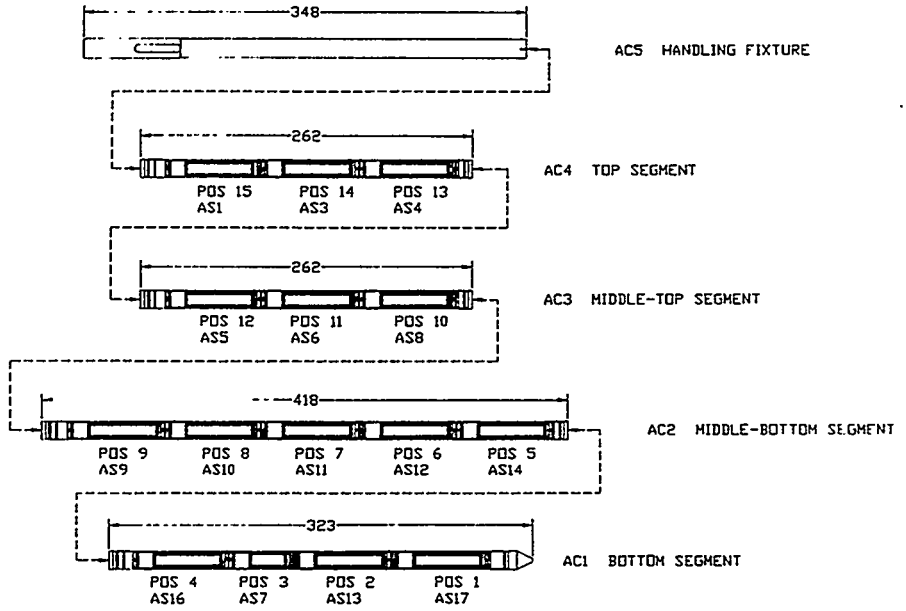

* Work supported by Office of Fusion Energy, U.S. Department of Energy, under Contract W-31-109-Eng-38.

The specimens included in the experiment are tensile, Charpy, compact tension, transmission electron microscopy disks, and creep (pressurized tubes). The configurations of the specimens are shown in Table 1. Flux dosimeters and melt-wire temperature monitors were incorporated in selected subcapsules, and their descriptions are shown in Tables 2 and 3, respectively. The loading of specimens in the subcapsules is summarized in Table 4 and the detailed listing of the specimens is shown in Appendix 1.

Table 1. Complement of Specimens in the ATR-A1 Experiment

Type	Material	Origin	Nominal Dimensions (mm)	Approx. Wt. (g)	
				V	Fe
SS-3 Tensile	V	US	25.4 l x 4.95 w x 0.76 t	0.33	–
MT Tensile	V, Fe	JP, US	16.0 l x 4.0 w x 0.25 t	0.06	0.09
1/3 CVN	V	US	25.4 l x 3.33 w x 3.33 t	1.7	–
1.5 CVN	V, Fe	JP, US	20.0 l x 1.5 w x 1.5 t	0.26	0.35
DCT-A	V	US, JP	9.60 d x 3.56 t	1.3	–
Creep	V	US, JP	25.4 l x 4.57 OD x 4.06 ID	0.65	–
TEM	V, Fe	US, JP	3.0d x 0.25 t	0.01	0.01

Table 2. Description of Flux Dosimeters

Material	Reactions	Half-life	Energy Range (MeV)
Spectral Set (6 Materials)			
Fe	^{58}Fe (n,γ) ^{59}Fe	45 d	3.6×10^{-4} – 0.5
	^{54}Fe (n,p) ^{54}Mn	312 d	2.3 – 6.7
Ti	^{46}Ti (n,p) ^{46}Sc	84 d	3.7 – 9.0
Nb	^{93}Nb (n,γ) ^{94}Nb	20,300 y	4.0×10^{-4} – 0.4
	^{93}Nb (n,n) ^{93M}Nb	16 y	0.55 – 4.5
Cu	^{63}Cu (n,α) ^{60}Co	5.3 y	5.0 – 10.0
Mn-20%Cu	^{55}Mn (n,2n) ^{54}Mn	312 d	12.0 – 15.0
0.1%Co-Al	^{59}Co (n,γ) ^{60}Co	5.3 y	1.4×10^{-6} – 0.19
Gradient Set (2 Materials)			
Fe	^{58}Fe (n,γ) ^{59}Fe	45 d	3.6×10^{-4} – 0.5
	^{54}Fe (n,p) ^{54}Mn	312 d	2.3 – 6.7
0.1%Co-Al	^{59}Co (n,γ) ^{60}Co	5.3 y	1.4×10^{-6} – 0.19

Table 3. Description of Temperature (Melt-Wire) Monitors

Monitors	Melt Materials	Melting Temp. (°C)
MW01	63Sn/37Pb	183
MW02	Se	221
MW04	Sn	232
	Bi	271
MW08	Sn	232
MW09	Bi	271
MW10	Pb	327
	Zn	420

Status of Specimen Retrieval

Shipment of Irradiated Capsule to ANL

A dry cask from ANL was used to ship the capsule from the ATR complex to ANL-E for disassembly. Loading of the capsule into the cask required the capsule to be out of the ATR water pool, i.e., without shielding, for ≈1 min while being inserted into the cask. Because of the high radioactivity of the capsule, ≈80 R/h at 1 m in air, extensive preparation was required. Thorough planning allowed this task to be accomplished at ATR without significant difficulties. The loaded cask was immediately shipped to ANL-E and was received in January 1997.

Disassembly of Capsule Segments

The capsule segments were disassembled in an alpha-free cell at ANL-E. To minimize the spread of loose contamination, a tubing cutter, instead of a saw, was used to remove the top and bottom end caps of the four capsule segments. After the cutting, a small hydraulic ram mounted on a platform (Fig. 2) was used to push the subcapsules out of the opened capsule tubes. (The ram provided the necessary force to overcome the resistance from the cutting burr and the tight fit between the subcapsule spacer pads and the capsule tube.) In this manner, all subcapsules from the four segments were successfully retrieved.

The subcapsules were individually surveyed for their gamma activity after retrieval. The peak readings were substantial, ≈50-60 R/h at a distance of ≈35 cm for the midplane subcapsules. The distribution profile among the subcapsules appeared to follow approximately the reactor axial power profile, i.e., immaterial of the specimen loading inside. This result suggested that the bulk of the induced activity was due to the activation of the subcapsule hardware and the Gd filter.

Disassembly of Subcapsules

The subcapsules were disassembled in the same alpha-free cell. The task consisted of removal of the top and bottom end caps, dissolving the bond lithium with ammonia, and cleaning the specimens with alcohol.

pressurization, a rupture of the creep specimen would result in an increase in the subcapsule plenum pressure from the nominal ≈1 atm to ≈5-10 atm.) The results showed all punctured subcapsules to have the normal plenum pressure, thus confirming all of the pressurized creep specimens were intact.

As in the case of the capsule segments, the top and bottom end plugs of the subcapsules were removed with a tubing cutter, with the assistance of a hydraulic ram in a setup similar to that shown in Fig. 2.

Fig. 2. Capsule Disassembly Fixture and A Retrieved Subcapsule

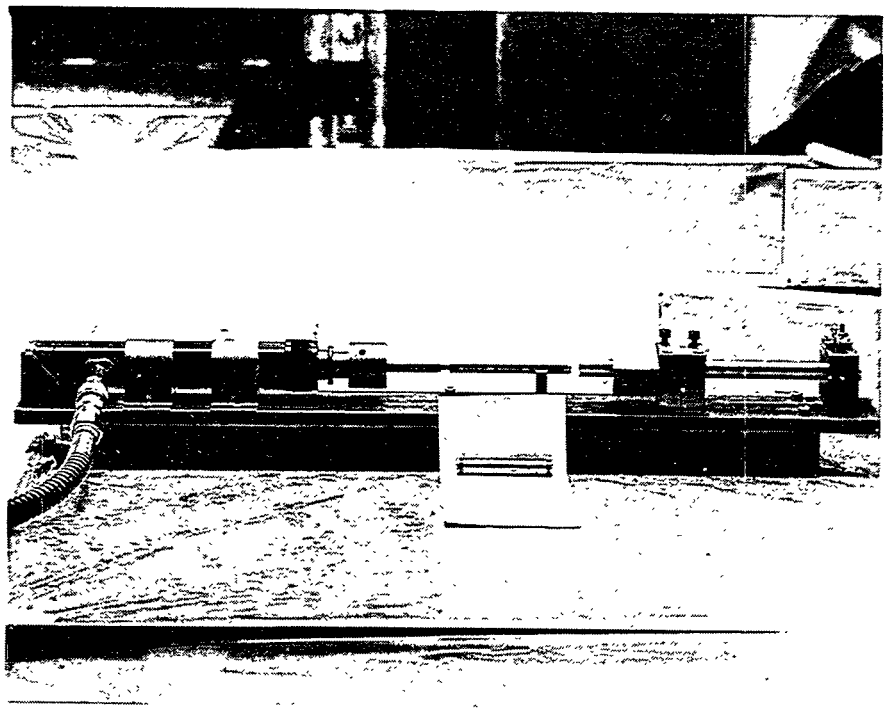

Dissolution of lithium with ammonia and cleaning of the retrieved specimens with alcohol was performed according to established procedures and no significant difficulties were encountered. The possibly fragile creep specimens were the first to be retrieved and were immediately put away to prevent possible damage from contact with the other specimens.

Additional gamma surveys were performed on the disassembled subcapsule components, and the results confirmed that much of the high activities noted before were due to the subcapsule hardware and the Gd filter. Gamma scans of the subcapsule hardware revealed the expected peaks of ^{60}Co, ^{54}Mn from activation of the stainless steels and ^{160}Tb, ^{153}Gd, and ^{154}Eu from the activation of the Gd. The scans also revealed the presence of ^{82}Ta, probably from the Ta impurity (<≈60 wppm) in the gadolinium filter. (^{82}Ta produces energetic gammas and can be a significant dose contributor within few years after the irradiation, as in the case of ATR-A1.) Gamma scanning of the specimens was limited to only one compact tension specimen (BL-47 material), due to the concern over alpha contamination. (The scanner is located in the alpha-side of the hot cell.) In that scan, gamma peaks suggesting ^{91M}Nb, ^{54}Mn, and ^{182}Ta were detected. (This specimen was subsequently retrieved from the alpha-cell contamination-free.)

Status of Retrieved Specimens

The retrieved specimens and monitors were transferred from the high-background disassembly cell to a low-background β-γ cell and the inventory of the specimens has been completed.

All mechanical testing specimens and monitors were accounted for. Except for a slight bend in a tensile specimen, all appear to be in good condition. The counts of the TEM disks were in good agreement with the loading data, except possibly for a few missing disks from subcapsule AS10.

A thorough and accurate radiation survey of the separated specimens has been conducted. The results, summarized in Table 5, indicate greater activation of the steel specimens (subcapsules AS3 and AS16) than the vanadium alloys. This was probably due to the inclusion of austenitic stainless steel specimens and the substantial contents of Ta and Nb in some of the ferritic alloys. For the vanadium alloys, the survey results show that as a whole, the Monbusho vanadium alloys seem to have greater activation than the U.S. vanadium alloys.

Future Activities

Disposition of the specimens will be determined. The specimens will be packaged and shipped to the collaborating laboratories. The flux dosimeters will be counted and calculations will be performed to determine the displacement damage in the specimens. The temperature monitors (melt wires) will be examined by radiography and possibly metallography.

Table 4. ATR-A1 Specimen and Monitor Loading Diagram

Subcap.		Test		US							JP				
No.	Temp.	Mat'l	Tier	DCT	1/3 CVN	SS-3 TS	MT TS	Creep	TEM	T.Mtr	F.Mtr	DCT	1.5 CVN	MT TS	TEM	Creep
AS1	Low	V	Top	–	–	2	–	A5	–	–	Gr.(2)	–	4	4	–	–
			Bot	–	3	1	–	–	–	–	–	–	2	4	–	–
AS3	Low	V	–	9	–	–	–	–	–	MW01	–	3	–	–	–	–
AS4	Low	Fe	Top	–	–	–	–	–	–	MW02	–	–	12	12	–	–
			Bot	–	–	–	–	–	–	–	–	–	12	15	126	–
AS5	Low	V	Top	–	–	2	–	–	–	–	–	–	4	4	–	J3
			Bot	–	3	1	2	–	65	–	–	–	2	2	–	–
AS6	Low	V	Top	–	–	2	–	A2	–	–	–	–	4	4	–	–
			Bot	–	3	1	4	–	50	–	–	–	2	–	–	–
AS8	Low	V	Top	–	–	2	–	A3	–	MW04	–	–	4	4	–	–
			Bot	–	3	1	–	–	–	–	–	–	2	4	64	–
AS9	High	V	Top	–	–	2	–	A1	–	–	–	–	4	4	–	–
			Bot	–	2+4*	1	–	–	41	–	–	–	2	4	–	–
					*1.5CVN											
AS10	High	V	Top	–	–	2	–	A10	–	–	Sp.(6)	–	4	4	–	–
			Bot	–	3	1	–	–	50	–	–	–	2	4	–	–
AS11	High	V	Top	–	–	2	–	A7	–	MW08	–	–	4	4	–	–
			Bot	–	3	1	4	–	24	–	–	–	2	–	–	–
AS12	High	V	Top	–	–	2	–	A11	–	–	Gr.(2)	–	4	4	–	–
			Bot	–	3	1	–	–	–	–	–	–	2	4	41	–
AS14	High	V	Top	–	–	2	–	–	–	MW09	–	–	4	4	–	J2
			Bot	–	3	1	–	–	–	–	–	–	2	3	23	–
AS16	High	Fe	Top	–	–	–	–	–	–	–	Gr.(2)	–	12	12	–	–
			Bot	–	–	–	–	–	–	–	–	–	12	15	126	–
AS7	High	V	Bot	–	3	1	2	–	–	–	–	–	–	–	–	–
AS13	High	V	–	10	–	–	–	–	–	MW10	–	3	–	–	–	–
AS17	Low	V	Top	–	–	2	–	A4	–	–	Sp.(6)	–	4	4	–	–
			Bot	–	3	1	–	–	–	–	–	–	2	4	–	–
Total																
Low Temp., V				9	15	15	6	4	115			3	30	34	64	1
High Temp., V				10	21	16	6	4	115			3	30	35	64	1
Low Temp., Fe				0	0	0	0	0	0			0	24	27	126	0
High Temp., Fe				0	0	0	0	0	0			0	24	27	126	0

Creep Specimen Hoop Stress Loading

High. T		Low T.	
A1	0 MPa	A5	0 MPa
A10	100 MPa	A4	100 MPa
A7	150 Mpa	A2	150 Mpa
A11	200 MPa	A3	200 MPa
J2	200 MPa	J3	200 MPa

Table 5. Summary of Radiation Survey of ATR-A1 Specimens (Full Scale Reading 2000 mR/h)

Sub-cap	Content	Gamma Activity (mR/h) @ Contact	Gamma Activity (mR/h) @ ~ 10 cm
AS1	3 CVN + 3 TS (US)	78	16
	6 CVN + 8 TS (JP)	585	75
	Creep A5 (US)	14	7
	2 Flux Monitors	52	12
AS3	9 DCT (US)	210	40
	3 DCT (JP)	>2000	290
	Temp. Monitors	150	28
AS4	Ferritic (all, JP)*	>>2000	>>2000
	Temp. Monitors	275	35
AS5	3 CVN + 5 TS (US)	270	42
	6 CVN + 6 TS (JP)	>2000	283
	Creep J3 (JP)	>2000	300
	TEM (US)	55	16
AS6	3 CVN + 7 TS (US)	350	52
	6 CVN + 4 TS (JP)	1140	160
	Creep A2 (US)	40	10
	TEM (US)	48	11
AS8	3 CVN + 3 TS (US)	260	60
	6 CVN + 8 TS (JP)	1480	210
	Creep A3 (US)	46	14
	TEM (JP)	720	100
	Temp. Monitors	280	45
AS9	6 CVN + 3 TS (US)	520	75
	6 CVN + 8 TS (JP)	1410	190
	Creep A1 (US)	60	12
	TEM (US)	91	17
AS10	3 CVN + 3 TS (US)	295	51
	6 CVN + 8 TS (JP)	1910	268
	Creep A10 (US)	60	15
	TEM (US)	113	24
	6 Flux Monitors	235	36
AS11	3 CVN + 7 TS (US)	410	60
	6 CVN + 4 TS (JP)	1510	210
	Creep A7 (US)	45	11
	TEM (US)	80	15
	Temp. Monitors	22	9
AS12	3 CVN + 3 TS (US)	360	55
	6 CVN + 8 TS (JP)	900	120
	Creep A11 (US)	54	16
	TEM (JP)	410	48
	2 Flux Monitors	185	28
AS14	3 CVN + 3 TS (US)	300	50
	6 CVN + 7 TS (JP)	>2000	360
	Creep J2 (JP)	>2000	380
	TEM (JP)	425	53
	Temp. Monitors	80	15
AS16	Ferritic (all, JP)*	>>2000	>>2000
	2 Flux Monitors	190	24
AS7	3 CVN + 3 TS (US)	165	35
AS13	10 DCT (US)	1760	269
	3 DCT (JP)	>>2000	590
	Temp. Monitors	385	56
AS17	3 CVN + 3 TS (US)	152	25
	6 CVN + 8 TS (JP)	575	70
	Creep A4 (US)	22	8
	6 Flux Monitors	95	17

*Reading ≈ 2000 mR/h at 45 cm.

Appendix 1 Listing of Specimens in the ATR-A1 Experiment

Specimen ID No.	Lab.	Specimen Type	Mat'l/Heat	Mass (g)	Subcap.
		Subcapsule AS1			
A5	ANL	Creep	832665	0.650	AS1
AJX0	Abe	1.5CVN	V-5Cr-5TI-1SiAlY	0.265	AS1
AJX1	Abe	1.5CVN	V-5Cr-5TI-1SiAlY	0.265	AS1
AJX2	Abe	1.5CVN	V-5Cr-5TI-1SiAlY	0.265	AS1
AJX3	Abe	1.5CVN	V-5Cr-5TI-1SiAlY	0.265	AS1
AJX4	Abe	1.5CVN	V-5Cr-5TI-1SiAlY	0.265	AS1
AJZ0	Abe	1.5CVN	V-5Cr-5TI-1SiAlY	0.265	AS1
QC08	ORNL	CVNM	832665	1.660	AS1
71	ANL	CVNM30	832665	1.662	AS1
47	ANL	CVNM45	BL-47	1.680	AS1
47	ANL	SS-3 TS	BL-47	0.318	AS1
71	ANL	SS-3 TS	832665	0.318	AS1
72	ANL	SS-3 TS	T87	0.318	AS1
AJA0	Abe	MT TS	V-5Cr-5TI-1SiAlY	0.059	AS1
AJA1	Abe	MT TS	V-5Cr-5TI-1SiAlY	0.059	AS1
AJA2	Abe	MT TS	V-5Cr-5TI-1SiAlY	0.059	AS1
AJA3	Abe	MT TS	V-5Cr-5TI-1SiAlY	0.059	AS1
AJB0	Abe	MT TS	V-5Cr-5TI-1SiAlY	0.059	AS1
AJB1	Abe	MT TS	V-5Cr-5TI-1SiAlY	0.059	AS1
AJB2	Abe	MT TS	V-5Cr-5TI-1SiAlY	0.059	AS1
AJB3	Abe	MT TS	V-5Cr-5TI-1SiAlY	0.059	AS1
		Subcapsule AS3			
--	Matsui	DCT-A	V-3Fe-4Ti	1.253	AS3
47	ANL	DCT-A	BL-47	1.255	AS3
47	ANL	DCT-A	BL-47	1.255	AS3
71	ANL	DCT-A	832665	1.223	AS3
71	ANL	DCT-A	832665	1.223	AS3
71	ANL	DCT-A	832665	1.223	AS3
72	ANL	DCT-A	T87	1.245	AS3
72	ANL	DCT-A	T87	1.245	AS3
M	Matsui	DCT-A	V-3Fe-4Ti	1.253	AS3
M	Matsui	DCT-A	V-3Fe-4Ti	1.253	AS3
QA05	ORNL	DCT-A	832665	1.375	AS3
QA06	ORNL	DCT-A	832665	1.375	AS3
		Subcapsule AS4			
G2F1	A.Kimura	1.5CVN	NLM-E	0.334	AS4
G2F2	A.Kimura	1.5CVN	NLM-E	0.334	AS4
G2F3	A.Kimura	1.5CVN	NLM-E	0.334	AS4
G2F4	A.Kimura	1.5CVN	NLM-E	0.334	AS4
G2F5	A.Kimura	1.5CVN	NLM-E	0.334	AS4
G2F6	A.Kimura	1.5CVN	NLM-E	0.334	AS4
G2F7	A.Kimura	1.5CVN	NLM-E	0.334	AS4
G2F8	A.Kimura	1.5CVN	NLM-E	0.334	AS4
LF01	Kohno	1.5CVN	JLF1	0.353	AS4
LF02	Kohno	1.5CVN	JLF1	0.353	AS4
LF03	Kohno	1.5CVN	JLF1	0.353	AS4
LF04	Kohno	1.5CVN	JLF1	0.353	AS4
LF05	Kohno	1.5CVN	JLF1	0.353	AS4
LF06	Kohno	1.5CVN	JLF1	0.353	AS4
LF07	Kohno	1.5CVN	JLF1	0.353	AS4
LF08	Kohno	1.5CVN	JLF1	0.353	AS4
LH01	Kohno	1.5CVN	F82H	0.335	AS4
LH02	Kohno	1.5CVN	F82H	0.335	AS4

Specimen ID No.	Lab.	Specimen Type	Mat'l/Heat	Mass (g)	Subcap.
LH03	Kohno	1.5CVN	F82H	0.335	AS4
LH04	Kohno	1.5CVN	F82H	0.335	AS4
LH05	Kohno	1.5CVN	F82H	0.335	AS4
LH06	Kohno	1.5CVN	F82H	0.335	AS4
LH07	Kohno	1.5CVN	F82H	0.335	AS4
LH08	Kohno	1.5CVN	F82H	0.335	AS4
G211	A.Kimura	MT TS	JLM-1	0.092	AS4
G212	A.Kimura	MT TS	JLM-1	0.092	AS4
G213	A.Kimura	MT TS	JLM-1	0.092	AS4
G214	A.Kimura	MT TS	JLM-1	0.092	AS4
G2D1	A.Kimura	MT TS	NLM-D	0.092	AS4
G2D2	A.Kimura	MT TS	NLM-D	0.092	AS4
G2D3	A.Kimura	MT TS	NLM-D	0.092	AS4
G2D4	A.Kimura	MT TS	NLM-D	0.092	AS4
G2F1	A.Kimura	MT TS	NLM-E	0.092	AS4
G2F2	A.Kimura	MT TS	NLM-E	0.092	AS4
G2F3	A.Kimura	MT TS	NLM-E	0.092	AS4
G2F4	A.Kimura	MT TS	NLM-E	0.092	AS4
LB01	Kohno	MT TS	JLF1B	0.031	AS4
LB02	Kohno	MT TS	JLF1B	0.031	AS4
LB03	Kohno	MT TS	JLF1B	0.031	AS4
LF01	Kohno	MT TS	JLF1	0.031	AS4
LF02	Kohno	MT TS	JLF1	0.031	AS4
LF03	Kohno	MT TS	JLF1	0.031	AS4
LF04	Kohno	MT TS	JLF1	0.031	AS4
LH01	Kohno	MT TS	F82H	0.031	AS4
LH02	Kohno	MT TS	F82H	0.031	AS4
LH03	Kohno	MT TS	F82H	0.031	AS4
LH04	Kohno	MT TS	F82H	0.031	AS4
LM10	Kohno	MT TS	JLF1Mn1	0.031	AS4
LM11	Kohno	MT TS	JLF1Mn1	0.031	AS4
LM20	Kohno	MT TS	JLFMn2	0.031	AS4
LM21	Kohno	MT TS	JLFMn2	0.031	AS4
G211	A.Kimura	TEM	JLM-1	0.008	AS4
G212	A.Kimura	TEM	JLM-1	0.008	AS4
G213	A.Kimura	TEM	JLM-1	0.008	AS4
G214	A.Kimura	TEM	JLM-1	0.008	AS4
G241	A.Kimura	TEM	NLM-D	0.008	AS4
G242	A.Kimura	TEM	NLM-D	0.008	AS4
G243	A.Kimura	TEM	NLM-D	0.008	AS4
G244	A.Kimura	TEM	NLM-D	0.008	AS4
G271	A.Kimura	TEM	NLM-E	0.008	AS4
G272	A.Kimura	TEM	NLM-E	0.008	AS4
G273	A.Kimura	TEM	NLM-E	0.008	AS4
G274	A.Kimura	TEM	NLM-E	0.008	AS4
LB01	Kohno	TEM	JLF1B	0.010	AS4
LB02	Kohno	TEM	JLF1B	0.010	AS4
LB03	Kohno	TEM	JLF1B	0.010	AS4
LB04	Kohno	TEM	JLF1B	0.010	AS4
LB05	Kohno	TEM	JLF1B	0.010	AS4
LB06	Kohno	TEM	JLF1B	0.010	AS4
LB07	Kohno	TEM	JLF1B	0.010	AS4
LB08	Kohno	TEM	JLF1B	0.010	AS4
LF01	Kohno	TEM	JLF1	0.010	AS4
LF02	Kohno	TEM	JLF1	0.010	AS4
LF03	Kohno	TEM	JLF1	0.010	AS4
LF04	Kohno	TEM	JLF1	0.010	AS4
LF05	Kohno	TEM	JLF1	0.010	AS4
LF06	Kohno	TEM	JLF1	0.010	AS4
LF07	Kohno	TEM	JLF1	0.010	AS4
LF08	Kohno	TEM	JLF1	0.010	AS4
LH01	Kohno	TEM	F82H	0.010	AS4

Specimen ID No.	Lab.	Specimen Type	Mat'l/Heat	Mass (g)	Subcap.
LH02	Kohno	TEM	F82H	0.010	AS4
LH03	Kohno	TEM	F82H	0.010	AS4
LH04	Kohno	TEM	F82H	0.010	AS4
LH05	Kohno	TEM	F82H	0.010	AS4
LH06	Kohno	TEM	F82H	0.010	AS4
LH07	Kohno	TEM	F82H	0.010	AS4
LH08	Kohno	TEM	F82H	0.010	AS4
LM11	Kohno	TEM	JLF1Mn1	0.010	AS4
LM12	Kohno	TEM	JLF1Mn1	0.010	AS4
LM13	Kohno	TEM	JLF1Mn1	0.010	AS4
LM14	Kohno	TEM	JLF1Mn1	0.010	AS4
LM15	Kohno	TEM	JLF1Mn1	0.010	AS4
LM16	Kohno	TEM	JLF1Mn1	0.010	AS4
LM17	Kohno	TEM	JLFMn1	0.010	AS4
LM18	Kohno	TEM	JLFMn1	0.010	AS4
LM21	Kohno	TEM	JLFMn2	0.010	AS4
LM22	Kohno	TEM	JLFMn2	0.010	AS4
LM23	Kohno	TEM	JLFMn2	0.010	AS4
LM24	Kohno	TEM	JLFMn2	0.010	AS4
LM25	Kohno	TEM	JLFMn2	0.010	AS4
LM26	Kohno	TEM	JLFMn2	0.010	AS4
LM27	Kohno	TEM	JLFMn2	0.010	AS4
LM28	Kohno	TEM	JLFMn2	0.010	AS4
TR17	Ohnuki	TEM	316L	0.011	AS4
TR18	Ohnuki	TEM	316L	0.011	AS4
TR19	Ohnuki	TEM	316-0.3Ti	0.011	AS4
TR20	Ohnuki	TEM	316-0.3Ti	0.011	AS4
TR21	Ohnuki	TEM	316-0.3Zr	0.011	AS4
TR22	Ohnuki	TEM	316-0.3Zr	0.011	AS4
TR23	Ohnuki	TEM	316-0.3Hf	0.011	AS4
TR24	Ohnuki	TEM	316-0.3Hf	0.011	AS4
TR25	Ohnuki	TEM	316-0.3Nb	0.011	AS4
TR26	Ohnuki	TEM	316-0.3Nb	0.011	AS4
TR27	Ohnuki	TEM	316L/CW	0.011	AS4
TR28	Ohnuki	TEM	316L/CW	0.011	AS4
TR29	Ohnuki	TEM	316L/CW	0.011	AS4
TR30	Ohnuki	TEM	316-0.3Ti/CW	0.011	AS4
TR31	Ohnuki	TEM	316-0.3Ti/CW	0.011	AS4
TR32	Ohnuki	TEM	316-0.3Ti/CW	0.011	AS4
TR33	Ohnuki	TEM	316-0.3Zr/CW	0.011	AS4
TR34	Ohnuki	TEM	316-0.3Zr/CW	0.011	AS4
TR35	Ohnuki	TEM	316-0.3Zr/CW	0.011	AS4
YA01	Yoshida	TEM	FeCrNi(1)	0.010	AS4
YA02	Yoshida	TEM	FeCrNi(1)	0.010	AS4
YA03	Yoshida	TEM	FeCrNi(2)	0.010	AS4
YA04	Yoshida	TEM	FeCrNi(2)	0.010	AS4
YA05	Yoshida	TEM	FeCrNi(3)	0.010	AS4
YA06	Yoshida	TEM	FeCrNi(3)	0.010	AS4
YA07	Yoshida	TEM	FeCrNi(4)	0.010	AS4
YA08	Yoshida	TEM	FeCrNi(4)	0.010	AS4
YA09	Yoshida	TEM	FeCrNi(5)	0.010	AS4
YA10	Yoshida	TEM	FeCrNi(5)	0.010	AS4
YA11	Yoshida	TEM	FeCrNi(6)	0.010	AS4
YA12	Yoshida	TEM	FeCrNi(6)	0.010	AS4
YA13	Yoshida	TEM	FeCrNi(7)	0.010	AS4
YA14	Yoshida	TEM	FeCrNi(7)	0.010	AS4
YA15	Yoshida	TEM	FeCrNi(8)	0.010	AS4
YA16	Yoshida	TEM	FeCrNi(8)	0.010	AS4
YA17	Yoshida	TEM	FeCrNi(9)	0.010	AS4
YA18	Yoshida	TEM	FeCrNi(9)	0.010	AS4
YA19	Yoshida	TEM	FeCrNi(10)	0.010	AS4
YA20	Yoshida	TEM	FeCrNi(10)	0.010	AS4

Specimen ID No.	Lab.	Specimen Type	Mat'l/Heat	Mass (g)	Subcap.
YA21	Yoshida	TEM	FeCrNi(11)	0.010	AS4
YA22	Yoshida	TEM	FeCrNi(11)	0.010	AS4
G215	A.Kimura	TEM	JLM-1	0.010	AS4
G216	A.Kimura	TEM	JLM-1	0.010	AS4
G217	A.Kimura	TEM	JLM-1	0.010	AS4
G218	A.Kimura	TEM	JLM-1	0.010	AS4
G219	A.Kimura	TEM	JLM-1	0.010	AS4
G220	A.Kimura	TEM	JLM-1	0.010	AS4
G221	A.Kimura	TEM	JLM-1	0.010	AS4
G222	A.Kimura	TEM	JLM-1	0.010	AS4
G223	A.Kimura	TEM	JLM-1	0.010	AS4
G224	A.Kimura	TEM	JLM-1	0.010	AS4
G225	A.Kimura	TEM	JLM-1	0.010	AS4
G245	A.Kimura	TEM	NLM-D	0.010	AS4
G246	A.Kimura	TEM	NLM-D	0.010	AS4
G247	A.Kimura	TEM	NLM-D	0.010	AS4
G248	A.Kimura	TEM	NLM-D	0.010	AS4
G249	A.Kimura	TEM	NLM-D	0.010	AS4
G250	A.Kimura	TEM	NLM-D	0.010	AS4
G251	A.Kimura	TEM	NLM-D	0.010	AS4
G252	A.Kimura	TEM	NLM-D	0.010	AS4
G253	A.Kimura	TEM	NLM-D	0.010	AS4
G254	A.Kimura	TEM	NLM-D	0.010	AS4
G255	A.Kimura	TEM	NLM-D	0.010	AS4
G275	A.Kimura	TEM	NLM-E	0.010	AS4
G276	A.Kimura	TEM	NLM-E	0.010	AS4
G277	A.Kimura	TEM	NLM-E	0.010	AS4
G278	A.Kimura	TEM	NLM-E	0.010	AS4
G279	A.Kimura	TEM	NLM-E	0.010	AS4
G280	A.Kimura	TEM	NLM-E	0.010	AS4
G281	A.Kimura	TEM	NLM-E	0.010	AS4
G282	A.Kimura	TEM	NLM-E	0.010	AS4
G283	A.Kimura	TEM	NLM-E	0.010	AS4
G284	A.Kimura	TEM	NLM-E	0.010	AS4
G285	A.Kimura	TEM	NLM-E	0.010	AS4
		Subcapsule AS5			
J3	Monbusho	Creep	V-3Fe-4TI-0.1Si	0.650	AS5
1XR5	Matsui	1.5CVN	V-4Cr-4TI-0.1Si	0.264	AS5
95F1	Matsui	1.5CVN	V-3Fe-4TI-0.1Si	0.264	AS5
95F2	Matsui	1.5CVN	V-3Fe-4TI-0.1Si	0.264	AS5
95F3	Matsui	1.5CVN	V-3Fe-4TI-0.1Si	0.264	AS5
95F4	Matsui	1.5CVN	V-3Fe-4TI-0.1Si	0.264	AS5
95F5	Matsui	1.5CVN	V-3Fe-4TI-0.1Si	0.264	AS5
71	ANL	CVNM30	832665	1.662	AS5
71E	ANL	CVNM-Weld	832665	1.660	AS5
71E	ANL	CVNM-Weld	832665	1.660	AS5
XC08	ORNL	SS-3 TS	T91	0.340	AS5
XC09	ORNL	SS-3 TS	T91	0.340	AS5
ZC09	ORNL	SS-3 TS	T92	0.345	AS5
AJD8	Abe	MT TS	V-5Cr-5TI-1SiAlY	0.059	AS5
P140	PNL	MT TS	T91	0.075	AS5
P141	PNL	MT TS	T91	0.075	AS5
XF21	Matsui	MT TS	V-3Fe-4TI-0.1Si	0.051	AS5
XF22	Matsui	MT TS	V-3Fe-4TI-0.1Si	0.051	AS5
XF23	Matsui	MT TS	V-3Fe-4TI-0.1Si	0.051	AS5
XF24	Matsui	MT TS	V-3Fe-4TI-0.1Si	0.051	AS5
XRX5	Matsui	MT TS	V-4Cr-4TI-0.1Si	0.051	AS5
47	ANL	TEM	BL-47	0.012	AS5
47	ANL	TEM	BL-47	0.012	AS5
47	ANL	TEM	BL-47	0.012	AS5

Specimen ID No.	Lab.	Specimen Type	Mat'l/Heat	Mass (g)	Subcap.
47	ANL	TEM	BL-47	0.012	AS5
47	ANL	TEM	BL-47	0.012	AS5
47	ANL	TEM	BL-47	0.012	AS5
47	ANL	TEM	BL-47	0.012	AS5
47	ANL	TEM	BL-47	0.012	AS5
47	ANL	TEM	BL-47	0.012	AS5
47	ANL	TEM	BL-47	0.012	AS5
70	ANL	TEM	BL-70	0.012	AS5
70	ANL	TEM	BL-70	0.012	AS5
70	ANL	TEM	BL-70	0.012	AS5
70	ANL	TEM	BL-70	0.012	AS5
70	ANL	TEM	BL-70	0.012	AS5
70	ANL	TEM	BL-70	0.012	AS5
70	ANL	TEM	BL-70	0.012	AS5
70	ANL	TEM	BL-70	0.012	AS5
70	ANL	TEM	BL-70	0.012	AS5
71	ANL	TEM	832665	0.012	AS5
71	ANL	TEM	832665	0.012	AS5
71	ANL	TEM	832665	0.012	AS5
71	ANL	TEM	832665	0.012	AS5
71	ANL	TEM	832665	0.012	AS5
71	ANL	TEM	832665	0.012	AS5
71	ANL	TEM	832665	0.012	AS5
71	ANL	TEM	832665	0.012	AS5
71	ANL	TEM	832665	0.012	AS5
71	ANL	TEM	832665	0.012	AS5
72	ANL	TEM	T87	0.012	AS5
72	ANL	TEM	T87	0.012	AS5
72	ANL	TEM	T87	0.012	AS5
72	ANL	TEM	T87	0.012	AS5
72	ANL	TEM	T87	0.012	AS5
72	ANL	TEM	T87	0.012	AS5
72	ANL	TEM	T87	0.012	AS5
72	ANL	TEM	T87	0.012	AS5
72	ANL	TEM	T87	0.012	AS5
72	ANL	TEM	T87	0.012	AS5
P109	PNL	TEM	T91	0.013	AS5
P112	PNL	TEM	T91	0.013	AS5
P113	PNL	TEM	T91	0.013	AS5
P116	PNL	TEM	T91	0.013	AS5
P117	PNL	TEM	T91	0.013	AS5
P125	PNL	TEM	T91	0.013	AS5
P203	PNL	TEM	T92	0.013	AS5
P218	PNL	TEM	T92	0.013	AS5
P224	PNL	TEM	T92	0.013	AS5
P225	PNL	TEM	T92	0.013	AS5
P226	PNL	TEM	T92	0.013	AS5
P228	PNL	TEM	T92	0.013	AS5
P702	PNL	TEM	T87	0.013	AS5
P703	PNL	TEM	T87	0.013	AS5
P706	PNL	TEM	T87	0.013	AS5
P723	PNL	TEM	T87	0.013	AS5
P728	PNL	TEM	T87	0.013	AS5
P732	PNL	TEM	T87	0.013	AS5
P803	PNL	TEM	832665	0.013	AS5
P804	PNL	TEM	832665	0.013	AS5
P816	PNL	TEM	832665	0.013	AS5
P827	PNL	TEM	832665	0.013	AS5
P834	PNL	TEM	832665	0.013	AS5
P837	PNL	TEM	832665	0.013	AS5
LZ	ANL	TEM-LZ	832665	0.012	AS5

Specimen ID No.	Lab.	Specimen Type	Mat'l/Heat	Mass (g)	Subcap.
		Subcapsule AS6			
A2	ANL	Creep	832665	0.650	AS6
1XR1	Matsui	1.5CVN	V-4Cr-4TI-0.1Si	0.264	AS6
1XR2	Matsui	1.5CVN	V-4Cr-4TI-0.1Si	0.264	AS6
1XR3	Matsui	1.5CVN	V-4Cr-4TI-0.1Si	0.264	AS6
1XR4	Matsui	1.5CVN	V-4Cr-4TI-0.1Si	0.264	AS6
95R5	Matsui	1.5CVN	V-4Cr-4TI-0.1Si	0.264	AS6
AN12	Matsui	1.5CVN	V-4Cr4Ti/832665	0.264	AS6
71	ANL	CVNM30	832665	1.662	AS6
BL71W-39	ANL	CVNM30	832665	1.662	AS6
BL71W-54	ANL	CVNM30	832665	1.662	AS6
UC08	ORNL	SS-3 TS	T90	0.345	AS6
UC09	ORNL	SS-3 TS	T90	0.345	AS6
ZC08	ORNL	SS-3 TS	T92	0.345	AS6
P747	PNL	MT TS	T87	0.075	AS6
P753	PNL	MT TS	T87	0.075	AS6
P845	PNL	MT TS	832665	0.075	AS6
P853	PNL	MT TS	832665	0.075	AS6
XFX1	Matsui	MT TS	V-3Fe-4TI-0.1Si	0.051	AS6
XFX2	Matsui	MT TS	V-3Fe-4TI-0.1Si	0.051	AS6
XFX3	Matsui	MT TS	V-3Fe-4TI-0.1Si	0.051	AS6
XFX4	Matsui	MT TS	V-3Fe-4TI-0.1Si	0.051	AS6
ET11	ORNL	TEM	T89	0.010	AS6
ET12	ORNL	TEM	T89	0.010	AS6
ET13	ORNL	TEM	T89	0.010	AS6
ET14	ORNL	TEM	T89	0.010	AS6
ET15	ORNL	TEM	T89	0.010	AS6
ET16	ORNL	TEM	T89	0.010	AS6
ET17	ORNL	TEM	T89	0.010	AS6
ET18	ORNL	TEM	T89	0.010	AS6
ET19	ORNL	TEM	T89	0.010	AS6
ET20	ORNL	TEM	T89	0.010	AS6
FT11	ORNL	TEM	T90	0.010	AS6
FT12	ORNL	TEM	T90	0.010	AS6
FT13	ORNL	TEM	T90	0.010	AS6
FT14	ORNL	TEM	T90	0.010	AS6
FT15	ORNL	TEM	T90	0.010	AS6
FT16	ORNL	TEM	T90	0.010	AS6
FT17	ORNL	TEM	T90	0.010	AS6
FT18	ORNL	TEM	T90	0.010	AS6
FT19	ORNL	TEM	T90	0.010	AS6
FT20	ORNL	TEM	T90	0.010	AS6
GT11	ORNL	TEM	T91	0.011	AS6
GT12	ORNL	TEM	T91	0.011	AS6
GT13	ORNL	TEM	T91	0.011	AS6
GT14	ORNL	TEM	T91	0.011	AS6
GT15	ORNL	TEM	T91	0.011	AS6
GT16	ORNL	TEM	T91	0.011	AS6
GT17	ORNL	TEM	T91	0.011	AS6
GT18	ORNL	TEM	T91	0.011	AS6
GT19	ORNL	TEM	T91	0.011	AS6
GT20	ORNL	TEM	T91	0.011	AS6
HT11	ORNL	TEM	T92	0.011	AS6
HT12	ORNL	TEM	T92	0.011	AS6
HT13	ORNL	TEM	T92	0.011	AS6
HT14	ORNL	TEM	T92	0.011	AS6
HT15	ORNL	TEM	T92	0.011	AS6
HT16	ORNL	TEM	T92	0.011	AS6
HT17	ORNL	TEM	T92	0.011	AS6
HT18	ORNL	TEM	T92	0.011	AS6

Specimen ID No.	Lab.	Specimen Type	Mat'l/Heat	Mass (g)	Subcap.
HT19	ORNL	TEM	T92	0.011	AS6
HT20	ORNL	TEM	T92	0.011	AS6
NT11	ORNL	TEM	832665	0.010	AS6
NT12	ORNL	TEM	832665	0.010	AS6
NT13	ORNL	TEM	832665	0.010	AS6
NT14	ORNL	TEM	832665	0.010	AS6
NT15	ORNL	TEM	832665	0.010	AS6
NT16	ORNL	TEM	832665	0.010	AS6
NT17	ORNL	TEM	832665	0.010	AS6
NT18	ORNL	TEM	832665	0.010	AS6
NT19	ORNL	TEM	832665	0.010	AS6
NT20	ORNL	TEM	832665	0.010	AS6
		Subcapsule AS7			
QC02	ORNL	CVNM	832665	1.662	AS7
71E	ANL	CVNM-Weld	832665	1.650	AS7
71E	ANL	CVNM-Weld	832665	1.650	AS7
WF22	ORNL	SS-3-EB	832665	0.340	AS7
P143	PNL	MT TS	T91	0.072	AS7
P144	PNL	MT TS	T91	0.072	AS7
		Subcapsule AS8			
A3	ANL	Creep	832665	0.650	AS8
95R1	Matsui	1.5CVN	V-4Cr-4TI-0.1Si	0.264	AS8
95R2	Matsui	1.5CVN	V-4Cr-4TI-0.1Si	0.264	AS8
95R3	Matsui	1.5CVN	V-4Cr-4TI-0.1Si	0.264	AS8
95R4	Matsui	1.5CVN	V-4Cr-4TI-0.1Si	0.264	AS8
AJZ1	Abe	1.5CVN	V-5Cr-5TI-1SiAlY	0.265	AS8
AJZ2	Abe	1.5CVN	V-5Cr-5TI-1SiAlY	0.265	AS8
QC07	ORNL	CVNM	832665	1.660	AS8
QC09	ORNL	CVNM	832665	1.660	AS8
QC10	ORNL	CVNM	832665	1.660	AS8
71	ANL	SS-3 TS	832665	0.318	AS8
71	ANL	SS-3 TS	832665	0.318	AS8
71-LZ	ANL	SS-3-LZ	832665	0.318	AS8
XR21	Matsui	MT TS	V-4Cr-4TI-0.1Si	0.051	AS8
XR22	Matsui	MT TS	V-4Cr-4TI-0.1Si	0.051	AS8
XR23	Matsui	MT TS	V-4Cr-4TI-0.1Si	0.051	AS8
XR24	Matsui	MT TS	V-4Cr-4TI-0.1Si	0.051	AS8
XRX1	Matsui	MT TS	V-4Cr-4TI-0.1Si	0.051	AS8
XRX2	Matsui	MT TS	V-4Cr-4TI-0.1Si	0.051	AS8
XRX3	Matsui	MT TS	V-4Cr-4TI-0.1Si	0.051	AS8
XRX4	Matsui	MT TS	V-4Cr-4TI-0.1Si	0.051	AS8
1RX1	Matsui	TEM	V-4Cr-4TI-0.1Si	0.011	AS8
1RX2	Matsui	TEM	V-4Cr-4TI-0.1Si	0.011	AS8
1RX3	Matsui	TEM	V-4Cr-4TI-0.1Si	0.011	AS8
1SX1	Matsui	TEM	V-1Si	0.011	AS8
5CX1	Matsui	TEM	V-5Cr	0.011	AS8
5FX1	Matsui	TEM	V-5Fe	0.011	AS8
5MX1	Matsui	TEM	V-5Mo	0.011	AS8
5NX1	Matsui	TEM	V-5Nb	0.011	AS8
5TX1	Matsui	TEM	V-5Ti	0.011	AS8
9RX1	Matsui	TEM	V-4Cr-4TI-0.1Si	0.011	AS8
9RX2	Matsui	TEM	V-4Cr-4TI-0.1Si	0.011	AS8
9RX3	Matsui	TEM	V-4Cr-4TI-0.1Si	0.011	AS8
AJ11	Abe	TEM	V-5Cr-5TI-1SiAlY	0.010	AS8
AJ12	Abe	TEM	V-5Cr-5TI-1SiAlY	0.010	AS8
AJ13	Abe	TEM	V-5Cr-5TI-1SiAlY	0.010	AS8
AJ14	Abe	TEM	V-5Cr-5TI-1SiAlY	0.010	AS8
AJ20	Abe	TEM	V-5Cr-5TI-1SiAlY	0.010	AS8

Specimen ID No.	Lab.	Specimen Type	Mat'l/Heat	Mass (g)	Subcap.
AJ30	Abe	TEM	V-5Cr-5TI-1SiAlY	0.010	AS8
AJ31	Abe	TEM	V-5Cr-5TI-1SiAlY	0.010	AS8
AJ32	Abe	TEM	V-5Cr-5TI-1SiAlY	0.010	AS8
AJ33	Abe	TEM	V-5Cr-5TI-1SiAlY	0.010	AS8
AJ34	Abe	TEM	V-5Cr-5TI-1SiAlY	0.010	AS8
AJ50	Abe	TEM	V-5Cr-5TI-1SiAlY	0.010	AS8
AJ51	Abe	TEM	V-5Cr-5TI-1SiAlY	0.010	AS8
AJ52	Abe	TEM	V-5Cr-5TI-1SiAlY	0.010	AS8
AJ53	Abe	TEM	V-5Cr-5TI-1SiAlY	0.010	AS8
AJ54	Abe	TEM	V-5Cr-5TI-1SiAlY	0.010	AS8
AJ55	Abe	TEM	V-5Cr-5TI-1SiAlY	0.010	AS8
AJ56	Abe	TEM	V-5Cr-5TI-1SiAlY	0.010	AS8
AJ57	Abe	TEM	V-5Cr-5TI-1SiAlY	0.010	AS8
AJ58	Abe	TEM	V-5Cr-5TI-1SiAlY	0.010	AS8
AJ59	Abe	TEM	V-5Cr-5TI-1SiAlY	0.010	AS8
AJ80	Abe	TEM	V-5Cr-5TI-1SiAlY	0.010	AS8
AJ81	Abe	TEM	V-5Cr-5TI-1SiAlY	0.010	AS8
AJ82	Abe	TEM	V-5Cr-5TI-1SiAlY	0.010	AS8
AJ83	Abe	TEM	V-5Cr-5TI-1SiAlY	0.010	AS8
AJ84	Abe	TEM	V-5Cr-5TI-1SiAlY	0.010	AS8
F9X1	Matsui	TEM	V-3Fe-4TI-0.1Si	0.011	AS8
F9X2	Matsui	TEM	V-3Fe-4TI-0.1Si	0.011	AS8
F9X3	Matsui	TEM	V-3Fe-4TI-0.1Si	0.011	AS8
PVX1	Matsui	TEM	PureV	0.011	AS8
TR01	Ohnuki	TEM	pure V	0.008	AS8
TR02	Ohnuki	TEM	pure V	0.008	AS8
TR03	Ohnuki	TEM	V-0.5Cr	0.008	AS8
TR04	Ohnuki	TEM	V-0.5Cr	0.008	AS8
TR05	Ohnuki	TEM	V-1Cr	0.008	AS8
TR06	Ohnuki	TEM	V-1Cr	0.008	AS8
TR07	Ohnuki	TEM	V-2Cr	0.008	AS8
TR08	Ohnuki	TEM	V-2Cr	0.008	AS8
TR09	Ohnuki	TEM	V-5Cr	0.008	AS8
TR10	Ohnuki	TEM	V-5Cr	0.008	AS8
TR11	Ohnuki	TEM	V-10Cr	0.008	AS8
TR12	Ohnuki	TEM	V-10Cr	0.008	AS8
TR13	Ohnuki	TEM	V-4Cr-4Ti	0.008	AS8
TR14	Ohnuki	TEM	V-4Cr-4Ti	0.008	AS8
TR15	Ohnuki	TEM	V-1Y	0.008	AS8
TR16	Ohnuki	TEM	V-1Y	0.008	AS8
X2X1	Matsui	TEM	VM9402	0.011	AS8
X3X1	Matsui	TEM	VM9403	0.011	AS8
X4X1	Matsui	TEM	VM9404	0.011	AS8
X5X1	Matsui	TEM	VM9405	0.011	AS8
X6X1	Matsui	TEM	VM9406	0.011	AS8
X8X1	Matsui	TEM	VM9408	0.011	AS8
X9X1	Matsui	TEM	VM9409	0.011	AS8
			Subcapsule AS9		
A1	ANL	Creep	832665	0.650	AS9
1XR6	Matsui	1.5CVN	V-4Cr-4TI-0.1Si	0.268	AS9
1XR7	Matsui	1.5CVN	V-4Cr-4TI-0.1Si	0.268	AS9
95R6	Matsui	1.5CVN	V-4Cr-4TI-0.1Si	0.268	AS9
95R7	Matsui	1.5CVN	V-4Cr-4TI-0.1Si	0.268	AS9
95R8	Matsui	1.5CVN	V-4Cr-4TI-0.1Si	0.268	AS9
95R9	Matsui	1.5CVN	V-4Cr-4TI-0.1Si	0.268	AS9
---	ANL	1.5CVN-IG	BL-47	0.264	AS9
---	ANL	1.5CVN-IG	BL-47	0.264	AS9
---	ANL	1.5CVN-IG	BL-47	0.264	AS9
---	ANL	1.5CVN-IG	BL-47	0.264	AS9
47-09	ANL	CVNM30	BL-47	1.678	AS9

Specimen ID No.	Lab.	Specimen Type	Mat'l/Heat	Mass (g)	Subcap.
BL71W-20	ANL	CVNM30	832665	1.674	AS9
71	ANL	SS-3 TS	832665	0.320	AS9
71	ANL	SS-3 TS	832665	0.320	AS9
71	ANL	SS-3 TS	832665	0.320	AS9
XR25	Matsui	MT TS	V-4Cr-4TI-0.1Si	0.053	AS9
XR26	Matsui	MT TS	V-4Cr-4TI-0.1Si	0.053	AS9
XR27	Matsui	MT TS	V-4Cr-4TI-0.1Si	0.053	AS9
XR28	Matsui	MT TS	V-4Cr-4TI-0.1Si	0.053	AS9
XRX6	Matsui	MT TS	V-4Cr-4TI-0.1Si	0.053	AS9
XRX7	Matsui	MT TS	V-4Cr-4TI-0.1Si	0.053	AS9
XRX8	Matsui	MT TS	V-4Cr-4TI-0.1Si	0.053	AS9
XRX9	Matsui	MT TS	V-4Cr-4TI-0.1Si	0.053	AS9
47	ANL	TEM	BL-47	0.012	AS9
47	ANL	TEM	BL-47	0.012	AS9
47	ANL	TEM	BL-47	0.012	AS9
47	ANL	TEM	BL-47	0.012	AS9
47	ANL	TEM	BL-47	0.012	AS9
47	ANL	TEM	BL-47	0.012	AS9
47	ANL	TEM	BL-47	0.012	AS9
47	ANL	TEM	BL-47	0.012	AS9
47	ANL	TEM	BL-47	0.012	AS9
47	ANL	TEM	BL-47	0.012	AS9
47	ANL	TEM	BL-47	0.012	AS9
70	ANL	TEM	BL-70	0.012	AS9
70	ANL	TEM	BL-70	0.012	AS9
70	ANL	TEM	BL-70	0.012	AS9
70	ANL	TEM	BL-70	0.012	AS9
70	ANL	TEM	BL-70	0.012	AS9
70	ANL	TEM	BL-70	0.012	AS9
70	ANL	TEM	BL-70	0.012	AS9
70	ANL	TEM	BL-70	0.012	AS9
70	ANL	TEM	BL-70	0.012	AS9
70	ANL	TEM	BL-70	0.012	AS9
71	ANL	TEM	832665	0.012	AS9
71	ANL	TEM	832665	0.012	AS9
71	ANL	TEM	832665	0.012	AS9
71	ANL	TEM	832665	0.012	AS9
71	ANL	TEM	832665	0.012	AS9
71	ANL	TEM	832665	0.012	AS9
71	ANL	TEM	832665	0.012	AS9
71	ANL	TEM	832665	0.012	AS9
71	ANL	TEM	832665	0.012	AS9
71	ANL	TEM	832665	0.012	AS9
72	ANL	TEM	T87	0.012	AS9
72	ANL	TEM	T87	0.012	AS9
72	ANL	TEM	T87	0.012	AS9
72	ANL	TEM	T87	0.012	AS9
72	ANL	TEM	T87	0.012	AS9
72	ANL	TEM	T87	0.012	AS9
72	ANL	TEM	T87	0.012	AS9
72	ANL	TEM	T87	0.012	AS9
72	ANL	TEM	T87	0.012	AS9
72	ANL	TEM	T87	0.012	AS9
LZ	ANL	TEM-LZ	832665	0.012	AS9
		Subcapsule AS10			
A10	ANL	Creep	832665	0.650	AS10
AJT5	Abe	1.5CVN	V-5Cr-5TI-1SiAlY	0.264	AS10
AJT6	Abe	1.5CVN	V-5Cr-5TI-1SiAlY	0.264	AS10
AJZ5	Abe	1.5CVN	V-5Cr-5TI-1SiAlY	0.264	AS10
AJZ6	Abe	1.5CVN	V-5Cr-5TI-1SiAlY	0.264	AS10
AJZ7	Abe	1.5CVN	V-5Cr-5TI-1SiAlY	0.264	AS10

Specimen ID No.	Lab.	Specimen Type	Mat'l/Heat	Mass (g)	Subcap.
AJZ8	Abe	1.5CVN	V-5Cr-5TI-1SiAlY	0.264	AS10
BL71W-21	ANL	CVNM30	832665	1.674	AS10
BL71W-22	ANL	CVNM30	832665	1.674	AS10
BL71W-30	ANL	CVNM30	832665	1.674	AS10
47	ANL	SS-3 TS	BL-47	0.320	AS10
47	ANL	SS-3 TS	BL-47	0.320	AS10
71-LZ	ANL	SS-3-LZ	832665	0.320	AS10
AJB4	Abe	MT TS	V-5Cr-5TI-1SiAlY	0.056	AS10
AJB5	Abe	MT TS	V-5Cr-5TI-1SiAlY	0.056	AS10
AJB6	Abe	MT TS	V-5Cr-5TI-1SiAlY	0.056	AS10
AJB7	Abe	MT TS	V-5Cr-5TI-1SiAlY	0.056	AS10
AJF0	Abe	MT TS	V-5Cr-5TI-1SiAlY	0.056	AS10
AJF1	Abe	MT TS	V-5Cr-5TI-1SiAlY	0.056	AS10
AJF2	Abe	MT TS	V-5Cr-5TI-1SiAlY	0.056	AS10
AJF3	Abe	MT TS	V-5Cr-5TI-1SiAlY	0.056	AS10
ET01	ORNL	TEM	T89	0.010	AS10
ET02	ORNL	TEM	T89	0.010	AS10
ET03	ORNL	TEM	T89	0.010	AS10
ET04	ORNL	TEM	T89	0.010	AS10
ET05	ORNL	TEM	T89	0.010	AS10
ET06	ORNL	TEM	T89	0.010	AS10
ET07	ORNL	TEM	T89	0.010	AS10
ET08	ORNL	TEM	T89	0.010	AS10
ET09	ORNL	TEM	T89	0.010	AS10
ET10	ORNL	TEM	T89	0.010	AS10
FT01	ORNL	TEM	T90	0.010	AS10
FT02	ORNL	TEM	T90	0.010	AS10
FT03	ORNL	TEM	T90	0.010	AS10
FT04	ORNL	TEM	T90	0.010	AS10
FT05	ORNL	TEM	T90	0.010	AS10
FT06	ORNL	TEM	T90	0.010	AS10
FT07	ORNL	TEM	T90	0.010	AS10
FT08	ORNL	TEM	T90	0.010	AS10
FT09	ORNL	TEM	T90	0.010	AS10
FT10	ORNL	TEM	T90	0.010	AS10
GT01	ORNL	TEM	T91	0.011	AS10
GT02	ORNL	TEM	T91	0.011	AS10
GT03	ORNL	TEM	T91	0.011	AS10
GT04	ORNL	TEM	T91	0.011	AS10
GT05	ORNL	TEM	T91	0.011	AS10
GT06	ORNL	TEM	T91	0.011	AS10
GT07	ORNL	TEM	T91	0.011	AS10
GT08	ORNL	TEM	T91	0.011	AS10
GT09	ORNL	TEM	T91	0.011	AS10
GT10	ORNL	TEM	T91	0.011	AS10
HT01	ORNL	TEM	T92	0.011	AS10
HT02	ORNL	TEM	T92	0.011	AS10
HT03	ORNL	TEM	T92	0.011	AS10
HT04	ORNL	TEM	T92	0.011	AS10
HT05	ORNL	TEM	T92	0.011	AS10
HT06	ORNL	TEM	T92	0.011	AS10
HT07	ORNL	TEM	T92	0.011	AS10
HT08	ORNL	TEM	T92	0.011	AS10
HT09	ORNL	TEM	T92	0.011	AS10
HT10	ORNL	TEM	T92	0.011	AS10
NT01	ORNL	TEM	832665	0.010	AS10
NT02	ORNL	TEM	832665	0.010	AS10
NT03	ORNL	TEM	832665	0.010	AS10
NT04	ORNL	TEM	832665	0.010	AS10
NT05	ORNL	TEM	832665	0.010	AS10
NT06	ORNL	TEM	832665	0.010	AS10
NT07	ORNL	TEM	832665	0.010	AS10

Specimen ID No.	Lab.	Specimen Type	Mat'l/Heat	Mass (g)	Subcap.
NT08	ORNL	TEM	832665	0.010	AS10
NT09	ORNL	TEM	832665	0.010	AS10
NT10	ORNL	TEM	832665	0.010	AS10
		Subcapsule AS11			
A7	ANL	Creep	832665	0.650	AS11
AJX5	Abe	1.5CVN	V-5Cr-5TI-1SiAlY	0.264	AS11
AJX6	Abe	1.5CVN	V-5Cr-5TI-1SiAlY	0.264	AS11
AJX7	Abe	1.5CVN	V-5Cr-5TI-1SiAlY	0.264	AS11
AJX8	Abe	1.5CVN	V-5Cr-5TI-1SiAlY	0.264	AS11
AJX9	Abe	1.5CVN	V-5Cr-5TI-1SiAlY	0.264	AS11
AJZ9	Abe	1.5CVN	V-5Cr-5TI-1SiAlY	0.264	AS11
47	ANL	CVNM45	BL-47	1.678	AS11
47	ANL	CVNM45	BL-47	1.678	AS11
47	ANL	CVNM45	BL-47	1.678	AS11
UC06	ORNL	SS-3 TS	T90	0.345	AS11
UC07	ORNL	SS-3 TS	T90	0.345	AS11
ZC06	ORNL	SS-3 TS	T92	0.340	AS11
AJA4	Abe	MT TS	V-5Cr-5TI-1SiAlY	0.056	AS11
AJA5	Abe	MT TS	V-5Cr-5TI-1SiAlY	0.056	AS11
AJA6	Abe	MT TS	V-5Cr-5TI-1SiAlY	0.056	AS11
AJA7	Abe	MT TS	V-5Cr-5TI-1SiAlY	0.056	AS11
P751	PNL	MT TS	T87	0.072	AS11
P752	PNL	MT TS	T87	0.072	AS11
P841	PNL	MT TS	832665	0.072	AS11
P842	PNL	MT TS	832665	0.072	AS11
P103	PNL	TEM	T91	0.013	AS11
P105	PNL	TEM	T91	0.013	AS11
P107	PNL	TEM	T91	0.013	AS11
P123	PNL	TEM	T91	0.013	AS11
P124	PNL	TEM	T91	0.013	AS11
P128	PNL	TEM	T91	0.013	AS11
P209	PNL	TEM	T92	0.013	AS11
P213	PNL	TEM	T92	0.013	AS11
P215	PNL	TEM	T92	0.013	AS11
P219	PNL	TEM	T92	0.013	AS11
P221	PNL	TEM	T92	0.013	AS11
P227	PNL	TEM	T92	0.013	AS11
P707	PNL	TEM	T87	0.013	AS11
P708	PNL	TEM	T87	0.013	AS11
P710	PNL	TEM	T87	0.013	AS11
P712	PNL	TEM	T87	0.013	AS11
P726	PNL	TEM	T87	0.013	AS11
P738	PNL	TEM	T87	0.013	AS11
P801	PNL	TEM	832665	0.013	AS11
P808	PNL	TEM	832665	0.013	AS11
P811	PNL	TEM	832665	0.013	AS11
P825	PNL	TEM	832665	0.013	AS11
P826	PNL	TEM	832665	0.013	AS11
P831	PNL	TEM	832665	0.013	AS11
		Subcapsule AS12			
A11	ANL	Creep	832665	0.650	AS12
AJT7	Abe	1.5CVN	V-5Cr-5TI-1SiAlY	0.264	AS12
AJT8	Abe	1.5CVN	V-5Cr-5TI-1SiAlY	0.264	AS12
AN13	Matsui	1.5CVN	V-4Cr4Ti/832665	0.268	AS12
AN14	Matsui	1.5CVN	V-4Cr4Ti/832665	0.268	AS12
AN15	Matsui	1.5CVN	V-4Cr4Ti/832665	0.268	AS12
AN16	Matsui	1.5CVN	V-4Cr4Ti/832665	0.268	AS12
QC03	ORNL	CVNM	832665	1.662	AS12

Specimen ID No.	Lab.	Specimen Type	Mat'l/Heat	Mass (g)	Subcap.
QC04	ORNL	CVNM	832665	1.662	AS12
QC05	ORNL	CVNM	832665	1.662	AS12
XC06	ORNL	SS-3 TS	T91	0.335	AS12
XC07	ORNL	SS-3 TS	T91	0.335	AS12
ZC07	ORNL	SS-3 TS	T92	0.340	AS12
AJF4	Abe	MT TS	V-5Cr-5TI-1SiAlY	0.056	AS12
AJF5	Abe	MT TS	V-5Cr-5TI-1SiAlY	0.056	AS12
AJG1	Abe	MT TS	V-5Cr-5TI-1SiAlY	0.056	AS12
AJG2	Abe	MT TS	V-5Cr-5TI-1SiAlY	0.056	AS12
AJG3	Abe	MT TS	V-5Cr-5TI-1SiAlY	0.056	AS12
AJG4	Abe	MT TS	V-5Cr-5TI-1SiAlY	0.056	AS12
XF28	Matsui	MT TS	V-3Fe-4TI-0.1Si	0.053	AS12
XR1X	Matsui	MT TS	V-4Cr-4TI-0.1Si	0.053	AS12
AJ15	Abe	TEM	V-5Cr-5TI-1SiAlY	0.010	AS12
AJ16	Abe	TEM	V-5Cr-5TI-1SiAlY	0.010	AS12
AJ17	Abe	TEM	V-5Cr-5TI-1SiAlY	0.010	AS12
AJ18	Abe	TEM	V-5Cr-5TI-1SiAlY	0.010	AS12
AJ19	Abe	TEM	V-5Cr-5TI-1SiAlY	0.010	AS12
AJ35	Abe	TEM	V-5Cr-5TI-1SiAlY	0.010	AS12
AJ36	Abe	TEM	V-5Cr-5TI-1SiAlY	0.010	AS12
AJ37	Abe	TEM	V-5Cr-5TI-1SiAlY	0.010	AS12
AJ38	Abe	TEM	V-5Cr-5TI-1SiAlY	0.010	AS12
AJ39	Abe	TEM	V-5Cr-5TI-1SiAlY	0.010	AS12
AJ60	Abe	TEM	V-5Cr-5TI-1SiAlY	0.010	AS12
AJ61	Abe	TEM	V-5Cr-5TI-1SiAlY	0.010	AS12
AJ62	Abe	TEM	V-5Cr-5TI-1SiAlY	0.010	AS12
AJ63	Abe	TEM	V-5Cr-5TI-1SiAlY	0.010	AS12
AJ64	Abe	TEM	V-5Cr-5TI-1SiAlY	0.010	AS12
AJ65	Abe	TEM	V-5Cr-5TI-1SiAlY	0.010	AS12
AJ66	Abe	TEM	V-5Cr-5TI-1SiAlY	0.010	AS12
AJ67	Abe	TEM	V-5Cr-5TI-1SiAlY	0.010	AS12
AJ68	Abe	TEM	V-5Cr-5TI-1SiAlY	0.010	AS12
AJ69	Abe	TEM	V-5Cr-5TI-1SiAlY	0.010	AS12
AJ85	Abe	TEM	V-5Cr-5TI-1SiAlY	0.010	AS12
AJ86	Abe	TEM	V-5Cr-5TI-1SiAlY	0.010	AS12
AJ87	Abe	TEM	V-5Cr-5TI-1SiAlY	0.010	AS12
AJ88	Abe	TEM	V-5Cr-5TI-1SiAlY	0.010	AS12
AJ89	Abe	TEM	V-5Cr-5TI-1SiAlY	0.010	AS12
TR41	Ohnuki	TEM	pure V	0.006	AS12
TR42	Ohnuki	TEM	pure V	0.006	AS12
TR43	Ohnuki	TEM	V-0.5Cr	0.006	AS12
TR44	Ohnuki	TEM	V-0.5Cr	0.006	AS12
TR45	Ohnuki	TEM	V-1Cr	0.006	AS12
TR46	Ohnuki	TEM	V-1Cr	0.006	AS12
TR47	Ohnuki	TEM	V-2Cr	0.006	AS12
TR48	Ohnuki	TEM	V-2Cr	0.006	AS12
TR49	Ohnuki	TEM	V-5Cr	0.006	AS12
TR50	Ohnuki	TEM	V-5Cr	0.006	AS12
TR51	Ohnuki	TEM	V-10Cr	0.006	AS12
TR52	Ohnuki	TEM	V-10Cr	0.006	AS12
TR53	Ohnuki	TEM	V-4Cr-4Ti	0.006	AS12
TR54	Ohnuki	TEM	V-4Cr-4Ti	0.006	AS12
TR55	Ohnuki	TEM	V-1Y	0.006	AS12
TR60	Ohnuki	TEM	V-1Y	0.006	AS12
		Subcapsule AS13			
47	ANL	DCT-A	BL-47	1.255	AS13
47	ANL	DCT-A	BL-47	1.255	AS13
71	ANL	DCT-A	832665	1.220	AS13
71	ANL	DCT-A	832665	1.220	AS13
71	ANL	DCT-A	832665	1.220	AS13

Specimen ID No.	Lab.	Specimen Type	Mat'l/Heat	Mass (g)	Subcap.
72	ANL	DCT-A	T87	1.240	AS13
72	ANL	DCT-A	T87	1.240	AS13
M	Matsui	DCT-A	V-3Fe-4Ti	1.257	AS13
M	Matsui	DCT-A	V-3Fe-4Ti	1.257	AS13
M	Matsui	DCT-A	V-3Fe-4Ti	1.257	AS13
QA01	ORNL	DCT-A	832665	1.377	AS13
QA02	ORNL	DCT-A	832665	1.377	AS13
QA04	ORNL	DCT-A	832665	1.377	AS13
		Subcapsule AS14			
J2	Monbusho	Creep	V-3Fe-4TI-0.1Si	0.650	AS14
95F0	Matsui	1.5CVN	V-3Fe-4TI-0.1Si	0.268	AS14
95F6	Matsui	1.5CVN	V-3Fe-4TI-0.1Si	0.268	AS14
95F7	Matsui	1.5CVN	V-3Fe-4TI-0.1Si	0.268	AS14
95F8	Matsui	1.5CVN	V-3Fe-4TI-0.1Si	0.268	AS14
95F9	Matsui	1.5CVN	V-3Fe-4TI-0.1Si	0.268	AS14
95RX	Matsui	1.5CVN	V-4Cr-4TI-0.1Si	0.268	AS14
BL71W-27	ANL	PCVN30	832665	1.667	AS14
BL71W-40	ANL	PCVN30	832665	1.667	AS14
BL71W-45	ANL	PCVN30	832665	1.667	AS14
72	ANL	SS-3 TS	T87	0.320	AS14
72	ANL	SS-3 TS	T87	0.320	AS14
WF21	ORNL	SS-3-EB	832665	0.340	AS14
XF25	Matsui	MT TS	V-3Fe-4TI-0.1Si	0.053	AS14
XF26	Matsui	MT TS	V-3Fe-4TI-0.1Si	0.053	AS14
XF27	Matsui	MT TS	V-3Fe-4TI-0.1Si	0.053	AS14
XFX5	Matsui	MT TS	V-3Fe-4TI-0.1Si	0.053	AS14
XFX6	Matsui	MT TS	V-3Fe-4TI-0.1Si	0.053	AS14
XFX7	Matsui	MT TS	V-3Fe-4TI-0.1Si	0.053	AS14
XFX8	Matsui	MT TS	V-3Fe-4TI-0.1Si	0.053	AS14
1RX4	Matsui	TEM	V-4Cr-4TI-0.1Si	0.010	AS14
1RX5	Matsui	TEM	V-4Cr-4TI-0.1Si	0.010	AS14
1RX6	Matsui	TEM	V-4Cr-4TI-0.1Si	0.010	AS14
1SX2	Matsui	TEM	V-1Si	0.010	AS14
5CX2	Matsui	TEM	V-5Cr	0.010	AS14
5FX2	Matsui	TEM	V-5Fe	0.010	AS14
5MX2	Matsui	TEM	V-5Mo	0.010	AS14
5NX2	Matsui	TEM	V-5Nb	0.010	AS14
5TX2	Matsui	TEM	V-5Ti	0.010	AS14
9RX4	Matsui	TEM	V-4Cr-4TI-0.1Si	0.010	AS14
9RX5	Matsui	TEM	V-4Cr-4TI-0.1Si	0.010	AS14
9RX6	Matsui	TEM	V-4Cr-4TI-0.1Si	0.010	AS14
F9X4	Matsui	TEM	V-3Fe-4TI-0.1Si	0.010	AS14
F9X5	Matsui	TEM	V-3Fe-4TI-0.1Si	0.010	AS14
F9X6	Matsui	TEM	V-3Fe-4TI-0.1Si	0.010	AS14
PVX2	Matsui	TEM	PureV	0.010	AS14
X2X2	Matsui	TEM	VM9402	0.010	AS14
X3X2	Matsui	TEM	VM9403	0.010	AS14
X4X2	Matsui	TEM	VM9404	0.010	AS14
X5X2	Matsui	TEM	VM9405	0.010	AS14
X6X2	Matsui	TEM	VM9406	0.010	AS14
X8X2	Matsui	TEM	VM9408	0.010	AS14
X9X2	Matsui	TEM	VM9409	0.010	AS14
		Subcapsule AS16			
G3F1	A.Kimura	1.5CVN	NLM-E	0.341	AS16
G3F2	A.Kimura	1.5CVN	NLM-E	0.341	AS16
G3F3	A.Kimura	1.5CVN	NLM-E	0.341	AS16
G3F4	A.Kimura	1.5CVN	NLM-E	0.341	AS16
G3F5	A.Kimura	1.5CVN	NLM-E	0.341	AS16

Specimen ID No.	Lab.	Specimen Type	Mat'l/Heat	Mass (g)	Subcap.
G3F6	A.Kimura	1.5CVN	NLM-E	0.341	AS16
G3F7	A.Kimura	1.5CVN	NLM-E	0.341	AS16
G3F8	A.Kimura	1.5CVN	NLM-E	0.341	AS16
LF09	Kohno	1.5CVN	JLF1	0.355	AS16
LF0A	Kohno	1.5CVN	JLF1	0.355	AS16
LF0B	Kohno	1.5CVN	JLF1	0.355	AS16
LF0D	Kohno	1.5CVN	JLF1	0.355	AS16
LF0F	Kohno	1.5CVN	JLF1	0.355	AS16
LF0G	Kohno	1.5CVN	JLF1	0.355	AS16
LF0H	Kohno	1.5CVN	JLF1	0.355	AS16
LF0K	Kohno	1.5CVN	JLF1	0.355	AS16
LH09	Kohno	1.5CVN	F82H	0.340	AS16
LH0A	Kohno	1.5CVN	F82H	0.340	AS16
LH0B	Kohno	1.5CVN	F82H	0.340	AS16
LH0D	Kohno	1.5CVN	F82H	0.340	AS16
LH0F	Kohno	1.5CVN	F82H	0.340	AS16
LH0G	Kohno	1.5CVN	F82H	0.340	AS16
LH0H	Kohno	1.5CVN	F82H	0.340	AS16
LH0K	Kohno	1.5CVN	F82H	0.340	AS16
G311	A.Kimura	MT TS	JLM-1	0.093	AS16
G312	A.Kimura	MT TS	JLM-1	0.093	AS16
G313	A.Kimura	MT TS	JLM-1	0.093	AS16
G314	A.Kimura	MT TS	JLM-1	0.093	AS16
G3D1	A.Kimura	MT TS	NLM-D	0.093	AS16
G3D2	A.Kimura	MT TS	NLM-D	0.093	AS16
G3D3	A.Kimura	MT TS	NLM-D	0.093	AS16
G3D4	A.Kimura	MT TS	NLM-D	0.093	AS16
G3F1	A.Kimura	MT TS	NLM-E	0.093	AS16
G3F2	A.Kimura	MT TS	NLM-E	0.093	AS16
G3F3	A.Kimura	MT TS	NLM-E	0.093	AS16
G3F4	A.Kimura	MT TS	NLM-E	0.093	AS16
LB04	Kohno	MT TS	JLF1B	0.031	AS16
LB05	Kohno	MT TS	JLF1B	0.031	AS16
LB06	Kohno	MT TS	JLF1B	0.031	AS16
LF05	Kohno	MT TS	JLF1	0.031	AS16
LF06	Kohno	MT TS	JLF1	0.031	AS16
LF07	Kohno	MT TS	JLF1	0.031	AS16
LF08	Kohno	MT TS	JLF1	0.031	AS16
LH05	Kohno	MT TS	F82H	0.031	AS16
LH06	Kohno	MT TS	F82H	0.031	AS16
LH07	Kohno	MT TS	F82H	0.031	AS16
LH08	Kohno	MT TS	F82H	0.031	AS16
LM12	Kohno	MT TS	JLF1Mn1	0.031	AS16
LM13	Kohno	MT TS	JLF1Mn1	0.031	AS16
LM22	Kohno	MT TS	JLFMn2	0.031	AS16
LM23	Kohno	MT TS	JLFMn2	0.031	AS16
G311	A.Kimura	TEM	JLM-1	0.007	AS16
G312	A.Kimura	TEM	JLM-1	0.007	AS16
G313	A.Kimura	TEM	JLM-1	0.007	AS16
G314	A.Kimura	TEM	JLM-1	0.007	AS16
G341	A.Kimura	TEM	NLM-D	0.007	AS16
G342	A.Kimura	TEM	NLM-D	0.007	AS16
G343	A.Kimura	TEM	NLM-D	0.007	AS16
G344	A.Kimura	TEM	NLM-D	0.007	AS16
G371	A.Kimura	TEM	NLM-E	0.007	AS16
G372	A.Kimura	TEM	NLM-E	0.007	AS16
G373	A.Kimura	TEM	NLM-E	0.007	AS16
G374	A.Kimura	TEM	NLM-E	0.007	AS16
LB09	Kohno	TEM	JLF1B	0.010	AS16
LB0A	Kohno	TEM	JLF1B	0.010	AS16
LB0B	Kohno	TEM	JLF1B	0.010	AS16
LB0D	Kohno	TEM	JLF1B	0.010	AS16

Specimen ID No.	Lab.	Specimen Type	Mat'l/Heat	Mass (g)	Subcap.
LB0F	Kohno	TEM	JLF1B	0.010	AS16
LB0G	Kohno	TEM	JLF1B	0.010	AS16
LB0H	Kohno	TEM	JLF1B	0.010	AS16
LB0K	Kohno	TEM	JLF1B	0.010	AS16
LF09	Kohno	TEM	JLF1	0.010	AS16
LF0A	Kohno	TEM	JLF1	0.010	AS16
LF0B	Kohno	TEM	JLF1	0.010	AS16
LF0D	Kohno	TEM	JLF1	0.010	AS16
LF0F	Kohno	TEM	JLF1	0.010	AS16
LF0G	Kohno	TEM	JLF1	0.010	AS16
LF0H	Kohno	TEM	JLF1	0.010	AS16
LF0K	Kohno	TEM	JLF1	0.010	AS16
LH09	Kohno	TEM	F82H	0.010	AS16
LH0A	Kohno	TEM	F82H	0.010	AS16
LH0B	Kohno	TEM	F82H	0.010	AS16
LH0D	Kohno	TEM	F82H	0.010	AS16
LH0F	Kohno	TEM	F82H	0.010	AS16
LH0G	Kohno	TEM	F82H	0.010	AS16
LH0H	Kohno	TEM	F82H	0.010	AS16
LH0K	Kohno	TEM	F82H	0.010	AS16
LM19	Kohno	TEM	JLFMn1	0.010	AS16
LM1A	Kohno	TEM	JLFMn1	0.010	AS16
LM1B	Kohno	TEM	JLFMn1	0.010	AS16
LM1D	Kohno	TEM	JLFMn1	0.010	AS16
LM1F	Kohno	TEM	JLFMn1	0.010	AS16
LM1G	Kohno	TEM	JLFMn1	0.010	AS16
LM1H	Kohno	TEM	JLFMn1	0.010	AS16
LM1K	Kohno	TEM	JLFMn1	0.010	AS16
LM29	Kohno	TEM	JLFMn2	0.010	AS16
LM2A	Kohno	TEM	JLFMn2	0.010	AS16
LM2B	Kohno	TEM	JLFMn2	0.010	AS16
LM2D	Kohno	TEM	JLFMn2	0.010	AS16
LM2F	Kohno	TEM	JLFMn2	0.010	AS16
LM2G	Kohno	TEM	JLFMn2	0.010	AS16
LM2H	Kohno	TEM	JLFMn2	0.010	AS16
LM2K	Kohno	TEM	JLFMn2	0.010	AS16
TR56	Ohnuki	TEM	316-0.3Ti	0.011	AS16
TR57	Ohnuki	TEM	316L	0.011	AS16
TR58	Ohnuki	TEM	316L	0.011	AS16
TR59	Ohnuki	TEM	316-0.3Ti	0.011	AS16
TR61	Ohnuki	TEM	316-0.3Zr	0.011	AS16
TR62	Ohnuki	TEM	316-0.3Zr	0.011	AS16
TR63	Ohnuki	TEM	316-0.3Hf	0.011	AS16
TR64	Ohnuki	TEM	316-0.3Hf	0.011	AS16
TR65	Ohnuki	TEM	316-0.3Nb	0.011	AS16
TR66	Ohnuki	TEM	316-0.3Nb	0.011	AS16
TR67	Ohnuki	TEM	316L/CW	0.011	AS16
TR68	Ohnuki	TEM	316L/CW	0.011	AS16
TR69	Ohnuki	TEM	316L/CW	0.011	AS16
TR70	Ohnuki	TEM	316-0.3Ti/CW	0.011	AS16
TR71	Ohnuki	TEM	316-0.3Ti/CW	0.011	AS16
TR72	Ohnuki	TEM	316-0.3Ti/CW	0.011	AS16
TR73	Ohnuki	TEM	316-0.3Zr/CW	0.011	AS16
TR74	Ohnuki	TEM	316-0.3Zr/CW	0.011	AS16
TR75	Ohnuki	TEM	316-0.3Zr/CW	0.011	AS16
YA23	Yoshida	TEM	FeCrNi(1)	0.010	AS16
YA24	Yoshida	TEM	FeCrNi(1)	0.010	AS16
YA25	Yoshida	TEM	FeCrNi(2)	0.010	AS16
YA26	Yoshida	TEM	FeCrNi(2)	0.010	AS16
YA27	Yoshida	TEM	FeCrNi(3)	0.010	AS16
YA28	Yoshida	TEM	FeCrNi(3)	0.010	AS16
YA29	Yoshida	TEM	FeCrNi(4)	0.010	AS16

Specimen ID No.	Lab.	Specimen Type	Mat'l/Heat	Mass (g)	Subcap.
YA30	Yoshida	TEM	FeCrNi(4)	0.010	AS16
YA31	Yoshida	TEM	FeCrNi(5)	0.010	AS16
YA32	Yoshida	TEM	FeCrNi(5)	0.010	AS16
YA33	Yoshida	TEM	FeCrNi(6)	0.010	AS16
YA34	Yoshida	TEM	FeCrNi(6)	0.010	AS16
YA35	Yoshida	TEM	FeCrNi(7)	0.010	AS16
YA36	Yoshida	TEM	FeCrNi(7)	0.010	AS16
YA37	Yoshida	TEM	FeCrNi(8)	0.010	AS16
YA38	Yoshida	TEM	FeCrNi(8)	0.010	AS16
YA39	Yoshida	TEM	FeCrNi(9)	0.010	AS16
YA40	Yoshida	TEM	FeCrNi(9)	0.010	AS16
YA41	Yoshida	TEM	FeCrNi(10)	0.010	AS16
YA42	Yoshida	TEM	FeCrNi(10)	0.010	AS16
YA43	Yoshida	TEM	FeCrNi(11)	0.010	AS16
YA44	Yoshida	TEM	FeCrNi(11)	0.010	AS16
G315	A.Kimura	TEM	JLM-1	0.010	AS16
G316	A.Kimura	TEM	JLM-1	0.010	AS16
G317	A.Kimura	TEM	JLM-1	0.010	AS16
G318	A.Kimura	TEM	JLM-1	0.010	AS16
G319	A.Kimura	TEM	JLM-1	0.010	AS16
G320	A.Kimura	TEM	JLM-1	0.010	AS16
G321	A.Kimura	TEM	JLM-1	0.010	AS16
G322	A.Kimura	TEM	JLM-1	0.010	AS16
G323	A.Kimura	TEM	JLM-1	0.010	AS16
G324	A.Kimura	TEM	JLM-1	0.010	AS16
G325	A.Kimura	TEM	JLM-1	0.010	AS16
G345	A.Kimura	TEM	NLM-D	0.010	AS16
G346	A.Kimura	TEM	NLM-D	0.010	AS16
G347	A.Kimura	TEM	NLM-D	0.010	AS16
G348	A.Kimura	TEM	NLM-D	0.010	AS16
G349	A.Kimura	TEM	NLM-D	0.010	AS16
G350	A.Kimura	TEM	NLM-D	0.010	AS16
G351	A.Kimura	TEM	NLM-D	0.010	AS16
G352	A.Kimura	TEM	NLM-D	0.010	AS16
G353	A.Kimura	TEM	NLM-D	0.010	AS16
G354	A.Kimura	TEM	NLM-D	0.010	AS16
G355	A.Kimura	TEM	NLM-D	0.010	AS16
G375	A.Kimura	TEM	NLM-E	0.010	AS16
G376	A.Kimura	TEM	NLM-E	0.010	AS16
G377	A.Kimura	TEM	NLM-E	0.010	AS16
G378	A.Kimura	TEM	NLM-E	0.010	AS16
G379	A.Kimura	TEM	NLM-E	0.010	AS16
G380	A.Kimura	TEM	NLM-E	0.010	AS16
G381	A.Kimura	TEM	NLM-E	0.010	AS16
G382	A.Kimura	TEM	NLM-E	0.010	AS16
G383	A.Kimura	TEM	NLM-E	0.010	AS16
G384	A.Kimura	TEM	NLM-E	0.010	AS16
G385	A.Kimura	TEM	NLM-E	0.010	AS16
			Subcapsule AS17		
A4	ANL	Creep	832665	0.650	AS17
AJZ3	Abe	1.5CVN	V-5Cr-5TI-1SiAlY	0.265	AS17
AJZ4	Abe	1.5CVN	V-5Cr-5TI-1SiAlY	0.265	AS17
AN08	Matsui	1.5CVN	V-4Cr4Ti/832665	0.264	AS17
AN09	Matsui	1.5CVN	V-4Cr4Ti/832665	0.264	AS17
AN10	Matsui	1.5CVN	V-4Cr4Ti/832665	0.264	AS17
AN11	Matsui	1.5CVN	V-4Cr4Ti/832665	0.264	AS17
47	ANL	CVNM45	BL-47	1.680	AS17
47	ANL	CVNM45	BL-47	1.680	AS17
47	ANL	CVNM45	BL-47	1.680	AS17
47	ANL	SS-3 TS	BL-47	0.318	AS17

Specimen ID No.	Lab.	Specimen Type	Mat'l/Heat	Mass (g)	Subcap.
47	ANL	SS-3 TS	BL-47	0.318	AS17
72	ANL	SS-3 TS	T87	0.318	AS17
AJD0	Abe	MT TS	V-5Cr-5TI-1SiAlY	0.059	AS17
AJD1	Abe	MT TS	V-5Cr-5TI-1SiAlY	0.059	AS17
AJD2	Abe	MT TS	V-5Cr-5TI-1SiAlY	0.059	AS17
AJD3	Abe	MT TS	V-5Cr-5TI-1SiAlY	0.059	AS17
AJD4	Abe	MT TS	V-5Cr-5TI-1SiAlY	0.059	AS17
AJD5	Abe	MT TS	V-5Cr-5TI-1SiAlY	0.059	AS17
AJD6	Abe	MT TS	V-5Cr-5TI-1SiAlY	0.059	AS17
AJD7	Abe	MT TS	V-5Cr-5TI-1SiAlY	0.059	AS17

SCHEDULE AND STATUS OF IRRADIATION EXPERIMENTS

– A. F. Rowcliffe, M. L. Grossbeck, and J. P. Robertson (Oak Ridge National Laboratory)

OBJECTIVE

To provide an updated summary of the status of irradiation experiments for the neutron-interactive materials program.

SUMMARY

The current status of reactor irradiation experiments is presented in tables summarizing the experimental objectives, conditions, and schedule.

PROGRESS AND STATUS

Currently, the program has three irradiation experiments in reactor; and 6 experiments in the planning or design stages. Postirradiation examination and testing is in progress on 18 experiments.

Summary of Reactor Irradiation Experiments

Experiment	Lead Lab	Collaborators	Responsible Person	Major Objectives	Materials	Temperature °C	Dose (dpa) or fluence	Irrad. Start	Irrad. Finish	Status
EBR-II, Reactor, ANL, Idaho Falls, ID										
COBRA 1A1	PNL	ORNL, ANL, MONBUSHO	M.L. Hamilton	Tensile and fatigue prop., Charpy impact, fracture toughness, TEM	Austenitic and ferritic steels, Fe-alloys, V, Be, low act. materials, Cu alloys, Ti-Al, SiC, C-C comp.	370, 500, 600	9	Nov-92	Apr-93	
COBRA 1A2	PNL	ORNL, ANL, MONBUSHO	M.L. Hamilton	Tensile and fatigue prop., Charpy impact, fracture toughness, TEM	Austenitic and ferritic steels, Fe-alloys, V, Be, low act. materials, Cu alloys, Ti-Al, SiC, C-C comp.	370, 400, 800	33	Nov-92	Sep-94	
X530	ANL		H. Tsai, H.M. Chung	He-effects, swelling, Charpy impact, fracture toughness, tensile prop.	V alloys	370	5	Aug-94	Sep-94	
High Flux Isotope Reactor, ORNL, Oak Ridge, TN										
HFIR-CTR-60	ORNL		S.J. Zinkle	Flexure bars, TEM, indentation disks	Isotopically tailored ceramics	100-600	2.4E+26 n/m2	Dec-94	Aug-95	
HFIR-CTR-61	ORNL		S.J. Zinkle	Similar to HFIR-CTR-60			7.20E+26	Dec-94	Aug-97	
HFIR-JP-9	ORNL	JAERI	P.J. Maziasz/ J.E. Pawel	He effects by isotopic tailoring, tensile prop., TEM	Austenitic and ferritic steels	300-600	57	Jul-90	Apr-94	
HFIR-JP-10	ORNL	JAERI	P.J. Maziasz/ J.E. Pawel	He effects by isotopic tailoring, tensile prop., TEM	Austenitic and ferritic steels	300-600	17	Jul-90	Sep-91	
HFIR-JP-11	ORNL	JAERI	P.J. Maziasz/ J.E. Pawel	Similar to HFIR-JP-10			17	Jul-90	Sep-91	
HFIR-JP-12	ORNL	JAERI	P.J. Maziasz/ J.E. Pawel	Similar to HFIR-JP-9			57	Jul-90	Apr-94	
HFIR-JP-13	ORNL	JAERI	P.J. Maziasz/ J.E. Pawel	Similar to HFIR-JP-10			17	Jul-90	Sep-91	
HFIR-JP-14	ORNL	JAERI	P.J. Maziasz/ J.E. Pawel	He effects by isotopic tailoring, tensile prop., TEM	Austenitic and ferritic steels	300-600	34	Jul-90	Sep-92	

Summary of Reactor Irradiation Experiments

Experiment	Lead Lab	Collaborators	Responsible Person	Major Objectives	Materials	Temperature °C	Dose (dpa) or fluence	Irrad. Start	Irrad. Finish	Status
HFIR-JP-15	ORNL	JAERI	P.J. Maziasz/ J.E. Pawel	Similar to HFIR-JP-9			57	Jul-90	Apr-94	
HFIR-JP-16	ORNL	JAERI	P.J. Maziasz/ J.E. Pawel	Similar to HFIR-JP-10			17	Jul-90	Sep-91	
HFIR-JP-17	ORNL	JAERI	M.L. Grossbeck/ J.E. Pawel	Fracture toughness, tensile prop. TEM	Austenitic and ferritic steels	250-300	3	Dec-91	Feb-92	
HFIR-JP-18	ORNL	JAERI	M.L. Grossbeck/ J.E. Pawel	Fracture toughness, tensile prop. TEM	Austenitic and ferritic steels	60-125	3	Aug-91	Oct-91	
HFIR-JP-19	ORNL	JAERI	M.L. Grossbeck/ J.E. Pawel	Similar to HFIR-JP-18		60-125	3	Aug-91	Oct-91	
HFIR-JP-20	ORNL	JAERI	J.E. Pawel	Tensile Prop., TEM, He effects by isotopic tailoring	Austenitic and ferritic steels	300-600	8	Dec-93	Jun-94	
HFIR-JP-21	ORNL	JAERI	J.E. Pawel	Similar to HFIR-JP-20			18	Dec-93	Apr-95	
HFIR-JP-22	ORNL	JAERI	J.E. Pawel	Similar to HFIR -JP-20			34	Dec-93	Jan-96	
HFIR-JP-23	PNL	MONBUSHO	D.S. Gelles	TEM	Austenitic and ferritic steels, Cu, Mo, V alloys, TiAl	300-600	8	Dec-93	Jun-94	
HFIR-MFE-60J	ORNL	JAERI	J.L. Scott/ M.L. Grossbeck	Spectrally tailored for fusion He prod. Began in ORR as ORR-MFE-6J (6.9 dpa). TEM, Charpy, irrad. creep, tensile and crack growth prop.	Austenitic and ferritic steels, and Ni alloys	60	19 (total)	Jul-90	Nov-92	
HFIR-MFE-330J	ORNL	JAERI	J.L. Scott/ M.L. Grossbeck	Similar to HFIR-MFE-60J. Began in ORR as ORR-MFE-7J (7.4 dpa)		330	19 (total)	Jul-90	Nov-92	
HFIR-MFE-200J	ORNL	JAERI	M.L. Grossbeck/ J.E. Pawel	Similar to HFIR-MFE-60J. Began in ORR as ORR-MFE-6J (6.9 dpa)		200	17 (total)	Nov-92	Jan-95	
HFIR-MFE-400J	ORNL	JAERI	M.L. Grossbeck/ J.E. Pawel	Similar to HFIR-MFE-60J. Began as ORR-MFE-7J (7.4 dpa)		400	17 (total)	Nov-92	Jan-95	
HFIR-HT-S1, -S7	ORNL		L.L. Snead	Thermal conductivity	Various Insulators	80-350	0.01-1.0	Jun-95	Aug-95	
HFIR-HT-F Series	ORNL		L. L. Snead	Fiber tensile	SiC	80-800	0.001-1.0	Jan-95	Mar-96	

Summary of Reactor Irradiation Experiments

Experiment	Lead Lab	Collaborators	Responsible Person	Major Objectives	Materials	Temperature °C	Dose (dpa) or fluence	Irrad. Start	Irrad. Finish	Status
HFIR-TRIST-ER1	ORNL	MONBUSHO/ JAERI	S.J. Zinkle	In-situ electrical conductivity	Al2O3	450	3E+25 n/m2	Apr-96	Jun-96	
HFIR-MFE-RB-10J	ORNL	JAERI	J.E. Pawel	Tensile, fracture	Vanadium, 316LN-1G, J316	200, 500	5	Feb-98	Feb-99	
HFIR-MFE-RB-11J	ORNL	MONBUSHO/ JAERI	M. L. Grossbeck	Tensile, fracture, TEM	Low activation ferritics, V alloys, SiC	300	5	Feb-97	Feb-98	
HFIR-MFE-RB-12J	ORNL	MONBUSHO/ JAERI	M. L. Grossbeck	Tensile, fracture, TEM	Low activation ferritics, V alloys, SiC	500	5	Feb-97	Feb-98	
HFIR-CTR-62	ORNL	JAERI	R.L. Klueh	Charpy impact and He effects	Reduced act. and conventional ferritic steels	300, 400	13	Apr-95	Dec-95	
HFIR-CTR-63	ORNL	JAERI	R.L. Klueh	Charpy impact and tensile, TEM, He effects	Reduced act. and conventional ferritic steels	300, 400	13	Apr-95	Dec-95	
HFIR-JP25	ORNL	JAERI	R.L. Klueh	Tensile, fracture, TEM	Low activation ferritics	300, 500	20	Apr-98	Jun-99	
HFIR-JP27	ORNL	JAERI	L.L. Snead	Fracture, TEM	Intermetallics, SiC	500-800	10	Apr-98	Jul-98	
HFIR-JP28	ORNL	JAERI	L.L. Snead	Fracture, TEM	SiC	500-800	10	Mar-98	Sep-98	
HFIR-P3-6	ORNL	MONBUSHO	A. L. Qualls	Varying Temperature	TOS	400-600	5	Feb-98	Feb-99	
High Flux Beam Reactor, Brookhaven National Laboratory										
HFBR-ISEC-3	ORNL		L.L. Snead	In-situ electrical	WESGO Al2O3	450	1.5	Jul-95	Sep-95	
HFBR-V1	ORNL		L.L. Snead	Tensile, fracture	V-4Cr-4Ti	75, 150, 225	0.4	May-95	Jun-95	
HFBR-V2	ORNL		L.L. Snead	Tensile, fracture	V-4Cr-4Ti	75, 225, 300, 375	0.4	Jul-95	Aug-95	
HFBR-V3	ORNL		L.L. Snead	Tensile, fracture	V-4Cr-4Ti	160, 265, 315, 420	0.4	Aug-96	Sep-96	
HFBR-V4	ORNL		L.L. Snead	Tensile, fracture	V-4Cr-4Ti	105-505	0.1	Aug-96	Sep-96	
Advanced Test Reactor, Idaho Falls										
ATR-A1	ANL	MONBUSHO	D.L. Smith	Tensile, fracture toughness, TEM, creep	Vanadium alloys	200, 300	5	Dec-95	May-96	

Summary of Reactor Irradiation Experiments

Experiment	Lead Lab	Collaborators	Responsible Person	Major Objectives	Materials	Temperature °C	Dose (dpa) or fluence	Irrad. Start	Irrad. Finish	Status
BOR-60 Reactor, RIAR, Dimitrovgrad, Russia										
BOR-60-Fusion-1	ORNL, ANL	RDIPE, RIAR	A.F. Rowcliffe, D.L. Smith	Mechanical and microstructural properties	V alloys	350-380	10	Jul-95	Mar-96	
SM-2 Reactor, RIAR, Dimitrovgrad, Russia										
SM-2.1	ORNL, PNL	RIAR	S.J. Zinkle	Tensile, electrical, microstructural, and creep properties	Cu alloys	100, 200, 330	1, 5	Dec-93	Feb-94	
SM-2.2	PNL	SRIAR	D.J. Edwards	Mechanical behavior of bonded materials	Cu alloys/SS, Cu/Be	120, 300	0.2	Mar-96	May-96	
SM-2.3	PNL	SRIAR	D.J. Edwards	Mechanical behavior of bonded materials	Cu alloys/SS, Cu/Be	100, 250	0.2	Jul-97	Dec-97	
	Irradiation complete									
	Irradiation in progress									
	Irradiation planned									

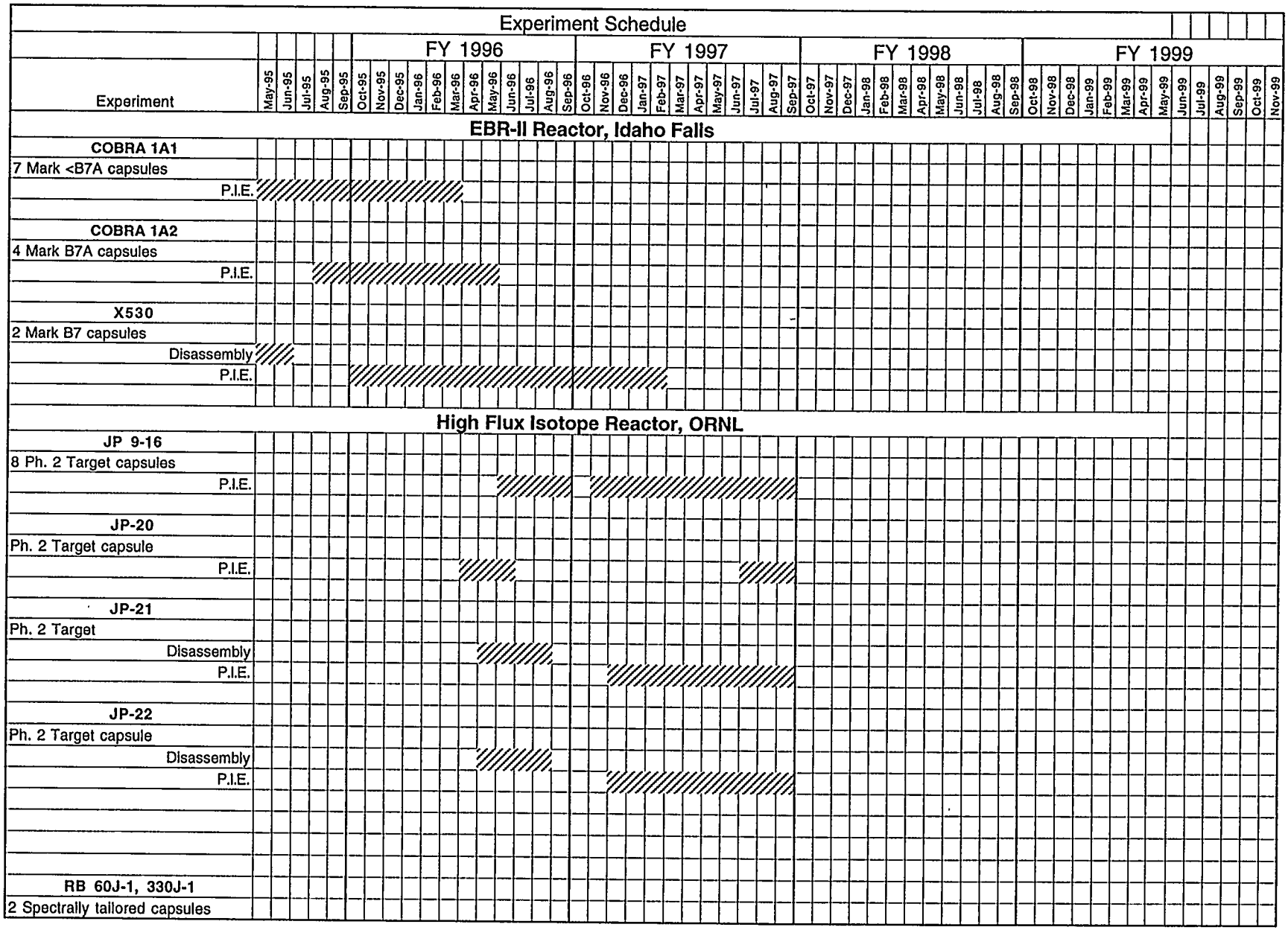
Experiment Schedule
FY 1996
FY 1997
FY 1998
FY 1999
Experiment
May-95 Jun-95 Jul-95 Aug-95 Sep-95 Oct-95 Nov-95 Dec-95 Jan-96 Feb-96 Mar-96 Apr-96 May-96 Jun-96 Jul-96 Aug-96 Sep-96 Oct-96 Nov-96 Dec-96 Jan-97 Feb-97 Mar-97 Apr-97 May-97 Jun-97 Jul-97 Aug-97 Sep-97 Oct-97 Nov-97 Dec-97 Jan-98 Feb-98 Mar-98 Apr-98 May-98 Jun-98 Jul-98 Aug-98 Sep-98 Oct-98 Nov-98 Dec-98 Jan-99 Feb-99 Mar-99 Apr-99 May-99 Jun-99 Jul-99 Aug-99 Sep-99 Oct-99 Nov-99
EBR-II Reactor, Idaho Falls
COBRA 1A1
7 Mark <B7A capsules
P.I.E.
COBRA 1A2
4 Mark B7A capsules
P.I.E.
X530
2 Mark B7 capsules
Disassembly
P.I.E.
High Flux Isotope Reactor, ORNL
JP 9-16
8 Ph. 2 Target capsules
P.I.E.
JP-20
Ph. 2 Target capsule
P.I.E.
JP-21
Ph. 2 Target
Disassembly
P.I.E.
JP-22
Ph. 2 Target capsule
Disassembly
P.I.E.
RB 60J-1, 330J-1
2 Spectrally tailored capsules

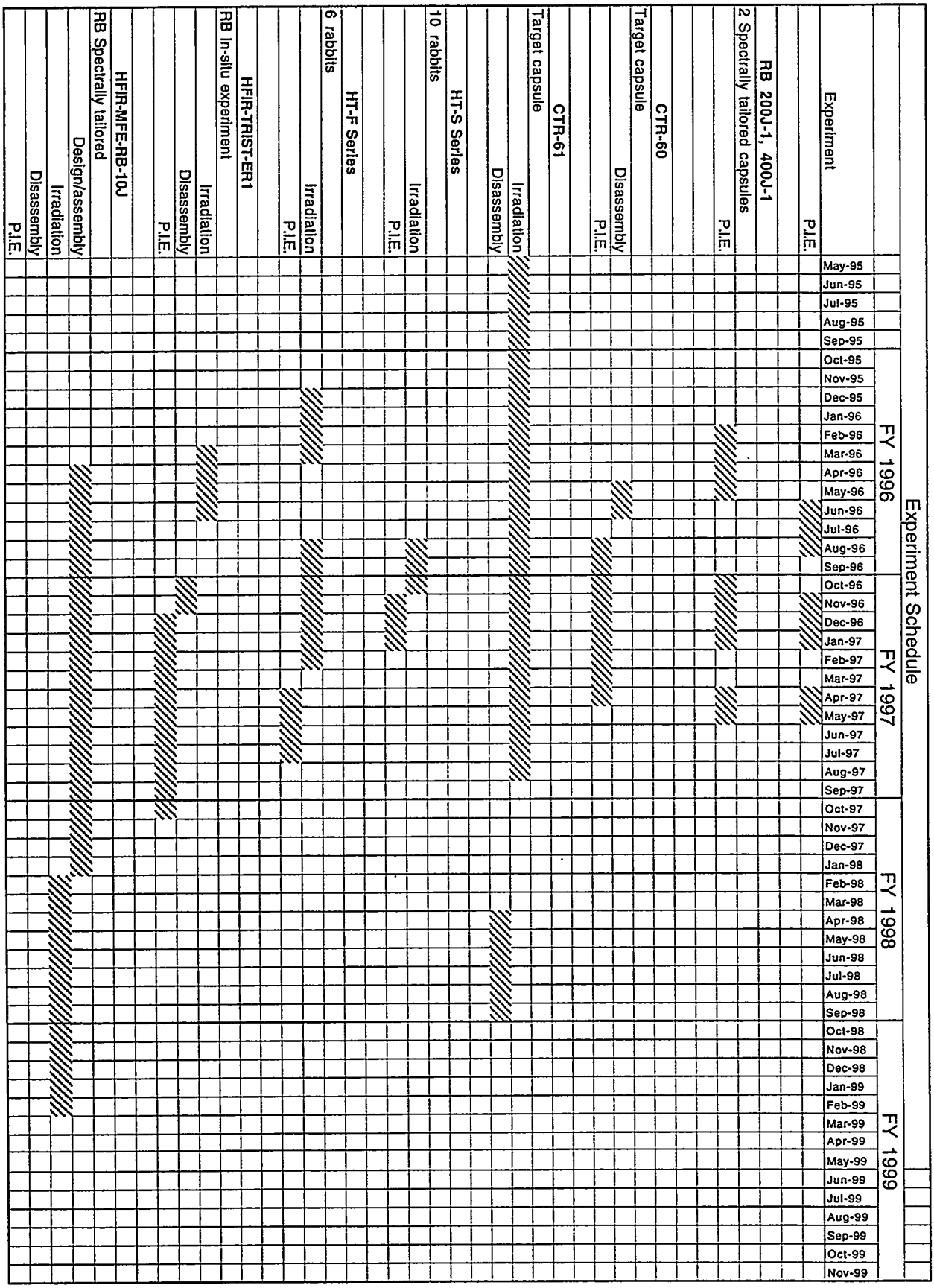
Experiment Schedule
FY 1996
FY 1997
FY 1998
FY 1999
Experiment
P.I.E.
RB 200J-1, 400J-1
2 Spectrally tailored capsules
P.I.E.
CTR-60
Target capsule
Disassembly
P.I.E.
CTR-61
Target capsule
Irradiation
Disassembly
HT-S Series
10 rabbits
Irradiation
P.I.E.
HT-F Series
6 rabbits
Irradiation
P.I.E.
HFIR-TRIST-ER1
RB In-situ experiment
Irradiation
Disassembly
P.I.E.
HFIR-MFE-RB-10J
RB Spectrally tailored
Design/assembly
Irradiation
Disassembly
P.I.E.
May-95
Jun-95
Jul-95
Aug-95
Sep-95
Oct-95
Nov-95
Dec-95
Jan-96
Feb-96
Mar-96
Apr-96
May-96
Jun-96
Jul-96
Aug-96
Sep-96
Oct-96
Nov-96
Dec-96
Jan-97
Feb-97
Mar-97
Apr-97
May-97
Jun-97
Jul-97
Aug-97
Sep-97
Oct-97
Nov-97
Dec-97
Jan-98
Feb-98
Mar-98
Apr-98
May-98
Jun-98
Jul-98
Aug-98
Sep-98
Oct-98
Nov-98
Dec-98
Jan-99
Feb-99
Mar-99
Apr-99
May-99
Jun-99
Jul-99
Aug-99
Sep-99
Oct-99
Nov-99

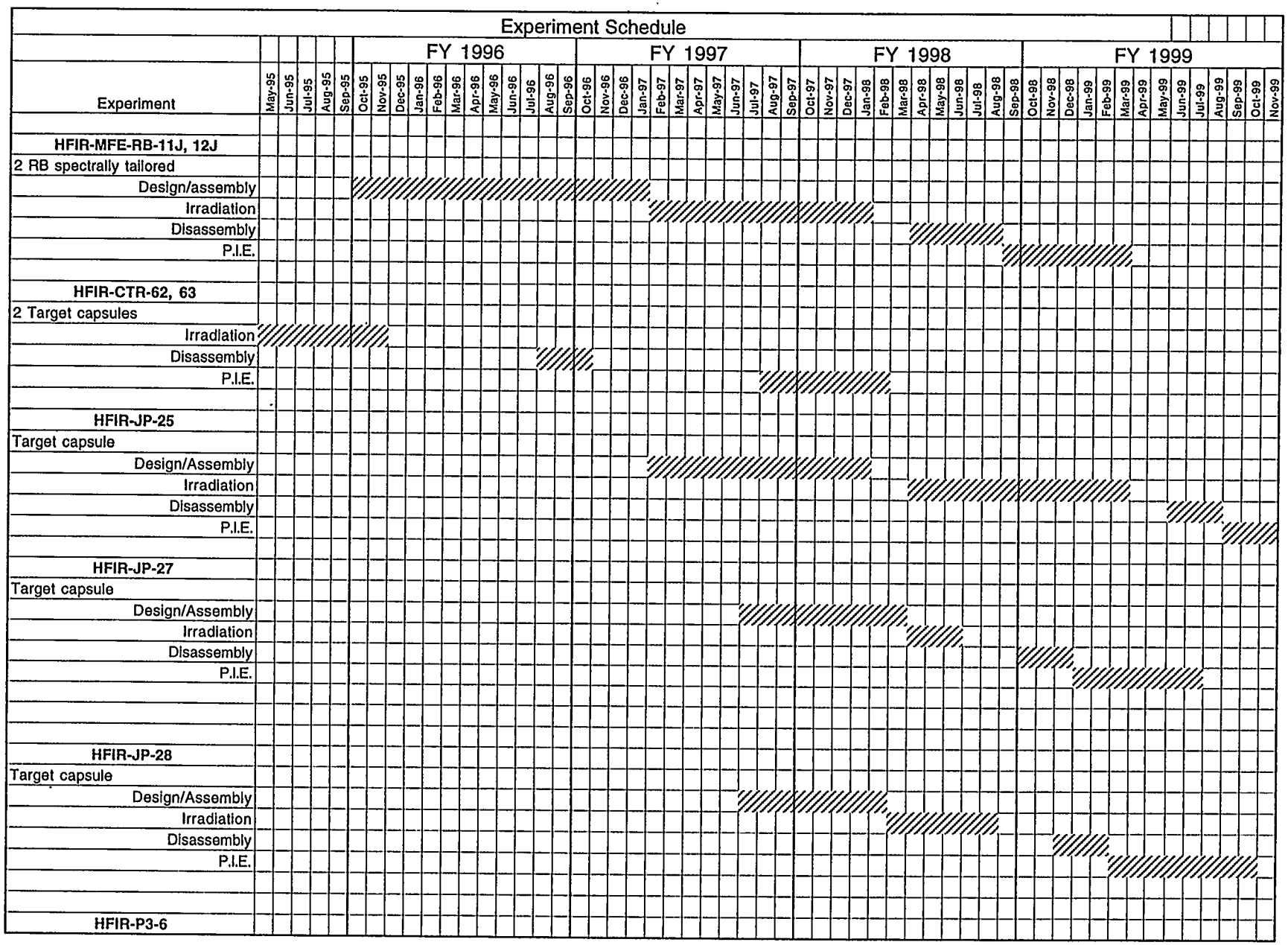
Experiment Schedule
FY 1996
FY 1997
FY 1998
FY 1999
Experiment
May-95
Jun-95
Jul-95
Aug-95
Sep-95
Oct-95
Nov-95
Dec-95
Jan-96
Feb-96
Mar-96
Apr-96
May-96
Jun-96
Jul-96
Aug-96
Sep-96
Oct-96
Nov-96
Dec-96
Jan-97
Feb-97
Mar-97
Apr-97
May-97
Jun-97
Jul-97
Aug-97
Sep-97
Oct-97
Nov-97
Dec-97
Jan-98
Feb-98
Mar-98
Apr-98
May-98
Jun-98
Jul-98
Aug-98
Sep-98
Oct-98
Nov-98
Dec-98
Jan-99
Feb-99
Mar-99
Apr-99
May-99
Jun-99
Jul-99
Aug-99
Sep-99
Oct-99
Nov-99
HFIR-MFE-RB-11J, 12J
2 RB spectrally tailored
Design/assembly
Irradiation
Disassembly
P.I.E.
HFIR-CTR-62, 63
2 Target capsules
Irradiation
Disassembly
P.I.E.
HFIR-JP-25
Target capsule
Design/Assembly
Irradiation
Disassembly
P.I.E.
HFIR-JP-27
Target capsule
Design/Assembly
Irradiation
Disassembly
P.I.E.
HFIR-JP-28
Target capsule
Design/Assembly
Irradiation
Disassembly
P.I.E.
HFIR-P3-6

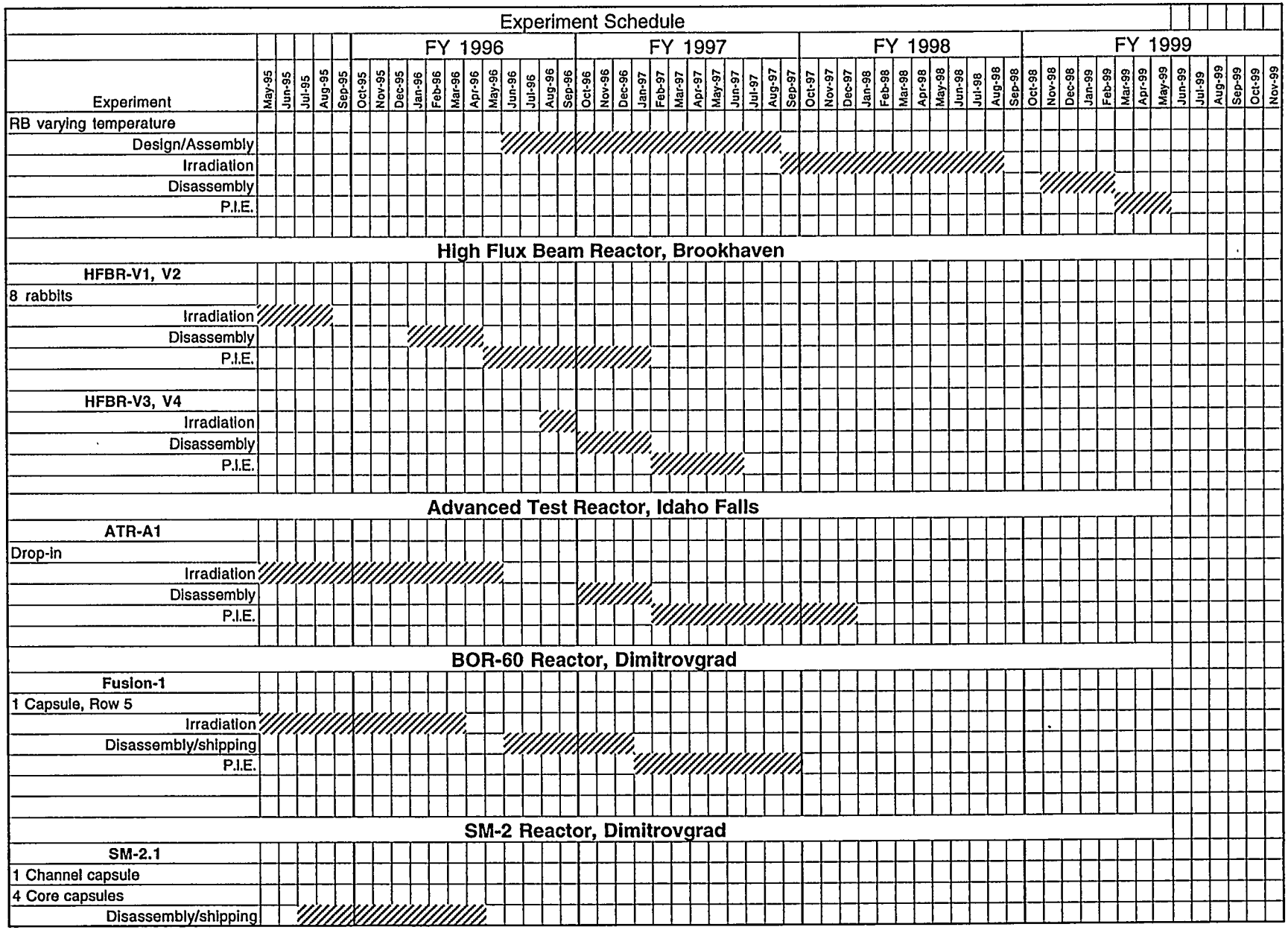
Experiment Schedule
FY 1996
FY 1997
FY 1998
FY 1999
Experiment
May-95 Jun-95 Jul-95 Aug-95 Sep-95 Oct-95 Nov-95 Dec-95 Jan-96 Feb-96 Mar-96 Apr-96 May-96 Jun-96 Jul-96 Aug-96 Sep-96 Oct-96 Nov-96 Dec-96 Jan-97 Feb-97 Mar-97 Apr-97 May-97 Jun-97 Jul-97 Aug-97 Sep-97 Oct-97 Nov-97 Dec-97 Jan-98 Feb-98 Mar-98 Apr-98 May-98 Jun-98 Jul-98 Aug-98 Sep-98 Oct-98 Nov-98 Dec-98 Jan-99 Feb-99 Mar-99 Apr-99 May-99 Jun-99 Jul-99 Aug-99 Sep-99 Oct-99 Nov-99
RB varying temperature
Design/Assembly
Irradiation
Disassembly
P.I.E.
High Flux Beam Reactor, Brookhaven
HFBR-V1, V2
8 rabbits
Irradiation
Disassembly
P.I.E.
HFBR-V3, V4
Irradiation
Disassembly
P.I.E.
Advanced Test Reactor, Idaho Falls
ATR-A1
Drop-in
Irradiation
Disassembly
P.I.E.
BOR-60 Reactor, Dimitrovgrad
Fusion-1
1 Capsule, Row 5
Irradiation
Disassembly/shipping
P.I.E.
SM-2 Reactor, Dimitrovgrad
SM-2.1
1 Channel capsule
4 Core capsules
Disassembly/shipping

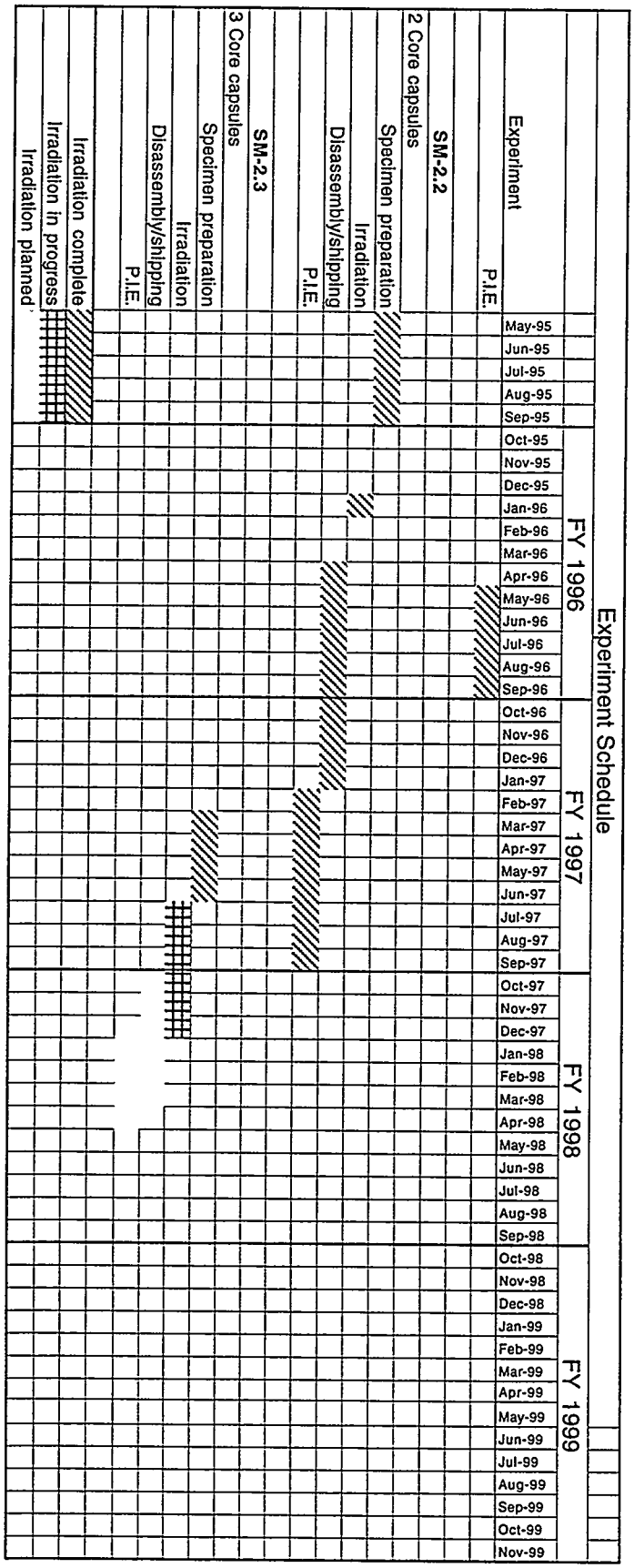
Experiment Schedule
Experiment
P.I.E.
SM-2.2
2 Core capsules
Specimen preparation
Irradiation
Disassembly/shipping
P.I.E.
SM-2.3
3 Core capsules
Specimen preparation
Irradiation
Disassembly/shipping
P.I.E.
Irradiation complete
Irradiation in progress
Irradiation planned
FY 1996
FY 1997
FY 1998
FY 1999
May-95
Jun-95
Jul-95
Aug-95
Sep-95
Oct-95
Nov-95
Dec-95
Jan-96
Feb-96
Mar-96
Apr-96
May-96
Jun-96
Jul-96
Aug-96
Sep-96
Oct-96
Nov-96
Dec-96
Jan-97
Feb-97
Mar-97
Apr-97
May-97
Jun-97
Jul-97
Aug-97
Sep-97
Oct-97
Nov-97
Dec-97
Jan-98
Feb-98
Mar-98
Apr-98
May-98
Jun-98
Jul-98
Aug-98
Sep-98
Oct-98
Nov-98
Dec-98
Jan-99
Feb-99
Mar-99
Apr-99
May-99
Jun-99
Jul-99
Aug-99
Sep-99
Oct-99
Nov-99

Distribution

1-16. Argonne National Laboratory, 9700 South Cass Avenue, Argonne, IL 60439

M. C. Billone	C. E. Johnson	J. H. Park
O. K. Chopra	F. Kassner	D. L. Smith
H. M. Chung	J. P. Kopasz	W. Tam
D. R. Diercks	R. F. Mattas	H. C. Tsai
J. Gazda	K. Nateson	
A. B. Hull	L. A. Niemark	

17-18. Argonne National Laboratory, EBR-II Division, P.O. Box 2528, Idaho Falls, ID 83403-2528

H. P. Planchon D. L. Porter

19. Auburn University, Department of Mechanical Engineering, 201 Ross Hall, Auburn, AL 36849

B. A. Chin

20-32. Pacific Northwest National Laboratory, P.O. Box 999, Richland, WA 99352

D. J. Edwards	L. R. Greenwood	G. W. Hollenberg
F. A. Garner (5)	M. L. Hamilton	R. H. Jones
D. S. Gelles	H. L. Heinisch	J. Youngblood

33. Carnegie Institute of Technology, Carnegie-Mellon University, Schenley Park, Pittsburgh, PA 15213

W. M. Garrison, Jr.

34. Commissariat à l'Energie Atomique, Direction des Technologies Advancées, M2R1/DECM Cen-Saclay, Gif Sur Yvette, Cedex, France

F. Tavassoli

35-37. General Atomics, P.O. Box 85608, San Diego, CA 92138

W. R. Johnson K. R. Schultz C. Wong

38. Georgia Institute of Technology, Fusion Research Center, 0225, Atlanta, GA 30332

W. M. Stacey

39. Grand Canyon University, Department of Natural Science, 3300 W. Camelback Rd., Phoenix, AZ 85017

W. A. Coghlan

40-42. Idaho National Engineering Laboratory, Fusion Safety Program, P.O. Box 1625, Idaho Falls, ID 83415-3523

G. Longhurst K. McCarthy D. Petti

43. Knolls Atomic Power Laboratory, P.O. Box 1072, Schenectady, NY 12301

G. Newsome

44-45. Lawrence Livermore National Laboratory, P.O. Box 808, Livermore, CA 94550

E.C.N. Dalder J. Perkins

46-52. Los Alamos National Laboratory, Los Alamos, NM 87545

J. L. Anderson	E. H. Farnum	W. F. Sommer
R. G. Castro	R. E. Siemon	K. E. Sickafus
D. W. Cooke		

53-55. Massachusetts Institute of Technology, Department of Metallurgy and Materials Science, Cambridge, MA 02139
L. W. Hobbs N. J. Grant K. C. Russell

56. Massachusette Institute of Technology, Plasma Fusion Center Headquarters, Cambridge, MA 02139
D. B. Montgomery

57-58. McDonnell-Douglas Corporation, Mail Code 1067220, P.O. Box 516, St. Louis, MO 63166-0516
J. W. Davis G. W. Wille

59. MER Corp., 7960 South Kolb Rd., Tucson, AZ 85706
W. Kowbel

60. Merrimack College, Dept. of Physics, 315 Turnpike Street, North Andover, MA 01845
D. P. White

61. M. J. Schiff & Associates, 1291 N. Indian Hill Blvd., Claremont, CA 91711-3897
G.E.C. Bell

62. NASA Lewis Research Center, MS-106-5, Cleveland, OH 44135
G. Morscher

63-65. National Institute of Standards and Technology, Boulder, CO 80302
F. R. Fickett H. I. McHenry R. P. Reed

66-67. Naval Research Laboratory, Code 6506, Washington, DC 20375
D. L. Gibson J. A. Sprague

68-111. Oak Ridge National Laboratory, P.O. Box 2008, Oak Ridge, TN 37831

Central Research Library	M. L. Grossbeck	A. F. Rowcliffe (10)
Document Reference Section	N. Hashimoto	M. J. Saltmarsh
Laboratory Records Department (2)	J. F. King	J. Sheffield
Laboratory Records-RC	E. A. Kenik	L. L. Snead
Patent Section	R. L. Klueh	R. E. Stoller
D. J. Alexander	E. H. Lee	K. R. Thoms
J. Bentley	L. K. Mansur	P. F. Tortorelli
E. E. Bloom	P. J. Maziasz	R. L. Wallace
T. D. Burchell	L. Qualls	E. Wakai
S. D. Connery	P. M. Rice	S. J. Zinkle
G. M. Goodwin	J. P. Robertson	
R. H. Goulding	T. C. Reuther	

112. Oregon Graduate Institute, Dept. of Materials Science & Engineering, 19600 N.W. Von Neumann Drive, Beaverton, OR 97006
J. M. McCarthy

113-115. Princeton University, Princeton Plasma Physics Laboratory, P.O. Box 451, Princeton, NJ 08540
R. C. Davidson Long-Poe Ku D. M. Meade

116-117. Rensselaer Polytechnic Institute, Troy, NY 12181
D. Duquette D. Steiner

118. Rockwell International Corporation, NA02, Rocketdyne Division, 6633 Canoga Avenue,Canoga Park, CA 91304
D. W. Kneff

119-121. Sandia National Laboratories, Fusion Technology Dept., Dept. No 6531, P.O. Box 5800, Albuquerque, NM 87185-5800
M. J. Davis M. Ulrickson R. D. Watson

122-124. Sandia National Laboratories, Livermore Division 8316, Livermore, CA 94550
W. Bauer K. Wilson W. G. Wolfer

125. San Diego State University, Mechanical Engineering Dept., San Diego, CA 92182-0191
L. D. Thompson

126. Texas A&M University, Box 397, Prairie View, TX 77446
D. Baker

127. TSI Research, 225 Stevens Ave., #110, Solana Beach, CA 92075
E. T. Cheng

128-129. University of California at San Diego, U.S. ITER Project Office, 9500 Gilman Drive, Bldg. 302, La Jolla, CA 92093-0035
C. C. Baker T. R. James

130-131. University of California, Dept. of Mechanical and Environmental Engineering, Engineering II, Room 2355, Santa Barbara, CA 93106-5070
G. E. Lucas G. R. Odette

132-134. University of California, Dept. of Chemical, Nuclear, and Thermal Engineering, Los Angeles, CA 90024
M. A. Abdou N. M. Ghoniem S. Sharafat

135. University of Illinois, Dept. of Nuclear Engineering, Urbana, IL 61801
J. Stubbins

136. University of Michigan, Dept. of Nuclear Engineering, Ann Arbor, MI 48109
T. Kammash

137. University of Missouri, Department of Nuclear Engineering, Rolla, MO 65401
A. Kumar

138-139. University of Tennessee, Dept. of Materials Science and Engineering, 427-B Dougherty Bldg., Knoxville, TN 37996-2200
P. K. Liaw C. J. McHargue

140-141. University of Wisconsin, Nuclear Engineering Dept., 1500 Johnson Drive, Madison, WI 53706
J. B. Blanchard G. L. Kulcinski

142-144. Hokkaido University, Faculty of Engineering, Kita 13, Nishi 8, Kita-ku, Sapporo 060, Japan
Heischichiro Takahashi Somei Ohnuki Akira Okada

145-146. Japan Atomic Energy Research Institute, Tokai Research Establishment, Tokai-mura, Naka-gun, Ibaraki-ken 319-11, Japan
Akimichi Hishinuma K. Noda

147-148. Kyoto University, Institute of Advanced Energy, Gokasho, Uji, Kyoto 611, Japan
Yutai Katoh — Akira Kohyama

149. Kyushu University, Dept. of Nuclear Engineering, Faculty of Engineering, Kyushu University 36, Hakozaki, Fukuoka 812, Japan
C. Kinoshita

150. Kyushu University, Research Institute for Applied Mechanics, Kasuga, Fukuoka 816, Japan
Naoaki Yoshida

151-152. Muroran Institute of Technology, Dept. of Metallurgical Engineering, 27-1 Mizumoto-cho, Mororan 050, Japan
Toshihei Misawa — Akihiko Kimura

153-154. Nagoya University, Dept. of Nuclear Engineering, Furo-Cho, Chikusa-ku, Nagoya 464-01, Japan
Michio Kiritani — Tetuo Tanabe

155-158. National Institute for Fusion Science, Furo-cho, Chikusa-ku, Nagoya 464-01, Japan
Osamu Motojima — Chusei Namba
Takeo Muroga — Nobuaki Noda

159-162. National Research Institute for Metals, Tsukuba Branch, Sengen, Tsukuba-shi, Ibaraki-ken, 305, Japan
Fujio Abe — Tetsuji Noda
Josei Nagakawa — Haruki Shiraishi

163. PNC Oarai, 4002 Narita, Oarai, Ibaraki 311-13, Japan
Itaru Shibahari

164. Science University of Tokyo, Dept. of Materials Science & Technology, 2641 Yamazaki, Noda City, Chiba Prefecture 278, Japan
Naohira Igata

165. Teikyo University, Otsuka, Hachioji, Tokyo 192-03, Japan
Akira Miyahara

166. Tohoku University, Institute for Materials Research, Katahira 2-2-1, Sendai 980-77, Japan
Hideki Matsui

167-170. Tohoku University, Institute for Materials Research, Oarai Branch, Oarai, Ibaraki 311-13, Japan
Hideo Kayono — Tamaki Shibayama
Hiroaki Kurishita — Tatsuo Shikama

171-172. Tohoku University, Dept. of Nuclear Engineering, Aoba, Aramaki, Sendai 980-77, Japan
Katsunori Abe — Akira Hasegawa

173. Tohoku University, Dept. of Machine Intelligence and Systems Engineering, Aramaki, Aoba-ku, Sendai 980-77, Japan
Tatsuo Kondo

174. Tokai University, Dept. of Nuclear Engineering, 1117 Kitakaname, Hiratsuka-shi, Kanagawa-ken 259-12, Japan
Shiori Ishino

175. University of Tokyo, Dept. of Nuclear Engineering, 3-1, Hongo 7-Chome, Bunkyo-Ku, Tokyo 113, Japan
Naoto Sekimura

176. University of Tokyo, Dept. of Materials Science, 3-1, Hongo 7-Chome, Bunkyo-ku, Tokyo 113, Japan
Yutaka Kohno

177. Commission of European Communities, Directorate-General for Research Science and Education, Fusion Programme RUE De La Loi 200, B-1049 Brussels, Belgium
F. Cozzani

178-179. Chalk River Nuclear Laboratories, Atomic Energy of Canada, Ltd., Chalk River, Ontario KOJ 1J0, Canada
I. J. Hastings D. P. Jackson

180-181. Southwestern Institute of Physics, P.O. Box 432, Chenedu 610041, Sichuan, P.R. China
J. P. Qian Zeng Yu Xu

182. Institute of Atomic Energy, Academia Sinica, P.O. Box 275-51, Beijing, P.R. China
J. Yu

183. Riso National Laboratory, Materials Dept., P.O. Box 49, DK-4000, Roskilde, Denmark
B. N. Singh

184. Centre d'Etudes Nucleaires, Saclay, DLPC/SMCM, Commissariat a l'Energie Atomique, 91191 Gif-Sur-Yvette, Cedex, France
N. Roux

185. Commission for European Communities, Joint Research Centre, I.A.M. Ispra Establishment, 21020 Ispra (Varese), Italy
P. Fenici

186. EURATOM/CIEMAT Fusion Association, Avenida Complutense 22, 28040, Madrid, Spain
E. R. Hodgson

187. Paul Scherrer Institute, CH-5232 Villigen, Wuerenlingen PSI, Switzerland
M. Victoria

188. Harwell Laboratory, B393, Radiation Damage Dept., Oxfordshire, OX11 ORA, United Kingdom
C. A. English

189. Metallurgical and Nuclear Consultant, 9A Cumnor Rise Road, Cumnor Hill, Oxford OX2 9HD,
United Kingdom
D. R. Harries

190. Hahn-Mietner-Institut fur Kernforschung Berlin, Postfach 390128, Glienicker Str. 100, D-14109, Germany
H. Wollenberger

191. Institut fur Festkorperforschung Forschungszentrum Jülich, Postfach 1913, D-52425 Jülich, Germany
H. Ullmaier

192-195. ITER Garching Joint Work Site, Max-Planck-Institute für Plasmaphysik, Boltzmannstrasse 2, D-85748 Garching bei München, Germany
B. Barabash G. Kalinin
Y. Gohar R. Parker

196-197. ITER Naka Joint Work Site, 801-1 Mukouyama, Naka-machi, Naka-gun, Ibaraki-Ken, 311-01, Japan
M. Huguet (2)

198-201. ITER San Diego Joint Work Site, 11025 N. Torrey Pines Road, La Jolla, CA 92037
V. Chuyanov F. Puhn
S. J. Piet P. Smith

202-203. Kernforschungszentrum Karlsruhe, Postfach 3640, 75 Karlsruhe 1, Germany
M. Dalle-Donne (INR) K. Ehrlich (IMF-II)

204. Max-Planck-Institut für Plasmaphysik, Boltzmannstrasse 2, D-85748 Garching bei München, Germany
Patrick Lorenzetto

205. A. A. Baikov Institute of Metallurgy, USSR Academy of Sciences, Leninsky Prospect 49, Moscow, Russia
L. I. Ivanov

206. CRISM "Prometey," Naberezhnava r. Monastyrick 1, 193167, St. Petersburg, Russia
V. V. Rybin

207. D. V. Efremov Institute of Electro-Physical Apparatus, 189631, St. Petersburg, Russia
S. A. Fabritsiev

208. Kharkov Institute of Physics & Technology, Radiation Damage and Materials Dept., Akademicheskaya 1, 310108 Kharkov, Ukraine
I. M. Neckludov

209-211. V. I. Lenin Research Institute of Atomic Reactors, 433510 Dimitrovgrad-10, Ulyanovsk Region, Russia
V. Kazakov A. S. Pokrovsky V. K. Shamardin

212. Korea Advanced Institute of Science and Technology, Department of Nuclear Engineering, DaeDukDanji, Taejon, 305-701, Korea
I-S. Kim

213-214. Korean Atomic Energy Research Institute, P.O. Box 105, Yusung, Taejon, 305-600, Korea
Thak-Sang Byun Jun Hwa Hong

215. Seoul National University, Dept. of Nuclear Engineering, 56-1 Shinrim-Dong, Kwanak-Ku Seoul, 151-742, Korea
K. H. Chung

216. Sung Kyun Kwan University, Dept. of Metallurgical Engineering, 300 Chunchun-dong, Jangan-gu, Suwon, 440-746, Korea
J. G. Han

217. Department of Energy, DOE Oak Ridge Field Office, P.O. Box 2008, Oak Ridge, TN 37831-6269
Assistant Manager for Energy Research and Development

218. Department of Energy, DOE Oak Ridge Field Office, P.O. Box 2008, Oak Ridge, TN 37831-6269
S. D. Frey

219. Department of Energy, Office of Basic Energy Sciences, Washington, D.C. 20585
R. J. Gottschall

220-225. Department of Energy, Office of Fusion Energy, Germantown, MD 20874

S. E. Berk	W. F. Dove	W. Marton
N. A. Davies	R. McKnight	F. W. Wiffen

226. Department of Energy, Richland Operations Office, P.O. Box 550, MS-K850, Richland, WA 99352
J. Turner

227-228. Department of Energy, Office of Scientific and Technical Information, Office of Information Services, P.O. Box 62, Oak Ridge, TN 37831
For distribution by microfiche as shown in DOE/OSTI-4500-R75, Distribution Categories UC-423 (Magnetic Fusion Reactor Materials) and UC-424 (Magnetic Fusion Energy Systems)